

**Document  
for  
ND280 review**

# Contents

<b>1</b>	<b>Physics Overview with the ND280 detector</b>	<b>8</b>
1.1	Introduction . . . . .	8
1.1.1	ND280 overview . . . . .	8
1.1.2	Physics goal of T2K . . . . .	10
1.1.3	Requirements of the ND280 detector . . . . .	15
1.2	$\nu_\mu$ flux and spectrum measurement . . . . .	16
1.2.1	Beam direction and stability monitoring by INGrid . . . . .	16
1.2.2	CCQE selection in the tracker . . . . .	16
1.2.3	Detection efficiency of CCQE . . . . .	17
1.2.4	Near to far extrapolation of the $\nu_\mu$ flux . . . . .	19
1.3	$\nu_e$ flux and spectrum measurement . . . . .	22
1.4	Neutrino cross section studies . . . . .	23
1.4.1	Single pion productions . . . . .	23
1.4.2	CC-1pi for $\nu_\mu$ disappearance measurement . . . . .	26
1.4.3	NC $\pi^+$ for $\nu_\mu$ disappearance measurement . . . . .	28
1.4.4	NC $\pi^0$ for $\nu_e$ appearance search . . . . .	28
1.4.5	Other cross section measurements . . . . .	29
<b>2</b>	<b>Neutrino Beam Monitor: INGRID Detector</b>	<b>30</b>
2.1	Introduction . . . . .	30
2.2	Detector overview and specification . . . . .	32
2.3	Expected Performance . . . . .	34
2.3.1	Basic Beam Property . . . . .	34
2.3.2	Event Selection . . . . .	34
2.3.3	Sensitivity to the beam direction . . . . .	36
2.3.4	Systematic Uncertainty . . . . .	38
2.3.5	Background Issues . . . . .	39
2.4	Electronics and DAQ . . . . .	41
2.5	Mechanical structure . . . . .	42
2.5.1	Preliminary design . . . . .	42
2.5.2	Structural analysis . . . . .	45
2.5.3	Manufacturing plan . . . . .	47
2.6	Detector technology R&D . . . . .	49
2.6.1	Test of the prototype INGRID module at the K2K neutrino beam. . . . .	50
2.7	Calibration systems . . . . .	52
2.8	Construction and installation schedule . . . . .	52
<b>3</b>	<b>The magnet</b>	<b>55</b>
3.1	Description . . . . .	55
3.2	Installation . . . . .	57

<b>4</b>	<b>FGD</b>	<b>59</b>
4.1	Introduction . . . . .	59
4.1.1	Overview . . . . .	59
4.1.2	Physics requirements . . . . .	59
4.1.3	About this document . . . . .	62
4.2	Detector design and specification . . . . .	62
4.2.1	Mechanical design overview . . . . .	62
4.2.2	Scintillator bars . . . . .	64
4.2.3	Wavelength-shifting fibers . . . . .	65
4.2.4	Photosensors . . . . .	66
4.2.5	Electronics . . . . .	67
4.2.6	Target water modules . . . . .	69
4.3	Detector technology R&D . . . . .	71
4.4	Detector construction schedule . . . . .	73
4.4.1	Schedule . . . . .	73
4.4.2	Quality control . . . . .	74
4.5	Detector installation & commissioning . . . . .	75
4.5.1	FGD services . . . . .	75
4.5.2	FGD Transportation . . . . .	75
4.5.3	Reception at ND280 . . . . .	75
4.5.4	FGD Installation . . . . .	76
4.5.5	ND280 Service Routing . . . . .	76
4.6	Detector calibration . . . . .	77
4.6.1	Calibration of mechanical aspects . . . . .	77
4.6.2	Electronics calibration . . . . .	77
4.6.3	Photosensor calibration . . . . .	77
4.6.4	Scintillator/fiber calibration . . . . .	77
4.6.5	Physics calibration . . . . .	77
4.7	Physics Performance . . . . .	78
4.7.1	Hit finding efficiency . . . . .	78
4.7.2	Pion rejection in FGD using Michel electron . . . . .	81
4.7.3	Statistical accuracy of interaction rate measurements . . . . .	85
<b>5</b>	<b>TPC(Time Projection Chambers)</b>	<b>87</b>
5.1	Overview . . . . .	87
5.1.1	Key Roles for the Tracker . . . . .	87
5.1.2	Key measurements by the TPCs . . . . .	88
5.1.3	Basic Design Considerations for the ND280 TPCs . . . . .	89
5.2	TPC mechanical . . . . .	90
5.2.1	Overview of Mechanical Design . . . . .	90
5.2.2	Inner Box/Field Cage . . . . .	91
5.2.3	Outer Box . . . . .	95
5.2.4	Service Spacers and Covers . . . . .	96
5.2.5	Assembly and Testing . . . . .	96
5.2.6	Analysis of the Electric Field . . . . .	99
5.3	Gas system . . . . .	105
5.3.1	Gas choice . . . . .	105
5.3.2	Gas handling system . . . . .	106
5.3.3	Monitors . . . . .	111
5.3.4	Safety . . . . .	112
5.4	Micromegas modules . . . . .	114

5.4.1	The T2K TPC Micromegas Module . . . . .	114
5.4.2	Micromegas Module production and Assembly . . . . .	117
5.4.3	Micromegas Modules Calibration . . . . .	121
5.5	Micromegas mechanical . . . . .	125
5.5.1	Introduction . . . . .	125
5.5.2	Mechanical Description . . . . .	125
5.5.3	Interfaces Description . . . . .	126
5.5.4	Services . . . . .	126
5.5.5	Module Construction . . . . .	128
5.6	Readout electronics . . . . .	128
5.6.1	Summary of requirements and constraints . . . . .	128
5.6.2	Outline of the architecture . . . . .	129
5.6.3	Detailed description of main components . . . . .	129
5.7	Integration . . . . .	139
5.7.1	TPC Services . . . . .	140
5.7.2	TPC Transportation . . . . .	140
5.7.3	ND280 Service routing . . . . .	142
5.8	Offline software . . . . .	142
5.8.1	Monte Carlo simulation . . . . .	143
5.8.2	Data model . . . . .	144
5.8.3	Reconstruction . . . . .	145
5.8.4	Particle Identification . . . . .	151
5.8.5	Data Base . . . . .	151
5.9	Calibration . . . . .	152
5.9.1	Overview . . . . .	152
5.9.2	Calibration methods . . . . .	153
5.9.3	Calibration procedure . . . . .	154
5.10	Prototype results . . . . .	158
5.10.1	Prototype field cage with GEM readout . . . . .	158
5.10.2	Prototype Micromegas and GEM studies with HARP field cage . . . . .	163
5.11	TPC performance . . . . .	169
5.11.1	Simulation and reconstruction . . . . .	169
5.11.2	TPC tracking capability . . . . .	171
5.11.3	Space point resolution . . . . .	171
5.11.4	Momentum resolution . . . . .	171
5.11.5	Further studies . . . . .	175
5.12	Schedule . . . . .	175
5.12.1	Schedule for construction . . . . .	175
5.12.2	Workpackages for the TPC project . . . . .	179
<b>6</b>	<b>P0D (<math>\pi^0</math> Detector)</b>	<b>183</b>
6.1	Introduction . . . . .	183
6.1.1	P0D Event Reconstruction Capabilities . . . . .	184
6.1.2	Predicting the $\nu_e$ Appearance Background . . . . .	187
6.2	Detector Design, Specification and Assembly . . . . .	190
6.2.1	The Water Target Design . . . . .	192
6.2.2	PØDule Design and Assembly . . . . .	194
6.2.3	Super-PØDule Assembly . . . . .	199
6.2.4	Electronics and Photosensors . . . . .	200
6.2.5	Mounting in the Basket . . . . .	202
6.2.6	P0D Heat Shield . . . . .	204

6.3	Detector Technology R&D . . . . .	205
6.3.1	PØDule Mechanical Prototypes . . . . .	205
6.3.2	Functional Prototypes . . . . .	207
6.4	Detector Construction Schedule . . . . .	209
6.5	Detector Installation/Commissioning . . . . .	209
6.5.1	Detector Integration and Shake-Down Tests . . . . .	209
6.5.2	Detector Installation and Commissioning . . . . .	210
6.6	Detector Calibration . . . . .	210
6.6.1	Preinstallation Detector Calibrations . . . . .	210
6.6.2	Optical Calibration System . . . . .	211
6.6.3	Cosmic Ray Calibrations . . . . .	211
<b>7</b>	<b>SMRD(Side Muon Range Detector)</b>	<b>214</b>
7.1	Introduction . . . . .	214
7.2	Detector design and specification . . . . .	217
7.2.1	Layout . . . . .	217
7.2.2	Scintillator and WLS fiber detectors . . . . .	218
7.2.3	Optical Connectors and Mechanical Module . . . . .	222
7.2.4	Photon Sensor + Electronics . . . . .	225
7.3	Detector Technology R&D . . . . .	225
7.3.1	Performance of SMRD Prototype modules . . . . .	225
7.4	Detector construction schedule . . . . .	225
7.4.1	Schedule . . . . .	225
7.4.2	Quality Control . . . . .	227
7.5	Detector installation/commissioning . . . . .	227
7.6	Detector calibration . . . . .	228
<b>8</b>	<b>ECAL</b>	<b>231</b>
8.1	Introduction . . . . .	231
8.1.1	Overview of ECAL Physics . . . . .	231
8.1.2	The Tracker ECAL . . . . .	231
8.1.3	Gamma/Muon Tagger (POD ECAL) . . . . .	232
8.2	Detector design and specification . . . . .	233
8.2.1	ECAL cluster reconstruction . . . . .	238
8.2.2	Electron and photon energy measurement . . . . .	238
8.2.3	Energy measurement using shower shape information . . . . .	238
8.2.4	Reconstruction of $\pi^0$ in the Tracker ECAL . . . . .	239
8.2.5	Particle identification: muon-electron separation . . . . .	242
8.2.6	Particle identification: electron-pion separation . . . . .	243
8.3	Detector technology R&D . . . . .	243
8.4	Detector construction schedule . . . . .	244
8.4.1	Facilities used in ECAL construction . . . . .	244
8.4.2	Timescales and notation . . . . .	244
8.4.3	Design . . . . .	245
8.4.4	Major procurements . . . . .	245
8.4.5	Fibre preparation . . . . .	245
8.4.6	Layer preparation for the Tracking and Downstream ECAL modules . . . . .	245
8.4.7	Module assembly for the Tracking and Downstream ECAL . . . . .	246
8.4.8	POD ECAL modules . . . . .	246
8.4.9	QA and initial calibration . . . . .	246
8.5	Detector installation/commissioning . . . . .	247

8.6	Detector calibration . . . . .	248
8.6.1	Fibre and Scintillator characterisation and quality control . . . . .	248
8.6.2	Electronics Calibration . . . . .	248
8.6.3	Photosensor Linearity and Monitoring . . . . .	249
8.6.4	Relative response correction . . . . .	249
8.6.5	Determination of the absolute energy scale . . . . .	250
<b>9</b>	<b>Photo-sensor</b>	<b>251</b>
9.1	Introduction . . . . .	251
9.2	Operation principle . . . . .	252
9.3	Requirements from detectors . . . . .	252
9.4	R&D status of the MRS-APD's . . . . .	253
9.4.1	Tested samples . . . . .	254
9.4.2	Gain . . . . .	254
9.4.3	Photon detection efficiency . . . . .	254
9.4.4	Dark rate . . . . .	255
9.4.5	Optical cross-talk . . . . .	257
9.4.6	Temperature dependence . . . . .	257
9.4.7	Recovery time . . . . .	258
9.4.8	Dynamic range and linearity . . . . .	258
9.4.9	Timing . . . . .	259
9.4.10	Life time . . . . .	259
9.4.11	Dispersion of parameters . . . . .	260
9.4.12	Summary and prospects . . . . .	260
9.5	R&D status of MPPC . . . . .	261
9.5.1	Tested samples . . . . .	261
9.5.2	Raw signal . . . . .	262
9.5.3	Gain . . . . .	262
9.5.4	Dark noise rate . . . . .	263
9.5.5	Photon detection efficiency (PDE) . . . . .	264
9.5.6	Cross-talk rate . . . . .	269
9.5.7	Linearity . . . . .	269
9.5.8	Recovery time . . . . .	270
9.5.9	Calibration . . . . .	271
9.5.10	Summary and prospects . . . . .	273
9.6	Summary of device performance . . . . .	274
<b>10</b>	<b>POD/ECAL/SMRD/INGRID Electronics</b>	<b>277</b>
10.1	Introduction . . . . .	277
10.2	Electronics design and specification . . . . .	278
10.2.1	TRIP-t ASIC . . . . .	278
10.2.2	TRIP-t Front-end Board (TFB) . . . . .	280
10.2.3	Readout Merger Module (RMM) . . . . .	281
10.2.4	TRIP-t Power Supply (TPS) . . . . .	281
10.2.5	Timing and Trigger System . . . . .	281
10.3	Construction Schedule . . . . .	282
10.3.1	TFB . . . . .	282
10.3.2	Back-end boards (BEB): RMM, GTM, SCM, MCM . . . . .	283
10.3.3	TPS . . . . .	283
10.3.4	Vertical Slice Test . . . . .	283
10.4	Installation/commissioning . . . . .	283

<b>11 Data Acquisition</b>	<b>285</b>
11.1 Introduction . . . . .	285
11.1.1 DAQ System Requirements . . . . .	285
11.1.2 The Proposed DAQ Implementation . . . . .	287
11.2 Inputs . . . . .	290
11.3 Objectives and Milestones . . . . .	291
11.3.1 TASK I: DAQ System Specification and Design . . . . .	291
11.3.2 TASK II: DAQ Software Development . . . . .	291
11.3.3 TASK III: Vertical Slice Demonstrator . . . . .	292
11.3.4 TASK IV: Full System Demonstrator . . . . .	292
11.3.5 TASK V: Test Beam and Subdetector Support . . . . .	292
11.3.6 TASK VI: Installation and Commissioning . . . . .	292
11.4 Outputs . . . . .	293
<b>12 Comissioning schedule + run plan</b>	<b>294</b>
<b>13 Reference</b>	<b>296</b>
13.1 Neutrino experimental hall . . . . .	296

# Chapter 1

## Physics Overview with the ND280 detector

### 1.1 Introduction

#### 1.1.1 ND280 overview

The near detector complex (ND280) consists of a finely segmented detectors acting as neutrino targets and tracking detectors surrounded by a magnet to measure the neutrino beam's energy spectrum, flux, flavor contents, and interaction cross-sections before the neutrino oscillation. The ND280 detector is located 280m from the target in the off-axis direction of the neutrino beam between the average pion decay point in the decay volume and the Super-Kamiokande detector.

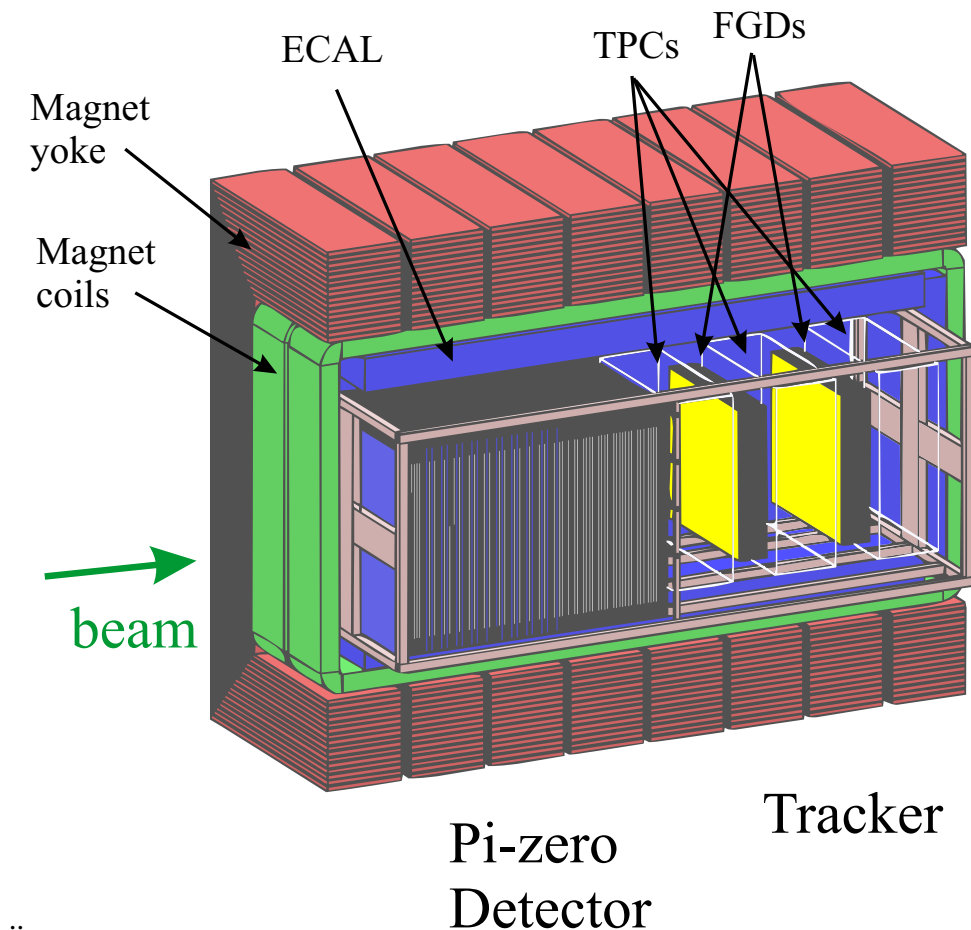


Figure 1.1: The ND280 detector.

The ND280 detector consists of the following elements, illustrated in Figure 1.1:

- Magnet: ND280 uses the UA1 magnet operated with a magnetic field of 0.2 T. Momenta of charged particles produced by neutrino interactions in the near detector is measured. The inner size of the magnet is  $3.5 \text{ m} \times 3.6 \text{ m} \times 7.0 \text{ m}$ .
- Tracker: Downstream of the POD is a tracking detector optimized to measure momenta of charged particles, particularly muons and pions produced by charged current interactions.
  1. Time Projection Chambers (TPCs): Three time projection chambers will measure the momenta of muons produced by charged current interactions in the detector, it will be used to reconstruct the neutrino energy spectrum. The TPC tracking and  $dE/dx$  measurements in the TPC will also determine the sign of charged particles and identify muons, pions, and electrons.
  2. Fine Grained Detectors (FGDs): Two FGD modules, placed after the first and second TPCs, consist of layers of finely segmented scintillator bars. The FGDs provide the target mass for neutrino interactions in the tracker. Direction and ranges of short tracks such as recoil protons produced by CC interactions in the FGDs are measured. One FGD module is made of plastic scintillator bars, while the second one is made of alternating plastic scintillator layers and water layers to allow the cross section measurement on water.
- Pi-Zero Detector (POD): The POD detector locates at the upstream end of the magnet inner volume. The detector is optimized to measure the rate of neutral current  $\pi^0$  production. The POD consists of tracking planes composed of scintillating bars alternating with lead foil. Water target is included part of the running time to measure neutrino cross section on water.
- Electromagnetic calorimeter (ECAL): ECAL Surrounds the POD and the tracker. The ECAL is a made of layers of scintillator bars interleaved with lead foils. The main purpose is to measure those  $\gamma$ -rays produced in ND280 that do not convert in the inner detectors and is critical for the reconstruction of  $\pi^0$  decays.
- Side Muon Range Detector (SMRD): Part of air gaps in the magnet iron yolk, which was originally used for hadron calorimeter in the UA1 experiment, will be instrumented with plastic scintillator to measure the ranges of muons that go in the side ways and miss TPC's. The SMRD also provide cosmic ray trigger for calibration.

In addition to these detectors which locates at the off-axis position of the neutrino beam, there will be an on-axis neutrino monitor (INGRID) to directly measure the direction of the neutrino beam.

Physics studied is underway using GEANT4 detector simulation and neutrino interaction simulation code (NEUT). An example of event display for the GEANT4 Monte Carlo simulation and a display of a tracking code are shown in Figure 1.2.

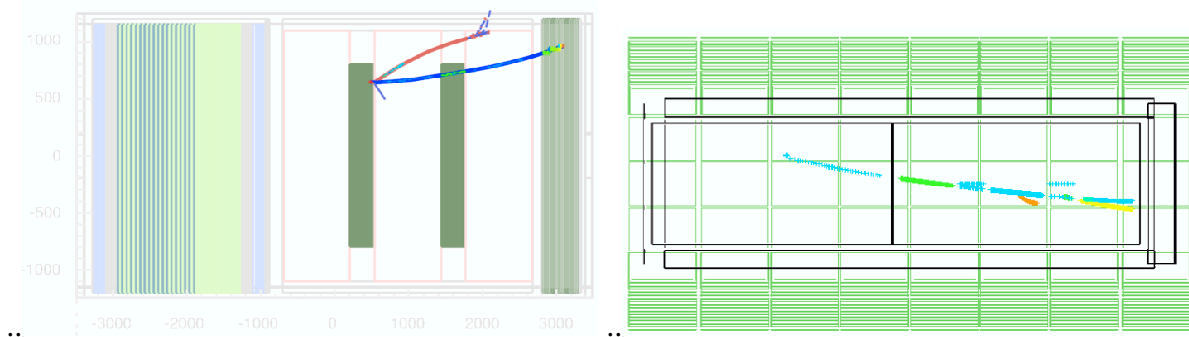


Figure 1.2: Event displays of the GEANT4 Monte Carlo simulation and a tracking code.

	$\nu_\mu$ CC BG	$\nu_\mu$ NC BG	beam $\nu_e$ BG	$\nu_e$ CC signal
Fully-contained, $E_{vis} \geq 100\text{MeV}$	2215	847	184	243
1 ring e-like, no decay-e	12	156	71	187
$0.35 \leq E_\nu^{rec.} \leq 0.85\text{GeV}$	1.8	47	21	146
e/ $\pi^0$ separations	0.7	9	13	103

Table 1.1: The number of events selected by the  $\nu_e$  appearance analysis, as predicted by NEUT Monte Carlo for  $5 \times 10^{21}$  POT exposure. For the calculation of oscillated  $\nu_e$ ,  $\Delta m^2 = 2.5 \times 10^{-3}\text{eV}^2$  and  $\sin^2 2\theta_{13} = 0.1$  are assumed.

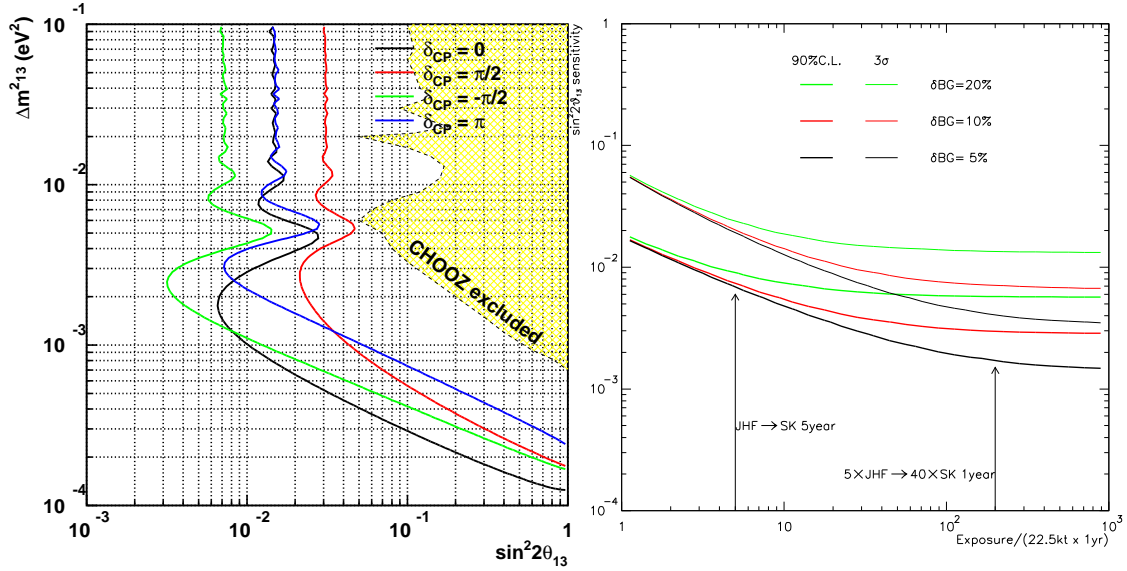


Figure 1.3: (Left) The 90% C.L. sensitivity to  $\sin^2 2\theta_{13}$  for an exposure of  $5 \times 10^{21}$  POT with the assumption of maximum mixing,  $\sin^2 2\theta_{23} = 1.0$ , and the CP violation phase  $\delta = 0, \pi/2, -\pi/2, \pi$ . The 90% excluded region of CHOOZ is overlaid for comparison with  $\sin^2 2\theta_{23} = 1.0$ . (Right) The expected 90% C.L. and  $3\sigma$  sensitivities of  $\sin^2 2\theta_{13}$  as a function of exposure time (5 years  $\equiv 5 \times 10^{21}$  POT) for three different uncertainties in background subtraction. We assume  $\Delta m^2 = 2.5 \times 10^{-3}\text{eV}^2$  and  $\delta = 0$ .

## 1.1.2 Physics goal of T2K

### $\nu_e$ appearance

The  $\nu_e$  selection criteria are based on the SK-1 atmospheric neutrino analysis. Events are required to be fully contained within the 22.5kt fiducial volume, have visible energy ( $E_{vis}$ ) greater than 100MeV, a single electron like (e-like) ring, and no decay electrons. The dominant source of background events are beam  $\nu_e$  contamination and single  $\pi^0$  production in neutral current (NC) interactions. The backgrounds can be further reduced by requiring the reconstructed neutrino energy to be around the oscillation maximum,  $0.35 \text{ GeV} \leq E_\nu^{rec.} \leq 0.85\text{GeV}$ , and by specific “e/ $\pi^0$  separation” requirement. Table 1.1 summarizes the number of events after the event selections for  $5 \times 10^{21}$  proton on target (POT) exposure at  $\Delta m^2 = 2.5 \times 10^{-3}\text{eV}^2$  and  $\sin^2 2\theta_{13} = 0.1$ .

Figure 1.3 (Left) shows the 90% C.L.  $\nu_e$  sensitivity for  $5 \times 10^{21}$  POT exposure and for  $\sin^2 2\theta_{23} = 1$  and  $\delta = 0, \pi/2, -\pi/2, \pi$ , assuming a 10% systematic uncertainty in the background subtraction. The sensitivity is  $\sin^2 2\theta_{13} = 0.008$  at 90% C.L. for  $\Delta m^2 \sim 2.5 \times 10^{-3}\text{eV}^2$ . This represents an order of magnitude improvement over the CHOOZ limit. Figure 1.3 (Right) shows the 90% C.L. and  $3\sigma$   $\nu_e$  sensitivities as a function of the exposure time for  $\Delta m^2 = 2.5 \times 10^{-3}\text{eV}^2$  for systematic uncertainties

	CC-QE	CC-nonQE	NC	All $\nu_\mu$
Generated in FV	4,114	3,737	3,149	11,000
(1) FCFV	3,885	3,011	1,369	8,265
(2) $E_{vis.} \geq 30$ MeV	3,788	2,820	945	7,553
(3) Single ring $\mu$ -like	3,620	1,089	96	4,805

Table 1.2: The expected number of neutrino events for  $5 \times 10^{21}$  POT for  $\nu_\mu$  disappearance analysis without oscillation. CC-QE refers to charged current quasi-elastic events and CC-nonQE to other charged current events, while NC refers to neutral current events.

$\Delta m^2$ (eV <sup>2</sup> )	CC-QE	CC-nonQE	NC	All $\nu_\mu$
No oscillation	3,620	1,089	96	4,805
$2.0 \times 10^{-3}$	933	607	96	1,636
$2.3 \times 10^{-3}$	723	525	96	1,344
$2.7 \times 10^{-3}$	681	446	96	1,223
$3.0 \times 10^{-3}$	800	414	96	1,310

Table 1.3: The expected number of neutrino events for  $5 \times 10^{21}$  POT for  $\nu_\mu$  disappearance analysis with neutrino oscillation for different values of  $\Delta m_{23}^2$  with  $\sin^2 2\theta_{23} = 1.0$  and  $\sin^2 2\theta_{13} = 0.0$ .

in the background subtraction of 5%, 10%, and 20%. Systematic uncertainty in the subtraction of beam  $\nu_e$  and NC  $\pi^0$  at SK is required to be 10% or less for the exposure of  $5 \times 10^{21}$  POT, which corresponds to a nominal 5 years of running.

### $\nu_\mu$ disappearance

The neutrino oscillation parameters,  $(\sin^2 2\theta_{23}, \Delta m^2)$ , will be determined by measuring the survival probability of  $\nu_\mu$  after traveling 295 km. The expected number of events without oscillation for an off-axis angle of  $2.5^\circ$  and  $5 \times 10^{21}$  POT are summarized in Table 1.2. The numbers of events after oscillation as a function of  $\Delta m_{23}^2$  are shown in Table 1.3 for the values of oscillation parameters  $\sin^2 2\theta_{23} = 1.0$  and  $\sin^2 2\theta_{13} = 0.0$ .

Figure 1.4 (Left) shows the reconstructed neutrino energy distribution of the fully-contained single ring  $\mu$ -like events. The hatched area shows the non-QE component. The distribution is fitted to extract oscillation parameters using an extended-maximum likelihood method. The right figure shows the ratio of reconstructed energy with and without oscillation. The expected statistical uncertainty on the measurements is 0.009 for  $\sin^2 2\theta_{23}$  and  $5 \times 10^{-5}$ eV<sup>2</sup> for  $\Delta m_{23}^2$ , and is shown as a function of the true  $\Delta m_{23}^2$  in Figure 1.5.

Figure 1.6 shows the effect of the systematic uncertainties. The dashed line corresponds to the statistical error for an exposure of  $5 \times 10^{21}$  POT and the following source of systematic uncertainties are considered in this analysis.

1. Uncertainty in the predicted number of the fully-contained single ring  $\mu$ -like events (event normalization). The red curve shows the systematic bias on oscillation parameters when the event normalization is shifted by 10 %.
2. Uncertainty in the non-QE/QE cross section ratio (non-QE/QE ratio). The green curve shows the systematic bias on oscillation parameters when the non-QE/QE ratio is shifted by 20 %.
3. Uncertainty in the energy scale. The blue curve shows the systematic bias on oscillation parameters when the energy scale is shifted by 4 %.

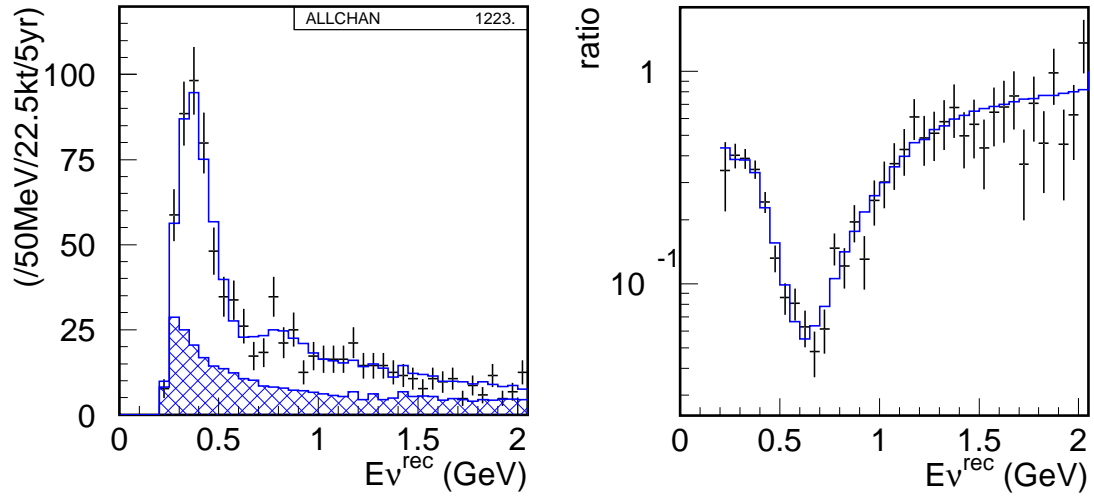


Figure 1.4: (Left) The reconstructed neutrino energy distribution with predicted for the best-fit oscillation parameters  $(\sin^2 2\theta_{23}, \Delta m^2) = (1.0, 2.7 \times 10^{-3} \text{eV}^2)$ . The hatched area shows the non-QE component. (Right) The ratio of the reconstructed neutrino energy distribution with oscillation to one without oscillation.

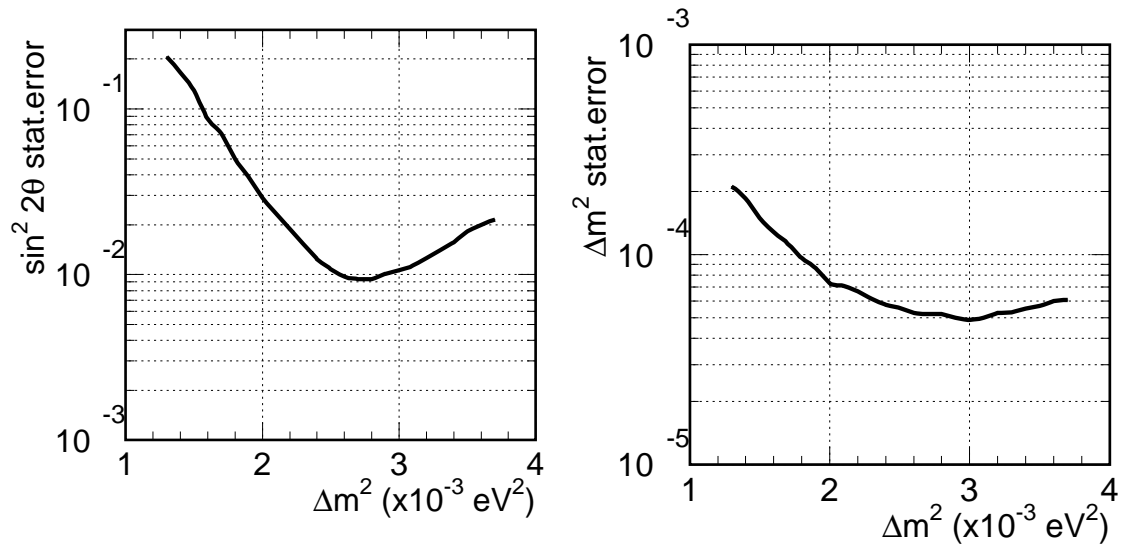


Figure 1.5: The statistical uncertainty of the oscillation parameters as a function of true  $\Delta m^2_{23}$ . The value of  $\sin^2 2\theta_{23}$  is assumed to be one.

4. Uncertainty in the predicted neutrino energy spectrum shape at far detector is considered in two ways. The pink curve shows the systematic bias on the oscillation parameters when a 20% linear distortion of  $1 + 0.2(1 - E_\nu)$  is introduced to the neutrino spectrum. This change roughly corresponds to the difference in spectra predicted by MARS and FLUKA hadron production models. The light blue curve shows the systematic bias on the oscillation parameters when width of the spectrum is changed by 10 %.

In order to keep the systematic uncertainties below the statistical error, the systematic uncertainties are required to be less than about 5 % in event normalization, less than 2 % for the energy scale, less than 5-10 % for the non-QE/QE ratio, less than 20% in linear spectrum distortion and less than 10% for the spectrum width.

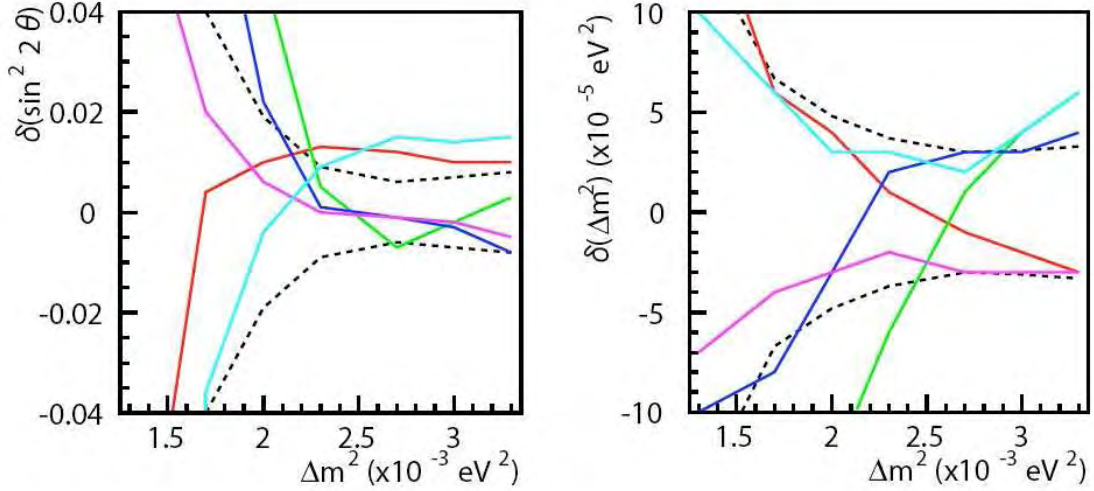


Figure 1.6: Systematic biases on the oscillation parameters. Red curve corresponds to event normalization changed by 10%, green curve is for nonQE/QE ratio changed by 20%, blue curve is for energy scale changed by 4%, pink curve is for 20% linear distortion in the spectrum shape (see text), and light blue is for the width of the spectrum to be changed by 10%. The dashed curve shows  $1\sigma$  statistical error for  $5 \times 10^{21}$  POT.

### Physics goal of the first year

In the first year of operation, on-axis detector, magnet, tracker (TPC and FGD), and part of SMRD will be operational. The beam intensity is expected to be limited to 100kW during this period, or  $2 \times 10^{20}$  POT. The main goal during this period is to understand the neutrino beam and measure the off-axis neutrino beam flux. At first, the neutrino beam will carefully be tuned and studied by the proton beam monitors in the beamline, optical transition radiation (OTR) monitor at the target, and the muon monitor behind the beamline. The direction of the horn focused neutrino beam is measured by the on-axis neutrino detector at the ND280m hall.

Although the total number of proton on target is expected to be at the similar level as exposure of MINOS experiment in the initial year, significant improvement in  $\nu_\mu$  disappearance sensitivity is expected because of the off-axis beam tuned at the oscillation maximum. Figure 1.7 shows  $\nu_\mu$  disappearance sensitivity of the first year, or  $2 \times 10^{20}$  POT. Expected  $1\sigma$  sensitivities are  $\delta(\sin^2 2\theta_{23})=0.03$  and  $\delta\Delta m_{23}^2=1.6 \times 10^{-4}$ . The sensitivity is expected to be limited by statistics. Figure 1.8 shows expected oscillation probability for  $2 \times 10^{20}$  POT. Even the first year of data, there is a chance of observing the "reappearance" effect at lower reconstructed neutrino energy, if we understand the background in particularly from NC1pi events.

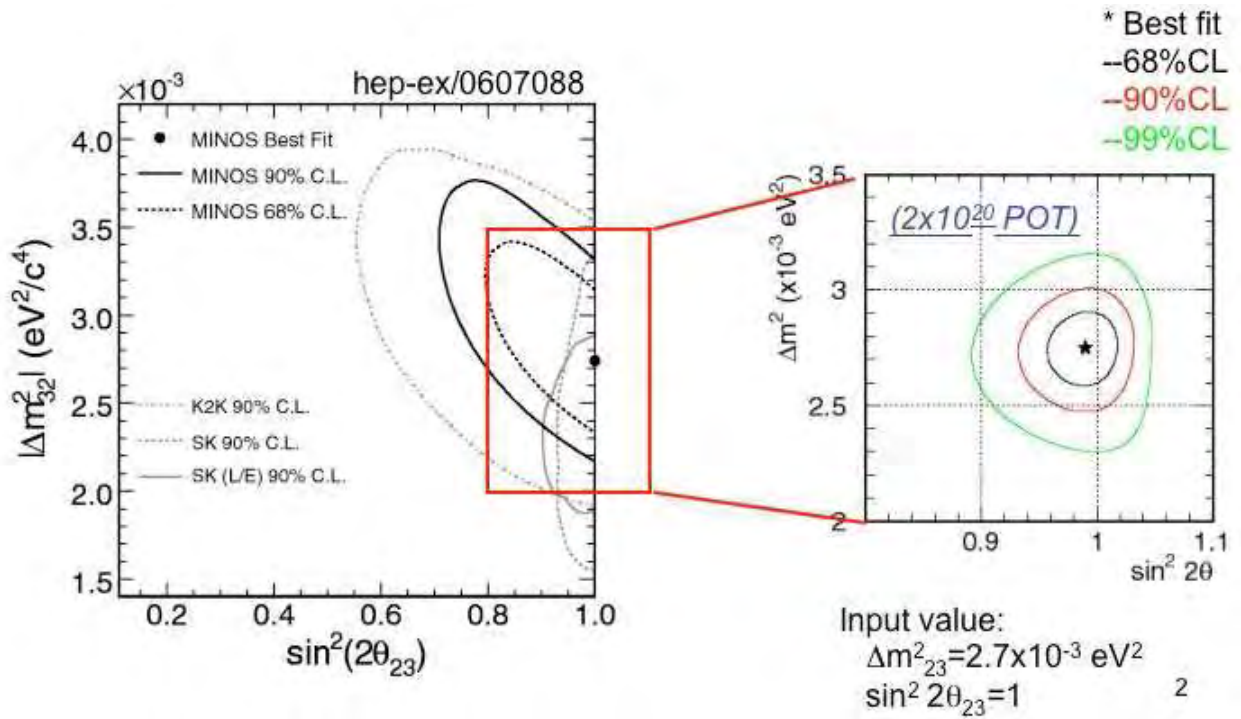


Figure 1.7:  $\nu_\mu$  disappearance sensitivity of the first year, or  $2 \times 10^{20}$  POT.

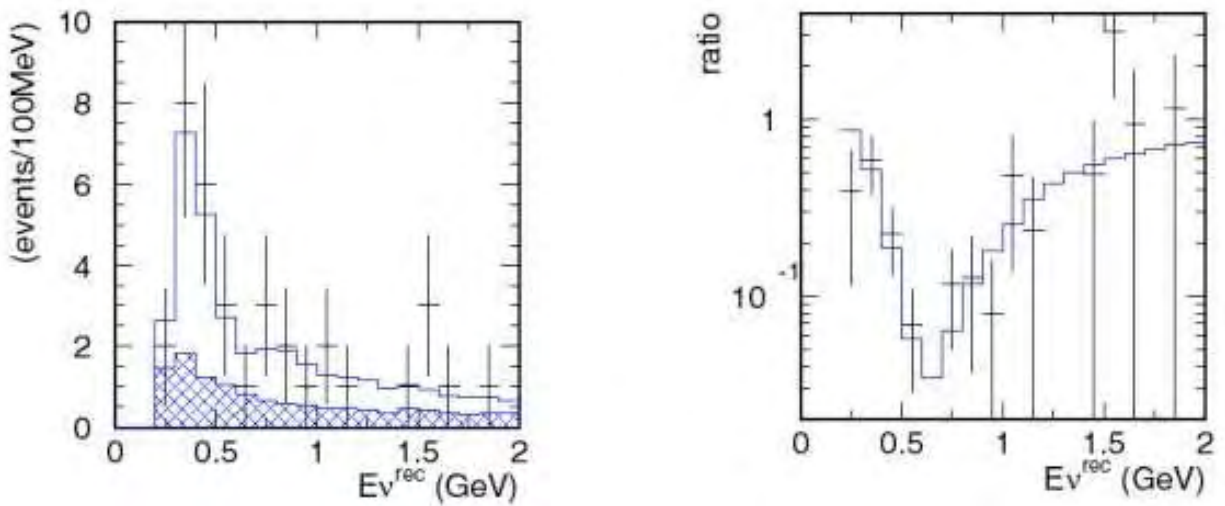


Figure 1.8: Expected oscillation probability for  $2 \times 10^{20}$  POT.

### 1.1.3 Requirements of the ND280 detector

#### Strategy of ND280 detector measurement

The neutrino spectrum at the far detector is estimated by correcting the neutrino spectrum measured at the near detector by an extrapolation function obtained from the beam Monte Carlo simulation (far/near ratio). The goal of the ND280 detector is to measure the neutrino ( $\nu_\mu$  and  $\nu_e$ ) spectra and to study the neutrino cross sections to predict the response at the far detector.

The main process at around the T2K peak neutrino energy is Charged-Current Quasi-Elastic (CCQE),  $\nu_\mu n \rightarrow \mu^- p$ , whose cross section will be used as a reference cross section. In the near detector, the product of flux and the CCQE cross section ( $\Phi_\nu \times \sigma_{CCQE}$ ) is measured, which is compared with the same quantity at the far detector. For specific neutrino interaction the ratio of the cross section to the CCQE ( $\sigma/\sigma_{CCQE}$ ) will be determined. In the neutrino oscillation analyses,  $\sigma_{CCQE}$  cancels out between the near and far detector measurements. Because the neutrino oscillations make the  $\nu_\mu$  spectrum at the far detector significantly different from that at the near detector due to far to near solid angle difference and neutrino oscillation, it is necessary to measure all the significant neutrino reactions as a function of neutrino energy (normalized to the CCQE cross section). Since the CCQE is a 2 body process, the initial neutrino energy can be reconstructed from the out-going muon momentum,  $E_\nu^{QE} = \frac{2E_l m_N - m_l^2}{2(m_N - E_l + P_l \cos\theta_l)}$ . For CC1pi process, one can use recoil mass to be  $\Delta$  mass instead of proton mass, to reconstruct the neutrino energy,  $E_\nu^{res} = \frac{2E_l m_N - m_l^2 + (M_\Delta^2 - m_N^2)}{2(m_N - E_l + P_l \cos\theta_l)}$ .

For the NC events, the energy of the neutrino cannot be reconstructed. The pions pre-dominantly come from NC-1pi process through the  $\Delta$  resonance. Since the Lorentz boost of  $\Delta$  is not so large due to its heavy mass, the pion energy spectrum from  $\Delta$  decay is almost independent of the initial neutrino energy. Therefore NC1pi pion energy spectrum measured in the near detector provides a good approximation of the NC1pi pion spectrum at the far detector. This hypothesis can be tested in the pion energy spectrum of the CC1pi events. The expected flux can be corrected using the far/near ratio estimated from the CCQE events.

#### ND280 detector requirements

As discussed in the previous subsection, the requirements for the systematic uncertainties of the T2K experiment are summarized as follows:

- Less than 10 % in uncertainty in the number of  $\nu_e$  appearance backgrounds.
- Less than 5 % in  $\nu_\mu$  event normalization.
- Less than 20% in the linear spectrum distortion and less than 10% in the  $\nu_\mu$  spectrum width.
- Less than 2 % for the energy scale.
- Less than 5-10 % for the non-QE/QE ratio.

The first one comes from  $\nu_e$  appearance measurement and the rest are from  $\nu_\mu$  disappearance measurement. The main  $\nu_e$  backgrounds at SK are beam  $\nu_e$  contamination and NC  $\pi^0$  background. The ND280 detector needs to be capable of identifying these process and have reasonable prediction to extrapolate the near detector measurement to the background prediction at the far detector. These are addressed in the following sections on " $\nu_e$  flux and spectrum measurement" and "NC $\pi^0$  for  $\nu_e$  appearance search" in the following sections.

The  $\nu_\mu$  event normalization and the spectrum shape (linear distortion and width of the spectrum) measurement will be done by measuring the  $\nu_\mu$  CCQE events in the near detector. The spectrum is then corrected by using far/near extrapolation function. The measurement of  $\nu_\mu$  flux is described in " $\nu_\mu$  flux and spectrum measurement".

The energy scale of the far detector is calibrated by cosmic rays, Michel electrons, and reconstructed  $\pi^0$  mass. The current SK calibration achieves the systematic uncertainty in the energy scale of 1-2%. The energy scale in the near detector is set by the Magnet-TPC spectrometer system. The field mapping of the magnet is required to be better than 1%.

Figure 1.9 shows the contributions of different non-QE backgrounds to the CCQE selection as a function of reconstructed neutrino energy in the far detector. NC1 $\pi$  events is the dominant background at lower energy region where oscillation "re-appearance" takes place, and CC1 $\pi$  events dominate in the rest of the energy region, in particular at the oscillation maximum region. Cross sections and

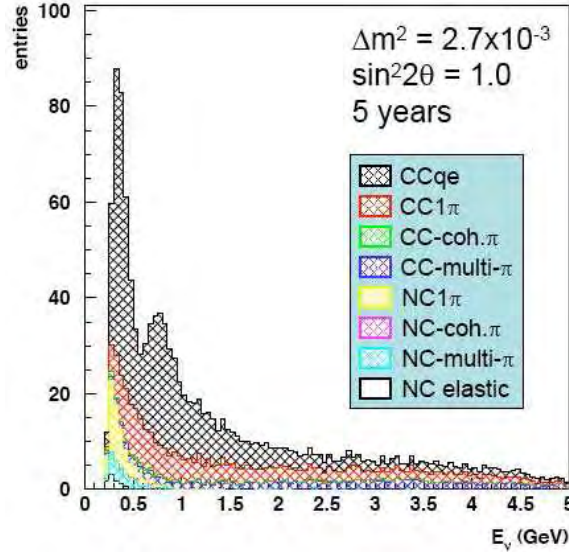


Figure 1.9: Contributions of different non-QE backgrounds to the CCQE selection as a function of reconstructed neutrino energy in the far detector.

detection efficiencies needs to be measured in detail, which are described in the sections of "CC-1pi for  $\nu_\mu$  disappearance measurement" and "NC  $\pi^+$  for  $\nu_\mu$  disappearance measurement".

## 1.2 $\nu_\mu$ flux and spectrum measurement

### 1.2.1 Beam direction and stability monitoring by INGrid

Off-axis angle of the beam can fluctuate during the operation due to the change in beam emittance, proton beam optics, horn alignment, and other factors. Proton beam monitors and muon monitors will monitor the proton and hadron beam axes. The on-axis INGrid detector provides the direct measurement of the neutrino beam direction and relative flux using the neutrinos. The requirement in the uncertainty of the beam direction is better than 1mrad, which corresponds to 14MeV or 2% shift in the peak neutrino energy.

### 1.2.2 CCQE selection in the tracker

CCQE selection procedure is first studied by event vector of the NEUT Monte Carlo generated on the 2.5 degree off-axis beam Monte Carlo data. CC events has  $\mu^-$  in the final state and can be selected by choosing negative charged track in the TPC. Figure 1.10 shows the momentum distribution of single negative charged particles. Those events with pions with momentum larger than 100MeV/c, which has a range of more than 12cm in FGD, are vetoed to simulate the single track selection. 96% of these negative charged single tracks are CC events. The rest of the events are  $\pi^-$ . With a  $\mu^-/\pi^-$

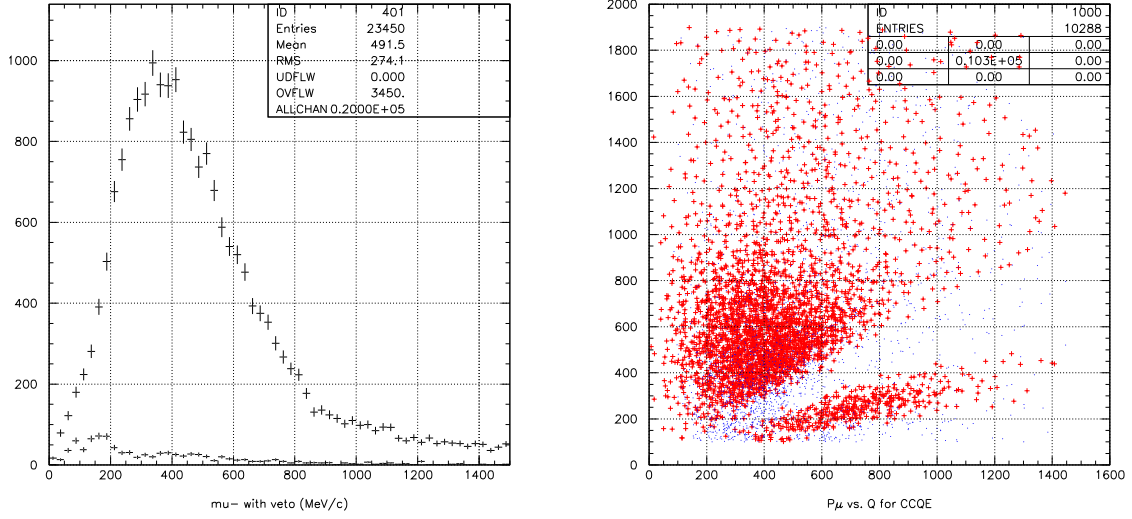


Figure 1.10: Left: Momentum distributions of negative charged particles at the off-axis near detector. The larger histogram is for  $\mu^-$  (Charged current) whereas the lower histogram is for  $\pi^-$  backgrounds. Right: Muon momentum versus reconstructed  $\sqrt{Q^2}$  distribution for CCQE signal events (red cross) and non-CCQE background events (blue dots).

identification of 5 or better by the downstream Ecal, the NC contamination is expected to be less than 1%.

Out of these single track CC events, 72% are CCQE. By applying photon ( $\pi^0$  and  $\eta$ ) veto in Ecal and Michel electron veto to suppress low energy  $\pi^+$  stopping in FGD, as will also be done in the SK analysis, the CCQE purity is further improved to 83%. 84% of the remaining backgrounds comes from CC1pi and the rest are from multi-pi/DIS processes. For both of these processes, pions are absorbed before exiting the nucleus. These background events occupy phase space different from the CCQE signal in  $P_\mu$  and  $Q^2$  space (Figure 1.10). The gap in the signal distribution corresponds to the requirement of ( $|\cos\theta| > 0.5$ ) to simulate muons going into upstream or downstream TPC. By fitting the observed distribution with signal and background, the background level can be estimated using the near detector data sample itself. An independent way to estimate the background is to use the proton direction compared to the expected proton direction assuming the event is CCQE ( $\Delta\theta_P$ ). This approach was used in the K2K experiment and provides a way to enhance signal and background samples to evaluate the systematic uncertainty. By taking an interpolation error of 20% in estimating the non-QE contamination, the systematic error on  $\nu_\mu$  event normalization due to background subtraction would be  $20\% \times 17\% = 3.4\%$ .

A full GEANT4 Monte Carlo simulation has been done, taking into account the pion interaction in FGD, to confirm the vector level study (Table 1.4). A CCQE purity of 81% is obtained. After rejecting  $\pi^-$  by downstream Ecal, the purity becomes 83%, which is consistent with the vector level study, with an overall acceptance of 60%. Figure 1.11 shows reconstructed  $E_\nu$  distributions for the remaining CCQE (solid line) and non-CCQE events (dotted line).

### 1.2.3 Detection efficiency of CCQE

As described in the previous section, selection of CCQE events rely primarily on muons reaching into the TPC. Tracker TPC has finite angular acceptance for muons. Acceptance has to be estimated in particular for those events with muons going perpendicular to the neutrino direction. Figure 1.12 shows muon momentum and angular distributions of muons from CCQE events. Figure 1.13 shows  $Q^2$  vs.  $E_\nu$  distribution of the detected CCQE events in the forward/backward direction (box) and

Table 1.4: Selection of CCQE events using ND280 GEANT4 simulation

	total	CCQE	CCQE eff.	CCQE purity
generated	5000	1767	1	0.3534
negative track in TPC	1971	1086	0.614	0.551
$\pi^+$ veto in TPC	1700	1084	0.613	0.638
$\pi^+$ veto in FGD	1577	1080	0.611	0.685
photon veto in Ecal	1303	1054	0.596	0.809
$\mu^-$ ID in Ecal	1270	1049	0.594	0.826

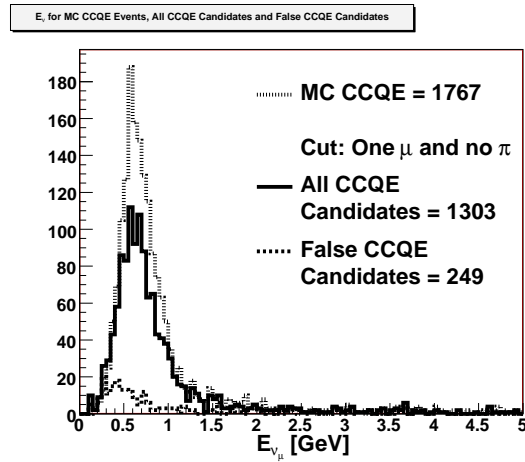


Figure 1.11: Reconstructed  $E_\nu$  distributions for all the CCQE events before the cuts, and selected CCQE and non-QE contaminations (false CCQE candidates).

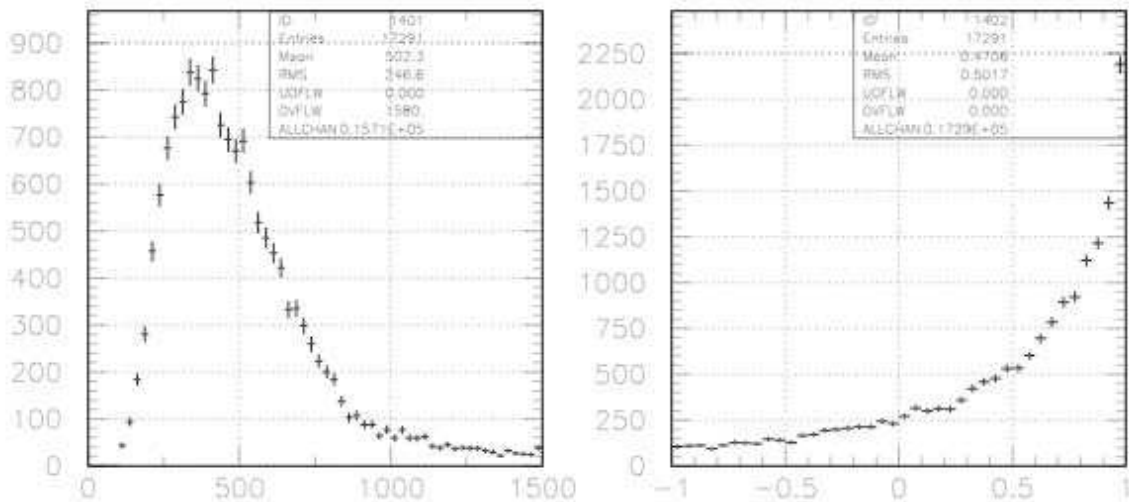


Figure 1.12: Muon momentum and angular ( $\cos \theta$ ) distributions of CCQE events.

for those events escaping in the side ways (dots). By interpolating the CCQE muon distribution

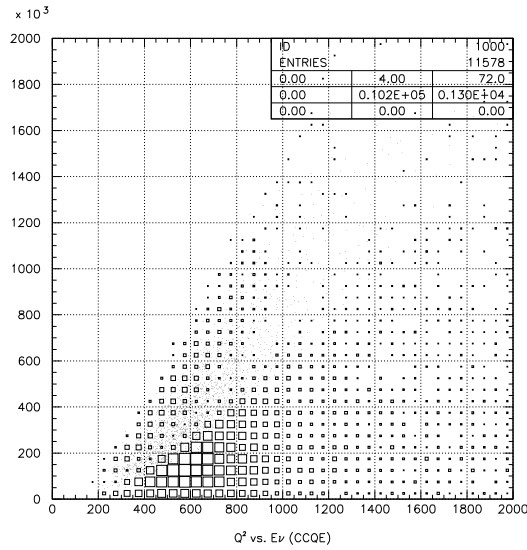


Figure 1.13:  $Q^2$  vs.  $E_\nu$  distribution for detected CCQE events in the forward/backward direction (box) and for those escaped events in the side ways (dots).

between the forward and backward directions the cross section in the side direction can be estimated. A 10% error due to this interpolation results in  $(100\%-60\%) \times 10\% = 4\%$  systematic uncertainty in  $\nu_\mu$  flux normalization. An independent way to measure muons going into the side direction is to tag muons by SMRD. This measurement will provide a way to improve the interpolation function and to understand the systematic uncertainties.

Since the CCQE measurement relies on muons going into the TPC, the detection efficiency is basically the same for water FGD and plastic FGD. The chemical composition is adjusted in such a way that water FGD is approximated as 55% of plastic and 45% of water. The CCQE measurement on water is performed by subtracting the plastic FGD spectrum from water FGD spectrum for both signal and backgrounds. For a nominal 1-year exposure of  $10^{21}$ POT, 40000 CCQE events are expected for each FGD's. The corresponding statistical uncertainty for the flux measurement in water becomes,

$$\sqrt{\frac{1}{0.45^2} \frac{1}{40000} + \left(\frac{0.55}{0.45}\right)^2 \frac{1}{40000}} = 1.1\%.$$

## 1.2.4 Near to far extrapolation of the $\nu_\mu$ flux

Un-oscillated Neutrino spectrum at the far detector is estimated by correcting the neutrino spectrum measured at the near detector. In principle, the flux will be reduced simply by the solid angle factor  $L_{near}^2/L_{far}^2$ , where  $L_{near}$  and  $L_{far}$  are the distances to the near and far detectors. In reality, because the length of the pion and kaon decay region is 110m, which is not negligible compared to the distance to the near detector of 280m, this scheme does not work. When the decays occur further downstream, the solid angle and the off-axis angle of the near detector get larger. The decay vertex distribution depends on the hadron production as well as alignment of the focusing components, and the geometry of the beam line, which causes the systematic uncertainty in near to far extrapolation. For example, a 5m shift in the pion decay vertex corresponds to 5% change in the solid angle and 1mrad change in the off-axis angle or 14MeV (2%) shift in the peak neutrino energy in the near detector. An uncertainty of 5m thus creates 5% in the  $\nu_\mu$  event normalization at the oscillation maximum and 2% shift in energy, which are at the limit of what are required for the systematic uncertainties.

Figure 1.14 (Left) shows the decay vertex distributions in the decay pipe for  $\nu_\mu$ 's detected in the near and far detector. The number of events decaying in the downstream region for the near

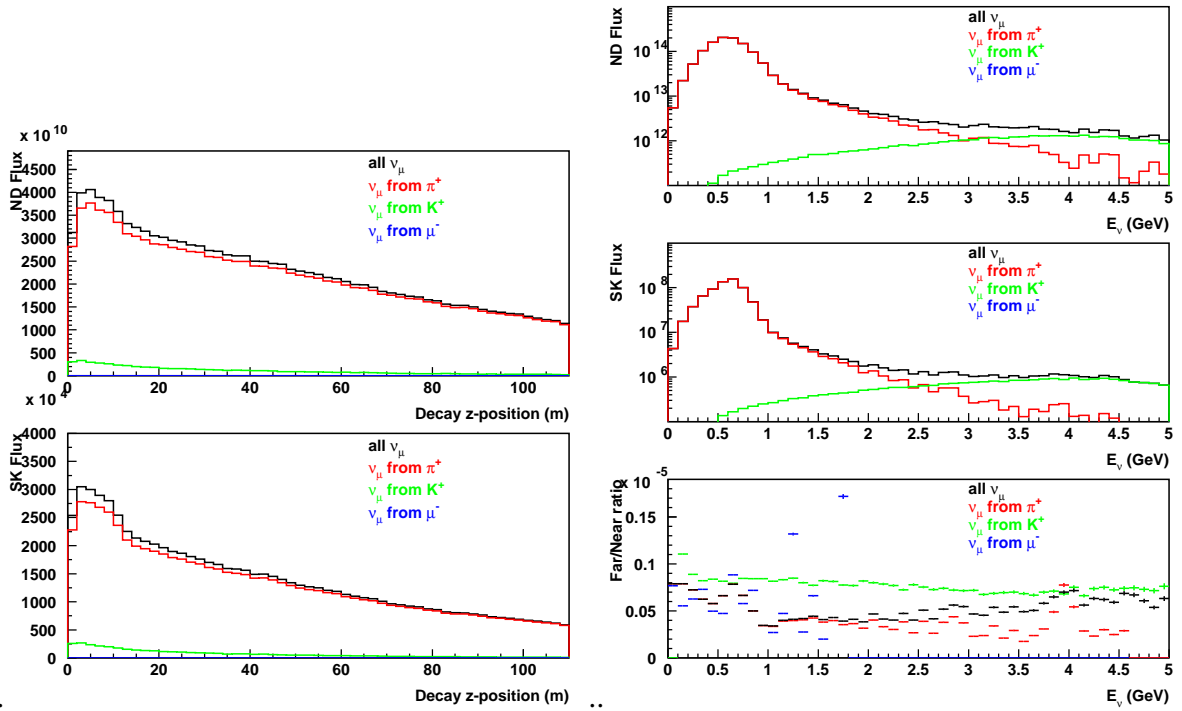


Figure 1.14: **Left:** Decay vertex distributions in the decay pipe for  $\nu_\mu$ 's detected in the near (top) and far (bottom) detector. Black line is for all the events, red is for pion decays and green is for kaon decays. **Right:**  $\nu_\mu$  energy spectra in the near (top) and far (middle) detectors and their ratios.

detector is enhanced because of the solid angle effect. The right figure shows the muon neutrino energy spectra in the near and far detectors and their ratio (Far/Near). The ratio is large in the region below  $E_\nu < 0.5\text{GeV}$  where pions have lower momentum and decay upstream. In the peak region of  $0.5 < E_\nu < 1\text{GeV}$ , the far/near ratio shows a peak because of the wider  $E_\nu$  peak in the near detector due to its larger solid angle and the spread of the decay vertex causing wider range in off-axis angle. The ratio is smaller in the  $1 < E_\nu < 2.5\text{GeV}$  region which comes from higher energy pions with longer decay length. In the region above  $E_\nu > 2.5\text{GeV}$ , the far/near ratio rises up again as kaon decays (green) that decays more upstream region dominate.

A detailed study is in progress to understand the systematic uncertainties in the near to far extrapolation. Here, we provide a snap shot of the study that is in progress. Figure 1.15 shows the decay vertex distributions of pions whose decay neutrinos are detected in the near detector for different pion energy bins. For pion momenta of  $0\text{-}1\text{GeV}/c$  and  $1\text{-}2\text{GeV}/c$ , the decay vertex distribution is consistent with pion decay length. For pion momenta above  $2\text{GeV}/c$ , the decay vertex distributions have almost the same shape. This is because of the cancelation of two competing processes; high momentum pions are more likely to decay downstream due to its longer decay length but harder to send neutrinos into the near detector from downstream position due to Lorentz boost. The right hand figure shows analytical estimation of decay vertex distribution for pencil beam pions by taking into account solid angle, pion decay probability, and acceptance change due to Lorentz boost, and it explains the decay vertex distributions reasonably well. This small pion momentum dependence in decay vertex distribution makes the near to far extrapolation insensitive to the parent pion momentum distribution. Figure 1.16 shows the pion decay vertex distributions for each  $E_\nu$  bins. Because of the off-axis nature, most of the events falls into the peak energy bin of  $E_\nu=0.5\text{-}0.75\text{GeV}$ , whose distribution is not sensitive to the pion energy distributions as discussed above. In the  $E_\nu=0.25\text{-}0.5\text{GeV}$  region, the distribution has faster drop until the middle of the decay pipe due to decays of pions below  $1\text{GeV}$ , but then recovers due to contributions from the high energy pions decaying downstream of the pipe. One way to separate components from the low energy pions and high energy pions is to examine the  $E_\nu$  distributions

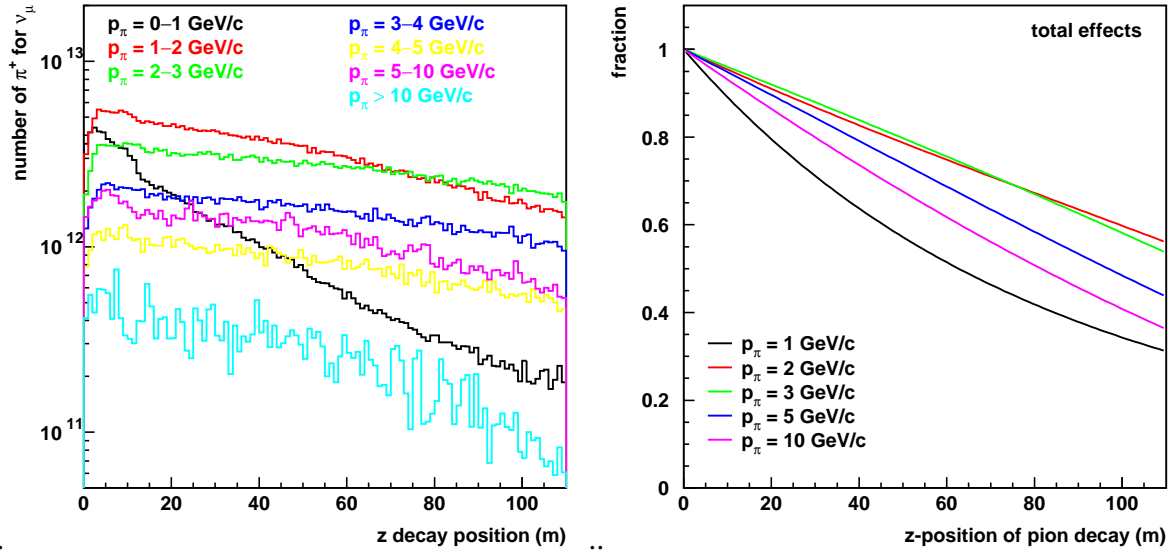


Figure 1.15: **Left:** Decay vertex distributions of pions that are detected in the near detector for different pion energy bins. **Right:** Analytical estimation of decay vertex distribution for pencil beam pions by taking into account solid angle, pion decay probability, and acceptance change due to Lorentz boost.

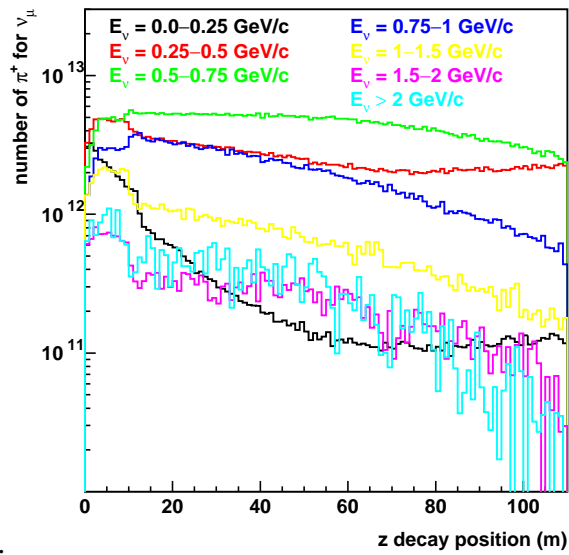


Figure 1.16: Decay vertex distributions of pions that are detected in the near detector for different neutrino energy ( $E_\nu$ ) bins.

at different hit position in the near detector (Figure 1.17). The  $E_\nu$  from pions below 1GeV/c does not depend much on the off-axis angle and thus the interaction point in the near detector (see the right figure), whereas the  $E_\nu$  from high energy pion decays shifts. Above  $E_\nu > 0.75\text{GeV}$ , the distribu-

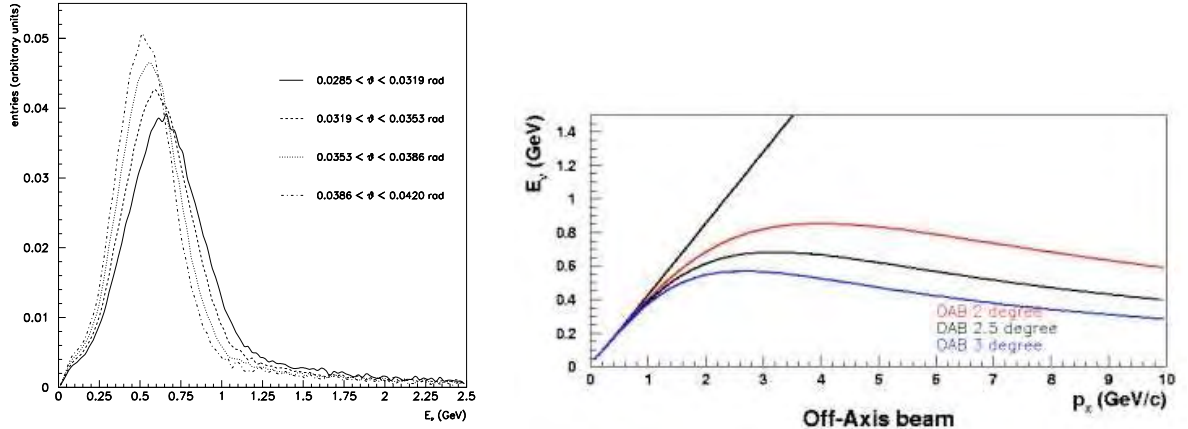


Figure 1.17:  $E_\nu$  distributions at different near detector positions.

tions have faster drop at downstream, because neutrinos from those pions decaying downstream have larger off-axis angle towards the near detector causing suppression and energy downshifting. Above  $E_\nu > 2.5\text{GeV}$ , kaon contribution becomes important, as discussed before. The interaction position dependence of the  $E_\nu$  distribution would also help in estimating the ratio between kaon contribution and pion contributions.

The peak  $E_\nu$  region, is the main contribution to the  $\nu_\mu$  normalization, and the near to far extrapolation needs to be understood at 5% level in this region, which appears to be achievable. For example, the difference between two pion production codes, MARS and FLUKA, is 2% in far/near ratio in the peak  $E_\nu$  region and 5% in the tail region. Some of the T2K collaboration members participate in the proposal to directly measure pion and kaon production using proton beam at CERN (NA49). This hadron production measurement along with a good understanding of the alignment of beam, target, and horn provide further information on the Monte Carlo estimation of the extrapolation function.

### 1.3 $\nu_e$ flux and spectrum measurement

The  $\nu_e$  CC events are selected by choosing negative charged track with electron identification in the TPC and downstream Ecal. In order to select  $\nu_e$ 's which is 0.5-1% of the number of  $\nu_\mu$ 's,  $e/\mu$  separation of  $10^{3-4}$  by TPC  $dE/dx$  and Ecal is sufficient to tag electrons from the muon background. Because of the smaller statistics for  $\nu_e$  events, the requirement for CCQE- $\nu_e$  selection is not as stringent as the muon case. A total of 2000 events are expected in each FGD for nominal 5-year exposure of  $5 \times 10^{21}\text{POT}$ , which corresponds to a statistical uncertainty of 5% for the cross section in water. Contamination of the CC1pi and multi-pi backgrounds can be estimated from those cross sections measured in the  $\nu_\mu$  interactions.

Figure 1.18 shows the  $\nu_e$  flux at ND280 and SK, and the ratio of the two distributions. The ratio is almost flat but slight positive slope which is determined by the ratio between those from muon decays and kaon decays. Beam  $\nu_e$  below  $E_\nu < 1.3\text{GeV}$  is mainly from  $\mu$  decays whereas above  $E_\nu > 1.3\text{GeV}$  is from kaon decays. Because the decay position distribution of muons spread throughout the decay volume, the flux ratio between far detector and near detector (far/near ratio) in this region is lower and does not depend much on the pion (muon) momentum distribution. The decay point distribution of kaons are concentrated near the target and thus far/near ratio is larger. Once a smooth fit to separate the kaon and muon components in the  $\nu_e$  spectrum, a relatively reliable far/near extrapolation could

be done. For example, a difference in  $\pi/K$  ratio for MARS and FLUKA simulation codes is 10%. In order to achieve the goal of 10% systematic uncertainty in  $\nu_e$  beam background normalization, the far/near ratio requirement for the  $\nu_e$  beam needs to be less than 10%.

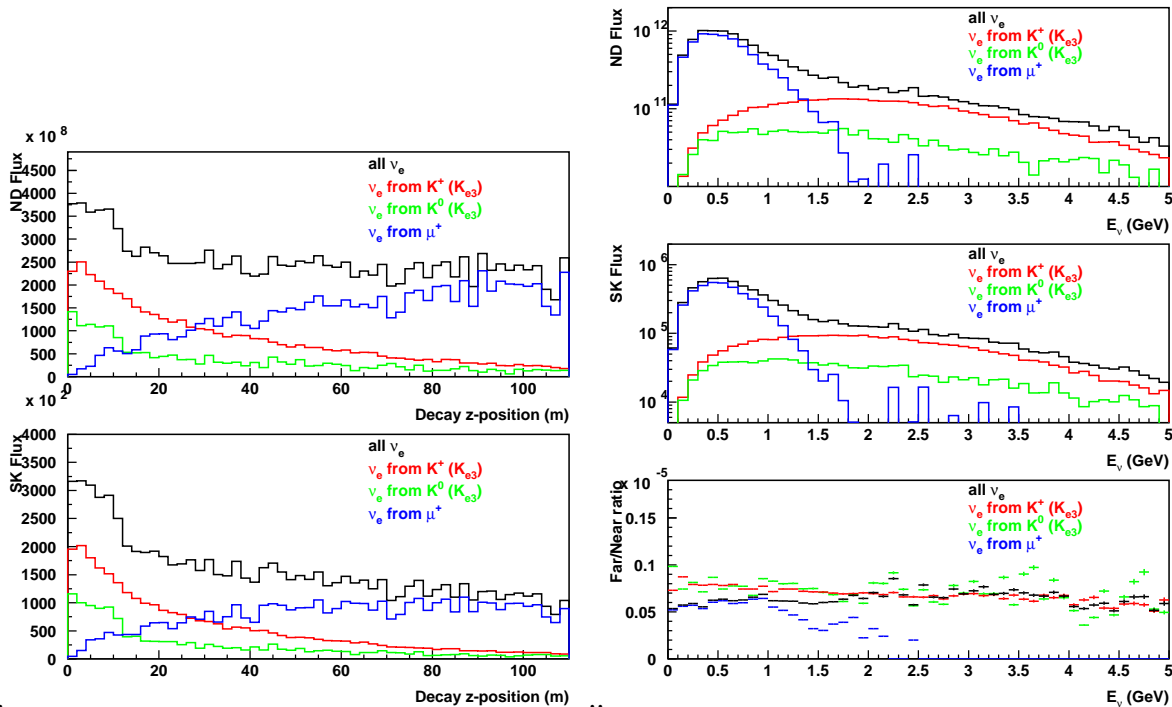


Figure 1.18: **Left:** Decay vertex distributions in the decay pipe for  $\nu_e$ 's detected in the near (top) and far (bottom) detector. Black line is for all the events, red is for pion decays and green is for kaon decays. **Right:**  $\nu_e$  energy spectra in the near (top) and far (middle) detectors and their ratios.

## 1.4 Neutrino cross section studies

### 1.4.1 Single pion productions

The goal of the neutrino cross section measurements in the near detector is to estimate of the backgrounds at the far detector, SK. The main backgrounds at the far detector are single pion production processes, the  $\text{NC}1\pi$  and  $\text{CC}1\pi$  for  $\nu_\mu$  disappearance measurement and  $\text{NC}1\pi^0$  for  $\nu_\mu$  disappearance measurement. The SK detection efficiency of  $\text{CC}1\pi$  events in the CCQE selection depends on the pion momentum. Figure 1.19 shows the effect of "1-ring  $\mu$ -like" selection on  $\text{CC}1\pi$  events as a function of their momenta. The pion ring is likely to be detected when it is above the Čerenkov threshold.

Single pion production processes proceed by exciting  $\Delta$  and other resonances. Figure 1.20 shows NC- $\pi$  cross section. The dominant cross section below  $E_\nu < 2\text{GeV}$  is  $\Delta$  resonance and contributions from other resonances are small. The cross section rises up from 0.5GeV to 1.0GeV and stays almost flat. Figure 1.21 shows the expected NC pion energy distribution for iron target. The dashed line corresponds to the pion energy spectrum without nuclear medium effect and the solid line is with nuclear effect. Pions with kinetic energy of around 0.2GeV tends to interact in the nucleus and its energy is shifted down. The shape of the energy distribution is dictated by the  $\Delta$  decay and the nuclear re-scattering effect in the nucleus, and it is almost independent of the incident neutrino energy, except for the higher energy cut off. Thus, the shape of the pion momentum distribution in the near detector is a good representative of that of the far detector. The pion momentum spectrum measured by the

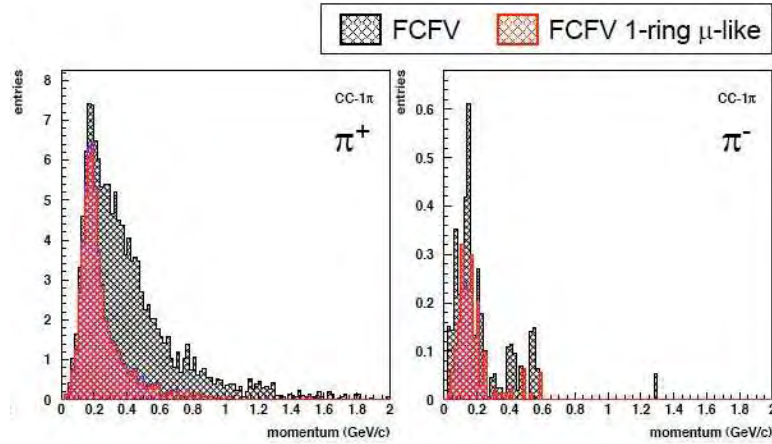


Figure 1.19: Pion momentum distributions of fully contained fiducial volume (FCFV) events at SK before (black) and after (red) single ring  $\mu$ -like selection.

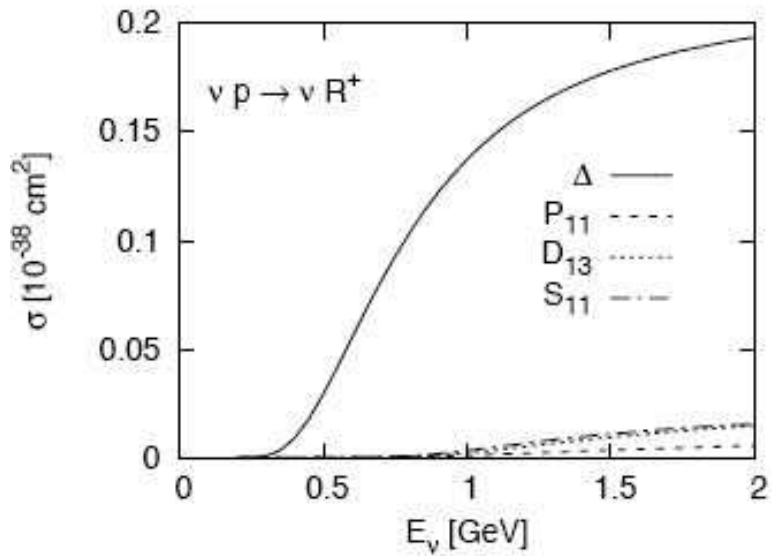


Figure 1.20: NC1 $\pi$  cross section as a function of neutrino energy.

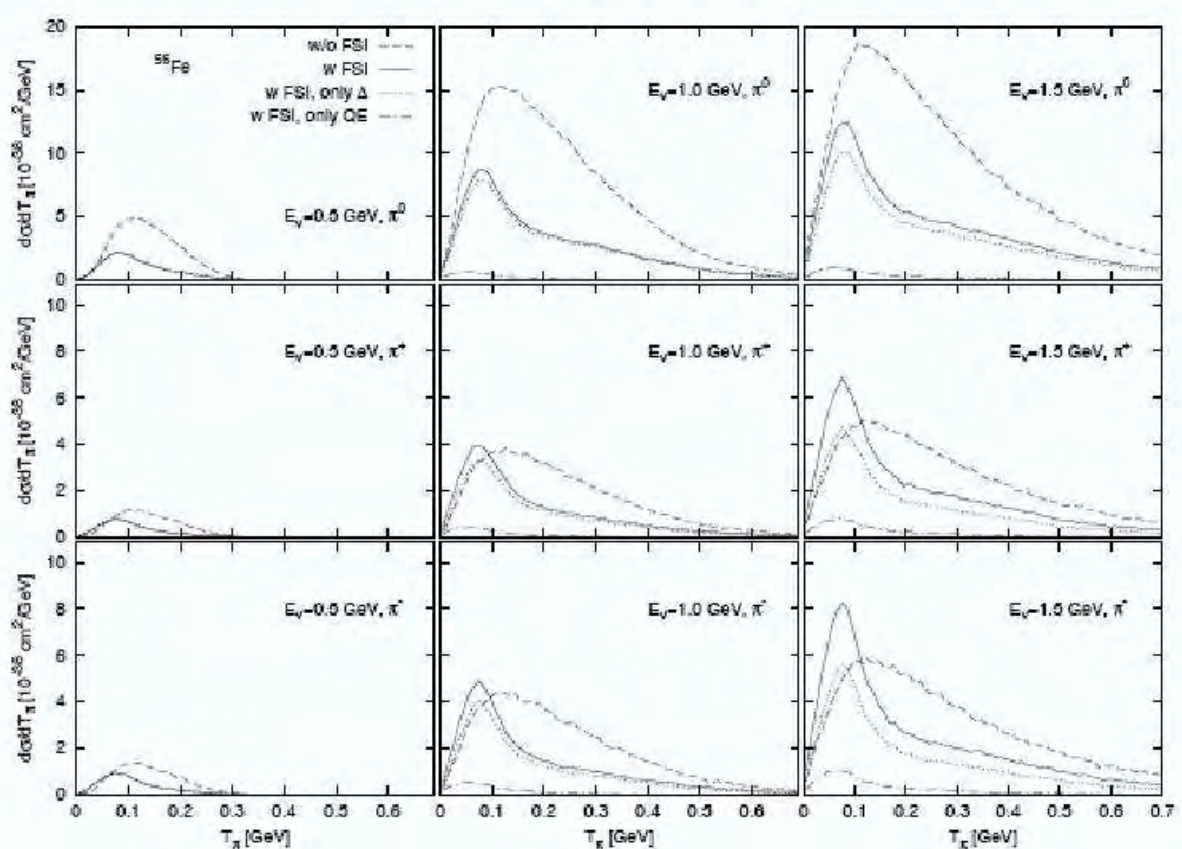


Figure 1.21: NC pion energy distribution for iron target with (bold line) and without (dashed line) final state interaction in the nucleus.

ND280 tracker even without far/near correction provides reasonable pion momentum distribution at SK.

## 1.4.2 CC-1pi for $\nu_\mu$ disappearance measurement

The goal of this study is to measure the differential cross section at SK. Figure 1.22 shows the CC1 $\pi$  cross section as a function of neutrino energy. The cross section rises between neutrino energy of 0.5

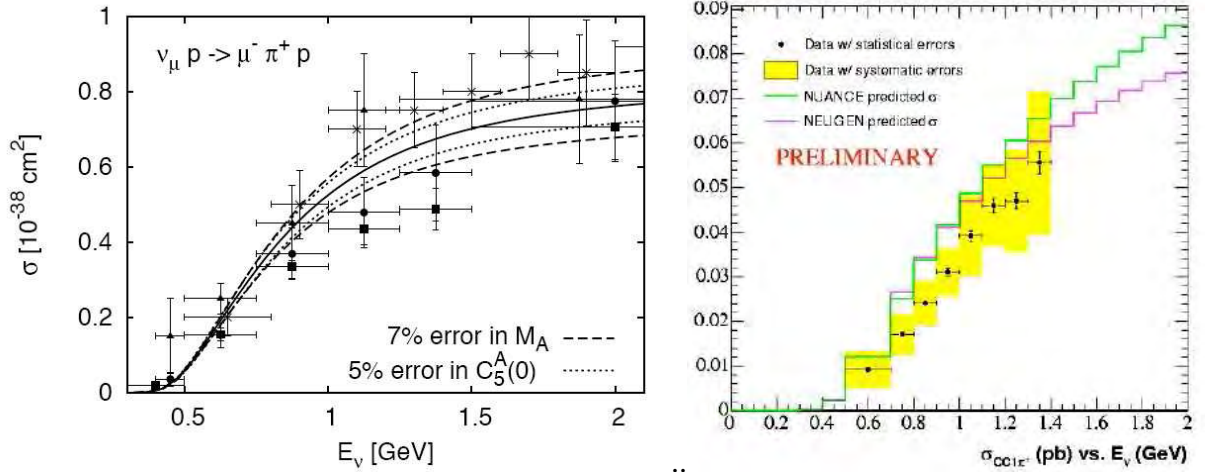


Figure 1.22: CC1pi cross section as a function of neutrino energy. The right hand figure is from the recent preliminary result by the MiniBooNE experiment.

and 1.5 GeV and the data scatters. The preliminary result from mini-BooNE experiment observed lower cross section than Monte Carlo prediction. The neutrino energy for CC1pi events can be reconstructed assuming recoil  $\Delta$ ,  $E_\nu^{res} = \frac{2E_l m_N - m_l^2 + (M_\Delta^2 - m_N^2)}{2(m_N - E_l + P_l \cos\theta_l)}$ . Because the  $\nu_\mu u$  flux, CC1pi cross section, and  $\nu_\mu$  oscillation probability also change rapidly in this region, it is important to measure the energy dependent CCqpi cross section. Figure 1.23 shows  $E_\nu$  distributions of CC1pi events that survived the CCQE selection. After oscillation, the survived CC1pi events for the oscillation maximum of  $E_\nu^{QE} = 0.5-0.7\text{GeV}$  (green line) comes from those with  $E_\nu > 0.8\text{GeV}$ , where the relative uncertainty of the cross section is less. With a reconstructed neutrino energy resolution of 50MeV, as achieved by mini-BooNE, the cross section uncertainty in the CC1pi background after oscillation is kept below 10%.

Out of ND280 GEANT4 events, CC1pi candidates are selected with the following selection criteria:

- $\mu^-$  selection: one and only one negative charged track in TPC
- $\pi^+$  selection: one positive minimum ionizing track in TPC or one minimum ionizing track in FGD with more than 15cm in path length
- Veto on extra minimum ionizing charged track in TPC
- Veto on extra minimum ionizing track in FGD with a track length of more than 15cm.
- Veto on extra electrons and positrons (Michel electron/positron) coming 50nsec or more later.
- Veto on gammas ( $\pi^0$  and  $\eta$ ) in Ecal with a true energy of more than 67MeV.

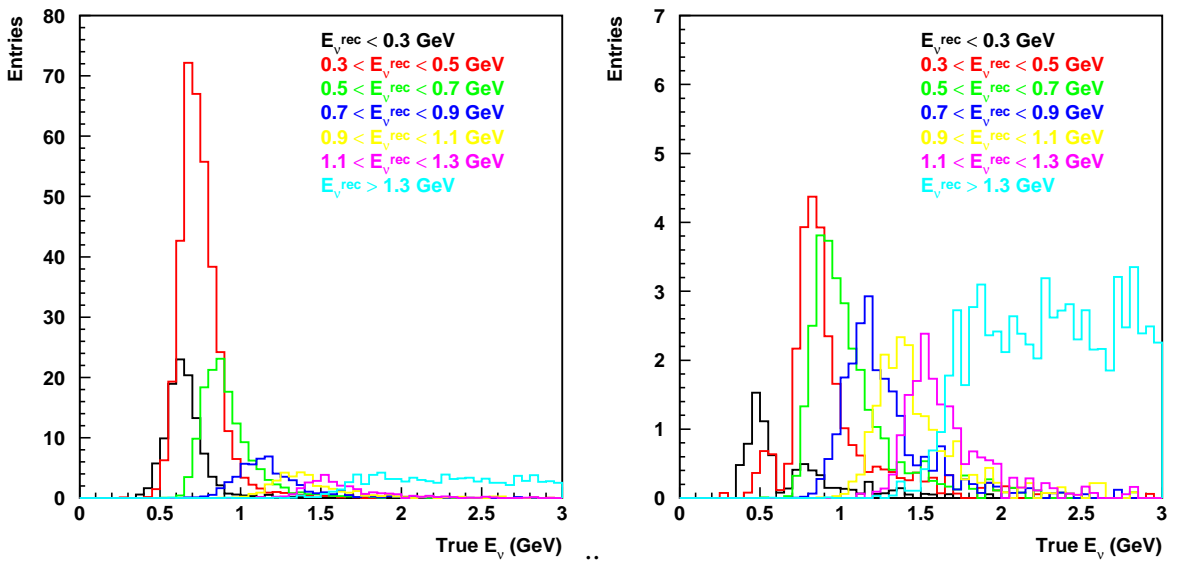


Figure 1.23:  $E_\nu$  distribution of CC1pi events that survived the CCQE selection before (left) and after (right) oscillation effect.

Figure 1.24 (Left) shows the reconstructed neutrino energy distribution for the CC1pi candidate events. Assuming recoil  $\Delta$  mass, one can reconstruct the neutrino energy just from the muon momentum. The CC1pi purity is 81.7% and an overall detection efficiency is 17.7%. The histogram on the right shows the reconstructed neutrino energy distribution for those events with both pion and muon are detected in TPC. The CC1pi purity is 84.7% and an overall detection efficiency is 10.4%. The remaining background comes from DIS and multi-pi events with other pions absorbed in the nucleus before exiting and this is the the main source of systematic uncertainty in CC1pi measurement. The contamination of these backgrounds can be estimated from the rejection power of gamma and Michel electron vetoes. With 50% uncertainties in estimating DIS/multi-pi contaminations, the CC1pi cross section relative to CCQE can be measured at 5-10% level, satisfying the non-QE/QE systematic uncertainty of 5-10%.

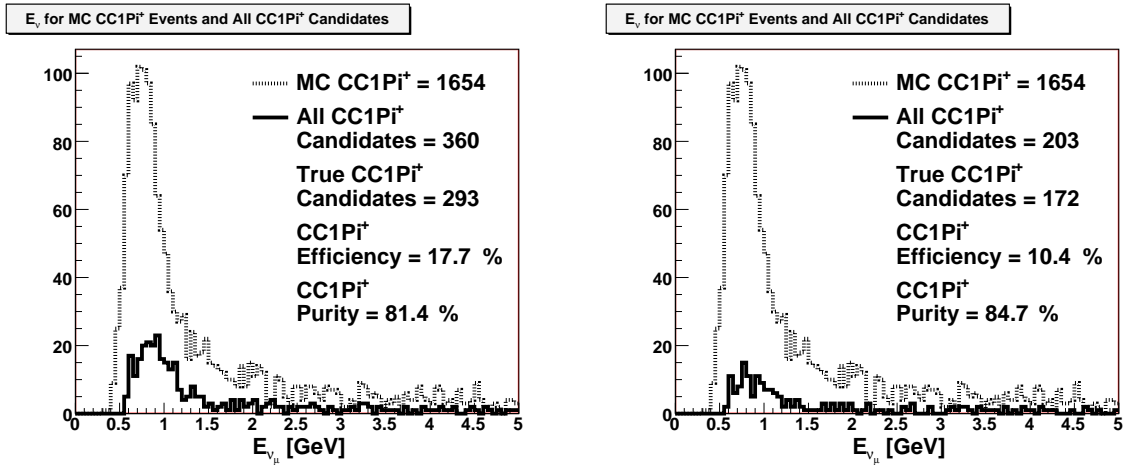


Figure 1.24: Reconstructed neutrino energy distribution for the CC1pi candidate events (left) and for those events with pions detected in TPC.

### 1.4.3 NC $\pi^+$ for $\nu_\mu$ disappearance measurement

NC $\pi^\pm$  background ( $\nu_\mu A \rightarrow \nu_\mu \pi^\pm (A-1)n$ ) is the main background for  $\nu_\mu$  disappearance at lower  $E_\nu$  region, which is important in observing the "re-appearance" effect in the neutrino oscillation.

Out of ND280 GEANT4 events, NC1pi+ candidates are selected with the following selection criteria:

- $\pi^+$  selection: one positive minimum ionizing track in TPC.
- Veto on extra minimum ionizing charged track in TPC
- Veto on extra minimum ionizing track in FGD with a track length of more than 15cm.
- Veto on extra electrons and positrons (Michel electron/positron) coming 50nsec or more later.
- Veto on gammas ( $\pi^0$  and  $\eta$ ) in Ecal with a true energy of more than 67MeV.

Figure 1.25 shows the momentum distribution of single positive charged track in TPC. The purity is 78% (32 out of 41 events) with a overall detection efficiency of 18.3% of those events with  $\pi^+$  coming out of the nucleus in which neutrino interaction takes place. The background comes from CC1pi events with muons not detected (6 events) and NC multi-pion events (3 events). A simulation with higher statistics is required to further understand the impurity.

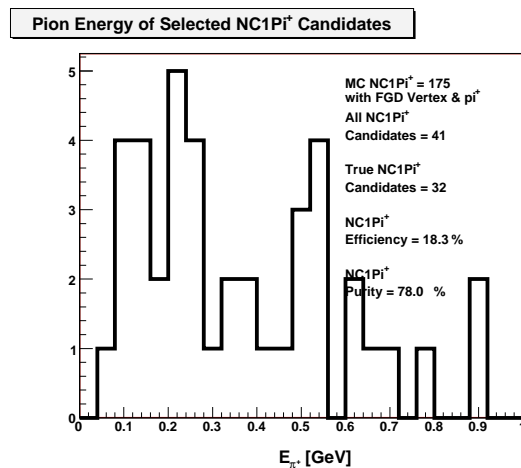


Figure 1.25: Momentum distribution of single positive charged track in TPC.

### 1.4.4 NC $\pi^0$ for $\nu_e$ appearance search

Neutral current  $\pi^0$  process is one of the two main background processes in  $\nu_e$  appearance search. There are three complimentary ways of measuring this important background in T2K.

- $\pi^0$  measurement by POD:  
POD is a dedicated  $\pi^0$  detector which provides high statistics sample of inclusive  $\pi^0$  production events.
- $\pi^0$  measurement using Ecal surrounding the tracker:  
 $\pi^0$  measurement with tracker provides exclusive measurement of  $\pi^0$ . For example it provides clean separation between NC and CC  $\pi^0$  production processes, which is needed in taking the neutrino oscillation effect into account. Statistics is limited to 6000 events/year ( $10^{21}$ POT) for each FGD.

- $\pi^0$  measurement at SuperK:

Although the statistics is very limited ( $\sim 100$  events over 5 years), the background contamination, far/near extrapolation, neutrino cross section, and neutrino flux are automatically taken into account. The statistics is just enough to satisfy the requirement of 10% error in number of  $\nu_e$  background, but not enough to study the systematic uncertainties in detail.

The first two measurements will be performed in the near detector.

### 1.4.5 Other cross section measurements

ND280m detector is a general purpose detector like a collider detector and has a potential of measuring various neutrino interaction modes in detail. Table 1.5 shows the expected numbers of  $\nu_\mu$  interactions for  $10^{21}$  POT on 1ton FGD. Similar measurement can be done for  $\nu_e$  as well as for  $\bar{\nu}_\mu$  and  $\bar{\nu}_e$  when the horn polarity is reversed.

Table 1.5: Numbers of  $\nu_\mu$  interactions for 40GeV  $10^{21}$ POT on 1ton FGD predicted by NEUT simulation code.

Int. Mode	Frac.	Events
<i>CC - QE</i>	38 %	65038
<i>CC - p<math>\pi^+</math></i>	11 %	17846
<i>CC - p<math>\pi^0</math></i>	3 %	4887
<i>CC - n<math>\pi^+</math></i>	3 %	5107
<i>CC - Coherent <math>\pi^+</math></i>	1 %	2189
<i>CC - multi <math>\pi</math></i>	7 %	11943
<i>CC - p<math>\rho^0</math></i>	0.5 %	835
<i>CC - <math>\Lambda K^+</math></i>	0.1 %	159
<i>CC - DIS</i>	8 %	13057
<i>NC - Elastic n</i>	9 %	15671
<i>NC - Elastic p</i>	8 %	13581
<i>NC - n<math>\pi^0</math></i>	2 %	2837
<i>NC - p<math>\pi^0</math></i>	2 %	3519
<i>NC - p<math>\pi^-</math></i>	1 %	1931
<i>NC - n<math>\pi^+</math></i>	1 %	2300
<i>NC - Coherent <math>\pi^0</math></i>	1 %	1099
<i>NC - multi <math>\pi</math></i>	2 %	3639
<i>NC - n<math>\rho^0</math></i>	0.1 %	150
<i>NC - p<math>\rho^0</math></i>	0.1 %	120
<i>NC - DIS</i>	2 %	4022

# Chapter 2

## Neutrino Beam Monitor: INGRID Detector

### 2.1 Introduction

A neutrino detector in a position on the beam axis (hereafter “on-axis”) will monitor the neutrino beam directly by observing neutrino interactions in the T2K 280m detector location [1]. The detector, “Interactive Neutrino GRID” (INGRID), is designed to monitor the neutrino beam direction, intensity and mean energy with sufficient statistics to provide a daily measurement at design intensity. The design of the detector corresponds to the 2.5 degree off-axis configuration.

The neutrino beam profile at the ND280 hall is shown in Figure 2.1 The INGRID detector is

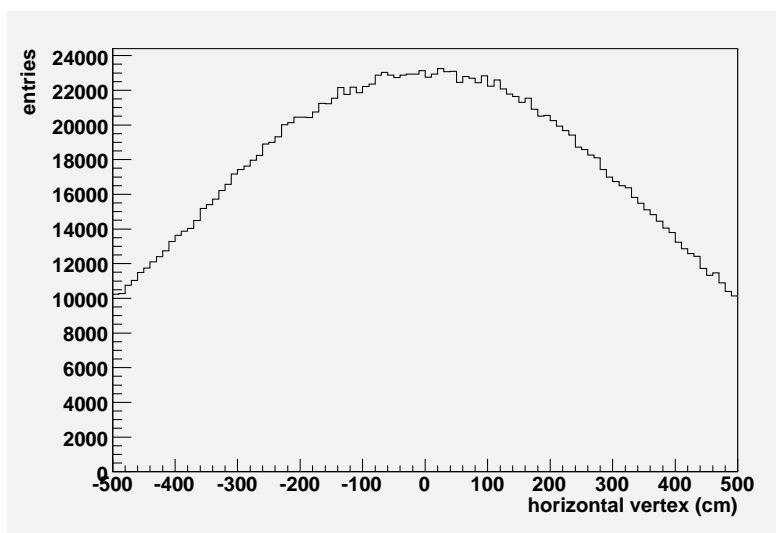


Figure 2.1: The beam profile of neutrinos which have interactions at the ND280 hall. The neutrino events are sampled in the region of  $\pm 5$  m horizontal and  $\pm 50$  cm vertical region.

designed to covered the neutrino beam profile of Figure 2.1 with 7 identical modules. Fourteen modules are arranged on a horizontal axis and a vertical axis, which samples the beam on  $10 \times 10\text{m}^2$  ( $\pm 5\text{m} \times \pm 5\text{m}$ ) area. The configuration of INGRID in the ND280 hall is shown in Figure 2.2. In addition, two more additional modules will be installed at the diagonal positions to confirm the off-diagonal neutrino flux.

One of the main purposes of INGRID is to monitor the direction of the neutrino beam. In Figure 2.3, we show the variation of the neutrino beam flux and the peak energy in the Super-Kamiokande detector as a function of the angle between the beam direction and the direction from the T2K beam to Super-K (the “off-axis angle”). A variation of the beam direction results in the different off-axis angle from its design value. Thus, in order to minimize a systematic error from the uncertainty of the off-axis angle, the beam direction must be monitored with precision better than 1 mrad.

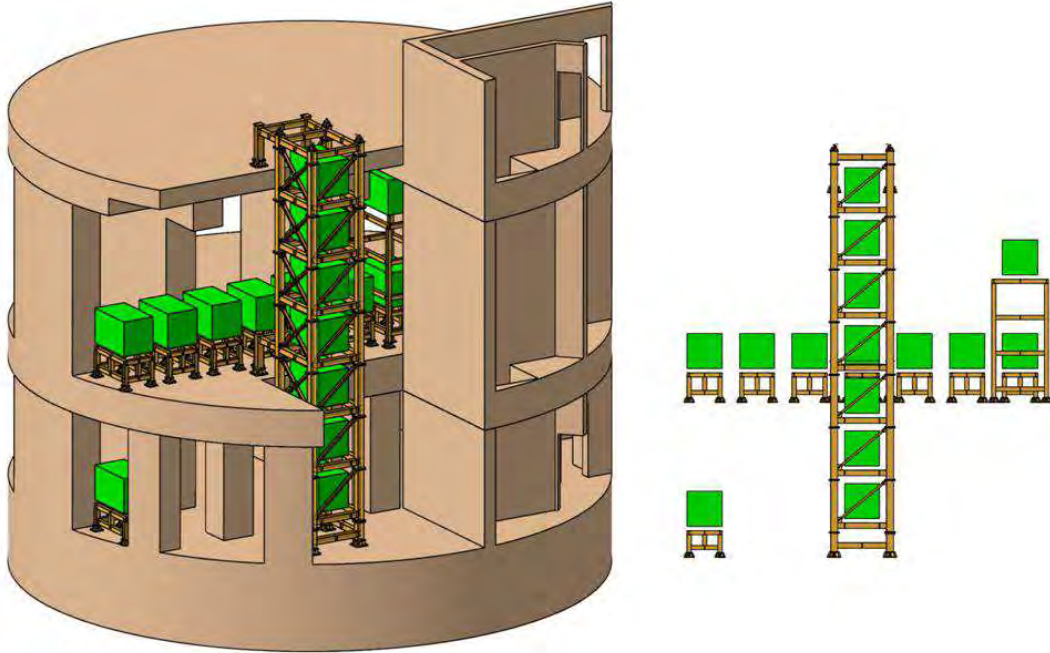


Figure 2.2: The INGRID detector configuration in the ND280 hall. The neutrino beam enters the detector from the bottom right of this drawing.

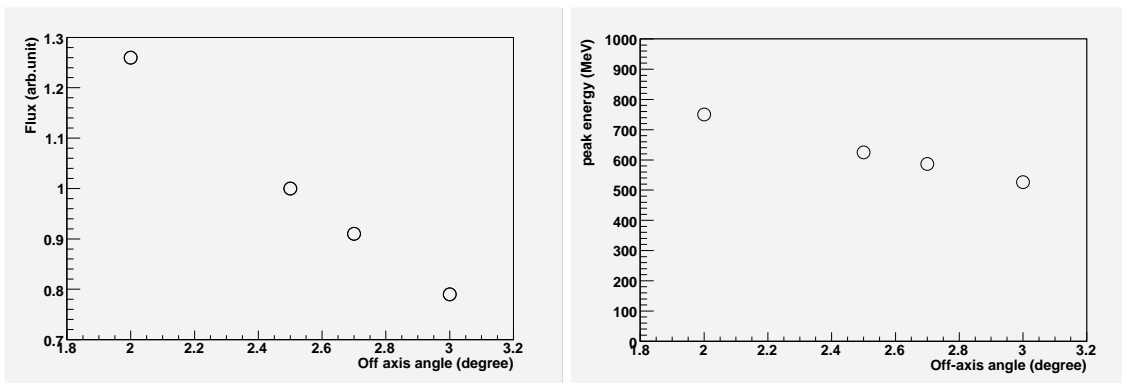


Figure 2.3: The variation of the neutrino beam flux (left) and peak energy (right) seen at Super-Kamiokande as a function of the off-axis angle. A change of the beam direction results in the different off-axis angle. The goal of INGRID is to monitor the angle to a precision of 1 mrad ( $0.06^\circ$ ) each day at design intensity.

## 2.2 Detector overview and specification

Each INGIRD module is a sandwich structure of iron and scintillators surrounded by the veto scintillator counters. A sketch of the INGRID module is shown in Figure 2.4. The module has ten iron

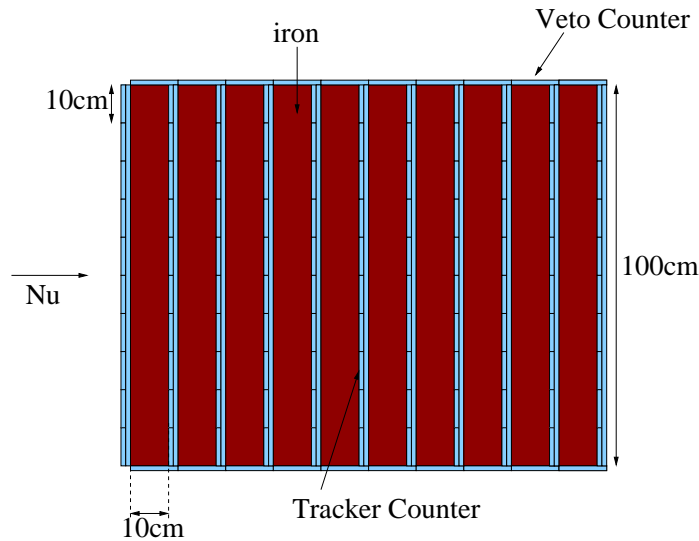


Figure 2.4: Sketch of the INGRID module.

plates with each dimension of  $1 \times 1 \times 0.1 \text{ m}^3$ . Thus, the total mass of iron serving as a neutrino target is 7.8 tons. The module has eleven scintillator tracking planes, named "tracker", with the dimension of  $1 \times 1 \times 0.03 \text{ m}^3$ . Each tracking plane consists of one vertical and one horizontal scintillator layers. Four veto planes of scintillators surround the sandwich structure. At this stage, we are developing two types of scintillators used for INGRID.

### Scintillator Design A

This design uses  $100 \times 5 \times 1.3 \text{ cm}^3$  scintillator strips produced at Fermilab. It is the same type of scintillator as that used for the K2K SciBar detector [6, 7]. Thus, the quality of this Fermilab scintillator is well established by the MINOS and K2K experiments, and it is worth noting that the Kyoto INGRID collaborators have significant experience with this scintillator on the K2K SciBar detector. The drawing of the scintillator is shown in Figure 2.5. In this design, the veto counters would consist of the same scintillator in 1.2 m lengths. The scintillator has a hole in the center to insert the 1 mm diameter WLS fiber for light collection. A photo-sensor, HPK MPPC, is used to measure the light at one end of the fiber. Since the length of fiber, 1 m, is relatively short compared with the attenuation length of the fiber ( $\sim 4 \text{ m}$ ), we expect to have enough light yield with one photo-sensor, and dark noise from the MPPC can be distinguished from true tracks by requiring multi-layer coincidences.

### Scintillator Design B

An alternative design uses  $100 \times 10 \times 1 \text{ cm}^3$  scintillator strip made at the Uniplast Factory at Vladimir in Russia [2, 3]. It is the same scintillator which is to be used in the SMRD [5]. Each tracker layer consists of ten  $100 \times 10 \times 1 \text{ cm}^3$  scintillator strips, and each veto layer consists of eight  $120 \times 18 \times 1 \text{ cm}^3$  strips. Scintillation light is collected by a 1 mm diameter wave-length-shifting (WLS) fiber, Kuraray Y-11 MS(200). The 2 m (2.5 m) long WLS fiber is embedded in the S-shape groove on the tracker (veto) scintillator as shown in Figure 2.6. Two photo-sensors, HPK MPPC's, are attached at both sides of the fiber to gain the light collection and to reduce the intrinsic noise of MPPC by taking coincidence of two.

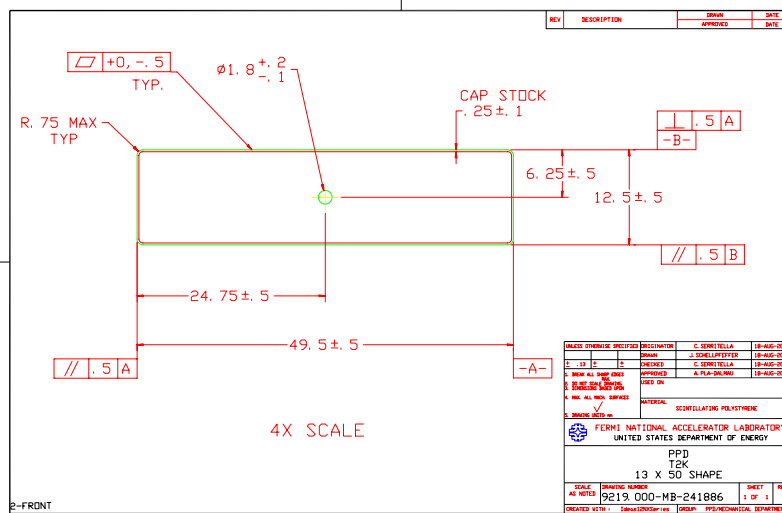


Figure 2.5: An engineering drawing illustrating the cross-section of scintillator to be produced at Fermilab.



Figure 2.6: A picture of a scintillator strip from the Uniplast Factory at Vladimir in Russia.

## 2.3 Expected Performance

We will measure the number of neutrino interactions occurring inside the INGRID detector to monitor the beam properties. To demonstrate the detector performance, we must determine the reconstructed event rate with a reasonable event selection, show that the detector is sensitive to beam properties, and finally demonstrate that systematic uncertainties and background events originating from neutrino interactions outside INGRID will not bias the reconstructed beam properties.

### 2.3.1 Basic Beam Property

In Figure 2.7, we show the neutrino flux at the position of the central INGRID module. A typical event

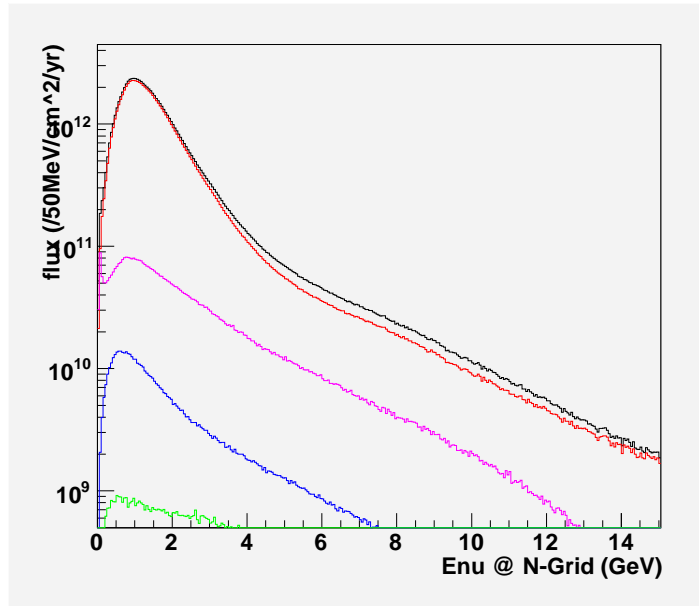


Figure 2.7: The neutrino flux at the INGRID position (on-axis) of  $\nu_\mu$ ,  $\bar{\nu}_\mu$ ,  $\nu_e$ , and  $\bar{\nu}_e$  listed in order of integrated flux from highest to lowest.

rate of muon neutrino interactions at the central INGRID module is  $0.54 \text{ events/ton}/(3.3 \times 10^{14} \text{ POT})$  where the  $3.3 \times 10^{14} \text{ POT}$  is a full proton intensity of one spill in T2K. The event rate at the far side INGRID module is about half of the rate at the center, and expected number of interactions per INGRID module is between two and four in each spill at the full T2K intensity.

The neutrino beam horizontal and vertical profiles in the vicinity of INGRID are shown in Figure 2.8 for the several neutrino energy ranges. One of the beam stability concerns that INGRID is to address is the change of the neutrino flux from a change in the proton beam position or angle on the target. As an example, Figure 2.8 shows the effect on the beam profile if the proton beam hits the off-center on the target by 3 mm. The change in beam position also causes changes in the beam as seen at Super-Kamiokande as shown in Figure 2.9. As can be seen, the effect of a 3 mm shift is significant, and INGRID is designed to measure such a beam shift.

### 2.3.2 Event Selection

The neutrino events in INGRID are identified by requiring hits in multiple layers of the tracking scintillator and removing events with hits in the veto scintillators. The contamination of background by neutrinos interacting outside of INGRID is expected to be less than one percent of the event rate. The event selection to obtain the neutrino interaction measurement is:

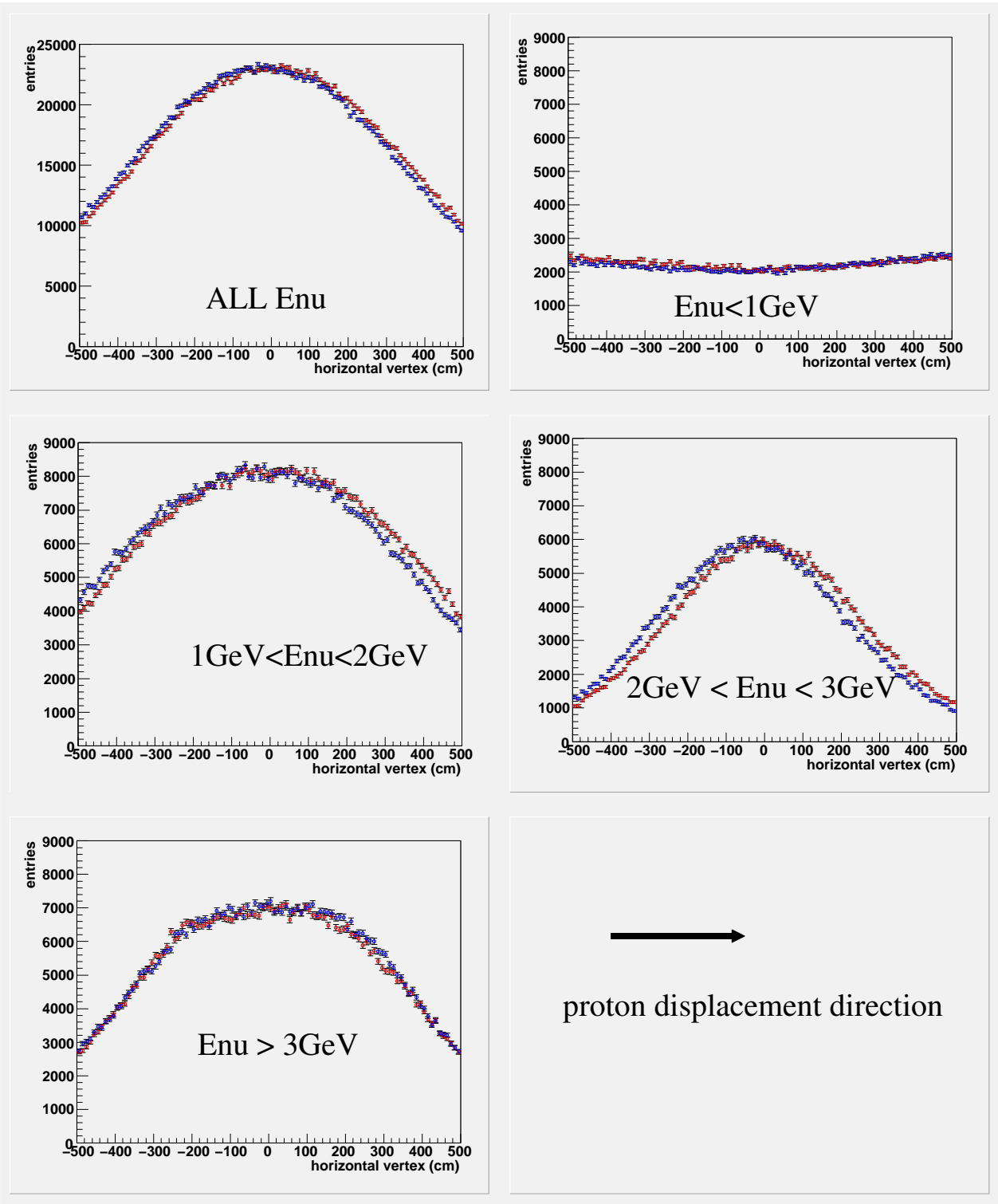


Figure 2.8: The neutrino beam profile distributions as a function of position from the beam axis at the location of the INGRID detectors. The red distributions show the profile when the proton beam hits the center of the target, and the blue distributions are for the case when the proton beam hits the target 3 mm off-center in the horizontal direction.

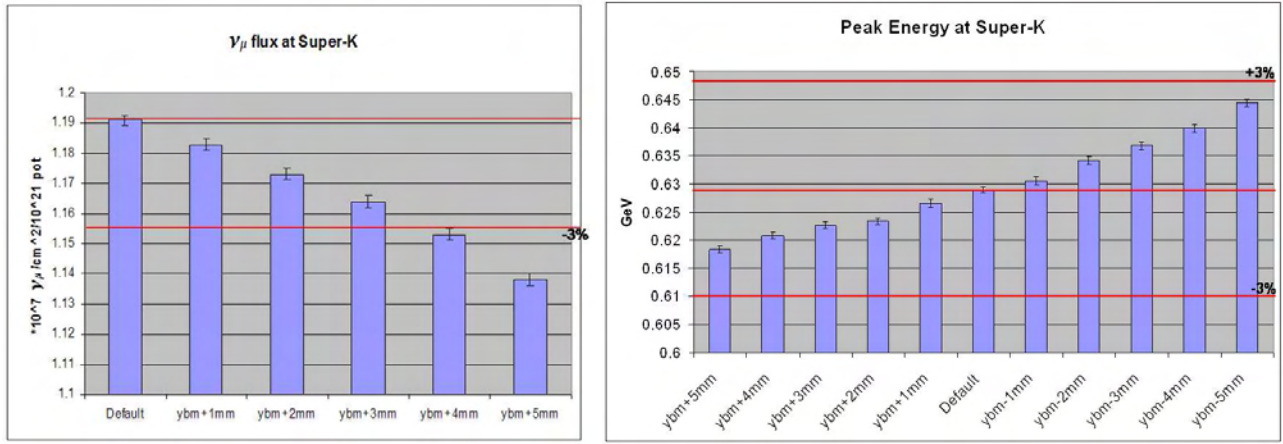


Figure 2.9: The effect on the neutrino beam flux (left) and peak energy (right) at Super-K when the proton beam position on the target is offset from its design position.

**Tracker cut:** events are selected with hits on at least three successive tracker planes in which both horizontal and vertical layers have hits.

**Veto cut:** events are rejected if a veto scintillator upstream of the selected tracker planes has an in-time hit. Such events have a high probability of being background interactions outside of INGRID entering from the direction of the incoming beam. There is little background from events originating downstream of INGRID, so no cut is applied on downstream veto counters.

**Optional  $\theta$  cut:** events could be required to have a track with the angle greater than 20 degree with respect to the neutrino beam direction. Such a cut would remove high energy events from the sample. High energy events are less sensitive to the condition of horns and the proton beam position on the target as shown in Figure 2.8.

Efficiencies of the event selections are shown in Table 2.1. Examples of the rejected and selected events are shown in Figure 2.10. Neutrino energy distributions of the events passing the selection criteria are shown in Figure 2.11. Before the optional  $\theta$  cut, we expect more than  $10^4$  observed events even in the far side module in a day with the full T2K intensity.

Module position (horizontal)	0.0m		1.5m		3.0m		4.5m	
	# events	eff.						
Generated	102227		95673		75857		51733	
tracker cut	36977	0.36	34590	0.36	26393	0.35	16723	0.32
veto cut	100593	0.98	94110	0.98	74420	0.98	50777	0.98
tracker+veto	36743	0.36	34273	0.36	26190	0.35	16557	0.32
+ $\theta > 20$ cut	14260	0.14	13810	0.14	10360	0.14	6570	0.13

Table 2.1: Summary of the event selection. The number of generated events are normalized for one day with the full T2K intensity ( $7.8 \times 10^{18}$  POT). The "eff" is the fraction of the event passing the selection.

### 2.3.3 Sensitivity to the beam direction

The sensitivity of INGRID to the neutrino beam direction is studied assuming the intensity of the commissioning period of T2K with a beam intensity of 1% of the design intensity. In this scenario,

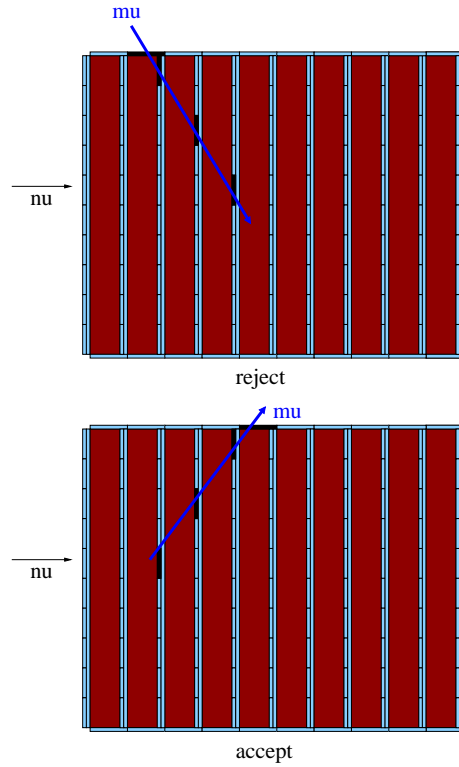


Figure 2.10: Examples of the rejected and selected events by the selection criteria including removal of events with upstream veto hits.

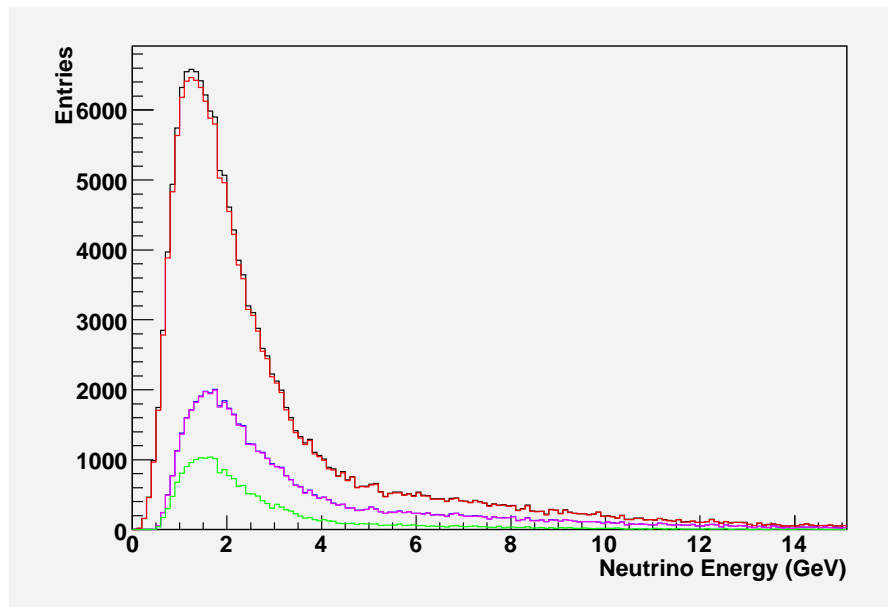


Figure 2.11: The neutrino energy distributions of the events passing the selection criteria. The black histogram is for the generated events, the red one is for the events passing the veto cut, the purple one is for the events passing the tracker + veto cuts, and the green one is with all cuts with the track angle greater than 20 degree.

one month running time corresponding to  $2.4 \times 10^{18}$  POT. After INGRID event selection, we would measure the beam profiles as shown in Figure 2.12 Before systematic uncertainties, the beam profile

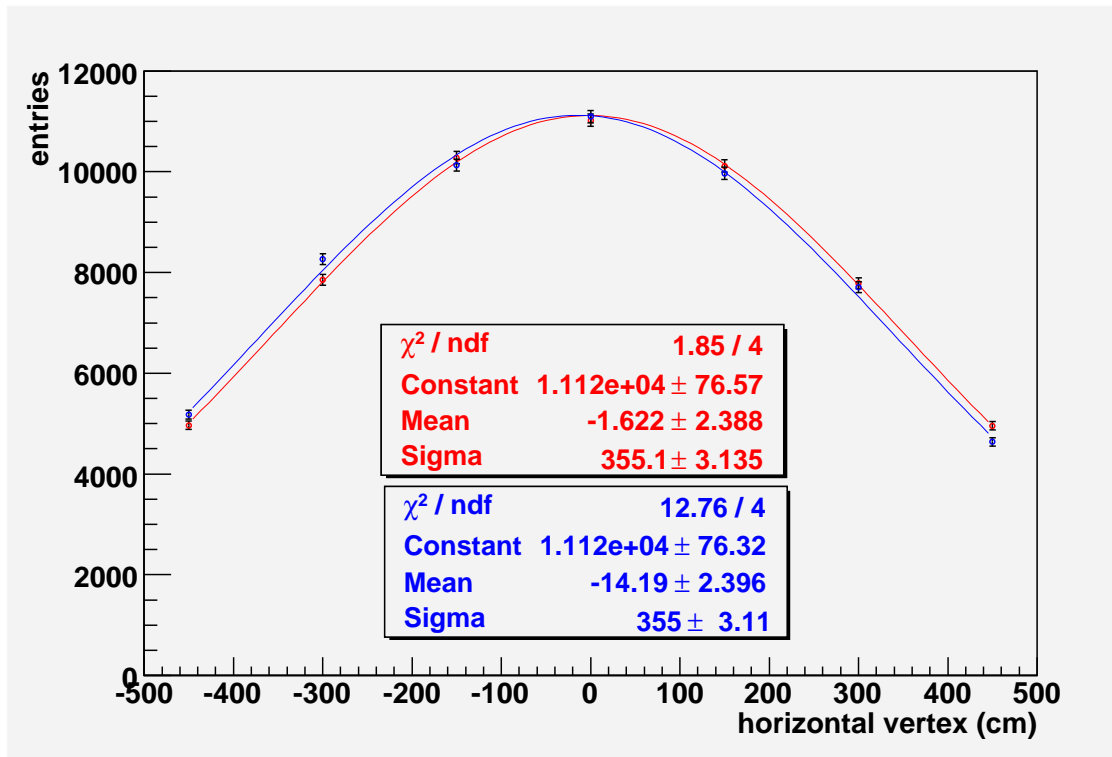


Figure 2.12: The reconstructed neutrino beam profile by the INGRID detector with one month of data at 1% of design intensity (the commissioning period). The measured error in the beam profile center at INGRID is 3.2 cm. A 3 mm beam shift would shift the beam center by  $\approx 10$  cm. The red dots and line show the profile if the proton beam hits the center of the target, and the blue ones show the effect when the beam hits the off-center of the target by 3 mm.

center at INGRID is measured to a precision of 2.3 cm. This corresponds to an error in the neutrino beam angle of  $\sim 0.1$  mrad, which is significantly better than the requirement of  $\sim 1$  mrad precision. In terms of a shift of the proton beam center, Figure 2.12 illustrates that a 3 mm beam shift results in a  $\approx 10$  cm beam shift, again much larger than the statistical uncertainty of the beam position determination during commissioning. The effect of the systematic errors on this conclusion is discussed below.

### 2.3.4 Systematic Uncertainty

In order to detect a change of the beam condition, such as the proton beam hitting position changes as mentioned above, the center of the neutrino beam profile must be measured with a precision of  $\sim 5$  cm. To achieve the goal, we find that the systematic error of the number of events in INGRID detectors must be controlled with an accuracy of 2 %. This in turn requires that the hit efficiency of scintillator should be understood with 0.5 % level.

In K2K SciBar detector, we achieve the 99.5 % hit efficiency of the scintillator plane. For the INGRID scintillator, we must have the same level of light yield of scintillator as that of K2K SciBar. Although we believe that we will have the similar quality of scintillators for INGRID, we are currently testing two types of scintillators. The goal of hit efficiency of scintillator plane for INGRID is 99.5 %, so that the systematic uncertainty from the scintillator efficiency will be small.

### 2.3.5 Background Issues

The event profile could be significantly altered from background events originating outside of the INGRID detectors. To study these background, we simulated the neutrino interactions occurring in the entire experimental hall. Figure 2.13 shows the plan view of the ND280 hall. Figure 2.14 shows

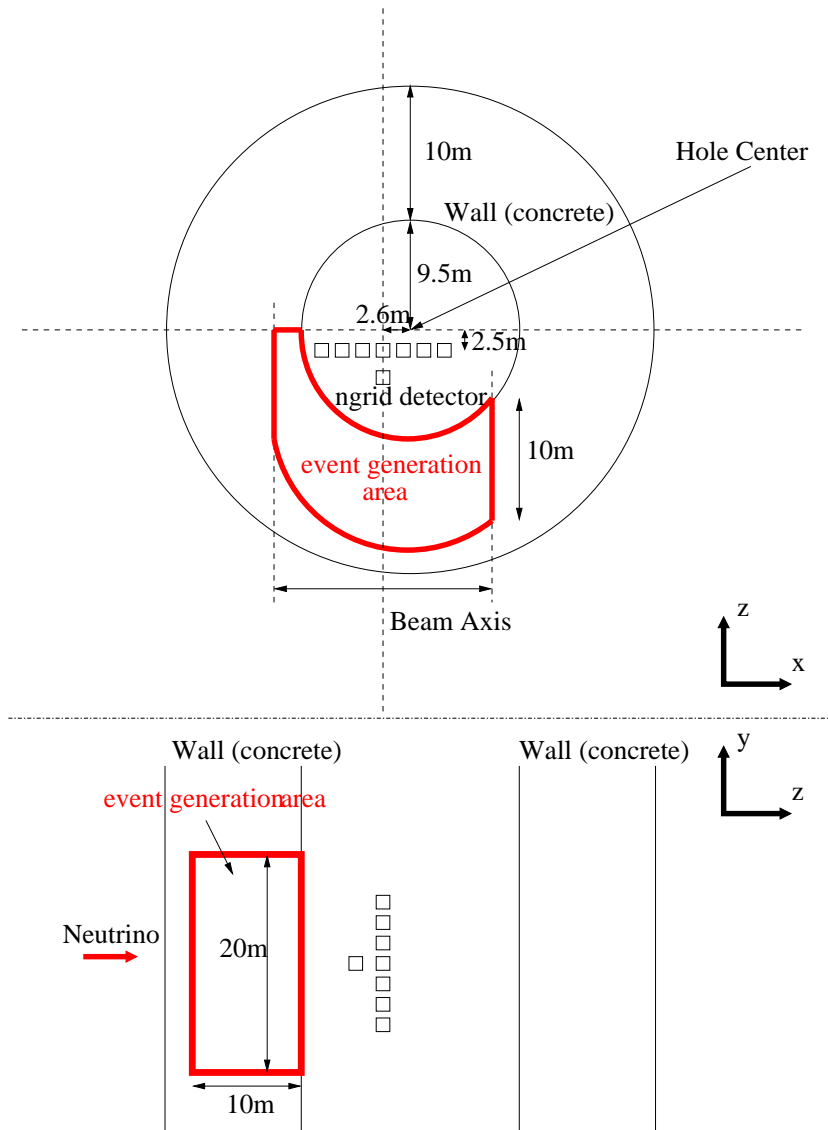


Figure 2.13: The top and side views of the ND280 experimental hall. The region where the neutrino interactions are simulated is shown.

the locations of neutrino interactions which cause a hit in the INGRID detector. We find that the most background hits come from the interactions in the upstream wall of the ND280 hall.

In Table 2.2, we show the number of remaining background events as normalized to 2 days of running with 1 % intensity of T2K. The simulation statistics was limited by the computing power. From this study, we find that the background events are less than 1 % of the signal events. Since a goal of INGRID is to understand the detector systematic less than 2 %, the background level is below the required level to control the systematic uncertainty from background. We show the event display of some remaining background events in Figure 2.15.

Since the previous background study is limited by MC statistics, we also study the background events with a partial simulation method. In the simulation, we only trace neutrons and  $\pi^0$  generated in neutrino interaction because the background particles entering INGRID without triggering the veto were found to be mostly neutrons and gamma-rays from the full simulation. With this method, we

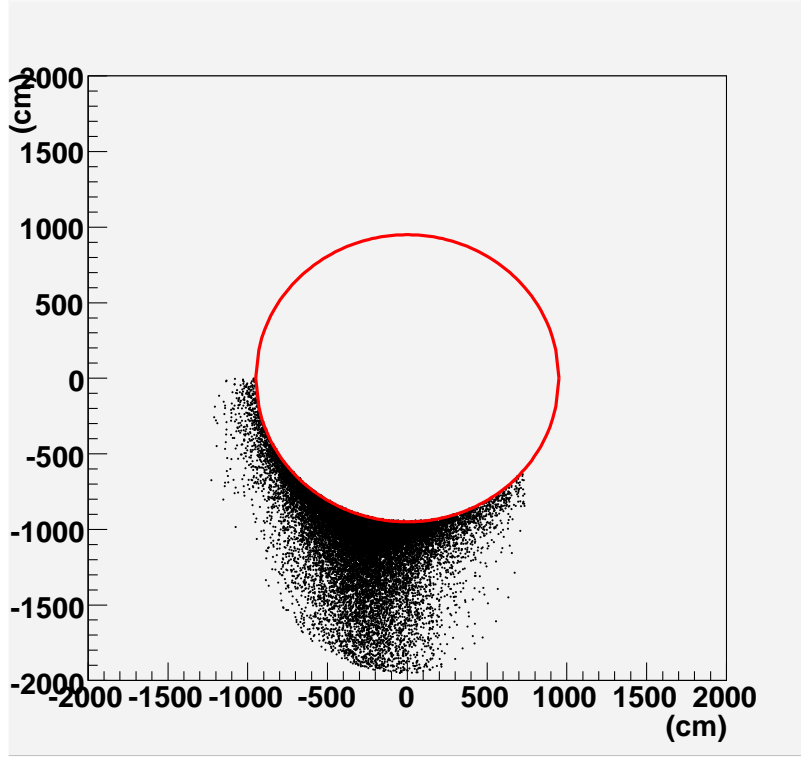


Figure 2.14: The locations of neutrino interactions which cause a hit in the INGRID detector.

Module position	-4.5	-3.0	-1.5	0.0	1.5	3.0	4.5
a hit	1330 (2.3)	1585 (1.6)	1622 (1.4)	1168 (1.7)	1503 (1.3)	1438 (1.7)	1206 (1.8)
tracker cut	399 (1.4)	539 (1.1)	629 (1.2)	483 (1.2)	585 (1.0)	510 (1.3)	392 (1.3)
+ front veto cut	97 (0.38)	127 (0.28)	114 (0.23)	137 (0.23)	105 (0.2)	106 (0.28)	84 (0.30)
+ all veto cut	0 (0)	2 (0.005)	2 (0.005)	0 (0)	2 (0.004)	1 (0.003)	0 (0)

Table 2.2: Summary of background events for the horizontal INGRID detectors. The number of background events are normalized to 2 days of running with 1 % of the design intensity of T2K. In parentheses, the ratio of the number of background events to the signal events are shown. "a hit" is the events which has a hit in INGRID, and "front veto cut" is the selection where only the most upstream tracker plane is used as veto. The standard event selection is shown as "+ all veto cut".

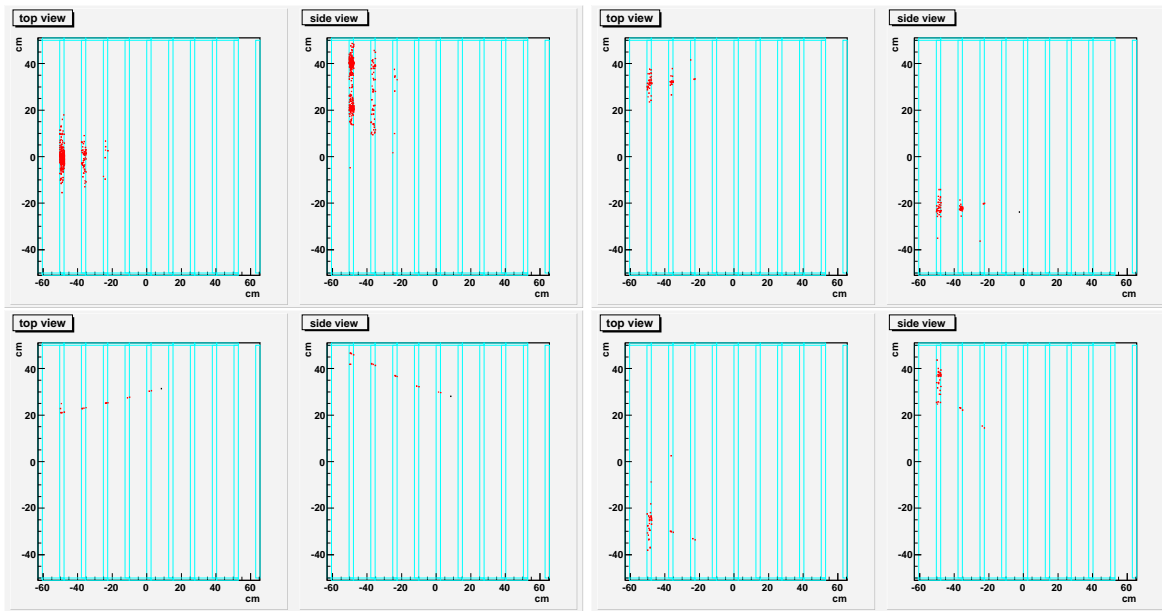


Figure 2.15: The event display of four remaining background events, with two views (horizontal and vertical) per event

simulate the background events corresponding to 200 days of 1 % T2K beam intensity. The fraction of the remaining background to the signal events is shown in Table 2.3 From this study, we find that

Module position	-4.5	-3.0	-1.5	0.0	1.5	3.0	4.5
Neutron Origin	0.07	0.04	0.07	0.09	0.08	0.09	0.09
$\pi^0$ Origin	0.11	0.05	0.04	0.04	0.04	0.06	0.03

Table 2.3: The fraction of background events to the signal ones (%). The background events are only generated from neutrons and  $\pi^0$ 's from neutrino interactions in the ND280 hall.

the fraction of the background events is an order of 0.1 % of the signal events. This gives us further confidence in our conclusion that the background from the ND280 hall should be small enough not to bias the INGRID beam profile measurements.

Other sources of background events we expect are from neutrons produced in the beam dump, accidental overlap of multiple events and from cosmic-rays. The neutron background is discussed in Section 2.6.1, and is found to be negligible. The accidental overlap events are suppressed by requiring the tight beam time window for each hit because every INGRID counter has timing information of  $\sim nsec.$ . In addition, an event loss by an accidental veto is also negligible because of good timing information. The accidental loss and event pile-up will be experimentally studied by looking at the hits outside of the time window. The cosmic-ray background events will be studied by looking at the timing because the cosmic-ray events are not synchronized with the accelerator (beam) timing.

## 2.4 Electronics and DAQ

For INGRID, we plan to use the common electronics of all the ND280 scintillator detectors that is being developed by the UK group. Although INGRID has an independent DAQ system from the off-axis detector, the design is common. The details of this system are described in reference [8].

The common electronics consists of TFB (Front-End electronics card) and RMM (Back-End electronics board) as described in the reference [8]. Since one TFB can handle up to 64 channels, we need

8 TFBs in each module, and 126 (112) in total for Design A (Design B). Three or four RMM boards will be required for the INGRID system. If we build the two additional “diagonal” modules, we would need 144 (128) TFBs and four or five RMMs for Design A (Design B).

The specifications of the INGRID detector are summarized in Table 2.4.

## 2.5 Mechanical structure

The INGRID detector will be installed in the 280m hall on the B2 and B3 floors. Beside gravity, the important criterion for the design of the support structure is the anti-seismic specifications. The vertical tower should in particular support roughly 60 tons for a total height of 12 meters. An important issue will also be the space available in the pit for the installation and the maintenance of the modules.

The detector is built as a modular system with sixteen identical modules. Those modules are aligned in a cross shape configuration with seven horizontal modules and seven vertical modules. Two additional modules placed in the diagonal account for shape asymmetry of the beam. The mechanical structure of the detector can be separated in four independent sub-structures related to the modularity of the system. They are the tracking planes, the VETO planes, the mechanics of the modules and their supports.

### 2.5.1 Preliminary design

#### Tracking plane

The tracking planes are built as fully functional, integrated units that can be tested prior to integration in the module. Each tracker plane includes 20 (design A) scintillator strips, each equipped with a WLS fiber and a MPPC photo sensor. Depending on the supplier that will be chosen (Fermilab or Uniplast), the dimensions of the scintillator strips can be different, which impacts the number of strips per plane and the thickness of the planes. The flexibility of current CAD tools allows an easy update of the design and the mechanical structure will in any case be similar.

The main constraints for the design will be given by the interfaces between the front-end electronics, the photo sensors and the scintillator strips. Developments are in progress to finalize those interfaces. Figure 2.16 shows preliminary conceptual designs for the scintillator strip assembly and tracking plane assembly. The fiber is held by one plastic sleeve at each end, bonded inside holes machined in the plastic scintillator. The sleeves also serve as alignment pins when assembling the layers. The optical coupling between the photo sensor and the fiber is an air gap. A spring provides the contact to keep the gap minimum.

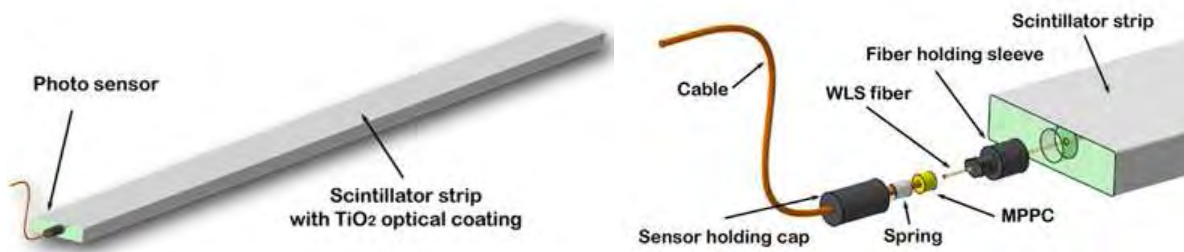


Figure 2.16: Scintillator strip assembly

Figure 2.17 shows the layout of the scintillator strips in a X-Y configuration and possible positions for the front end electronic boards. The cables of the photo sensors are connected to the PCB placed at the center of the layer. Aluminum housing will be used to protect the strips and the circuit boards. This sealed enclosure will also provide protection against outside light. A black anodizing is foreseen as a

INGRID system	# modules	7 + 7 (+4)
Module	Sandwich structure + Veto surrounding	11 tracking planes + 10 iron plates 4 veto planes
Iron	Dimension of plate #plates of module Weight of iron module	$100 \times 100 \times 10 \text{ cm}^3$ 10 7.8 ton
Scintillator	# tracker plane / module # veto plane / module	11 (22 layers) 4
Design A	<b>Tracker Part</b> Dimension of scintillator # scintillators / layer # scintillators / module [all modules] Dimension of the WLS fiber # MPPC's / module [all modules]	$100 \times 5 \times 1.25 \text{ cm}^3$ 20 440 [6160 (+880)] 1 mm $\phi \times 1 \text{ m}$ 440 [6160 (+880)]
	<b>Veto Part</b> Dimension of scintillator # scintillators / plane # scintillators / module [all modules] Dimension of the WLS fiber # MPPC's / module [all modules]	$120 \times 5 \times 1.25 \text{ cm}^3$ 30 120 [1680 (+240)] 1 mm $\phi \times 1.2 \text{ m}$ 120 [1680 (+240)]
	<b>TOTAL</b> # MPPC's Total length of WLS fibers # TFB's # RMM's	7840 (+1120) 8.176 (+1.168) km 126 (+18) 3 ~ 4 (+1)
Design B	<b>Tracker Part</b> Dimension of scintillator # scintillators / layer # scintillators / module [all modules] Dimension of the WLS fiber # MPPC's / module [all modules]	$100 \times 10 \times 1 \text{ cm}^3$ 10 220 [3080 (+440)] 1 mm $\phi \times 2 \text{ m}$ 440 [6160 (+880)]
	<b>Veto Part</b> Dimension of scintillator # scintillators / plane # scintillators / module [all modules] Dimension of the WLS fiber # MPPC's / module [all modules]	$120 \times 18 \times 1 \text{ cm}^3$ 8 32 [448 (+64)] 1 mm $\phi \times 2.5 \text{ m}$ 64 [896 (+128)]
	<b>TOTAL</b> # MPPC's Total length of WLS fibers # TFB's # RMM's	7056 (+2016) 7.28 (+2.08) km 112 (+16) 3 ~ 4 (+1)

Table 2.4: Summary of the INGRID specification. The numbers in parentheses are for the possible two additional “diagonal” modules.

surface treatment to more efficiently protect the photo sensors and scintillator strips against unwanted light. Surfaces will be spared to allow electrical continuity, for an efficient grounding, if required.

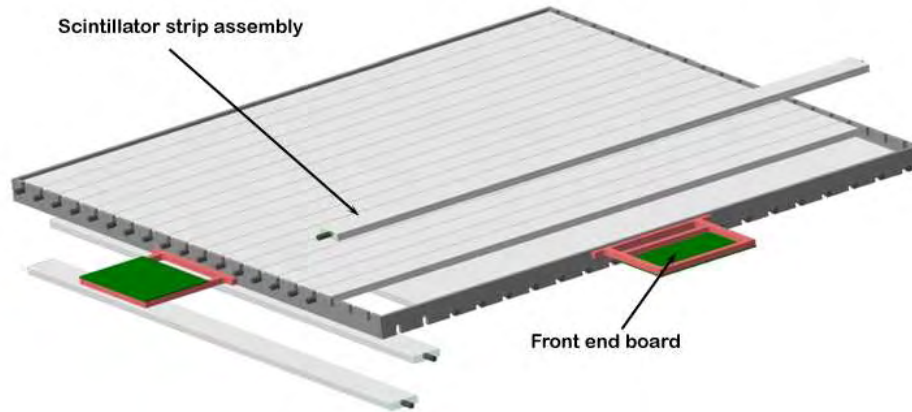


Figure 2.17: Tracking plane assembly

### Veto planes

The mechanical design of the VETO counters will be similar to the one developed for the tracking plane but with different dimensions. The same detector techniques are used namely scintillator strips with WLS fibers and MPPC.

### Mechanical structure of the modules

The steel plates provide the target material for the neutrinos. They are the main component of the mechanical structure of the INGRID modules. The plates will be assembled on two support I beams. Bolted corners will provide the attachment of the plates onto the beams. The dimensions of the plates are  $1000 \times 1000 \text{ mm}^2$  and their thickness 100 mm. The amount of target material between the tracking planes needs to be known with a precision better than 1%. This parameter defines the required precision for the thickness of the plates.

The plates will be made of standard structural steel S235JR (carbon-manganese steel). Raw material is produced in accordance to EN 10025 specifications. The plates will be cut from hot-rolled material and machined to the required dimensions. The design driver for those plates is to minimize the machining, to save on cost. Machining is needed for transverse dimensions and holes for connection. Thickness and flatness tolerances on hot-rolled plates might not meet the requirement which means that 100 mm dimension could also require machining.

The structure shown in Figure 2.18 is designed so that it can be fully mounted before the integration of the tracking planes. Both components are manufactured independently and share minimum interfaces. Guiding rails attached to the steel plates will allow an easy insertion (or removal) of the planes inside the structure. The position of the tracking planes will be secured by fasteners.

### Support structures for the modules

Depending on the position of the modules, horizontal, vertical or diagonal, different type of support structures will be used. The structures will be fabricated from welded standard industrial beams. Bolted connection will be used for bracing members where applicable.

The support structures for the horizontal modules will be quite simple. For the vertical modules, a more complex design is required. Seven modules need to be stacked with a 1.5 meter pitch to form

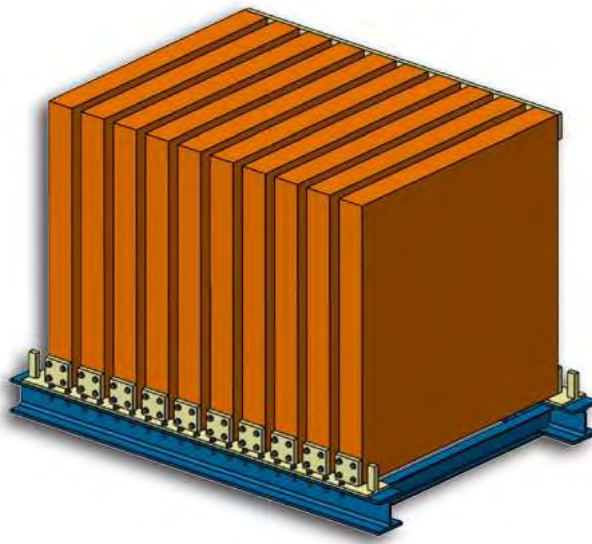


Figure 2.18: Mechanical structure of the INGRID modules

the vertical harm of the detector. This means a 14 meters high tower able to support around 60 tons and withstand seismic loads in case of an earthquake.

The tower will be built with seven identical structures bolted together as shown in Figure 2.19. The module will be installed prior to lift and stack the structures. This operation will be done with the 10 ton crane of the facility. The four bases of the tower will be anchored on B3 floor. Requests for additional attachments on B2 and B1 floors have been made. The design of the pit will account for those additional connection points.

## 2.5.2 Structural analysis

### Requirements

The load on the mechanical structures of the INGRID detector is mainly gravity but, since the detector will be installed in a site where seismic hazard is high, the structure must be designed to resist earthquake ground motion. NHERP recommended provisions for seismic regulations for new buildings and other structures will be used as a guideline document for the structural analysis of the support structures of the detector.

### Analysis

The tower assembly is a structure very sensitive to any transverse acceleration because of its height and the total mass of the stacked modules. A detailed structural analysis is planned to verify the design of this tower. It will include a response spectrum analysis and local stress analysis of the connections between the beams and the attachment of the bases of the columns on the ground. The strength of the other support structure will be checked with an equivalent lateral force procedure. The preliminary results of the ongoing analysis are presented in this chapter.

### Modal analysis of the tower

A modal analysis of the structure has been performed to evaluate its sensitivity to seismic loading. The result is shown in Table 2.5. Figure 2.20 shows the fundamental mode of the structure. As expected, it is a bending mode. A torsion effect, due to the lack of bracing on one of the sides of the support structures, can also be noticed. The fundamental frequency of the structure is around 12 Hz

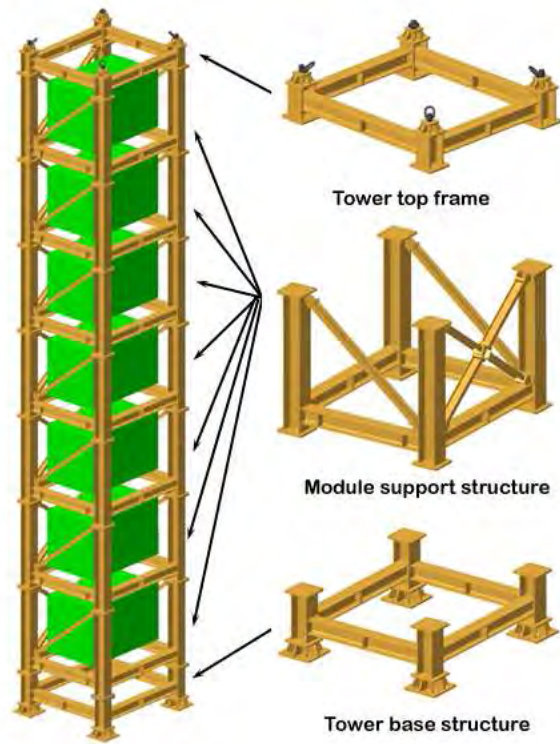


Figure 2.19: Support tower for vertical module



Figure 2.20: Fundamental mode of the tower

Mode #	Frequency (Hz)	Generalized mass (kg)	Type
1	11.9	14187	Bending Y
2	13.6	22309	Bending X
3	18.1	9457	Torsion
4	21.0	26596	Bending Y
5	21.6	4147	Torsion

Table 2.5: Mode and frequency of the structure.

### Static analysis of the tower

A static analysis has been performed to evaluate the interface loads between the tower and the pit so that proper anchor frames can be designed. In addition to the gravity load, a combination of the expected seismic acceleration (0.5 g) plus 40% along the perpendicular direction has been taken into account for the analysis. The standard recommendation of 30% has been increased to be more conservative. The main transverse load has been applied along Y direction, which corresponds to the worst case, due to the geometry of the tower.

Table 2.6 provides a summary of the results. Shear and tensile loads are given for each of the attachment points. The numbers are the total value per column base. The average shear and tensile stress are calculated assuming an evenly distributed load on 8 M24 high strength bolts of each bearing plate. The margins of safety have been calculated with proper factors of safety.

Attachment point	Shear load (N)	Tension load (N)	Average shear Stress (Mpa)	Mean tensile Stress (MPa)	Margin of safety
B3 Floor 1	57521	298406	20.37	105.67	1.46
B3 Floor 2	84000	115787	29.75	41.00	5.34
B3 Floor 3	76183	653666	26.98	231.47	0.12
B3 Floor 4	45295	412638	16.04	146.12	0.78
B2 Floor 1	28433	45764	10.07	16.21	15.04
B2 Floor 2	44174	56545	15.64	20.02	11.99
B1 Floor 1	18476	30796	6.54	10.91	22.84
B1 Floor 2	34771	44953	12.31	15.92	15.33

Table 2.6: Result of static analysis

### 2.5.3 Manufacturing plan

The manufacturing of the components of the INGRID detector will be a shared responsibility between the KYOTO University and LLR. The Japanese groups will be in charge of the procurements of the components of the scintillators, fibers and MPPC detectors. The LLR laboratory will be in charge of the procurement of all the mechanical parts of the modules and their support structures.

#### Tracking planes assemblies

The assembly flow-charts are presented in Figure 2.21. They correspond to the design that is been previously described, which is still in a conceptual form.

At the level of the scintillator strip assembly, only lot acceptance test should be performed. A good uniformity of the characteristics of the extruded scintillator strips is expected.



## Mechanical assembly

All the components of the mechanical structure of the INGRID modules will be delivered to LLR, where they will be assembled. Receiving inspection should be limited to the verification of the conformity of the materials. Once assembled, the structures will be mounted on their associated support structure to be shipped as a unit to the facility in Japan. Standard 20' marine containers are planned to be used for the shipping. They should be able to accommodate each 2 assembled mechanical structures with their support.

The integration of the tracking planes will be a simple operation. The planes will be inserted between the steel plates and secured with fasteners. Interconnect cabling will be performed once all the planes are in place. The VETO counters will be fastened to the sides of the module. Proper attached parts still have to be designed. The counter on the bottom surface will be inserted between "I" beams supporting the target plates. Full coverage of the surface is not possible but maximizing the surface is a design driver.

The current planning for the mechanical activities is given in Figure 2.23.

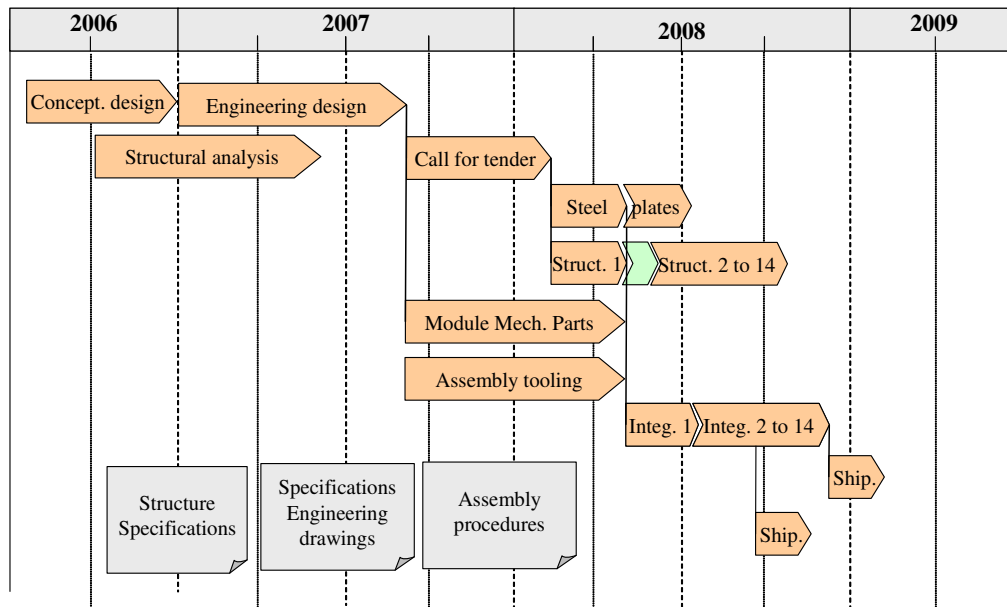


Figure 2.23: Planning for mechanical structures

## 2.6 Detector technology R&D

For the detector construction, most of the detector technology adopted in INGRID are well established except for the photo-sensor, MPPC. The details of the photo-sensor R&D are described in Ref. [9, 10].

The Design A scintillator is the same scintillator used in K2K-SciBar. In K2K, we measured the light yield of Fermilab scintillator to be 18.7 photo-electrons per centimeter for a minimum ionizing particle [6]. After correcting the different fiber diameter in INGRID, we expect 12 photo-electrons per centimeter INGRID. With this high light yield, an inefficiency of the scintillator is less than 0.5 %, again satisfying the design requirement or INGRID. The FNAL Design B scintillator will first be produced at Fermilab in March 2007.

Scintillators made at the Uniplast Factory at Vladimir in Russia are used in the Design B. The scintillator provides 80% of the light yield of Bicron BC408. The scintillator was tested by the pion beam at KEK-PS [10] to demonstrate that this scintillator with WLS fiber meets the INGRID requirements.

The WLS fiber planned for INGRID is KURARY Y-11 MS(200), which is same fiber used in K2K-SciBar. We plan to purchase the fiber in 2006.

The photo-sensor, MPPC, readout electronics, and DAQ system are developed as a common effort by the ND280 group. The status of developments are described in other documents [10, 8].

### 2.6.1 Test of the prototype INGRID module at the K2K neutrino beam.

In order to prove the concept of INGRID, a first prototype detector was built and installed in the K2K neutrino beam as shown in Figure 2.24

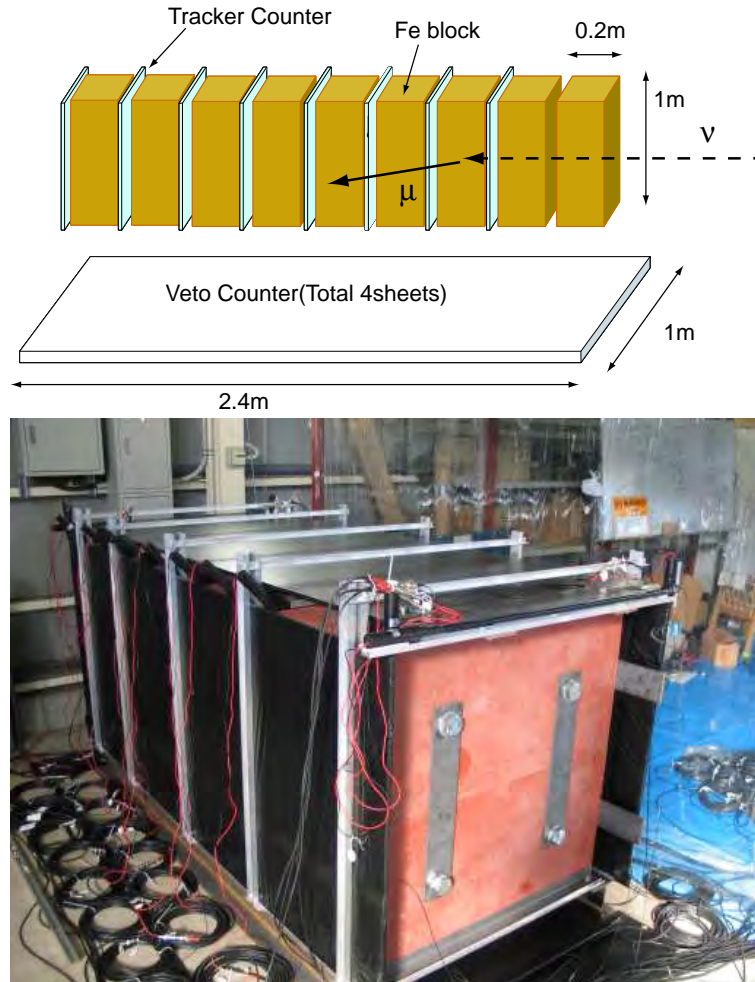


Figure 2.24: The design of prototype INGRID detector installed in K2K (top) and the picture of the prototype detector. This detector has 20 cm thick iron plates with non-segmented scintillator trackers.

The prototype detector differed substantially from the current INGRID design because of its thick iron plates (20 cm) and non-segmented tracker scintillators. Data from the prototype detector was very limited because of the early termination of K2K due to a failed horn.. With the small amount of neutrino data, we observed many beam-correlated background, most of which are originated by neutrons coming from the proton target or from the beam dump. The observed number of hits in the tracker scintillator of the prototype in the K2K neutrino beam is shown in Figure 2.25

However, by requiring at least two in-time hits in the tracker counters and no hit in the veto counter, we found a dramatic reduction in background events, with only two events surviving in-time with the beam. Figure 2.26 show the remaining events in a wide timing window around the beam time. Although we observed the consistent number of events with the expected neutrino events, we could not conclude that we observed the neutrino events because of low statistics in the large number of events arriving at times after the beam window.

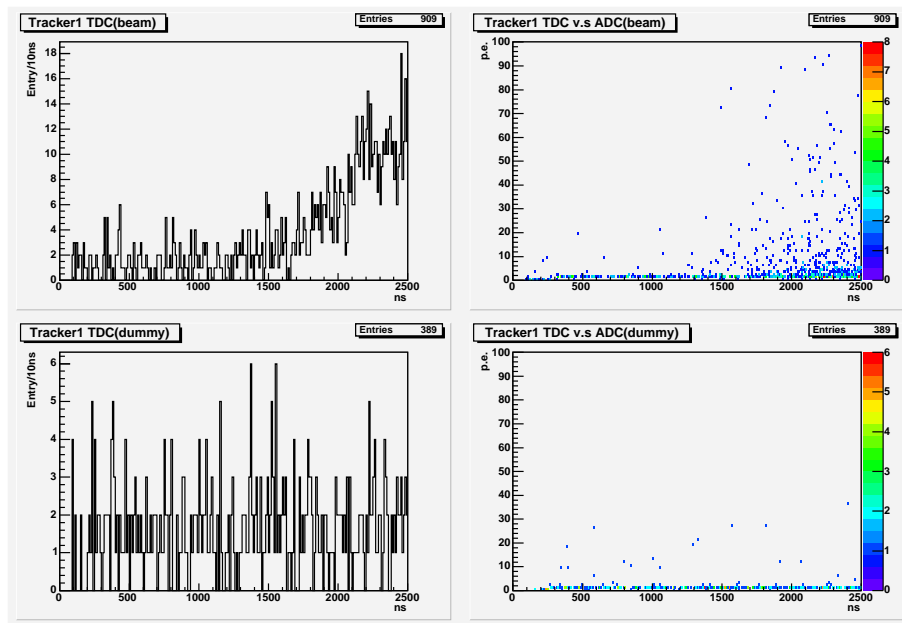


Figure 2.25: Charge and timing information of hits observed at the tracker scintillator of prototype INGRID in the K2K neutrino beam. Upper plots are taken with the neutrino beam, and the lower plots are taken by the random trigger without the beam. The left plots are the timing distributions where the beam interval is between 800 and 1900 nsec. Note the increase of events with time which results from backgrounds from neutrons created in the K2K beam dump. The right plots are the scatter plots of the time versus the charge.

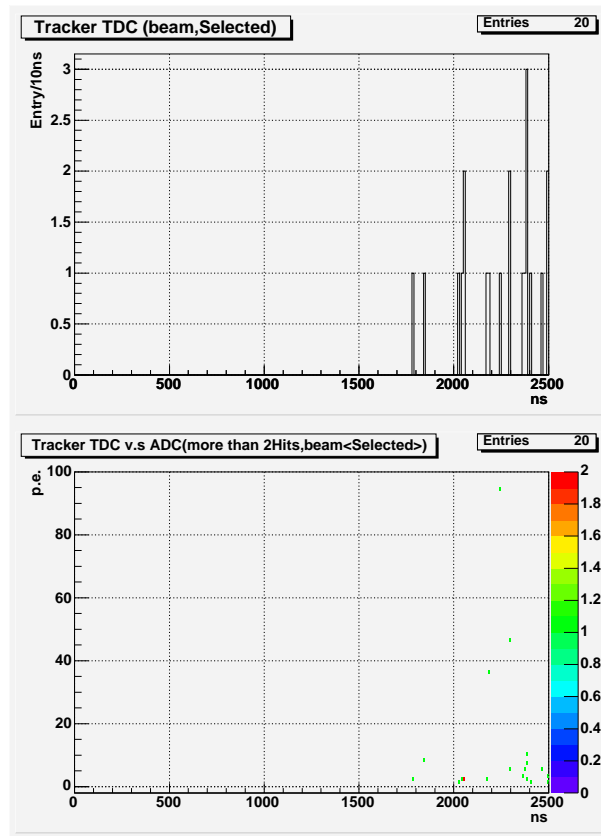


Figure 2.26: The charge and timing information of hits of events passing the selection criteria mentioned in the text. The upper plot is the timing distribution where three events are observed in the beam window between 800 and 1900 nsec. The lower plots are the scatter plots of the time versus the charge.

The test of the prototype detector taught us the following lessons which were applied to the INGRID design:

- The detector design must be more robust against background events. In the real design of INGRID, we have two scintillator layers per one tracker plane with segmentation. Thus, we can take a coincidence at each tracker plane to eliminate random hits. Another advantage of segmentation is that we can reconstruct the track, and measure the vertex position where the neutrino interaction happens. The vertex distribution is useful to identify the neutrino interaction and eliminate the background events.
- A thin iron thickness of INGRID has an advantage to the prototype because of higher efficiency for neutrino events.
- In T2K, we expect the better signal to background ratio by three orders of magnitude as follows. The neutrino flux at INGRID is three orders of magnitude higher than that at the K2K prototype because of the higher beam power of T2K and the different location of the detector. (In the K2K test, the prototype detector was installed at the ground level (off-axis) where the neutrino flux was lower by a factor of ten than the on-axis.) In addition, the number of background level in T2K is expected to be same or lower than that of K2K with because the number of neutrons exiting from the beam dump or target in T2K will be similar to that of K2K\* and because detector position in T2K is much deeper than the surface position for the K2K test.

## 2.7 Calibration systems

The calibration of the INGRID detector will be important for the performance of the detector such as for example tracking efficiencies. A combination of two or three techniques of calibration will be used:

- light injection for a selected sample of scintillates to check short and long variation during data taking
- cosmic-ray muons triggered by the veto counters
- test beams for scintillator proto-types

## 2.8 Construction and installation schedule

The detailed procedures for assembling the modules and the installation of INGRID in the 280m hall are still in progress. The general features are nonetheless already established. As already mentioned, the passive parts of the detector, iron plates and the corresponding support structures, will be constructed and assembled in France before shipping to JPARC. The active parts, scintillators, fibers and MPPC, will be assembled in Kyoto. The sixteen modules will be finally assembled at JPARC before the installation of INGRID in the pit.

The different active components of the detector will be tested before shipping to JPARC. It is nonetheless important to perform tests before the final installation of INGRID. Damages to scintillators, MPPC detectors and front-end electronics may occur during transportation. Assembly work and testing at JPARC should be kept to a minimum in order to achieve rapid installation of INGRID. This procedures will involve very close coordination between the Japanese and the French groups. A dedicated manager will be appointed for the organization and supervision of the on-site integration and installation.

---

\* The dump design in both K2K and T2K was set by the same criteria for allowable radiation levels.

Installation of INGRID in the 280m hall of the horizontal part (B2 floor) and, in particular, the vertical part (B3 floor) of the detector will be coordinated with installation of the off-axis detectors (B1 floor). The horizontal modules will be first moved down to B2 floor with the 10 tons crane. An air powered load moving system will be used to move the modules with their support structures on B2 and bring them into position. The procedure for the alignment is not defined yet. The requirements for the floor surface on B2 have been taken into account in the design, so that the load moving system can be used. The modules on the vertical arm of the detector will be directly stacked with the crane. A temporary platform will have to be installed to bolt the structures together as they are placed one on top of the other. The platform will also serve to deal with the cables and services. Support rails or equivalent will be used to support them.

The schedule of mechanical parts is shown in Figure 2.23. The schedule of active components and electronics is summarized below.

**Year2007 – the first half –**

- Selection of the scintillator based on the lab test and cost.
- Mass production of the WLS fibers.

**Year2007 – the second half –**

- Make the prototype of the tracker plane.
- Make the prototype of the veto plane.
- Mass production of the scintillators.
- Test the prototype of readout electronics.

**Year2008 – the first half –**

- Mass production of the photo-sensor
- Mass production of the tracker planes
- Mass production of the veto planes.
- Test the production version of readout electronics.

**Year2008 – the second half –**

- Mass production of the readout electronics.
- Mock-up test of one INGRID module
- Prepare the installation of INGRID module to the ND280 hall.

# Bibliography

- [1] T2K-ND280 group, Conceptual Design Report (unpublished), 2005.
- [2] Yu. G. Kudenko *et al.* Nucl. Instrum. Methods **A469**, 340-346 (2001)
- [3] O. Mineev *et al.*, NIM, A494 (200) 362-368; physics/0207033.
- [4] N. Yershov *et al.*, physics/0410080.
- [5] T2K-ND280 group, Technical Design Report of the SMRD detector (unpublished), 2006.
- [6] K. Nitta *et al.*, The K2K SciBar detector, Nucl. Instrum. Methods **A**, 535 (2004)147-151
- [7] H. Maesaka, The K2K SciBar Detector, Nucl. Phys. B (**Proc. Suppl.**) **139**, 2005 (289-294)
- [8] T2K-ND280 group, Technical Design Report of the Electronics and DAQ for the ND280 scintillator detector (unpublished), 2006.
- [9] M. Yokoyama *et al.*, "Development of Multi-Pixel Photon Counters", physics/0605241
- [10] T2K-ND280 group, Technical Design Report of the new photo-sensor for the ND280 scintillator detector (unpublished), 2006.

# Chapter 3

## The magnet

### 3.1 Description

The UA1 magnet is presently stored at CERN, and the CERN Council has approved its donation to the T2K experiment. The magnet will provide a horizontal uniform field of 0.2 T, perpendicular to the neutrino beam direction over an inner volume of  $88 \text{ m}^3$ . A schematic drawing of the magnet, placed on its support structure, is shown in Figure 3.1.

The magnet consists of two halves which are mirror symmetric about a vertical plane containing the beam axis. Each half consists of 8 C-shaped flux return yokes, made of low-carbon steel plates. The total weight of the yoke is 850 tons. The external dimensions of the magnet are 7.6m(L)x6.1m(H)x5.6m(W). Figure 3.1 shows the two halves of the magnet apart, to make visible the coils inside the magnet. The magnet will be in that open position when assembling the inner detectors. Normal operation will be with the two halves in contact. The coils consist of aluminum conductors of square cross-section ( $54.5 \times 54.5 \text{ mm}^2$ ). The peculiar shape of the coils, forming a hole along the magnet axis, was specifically designed to accommodate the beam pipe in the UA1 experiment. The coils will provide a uniform horizontal field, orthogonal to the beam axis. The magnet was originally designed to operate with a current of 10 kA, providing a field of 0.67 Tesla, with a power consumption of 6 MW. We propose to operate the magnet with a current of 3 kA corresponding to a field of 0.2 T and to a reduced power consumption of 0.6 MW. We note that the Nomad experiment provided excellent measurements of neutrino interactions with a field of 0.4 T, in a neutrino beam with average energy of 30 GeV, i.e. 40 times higher than for T2K.

The Nomad Collaboration, whose help for the use of the magnet we would like to acknowledge, has also provided us a program to compute the field map. It turns out that the field is quite uniform in intensity and direction. Transverse components larger than 1%, as well as variations of intensity exceeding 2%, are only present in regions at distances of few tens of centimeter from the coils. A more detailed description of the magnet is given in the following, starting with a list of relevant parameters presented in Table 3.1.

The 16 C's forming the yoke have all a very similar structure. Figure 3.2 shows that the C is segmented in 12 azimuthal sections. Each section is made of 16 iron plates 5 cm thick, with 1.7 cm air gap between plates. Apart from the corners, the plates at different depth have the same size. Their dimensions are  $0.88 \times 0.90 \text{ m}^2$  (vertical plates) or  $0.88 \times 0.70 \text{ m}^2$  (horizontal plates). In the UA1 experiment the gaps between plates were instrumented with scintillators and the iron yoke acted as hadron calorimeter. We plan to put scintillators in the gaps to identify laterally escaping muons and to measure their range (Side Muon Range Detector). This is described in Chapter 7.

The coils are made by aluminum bars with  $5.45 \times 5.45 \text{ cm}^2$  square cross-section, with a central 23 mm diameter bore. Demineralised water is pumped through the inner cavity of the conductor to provide cooling. The coils are composed by individual "pancakes" which will be connected hydraulically in parallel and electrically in series. The total thickness of the coils is 20 cm.

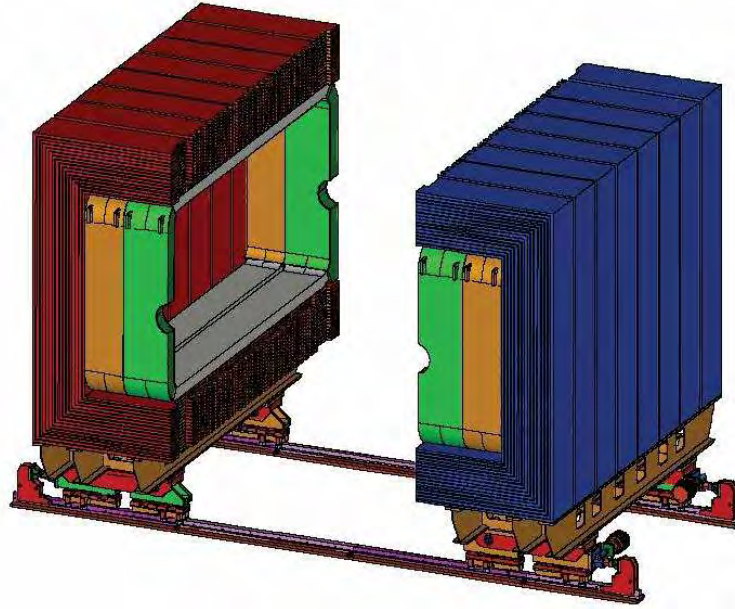


Figure 3.1: The UA1 magnet.

Magnetic field	0.2 T (maximum field 0.67 T)
External dimensions	7.6 m(L), 6.1 m(H), 5.6 m(W)
Internal dimensions	7.0 m(L), 3.6 m(H), 3.5 m(W) (Inner volume $\sim 88m^3$ )
Iron yoke weight (16 C)	850 tons
Coils material	Aluminum
Number of turns	208
Number of double pancakes	26
Total conductor weight	31 tons
Ohmic resistance (at $T = 40^0 C$ )	0.0576 $\Omega$
Inductance	0.36 H
Nominal current	3000 A (for $B = 0.2 T$ )
Power dissipation	0.6 MW (for $B= 0.2 T$ )
Cooling water flow in coils ( $\Delta T = 10^0 C$ )	15 liter/sec

Table 3.1: Specification of the magnet.

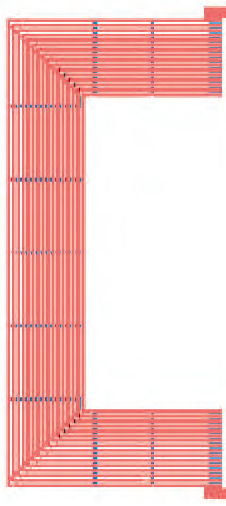


Figure 3.2: Lateral view of one of the 16 C's composing the iron yoke.

## 3.2 Installation

The magnet will be installed in the experimental area onto the original supporting structure, as schematically shown in Figure 3.1. The two halves of the magnet (8 C per side) will be mounted onto iron beams, parallel to the neutrino beam direction. Two groups of coils will be fixed inside each half of the yoke. The beams are mounted onto carriages which allow to move apart the two halves along rails orthogonal to the beam direction. The movement will be controlled by separate motors on the two sides. It will be possible to move the two halves apart by 5.5 meters, so to guarantee easy access for the assembling of the inner detector (the maximum transverse dimension of the inner detector is 3.5 meters).

For the assembling of the inner detector inside the magnet, we plan to adopt a technique similar to that of the NOMAD experiment, but to use a newly designed framework, adapted to our detector. With the exception of the electromagnetic calorimeter, all other detectors will be assembled inside a carbon fiber frame ("basket") with approximate dimensions of  $6.5 \times 2.6 \times 2.5 \text{m}^3$ . A preliminary design of the basket with its supporting structure is shown in Figure 3.3. The basket will be completely open at the top, to allow the insertion of the various detectors. Two short beams will be fixed at the center of the two faces of the basket perpendicular to the beam axis. The short beams will be connected outside the magnet to a structure fixed on the floor, which holds the basket. The beams will connect the basket to the external support structure passing through the holes in the coils, originally designed to allow the passage of the beam pipe. When opening the magnet, the C's and the coils move apart, while the basket and the inner detector remain in the position chosen for data taking. The design and construction of the basket and of the supporting structures, can be accomplished in less than one year. Therefore, we shall wait for the final engineering design of the inner detectors before to finalize the design of these structures.

Most of the magnet components are in good conditions and stored at CERN. These are the 16 C of the iron yoke, the coils, support carriages and rails, and manifold for the distribution of the water cooling. We foresee to perform at CERN a complete check and maintenance of these components (including a test of coils insulation). The maintenance will be completed by mid-2007. The motors for the displacement of the magnet are not available anymore. We have completely redesigned the system for movement. The motors and the transmission are new, and we have added a system of hydraulic jacks with central control, used to support with precise alignment the magnet, when in the working position. The magnet will be shipped to Japan in the second half of year 2007 and the installation of the magnet in the pit will be performed during spring 2008, before the construction of

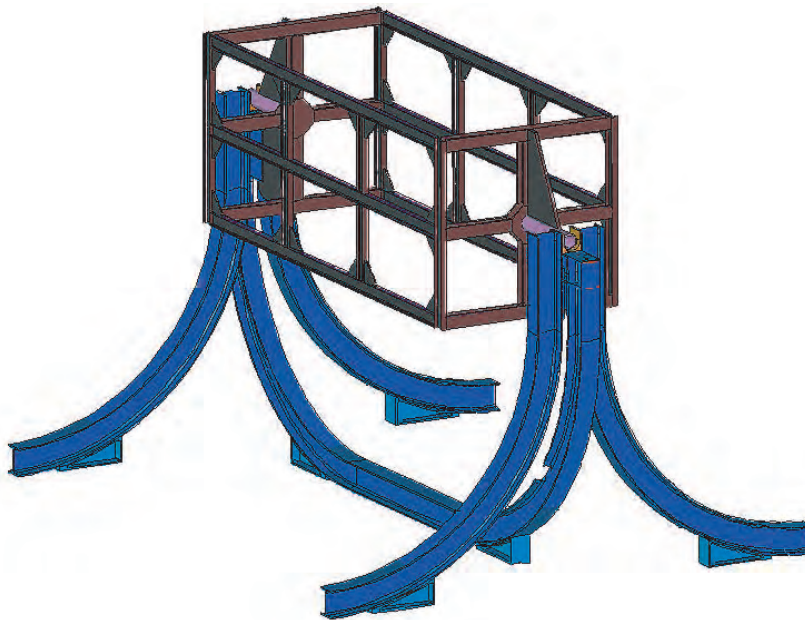


Figure 3.3: Preliminary drawing of the basket.

the roof of the experimental hall. The weight of a single C (53 tons) is in fact larger than the capacity (10 tons) of the crane in the experimental hall. Therefore, the rails, carriages, yoke and coils will be lowered in the pit by using external cranes and the installation of the magnet will be completed. We will then proceed to the coverage of the hall with its roof, before starting to install the detectors inside the magnet.

# Chapter 4

## FGD

*October 11, 2006: Updated water target Section 1.2.6 to give more details on water subtraction analysis, in response to review committee questions. Added Section 1.7 on physics performance.*

*October 23, 2006: Incremental changes in response to feedback/review from Clark.*

### 4.1 Introduction

#### 4.1.1 Overview

The ND280 detector will contain two massive fine-grained detectors (FGDs), which provide the target mass for neutrino interactions as well as tracking of charged particles coming from the interaction vertex. The FGDs are constructed from  $0.96\text{ cm} \times 0.96\text{ cm} \times 184.3\text{ cm}$  bars of extruded polystyrene scintillator, each of which is read out by a wavelength-shifting fiber going down its center. One end of each fiber is mirrored by vacuum deposition of aluminum, while the other end is attached to a silicon multi-pixel photon counter (see Chapter 9) and associated electronics, which digitize the light signal produced by scintillation inside the bar. Each FGD has outer dimensions of  $230\text{ cm}$  (width)  $\times$   $240\text{ cm}$  (height)  $\times$   $36.5\text{ cm}$  (depth in beam direction), and contains 1.0 tonnes of target material. The first FGD consists of 5760 scintillator bars, arranged into 30 layers of 192 bars each, with each layer oriented alternately in the  $x$  and  $y$  directions perpendicular to the neutrino beam. The scintillator provides the target mass for neutrino interactions, and having alternating  $x$  and  $y$  layers of fine-grained bars allows for tracking of charged particles produced in those interactions by the same principle used in K2K's Scibar near detector. The second FGD is a water-rich detector consisting of 7  $x$ - $y$  sandwiches of plastic scintillator layers alternating with six 2.5-cm thick layers of water (for a total of 2688 active scintillator bars and 15 cm total thickness of water). Comparing the interaction rates in the two FGDs permits separate determination of cross sections on carbon and on water. Both FGDs will be built with the same geometry, mounting, and readout for interoperability. Each FGD is contained in a light-tight dark box that contains the scintillator, fibers, and photosensors, while the FGD electronics are mounted in mini-crates around the outside of the dark box.

#### 4.1.2 Physics requirements

The FGDs form part of the ND280's tracker. The tracker, consisting of three TPCs (Chapter 5) and the two FGD modules, lies at the heart of the ND280. Its primary function is to measure the neutrino beam's flux, energy spectrum, and flavor composition by observing charged current neutrino interactions. The FGDs are thin enough ( $< 30\text{ cm}$ ) that most of the penetrating particles produced in neutrino interactions, especially muons, will reach the TPCs where their momenta and charges will be measured by their bending in the magnetic field. Short-ranged particles such as recoil protons are primarily measured in the FGDs themselves, which therefore must have fine granularity so that individual particle tracks can be separated and their directions measured. The TPCs provide excellent

3D tracking for forward and backward-going charged particles produced in the two FGDs. The TPCs measure the momenta and charges of penetrating particles and provide particle identification through  $dE/dx$  measurements.

An especially important reaction to measure is the CCQE interaction  $\nu_\ell + n \rightarrow \ell^- + p$ , which is the most common interaction at T2K's beam energy. For these interactions, the energy of the incident neutrino is calculable from only the energy and direction of the final lepton, which makes the CCQE reaction ideal for measuring the neutrino energy spectrum. However, although the CCQE interaction is the most common interaction mode, many other processes can occur. An important example is CC single pion (CC- $1\pi$ ) production ( $\nu_\ell + N \rightarrow \ell^- + N' + \pi$ ). This process, which often proceeds through excitation of a  $\Delta$  resonance, will often look just like a CCQE event in Super-K, where only the final state charged lepton will be above the Cherenkov threshold. Because CC- $1\pi$  produces a three-body final state, the initial neutrino's energy is not a simple function of the charged lepton's direction and energy. CC- $1\pi$  events will therefore smear out the energy spectrum measurement, and must be excluded from the energy spectrum analyses in both the near and far detector. At Super-K this is accomplished by selecting only events with a single charged lepton in the final state, although CC- $1\pi$  events with the pion below Cherenkov threshold form an irreducible background. The tracker is used to measure the size of this and other backgrounds to CCQE interactions at Super-K.

The tracker must yield high statistics measurements of the rates of CCQE and non-QE interactions from the T2K beam, which will then be used to predict event distributions at Super-K. Because the tracker can see all charged particles produced in an interaction, it can identify CCQE events by selecting just those events which contain a lepton and a recoil proton. Even this is not sufficient, however, since very short-ranged pions or protons may not be identified as separate tracks in the detector. Even worse, the pion from a CC- $1\pi$  event can even be reabsorbed inside the production nucleus and may not even make a track. Fortunately additional kinematic cuts can be applied to improve the CCQE selection purity. For CCQE interactions, the direction of the recoil proton can be calculated just from the direction and energy of the charged lepton. The angle between the observed proton momentum and the expected proton momentum will be distributed around zero for true CCQE events, but will have a much flatter distribution for non-QE events with additional, possibly undetected, particles in the final state (see Figure 4.1). The ability to distinguish CCQE events from non-QE events not only improves the energy spectrum measurement in the ND280, but also is essential for predicting the neutrino event distributions in SK where CCQE and non-QE events can often not be distinguished.

Another method of rejecting non-QE events is to tag Michel electrons produced from the decay of short-ranged pions that do not otherwise leave reconstructable tracks in the FGD. While most pions will leave usable tracks in the FGD, low-energy pions can stop in the FGD after leaving just a very short track. These pions can then decay into a muon, which then decays to produce a Michel electron. The presence of a Michel electron in the FGD within a few muon lifetimes after a neutrino interaction can be used to reject events in which a pion is produced.

The FGDs must therefore satisfy a variety of design criteria:

- They must be capable of detecting all charged particles produced at the interaction vertex with good efficiency, in order to determine the type of interaction.
- They must be thin enough that charged leptons will penetrate into the TPCs, where their momenta and flavor can be determined.
- The directions of recoil protons must be measured accurately so that CCQE events can be selected using kinematic cuts on the recoil proton's direction.
- Particle ID from  $dE/dx$  measurements must reliably distinguish between muons, electrons, protons, and pions.
- The tracker must contain  $\sim 1$  tonne of target mass for neutrino interactions in order to yield sufficient statistics ( $< \sim 5\%$  measurement of the CCQE rate on water,  $< 10\%$  for the CC- $1\pi$  rate, and  $< 10\%$  for the beam  $\nu_e$  background).

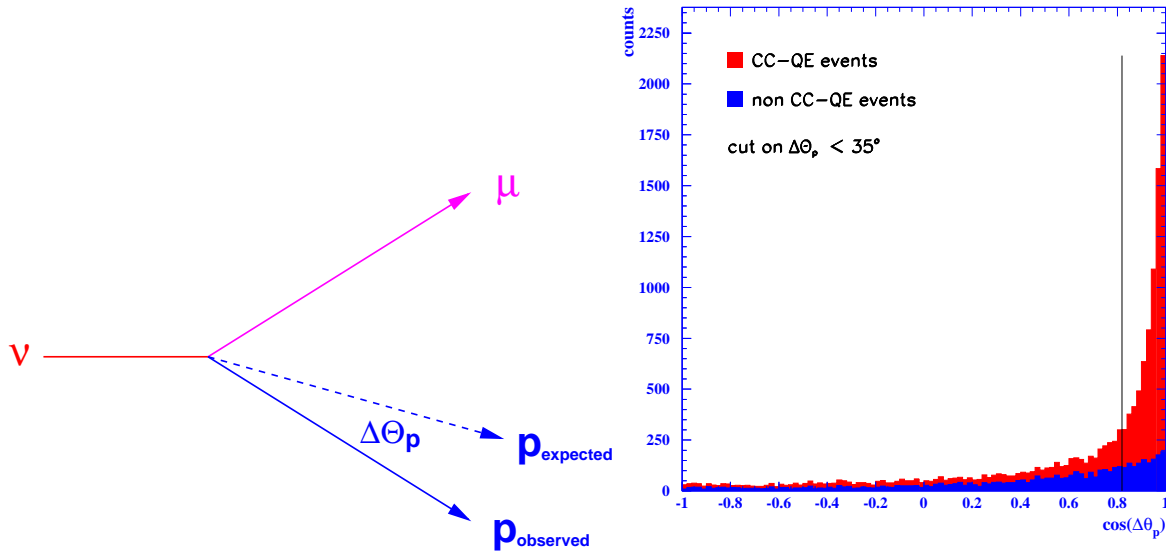


Figure 4.1: Left: For CCQE events, the direction of the recoil proton can be calculated just from the energy and direction of the lepton. The angle  $\Delta\theta_p$  between the observed proton momentum and the expected proton momentum is a kinematic variable that can be used to distinguish CCQE events from other types of interactions. Right: Histogram of the  $\Delta\theta_p$  distribution for CCQE and non-QE events in a fine-grained scintillator detector.

- Because the ND280 sits in an off-axis beam, the off-axis angle and hence the neutrino energy spectrum varies substantially across the face of the tracker. Non-uniformities in threshold or efficiency across the tracker would greatly complicate the extraction of the neutrino beam properties, and potentially could even bias the measurement. Therefore the detector response across the tracker needs to be as uniform as practically possible.
- Because the far detector is a water Cherenkov detector, the tracker must measure the neutrino interaction rates on water. All of the relevant neutrino cross sections depend at some level on the target nucleus through such effects as Pauli blocking, pion rescattering and absorption inside the nucleus, etc. These nuclear effects cannot be reliably corrected for from theory, and therefore the nuclear interaction rates must be measured on water so that the rates can be used to predict the rates for these processes in SK. Unfortunately, an all-water near detector, such as K2K's kiloton water Cherenkov detector, cannot see all final state particles or satisfy the other design criteria. The best that can be done is to measure neutrino interaction rates on a mixture of water and carbon-based scintillator, and to determine the rate on water from a statistical subtraction. For this reason, the amount of higher-Z material in the tracker must be minimized in order not to complicate the procedure of separating the contributions from water vs. carbon.
- The FGD electronics must provide excellent acceptance of late hits such as those due to Michel electrons.

The final FGD design is based upon K2K's Scibar detector with a number of modifications. The most important modifications are:

1. Reduced scintillator bar size for improved tracking of short-ranged particles
2. Use of silicon-based multi-pixel photon counters instead of multi-anode PMTs to allow robust operation in magnetic fields and elimination of crosstalk inside the photosensor
3. Reduced thickness and new mechanical support structure to accommodate the ND280 magnet

4. Addition of target water layers to permit cross section measurements on oxygen
5. Improved electronics to increase Michel electron acceptance.

Section 4.2 describes the FGD design in detail.

### 4.1.3 About this document

This document describes the basic design of the FGD as well as prototype results. A more detailed full-length technical design report is well underway and proceeding quickly.

## 4.2 Detector design and specification

### 4.2.1 Mechanical design overview

Each of the two fine-grained detector modules consists of 15 vertically hanging  $184.3\text{ cm} \times 184.3\text{ cm}$  dual planes of extruded polystyrene scintillator bars, each of which is  $9.6\text{ cm} \times 9.6\text{ cm}$  in cross section. Each such dual plane (which is called an “XY module”) consists of a plane of 192 horizontal bars glued to a similar plane consisting of the same number of vertical bars. Each bar has a photosensor at only one end. The criteria and issues related to the mechanical design include:

1. The XY modules must tolerate normal handling during assembly and servicing, while horizontal and supported at the edges.
2. The XY modules, consisting of a material with large thermal expansion coefficient, must be supported vertically, with a position resolution of order 1 mm. However, the lower edges of the monolithic XY modules offer little external load-bearing surface.
3. Earthquake accelerations of up to several  $g$ 's must be tolerated without damage.
4. A light-tight seal must be provided around the assembly of XY modules and photosensors.
5. A photosensor temperature stability of  $\pm 3^\circ\text{C}$  is needed for adequate gain stability.
6. Convenient service access to the front-end readout electronics is needed, without requiring removal of the module from the basket.
7. The design should minimize the mechanical space needed for readout around the margins of the planes to fit the largest feasible volume of scintillator inside the defined dimensions of the basket containing the FGDs and TPCs.

The scintillator bars are glued together to form the XY modules. The XY modules are made robust to handling (criterion 1) by laminating the outer surface of each XY module with a 0.3mm thick layer of G10 epoxy-fiberglass. As polystyrene is a material with low surface energy and poor bonding to conventional adhesives, a special adhesive with high performance with this material was chosen, based on extensive tests. Criteria 2 and 3 are addressed by suspending each XY module via five thin flexible straps passing under the plane. The straps are glued to the large faces of the plane. The stack of 15 XY modules in the FGD is lightly clamped together at the four corners. The straps hang from fixtures attached to a structural metal frame covering all four edge faces of the module. The frame mounts directly on the basket at its lower two corners, with only lateral stability provided at its upper corners.

The light-tight envelope is provided by a rectangular box containing the entire module stack. The four sides of this box that line the structural frame are penetrated in many locations as described below. The two large faces of the box are removable panels of G10 that are sealed to the frame liner

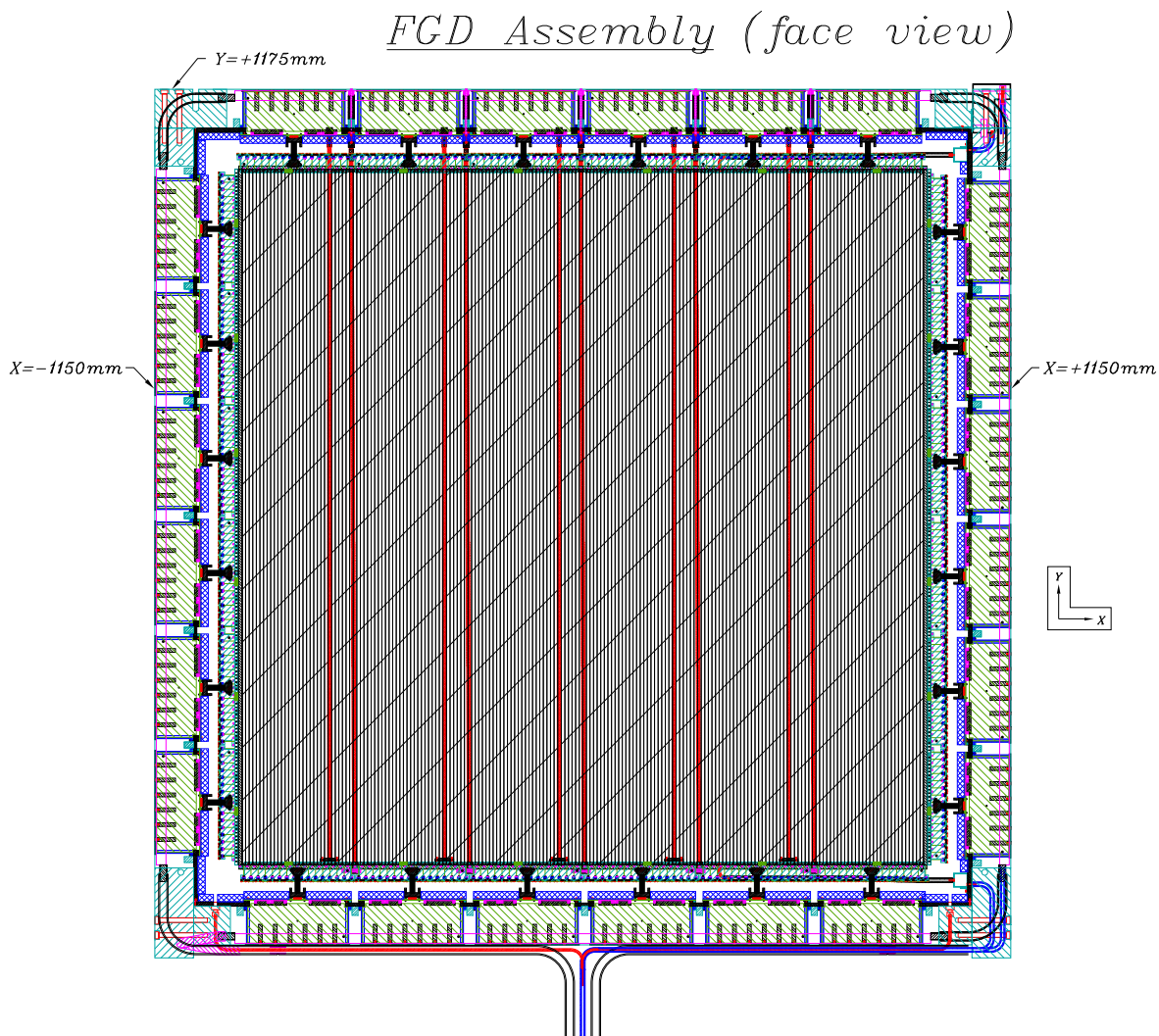


Figure 4.2: End view on one FGD. The XY scintillator layers hang from nylon straps (shown in magenta) inside the dark box. Twenty-four mini-crates on the four sides of the FGD contain the front-end electronics boards, while the photosensors themselves are mounted on bus boards attached directly to the edges of the scintillator.

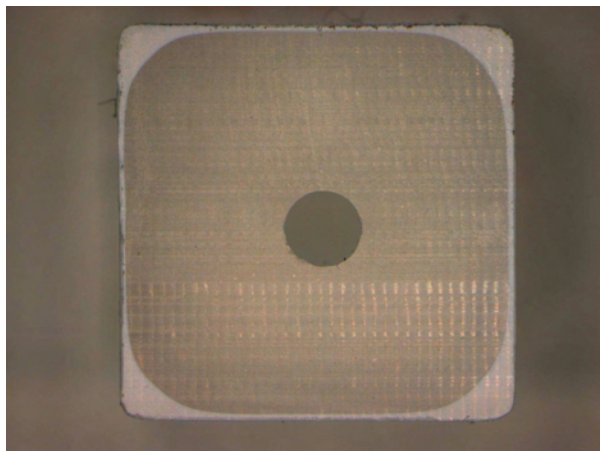


Figure 4.3: Cross-section view of prototype scintillator bar produced at Celco Plastics.

via gaskets. This “dark box” is reconciled with the required temperature stability by including no electronic elements inside the box except the photosensors, which have a tiny power dissipation of  $< 0.1\text{mW}$  per channel. This power is removed by a small flow of dry nitrogen through the box. The sensors for each edge of each plane service only every second bar. Hence all four edges of an XY module carry photosensors, which are mounted on “bus-boards” attached by screws to the scintillator plane itself. Each of the 12 bus-boards on each edge of a plane contains no active elements, but only gathers the connections from its 8 photosensors to a short ribbon cable attached to the board. The other ends of these flat cables plug into receptacles embedded in opaque printed-circuit boards that serve as both part of the dark box and as back-planes of the front-end electronic crates mounted on the outside of the box. Six of these crates appear on each of the four smaller edge faces of the light box, inside penetrations through the structural frame. Hence the crates are integrated onto the dark box. The location of the crates with respect to the structural beams of the enclosing basket is arranged to offer external access to the electronic cards in the crates while the FGD modules remain in the basket.

Figure 4.2 shows an end view of one FGD, illustrating the locations of the scintillator layer, dark box frame, and mini-crates.

## 4.2.2 Scintillator bars

The number of bars needed for the plastic FGD is  $192 \times 30 = 5760$  while for the water-rich FGD we need  $192 \times 14 = 2688$  bars. The total number of bars, including 1552 spares, is 10000. The geometrical specifications of each bar are as follows:

- Length (z dimension) =  $1843.2 \pm 1$  mm
- Outside x and y dimensions =  $9.6 \pm 0.3$  mm
- $\text{TiO}_2$  thickness =  $0.25 \pm 0.05$  mm, (co-extruded bar coating)
- Active dimensions =  $9.1 \pm 0.3$  mm
- Hole diameter =  $1.8 \pm 0.3$  mm

Figure 4.3 shows the bar profile.

The scintillator bars are made of polystyrene doped with PPO and POPOP, and are co-extruded with a reflective coating consisting of polystyrene doped with  $\text{TiO}_2$ . This is the same technique used by the MINOS and K2K experiments to produce plastic scintillator bars. The materials used in extruding the bars are as follows. For the basic polystyrene we use DOW Styron 663 W-27 general

purpose crystal polystyrene without additives, in pellet form. The fluors are purchased already mixed from Curtiss Laboratories. The primary fluor is 1% PPO (2,5-diphenyloxazole) and the secondary fluor is 0.03% POPOP (1,4-bis(5-phenyloxazol-2-yl) benzene). The  $\text{TiO}_2$  concentrate is purchased from Clariant (catalog number WHC-26311-A.). This concentrate has 60%  $\text{TiO}_2$  (rutile form). We use 1 part concentrate and 3 parts plain polystyrene pellets to bring the concentration of  $\text{TiO}_2$  in the coating to 15%.

The polystyrene pellets are weighed in 100 lb. batches and dried for  $\sim 8$  hours at  $170^\circ\text{F}$  with dry  $\text{N}_2$  flowing in the oven. The pellets are then mixed (in a small concrete mixer which has dry  $\text{N}_2$  from a liquid  $\text{N}_2$  dewar flowing through it) with the premixed PPO/POPOP fluor. This mixture is then stored in 200 lb. containers under dry  $\text{N}_2$  purge. The  $\text{TiO}_2$  coating (15 lbs polystyrene to 5 lbs  $\text{TiO}_2$  concentrate) is mixed by hand and similarly dried and stored. The materials and mixing procedures are identical to those utilized in producing extruded scintillator strips for MINOS and the K2K SciBar detector.

The mixed materials are transported to Celco Plastics Ltd, Surrey, B.C., where they are purged with dry  $\text{N}_2$ , then fed into hoppers. Separate hoppers are used for the doped plastic scintillator extrusion and for the  $\text{TiO}_2$  co-extrusion. The materials are heated to a molten state and forced through the die and sizer plate, which determine the bar cross-section. The bar is then cooled by pulling it through a water bath and cut to length by an automated saw which moves with the bar. A laser feedback system controls the bar thickness. During production all bars will be checked at Celco to ensure they are within geometrical tolerances and that the central hole is clear. A sample of the bars will be checked daily at TRIUMF by scanning the bars with a source and measuring light yield with a photodiode.

We have successfully produced production-quality bars in test runs at Celco Plastics. The results of these tests are described in Section 4.3.

### 4.2.3 Wavelength-shifting fibers

Light from each of the extruded plastic scintillator bars of the FGD is collected and transmitted by a blue-to-green double-clad wavelength shifting fiber (WLS). Double cladding improves the light output. The WLS is coupled at one end to a pixellated avalanche photodiode (see Section 4.2.4). The other end of the WLS fiber is mirrored to further increase the light yield.

The fiber absorption spectrum must match the light emitted by the scintillator and the emission spectrum must match the photosensor spectral sensitivity. With the photosensor coupled, the light output requirement is more than 10 photoelectrons for a minimum ionizing particle (MIP) striking the far end of a scintillator bar ( $\sim 2\text{m}$  from the photosensor).

After studies performed at TRIUMF, the well known Kuraray Y11 (200) S-35 WLS fibers were selected. These have the following specifications:

- 1 mm diameter
- Refractive index: 1.59 (outer clad) / 1.49 (middle clad) / 1.42 (core)
- Absorption wavelength: 430 nm (peak)
- Emission wavelength: 476 nm (peak)
- Attenuation length:  $\sim 350$  cm
- Decay time:  $\sim 7$  ns
- Trapping efficiency by total internal reflection:  $\sim 5\%$
- Fiber length:  $\sim 2$  m

The WLS fibers are inserted in 1.8 mm diameter holes in the scintillator bars. The coupling between the WLS fiber and scintillator is through an air gap. There is tolerable loss of light yield at the coupling as demonstrated by studies carried out at TRIUMF (see Section 4.3), with no need to glue the fibers into the scintillator. The attenuation length of the fiber is approximately 5 meters for the S-35 type, with a shorter attenuation component present at small distances from the photosensor due to the variation of the fiber attenuation with wavelength.

The FGD will use  $\sim 20$  km of fibers. This amount can be produced in roughly 6 batches by Kuraray. Upon delivery, samples from each batch of fibers, as delivered by the manufacturer, will be tested for initial quality control to verify the attenuation length and absolute light yield. One end of the fibers will then be mirrored using aluminum sputtering and protected with UV epoxy at the Fermi National Laboratory (FNAL) in the USA. Lab 7 at FNAL has extensive experience in this mirroring procedure. The mirroring increases the light output by a factor of  $> 50\%$  with respect to non-mirrored fibers as has been demonstrated in recent tests performed at TRIUMF. Once mirrored, the fibers will be delivered to Canada. During this time, the infrastructure for individual testing of all fibers will be completed.

All fibers will be tested in Canada after mirroring. The testing arrangement will include facilities for exciting scintillators, using radioactive sources and/or LED flashers to simultaneously test up to  $\sim 16$  fibers. The final polishing of the photosensor end of the fiber may be integrated with the installation of optical couplers that align and anchor the fibers to the photosensors. The tests done on each fiber will include relative light yield as a function of the distance between the light source and the photosensor, light output uniformity between fibers, and attenuation length. Particular attention must be paid to reproducibility of measurements, using reference fibers. Information for individual fibers will be recorded in a suitable data base. Monte Carlo simulations will also be used to compare with some of the measurements.

A sample of the fibers will be tested using the final version of the photosensors and FGD extruded scintillator bars excited with LED flashers, cosmic muons and/or radioactive sources. Finally tests in TRIUMF beam facilities will be undertaken after installation of the fibers in the FGD.

#### 4.2.4 Photosensors

The FGD photosensor needs to satisfy tight constraints:

- It must be able to count photons down to a few photoelectron level.
- It must work inside the 0.2 T magnetic field.
- It must fit in a very tight space constraint.

Multi-anode photomultipliers could work either by bringing the fibers out of the detector or by sacrificing fiducial space to install MCP-type ones. Avalanche photodiodes with good preamplifiers could also work after R&D. However, there is a concern on the very limited time of commissioning about identifying and treat electronic noise sources. Either multi-anode photomultipliers or avalanche photodiodes would greatly increase the complexity and cost of the detector.

Therefore the collaboration has chosen pixellated avalanche photodiodes that operate in Geiger mode from HPK (MPPC) and CPTA (MRS) as the default photosensors for the scintillator detectors. The sensor is compact, works in the magnetic field, and has excellent photon counting capability with higher quantum efficiency than photomultipliers for the light coming out of wavelength-shifting fibers. Successful prototyping of these sensors has been done, and the technology is mature enough to be ready for the experiment starting in a couple of years. Details on the photosensor are described in Chapter 9.

The particular photosensor requirements for the FGD are similar to those for the other scintillator detectors. The electronics requires a photosensor gain in excess of  $10^5$ , while the dynamic range

of the detector can be satisfied with a  $\sim 400$  pixel device. A single photoelectron dark noise of 1-2 MHz is tolerable, but the packaging of the device must be  $< 8$  mm in cross-section in order to fit within the FGD requirements. The photosensors will be mounted a few centimeters from the end of each scintillator bar directly inside the FGD itself. The extremely small power requirements of these photosensors makes this practical.

The FGD group is working actively with the ND280 photosensor working group to test prototype photosensors. We have already verified that existing prototype sensors meet our requirements, as described in Section 4.3.

## 4.2.5 Electronics

### Requirements and specifications

The electronics is designed to provide both timing and energy resolution. The timing resolution requirement is driven by background rejection. Detector activity associated with a single neutrino interaction is combined by using topological information (i.e. projecting the tracks back to their vertex in the FGD) but also timing information when matching calorimeter hits. The timing requirement has been estimated to be of the order of 3 ns for a FGD vertex, which consists of several hits.

Minimum ionizing particles produce 20-30 photo-electrons, which corresponds to about 20% energy resolution. The electronics noise must not contribute significantly to the energy resolution, which sets a very modest requirement. However, in order to calibrate the photosensor, we intend to identify single photo-electron peaks, which requires the electronics noise to be less than 0.1 photo-electron. The dynamic range is defined by the number of photosensor pixels, which is on the order of 500 pixels. Assuming a photosensor gain of  $10^6$  means that the maximum range is 80 pC, while having a noise of less than 1.6 fC (10,000 electrons ENC).

The neutrino beam structure is divided in 9 bunches separated by 600 ns. The electronics must be alive during each bunch. Furthermore it is advantageous to keep the electronics alive in between bunches and for several microseconds after the spill in order to measure the electrons from pion decay (produced from the decay of muons generated by the decaying pions). Measuring these Michel electrons provide a clean way of identifying pions stopping in the FGD.

### Architecture

The FGD electronics must rely on an Application Specific Integrated Circuit (ASIC) in order to meet the requirements, while fitting in the tight space available without consuming too much power. The Switch Capacitor Array chip designed for the T2K Time Projection Chamber has been selected for this purpose. This chip will be operated at 50 MHz sampling frequency and 100 ns (peaking) shaping time, which provides 10  $\mu$ s of integration time when the electronics is fully alive without compromising the timing resolution. Simulations show that a timing resolution of 3 ns can be achieved in such configuration as long as the signal-to-noise is on the order of 100/1. Such requirement implies that the noise correspond to about 0.1 photo-electrons.

The dynamic range of the TPC ASIC does not match the photosensor output. The photosensor signal needs to be attenuated by a factor that depends on the gain. Furthermore it is advantageous to split the signal in two branches, one with low attenuation, where 100/1 signal to noise is achieved for minimum ionizing particles, and one with high attenuation that allow measurement of large signal corresponding to several hundred pixels.

The FGD channels are separated by 2 cm, which is relatively sparse. On the other hand the TPC chip is about 1 cm<sup>2</sup> but it can handle up to 72 channels, which corresponds to 36 FGD channels after signal splitting. In addition the photosensors are very sensitive to temperature variation, while the ASIC and the other necessary electronics components dissipate significant power. It is thus important to separate the photosensors from the readout electronics. These considerations motivated the choice of housing the electronics front end boards in mini-crates surrounding the FGD scintillators. Only the

scintillators, fibers, and photosensors are housed within the light-tight box, which also provide thermal isolation. A set of connection boards and cables must then be designed to connect the photosensor to the front end boards. Data from the front end boards are concentrated per minicrate and shipped to a back-end receiver board outside the magnet by an optical fiber. The fibers also carry trigger and clock signals. A separate bus is used for slow control.

### **Photosensor connection**

There are 6 mini-crates per FGD side, which means that one crate reads out 16 photosensors per layer. The depth of the FGD is 30 cm, which corresponds to 15 X or Y layers. Hence the electronics in one mini-crate has to read out 240 channels. The channels are spread over a  $32 \times 30 \text{ cm}^2$  zone. A bus board fans in the signals from 16 photosensors onto a flat cable connector. The cable runs from the bus board to the mini-crate backplane. Hence, there are 15 bus boards and cables.

The 240 photosensor lines from the light-tight box are brought through the backplane to connectors where the front end boards are plugged in. The backplane also has to carry digital data between the front end boards. The slow control bus will also go through this backplane.

### **Front end boards**

There are two kind of front end boards. In each crate, there are 4 front end boards (FEB) housing 2 TPC ASICs each, and 1 control and collector board (CCB) housing an FPGA that controls all the FEBs in the crate.

One FEB handles 64 photosensor channels, which corresponds to 128 ASIC outputs because of the high/low attenuation scheme. The FEB also house one dual ADC per board. The ASIC control and ADC signals (e.g. SCA write, SCA read, sampling clock) are generated by the FPGA on the CCB. The FEBs also control the bias of each photosensor through the slow control bus. The FEBs generate one rail bias using a charge pump circuit, which is then tuned for each photosensor using independent DAC channels.

The CCB controls the ASICs and ADCs, and formats the data before shipping them to the Data Concentrator Card. The CCB also receives and distributes the trigger and clock.

### **Back end electronics**

The Data Concentrator Card (DCC) are located outside the magnet. It can handle 12 to 14 optical fibers, which corresponds to roughly half of an FGD. The two FGDs hence require 4 DCCs. The DCCs distribute both trigger and clock signals. The DCCs will hold one or two powerful FPGAs that will be used for data compression. Specific data compression algorithms will have to be developed for the FGD in order to cope with the Dark Noise rate without compromising the efficiency and the timing resolution. The compressed data will then be shipped off board for storage.

### **Slow control and monitoring**

The FGD slow control is responsible for setting the photosensor bias and monitoring the temperature, current and bias on the boards and close to the photosensors. The slow control relies on a separate bus in order to provide a mean of accessing the board even when the data path is broken. The slow control relies on the Midas Slow Control Bus (MSCB) developed at PSI (Switzerland). There will be one slow control bus per FGD side, which will control 30 or 36 nodes (24 FEB, 6 CCB and possible 6 light injection boards).

### **Electronics integration**

The minicrate architecture subdivides the FGD electronics in 24 pieces per FGD. Power will be brought in by bus bars running on the side of the crate. Water used for cooling the electronics will

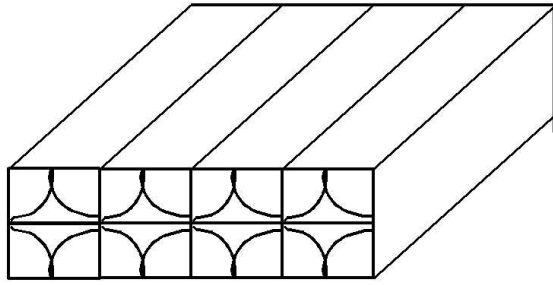


Figure 4.4: Cross-section diagram of polycarbonate panel for the target water module.

Element	XY Module	Water Module	Remainder
C	1.873	0.422	0
O	0.080	2.043	2.025
H	0.161	0.289	0.253
Ti	0.035	0	-0.008
Si	0.022	0	-0.005
Other	0.003	0	-0.001

Table 4.1: Elemental compositions of the XY modules (plastic scintillator) and target water modules, per  $\text{cm}^2$  of cross-sectional area. All amounts are in grams. The “remainder” column equals the water module mass minus the XY module mass, with the latter scaled by the ratio of the amounts of carbon in each so that the carbon remainder is zero by construction.

also run along the side of the crate. Metal (copper) bars and plates will transfer the heat from the electronics board to the water pipes. Cool dry gas will be flowed through the light tight box providing modest cooling, which should be sufficient to remove the very small amount of heat dissipated by the photosensors.

#### 4.2.6 Target water modules

The water-rich FGD will consist of  $x$ - $y$  layers of plastic scintillator of the same construction as those used in the plastic FGD, interleaved with layers of water enclosed in a vessel made of 25 mm thick polycarbonate hollow panel sealed at both ends with Stycast 1266 epoxy. The cross section of the panel is shown in Figure 4.4. There is an intricate structure of internal walls to enhance the mechanical strength of the panel with the minimum amount of plastic. The use of polycarbonate panel (Lexan), instead of polypropylene panel (Matraplast) as initially proposed in fall 2005, gives a significant improvement in the oxygen content of the water-bearing layer, namely an increase in the ratio of oxygen nucleons to carbon nucleons from 4.09 to 7.87. After exhaustive testing of many candidate sealants, Stycast 1266 was found to be the best, since it forms a bond with the polycarbonate which is stronger than the polycarbonate itself. Our group has successfully sealed corrugated plastic panels with a number of epoxies and achieved water-tight seals. Figure 4.6 shows a prototype polycarbonate test panel with a small buffer tank, filled under negative pressure. The water in the panel has been colored with green food dye to make it more visible. This setup is essentially identical to the final version in every respect except its width. Measurements show that the deformation in the thickness of the panel is  $< 0.2\%$  over the full range of operating pressures.

The two FGDs contain principally polystyrene, polycarbonate, and water, which are composed of the elements carbon, oxygen and hydrogen. Ideally, one would like to extract the neutrino interaction

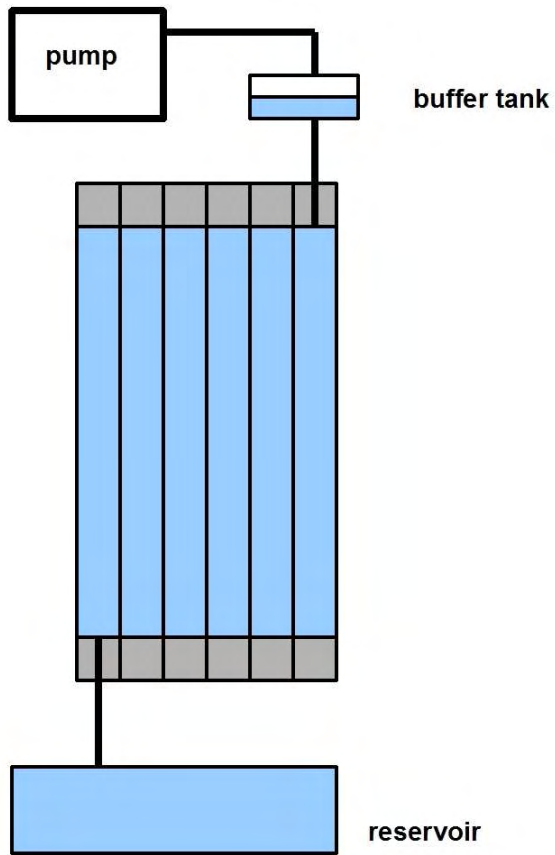


Figure 4.5: Water circulation system for the target water modules.



Figure 4.6: Test panel for the target water model. The panel is filled with water (dyed green) under negative pressure. A buffer tank is visible above the panel.

cross sections on each of these elements separately. In practice, since there are only two FGDs, we can extract the neutrino interaction cross sections on only two target materials, and there is no way of determining the neutrino interactions on each element separately. However, the Super-K far detector is composed of pure water, and for the purpose of comparing the interactions in the near and far detectors, it is this target material for which we need to know the neutrino interactions. We therefore elect to determine the neutrino interactions on water and polystyrene as the two independent measurements. To this end, we design the water-bearing layers have the elemental composition of H<sub>2</sub>O plus polystyrene. This can be achieved by adding a single layer of CH<sub>2</sub> of thickness  $\sim 1.6$  mm to one of the outer walls of the polycarbonate vessel. Since the plastic FGD is pure polystyrene, while the second FGD is equivalent to a mixture of polystyrene and water, the interaction rate in the first FGD can be subtracted from the interaction rate in the second FGD (with a scaling factor to account for the different masses and detection efficiencies) to determine the neutrino interaction rate on water alone. The small amounts of titanium and silicon in the XY modules themselves contribute only at the  $\sim 0.3\%$  to the residual rate after subtraction.

Table 4.1 illustrates this subtraction by listing the masses of the various elements that comprise the XY and water modules, per cm<sup>2</sup>. While the XY module is predominantly carbon, the water module is mostly oxygen, with some carbon as well. The basic concept behind the analysis when extracting interaction rates on water is to subtract the event rate in the all-plastic FGD from the event rate in the water-rich FGD, scaling the former rate by the ratio of the carbon masses in the two detectors, so that the contribution from carbon in the water-rich FGD is subtracted off. This ratio also needs to be corrected for the difference in the detection efficiencies in the two FGDs, although this efficiency difference is expected to be the same for all elements. Because the active layers of two FGDs are identical in construction, any such efficiency differences will be due almost entirely to the slightly different amounts of material that charged particles encounter in the two kinds of modules, and should be accurately modelled by Monte Carlo simulation. As can be seen from Table 4.1, the event rate per water module after subtracting off the rate seen in an XY module is overwhelmingly dominated by oxygen and hydrogen in a mass ratio of 8:1, identical to that for water. In effect, by carefully choosing the composition of the two kinds of FGD modules we ensure that the contributions to the interaction rates from anything but water is negligible after the subtraction. The systematic uncertainties in the water subtraction will be dominated by how well we can determine the relative efficiencies of the two FGDs for the various kinds of events. Monte Carlo studies are planned to quantify this, although the close similarity of the two FGDs gives us confidence that this can be quite accurately determined. As a consistency check we do have the option of running the second FGD with and without water in the target modules and directly comparing the rates in the same FGD.

The inside of the magnet will contain many detectors and electronics components which could be damaged by water. It is thus imperative that we take precautions to ensure that the water never leaks out of the polycarbonate vessel. This will be done by holding the water at negative pressure. A pump will suck from the top with just enough pressure to pull the water level in the polycarbonate vessel to the desired height. The setup is shown in Figure 4.5. system ensures that if a leak develops, the system will suck air into the module rather than leaking water into the dark box. In the event that negative pressure is removed by a pump failure, the target water will drain to a reservoir below the magnet.

### 4.3 Detector technology R&D

In Fall 2005 and Spring 2006 the FGD group carried out successive scintillator extrusion runs at Celco Plastics to refine the extrusion technique and geometry. These test runs successfully produced production-quality scintillator bars that satisfy the geometrical requirements of Section 4.2.2. We have since carried out a number of beam tests to verify the performance of these bars, in preparation for final scintillator extrusion in late 2006. These beam tests essentially are a complete test of one

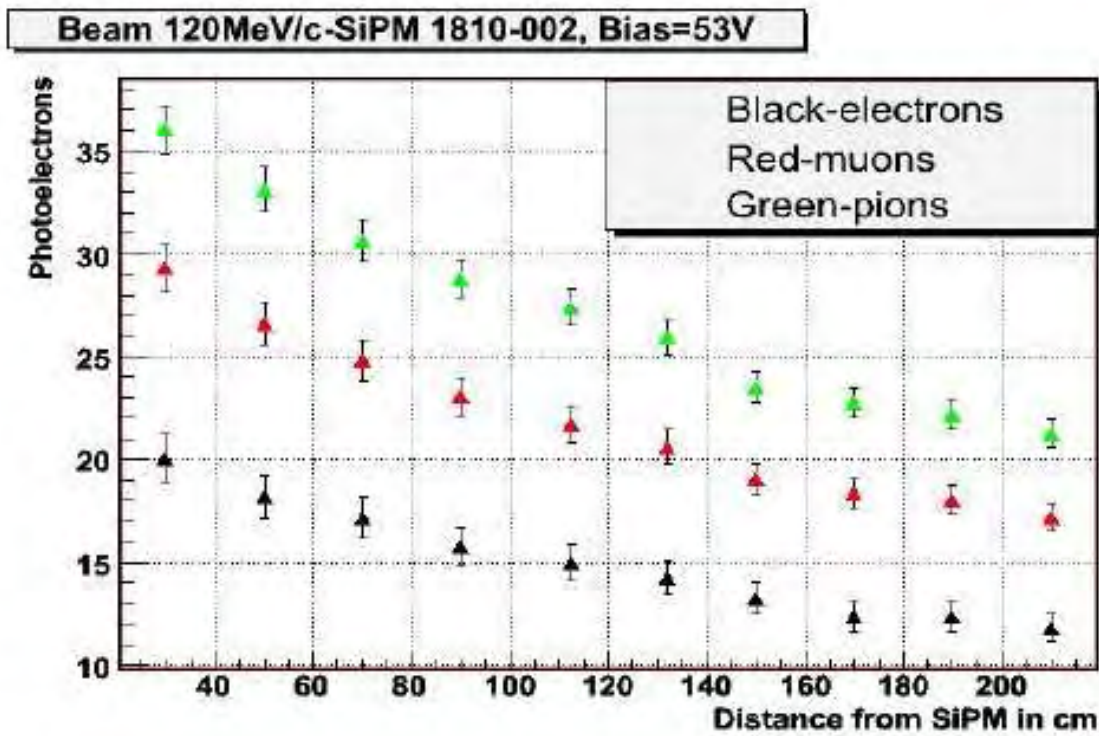


Figure 4.7: Light yield of an FGD scintillator bar for 120 MeV/c electrons, muons, and pions, as a function of the distance between the photosensor and the incident particle.

scintillator bar, fiber, and photosensor.

The light yield from the bars was measured in the M11 beam line at TRIUMF with a beam of electrons, muons and pions using time-of-flight to identify the particle type. The bars were read out with Kuraray Y11(200) S-type wavelength-shifting fibers, 1mm in diameter. One end of the fiber was closely coupled to a pixellated avalanche photodiode (see Section 4.2.4), manufactured by CPTA in Moscow. The measured light yield in photo-electrons as a function of distance from the photosensor is shown in Figure 4.7, for the case where the end of the fiber furthest from the photosensor was cut at 45 degrees and painted black. After correcting for  $dE/dx$ , the results for electrons, muons and pions are consistent and predict that the light yield will be  $>10$  pe from the far end of a 2 m bar if we do not mirror the far end of the bar. A single measurement with cosmic rays was consistent with this result. The effect of mirroring the far end of the fiber was measured and found to increase the light yield by more than 80% for particles striking the bar 2 m from the photosensor. This level of light exceeds that seen in the Scibar detector, which saw  $\sim 15$  photoelectrons for a minimum ionizing particle incident at a distance of 200 cm from the photosensor. Simulations of the FGD bars have shown that we will achieve hit efficiencies in excess of 99% with this level of light yield.

MINOS estimated that aging of the bars reduced the light yield by  $\sim 2\%$  per year. We are carrying out our own tests to check this, accelerating the aging by heating samples of the bars in an oven and measuring the light yield from a  $^{90}\text{Sr}$  source with a photo-diode. Results are expected by mid-September, 2006.

We have carried out a set of crosstalk measurements in which we measure the leakage of light through the reflective  $\text{TiO}_2$  coating between two adjacent bars. By triggering on muons striking one bar and looking at the signal in a neighboring bar, the optical crosstalk between bars is found to be  $< 1\%$ . This level of crosstalk is much smaller than that seen in the Scibar detector, in which crosstalk inside the multi-anode PMTs was as large as several percent between channels. (Because the FGD uses one photosensor per fiber, there is no crosstalk between scintillator bars inside the photosensors themselves.)

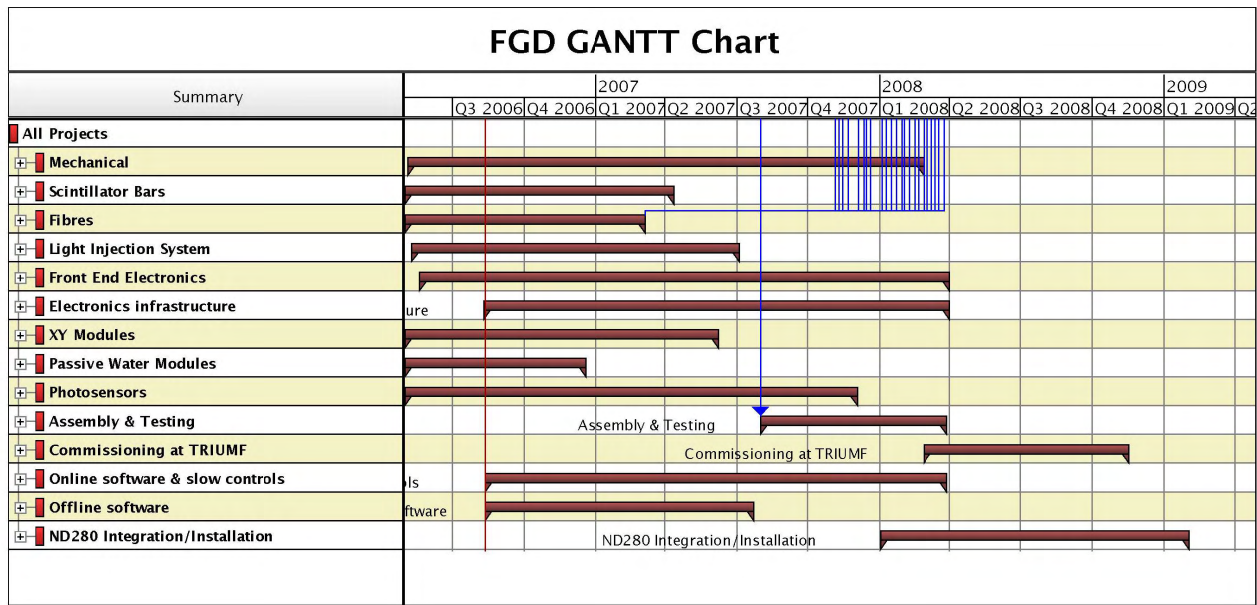


Figure 4.8: FGD schedule / GANTT chart.

A number of prototype target water modules have been constructed from corrugated polycarbonate and polypropylene sheets. The ends of these modules have been successfully sealed with epoxy and have been tested for months while filled with water, and show no sign of leakage or deformation.

The remaining R&D efforts for the FGD focus primarily on the electronics and photosensors (described in more detail in Chapter 9). While we have already demonstrated that the silicon multi-pixel photon counters yield enough detected light and meet our other specifications, the details of the optical coupling between the photosensor and fiber must still be finalized. For the electronics, we have assembled prototype bus boards and daughter cards, and have demonstrated that electronic crosstalk between channels is negligible.

Two independent waveform-based simulations of the waveform produced by the photosensor-ASIC combination suggest that the proposed electronics design will achieve a timing resolution of < 3 nsec, which is adequate for the FGD. In Fall 2006 a prototype front-end board composed of discrete components (already built) will be used to test the front-end board design with actual photosensors, and immediately afterwards a second prototype incorporating the ASIC itself will be built. These tests should be sufficient to finalize the last details of the FGD electronics design and move towards final board production. The prototype front-end board has already been used to successfully test the photosensor bias voltage regulator, current monitoring, and slow control systems.

## 4.4 Detector construction schedule

### 4.4.1 Schedule

A detailed schedule and WBS/GANTT chart exists for the FGD project, whose broad outline is shown in Figure 4.8. This schedule reflects available manpower and timescales for R&D and manufacturing, and culminates in the installation of the FGDs in the ND280 starting in early 2009. This schedule can comfortably be met with the available resources, while containing some contingency for unexpected delays.

In broad strokes, the schedule can be summarized as follows:

- October-December 2006: Scintillator production in Canada; finalization of mechanical design; fiber procurement; production of passive water modules.

- January-June 2007: assembly of XY scintillator layers; start of dark box construction; electronics prototyping.
- July 2007-November 2007: dark box construction; finalization of light injection system design; start of electronics board production.
- December 2007-March 2008: delivery of photosensors and optical couplers; instrumenting of XY layers with fibers and photosensors; continued electronics production
- April 2008: installation of final electronics
- April-November 2008: commissioning of FGDs at TRIUMF; beam tests with protons, pions, muons, and electrons; combined tests of FGDs+TPCs
- December 2008: shipment of FGDs and TPCs to Japan
- January-March 2009: installation of FGDs into ND280 detector
- April 2009: start of neutrino running

The lengthy commissioning period from April-November 2008 could be shortened if delivery of any component is delayed. The schedule is based upon the delivery of tested working photosensors starting in December 2007.

#### 4.4.2 Quality control

Quality control procedures are built in as integral parts of each FGD workpackage. Quality control procedures for major detector components are as follows:

- Scintillator bars: During the extrusion process, each bar will be tested for size and hole diameter, and individually labelled with a unique identifier. A sample of bars from each shift will be scanned with a radioactive source to verify light yield. After extrusion, every bar will be scanned along its length of a radioactive source to verify the level and uniformity of the light yield and to reject bad bars before the bars are glued into XY layers.
- Wavelength-shifting fibers: Fibers from every batch delivered by Kuraray will be tested with a radioactive source upon delivery. Fermilab's Lab 7 will perform spot checks on mirroring and polishing as fibers are processed. All fibers will be tested after mirroring in Canada with an LED test stand, and their attenuation lengths will be measured.
- Photosensors: All photosensors will be tested for gain, dark rate, and bias voltage before installation in the FGD.
- Assembled scintillator layers: Every channel on each assembled XY scintillator layer will be pulsed with the layer's light injection system immediately after assembly, before installation in the FGD, in order to verify that all photosensors, fiber couplers, and electronics channels are in working order.
- Passive water modules: Each passive water target module will be filled and checked for leaks under load after sealing.

In addition to quality control procedures that are implemented throughout the construction process, the construction schedule allows several months for calibration, testing, and shakedown of detector systems at TRIUMF before shipping the FGDs to Japan at the end of 2008.

## **4.5 Detector installation & commissioning**

### **4.5.1 FGD services**

The two FGD modules, forming part of the overall tracker of the ND280 experiment, are positioned in a supporting basket structure centered approximately five meters above the floor of the experimental hall. During regular operation, the tracker modules and basket structure are completely enclosed within the magnet yokes, and are surrounded by the ECAL calorimeter. The magnet comprises sixteen 'C' half-yokes formed into eight return yokes split along the central vertical axis of the assembly. Service access to all equipment positioned inside the magnet is made possible via slots located in the lower faces of the magnet yoke interface. Each of the central six yokes have four slots, 105mm in depth when viewed along the magnet axis and 260mm wide, transverse to the magnet axis. A custom designed array of service conduits will be provided to protect cables, optical links, and gas lines as they exit the magnet through this series of slots.

All FGD services are routed to the bottom side of the FGD through a gap between the bottom left and bottom right ECAL modules. It is foreseen to attach cable guides to the basket structure to secure all services in the event the FGD modules are disconnected and removed from the basket for maintenance. Similar cable guides will also be added to the underside of the basket to secure all cables, optical fibers, and water pipes making their transition from the side of the basket to the vertical service conduits passing through the magnet yokes.

Services for the FGD consist of optical fibers for data readout links and for light injection, power cables, negative-pressure water cooling lines for the electronics, control and monitoring cables, and water lines for the target water modules. In total the two FGDs will use 200 optical fibers for data readout and light injection, 16 power cables, 80 cables for slow control and monitoring, 10 pipes for the water cooling system, and 6 pipes for filling and draining the target water modules remotely.

### **4.5.2 FGD Transportation**

Upon completion of manufacture and testing at the TRIUMF site in Vancouver, it is foreseen to ship the FGD and other tracker modules to Japan using an ISO Intermodal forty-foot shipping container. While the overall transported load is relatively light, and well within the capacity of the shipping container, the large physical sizes of the various components dictate the use of a special 'high-cube' container which has an additional headroom of 300 mm. The door aperture of 2280 mm wide and 2560 mm high is the limiting factor influencing the design of a suitable FGD module transportation frame.

In order to maintain the lowest possible vertical profile, the transportation trolley will require side mounted castors and a maximum distance of 100 mm between the floor and the underside of the FGD module. The resulting 60 mm clearance at the door aperture will increase to 150 mm once the module is inside the container. Each transportation trolley will be provided with a mechanism to fasten one trolley to another, and also to remove each castor from contact with the floor to provide a stable platform for shipping. A framework will also be provided to constrain module movement with respect to the container floor and walls.

From the time each module passes inspection in Canada, until its re-inspection at ND280 in Japan, each module will be individually wrapped with a waterproof cover, and will be protected against humidity with an appropriate amount of packaged silica-gel. Working within the restrictive height limitations for the FGD modules, it is foreseen to add the maximum possible amount of damping material between the transportation trolley and module to minimize vibrations during shipping.

### **4.5.3 Reception at ND280**

The surface building of the ND280 facility provides a covered reception area, with gantry crane access, measuring approximately 6.0 × 14.0 meters. This area will be used for the unloading of the

TPC/FGD Intermodal container from its transport vehicle. With the container resting on the floor, the modules, on their individual transportation trolleys, will be unfastened one from another and removed from the container using their own castor system. Included in the same container will be a custom-designed clean room, previously assembled and tested in Canada, and shipped to Japan in kit form. Dedicated space for the clean room has been assigned on level B3 of the experimental hall, two floors below the experimental floor. Personnel access to the the cleanroom is provided by stairs and elevator with equipment access provided by an overhead 10 tonne gantry crane.

There will be a period of time, between unloading the container and the completion of the clean-room installation, when temporary module storage will be required. Sufficient space will be available for short term storage on level B3 while the cleanroom is being assembled. Each module will retain its protective wrap until such time it can be accommodated in the cleanroom for inspection, testing, and then given approval for installation into the basket structure.

Once all transportation frames and other fixtures have been removed from the shipping container, it will be transferred to a position adjacent the ND280 surface building for use as a part storage and workshop facility. The container will be modified to incorporate suitable doors and windows prior to leaving Canada. Arrangements will be made to provide lighting and power outlets conforming to Japanese building code standards.

#### **4.5.4 FGD Installation**

Upon being given approval for installation by the FGD technical group, each module will be provided with a temporary protective cover for its movement to the experimental floor. Mounted on a transportation trolley, each module will be removed from the clean room enclosure and wheeled the 14 meter distance to an area accessible by the overhead crane. After being lifted to the experimental floor, approximately 12 meters above the clean room level, the transportation trolley and protective cover will be removed in readiness for module assembly into the basket.

The vertical center of the basket is positioned almost 5 meters above the floor of the hall. Two scissor-lift working platforms will be provided to allow access to all areas of the basket during the installation process. It will be essential to have at least one person on each side of the basket to guide the approach of the FGD module into position and maintain the nominal 10 mm clearance between adjacent features. Securing of the module inside the basket structure is achieved via fasteners inserted from the underside of the basket into threaded holes in the base of the FGD frame. Alignment will be assured with datum pins and mating holes. Additional restraints will also be incorporated into the upper surface of the FGD modules to restrict movement during periods of seismic activity.

#### **4.5.5 ND280 Service Routing**

Equipment racks for the FGD and all other sub-detectors are located on the B2 floor immediately below the experimental area. Access from the basket to the B2 floor is provided in the form of six holes cast through the concrete floor of the experimental hall. These holes are located, three on each side of the centerline, in a position coincident with the walls of the lower central support pillar located directly under the basket. The distance from the centerline of the basket to the edge of the hole openings is 500 mm, and the cross-section of each hole will be of sufficient size to accommodate a standard range of cable trays in which to secure the services as they pass from one floor to another. The cooling water chillers may either be mounted on the B2 floor, or on the main floor in a location against the pit wall behind the right-hand magnet yoke.

An interconnecting steel floor beam of the basket support structure acts as a base for an array of conduits providing guidance for the various services exiting the magnet. There are six individual groups of four conduits, each one having the ability for adjustment to suit the position of mating slots in the central six yokes of the magnet. These conduits will have an approximate internal cross-section of 95 mm X 250 mm and will begin at a point 1125mm above the floor, continuing through

the magnet yokes and coils to terminate 3017 mm above floor level. To assist with segregation of the various service categories, the internal space of the conduits is sub-divided by 6mm diameter bars, spaced at 200 mm intervals along the length. It is anticipated fourteen of the conduits will be available for sharing between the TPC and FGD modules. Space, between the underside of the service conduits and the floor, provides sufficient room to allow routing of the services into their assigned cable trays, through the floor, and down to level B2.

## **4.6 Detector calibration**

### **4.6.1 Calibration of mechanical aspects**

The positions and shape of each scintillator/fiber modules will be measured before installation. The weight of each FGD planes as well as each “dead material” components, such as the dark box and electronics modules) are precisely measured before installation. Position of FGD will be surveyed after installation of components into the basked. During the data taking, the position of each FGD elements will be calibrated using extrapolated track from TPC. The weight of the FGD box will be monitored by the spring attached at the top

### **4.6.2 Electronics calibration**

The gain and timing of the front end electronics electronics will be tested and calibrated using the test pulse from ASIC and FPGA in the front end board. Leaky fiber and cosmic ray data will provide confirmation of this calibration procedure.

### **4.6.3 Photosensor calibration**

During the data taking, the single photoelectron gain of the photosensor will be measured by monitoring the single photoelectron peak position. Relative photon detection efficiency (PDE), gain, and its linearity will be calibrated by injecting the light by leaky fibers. This study will also provide an estimate of cross talk by its deviation from the Poisson distribution as well as stability of the pixel-by-pixel gain variation. A random trigger data will provide the measure of cross talk and the dark noise rate. Temperature and bias voltage ( $V_{op}$ ) will be constantly monitored during the experiment. The gain, PDE, cross talk, and noise rate of the photosensor can be parameterized by the voltage difference between breakdown voltage ( $V_{bd}$ ) and bias voltage,  $V_{bd}-V_{op}$ . The temperature and bias voltage dependences of gain, PDE, cross talk, and noise rate, will be measured as a function of  $V_{bd}-V_{op}$ , which will provide an independent check of the calibration.

### **4.6.4 Scintillator/fiber calibration**

Overall photoelectron yield for minimum ionizing particles (MIP) will be calibrated using cosmic rays and through going muons produced by neutrino interaction with upstream of the detector. These data will also provide attenuation length. Comparison of the leaky fiber measurement at near and far ends of the fibers will provide an independent measure of the attenuation length. Before assembly of FGD, the light yield and attenuation length of each scintillator/fiber module will be calibrated using the test beam at TRIUMF and LED.

### **4.6.5 Physics calibration**

Before installation, the FGD response will be calibrated using the proton, pion, muon, and electron beam at TRIUMF. This beam test will provide the saturation parameter (Birk’s constant) of the scintillator as well as the range of the particles as a function of momentum. During the data taking,

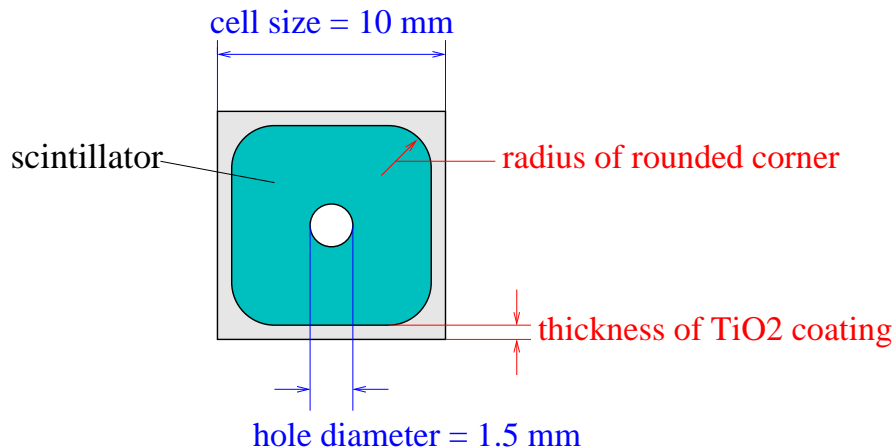


Figure 4.9: A cross-sectional view of a scintillator bar. A square shaped scintillator is coated with  $\text{TiO}_2$ -mixed polystyrene and has a hole of 1.5 mm diameter in its center. The outer width is fixed to be 10 mm. Due to the extrusion process, the scintillator has rounded corner. The actual FGD bars are slightly smaller (9.6 mm) with a nominal hole diameter of 1.8 mm.

protons and muons, whose momentum will be tagged by the upstream TPC, will be used to calibrate the saturation effect in the scintillator/photosensor and momentum/range calibrations.

## 4.7 Physics Performance

### 4.7.1 Hit finding efficiency

The “hit efficiency” for a plane of scintillator bars is defined as the probability that a particle crossing that plane will produce a signal in the photosensor above a specified detection threshold (typically specified in terms of some number of photoelectrons). The efficiency to find a hit in a plane of scintillator bars has been studied to determine the dimensions of the bar as well as the light yield needed to have sufficient efficiency. Fig. 4.9 shows a cross-sectional view of a model scintillator bar. It is square in shape, 10 mm wide, with  $\text{TiO}_2$ -mixed polystyrene reflector coating on the four sides. In the center of the bar, a hole of 1.5 mm diameter is made for the WLS fiber. Due to the extrusion process, the corner of the scintillator is rounded as shown in the figure, with a radius on the order of 2 mm. (Compare with Figure 4.3.) Since the reflector material is inactive, it may contribute to the inefficiency for detecting a hit, since a particle passing through a plane in the coating between two adjacent bars will not be detected. In order to determine the thickness of the reflector and the radius of rounded corners, the hit finding efficiency has been studied as a function of them. We need to estimate as well the minimum requirement for the light yield. This depends on the threshold to find a hit in a cell, the attenuation length of the WLS fiber, and the reflectivity of a reflector put on the end of the WLS fiber. The hit efficiency has therefore also studied as a function of these parameters.

A  $2\text{ m} \times 2\text{ m}$  plane geometry consisting of 200 scintillator bars, each of which has a length of 2 m and the cross-section shown in Fig. 4.9, was modeled in GEANT. The attenuation in the WLS fibers was taken into account during the light propagation through it. Each fiber had a reflector on an end and a SiPM photosensor on the other end. Once light comes to the mirrored end, it is reflected with a certain reflectivity and is propagated to the SiPM end. The left-right/top-bottom alternating readout scheme was correctly implemented, for example the first bar is read out from left (or top) end, the second one from right (or bottom) end, the third one from left (or top) end, and so on.

Individual minimum ionizing muons were generated in an event in front of the plane, which pass through the FGD. The angular distribution of the muons was taken from NEUT vectors, and corresponds to the distribution expected in the FGD. The muons are distributed randomly over the

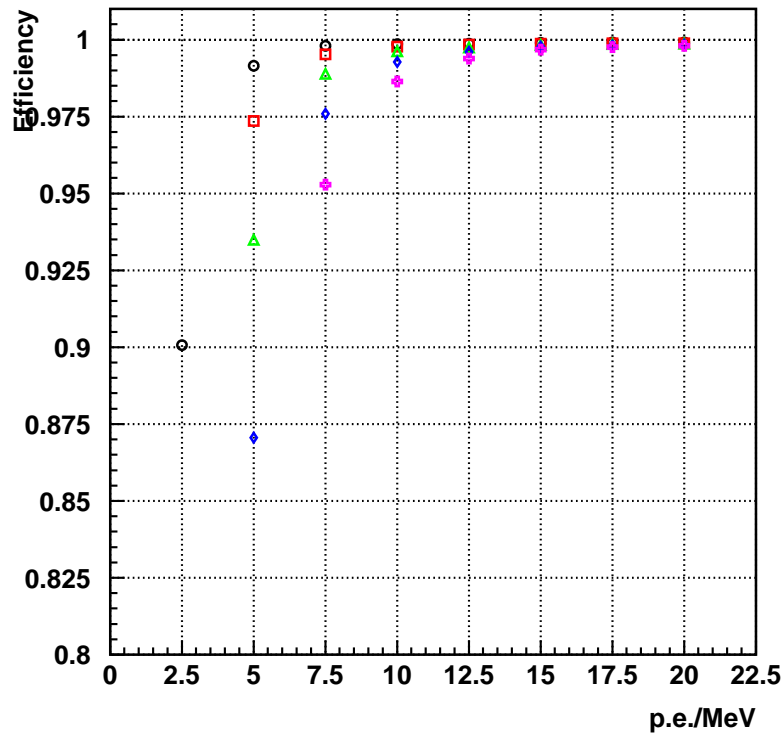


Figure 4.10: The hit finding efficiency as a function of the light yield and the threshold to find a hit in a cell. The horizontal axis is the light yield in units of the number of photoelectrons per MeV of deposited energy (p.e./MeV) for a hit in the near end of the bar. Different colors (markers) correspond to different threshold settings— black (circle): 1.5 p.e., red (square): 2.5 p.e., green (triangle): 3.5 p.e., blue (diamond): 4.5 p.e. and purple (cross): 5.5 p.e. The thickness of the TiO<sub>2</sub> reflective coating, the radius of the rounded corners, the attenuation length of the WLS fibers and the reflectivity of the reflector on the fiber ends are, respectively, set to be 0.2 mm, 2.0 mm, 300 cm and 0%.

plane area.

First, the hit finding efficiency as a function of the light yield and the threshold was studied. In this study, the thickness of TiO<sub>2</sub> reflective coating, the radius of the rounded corners, the attenuation length of the WLS fibers and the reflectivity of the reflector on the fiber ends are, respectively, set to be 0.2 mm, 2.0 mm, 300 cm and 0%. Fig. 4.10 shows the results. As seen in the figure, the efficiency is more than 99% when the light yield from the near end of the bar is larger than 7.5 p.e./MeV\* for a threshold setting below 2.5 p.e.

Second, the efficiency as a function of the TiO<sub>2</sub> thickness and the radius of the rounded corner was studied. Here, the light yield and the threshold are set to be 10 p.e./MeV and 1.5 p.e., respectively. Other parameters are the same as in Fig. 4.10. Fig. 4.11 shows the results. When the thickness of TiO<sub>2</sub> is less than 0.2 mm and the radius of the rounded corners is smaller than 2.0 mm, the efficiency gets larger than 99%.

Third, the efficiency as a function of the attenuation length of the WLS fiber was studied. In this case, the uniformity along the bar was investigated since the attenuation makes the response non-uniform. Fig. 4.12 shows the results. In the case that the light yield is 5 p.e./MeV, the efficiency is significantly non-uniform along the bar's length when the attenuation length is shorter than 300 cm, while it is uniform and more than 99% over the length of the bar in the case of 10 p.e./MeV light yield.

\* Here and throughout the section, the “light yield” refers to the number of photoelectrons per MeV of deposited energy generated by an MIP passing through the scintillator bar close to the readout side, for the nominal bar parameters.

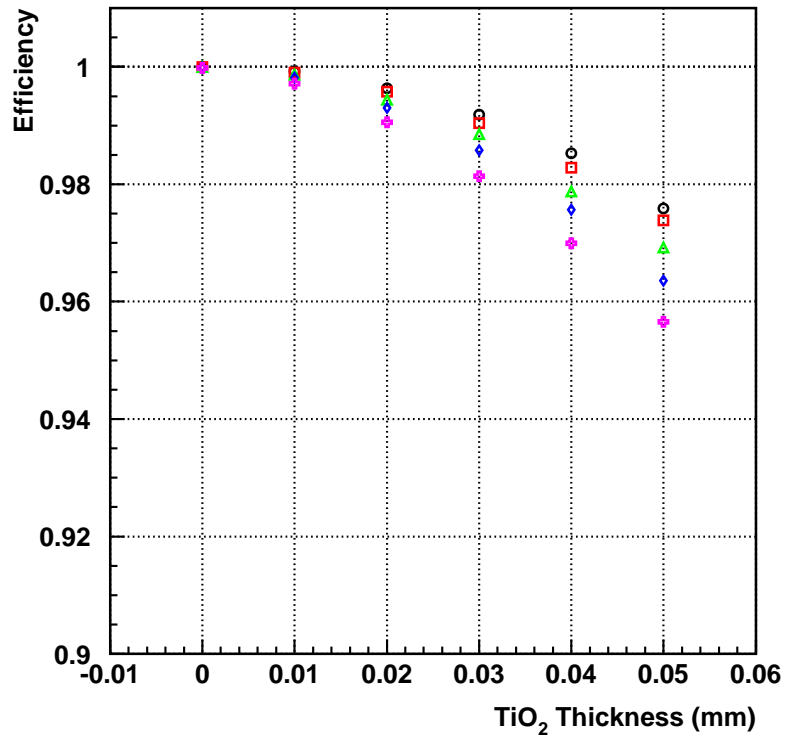


Figure 4.11: The hit finding efficiency as a function of the thickness of the TiO<sub>2</sub> reflective coating and the radius of the rounded corners. The horizontal axis is the thickness of the TiO<sub>2</sub>, and different colors (markers) show the different radii of the rounded corners—black (circle): 1.0 mm, red (square): 1.5 mm, green (triangle): 2.0 mm, blue (diamond): 2.5 mm and purple (cross): 3.0 mm. The light yield of the scintillators, the threshold to find a hit in a cell, the attenuation length of the WLS fibers and the reflectivity of the reflector on the fiber ends are, respectively, set to be 10 p.e./MeV, 1.5 p.e., 300 cm and 0%.

Finally, the efficiency as a function of the reflectivity of the mirror put on the end of the WLS fiber was studied. In this case, again, the uniformity along the bar is investigated since the the reflector makes the response more uniform. Fig. 4.13 shows the results. In the case that the light yield is 5 p.e./MeV, the efficiency has a non-uniform response along the bar when the reflectivity is less than 20% while it is uniform and more than 99% over the bar in the case of 10 p.e./MeV light yield.

In summary, the requirements for the light yield, the hit finding threshold, the thickness of the TiO<sub>2</sub> coating, the radius of the rounded corners, the attenuation length of the WLS fiber, and the reflectivity of the mirroring put on the fiber end are as follows:

- The light yield should be greater than 7.5 p.e./MeV.
- The threshold to find a hit in a cell should be below 2.5 p.e./MeV.
- The thickness of the TiO<sub>2</sub> coating should be less than 0.3 mm.
- The radius of the rounded corners should be smaller than 2.0 mm.
- The attenuation length of the WLS fiber should be longer than 300 cm.
- The reflectivity of the reflector on the fiber end should be greater than 20%.

With these parameters, the hit efficiency for any particle passing through a scintillator plane will be greater than 99%, matching the Scibar detector's performance and ensuring that a negligible number of hits are missed in an FGD track.

As shown in Figure 4.7, the CELCO scintillator bars and the Kuraray Y11 1 mm diameter WLS fiber yield 20 photoelectrons from the near end of the bar even without mirroring. This corresponds to a light yield of  $\sim 10$  p.e./MeV. The geometry of the extruded bars has been adjusted to satisfy the requirements on the coating and thickness, and even a modest quality mirroring of the far end of the fiber results in substantially more light than is needed to meet the minimum requirement. The additional light yield provides a safety margin, and also results in improved  $dE/dx$  resolution for particle ID.

## 4.7.2 Pion rejection in FGD using Michel electron

In order to study the CCQE cross section and understand the backgrounds to this measurement, we need to have particle identification capability to distinguish protons scattered in CCQE interactions from pions produced in any other background interactions. While protons from CCQE events in our energy range tend not to interact in the FGD (except by  $dE/dx$  ionization), pions often will undergo nuclear interactions before leaving the FGD. Pions stopping in the FGD may decay to a muon which then decays to emit a Michel electron. Therefore, some portion of pions have a "kink" in their tracks due to the Michel electron. Furthermore, in the case that a Michel electron is emitted, there may be a hit cluster delayed in time from the prompt pion track by the muon lifetime. Here, we show the possible capability of doing particle identification between protons and positive pions using these features.

The FGD geometry has been modeled in a GEANT simulation. A proton or a positive pion is generated in an event, where the momentum distribution for the proton is taken from CCQE interactions in a NEUT simulation and that for the pions is taken from any interaction in NEUT. This yields protons with momentum distributions corresponding to CCQE events and pion background events corresponding to all sources of pion background. The bunch structure of the neutrino beam in T2K is properly modeled: a beam spill has eight bunches with an interval of 600 ns between each other, and a bunch has a full width of 50 ns. When charged particles pass through a scintillator bar, its scintillation light is properly propagated to the readout photosensor put on the end of WLS fiber. The average light yield is assumed to be 10 p.e./MeV when a MIP passes through the scintillator at the position close to the readout end. (This matches the observed light yield from the FGD bars without

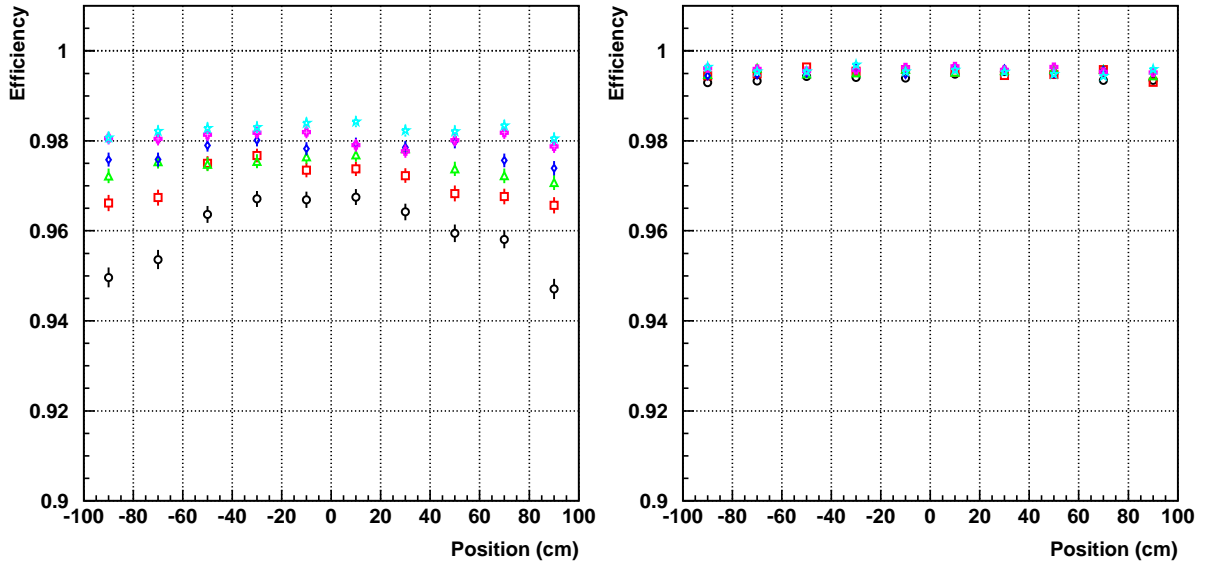


Figure 4.12: The hit finding efficiency as a function of the attenuation length of the WLS fiber. The horizontal axis is the hit position along the scintillator bar and different colors (markers) show the different attenuation lengths— black (circle): 250 cm, red (square): 300 cm, green (triangle): 350 cm, blue (diamond): 400 cm, purple (cross): 450 mm and light blue (star): 500 cm. The left figure shows the case that the light yield is 5 p.e./MeV, and the right figure shows the case that the light yield is 10 p.e./MeV. The threshold to find a hit in a cell, the thickness of  $\text{TiO}_2$  reflective coating, the radius of the rounded corners and the reflectivity of the mirror on the fiber ends are, respectively, set to be 1.5 p.e., 0.2 mm, 2.0 mm and 0%.

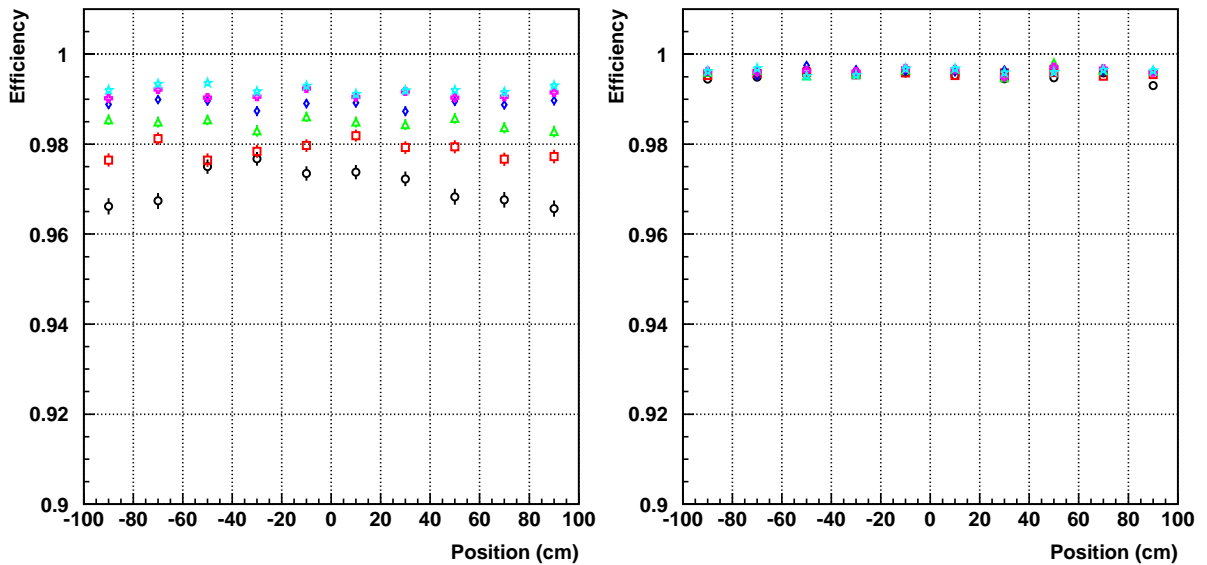


Figure 4.13: The hit finding efficiency as a function of the reflectivity of the reflector put on the end of the WLS fiber. The horizontal axis is the hit position along the scintillator bar, and different colors (markers) show the different reflectivities— black (circle): 0%, red (square): 20%, green (triangle): 40%, blue (diamond): 60%, purple (cross): 80% and light blue (star): 100%. The left figure shows the case that the light yield is 5 p.e./MeV, while the right figure shows the case that the light yield is 10 p.e./MeV. The attenuation length of the WLS fibers is set to be 300 cm and the other parameters are the same as Fig. 4.12.

Table 4.2: The fraction of events in each category. The number of events is normalized to the total number of interactions in the FGD *per*  $10^{20}$  *pot*?. The proton column includes only protons generated by CCQE interactions, while the pion column includes all charged pions.

Categories	Protons	Pions
Number of events	23,272	22,800
(1) Track entering TPC	9,135 (39.3%)	11,634 (51.0%)
(2) FGD-only track	8,437 (36.3%)	8,533 (37.4%)
(3) No track found	5,700 (24.5%)	2,633 (11.6%)

mirroring—with mirroring the light yield will be even higher.) The light attenuation and propagation time in WLS fiber are correctly taken into account.

Hits in each scintillator bar are recorded based on the specifications of the readout electronics described in Section 4.2.5. In the TPC chip case, the waveform sampling is enabled 50 ns before the first bunch comes and is kept enabled for 10  $\mu$ s. The pulse shape of the photosensor signal is recorded with a 50 MHz sampling rate during this time window. Therefore, the amount of charge and timing for each hit can be recorded, in principle. However, in this study, the charge is integrated over the whole 10  $\mu$ s time window for simplicity while the times of each hit occurring in the time window are recorded. To reflect the case of an actual waveform analysis, once a hit occurs, 50 ns dead time is created in the hit bar after the hit timing. During this dead time, additional hit timing cannot be recorded. (This corresponds to the inability to resolve closely spaced hits due to the 50 MHz sampling speed.)

A crude reconstruction algorithm is applied to each event. The vertex is assumed to be known from the associated muon track (which will be well measured by the TPC), and so the Monte Carlo truth interaction vertex is used. Hits close to each other or to the vertex are clustered in each view, where the threshold to find a hit in a cell is set at 1.5 p.e. Note that we don't care about the hit timings here, and all the hits close to each other are clustered regardless of time. When a series of hits in a cluster lies over two or more than two layers, it is recognized as a track segment. Starting and ending points of the track segments between  $x$  and  $y$  views are compared and  $x$  and  $y$  track segments are combined to build a reconstructed track if both starting and ending points are consistent within  $\pm 1$  layer. Once a track is found in an event, its straightness is examined by fitting the track to a straight line. If the reduced  $\chi^2$  of the fitting is less than 1.5, the track is recognized as a straight track without any kink. The series of hits in a track may have hits by a Michel electron. To identify it, the difference between the earliest and the latest hit timings among the hits in a cluster is calculated, which we call  $\Delta T$  here. If  $\Delta T$  is greater than 100 ns, the track is identified as the one possibly containing a Michel electron.

Here, we classify the events into three categories; (1) track entering the TPC, (2) FGD-only track and (3) no track found. The fraction of protons and pions in each category is summarized in Table 4.2. In case (1), the particle enters a neighboring TPC, and particle identification by momentum and  $dE/dx$  measured in the TPC is available as well as that in the FGD. Fig. 4.14, as an example to demonstrate the particle identification capability for protons and pions that enter a TPC, shows the two-dimensional plot of particle momenta measured by TPC v.s.  $dE/dx$  measured by FGD, where protons and pions are clearly separated below 1 GeV/ $c$ . In cases (2) and (3), the particle identification has to be done using only FGD information. We will discuss the particle identification capability for these categories below.

The particle identification capability for the FGD-only tracks (case 2) and the events with no track found (case 3) is examined based on the straightness and/or  $\Delta T$  of the track. As described above, these two parameters reflect the fact that the track has any kink and/or a delayed hit from a Michel electron. The results for case 2 are summarized in Table 4.3. By requiring tracks not to have any

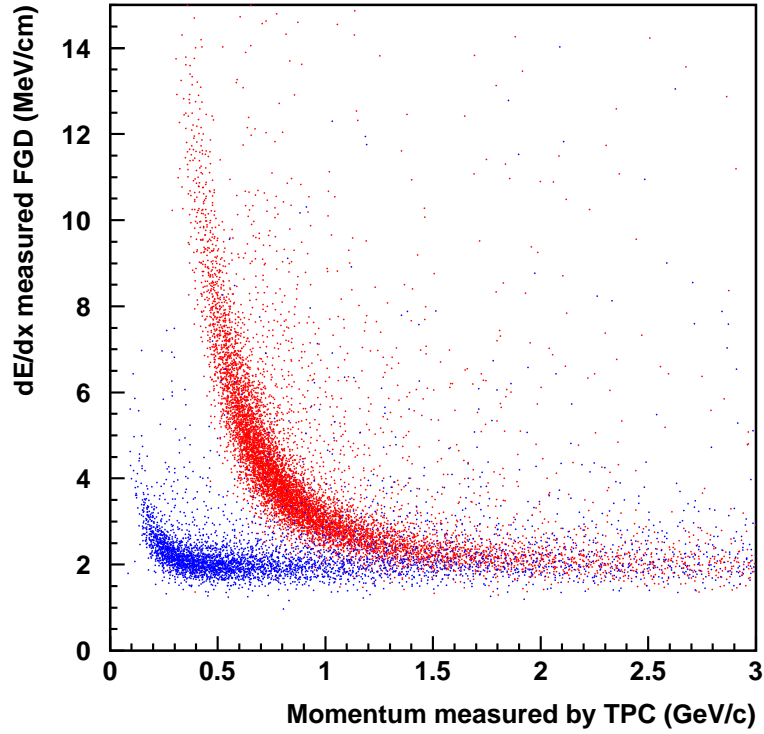


Figure 4.14: Two-dimensional plot of particle momenta measured by TPC v.s.  $dE/dx$  measured by FGD. Red dots are protons and blue ones are pions.

Table 4.3: The summary of the particle identification capability for the FGD-only tracks.

		Protons	Pions	$p/\pi$ ratio
Kink	Michel electron	8,437 events	8,533 events	0.989
Yes	Yes	2.3%	62.2%	0.037
No	Yes	0.8%	9.7%	0.082
Yes	No	10.8%	19.7%	0.399
No	No	86.0%	8.3%	10.2

kink or Michel electron, the protons from CCQE are very purely separated from the pions from any interactions. The purity is 91.1%. If needed, further separation between protons and pions is available using the range and deposited energy of the track although they are not used in this study.

Since we don't have any information on the straightness of tracks in case 3 (no reconstructable track), only  $\Delta T$  is used to examine the particle identification capability. The results are summarized in Table 4.4. The purity of CCQE protons separated from the pions from any interactions is 85.9% for the TPC chip.

In summary, the protons can be purely separated from pions using the difference of basic properties between protons and pions; protons in our energy region tends to stop inside the FGD without any interaction while pions interact in materials more often. Pions can also emit Michel electrons via a muon when they stop. Strong pion rejection is obtained for CCQE events even without using  $dE/dx$  information or kinematic constraints.

Table 4.4: The summary of the particle identification capability for the events with no track reconstructed in the FGD.

	Protons	Pions	$p/\pi$ ratio
Michel electron	5,700 events	2,633 events	2.165
Yes	0.5%	64.7%	0.023
No	99.5%	35.3%	6.10

Table 4.5: Estimated number of interactions in each FGD section and achievable statistical accuracy after 5 years running of the experiment (corresponding to  $5 \times 10^{21}$  protons on target).

Interaction modes	Active FGD	Passive FGD		efficiency	Statistical accuracy (after subtraction)
		Plastic	Water		
CCQE	289,900	165,600	118,300	40%	0.8%
CC- $1\pi^+$	141,600	80,900	57,800	40%	1.1%
CC- $1\pi^0$	27,400	15,700	11,200	10%	5.0%
NC- $1\pi^0$	40,800	23,300	16,700	10%	4.1%
beam $\nu_e$ CCQE	6,400	3,600	2,600	70%	3.8%

### 4.7.3 Statistical accuracy of interaction rate measurements

The FGDs have to provide the target mass for the neutrino interactions, and must allow us to estimate the rate of interactions occurring on water, which is the target material in Super-Kamiokande. The major modes to be measured are CCQE, CC- $1\pi$  and NC- $1\pi^0$  for muon neutrinos, and CCQE interactions for electron neutrinos.

One of the two FGD sections is totally active consisting of plastic scintillator bars. Its total mass is 1.0 tonnes. The other FGD section consists of active plastic scintillator layers alternating with passive water layers. The weight of plastic scintillator part is 0.56 ton and that of water is 0.44 ton, providing 1.99 tonnes of target mass in total. Table 4.5 summarizes the expected number of each interaction mode in each FGD section, as estimated from a simple GEANT3-based Monte Carlo. The efficiencies vary only slightly between the all=plastic FGD and the water FGD.

To estimate the interaction rates on water, we need to measure the rates in each FGD section and subtract the plastic components from the rate in the passive FGD. In the  $\nu_\mu$  CC events, the geometrical acceptance of the surrounding TPCS for muons produced in the FGDs is about 60%. Assuming that CCQE events are selected by requiring the proton to be tracked in the FGD and not having any kink or Michel electron as described in the previous section, the efficiency is about 70%, and hence overall efficiency for CCQE is about 40%. For the CC- $1\pi$  case, the pion has to be tracked in the FGD and identified as a pion by looking for kinks and/or a Michel electron in the track; the efficiency is about 70% and overall efficiency for CC- $1\pi$  is about 40%. The study on reconstructing  $\pi^0$  events using FGD, TPC and ECAL detectors show the efficiency of about 10%. As for the beam  $\nu_e$  events, the geometrical acceptance for the scattered electrons to enter the TPC is about 70%, all of which are assumed to be identified as electrons by momentum and  $dE/dx$  measurement in the TPC and energy measurement in the downstream ECAL.

Assuming the above efficiencies, the statistical accuracy for each interaction is calculated as shown in the last column of Table 4.5. The rates for CCQE and CC- $1\pi$  have to be measured within 5% and 10%, respectively, and the statistical accuracy is well below these requirements. For the NC- $1\pi^0$  and beam  $\nu_e$ , we need to understand their rate within 10%, and again, the statistical accuracy satisfies these requirements. Because the statistics significantly exceed the minimum requirements, we will be able to measure cross-sections accurately even with limited beam power. In addition, the high statistics will allow us to carry out a variety of systematic studies, such as subdividing the detector

and looking at the variation in energy vs. off-axis angle.

There may be backgrounds in the samples, and further selection may be required which lose efficiency. It is also expected that there is some difference of the efficiency and purity between totally active and passive FGDs, which can be corrected for in principle, but may introduce additional uncertainty. These issues have to be figured out by further studies.

# Chapter 5

## TPC(Time Projection Chambers)

The Time Projection Chambers (TPCs), along with the Fine Grained Detectors (FGDs), make up the Tracker for the off axis detector, which is optimized for the study of neutrino interactions that produce energetic charged particles.

This chapter describes the physics goals of the tracker and the TPCs in particular, followed by a description of the TPC mechanical design and its gas system. This is followed by a description of the micromegas gas amplification systems, the readout electronics, and integration into the ND280 hall. Considerations for offline software and calibration are then discussed. Prototype studies have been performed, and their results are shown along with expected performance of the full size modules. The chapter ends with a summary of the schedule, organization, and personnel involved.

### 5.1 Overview

#### 5.1.1 Key Roles for the Tracker

The ND280 tracker is intended to measure the  $\nu_\mu$  and  $\nu_e$  fluxes and spectra and various charged current cross sections. As neutrino cross-section measurements and flux determinations are always coupled, the charged current quasi-elastic (CCQE) cross-section is used as a reference cross-section.

#### Event classification

The first role for the tracker is to isolate a clean sample of CCQE events. In order to do that, both the proton and the muon track need to be reconstructed, the first mostly in the FGD. Detecting the recoil proton allows to select a high purity CCQE sample, using a method similar to the one used in K2K. The proton momentum is soft (a few hundred MeV/c) so that some will stop before entering the TPC volume. The TPC will also provide further information useful to study events with additional pion tracks. Given the fact that CCQE represents 40% of the total neutrino cross-section at these energies and that the TPC will provide 3-D information on the event, this classification is expected to be relatively straightforward.

It will also be important to distinguish the products from neutrino interactions inside the fiducial volume of the near detector from other beam related activity. In particular, neutrino interactions in the magnet iron will produce many charged particles that will enter the fiducial volume. The excellent 3D granularity of TPCs will allow these to be distinguished more easily than in a projective 2D tracker.

#### Neutrino spectrum

The measurement of the neutrino spectrum will be conducted using the reconstructed muon momentum in CCQE events. The muon momentum is only required to be measured with a moderate resolution since the neutrino energy reconstruction is affected by the relatively large smearing due to

the Fermi motion of the nucleon target. Typically this smearing is of the order of 10% for neutrinos around the peak of the beam energy. However, the muon momentum scale plays a crucial role in setting the scale of the neutrino energy and therefore in the  $\nu_\mu$  disappearance measurement. The energy scale is one of the main systematics in this measurement. The muon momentum scale is required to be understood at the 2% level.

## Beam composition

One of the major background to the  $\nu_e$  appearance measurement in Super-Kamiokande is due to the  $\nu_e$  component in the beam: it is necessary to measure this component in the ND280 detector. This can be done by reconstructing a sample of CCQE events where the high momentum particle is identified as an electron. This identification can be done using the TPC ionization measurement, and also with ECAL and SMRD information. The use of independent information from different detectors will help cross-check the selection efficiency and contamination of this analysis. The main difficulty will be to reliably identify electrons in a sample dominated by muons:  $\nu_e$  are expected to be 0.5% of the  $\nu_\mu$  in the 0.4-0.8 GeV energy range.

A further handle in this measurement will be given by the measurement of the neutrino spectrum in the high energy (1 to 3 GeV) region. These neutrinos are mainly due to kaon decays which are also responsible for a large fraction of the  $\nu_e$  component in the beam, through the Ke3 decays. Therefore the measurement of high momentum muons could help understand the hadron production model in the beam Monte Carlo simulations and help predict the  $\nu_e$  flux.

## Estimating backgrounds for SK

One of the main background contributions in Super-Kamiokande to the  $\nu_\mu$  disappearance measurement comes from charged current interactions with the production of one pion in the final state (CC1 $\pi$ ): in this case the charged pion is below the threshold to produce Cherenkov light or its ring is not reconstructed. Other backgrounds are due to the NC1 $\pi$  and NC-multi $\pi$  channels. The dominant backgrounds therefore include pions in the final states and thus understanding pion production and absorption mechanisms via nuclear re-interactions is fundamental to understand backgrounds at Super-Kamiokande. The goal in this domain will therefore be to measure the differential cross-section for CC1 $\pi$ .

## Constraining models of neutrino-nucleus interactions

A large fraction of low energy neutrino-nucleus interactions involves the production of very low energy hadrons. Monte Carlo simulations of these processes make use of empirical models which have not been well tested, owing to the fact that it is difficult to detect and measure the low energy particles within dense target material. The gas of the TPC will provide additional target nuclei, and neutrino interactions within the gas could provide interesting samples of a few thousand events per year to improve the understanding of neutrino-nucleus interactions, since all of the charged particles produced can be tracked in the TPC.

### 5.1.2 Key measurements by the TPCs

From the considerations above, the key measurements for the TPC system are:

- Momentum: here the goal is to reach a 10% resolution around 1 GeV/c. Given the limited curvature offered by the low magnetic field, this will require good space point resolution. The requirement on the momentum resolution drives the segmentation of the readout plane. A related but more challenging task is the measurement of the charge of high momentum muons. This will probably require the development of a combined and optimized fit algorithm using the space points of the muon track in several TPCs.

- Energy scale: the T2K physics goals require understanding the energy scale at the 2% level. This goal can be met using a combination of magnetic field measurement and mapping, absolute momentum calibration using a physical signal (the invariant mass of  $K^0$  produced in DIS neutrino events and decaying in the TPC volume), excellent control of the electric field distortions. Clearly this points to the importance of a dedicated calibration program as an integral part of the TPC project.
- Particle identification through ionization energy loss: here the purpose is to identify electron from muon in the 0.5 - 1.0 GeV/c momentum range. The typical separation between the electron and muon dE/dx is 30 to 40%. In order to achieve a  $3\sigma$  separation between the electron and the muon tracks, a dE/dx measurement below 10% is needed. Considering the number of samples and the track length and the resolution achieved by previous TPCs, this goal can be met. It requires however a careful calibration of the detector response both over the readout planes and as a function of time.

### 5.1.3 Basic Design Considerations for the ND280 TPCs

#### Geometry

The overall geometry of the TPC follows from the constraints given by the use of the UA1 magnet. Three TPCs are needed in order to measure the momenta of particles originating from the two FGD targets. The outer dimensions of each module are roughly  $2.5\text{ m} \times 2.5\text{ m}$  in the plane perpendicular to the neutrino beam direction, and 1.0 m along the beam direction. The transverse dimension is chosen to provide space between the inner wall of the magnet and the TPC modules for electromagnetic calorimeter and for a mechanical support cage. The dimension along the beam direction is chosen to achieve the required momentum resolution, including the necessary inactive elements. The upstream TPC will measure backscattered particles from the upstream FGD as well as high momentum muons exiting the POD in the forward direction.

#### Field cage

The field cage has been designed with the main criteria of robustness and simplicity of construction and excellent uniformity of the drift field. A simplified drawing of the TPC is shown in Fig. 5.1. Operation is considered at an electric field around 200 V/cm, the cathode being at a potential of  $-25\text{ kV}$ . The outer surface of the TPC module will be at nominal ground potential for safety considerations and for RF shielding. The field degradation will take place in a gas envelope between the outer and inner walls of the TPC. Given that the tracks to be measured have typical momenta in the few hundred MeV range, these walls will be built out of a very light material in order to minimize the amount of matter between the FGD and the TPC active volume. A central cathode will divide the drift space in two halves in order to limit the maximum drift distance to approximately 1m.

#### Gas options

Several gas mixtures are currently being considered for the TPC. All contain a dominant fraction of Argon to assure a large primary ionization yield. A few % fraction of an organic quencher (isobutane, ...) is studied in order to operate the gas amplification device well below the maximum voltage. This will give large flexibility and ease of operation. Small fraction of CF<sub>4</sub> or CO<sub>2</sub> are considered in order to lower the transverse diffusion coefficient of the mixture, to operate the gas close to its maximum drift velocity and to minimize the effect of small impurities.

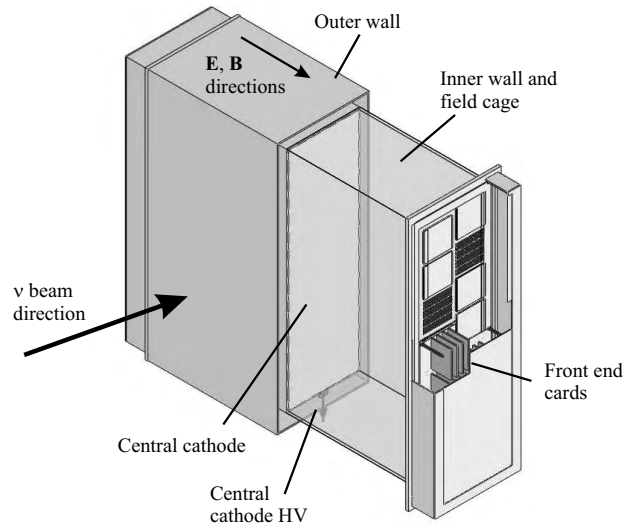


Figure 5.1: Simplified drawing of the TPC showing the inner and outer boxes and central cathode.

## Gas amplification

Micromegas has been chosen to be as the gas amplification device. The choice of a micropattern device is justified by the following considerations:

- the tracks will be produced almost isotropically. A micropattern device, having no preferred direction presents an advantage in term of resolution for large angle tracks with respect to a wire chamber.
- There will be no thin wires under tensions that present the risk of a breakage

The gas amplification device will cover a large detection surface of almost  $10 \text{ m}^2$ . Clearly a good uniformity of response of the O(100) modules will be at premium.

## Readout electronics

The readout electronics will have to instrument of the order of 100k channels: the maximum electronic density and cost are the major constraint driving the segmentation of the readout plane. Existing TPC-oriented ASIC (eg ALICE ALTRO chip) have been considered as a basis for this readout, however the combination of cost and dense integration has favored the choice of developing a new dedicated ASIC. This will offer a large flexibility in terms of sampling frequency, shaping time, and gain while taking advantage of the relatively low physics events rate of 0.3 Hz.

## 5.2 TPC mechanical

### 5.2.1 Overview of Mechanical Design

The major mechanical components of the TPC are shown in Fig. 5.1. The inner box forms the field cage and drift volume. The outer box surrounds the inner and forms a  $\text{CO}_2$  volume that provides the electrical insulation to hold off the substantial cathode voltage. The  $\text{CO}_2$  also serves to exclude oxygen, nitrogen, or other contaminants from entering the inner volume. The  $\text{CO}_2$  gap is 68 mm on the top and sides and 118 mm on the bottom, where extra space is needed for the cathode HV connection.

The inner box endplate mounts the micromegas module frame, to which each of the individual micromegas modules are mounted. The outer box endplate supports the service spacer and cover



Figure 5.2: Router to be used for much of the TPC mechanical construction at TRIUMF.

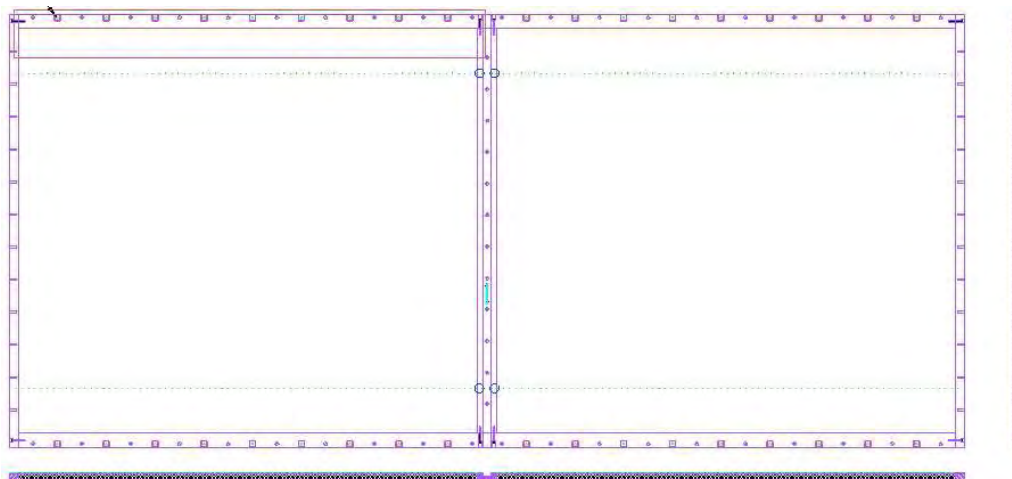


Figure 5.3: The inner box frame is assembled from bars of G10. An inner box wall is made by loading the frame with two (nearly square) sheets of rohocell and laminating both surfaces with 1/32 inch copper-clad G10. The central cathode is mounted to the central bar of the frame.

plate, which form the volume that contains the front end electronics. The service spacers also hold the cable and other service feedthroughs. The mounting and lifting fixtures attach to the outer box endplate.

The components are described in more detail below. Whenever possible, we have chosen a design that allows the device to be manufactured using TRIUMF resources. In particular, we will machine all of the large components using the new router purchased for this purpose (Fig. 5.2).

## 5.2.2 Inner Box/Field Cage

The inner box includes the central cathode, which defines the cathode plane of the drift field, the box walls, which define the field gradient, the endplate, and the module frame.

### Box walls

The box walls are constructed from 1/32 inch copper-clad G10 laminated onto both surfaces of 11.6 mm (nominal) thick rohocell, giving a total nominal thickness of 13.2 mm. To make the wall panels, a frame is constructed from glued and screwed G10 bars, which are machined to match the measured rohocell thickness. (The manufacturer's specification is  $\pm 0.5$  mm). The frame consists of four bars that form the outer edge of the sheet, with an additional central bar that provide an attachment area for the central cathode (Fig. 5.3).

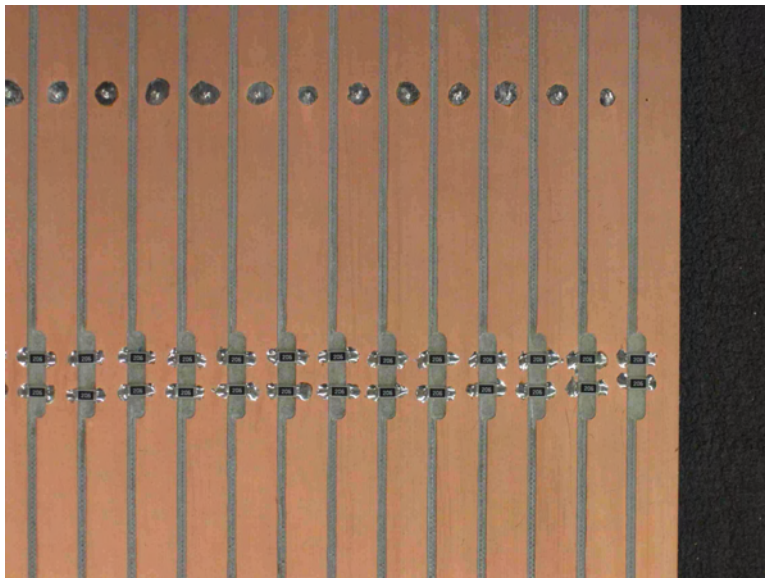


Figure 5.4: Copper strips on G10 form the electric field. This photograph of the outer wall of the prototype inner box shows the resistor chain soldered on the strips, and the jumpers that connect the inner and outer walls.

The frame is then loaded with rohacell and laminated to both copper-clad G10 sheets at the same time. The lamination is done on a granite flat table with a vacuum bag. The adhesive is Epon 826 with Versamid 140 hardener.

This assembly method assumes that the rohacell surfaces are parallel and flat within the tolerance provided by the glue. If this is not true, we will instead do the lamination in two stages. After the frame and rohacell is glued to the bottom sheet, the piece will be machined to the specified thickness prior to the gluing of the second.

The resulting laminated panels are then machined to size, and are drilled with screw holes for subsequent assembly. It is not yet decided whether the hole will be tapped using the router or done by hand. Note that no rohacell is exposed to the drift gas or the surrounding  $\text{CO}_2$  volume.

Both surfaces of each wall are then divided into a series of electrically isolated copper-clad strips on an 11.5 mm spacing, by cutting into but not through the G10 (Fig. 5.4). Two fine holes are drilled through each strip and jumpers soldered in place to ensure that the two copper-clad surfaces are electrically connected. The strip locations are referenced from the  $+x$  end of the panel during machining.

The strips are formed into two resistor chains (one for the drift volume on either side of the central cathode) by joining adjacent strips with a pair of  $20 \text{ M}\Omega$  resistors. The resistors are measured and sorted to ensure that the resulting resistance has an rms of 0.1% or less. Two resistors are needed to stop sparking if one of them fails open. The resistors are soldered onto the bottom wall, in the  $\text{CO}_2$  volume.

The joints are formed by screwing and gluing the panel edges. During gluing, the  $+x$  edges of the walls are screwed into a stiff plate to ensure a precision alignment of the reference edges. Note that the non-endplate edges of the top and bottom panels are chamfered to allow slightly more distance between the field-reducing corners and the outer box (Fig. 5.5). This joint design is not as strong as that used for the outer box, but the maximum differential pressure supported by the inner box is less than 1 mbar, compared to 10 mbar for the outer box.

### Central cathode/Laser calibration target

The central cathode is also a copper-clad G10/rohacell laminate component. The frame in this case is made from a solid G10 sheet, and includes an expanded rectangular region in each corner (Fig. 5.6).

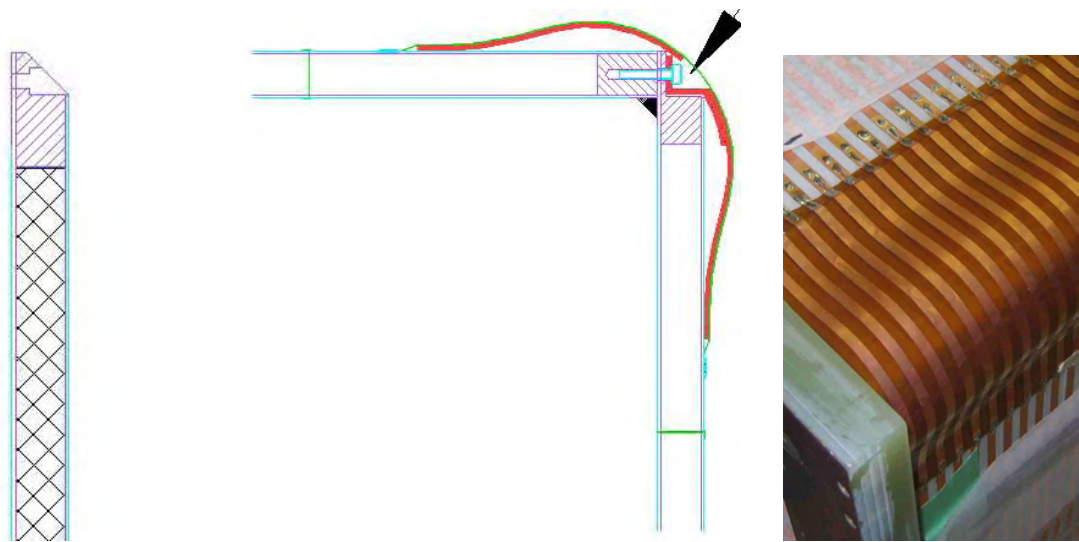


Figure 5.5: The inner box corners are chamfered (left) to allow the field-reduction corners to fit more tightly (middle). The right-hand photograph shows the corners on the prototype.

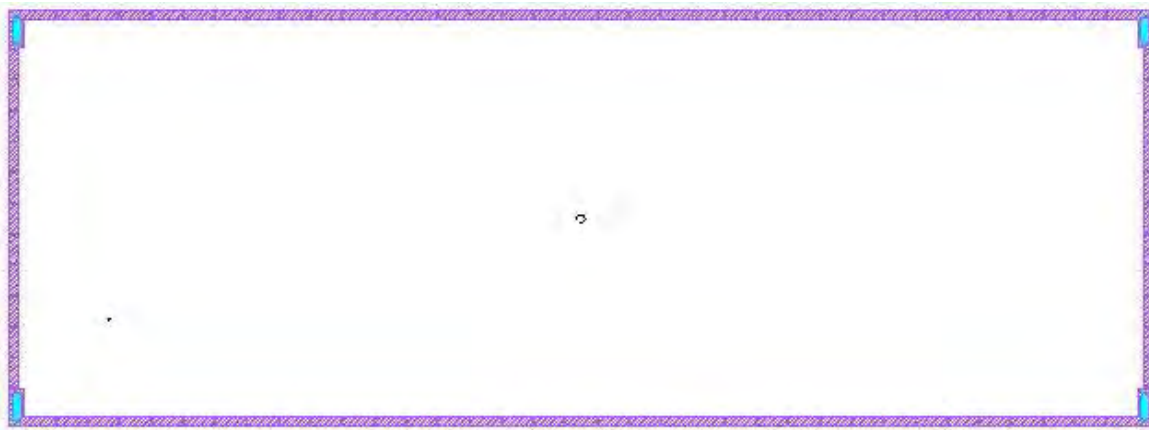


Figure 5.6: The central cathode is machined from a solid plate of G10 and includes gas ports in the four corners.

Gas holes are cut in each of these regions to connect the volumes on either side of the central cathode. The holes are covered with a metallic mesh to help maintain field uniformity in this region.

The high-voltage connection to the central cathode is made at the bottom of the box. The outer jacket and conductor of the high voltage cable terminate in a gas-tight socket mounted on the outer wall of the outer box. The central conductor and attached insulator pass through the outer box wall and terminate in a banana-plug socket mounted on the outer wall of the inner box. The socket is mechanically held by screws into the central G10 frame, and is electrically connected to the appropriate copper strip. Fine wires are soldered onto the cathode and fed through corresponding holes in the field cage during assembly. These are then soldered onto this strip.

The central cathode is the target for the laser calibration system. To provide sufficient contrast for the system to work, both surfaces are covered with carbon-loaded kapton, which is attached using transfer adhesive. The electrical connection between the kapton and the copper cladding is made using screws and washers near the gas holes. Slightly over-sized aluminum tape strips are then placed on the kapton, and trimmed to the correct width with a straight-edge and razor (Fig. 5.7). The strips will be placed with reasonable accuracy, but the final locations will be measured on the large router.



Figure 5.7: The bottom half of the prototype central cathode shows the carbon-loaded kapton with aluminum strips that will be used in the final design.

## Endplate

The endplate is machined from a solid plate of G10 (not copper clad) (Fig. 5.8). The inner surface will be machined to give the correct thickness, and to give the groove that captures the ends of the four box walls.

The outer surface is not machined, as we require the original smooth finish to achieve a good O-ring seal with the module frame. This requirement precludes an O-ring groove, so we instead use spacers and shims to capture the O-ring and establish the amount of compression.

Since the location in  $x$  of the module frame relative to the field cage is established by the O-ring spacers, variations in the distance from the top of the spacers to the joint groove on the inner surface are a contribution to the  $100\mu\text{m}$  tolerance on the planarity of the MicroMegas surface. We will machine the height of the spacers relative to the joint groove.

The threaded holes for the O-ring joints in the endplate will use brass inserts instead of holes tapped directly into the G10. The same is true of the O-ring holes in the module frame, but not of threaded holes that are used only once, such as those in glued joints.

## Module Frame and Stiffener

The Module Frame is a large G10 piece containing 12 almost-square cutouts for the 12 MicroMegas modules (Fig. 5.8). Both surfaces of the sheet need to be the original smooth G10 surfaces, since the bottom forms an O-ring seal to the endplate, while the top forms O-ring seal to the MicroMegas modules. Since G10 pieces of this size are not uniformly thick on the required scale, it will be produced from two pieces of G10 milled to thickness, then laminated.

As for the endplate, the O-ring spacers will need to be individually machined to achieve the planarity requirement on MM placement.

To help maintain the flatness requirements, a 20mm by 120mm G10 beam will be placed between the two columns of MM. It will be mounted to the top and bottom edges of the endplate, and will support the module frame using 8mm stainless steel rods at five locations. The rods rigidly support the module frame against both inwards and outwards deflections.

The endplate, module frame, module frame stiffener, and 12 dummy MM modules will be assembled on a granite table to ensure that the module frame is flat prior to the assembly being glued to the inner box panels.

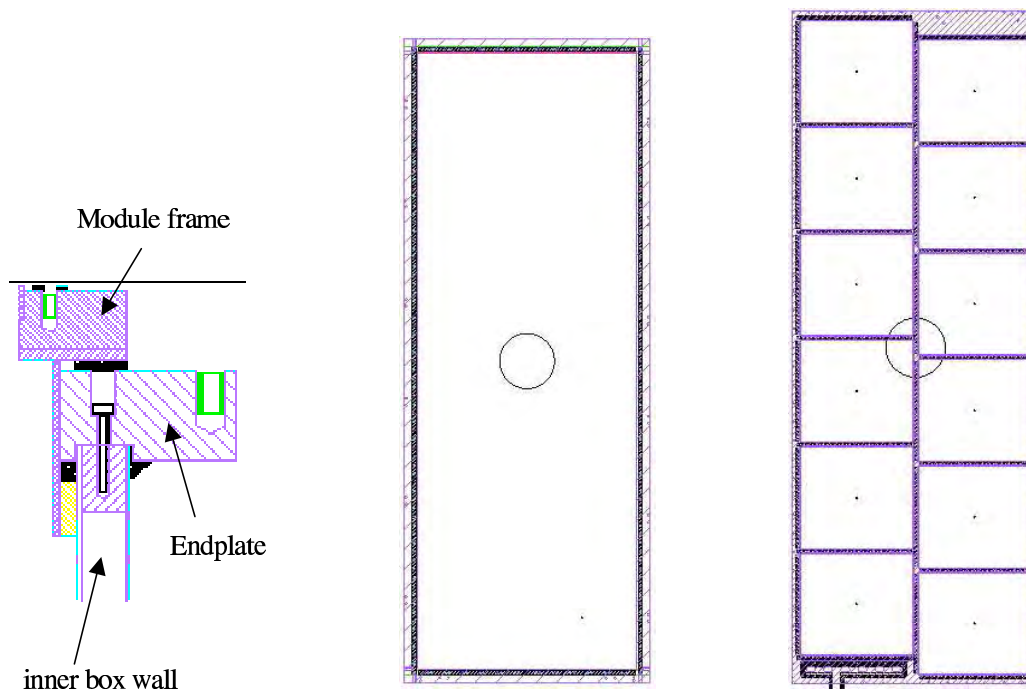


Figure 5.8: (left) Assembly detail of the inner box end. The box walls are glued and screwed into the endplate, then the module frame is mounted with an O-ring to the endplate. The module frame is constructed from two pieces of G10. (middle) Inner box endplate. (right) The 12 micromegas modules are mounted on the module frame, which is bolted to the inner box endplate. The gas manifold at each end is mounted near the bottom of the frame.

### Field reducing corners

The field-reducing corners are mounted on the non-endplate edges of the inner box to reduce the radius of curvature at the corner (Fig. 5.5). The resulting maximum electric field in the volume between the inner and outer boxes is 5 kV/cm for a drift field of 200 V/cm. The nominal breakdown in CO<sub>2</sub> is approximately 20 kV/cm.

### 5.2.3 Outer Box

The outer box consists of four walls and two endplates. It must be gas tight and reasonably robust to protect against incidental contact. The walls must be stiff enough that their deflection under the allowable CO<sub>2</sub> overpressure does not cause them to come in contact with any other surface, nor to infringe into the 10 mm stay-clear in  $z$  that surrounds each module.

The four walls are constructed from an aluminum-framed, aluminum-clad, rohacell laminate. The rohacell has a nominal thickness of 13.6 mm, with a manufacturer's specification of  $\pm 0.5$  mm. The aluminum cladding is 1/32 inch, giving a total nominal thickness of 15.2 mm. As with the inner box, no rohacell is exposed to the gas volume or to air.

To make each wall, four aluminum bars are machined to match the measured rohacell thickness, and are glued and screwed to form a frame. The bottom panel has an addition bar directly under the central cathode that provides a mounting point for the cathode HV socket. The front and back walls also have a central bar, because individual sheets of aluminum are not large enough to cover the entire surface.

The frame is then loaded with rohacell sheets and laminated to both aluminum surfaces at the same time. The lamination is done on a granite flat table with a vacuum bag, using the same adhesive as for the inner box.

Again, if the rohacell is not flat enough for this method, we will instead do the lamination in two stages. Either way, the resulting laminate sheet then undergoes final machining. The outer edge is cut



Figure 5.9: Test piece to study the outer box joints, constructed out of aluminum-clad rohocell laminate. In the actual detector, an aluminum frame will cover all rohocell edges.

to size, and holes are drilled and grooves machined for the subsequent assembly stage.

The box joints have the edges of the large upstream and downstream walls glued and screwed into grooves cut into the top and bottom panels (Fig. 5.9).

The endplate is in the shape of a picture frame, and is cut from a solid piece of aluminum. Grooves are cut into the endplate to allow the box walls to be glued and screwed into place. The endplate fully fills the specified 974 mm TPC envelope in  $z$ . The assembly groove locates the outer surface of the laminated walls 6 mm in from the envelope boundary. This establishes the allowable deflection of the outer box under the  $\text{CO}_2$  gas pressure.

#### 5.2.4 Service Spacers and Covers

The service spacers form an extension of the outer box wall, creating the volume that contains the front end electronics at each end of a TPC module. (Fig. 5.10). (Thus, the front end electronics are located in the  $\text{CO}_2$  atmosphere). Electrical, gas, and water feedthroughs are mounted on the service spacer, which is designed so that it can stay in place during the removal of a MicroMegas Module, or even the entire module frame. The only service item that does not pass through the service spacer is the central cathode HV.

The service spacer is constructed from aluminum. The bottom flange of the spacer forms an O-ring seal with the outer box endplate, while the top flange forms an O-ring seal with the cover plate.

The cover plate is an aluminum-clad rohocell laminate. It is similar in design to an outer box panel, except that the nominal rohocell thickness is 11.6 mm instead of 13.6 mm. The panels are light enough ( $\sim 10$  kg) that they can be removed and replaced by hand when accessing the electronics.

#### 5.2.5 Assembly and Testing

After the inner and outer boxes are separately assembled, the inner box is inserted into the outer using a removable rail system. The rail system is constructed from box beams, with commercial carriage

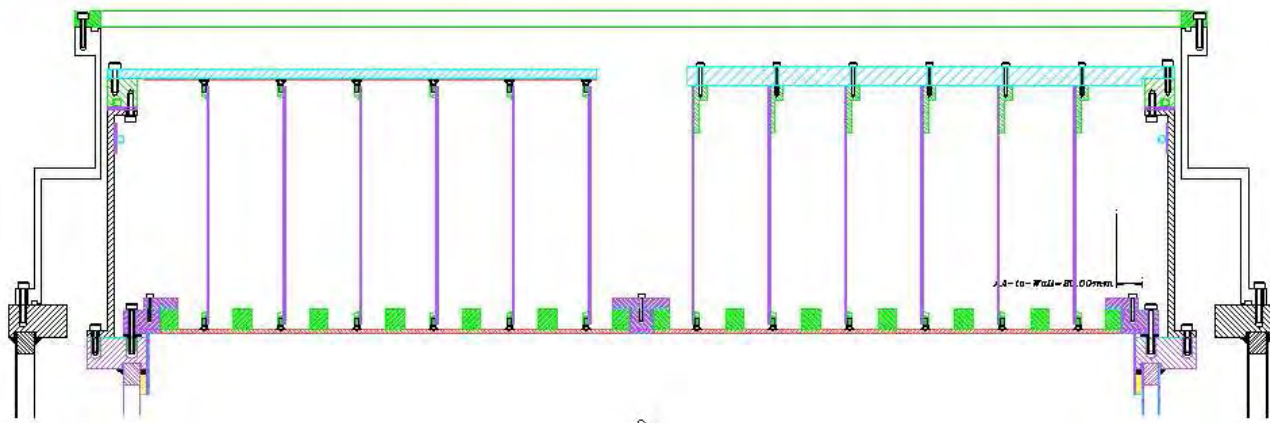


Figure 5.10: The service spacers are mounted to the outer box endplate and, together with the cover plate, enclose the front end electronics.

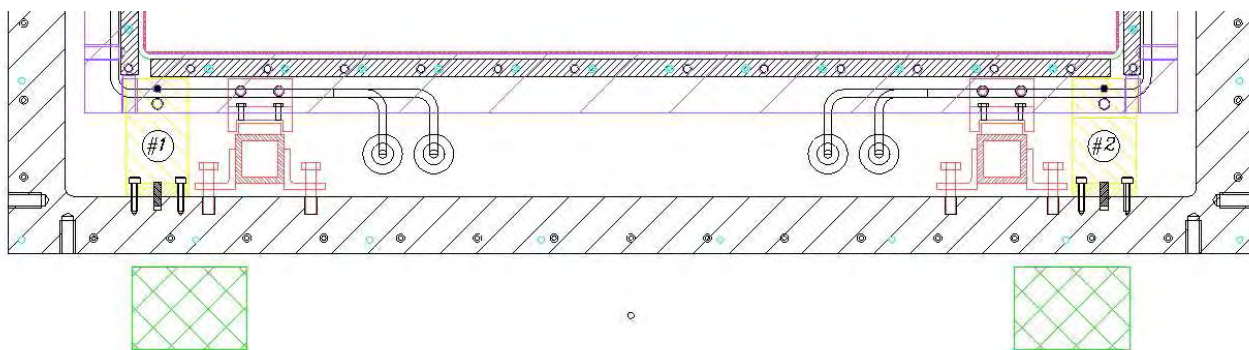


Figure 5.11: The rail system (in red) for installing the inner box into the outer. The mounting brackets that connect the two boxes are in yellow.

and rails, and includes a jacking system to adjust the vertical position of the inner box relative to the outer (Fig. 5.11).

The two boxes are connected at four bottom corners of the inner box. Since the two boxes have significantly different coefficients of thermal expansion, the mounts are designed to allow for (limited) relative motion. All four corners fix the vertical ( $y$ ) separation between the boxes. The  $-x$ ,  $-z$  mount constrains relative motion in both  $x$  and  $z$ , the  $+x$ ,  $+z$  mount constrains neither  $x$  nor  $z$ , while the other two mounts constrain only one of  $x$  or  $z$  by using a slot and pin system.

The gas manifolds are then mounted to the bottom edges of the module frame and the service spacers attached to the outer box endplate. Some services inside the service volume can be connected at this time: gas lines, pressure transducers, some temperature sensors, and the cooling lines (Fig. 5.12). The remainder will be connected after the front-end electronics are mounted.

At this stage of assembly, the module frames will be populated by blanks that will keep the inner volume clean and allow us to perform initial gas tightness and HV tests. The gas tests will include overpressure tests, and measurements of the  $O_2$  concentration in the outer box exhaust, and in the inner box exhaust when air is present in the outer box. All O-ring joints are accessible from the endplate region, so most potential leak locations can be reached without having to remove the inner box.

The MM modules will be installed after these tests, together with the available front end electronics (Fig. 5.12). After commissioning the MM modules and electronics, cosmic rays will be used to check the hit resolution and perform some calibration tests. Beam tests in the M11 beam line at TRIUMF can be used for both tracking and  $dE/dx$  measurements. The beam tests will also be performed with FGD modules to allow combined reconstruction tests.

The rail system will be shipped to Japan to allow the modules to be disassembled, albeit at the

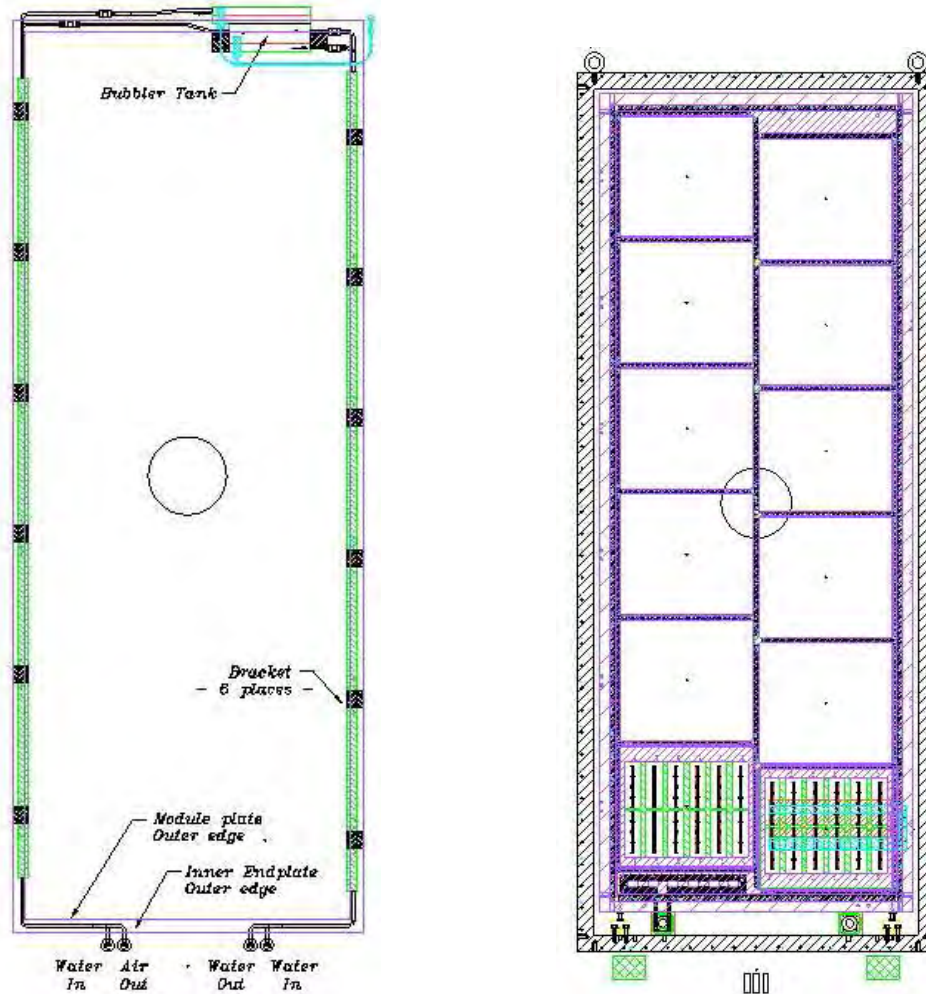


Figure 5.12: (a) The cooling lines mounted instead the service volume. (b) Assembled TPC, with two MicroMegas modules mounted. Note that the rails used to insert the inner box have been removed.

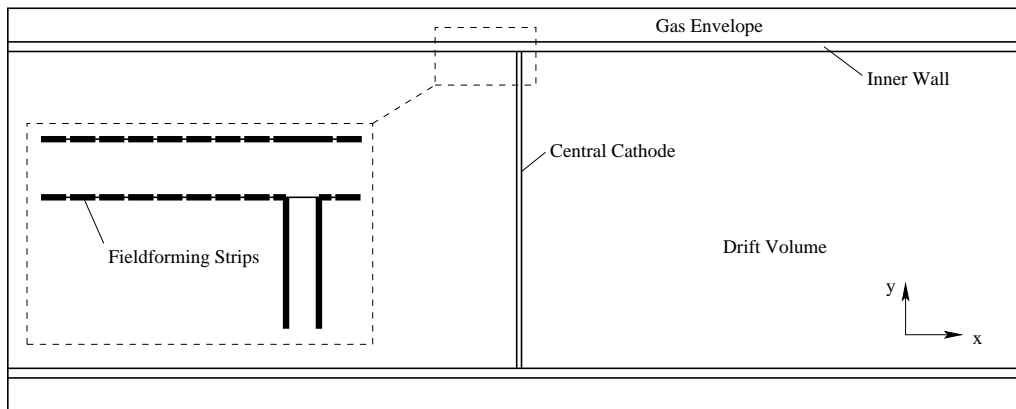


Figure 5.13: The 2-dimensional model used in the finite element analysis. The model's dimensions are close to those of the final design. The model ends at the endplates which are at ground potential (left and right in the figure) and at the inside of the outer wall also at ground. The inset shows a detail illustrating the arrangement of the field forming strips. Note that the central cathode is located such that it intersects with the inner wall in the middle of a strip.

cost of removing the services, service spacers, and gas manifolds.

## 5.2.6 Analysis of the Electric Field

### Basic Design of the Field Cage

The field cage described in some detail in the previous sections follows closely that of the STAR design [1]. There are strips on the inside and the outside of the side walls of the inner box. The two sets of strips are aligned. The strip width is 10 mm with a 1.5 mm gap in between the strips, giving an 11.5 mm pitch. The thickness of the inner wall is proposed to be 13.2 mm. The high electric potential on the inner wall, especially near the central cathode is dropped to ground across the gas envelope that surrounds the drift volume. The outer wall is at ground. A schematic of the arrangement is shown in Fig. 5.13. A detailed view of the strips is also given.

The electric field in the TPC was studied using the 2D finite element analysis suite COMSOL Multiphysics. Figure 5.14 shows the electric field for the geometry explained above. The field is uniform to better than  $10^{-4}$  for distances larger than 20 mm from the inner side wall.

The electric field uniformity worsens when the micromegas devices used for gas amplification are included in the model. Figure 5.15 shows the geometry near the readout with two micromegas devices. The Figure also shows a possible wiregrid that protects the drift volume from potential mismatches in the readout region. In the following studies the wiregrid is not included unless otherwise noted.

Figure 5.16 shows the electric field in one side of the TPC module including the micromegas readout. In this calculation the readout plane is at ground, the micromegas mesh located  $124 \mu\text{m}$  from the readout pads is at  $-400 \text{ V}$ , the nominal electric field in the drift volume is  $180 \text{ V/cm}$  and therefore the central cathode at a distance of 1.2535 m from the micromesh is at  $-22,963 \text{ V}$ . The figure shows that there is excellent field uniformity from the central cathode up to about 20 cm from the readout region. In the readout region the field distortions become larger than  $10^{-4}$  due to the non-continuous termination of the field by the micromegas devices and their support structures. In order to estimate the impact of these field distortions on the particle tracks, particles are propagated through the drift volume. In the simplest model, the velocity of the drifting electrons is constant and proportional to the electric field vector at any given point in the drift volume,  $\vec{v} = \mu \vec{E}$ , where  $\mu$  is the electron mobility. Based on this model particles were tracked through the field starting 0.25 m from the micromesh at various locations perpendicular to the drift direction. The algorithm then measures the perpendicular displacement of the track where it intersects with the micromesh with respect to the starting point of

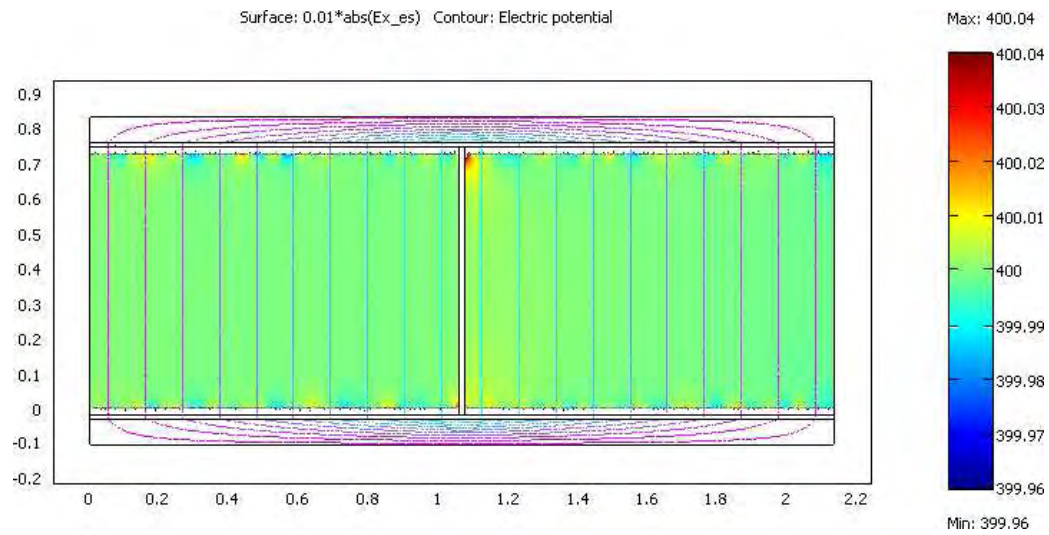


Figure 5.14: The electric field in a TPC module computed with finite element analysis. The surface shows the field component in the drift direction in the range of  $399.96 \text{ V/cm} < E < 400.04 \text{ V/cm}$  with  $400 \text{ V/cm}$  being the nominal electric field in this calculation. The contour shows equipotential lines. (Note that the dimensions used here do not correspond exactly to those of the final design.)

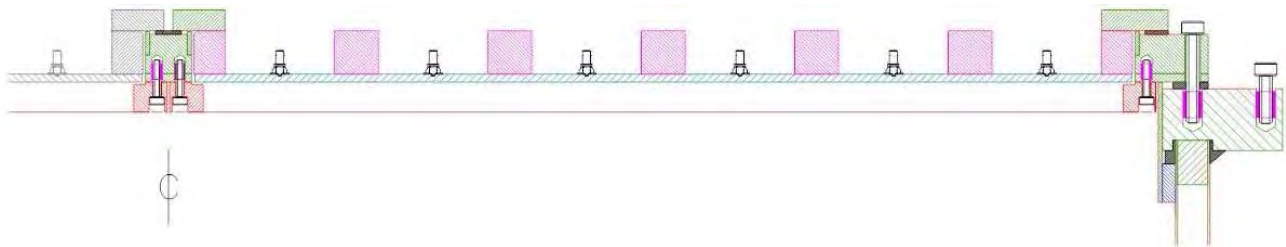


Figure 5.15: The geometry near the readout of the TPC with micromegas gas amplification. The proposed wiregrid is shown in red.

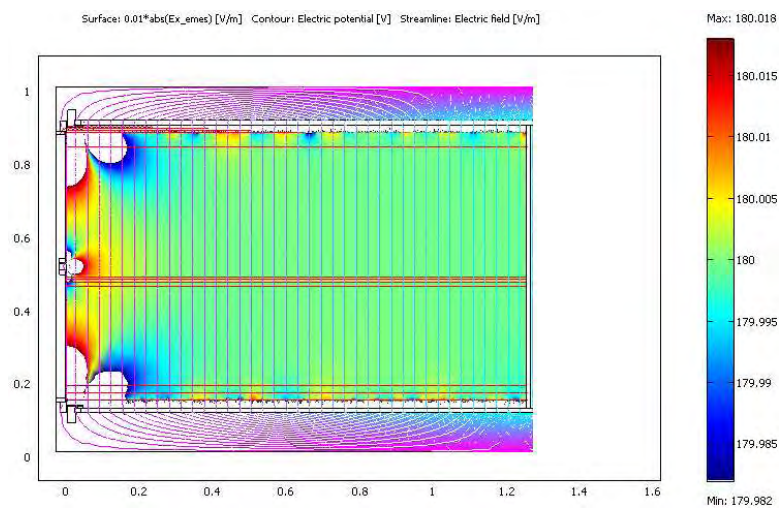


Figure 5.16: The electric field in one side of a TPC module including the micromegas based readout. The nominal electric field in the drift direction is  $180 \text{ V/cm}$  and the surface shows a range of  $179.982 \text{ V/cm} < E < 180.018 \text{ V/cm}$ . The *small* fluctuations along the side walls are due to the finite precision of the calculation.

the track. The displacements for a few starting positions ( $x$  is in the drift direction) are:

xStart[m]	yStart [m]	Displacement [mm]
0.25000	0.88950	-0.06910
0.25000	0.88500	-0.08423
0.25000	0.88000	-0.08246
0.25000	0.87500	-0.07761
0.25000	0.87000	-0.07170
0.25000	0.85000	-0.04970
0.25000	0.82000	-0.02923
0.25000	0.80000	-0.02141
0.25000	0.75000	-0.01110
0.25000	0.70000	-0.00653

These starting positions sample the distortions observed in the upper left corner in Fig. 5.16 where  $y = 0.8895$  corresponds to the upper end of the active area of the top micromegas device. The distortions are found to be below  $100 \mu\text{m}$  which is within the limits required for good resolution.

### Systematic Studies

The calculations presented in the previous subsection assume that the TPC will be built to perfect specifications. However, the TPC can only be constructed within certain mechanical limits and the resistor chain required to degrade the potential can only be set up with resistances of finite precision. In addition, the pressure differentials between the inner and the outer box and the finite mechanical rigidity may lead to bulging.

**Imperfect resistors** The resistors for the potential degrader will be paired and the resistance of each pair is anticipated to be accurate to better than 0.1%. For a given set of resistances  $\{R_i\}$  of the resistor pairs, the potential  $V_j$  on a strip  $j$  is given by

$$V_j = \frac{\sum_{i=0}^{j-1} R_i}{\sum_{i=0}^n R_i} (V_C - V_0) + V_0. \quad (5.1)$$

Here  $V_C$  is the potential of the cathode,  $V_0$  is the potential of the micromesh, and  $n$  is the number of strips on the sidewalls excluding the central cathode and the micromesh. The impact of imperfect resistances was studied using the finite element method by randomly drawing resistances with 0.1% accuracy (a Gaussian distribution with RMS of 0.1% was assumed) and recomputing the electric field for each set of resistances. Field maps for a variety of resistances with 0.1% accuracy are shown in Fig. 5.17. The field distortions due to variations in the resistor chain are more substantial than those found due to the geometry of the readout. One of these samples (column 2, row 1 in the Figure) was used to compute track displacements:

xStart[m]	yStart [m]	Displacement [mm]
0.40000	0.88000	-0.08845
0.40000	0.70000	-0.00960
0.40000	0.60000	-0.00517
0.40000	0.80000	-0.02717
1.20000	0.88000	-0.12178
1.20000	0.70000	-0.03103
1.20000	0.60000	-0.01476
1.20000	0.80000	-0.05714

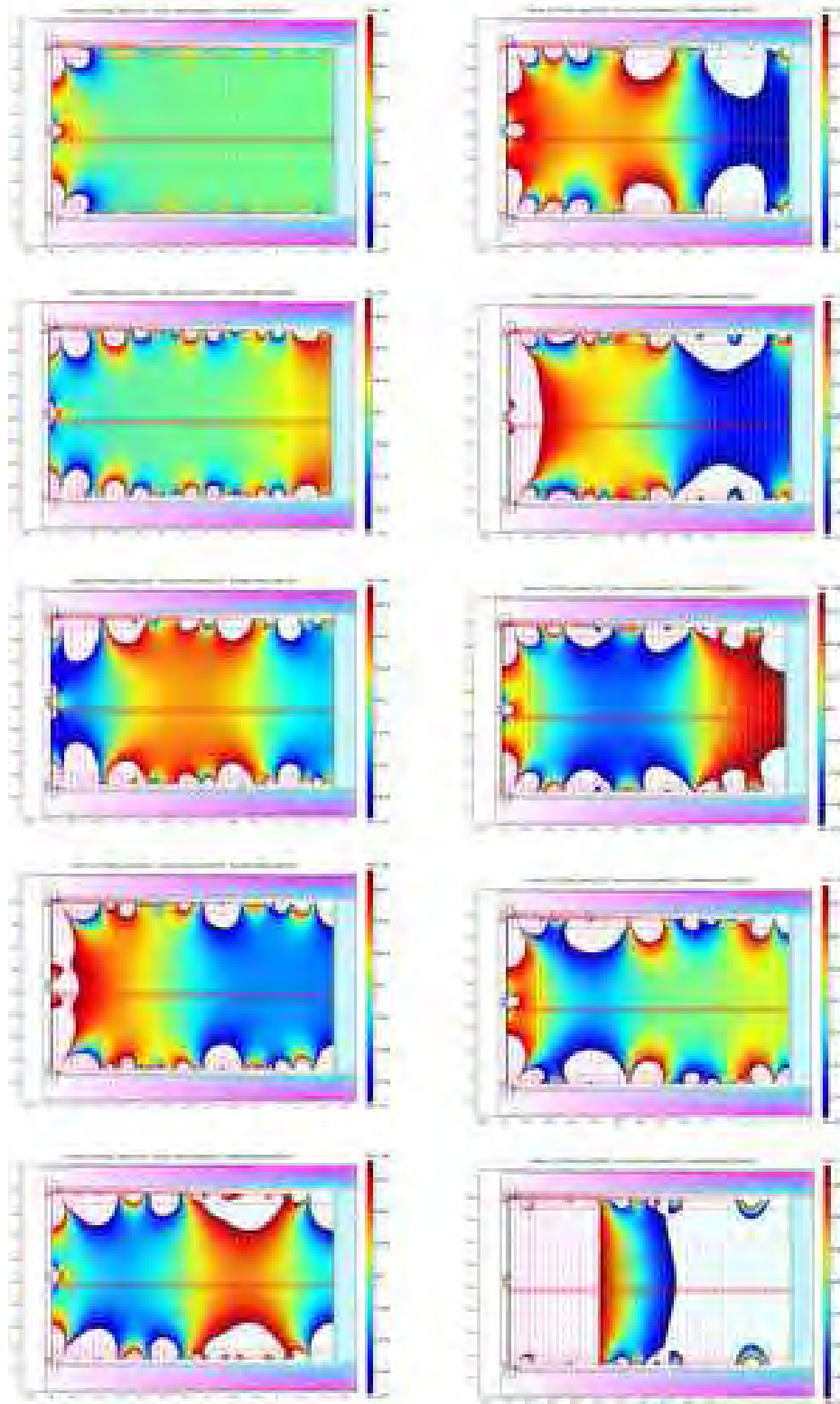


Figure 5.17: Field maps for 9 resistor chains with resistances of 0.1% accuracy. For comparison, the top left panel shows the electric field for perfect resistances. The range of the surface plot is  $179.982 \text{ V/cm} < E < 180.018 \text{ V/cm}$ , that is  $10^{-4}$  about the central value.

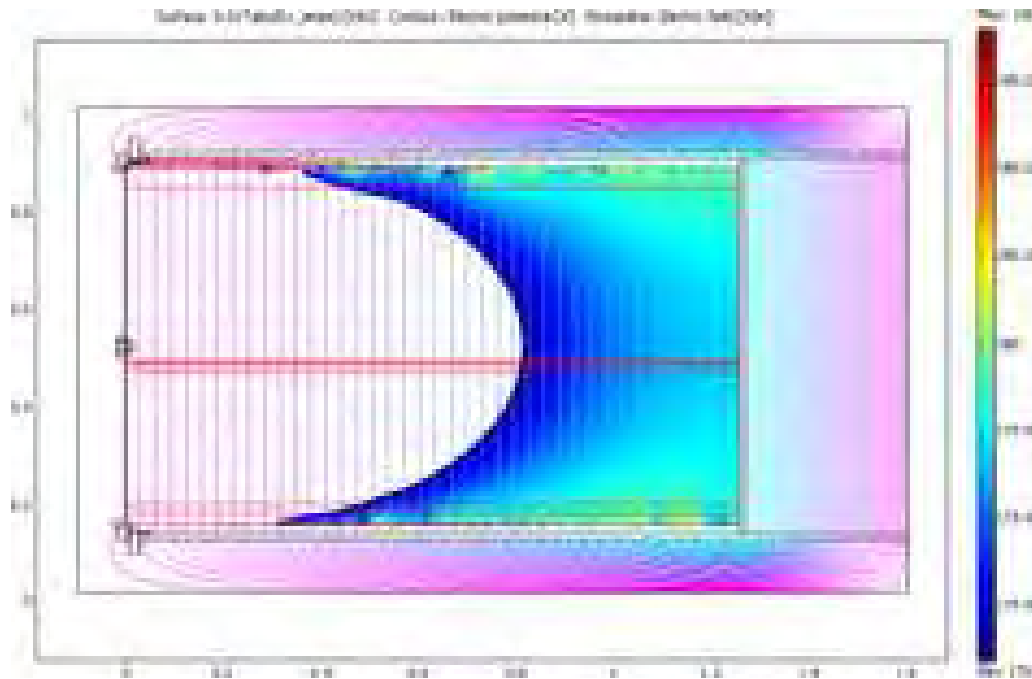


Figure 5.18: The electric field in the drift direction if the micromegas readout modules are shifted by  $-0.5$  mm. The range of the surface plot is  $179.982 \text{ V/cm} < E < 180.018 \text{ V/cm}$ .

The track displacements are below the  $100 \mu\text{m}$  in most cases except close to the edge of the micromegas active area. These values show that the distortions in a field cage built with resistances matched to  $0.1\%$  typically satisfy our target of  $100 \mu\text{m}$  distortion for a  $1 \text{ m}$  drift. However, larger distortions could result if the sequence of resistances is unfortunate.

**Imperfect placement of the readout modules** All components of the TPCs can only be aligned with finite precision. The central cathodes and the readout modules are most sensitive to improper placement as their surfaces define the location of the cathode and the anode with respect to each other and with respect to the potential degrader on the sidewalls. Here, two scenarios were studied: a shift of the readout plane by  $-0.5$  mm and a tilt of the plane such that the top end of the upper micromegas device was tilted  $0.5$  mm inwards and the bottom of the lower micromegas device was tilted  $0.5$  mm outwards. The electric fields for the shifted and tilted micromegas devices are shown in Figs. 5.18 and 5.19 respectively. In both cases the electric field is sizably distorted. The track distortions computed for a few starting points are

xStart[m]	yStart [m]	Shift: D [mm]	Tilt: D [mm]
0.60000	0.85000	0.59765	-0.33914
0.60000	0.70000	0.21098	0.14281
0.60000	0.60000	0.08122	0.21014
0.60000	0.55000	0.02273	0.22006

Corresponding to the large field distortions the track displacement exceed the limit of  $100$  micron in a number of cases. Thus the placement of the micromegas readout plane needs to be controlled to better than the  $0.5$  mm shift (and tilt) investigated here.

A potential solution to the large field distortions in the drift volume is the wiregrid indicated in Fig. 5.15. Under the assumption that the wiregrid is positioned perfectly and that it is unaffected by the shift or tilt of the micromegas readout, the electric field in the drift volume is much less affected by the misplacement of the readout module. The resulting electric field for the same  $0.5$  mm shift and the  $0.0775$  degree tilt are shown in Fig. 5.20. The field distortions are notably smaller than without the wiregrid. Track distortions have not been computed for these two cases. Note that the assumption

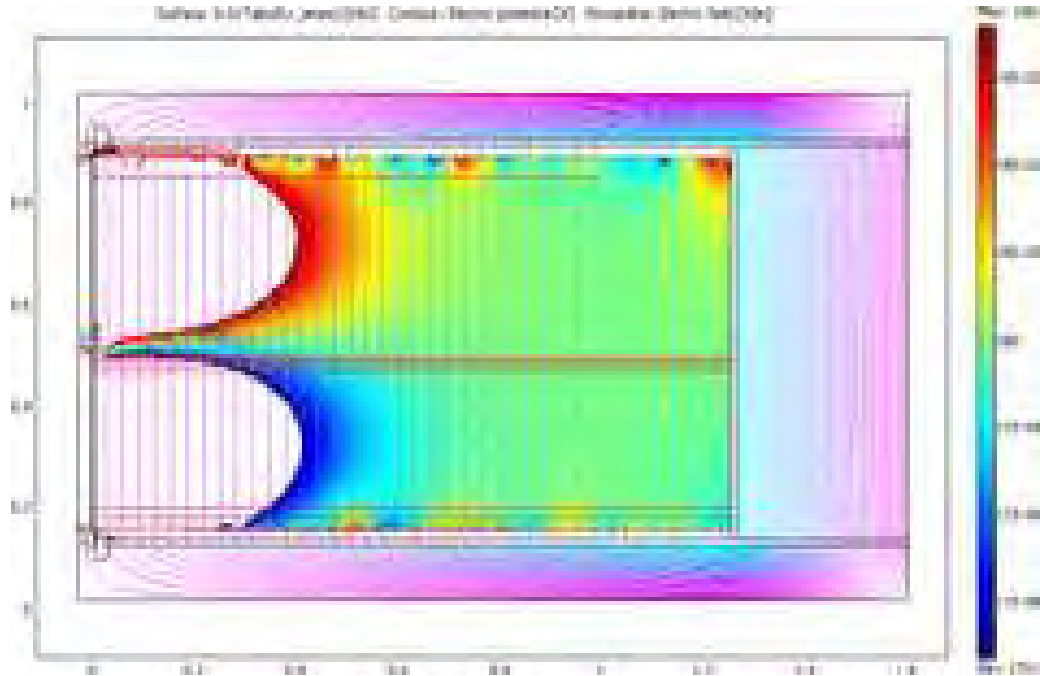


Figure 5.19: The electric field in the drift direction if the micromegas readout modules is tilted by 0.0775 degrees. The range of the surface plot is  $179.982 \text{ V/cm} < E < 180.018 \text{ V/cm}$ .

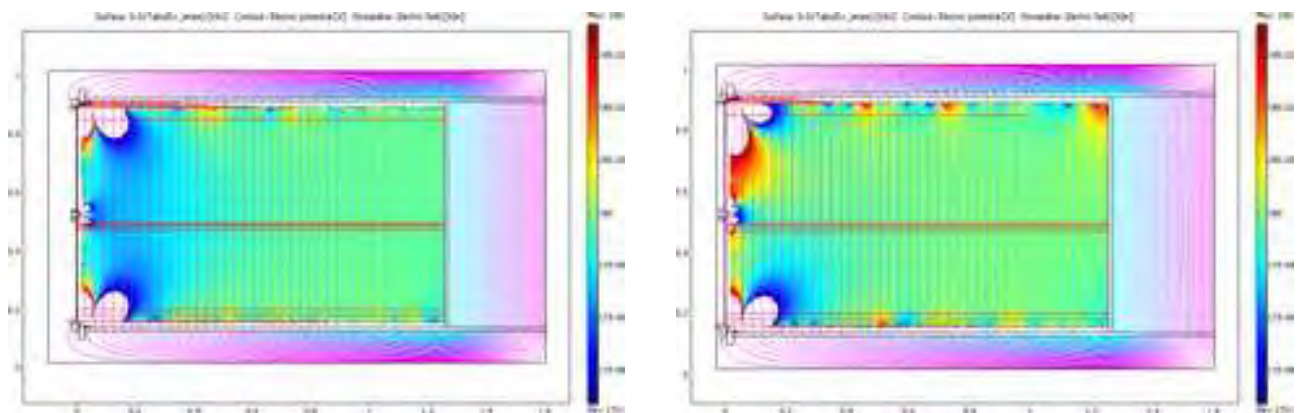


Figure 5.20: The electric field in a fieldcage with a wiregrid when the micromegas readout is shifted by -0.5 mm (left) or tilted by -0.0775 degrees (right). The range of the surface plot is  $179.982 \text{ V/cm} < E < 180.018 \text{ V/cm}$ .

of a perfectly positioned wiregrid is not very realistic. While the grid can in principle be aligned more precisely than the (removable) readout modules, it would need to be attached to the micromegas support frame in the middle. Therefore the wiregrid would become distorted if the readout modules are displaced. The impact on the electric field of this scenario has so far not been considered.

## Summary

The electric field uniformity in the proposed T2K TPC modules was studied using finite element analysis. For a perfectly built detector the electric field uniformity was sufficient to result in track displacements below 100 microns within the active area of the micromegas readout modules. The anticipated 0.1% accuracy of the resistors used in the potential degrader leads to track distortions on the same order. The positioning of the micromegas modules was found to lead to much larger track displacement when the modules can only be positioned with about a 0.5 mm precision. A perfectly located wiregrid placed in front of the readout modules was found to reduce these field (and track) distortions significantly.

Finally note that the track distortions were computed assuming that the particles follow the electric field lines exactly. Depending on the gas choice, however, the drift direction may be sizably influenced by the magnetic field in addition. Thus the displacements computed here represent the maximum possible due to non-uniformities in the electric field.

## 5.3 Gas system

### 5.3.1 Gas choice

Important parameters for the gas choice are the transverse diffusion coefficient which affects the momentum resolution and the achievable gain. Simulations indicated an upper limit on the transverse diffusion of  $400\text{--}500 \mu\text{m}/\sqrt{\text{cm}}$ . However, since not all the point resolution degrading effects are included in the simulation, the transverse diffusion coefficient of the selected gas should be well below this limit. Further boundary conditions are set by safety (e.g. non-flammability) and cost issues. In addition the gas mixture should be at the chosen working point as stable as possible against possible contaminations, mixing inaccuracies and density changing effects.

In the following the gas mixtures under consideration are first presented. Afterwards the choice of the insulation gas is discussed. Finally stability studies based on simulations with GARFIELD[3] and MAGBOLTZ[2] and measurements are presented.

### Gas Candidates

Argon is considered to be the main component of the gas mixture, since it is inexpensive and has a reasonable primary ionization ( $\sim 100 e^-/\text{cm}$ ). As additional components  $\text{CF}_4$ ,  $\text{iC}_4\text{H}_{10}$  and  $\text{CO}_2$  are investigated. A possible candidate is  $\text{Ar}:\text{CF}_4:\text{iC}_4\text{H}_{10}$  95:3:2 which was successfully tested with MicroMegas and GEMs in the HARP TPC. It has a small transverse diffusion coefficient of about  $280 \mu\text{m}/\sqrt{\text{cm}}$  at the electric field of the peak of drift velocity (290 V/cm) under the magnetic field of 0.2 T and showed during the tests small  $e^-$  attachment (attachment length  $> 30 \text{ m}$  at 140–160 V/cm), high gain at low operational voltage and a good point resolution with  $8 \times 8 \text{ mm}^2$  large pads.

An alternative under investigation is to replace  $\text{CF}_4$  by  $\text{CO}_2$ . This replacement might simplify the gas system. Depending on the  $\text{CO}_2$  and the working point a better stability against a contamination from the insulation gap and  $\text{CO}_2$  variations might be possible. The  $\text{CO}_2$  based gas mixtures have in general a smaller drift velocity which is in respect to magnetic field sensitivity an advantage but might lead to an increased sensitivity to attachment.

## Gas for outer flush gap volume

In the corners of this insulation gap electric fields up-to 10 kV/cm, corresponding to a drift field of 400 V/cm, will occur. Therefore a gas with a sufficient breakdown voltage has to be selected for the outer flush gap volume. In addition this gap protects the active volume for a contamination with air.

A reasonable candidate for this gap gas is CO<sub>2</sub> which has a breakdown voltage of about 20 kV/cm. It is inexpensive and easily available in large quantities. Furthermore filters exist which allow to reduce a possible CO<sub>2</sub> contamination in the drift gas to a few ppm.

### 5.3.2 Gas handling system

#### Overview of gas handling system

The TPC gas system will need to be put in place to maintain possible contaminants at the level of 10 ppm. In order to achieve this requirement, we expect to flow the inner and the outer gas volumes at up to one volume change every 6 hours. The inner and outer volumes are  $3.1 \times 3 \text{ m}^3$  and  $2.2 \times 3 \text{ m}^3$ , respectively, and their expected flow rates will be up to 30 l/min and 20 l/min. With these flow rates, the TPC can also be purged by 5 volumes within 1.5 days, after which it is ready for normal operation.

Fig. 5.21 shows a schematic diagram of the gas handling system. Here, Ar/CF<sub>4</sub>/isobutane mixture is assumed to be a baseline gas choice for the inner gas volume, while an alternative option will be Ar/CO<sub>2</sub>/isobutane mixture in the case of that any serious problem will be found in the future studies. For the outer gas volume, pure CO<sub>2</sub> is the baseline gas choice and N<sub>2</sub> will be an alternative option. The gas handling system will be almost the same for any gas choice.

Ar, CF<sub>4</sub> and isobutane for the main volume are provided from cylinders located at ground level. They are mixed in a gas mixing station and go through the gas purifier and filter system to remove contaminant oxygen, water, CO<sub>2</sub> and particulate. After that it is sent to the flow control system located on B2 floor, where the flow is restricted at a certain flow rate and the gas mixture enters each drift volume of TPC on B1 floor. The gas goes from an endplate on one side of the TPC, through holes in the central cathode, and exits from the other endplate. The exhaust from the chambers is collected in the chamber exhaust manifold and then returned by a pump to a buffer tank in the mixing station, which stores a certain amount of the gas in it. The flow rate will be  $\sim 10 \text{ l/min}$  for each drift volume at maximum, and hence  $\sim 30 \text{ l/min}$  in total.

CO<sub>2</sub> for the outer volume is directly sent from cylinders to B2 floor. The flow is controlled there and the gas is sent to the chamber. The exhaust is collected into the flush gap exhaust manifold, then sent to the ground level and exhausted to the atmosphere. The flow rate for the outer volume will be at maximum  $\sim 6 \text{ l/min}$  for each chamber, and hence  $\sim 20 \text{ l/min}$  in total.

The flow rate will be controlled and monitored by mass flow controllers and mass flow meters installed at several points in the line. The pressure in the outer volume should be the same as the atmosphere within 5-10 mBar to avoid outer wall distortion. The pressure difference between inner and outer volumes has to be more strictly controlled since even small deflection of the chamber wall, especially in endplates, could distort the electric field for the drift. The pressure difference between the inner and outer exhaust manifolds will be monitored by a pressure gauge and fed back to the pump system to control the output flow so that the pressure difference is kept stable at about 0.1 mBar. The buffer tank stores a certain amount of the gas mixture in order to supply necessary amount of gas when atmospheric pressure changes.

The properties of the gas has to be monitored for the stable operation. The mixing ratio will be monitored by mass flow controllers. CF<sub>4</sub> and isobutane analyzers will also be used to measure their fraction in the mixture. Oxygen, water and CO<sub>2</sub> analyzers will be used to monitor the concentration of these contaminants at the precision about of  $\sim 1 \text{ ppm}$ . Temperature will be monitored by temperature sensors put at various locations in the chamber. In addition, we will have small chambers to directly measure the amplification gain and the drift velocity for the input and output gases.



## Flow rate and recycling ratio controls

A set of mass flow controllers installed on the input of the chambers (FCD4–6 shown in Fig. 5.21) will control the total flow rate into the inner volume of the chambers. The gas mixture needs to be recycled in order to reduce the necessary amount of the fresh gases as well as to stabilize the mixing ratio as much as possible.

While there are several ways to accomplish recycling ratio control, we chose an option in which fresh gas input is kept at constant pressure and controlled by a variable exhaust flow rate. This has two advantages. One is that, for contaminants which cannot be removed by the filter, the concentration in the circulating gas flow will stabilize at the ratio of diffusion rate of the contaminant to fresh gas input flow rate when the input flow rate is kept constant and the input rate of the contaminant remains constant. The other advantage is that the mixing ratio errors can be reduced by operating the mass flow controllers at a constant flow since they typically have non-linearities in their response.

In the system shown in Fig. 5.21, the fresh gas input flow rate for the inner volume will be set by a set of mixing mass flow controllers (FCD1–3). The exhaust flow rate will be controlled by a pressure transducer on the buffer tank, so that the buffer tank pressure does not exceed a certain maximum value. In this scheme, the recycling ratio will be determined by the ratio of flow rate set by FCD1–3 to that set by FCD4–6 while any unnecessary amount of gas will be automatically exhausted from the buffer tank.

The buffer tank must have sufficient capacity to supply enough gas to the chamber during episodes of rapidly increasing atmospheric pressure, while retaining sufficient pressure to propel gas through the system. The buffer tank capacity will be ultimately determined by the minimum required fresh gas input flow rate (higher fresh gas input flow rate implies lower required buffer tank capacity), the maximum anticipated duration and rate of atmospheric pressure, and the volume of the chambers. Calculations based on an assumption that a maximum pressure disturbance is 50 mBar over 5 hours (in the case of typhoon passing) and the total volume of the chambers is 10,200 litres indicate that a buffer tank of 250 litres operated at 2 Barg (3 Bar absolute) would be sufficient for the fresh gas input flow rates greater than 1.0  $\ell$ /min. At fresh gas input flow rates greater than 2.0  $\ell$ /min, a buffer tank may not even be necessary, although some sort of small tank would probably still be advisable.

## Pressure control

The pressure inside the TPCs has to follow the atmospheric pressure in order to protect the chambers from distortion, or even destruction. While there are also several ways to accomplish chamber pressure control, we choose an option where a pressure controlled bypass valve connecting the outlet and inlet of a pump are used. This method results in the lowest compression ratio ((outlet pressure)/(inlet pressure)) for the pump. The schematic diagram shown in Fig 5.21 shows a pressure transducer (PXD1) which measures the differential pressure between the chamber and flush gap manifolds. This pressure in turn controls the bypass valve (VSD1) around the pump (PUD1) to maintain a constant differential pressure between the exhaust manifolds.

One possible problem with this technique may be that when the chambers are isolated from the pump by the chamber output shutoff valve (VAD3), the pressure control valve is isolated from the point at which the differential pressure is measured. This could cause the pressure at the inlet of the pump to drift to higher or lower pressures depending on what is happening to the differential pressure at the isolated chambers. When the shutoff valve is subsequently re-opened, there may be an uncontrolled rush of gas until the pressure control system stabilizes. Whether or not this presents a serious problem would depend on the pneumatic capacity of the chambers, the pneumatic capacity of the tubing between the shutoff valve and the pump, and the speed of response of the pressure control system.

Given the reasonably tolerant pressure stability requirements (several mBar), a better solution might be to use a pressure transducer at the inlet of the pump to control the pressure at the inlet to the pump. Provided that the conductance of the tubing between the outlet of the chambers and the pump

was reasonably high, any flow related pressure drops due to the tubing between the pressure control point and the chambers would be minimal, and easily compensated for normal operating flow rates. In this scenario, the differential pressure at the chambers would still be measured by another pressure transducer between the manifolds which would be used to signal safety interlock conditions, etc.

Two small buffer tanks (not shown in Fig. 5.21) would be located one at the inlet and one at the outlet of the pump. These tanks effectively act as mufflers, reducing the high frequency pressure fluctuations due to the pump stroke. This prevents the pump noise from interfering with the operation of the pressure control bypass valve, and also reduces venturi effects which can interfere with any pressure measurements at the inlet or outlet of the pump.

## **Purifiers and filters**

During recycling the gas mixture, contaminants getting into it have to be controlled at low level since they may change the properties of drift gas mixture. Particulate must also be removed to avoid sparking in the chambers and on MicroMegas modules. Possible contaminants are nitrogen, oxygen and water in the air and CO<sub>2</sub> in the outer volume of the chambers.

Oxygen, water and CO<sub>2</sub> can be relatively easily removed using a set of purifiers. Activated copper (BASF R3-11) will be used to remove oxygen while 13X sieves will be used to remove water and CO<sub>2</sub>. If the chamber gas will have CO<sub>2</sub> component, 3A sieves will be used instead. These purifiers would be regenerated in situ by heating to ~ 150°C and flowing a mixture of 5% H<sub>2</sub> and 95% Ar through them. The physical size of the purifiers will depend on flow rates and estimated contamination loads. Some of the desired gas components may be partially absorbed by the purifiers, and hence the purifiers need to be pre-saturated with the desired gas mixture to minimize changes to the composition of the circulating gas when fresh regenerated purifiers are switched into the gas stream.

Particles will be removed by a particulate filters located at the outlet of the purifiers, the inlet to the fresh gas supply flow control mass flow controllers, and possibly at the inlet to the chamber input flow control mass flow controllers.

The level of any other contaminants will be controlled by replacing a certain fraction of the gas mixture by fresh gas. The recycling ratio will be determined by the rate of contaminants getting into the mixture.

## **Safety system**

Several safety systems will be installed in the gas handling system to protect against unusual pressure differences and leaks.

A pressure relief bubbler is located on the outlet side of the chambers just before the chamber shutoff valve. The bubbler will relieve serious overpressure by bubbling out, and relieve serious underpressure by sucking air in. This is the pressure relief system of last resort. If the other control systems and safety interlock system work properly, the bubbler should never bubble. In order for the bubbler to provide "fail-safe" protection, there must be no valve or other obstruction between the chambers and this bubbler. The physical size and design of the bubbler depends critically on the maximum worst case flow rate it needs to provide in order to relieve a serious pressure excursion.

The bubbler could be located at the B2 level, approximately 10 m below the center of the chambers. Since Ar is 1.4 times more dense than air, this would cause an offset at the bubbler location of ~ 0.5 mBar, i.e. if the pressure with respect to atmosphere at the center of the chambers was 0 mBar, the pressure with respect to atmosphere at the bubbler location would be 0.5 mBar. The offset would result in a 0.5 mBar asymmetry in bubbler relief between over and under pressure conditions but this is not a significant problem.

The schematic shows shutoff valves at the input to the chamber mass flow controllers (VAD2) and at the outlet of the chambers between the bubbler and the pump (VAD3). These would be solenoid or air activated valves. The valves would be normally closed types (i.e. closed if no power applied)

and would be automatically closed if chamber pressures rise or fall beyond setpoint levels. In addition, solenoid (or air activated) valves are shown on the fresh gas input line (VAD1), the recycle line (VAD6) and the exhaust bypass line (VAD5). All of these valves would be under automatic control to prevent undesirable conditions from occurring. A programmable logic controller (PLC) would monitor pressures, flows, and valve states and take appropriate actions if necessary to prevent undesirable conditions. The PLC and all of the gas system variables would be monitored by the slow control system.

If atmospheric pressure were to rapidly increase while the chambers were isolated from the gas system (e.g. during a power outage resulting from a typhoon), the bubbler would relieve the negative pressure (with respect to atmosphere) in the chambers by sucking air into the chambers. To prevent this, the schematic shows an emergency gas supply. A cylinder of premixed gas feeds through a line regulator set to a pressure slightly below the normal chamber operating pressure (e.g. a few mBar with respect to atmosphere). The emergency supply is normally isolated from the gas system by a solenoid valve (VAD4, normally open type). If the power fails, the solenoid valve opens and connects the emergency supply to the outlet line of the chambers near the bubbler. If the chamber pressure falls with respect to atmosphere, the regulator valve (PRD1) will open and supply gas to maintain the chambers at the pressure set by the line regulator. The PLC logic could also be programmed to open the emergency gas supply valve under other conditions as well, e.g. if the chambers are intentionally isolated by closing the chamber input and output shutoff valves.

### **Outer flush gap gas system**

The flush gap system has many of the same features as the TPC chamber gas system. The major difference is that the gas is not recycled, hence purification and recycle ratio control systems are not needed. For monitoring purposes, there are mass flow meters at the supply and exhaust of the system (FMG1,2).

It may be possible to exhaust the gas to the surface without requiring a pump and pressure control system while the schematic diagram shows them (PUG1 and VSG1). The static pressure with respect to atmosphere of a 25 m column of CO<sub>2</sub> is  $\sim 1.6$  mBar. The pressure required to push 15  $\ell$ /min of CO<sub>2</sub> through a 50 m long, 22 mm inner diameter tube is  $\sim 0.5$  mBar. An output shutoff valve with a suitably large orifice can probably be purchased. Most mass flow meters require input pressures of greater than 10 mBar, however at least one manufacturer (Bronkhurst) lists a mass flow meter which requires less than 1 mBar for operation. Thus it may be possible to design a system with direct exhaust to atmosphere which would only require a gap pressure with respect to atmosphere of  $\sim 4 - 5$  mBar. Since such a system would be simpler, safer and less expensive, it may be worth pursuing this option, provided that the resulting backpressure at the flush gap was tolerable.

### **Gas bottle storage**

Given that the maximum flow rate for inner volume gas mixture will be 30  $\ell$ /min and that for outer volume CO<sub>2</sub> will be 20  $\ell$ /min, relatively large amount of gases need to be stored close to the mixing station.

During purging process, the inner volume gas mixture will be just exhausted without recycle. In order to purge the chamber 5 volumes, 46.5 m<sup>3</sup> of Ar, 1.4 m<sup>3</sup> (or 5.5 kg) of CF<sub>4</sub> and 0.93 m<sup>3</sup> (or 2.5 kg) of isobutane will be needed, which need 6.3 bottles of Ar (7 m<sup>3</sup> in a bottle), 0.17 bottle of CF<sub>4</sub> (32 kg in a bottle) and 0.25 bottle of isobutane (10 kg in a bottle). Much less consumption will be expected during normal operation due to recycling. Assuming 90% recycling ratio, 4.1 m<sup>3</sup> of Ar, 0.13 m<sup>3</sup> (or 0.5 kg) of CF<sub>4</sub> and 0.086 m<sup>3</sup> (or 0.22 kg) of isobutane will be needed every day during normal operation, corresponding to consumption of 0.58 bottle of Ar, 0.016 bottle of CF<sub>4</sub> and 0.022 bottle of isobutane every day. Therefore, seven 7 m<sup>3</sup> capacity bottles of Ar, one 32 kg capacity bottle of CF<sub>4</sub> and one 10 kg capacity bottle of isobutane have to be stored at once. We have to switch to new bottles when we run out of gas, and hence we need to have two sets of these bottles as well. With

these amount of storage, the frequency of bottle replacement will be once every 12 days for Ar, once every 45 days for CF<sub>4</sub> and once every 64 days for isobutane.

For the outer volume CO<sub>2</sub> gas, the expected consumption is 28.8 m<sup>3</sup> (or 56.7 kg) every day during both purging process and normal operation, which corresponds to 1.9 bottles per day. To make the replacement frequency reasonable, 15 bottles will be needed, which requires replacement work of once a week. Two sets of 15 bottles will be needed to switch to new bottles when one has run out.

In addition to the chamber gases, Ar/H<sub>2</sub> mixture will be needed for the filter regeneration purpose. The necessary amount of the mixture and required frequency of the replacement depend on the capacity of the filters and how much contaminants will get into the chamber gas mixture. Rough estimation give us 2 or 3 bottles (7 m<sup>3</sup> each) of Ar/H<sub>2</sub> needed for each regeneration process. Two sets of bottles will be desired in the case of bottle replacement.

### 5.3.3 Monitors

#### Flow rate, pressure and temperature monitors

Gas flows, pressures and temperature in the lines have to be monitored to ensure that all the system is working correctly, and rather to correct the effects of those variation in the data analysis. Most of the mass flow controllers and flow meters mentioned above will be of digital equipments, whose readings will be read out by slow control system and monitored appropriately. The readings of pressure gauges on the inner volume exhaust manifold, the flush gap exhaust manifold and the buffer tank are also be read out and monitored with slow control system. Pressures at input lines, the inlet and outlet of the pump, the filters, and gas supply bottles will also be monitored in order to ensure that those pressures are not too high or too low. A number of temperature sensors will be installed inside and outside the TPCs, which are also monitored by slow control system.

#### Gas analyzers

Variations of the mixture and contaminants in it change the drift properties, and hence those concentrations have to be monitored. For the components of the mixture, the concentrations of CF<sub>4</sub>, CO<sub>2</sub> and iC<sub>4</sub>H<sub>10</sub> will be measured by an infrared multi-gas analyzer. Possible contaminants are water, O<sub>2</sub> and N<sub>2</sub>; the concentrations of water and O<sub>2</sub> will be measured by appropriate analyzers. Although it is difficult to measure N<sub>2</sub> concentration, it can be inferred from measured O<sub>2</sub> concentration since both N<sub>2</sub> and O<sub>2</sub> would come from the air and those ratio has to be roughly 4:1. We plan to measure those concentration at several locations; just after the flow controllers for mixing, before and after the filter, and at the buffer tank, which are indicated by A–D in Fig. 5.21.

In addition, the concentration of iC<sub>4</sub>H<sub>10</sub> at the outlet of the filters will be continuously monitored by a flammable gas analyzer in order to ensure that we are always sending non-flammable gas to underground. The reading of this analyzer will be fed to the safety shutoff system for the fail-safe purpose.

#### Monitor chambers

For a given electric field the drift velocity, the gas amplification and the electron attachment are determined by the composition of the gas and its contaminants. In addition, they depend on environmental parameters as pressure and temperature. The gas composition is controlled by the gas system which also keeps the contaminants of oxygen, nitrogen and water at low values. Pressure and temperature are continuously monitored using precision sensors. The gas pressure, for example, is regulated at small overpressure with respect to the atmospheric pressure.

The simultaneous variation of these parameters will make it difficult to predict their total effect on drift velocity and gain. In addition, non detected changes of the gas quality, for example caused by leaks, cannot be registered by the individual monitoring of each of these parameters. It is therefore

desireable to monitor the drift velocity and the gas amplification continuously using dedicated monitor chambers. This will allow a calibration of the recorded TPC data according to the variations of the monitored parameters.

Currently, several designs for such monitor chambers are under study. To monitor the drift velocity a small monitor chamber has been operated successfully over years at the central drift chamber of the LEP experiment L3. For the CMS muon detector an improved version of this chamber will be used [4]. This chamber records pulses of the electrons from the  $\beta$  decay of two Sr-90 sources, which are installed at 42 mm distance from each other. The measured time difference between the pulses allows a precise measurement of the drift time.

In an alternative method, developed by a group in Saclay [5], UV laser pulses are directed onto two separate meshes in a micromegas detector. The photo electrons emitted from the meshes are amplified and registered with a time difference caused by the drift time of the electrons between the two meshes. The measurement of this time difference again allows to determine the drift velocity.

For the monitoring of the gas gain it is desirable to use the identical gas amplification device as it is used in the TPC chambers. Hence, a micromegas detector of same type as used in the TPCs will be irradiated with a Fe-55 source. Sufficient high activity of this source will allow to record an energy spectrum with a measurement time of less than a minute. The position of the photo peak in the recorded spectrum is a measure of the actual gas gain. Currently, small test chambers, used in previous studies on the charge transfer of GEM structures [6], are modified to accomplish the operation of a micromegas device.

### 5.3.4 Safety

#### Flammable gas

Argon/Isobutane mixtures are unconditionally non-flammable below  $\sim 4\%$  isobutane. Addition of  $\text{CF}_4$  should make mixture less flammable.

#### Toxic gas

Carbon dioxide is non toxic if its concentration in the air is less than 3%. The concentration of 3–5% causes headaches and/or respiratory phenomena, but no chronic harmful effects, 5–15% causes headaches, nausea, and/or vomiting which can lead to unconsciousness and death, and  $> 15\%$  causes rapid circulatory insufficiency which leads to coma and death.

Isobutane is an asphyxiant, and narcotic (central nervous system depressant) at high (much greater than flammable) concentrations.  $\text{CF}_4$  and Ar are asphyxiants.

#### Pressurized gas

The pressure at each section of the system is as following.

- Between pump PUD1 and MFC's FCD4–6:  $\sim 2$  barg
- Between mass flow controllers FCD4–6 and pump PUD1:  $< 15$  mbarg
- Between flow meters FMG1 and FMG2:  $\sim 1.5$  barg
- Between mass flow controllers FCG1–3 and flow meters FMG2:  $< 15$  mbarg
- Gas cylinder output pressures:  $\sim 3$  to 4 bar

## Operation

**Construction and commissioning** To ensure a safe environment, all components have to be leak tight. All the component assemblies will be checked by helium leak test before shipping to Japan. After installing the components, system leak test will be done by pressurizing sections and monitoring pressure over time. Small leaks which cannot be found by pressurizing test will be indicated by high oxygen levels in the gas system during the commissioning.

## Drift volume

**Continuous leak detection and prevention** Flow rates at several points will be monitored by mass flow controllers and flow meters. If there is no leak in the input system, the flow rate at FMD1 plus a sum of the flow rates at FCD1–3 should be equal to a sum of the flow rates at FCD4–6. If significant difference between them is detected, a programmable logic controller (PLC) will close the valves VAD1, VAD2, VAD3 and VAD6 to shut off the flow. If there is no leak in the detectors or output system, a sum of the flow rates at FCD4–6 should be equal to FCD7 plus FMD1 assuming that PXD2 is constant. In the case of significant difference, PLC will close the valves VAD1, VAD2, VAD3 and VAD6 to shut off the gas flow to the detector.

**Pressure protection** The difference between the inner and outer volume pressures will be monitored by a pressure transducer PXD1. If PXD1 reads too high or too low pressure, PLC will close the valves VAD2 and VAD3 to isolate the chambers. If any of PXD1, VAD2, VAD3 or PLC fails to act, a bubbler BUD1 will relieve the pressure in either direction to equalize the chamber and atmospheric pressures.

The maximum input pressure will be limited to 3–4 barg by pressure regulators on outputs of cylinders. Pump maximum output pressure will be  $\sim 4$  barg which is limited by the pump capacity and pressure regulator on the buffer tank. Mechanical pressure relief valves could be installed at the output of pump, on the buffer tank, and at the purifiers if it is necessary.

**Gas mixture** The gas mixture can be continuously analyzed for  $\text{H}_2\text{O}$ ,  $\text{O}_2$ ,  $\text{CO}_2$ , isobutane and  $\text{CF}_4$  concentrations by gas analyzers. Sample points will be A) output from mixer, B) input to purifiers, C) output from purifiers, and D) return from chambers. If isobutane concentration at point A, only where it is possible for the mixture to get flammable due to wrong mixing, becomes larger than a maximum allowed isobutane concentration, PLC will close the valve VAD1 not to supply flammable gas to the system.

**Chamber high voltage** If a lot of contaminants get into the chambers, the high voltage applied to chamber could spark. Possible location for the contaminants getting into the chamber is the bubbler BUD1 when sufficient gas could not be supplied and the pressure in the chamber would drop. To avoid it, PLC will disable the high voltage if the flow rates at FCD4–6 would become below a certain minimum flow rate.

## Flush gap volume

**Continuous leak detection** The concept similar to the drift volume system will be applied to the flush gap volume system. If there is no leak, the flow rate at FMG1, a sum of the flow rates at FCG1–3 and the flow rate at FMG2 have to be the same between each other. If FMG1 reads a flow rate significantly greater than the sum of FCG1–3, PLC will close the valve VAG1. If FMG2 reads a flow rate significantly smaller than the sum of FCG1–3, PLC will close the valve VAG2.

**Pressure protection** The pressure of the flush gap will be monitored by a pressure transducer PXG1. If PXG1 reads too high (low) pressure, PLC will close the valve VAG2 (VAG3). A bubbler BUG1 will relieve pressure in either direction if any of PXG1, VAG2, VAG3 or PLC fails to act.

The maximum input pressure will be limited to  $\sim 3-4$  barg by regulators on supply cylinders.

## **Gas mixing station and detector hall**

In order to avoid the TPC gases accumulating in the gas mixing station or the detector hall in the case of any leak, fresh air has to be sent continuously. The detector hall will be ventilated at the rate of about one entire volume change every two hours. The gas mixing station will also be ventilated at high rate. It will be possible that the gases accumulate much faster than the ventilation rate in the case of large leak. To keep people out of such environment, oxygen sensors have to be equipped in the gas mixing station and hall, which will indicate in front of the entrances the oxygen level inside and give alarm if it goes abnormal. The mixing station will have flammable gas sensor as well since flammable gas line will be there (isobutane).

## **5.4 Micromegas modules**

### **5.4.1 The T2K TPC Micromegas Module**

Micromegas technology is the micropattern device chosen to equip the T2K/TPCs of the ND280m near detector. A total of 72 of these Micromegas modules will be needed to instrument the 3 TPCs (12 Micromegas modules per readout planes).

This section describes the current design of the Micromegas modules, with a focus on the "Bulk" Micromegas detector, composed of an anode segmented Printed Circuit Board (PCB) on which is integrated an inox micromesh by means of photolithography technics.

#### **Overview**

The Micromegas modules will be each be  $36 \times 34$  cm<sup>2</sup> with pad size of  $6.9 \times 9.7$  mm<sup>2</sup> giving a module of 1728 channels, arranged in 48 rows and 36 columns. As explained below, we have chosen for the detector the "bulk" Micromegas technique [14] that is simple, easy to produce, and robust. This technique allows also to minimize the dead space between units. The fabrication process was developed in collaboration with the CERN/TS-DEM division lead by Rui de Oliveira [16] and is described in section 5.4.1.

We chose a design which enables the modules to be mounted from the outside of the TPC field cage and without any internal connections between a module and the readout plane. In case of failure, this makes the detector replacement easier, and prevent as much as possible dust from entering the field cage.

A Micromegas module is a "bulk" Micromegas detector glued on a mechanical support frame (the stiffener) which assures the rigidity of the structure. The pads are electrically connected by vias in the PCB inner layer to the connectors, soldered on the back side of the detector. A corner of the PCB is used to electrically connect the micromesh of the detector to the high voltage supply from the backside of the detector. The complete production process of a Micromegas module is described on figure 5.26. The main manufacturing steps are detailed in the following paragraphs.

#### **The "bulk" Micromegas**

For the TPC readout plane, the "bulk" Micromegas technology is the best technical solution to minimize the dead zones on the edges of the modules and to improve the gas gain uniformity, especially

in the corners. A woven mesh is laminated on a PC board covered by a photo-imageable polyimide film.

At the end of the process, the micromesh is sandwiched between 2 layers of insulating material which are removed after UV exposure and chemical development. A 2 mm wide border at the edge is thus naturally produced and avoids the need of an external additional frame to support the stretched micromesh. Regularly distributed 0,3 mm cylindrical pillars maintain the amplification gap with 12 pillars per pad (see figure 5.24). These design parameters minimize the dead zones in the detector and will be validated with the first prototypes. A backup design closer to the 2005 prototypes (see next section) with a 3 mm wide border, 20 pillars of 0,4 mm diameter per pad will be used in case of technical difficulties.

The components of the detector are :

- the PCB, described in the following section;
- the woven micromesh, produced by the Gantois company [17], using 19  $\mu\text{m}$  thick 304L stainless steel wires. Its thickness is reduced after weaving by 20-30% with a lamination process. The wires are spaced with a pitch of 59  $\mu\text{m}$  which is approximately equivalent to a 400 LPI (Lines Per Inch) micromesh
- three layers of a 62  $\mu\text{m}$  coverlay [18] (Pyrulux coverlay is a composite of DuPont Kapton polyimide film). Two layers are placed between the mesh and PCB to realize a 124  $\mu\text{m}$  amplification gap. The third layer is placed above the mesh.

The specifications of the micromesh, such as its thickness and the density and shape of its holes, define the fraction of the electrons that are transmitted from the drift space into the amplification gap. Similarly, they also define the fraction of the ions created in the amplification gap that are going back into the TPC drift volume. With such a micromesh and gap, the 5.9 KeV Fe55 energy resolution (FWHM/peak) was measured to be 23 % (see next section). The ions backflow in the TPC drift volume is expected to be at the few per mil level [8].

## The pad plane PCB

The Micromegas detector is built on top of a PCB that performs several functions :

- it acts as the anode of the Micromegas detector, implementing the read-out segmentation for 2D track information;
- it routes the electrical signal from the pads to the connectors;
- it assures the gas tightness and brings mechanical rigidity to the detector.

Our design is based on previous experience, most notably the HPMID Alice anode PCBs [19] (120 units produced at CERN/EST laboratory). In our case the PCB is 3mm thick for safe direct connection of the Front-End readout cards on the back. It is realized with a 3-layers structure with blind vias in the inner layer. This solution avoids the gas tightness problems arising from the conventional 2 layers structure with vias sealed with epoxide resins.

The drawing of the PCB is shown in figures 5.22 and 5.23. It has 1726 pads,  $9.7 \times 6.9 \text{ mm}^2$ , with a 100  $\mu\text{m}$  isolation between them. The pads are arranged in 48 rows of 36 pads each apart from the two rows where the high voltage connector is located (left figure 5.23).

A 2 pads equivalent surface is reserved in a corner for the Micromesh high voltage supply connection from the backside of the PCB. A 1 mm wide guard ring runs around the active surface for electrical and mechanical reasons. The top conductive layer is realized with 12  $\mu\text{m}$  thick copper deposited on FR4 (G10, presenting the same mechanical and electrical properties, can be used instead if outgassing would be proven to be a problem).

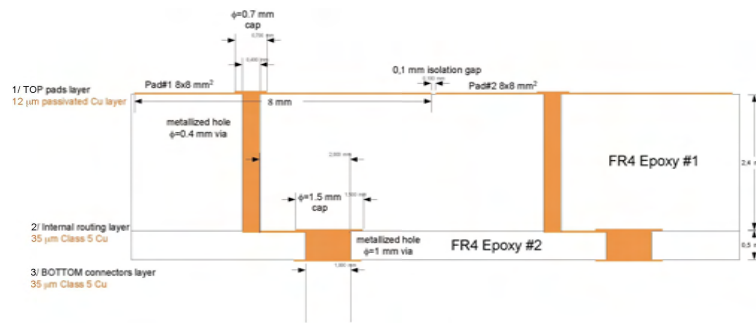


Figure 5.22: The pad plane PCB cross-section.

The 6x4 connectors are manually soldered onto the backplane after the production and validation of the "bulk" micromegas (see right figure 5.23).

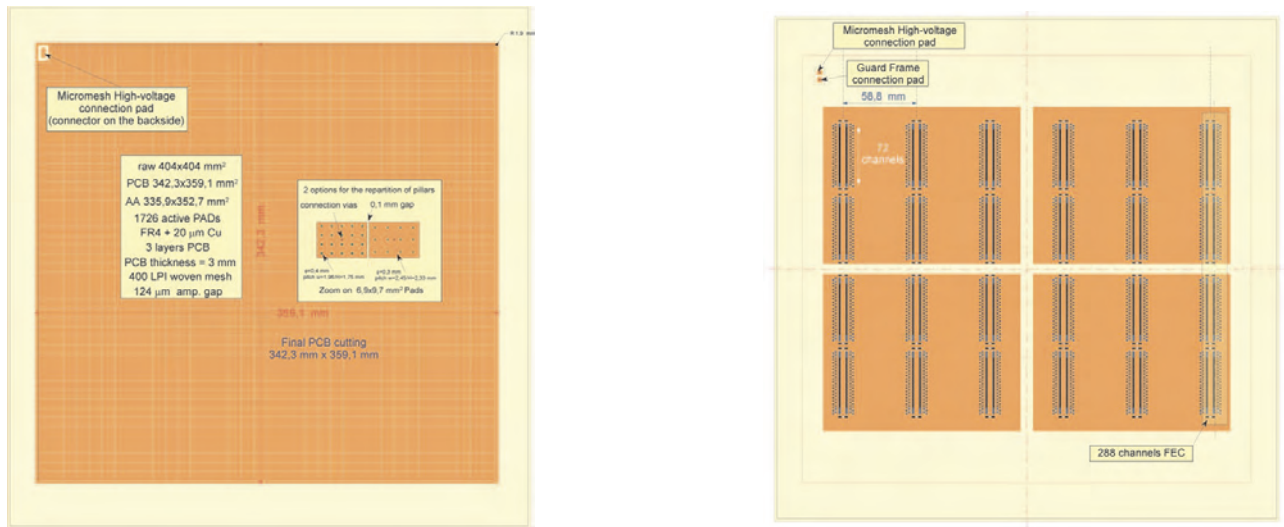


Figure 5.23: The pad plane PCB TOP view (anode pads' side) on left side and the pad plane PCB Bottom view (Front-End Cards connectors' side) on right side

### The "Bulk" micromegas production

The process begins with the above described anode PCB. At this stage, the  $36 \times 34 \text{ cm}^2$  effective area of the future detector is centered on a larger FR4 circuit ( $40 \times 40 \text{ cm}^2$ ) for handling and manufacturing purposes. We also asked the Gantois company to deliver cleaned, controlled and individually packed  $40 \times 40 \text{ cm}^2$  woven micromeshes. A special oxidation of the TOP copper layer of the PCB allows better adherence of the Micromegas pillars. The photo-imageable polyamide film is a Coverlay [18] instead of the standard Vacrel normally used in other Micromegas detectors. This film, after proper imaging and drying, produces strongly attached and more robust pillars to allow a better, complete and effective cleaning and drying of the detector at the end of the "bulk" Micromegas production.

The complete manufacturing process of the T2K/TPC "bulk" micromegas is described in reference [21], and the main steps are the following ( see fig. 5.25):

1. Preparation
2. UV exposure
3. Development, cleaning and drying

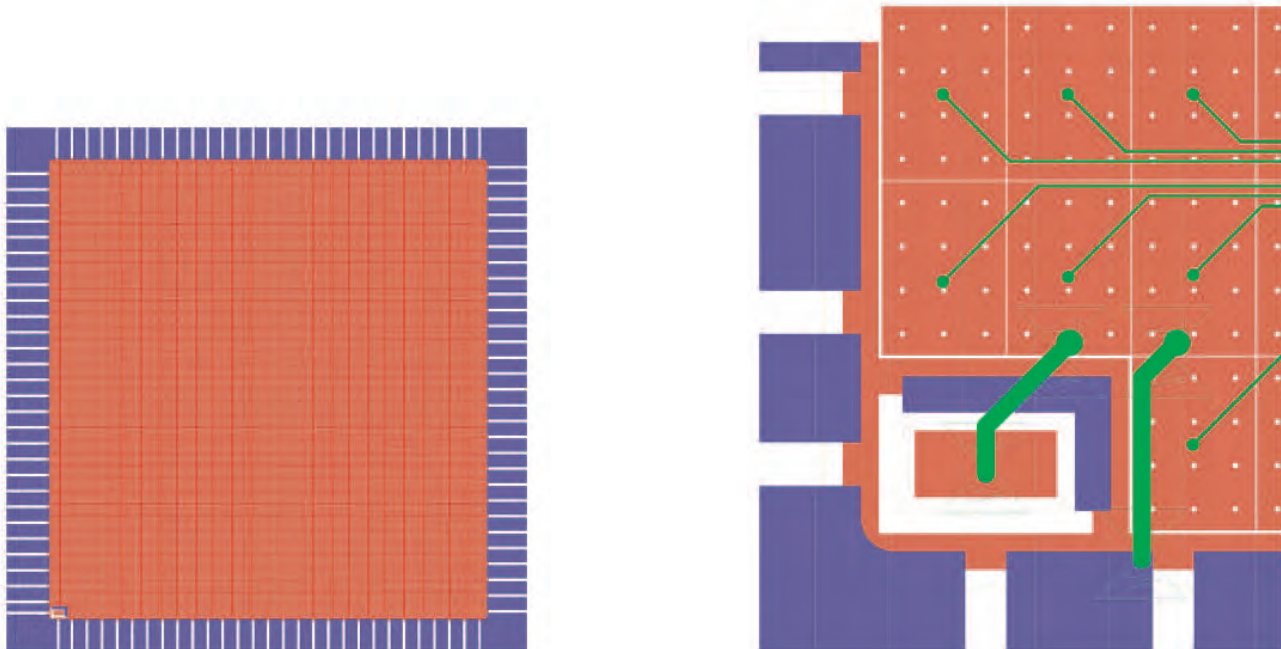


Figure 5.24: Coverlay layer (in blue) left on the pad plane PCB of the finalized detector (left) and zoom on the High-voltage connection pad (right). The coverlay layer is in blue, the copper pads in red, the inner layer routing strips in green and coverlay pillars in white.

4. Final disoxidation
5. Resistive gluing of the micromesh on its TOP copper pad for electrical contact,

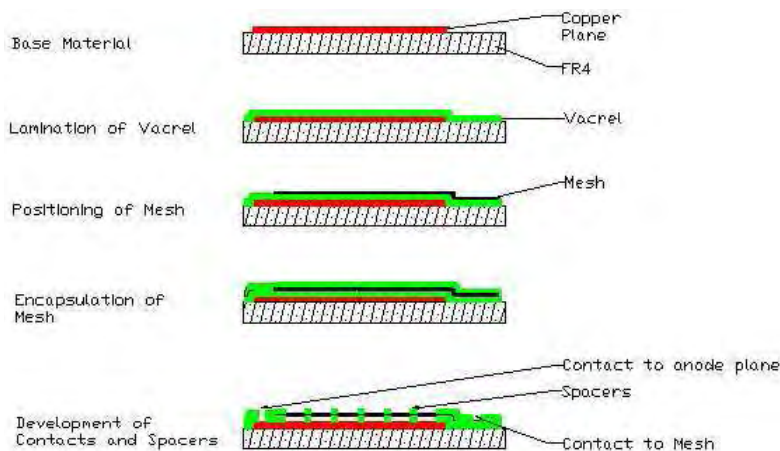


Figure 5.25: Production sequence of a "Bulk" Micromegas. In our case Coverlay is used instead of Vacrel.

## 5.4.2 Micromegas Module production and Assembly

This section presents the foreseen production line of the Micromegas modules which will be localized at CERN.

### The "bulk" Micromegas production and qualification

The Production sequence of a Micromegas Module, from the "bulk" Micromegas production to the Micromegas module Calibration, is shown on figure 5.26. The Quality Controls (Q/C) are described in the next section.

Figure 5.26: Production sequence of a Micromegas module from the pad plane PCB production to the final calibration of the module

T2K-TPC Micromegas modules WP#4

Task	Who	How	When
<b>Micromégas</b>			
<b>Design specifications*</b>	T2K/TPC gpe	following physics needs *included stiffening Frame, End frame, cooling	11/06
PCB CAD, Detector & Specifications file	Saclay / Cern		
<b>Contract Saclay/TS-DEM-PMT</b>	Saclay / Cern		12/06
<b>Quality Assurance Master file</b>	Saclay		05/07
<b>Anode PCB</b>			
PCB CAD*	Saclay	* control of files at Cern	05/07
Control	Cern	<i>CERN-TS-DEM-PMT Automated test bench</i>	06/07- 06/08
<b>"Bulk" Micromegas</b>			
Coverlay procurement	Cern	sub-contractor with Q/C	
Micromesh procurement	Saclay	Gantois company with Q/C	
production*	Cern	*European institutes participation	06/07- 06/08
Q/C test for 2nd cleaning-drying decision	Europe	<b>1st Quality control Global current test bench</b>	
Cutting & conditioning	Cern	Cover (mélamine)	
Shipping to connector soldering sub-contractor	Cern		
<b>ERNI connectors soldering</b>			
procurement	Saclay	(Q/C sheet)	
soldering & Q/C	Saclay / Cern	sub-contractor (with Q/C)	
Q/C for individual pad defects	Europe	<b>2nd Quality control Pad Q/C test bench</b>	

<b>Stiffening frame</b> WP#5
<b>FEC &amp; FEM</b> WP#6
<b>FEE Cooling system</b> WP#5

<b>Module assembly and calibration*</b>		*at Cern, European labs participation
production line organization	Saclay	lab specifications & organization (laminar flux, gaz ...) --> proposal for Saclay division lab at CERN
Gas procurement	Europe	
glue procurement	Europe	glue control , N <sub>2</sub> lot, "épreuve témoin", ageing tests (T, Gas,...), scratch tests
Assembly*	Europe	*European institutes participation ?
<b>detector baking</b>	Europe	<b>3rd Quality control baking test bench (2 days at 750V with current monitoring)</b>
<b>Module Calibration</b>	UG	<b>Calibration test bench</b>
conditionning	Europe	module cover mechanics
shipping to Triumf	Europe	

The "Bulk" Micromegas detectors will be produced at CERN/TS-DEM-PMT laboratory. In order to qualify the quality of the produced detector, a Global Current Quality Control (Q/C) is done. In case this Q/C is not passed, the detector can be improved by a new sequence of deionized water cleaning, compressed air jet drying, and final 12h heating at 80 degrees celcius. If this Global Q/C is passed, a second Pad Current Q/C is done to localize the defective pads. In case this second Q/C is not passed the same new sequence of cleaning-drying is done until the detector passes the quality criteria.

The top side of the Micromegas detector is then protected by fixing a 1 mm thick melamine plate with a double-side adhesive film on the outer inactive part of the PCB.

The detector is then partially cut to its final size of 342.3 (+0/-0.1) mm x 359.1 (+0/-0.1) mm on a computer aided cutting machine. Drilling of the positioning holes for the SMC connectors and the PCB centering pins is also done. The detector area is still linked to the outer PCB through 8 thin epoxy bars which will be removed after gluing of the PCB on the stiffening frame,

At this stage of the production process, the detector remains covered by the top melamine plate protection until its final cutting on its mechanical support. It is thus protected from dust pollution or handling incidents during the following complete assembly of the module, and it still can be tested in air with high voltage supply on the micromesh if needed.

### **The Micromegas Module Assembly**

Once the "bulk" micromegas has been produced and validated, the next step is to mount the SMC connectors on its backside (see figure 5.26). This is done by an external company by manual soft soldering of every contacts. The welding flux is chemically removed with a brush and the electrical continuities and isolations are controlled.

The detector must be finally glued on its mechanical stiffening frame. The gluing procedure needs to satisfy both gas tightness and assembling robustness and also needs to be done with the proper tools in order to precisely control the thickness of the assembly (goal thickness of 19,5 mm).

The complete gluing and final cutting is done on a flat bed under a laminar flow and the one used to produce the 2005 prototypes is described in reference [22]. The main steps are the following:

- Preparation
- Gluing with Araldite 2011 under 50 kg during 8 hours
- Final cutting of the detector
- Careful removal of epoxy dusts on the TOP detector surface with a compressed clean air jet in clean room.

On the backside of the Micromegas PCB, a high voltage wire is directly soldered to the connection provided in a corner of the PCB. This supplies the high voltage to the micromesh. A high-pass RC circuit filters the high voltage power supply equipped with a low current limitation (500 nA). One or several high voltage channels will be used for the readout plane guard frame high voltage power supply. The control-command of each of the 72 High Voltages and the monitoring of the associated currents drawn by the power supplies will be done through serial or low speed interface.

### **The "Bulk" Micromegas Quality controls**

At each step of the Micromegas module production and assembly, quality controls and validation tests are performed. These quality control procedures have been elaborated and tuned for the production of the 4 x 2005 prototypes. They will be fine tuned and finally fixed at the beginning of the final production with several detectors in order to get a high production yield needed for the 72 micromegas production. The main quality control tests are the following :

- "Bulk" micromegas production
  - Anode PCB : all electrical continuities and insulations between channels are tested on computer controlled equipment,
  - Woven Micromesh : cleaning, quality controls and selection of the micromesh by the manufacturer. Visual control prior to assembling in "bulk" micromegas.
  - At the end of the "bulk" micromegas production, the global Current Q/C test and the pad current Q/C test are done, and if these Q/C tests are passed, the "bulk" micromegas is cut to its final size and ready for module assembling
  
- Micromegas module
  - SMC connectors cabling : all electrical continuities and insulations are tested on a computer controlled equipment,
  - Control of the mechanical dimensions of the assembled module : thickness of the assembly, and insertion in a Module frame opening,
  - Baking of the detectors, in air, during several days,
  - Final validation on the Calibration test bench with an Fe55 X-ray source (see next section),

### **Global Current Test Bench**

This first Q/C test bench is used to globally and quickly evaluate the quality of the cleaning and drying of the detector. On a flat bed under a laminar flow, it consists to gradually increase the High Voltage between the micromesh and the pads polarized at ground in order to reach a stable operation without sparking. Following our past experience in Micromegas detectors production and operation, two criteria are used:

- for a 124  $\mu\text{m}$  amplification gap, the test is passed if the detector operates stably with a maximum high voltage at least 750 V,
- the current drawn by the power supply must be less than 100 nA.

If the current limit of 100 nA is reached below 750V, local defects are present either on the pad plane surface, or the micromesh, or between them (dusts). Part of these defects can be naturally "burnt" after several hours of operation at 750 V. If the current drawn still remains too high, the cleaning and drying is incomplete and ionized residuals are present. Another cleaning and drying of the detector can solve all or part of these defects. It can happen that the high-voltage cannot be maintained because of a short-circuit (few Ohms) between the micromesh and the pad plane. In that case, the pad current Q/C is used to locate the short-circuit. In case the short-circuit cannot be solved, it is decided whether to keep it (the pad is disconnected from ground and dead for reconstruction) or to chemically remove the micromesh and coverlay. The micromesh is then lost but the PCB can be used again to produce another "bulk" micromegas.

When this test is finally passed after proper cleaning and drying, only a few pads remains faulty (typically less than 10, i.e 0,6 percent of the total active area).

### **Pad current Q/C Test Bench**

This test is used to locate the faulty pads and decide whether or not their localization is acceptable for the physics requirements. For instance, a detector with too many adjacent faulty pads will be rejected. On a flat bed under a laminar flow, the test is done by grounding each pad individually (all the other floating) and measuring the current drawn through the micromesh High-voltage power

supply set around 750V. With a CAEN N471A power supply module, this current is typically lower than 2 nA, i.e. at the level of the measurement limit of the power supply. Another sequence of cleaning, compressed air drying and final heating can be done to further lower the defects. At this stage, the remaining faulty pads are definitely disconnected from ground as they present a very rare but potential risk to sparking during detector operation.

When the test is passed, the top side of the detector is protected with a thin melamine plate to prevent damage or dust pollution, and the "bulk" micromegas is partially cut to its final dimension.

## Baking Test Bench

Before the final calibration of the micromegas module (see next section), the detector is baked in air, in a clean room. This is done by gradually increasing the High Voltage between the micromesh and the remaining good pads polarized at ground in order to reach a stable operation. A typical 500 nA current limit is fixed on the micromesh high-voltage power supply, and the current drawn is monitored. After 24 to 48 hours at around 800V, the sparking rate has continually decreased and reached an asymptote. This way, most of the dusts have been burnt and most of the tiny surface asperities of the micromesh and/or the copper pads have been smoothed.

## 5.4.3 Micromegas Modules Calibration

### Overview

During the production, modules have to get through various electric tests before calibration and final integration onto the TPC. The goal of the test bench under construction at the University of Geneva is to characterize the delivered Micromegas modules on a pad-per-pad basis. Prior to the production of the Micromegas modules, this test bench will be used to perform further studies of the GEM prototype module (see [24]). In a second stage, a specific test box adapted to the Micromegas module geometry will be operated. It is foreseen to use first, the ALICE electronics used during the prototype study at CERN and once available, the dedicated final electronics developed by Saclay.

### The Calibration Test Bench

The test bench is designed to allow a full characterization of the Micromegas modules in a reasonable time. After production, a Micromegas module is mounted in the test box, a gas chamber which is operated as a small drift chamber. This test box is also used for transportation of the module after the assembly with the stiffeners from the assembly point to the test bench. The test bench and assembly chain will be located in the same premises. Fig. 5.27 shows a general view of the setup. The module is held in a similar position as in the final ND280 TPC, i.e. vertically with readout cards plugged-in vertically. The box is mounted on a rail system which allows it to move to the desired distance from the calibration source. This source is fixed on a set of two mechanical arms (X-Y stages) which will move it along the pad rows.

The pad plane and the cathode act as the walls of the test box. The cathode is made of an aluminized mylar foil and supported by a vetronite grid to avoid bending of the mylar foil under the inner pressure of the test box and to ensure protection. All services (gas and electronics) and environment sensors will be integrated onto the test box.

The  $^{55}\text{Fe}$  collimated source activity is chosen to be the best compromise between the following criteria:

- **collimation:** in order to allow the identification of a single faulty pad and to study the border effects, the illumination spot should cover a reasonable fraction of a pad.
- **count rate:** as high as possible, in order to perform the overall calibration process in a reasonable time, and to take advantage of the livetime pattern. The 190 ns shaping time of the

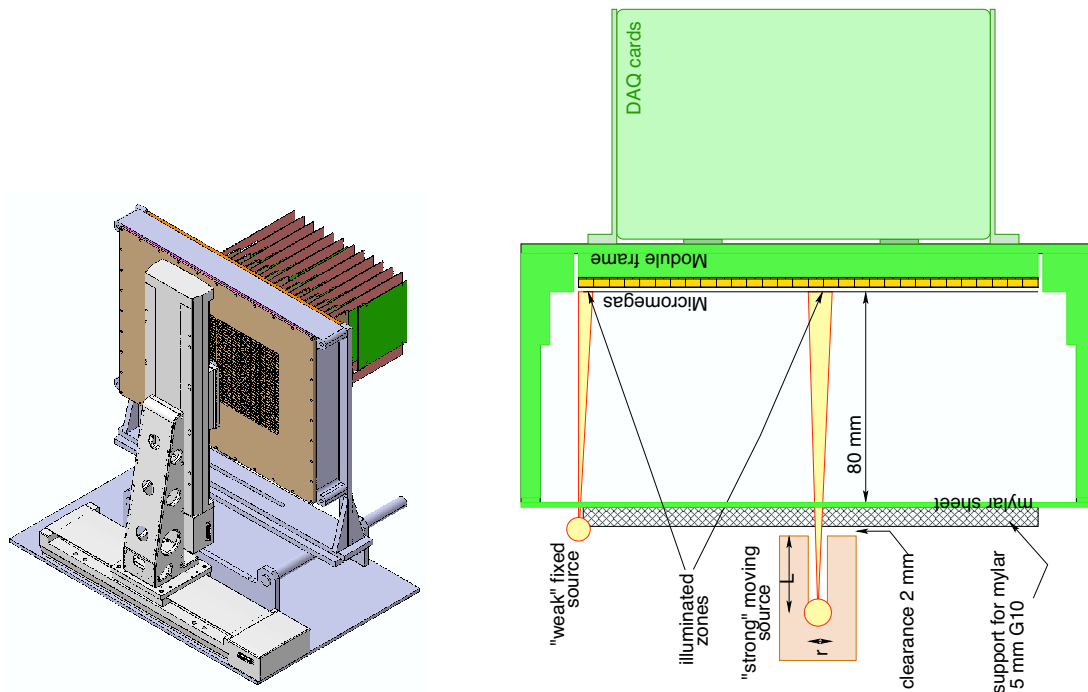


Figure 5.27: Technical 3D drawing of the test bench (left), schematical representation of a module integration on the test box (right).

ALICE electronics causes a pile-up of 0.001% for a 3 kHz counting rate, and 0.002% for 10 kHz; therefore it is not an issue.

- **radioprotection issues:** 6 keV X-rays are considered “not dangerous”, as they affect the dead layer of skin only, hence a very thin layer of material (even air) blocks the bulk of the radiation. An X-ray tube is not as trivial as a  $^{55}\text{Fe}$  source, as it needs an interlock system for the generator, and is far more expensive.
- **statistics:** the statistical error (defined by the strength of the source and the duration of the calibration runs) should be inferior to the systematic error on the overall resolution of the Micromegas. In the case of the GEM prototype,  $7.10^3$  hits yield an error of 0.7% on the location of the photopeak.

The calibrations will be performed using a  $^{55}\text{Fe}$  collimated source moving in the x-y plane, that will allow the characterization of each single pad, and a set of two fixed non-collimated  $^{55}\text{Fe}$  sources, to monitor the stability of the system over time. The sources have been ordered at Eckert&Ziegler ([25]): the moving source has an activity of 185 MBq over a diameter of 5.08 mm, and the fixed sources an activity of 37 MBq over a diameter of 3.0 mm. The two weak sources will be fixed at the corners of the cathode support grid and only a few pads will be illuminated at a rather low rate. Their activity will be matched in order to obtain enough statistics for a given period (after 100 pads are scanned for example) to monitor the gain versus time with sufficient sensitivity.

Because the DAQ livetime for the ALICE electronics is quite low (0.1%), two kinds of pad-per-pad measurements will be performed: 1) a “fast” scan, with a rather large illuminated area, will be performed to calibrate and measure a gain map for each module, and 2) a more “precise” scan will allow to pin down inhomogeneities (faulty pads, border between 2 pads) if any is found in the fast scan. This scan will obviously take longer but probably only part of the padplane would be scanned if any faulty pad was found. The scan setting is achieved by changing the collimation of the source; parameters are given in table 5.1 for the GEM prototype study and will easily be extrapolated for the Micromegas modules.

Temperature, pressure and humidity have to be monitored during the calibration process since both temperature and pressure can affect the gain of the modules. The pressure will be controlled

scan	$l_{coll}$ [mm]	$w_{coll}$ [mm]	$\theta$ [ $^\circ$ ]	$r_0$ [mm]	$A_0$ [Bq]	$t$ [h]	$\Gamma$ [Hz]
fast	80	4	5.7	2.32	249151	1.96	249.15
precise	100	2.5	2.8	1.16	46134	10.61	46.13
precise	150	4	3.0	1.25	109756	4.45	109.76

Table 5.1: Estimation of the duration of the scan  $t$  (illumination only, not taking into account the mechanics and DAQ settings) and count rate  $\Gamma$ , for  $10^3$  hits on the Micromegas;  $l_{coll}$  is the length of the collimation tube,  $w_{coll}$  its width,  $\theta$  the angle of aperture,  $r_0$  the radius of the illumination spot on the micromesh (diffusion is negligible between the micromesh and the pad plane) and  $A_0$  the activity reaching the micromesh.

and measured in time with very high precision inside the test bench. Temperature sensors fixed at different locations, including also electronics components, and a humidity probe will monitor the overall environment conditions. The dimensions of the test bench volume (drift distance  $\approx 7$  cm) and the choice of the operating gas (baseline mixture is  $\text{ArCF}_4\text{iC}_4\text{H}_{10}$ , 95:3:2, which is much less sensitive to charge attachment than  $\text{ArCO}_2$ , 90:10, for ex.) do not require the control of the  $\text{O}_2$  content during calibration of the modules.

The gas system distribution is described in Fig. 5.28. To flush the volume of the test box ( $\approx 16$  L), premix bottles (ordered via CERN to the CARBAGAS company) will be stored and directly connected to the inlet of the system. The inlet is equipped with two pressure regulators used to set a pressure of 100 mbars. A bypass can be used to purge the line before flushing the chamber and a set of valves and mass flow controllers is used to flush the chamber according to the appropriate operation flow rate (high or low rate). A 10 mbar overpressure is maintained in the test box with a set of valves and bubblers and will be monitored in time via a pressure transmitter. The exhaust of the system will simply be connected to the atmosphere. In the baseline scheme, the maximal measurement flow rate is set to 20L/h, which gives 1.25 volume exchange/h and a consumption of 10 bars/day. This means approximately one gas bottle exchange every two weeks considering 150 bar standard premix bottles ( $\text{ArCF}_4\text{iC}_4\text{H}_{10}$  premix bottles might be only available as 50 bars bottles, giving 3 bottle exchange every two weeks). These numbers represent an upper bound and will certainly be reduced. Procedures specific to the operation of the gas system will be part of the global procedure to follow for the calibration test bench.

The low and high voltage systems are specific to the electronics and readout modules respectively. At the time being, this description is only based on the ALICE electronics requirements. All the specifications can be found in [26]. The low voltage power supply system will consist in five power supplies: two Konstanter LSP (33K7 5/2 type) for the inverter, termination and U2F cards and three DC PSU (TSX1820P type) for the FECs (these references might be slightly different and are given for the voltage and current output ranges). Concerning the GEM prototype, the high voltage power supply system will consist of 5 NIM modules (N471A type with two channels) for the GEMs, guard ring, shield and cathode. This could also consist of 2 NIM modules (N470A type with four channels) and one N471A module. In the case of the Micromegas test box, the usual SY127 CAEN module which is to be preferred for debugging the operation, may be used if planned for the final distribution scheme. The mechanical integration of the low voltage distribution will be based on copper distribution bars for the different voltage channels and respective grounds of the boards. The overall analogue and digital ground connections will consist of a set of three connections per electronic module. The digital ground is connected to the detector ground while the analogue ground is let floating in order to decouple the two grounds as much as possible. A single NIM crate is necessary for the high voltage distribution.

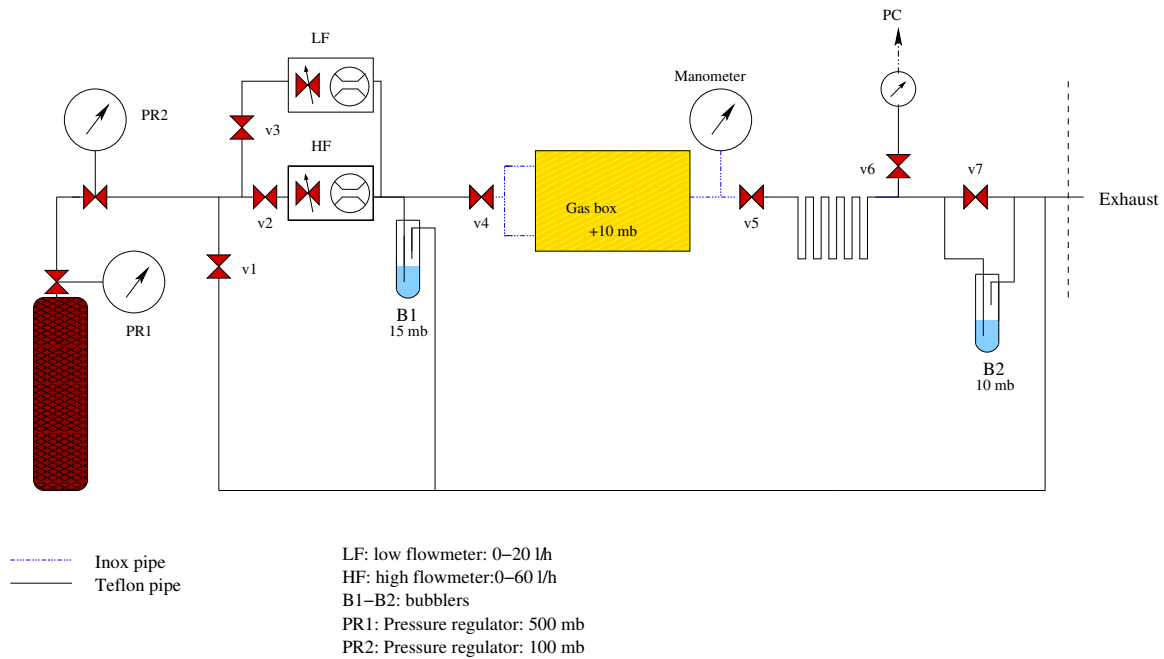


Figure 5.28: Schematic representation of the test bench gas system.

## Calibration Procedures

Precise procedures will be determined, tested and improved with studies using a GEM prototype. The pad-per-pad calibration will include the different parameters given below:

- gain:** The gain over a Micromegas module is subject to variations that need to be studied in order to interpret correctly the measurements. The gain can be computed as:  $G = \frac{\text{charge}[\text{ADCcounts}] \times C}{N}$ , where where C is the ADC/electrons conversion factor ( $C \approx 1 \text{ ADC count}/1000 e^-$  for the ALICE experiment electronics) and N is the mean number of ionisation electrons over the pad, estimated using the energy of the photons and the energy required for the creation of an ion-electron pair in the gas. The scanning of the pad plane will provide a calibration and gain map for each module. The gain variation over a module over time should also be monitored.
- pad response function and cross-talk:** The reconstruction of the centroid position as a function of the source displacement could help in studying the pad response function. The observation of induced signals on neighboring pads when moving the source from the center towards the border of a given pad would reveal cross-talk problems. Induced signals may also be observed on neighboring pads as a function of gain.
- source spectrum reconstruction:** To calibrate the modules, the spectrum of the  $^{55}\text{Fe}$  source will be reconstructed to observe any broadening or displacement of the photo-peaks.
- local charge collection:** Precisely measure the charge collection efficiency at the borders of the active area where charging up effects could affect the electric field. This study, performed at the level of the prototype, could give information about the necessity of an additional wire grid.
- pulse shape:** Check if the pulse shape is coherent with the expected function given by the front end electronics by quantifying for example the FWHM and the rise time.
- high voltage stability:** Monitor the number of sparks as a function of time and gain.

## 5.5 Micromegas mechanical

### 5.5.1 Introduction

The Micromegas mechanical workpackage, is deeply related to the TPC mechanical, Micromegas detector module and electronics workpackages. It includes both the aspects of the module mechanical integration on the TPC, and the services integration on the modules themselves.

### 5.5.2 Mechanical Description

#### Specifications

Twelve Micromegas modules ( $2 \times 6$ ) are mounted on each side of the TPC. Operation is foreseen at room temperature (22-23deg C) with an overpressure of  $\approx 5-10$  mbars. The electronics is situated in a closed volume (formed by the second wall of the TPC) at a pressure of 1 mbar below the TPC pressure. For safety reasons, the modules have to be able to support a maximal pressure of 20 mbars. The Micromegas modules have to be positioned with an accuracy of  $\pm 0.2$  mm in y and z and the micromeshes of the 12 modules, forming an array, have to be coplanar within 0.1 mm in z.

#### Mechanical Design

The Micromegas module consists of a micromesh precisely bonded to a PCB (see section 4.2). The PCB is reinforced by a G10 stiffener bonded on its connector face, allowing for the fixation and sealing of the module onto the TPC. Dimensions of the PCB have been fixed at  $342.3 \text{ mm} \times 359.1 \text{ mm}$ . This size allowing for two columns of six Micromegas modules to be mounted with minimal dead areas on each side of the TPC.

The stiffener also provides anchorage for a guiding, fixation and extraction system for the 6 front-end cards (FEC) plugged directly into the connectors soldered to the PCB. These 6 FECs are bridged by a front-end mezzanine card (FEM).

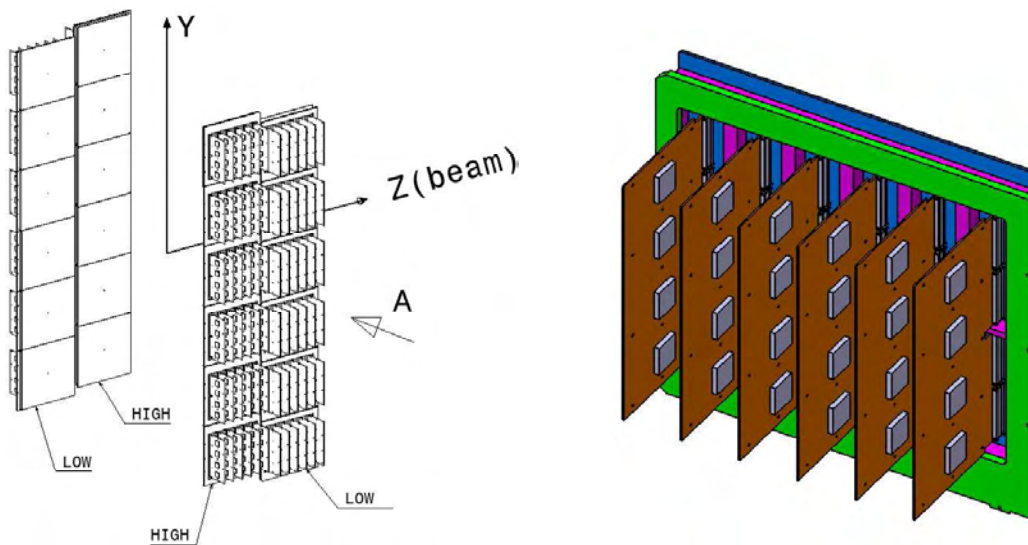


Figure 5.29: Global integration of the 24 Micromegas modules on the TPC end-plates (left), 3D view from connector side of a Micromegas module with 6 FECs plugged-in (right).

In situ accessibility to change a FEM or a FEC is mandatory. Changing a Micromegas module has also to be possible. Therefore a mounting-demounting tool is foreseen for the modules.



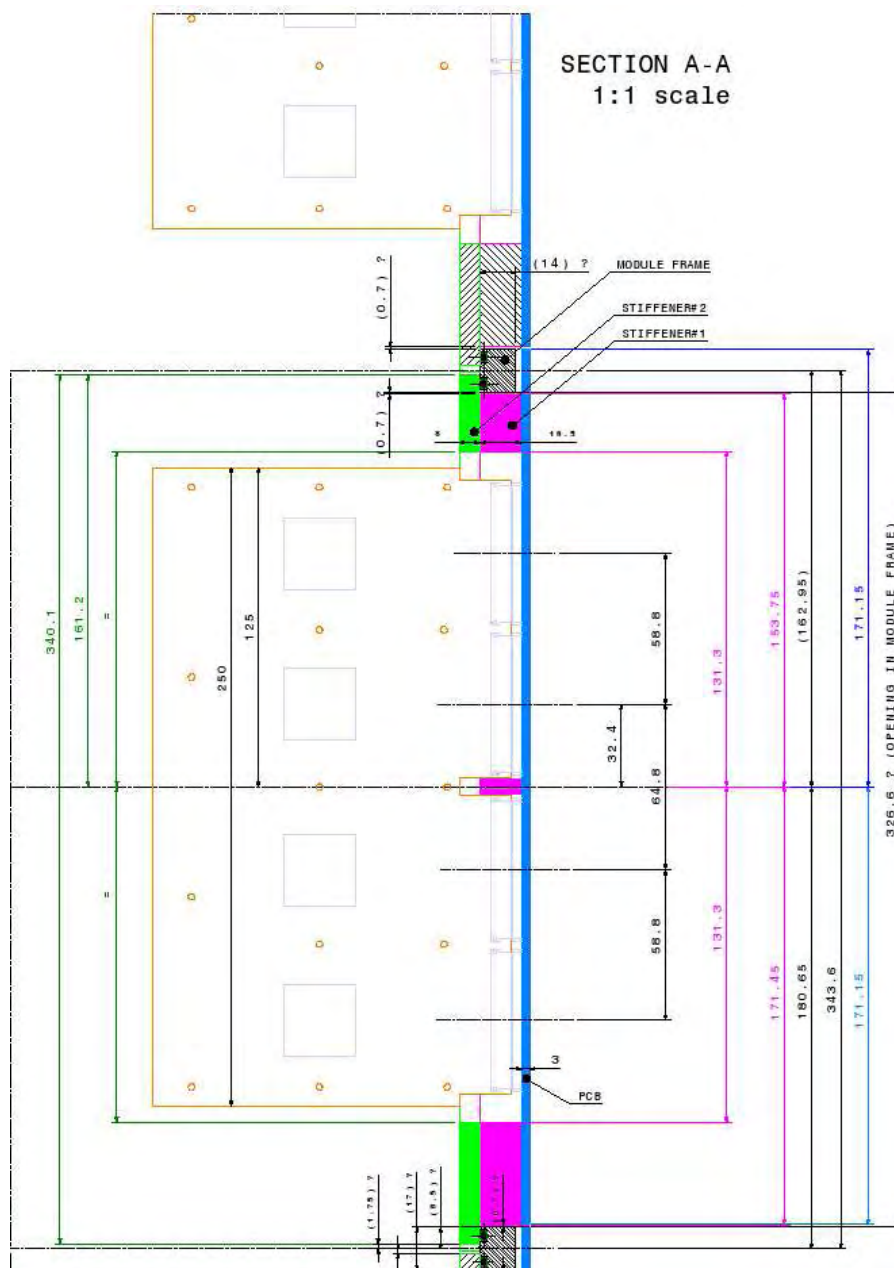


Figure 5.31: Interface drawing of the Micromegas module integration in the y-z plane.

- 1 single slow control cable at the input + one at the exit for the daisy chain. Each cable will be of the order of 5 mm diameter.
- 1 low voltage power supply cable (4 to 5 V) and ground return cable. The maximum current specified is 10 A and therefore a 10 mm<sup>2</sup> copper section cable should be considered. This is resulting into 2 cables of about 6 mm each.
- 1 cable for the HV power supply of the micromesh. Cable diameter is in the order of 4 mm.

### Cooling System

The present design of the TPC includes water pipes (liquid temperature 15-18deg C) running vertically on both sides of the 12 Micromegas modules array. A secondary cooling system has to be designed to transfer the heat produced in the FECs and the FEMs into the water pipes. Two options are presently studied:

- i) Use heat pipes from electronic cards to cooling pipes.

ii) Use also water to cool the cards directly.

In case the of ii) the cooling system has to be of the *leaklesstype* (operating under atmospheric pressure - in case a leak occurs, air is entering the system and no water is leaking).

## 5.5.5 Module Construction

### Tooling and Prototype

In order to assemble a bare Micromegas module with the stiffeners, dedicated jigs will be designed. The desired material for the stiffeners is G10 that has the same thermal expansion coefficient than the Micromegas PCB. Planarity tolerance of both the stiffeners and the Micromegas PCB will be far from the 100 microns initially required for the TPC. It is therefore expected to absorb the potential bowing and thickness variations via this assembly and two glue layers: one between the Micromegas PCB and the first stiffener and one between the first and second stiffener.

A few prototypes of the Micromegas modules are about to be completed at CERN and one of the goals in the framework of the module construction is to evaluate the assembly procedure with a set of prototype jigs.

### Logistics

The Micromegas modules production and tests will be mainly centralized at CERN. The production of the bare modules will be made in the TS DEM workshop. Once the modules, issued from this production, satisfy all the quality assurance requirements, they will be delivered to the collaboration for the final assembly and tests. The final assembly with the stiffeners will require dedicated tooling and a clean environment in order to avoid polluting the Micromegas when exposed to the atmosphere. Once assembled, a module will be embedded into the test box, with a close environment as in the TPC, for the calibration tests with an  $^{55}\text{Fe}$  source. Afterwards the module will be transferred to a transport box and will require another operation under laminar flow. Modules will finally be stored and ready to be shipped for the TPC assembly in Vancouver.

All the main steps of this production line will be recorded into a DB that will handle the items, assembly, test and shipment operations. More detailed operations should be kept onto a traveler document.

## 5.6 Readout electronics

This section describes the custom electronics designed for reading out pulses from the pads of the TPC modules.

### 5.6.1 Summary of requirements and constraints

In total, the three TPC modules have  $\sim 124,000$  pads. The spill rate is  $\sim 0.3$  Hz and the acquisition strategy is to record all events. The target maximum sustainable event rate for the TPC read-out electronics is 20 Hz. This provides a comfortable bandwidth for recording cosmic rays triggers, laser calibration events and various test events. The dead-time for processing an event can be up to 50 ms. Efficient data reduction is required due to the large size of raw events ( $\sim 130$  MB) and formatted events shall be delivered to the DAQ system over one (or a few) standard Gigabit Ethernet LAN connection(s). The typical data rate sent to tape by the TPC is  $\sim 10$  MB/s. Synchronization of the TPC with other T2K 280 m detectors shares the same primary 100 MHz clock locked to the GPS. The

global clock signal, along with a spill signal, trigger and other synchronization signals are distributed by a time-predictable fanout tree. Operating TPC electronics safely and in known conditions requires monitoring card supply voltages, currents, temperature, etc. A robust network is needed to perform these slow control operations.

## 5.6.2 Outline of the architecture

The architecture for TPC readout consists of two main parts: on-detector electronics mounted at the back of the gas amplification modules inside the magnet, and off-detector electronics, housed in standard racks at B2 floor. Each of the 2 end-plates of the 3 TPCs comprises 12 Micromegas modules arranged in 2 columns of 6 rows. On-detector electronics is composed of 72 identical readout modules, i.e. one readout module per Micromegas module. Each of the 72 Micromegas modules is segmented into  $48 \times 36$  pads. It is readout by 6 Front-End Cards (FECs) and 1 Front-End Mezzanine (FEM) card as shown in Fig. 5.32. Each FEC reads out 288 channels, i.e. a detector area of  $48 \times 6$  pads. Each FEC comprises 4 custom-made front-end ASICs “AFTER” (Asic For Tpc Electronic Readout). Each AFTER chip reads out 72 channels, i.e. a detector area of  $12 \times 6$  pads. The AFTER chip samples detector pad signals in a 511-bin Switch Capacitor Array (SCA) at a maximum rate of 50 MHz. The shortest sampling window is  $\sim 10 \mu\text{s}$  which is adequate for the fastest gas being considered. The FEC is mainly an analog electronic card but it also performs digitization. On the other hand, the FEM is a pure digital electronics card that controls several FECs, gathers event data digitized by the FECs, and interfaces to off-detector electronics. Each FEM has a full-duplex gigabit class optical link to communicate with off-detector Data Concentrator Cards (DCCs). The FEM to DCC path is used to transport event data and some control messages while the DCC to FEM path is used to transport the global clock, trigger and other synchronization signals as well as some protocol and configuration messages. Each FEM is also connected to a daisy-chained slow control network used to gather operating parameters and ensure the safe operation of the read-out electronics. Each readout module has a single low voltage power input. A power bar and a cable distribute power to the 6 FECs and to the FEM. Low voltage power supplies for all on-detector front-end electronics are placed in a rack at B2. The interface between on-detector electronics and off-detector electronics consists of 72 duplex optical fibers. Each DCC has 12 duplex fibers and services 1 TPC end-plate. There are 6 DCCs in the complete system. All DCCs are linked to a merger computer that performs a final data reduction and formatting and communicates with the experiment-wide DAQ system via a standard network connection. The 6 DCCs and the merger computer are housed in a standard, off-the-shelf, powered crate. A global view of the complete TPC readout system is depicted in Fig. 5.33.

## 5.6.3 Detailed description of main components

The following section gives details for the major components of the readout system.

### Front-end ASIC

The purpose of this electronic device is to provide information on the energy of charged particles and on their localization in the TPC (three dimensional space point). The large drift length (100 cm) of the TPC requires an accurate method to obtain the coordinate information by sampling continuously pad signals in analog memory arrays. The architecture of the AFTER chip has been defined to meet the specifications written at the beginning of 2005 (Table 5.2).

The asic AFTER contains 72 individual channels (Fig. 5.34); each channel handles one detector pad. A channel comprises an analog part dedicated to the conversion and the shaping of the input signal, and a switch capacitor array to store the analog signal until the reception of an external trigger signal. Global parameters (gain, peaking time, test mode and asic control) are managed by slow control, using a serial protocol. Two inputs are provided for calibration or a functional test of the 72 channels.

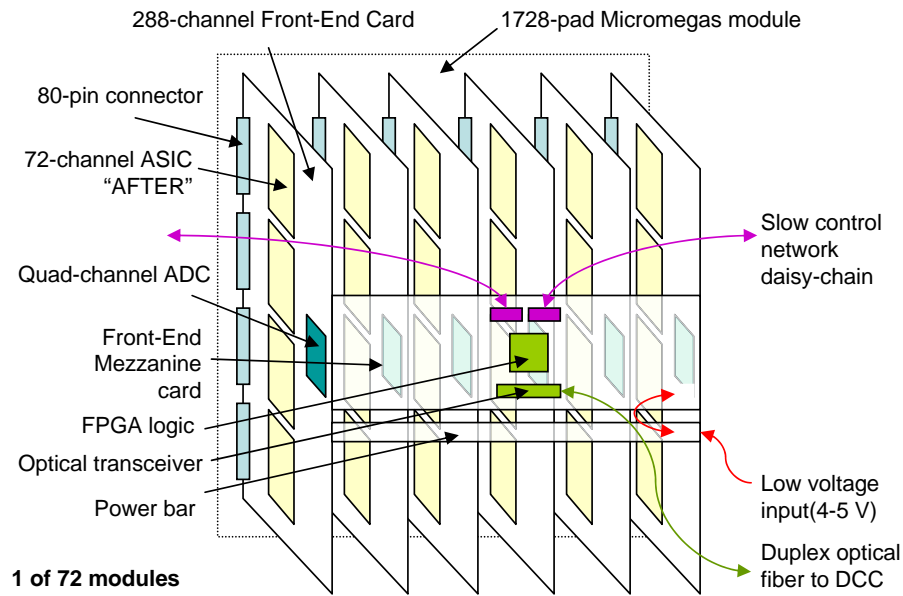


Figure 5.32: Readout architecture of a detector module.

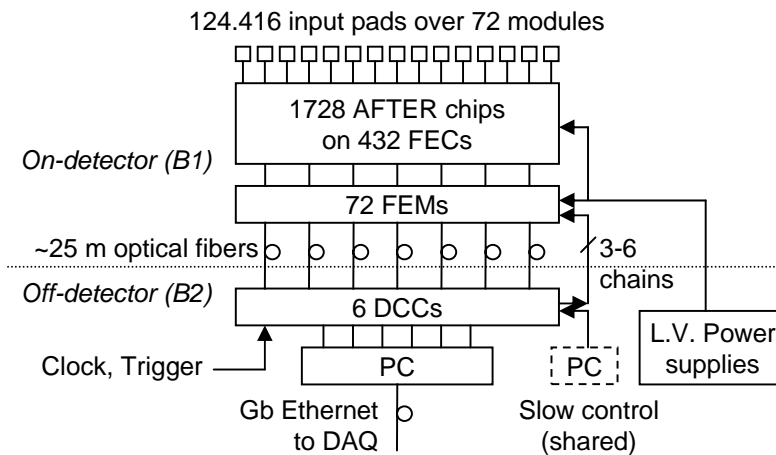


Figure 5.33: Overall TPC readout architecture.

The analog part is composed by: a Charge Sensitive Amplifier (CSA), a Pole-Zero Cancellation (PZC), a  $RC^2$  filter and a Gain-2 amplifier. The CSA is based on single-ended folded cascode architecture. The charge to voltage conversion is made by selecting via slow control one of the four feedback capacitors (200 fF, 400 fF, 600 fF or 1 pF). The PZC stage is used to avoid long duration undershoots at the output. It introduces a zero to cancel the low frequency pole of the CSA and replaces it by a higher tuneable pole. With this CR filter, the 2-pole Sallen-Key low pass filter gives the total  $CR - RC^2$  semi-Gaussian shaping of the analog channel. The peaking time of the global filter ( $CR - RC^2$ ) is defined by switching different combination of the resistors on each stage. The available range is 100 ns to 2  $\mu$ s (sixteen values). The last stage is an amplifier used to adjust the voltage dynamic range of the chain and to provide the necessary buffering for sampling the signal in the SCA. To perform common mode rejection, 4 extra channels, FPN (Fixed Pattern Noise), are included in the chip. These channels are only constituted by the Gain-2 stage and will be treated by the SCA exactly as the other channels. Their outputs will be subtracted off-line to the 72 analog channels.

The analog memory is based on a Switched Capacitor Array structure. It is used as a circular buffer in which the signal coming from the analog channel is continuously sampled and stored at a sampling

Table 5.2: Specifications of the AFTER chip.

Number of channels	72	Sampling frequency	1 MHz to 50 MHz
Number of Time bins	511	Shaping Time	100 ns to 2 $\mu$ s
MIP	12 fC to 60 fC	Read out frequency	20 to 25 MHz
MIP/noise	100	Signal Polarity	Negative (TPC) or positive
Dynamic range	10 MIPS on 12 bits	Calibration	Selection 1/72
I.N.L	1% [0-3 MIPS]; 5% [3-10 MIPS]	Test	1 capacitor / channel
Gain	Adjustable (4 values)		

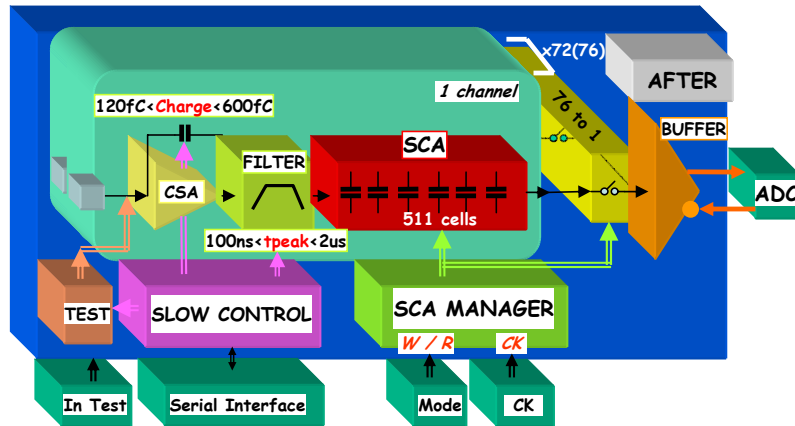


Figure 5.34: Architecture of the AFTER chip.

rate  $F_{wck}$ . The writing and sampling phases are defined by the external signals Write (CMOS level) and  $W_{ck}$  (LVDS level). Sampling is stopped by de-asserting the Write signal. This is achieved by the FEM when it receives an external trigger signal. The reading phase and readout frequency are defined by the external signals Read (CMOS level) and  $R_{ck}$  (LVDS level). Analog signals are sequentially multiplexed towards the analog output on each rising edge of the  $R_{ck}$  clock. The first column read is the oldest written. To read a column, 78  $R_{ck}$  clock periods are needed as shown in Fig. 5.35. The first two cycles correspond to the reset level of the read amplifiers; the 76 following cycles correspond to the analog data stored in the different lines of the current column starting from line 1. After the last ( $76^{th}$ ) cell of a column, the read pointer is shifted and the same operation is performed on the next column. When the signal Read comes back to 0, this sequence is asynchronously interrupted and the current address of the read pointer is encoded and multiplexed towards the output.

The data from the SCA are transmitted to an external ADC through an internal readout buffer. It performs the required single ended to differential conversion with a gain of 1.33 to match the input dynamic range of the ADC ( $\pm 1$  V on each input).

An important feature that was implemented is dedicated to testability. This will be used for: electrical calibration, asic test bench and functionality control. For calibration, the charge current generation is made outside of the chip, directly on the FEC. For the test and functionality check, generation is made inside the chip using one injection capacitor for all channels; for calibration, one capacitor per channel is used.

The design of AFTER is made in the standard AMS CMOS 0.35  $\mu$ m technology.

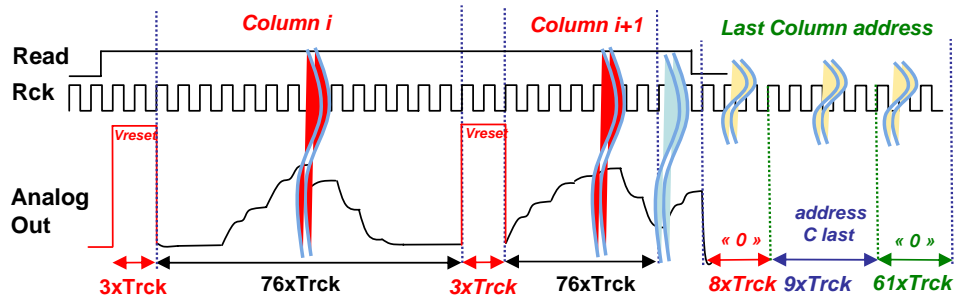


Figure 5.35: SCA read phase timing diagram.

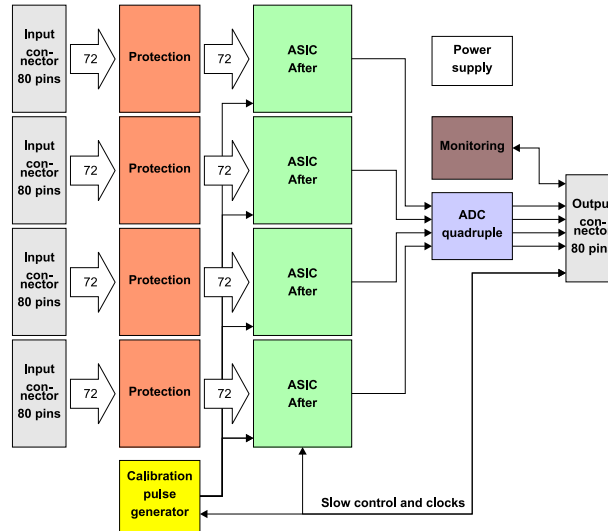


Figure 5.36: FEM card block diagram.

## Front-End Card

**Functions** The Front-End Card performs three main functions (see Fig. 5.36): the digital conversion of 288 analogue signals coming from a Micromegas detector, the calibration of this conversion function, and the monitoring of the board. Monitoring consists in measuring the board power supply voltage and current and the ambient temperature. A silicon identification chip provides a unique serial number for each board. In addition, the board establishes a link between the identification chip located on the Micromegas detector and the FEM card that is responsible for reading out all FEC and detector serial numbers.

The calibration of the conversion function consists in generating a voltage step signal through a capacitance in series to simulate an analogue input signal. The amplitude of this step is precisely known and is programmable. The digital conversion of the 288 analogue signals is performed in several stages. The first stage protects the FEC electronics against an accidental over voltage coming from the detector. The following stages are amplification and shaping, analogue storage, and signal multiplexing (288 channels towards 4 input channels to an ADC). These functions are performed by the AFTER ASIC described in the previous section. In the last stage, analogue signals are converted to digital values by a quadruple ADC and are sent to the FEM card.

**Requirements** The input protection circuits should protect the board components against sparks that can occur in the Micromegas detector, as well as against permanent short circuits between the mesh and one or several pads of the detector. This type of failure sets the DC input level of faulty channels to several hundred volts (up to 500 V). In such a case, the protection circuit should withstand

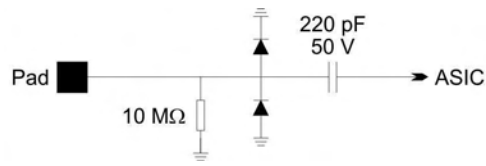


Figure 5.37: Basic protection circuit.

the high voltage while reading other parts of the detector should be unaffected by the defect.

Another requirement concerns the routing of the 288 analogue signals from the input connectors: crosstalk should, of course, be minimised, but also the capacitance between traces and ground planes. Minimizing parasitic capacitances reduces the noise added to input signals because the first stage of the analogue chain is a charge amplifier.

The precision of the calibration signal is also an important requirement. As already mentioned, a square signal charging a capacitor is used. The rise time is not critical because it has no significant influence on the measurement of the charge. However it should be faster than the shaping time of the shaping stage (i.e. at most 100 ns). On the other hand, the precision of the measurement is directly related to the precision on the amplitude of the calibration signal. This amplitude should be known to better than  $\pm 2\%$ .

Finally, the last requirement concerns the design of the printed circuit board and the implementation of components. A careful layout is mandatory to avoid noise perturbations between the analogue and the digital parts of the board.

**Main elements** (1) *Protection circuit* The first scheme that has been studied is shown in Fig. 5.37. It has been tested and validated during tests on the HARP prototype. The main advantage of this scheme is that both protection diodes are connected to ground (i.e. no auxiliary supply voltage is needed). Only ground noise may be injected at the input of the pre-amplifiers, and such noise can be minimized using a solid ground plane. Although this circuit fulfils the requirement of protection against sporadic sparks, it cannot cope with a permanent short between the mesh and a pad because the diode polarized in the forward direction would be destroyed unless the high voltage source is turned off.

An alternative scheme should be used (see Fig. 5.38). It uses a large value resistor to polarize the detector pad and a series capacitor to block the DC component for the downstream circuit. A large DC voltage can be applied to the pad without damaging the electronics. Nevertheless, it is mandatory that both the resistor and the coupling capacitor are specified for high voltage operation (up to 500 V). This kind of components exists, but they are more expensive and bulky (resistor in SMT 1206 package and capacitor in SMT 0805 package) than a low voltage rating counterpart. Using comparatively large components has some negative impact when trying to minimize trace lengths, but this cannot be avoided. Because the input of the amplifier must be polarized, one protection diode is referenced to an auxiliary supply voltage (instead of ground). A good de-coupling of this power supply is essential.

If a permanent short between a detector pad and the mesh appears, the current through the pad polarization resistor can reach  $5\ \mu\text{A}$ . Supplying excessive current on the high voltage side can be an issue, especially if several pads are shorted. To avoid this limitation, we designed a circuit to optionally remove the connection between subsets of the input resistors and the ground plane. Two photoMOS relays are placed between one-end of the polarization resistors and the ground plane. Each photoMOS is driven by the FEM card via slow control. When a photoMOS is turned off, one-half of the pads readout (i.e. 144) become floating. Each Micromegas detector is segmented into 12 sectors of 144 pads that can be independently polarized to ground or left floating.

(2) *Shaping - storage - multiplexing.*

These three tasks are performed by four AFTER chips. Each chip handles 72 analogue inputs. The storage procedure in the SCA is driven by the Write Clock and the reading procedure by the Read

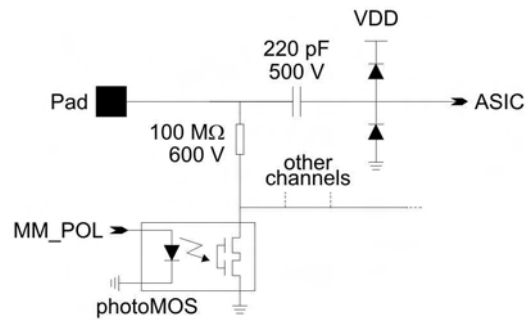


Figure 5.38: Improved protection circuit.

Clock. These two clocks are supplied by the FEM card. During the reading procedure, the analogue samples of each input channel are successively sent to the next stage for conversion to digital format.

(3) *Conversion.*

The analog to digital conversion is performed by a commercial device, the AD9229 from Analog Devices. This chip has four differential analogue inputs, each channel is linked to one of the 4 AFTER chips, and four differential digital outputs. It is driven by a sampling clock that is also used for the serial communication of data (after internal multiplication by 6). The sampling clock is supplied by the FEM card. The maximum sampling rate of the ADC is 50 MSPS; the operating range of the AFTER chip is 20-25 MHz.

(4) *Calibration.*

The square signal for calibration is generated by a digital-to-analogue converter (DAC) followed by a driver. The DAC chip used is an AD9744 from Analog Devices. It is a 14-bit resolution converter that features an extremely low output settling time of 11 ns (to 0.1 %). This avoids the need of an external fast switching circuit. An addition benefit is that the same DAC can be used to set the two levels of the square signal so any offset error can be exactly compensated. The maximal integral linearity error is  $\pm 5$  LSB ( $\pm 0.8$  LSB typ.) and the maximal differential nonlinearity is  $\pm 3$  LSB ( $\pm 0.8$  LSB typ.). Including the contribution of the voltage reference and of the output driver, the maximal amplitude error can be evaluated to 1.3 %. This calibration error can be further reduced by calibrating the pulse generator itself. The output signal of the generator is sent to the FEC output connector for this purpose. The levels will be measured during the characterization test of each FEC board before installation, and these parameters will be stored in a database. The only remaining error will then be the maximal differential nonlinearity, i.e. at most 0.036 % of the full scale value. In addition to the error on the amplitude of the generator, we also have to consider the tolerance of the four capacitors (one per AFTER chip) used for signal injection: +1.25 %; -0.15 %, so  $\pm 0.7$  % when centred.

The DAC is controlled over a SPI bus for loading the DAC value in two registers. The digital value loaded can be read back over the SPI bus. The signal “GEN\_GO” is used to set the output voltage of the DAC to the value previously loaded over the SPI bus. The frequency of the pulses generated is limited by the time required to load a new DAC setting over the serial control bus.

(5) *Self-monitoring.*

The chip used to perform the self-monitoring of the board is a DS2438 from Dallas Semiconductor. It uses a 1-Wire interface for communication and contains a unique 64-bit serial number. This will be used to uniquely identify each board. This chip also contains a temperature sensor and an analogue-to-digital converter that will be used to measure the temperature, the power supply voltage and current (using a  $0.2 \Omega$  sense resistor and an external operational amplifier). The chip can be read-out even when the card is not powered. It uses current derived from the 1-Wire interface in that case.

(6) *Power supply.*

All active devices can be powered at 3.3 V, so using only one voltage regulator is sufficient. Two

voltage regulators will be tested: the LD29150 and the LD29300 from STmicroelectronics. Both devices have identical characteristics except for the maximum current that can be supplied: 1.5 A or 3 A. These voltage regulators have a low dropout voltage, low noise, an inhibit pin, and an internal current and thermal limitation circuit. The proposed power supply connector is part number IC 2,5 4-G-5,08 from Phoenix Contact. Because it is rated for currents up to 12 A, the same connector can be used in various places, e.g. on the main power input of a detector module. This connector has four pins but a two pins version also exists.

#### *(7) Inputs - outputs.*

For connecting the 288 analogue inputs, four connectors type SMCB 80 F AB VV 6-03 (reference 114806) from Erni are used. These 80-pin connectors have been tested and validated during the tests on the HARP setup. Each connector takes 72 inputs and four pins at each extremity are grounded. In one place only, one connector pin is connected to the identification chip of the Micromegas detector instead of being connected to ground. The connector chosen for the interface between the FEC and the FEM card is model FX2-80S-1.27DSL from Hirose. This 80-pin connector is adequate for high speed signals and is more robust (though less compact) than the connectors placed on the detector side.

**Mechanical aspects** The PCB will be standard FR4. It will have 6 layers, in class 5. The thickness of layers should be calculated so that unipolar  $50 \Omega$  and differential  $100 \Omega$  microstrips and striplines have the right controlled impedance, while the capacity between the input lines (in surface) and the ground planes beyond are weak to minimise the noise. A good compromise is about  $300 \mu\text{m}$  per layer and a total PCB thickness of 1.74 mm.

The design of the printed circuit of the ASIC prototypes test card has validated the space required for components and routing in the FEC card:  $250 \text{ mm} \times 140 \text{ mm}$ . Indeed the minimal value for the length of the board (250 mm) is imposed by the length of the four input connectors plus the gap between the two central connectors (this gap is required by the central mechanical piece of the detector). The width of the board (140 mm) cannot be noticeably reduced without causing difficulties in PCB routing.

**Development procedure** The board for testing the prototype of the AFTER chip has been designed to serve also has a pre-prototype of the FEC. Then next step is the production of the first prototype of the FEC. It is foreseen to produce a sufficient number of cards to equip one detector module. After validation, the final prototype will be defined. Pre-series boards and series boards will then be manufactured.

Four kinds of tests are planned: “on table” functional tests, “on detector” tests, system test, and production validation tests. To perform them three main tools will be needed: a table test bench, a system test bench (including one detector module and a complete data acquisition system), and a board production test bench.

### **Front-End Mezzanine card**

The Front-End Mezzanine card performs several different tasks. It receives clock, trigger and synchronization information from its DCC and duplicates these signals for the 6 FECs that it controls. The FEM acts as a master device for programming the operating parameters of the front-end ASICs (gain, shaping time, etc). The FEM also sequences the read and write operations in the SCAs, receives and buffers event data digitized by the ADCs of the FECs, and delivers complete or compressed event fragments to its DCC upon requests from this card. The FEM also performs the local monitoring of current, supply voltage and operating temperature of various components. The required input bandwidth is one of the challenging aspects of the FEM: given a 20 MHz conversion rate for the quad-channel 12-bit ADC of each FEC, the FEM has to receive and store an aggregate data flow of 5.76 Gbit/s. Transmission to / reception from the DCC occurs at  $\sim 2$  Gbit/s each way. The core of the

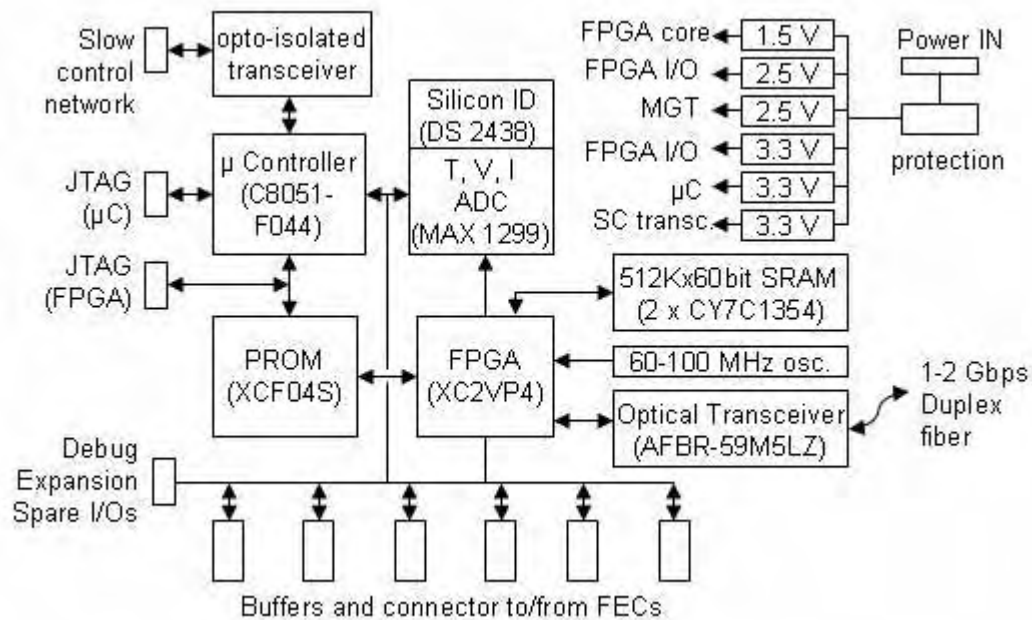


Figure 5.39: FEM card block diagram.

FEM is a large FPGA device that has to provide a few million gates, a couple of hundred I/O pins with an aggregate bandwidth of  $\sim 20$  Gbit/s. These features are well within the capacity and performance of modern FPGA devices, but a careful design is nonetheless of primary importance. A schematic view of the FEM card is shown in Fig. 5.39. The central component is a large FPGA. The selected part is a XC2VP4-FF672 from Xilinx Virtex-II Pro family. This part is a “system-on-chip” that offers over 300 user I/O pins, includes 4 Multi-Gigabit Transceivers (3.125 Gbit/s RocketIO MGTs), ample logic resources, memory blocks and an embedded 350 MHz PowerPC 405 CPU core. It is fully compatible with the XC2VP20 device on-board the commercial evaluation kit used during the R&D phase. Large parts of the firmware have already been prototyped, debugged and will be re-used. An in-situ configurable PROM is placed next to the FPGA to automatically load the configuration bitstream at power up. A JTAG header is used to set the initial firmware, while upgrades can be loaded remotely via slow control. At present, the current FPGA firmware does not make use of the embedded PowerPC processor. Later releases may use it to perform some more complex data reduction than what can be achieved in wired-logic.

The amount of buffer memory required on the FEM is too large to be found in today’s FPGAs and an external memory is needed. Assuming 12-bit ADC samples, 72 active channels per AFTER chip (plus 4 non-instrumented channel and 2 extra samples due to internal pipe-line delay in SCA readout), 511 time bins (plus 1 pseudo time bin used to encode the value of the last write pointer in the SCA), 4 AFTER chips per FEC and 6 FECs per FEM, the size of an uncompressed event in the FEM is  $\sim 11.5$  Mbit. Two 512 K  $\times$  36-bit Zero-Bus Turnaround (ZBT) SRAMs are used. These are interfaced to the FPGA by a 60-bit wide bus operating at 120 MHz single data rate. This bus provides the 7.2 Gbit/s capacity required to receive data from the 30-bit wide interface to the 6 quad-channel ADCs of the FECs (each line is clocked at 120 MHz, i.e. 6 times the 20 MHz sampling rate of the ADC, but operates at double data rate).

The FEM includes external logic to fanout signals from the FPGA to each of the 6 FECs, and multiplex some of the output signals of the FECs before feeding the FPGA. These simple discrete logic circuits allow a significant reduction in FPGA user I/O pin count.

An optical transceiver is attached directly to one of the RocketIO transceivers integrated on the FPGA die. A local oscillator is needed to clock the transceiver part, while the receiver part uses the clock recovered from the link to derive synchronization signals that are coherent in time among

all FEMs. The current firmware uses a 60 MHz primary clock and a 16-bit wide interface for the transceiver and receiver, leading to 960 Mbit/s (1.2 Gbaud after 8B/10B encoding) over the fiber. A later version may use a 100 MHz primary clock (for an exact match with other sub-detectors), leading to 1.6 Gbit/s (2 Gbaud) over the fiber. Both rates are within the operating range of the RocketIO transceiver (622-3125 Mbit/s) and the selected optical transceiver. The DCC to FEM path uses a custom protocol to preserve synchronous signals, while the FEM to DCC path uses standard Start-Of-Frame and End-Of-Frame packet delimiters and CRC-32 integrity check.

Another element of the FEM is a microcontroller dedicated to slow control. Using a device distinct from the core FPGA and a path different from the main data path was found preferable for various reasons: this makes FPGA firmware simpler and easier to upgrade in-situ, a low speed network is presumably more robust than a set of gigabit-class links, etc. Following the choice of the FGD group, a microcontroller from Silicon Laboratories was selected: the C8051F044. This component includes 64 programmable I/O pins, a 10-bit ADC, a CANbus interface, 2 serial ports and many other interfaces. It is used to control and monitor the following items: voltage, current, temperature and serial identification number of all 6 FECs, FEM and serial ID of the Micromegas detector, enable/disable the voltage regulators of the FEM and each FEC individually, open/close the 2 OptoMOS relays of each FEC to ground or leave floating groups of pad polarization resistors on the Micromegas module, read-out FPGA core temperature, optical transceiver temperature, laser transmission and reception power, upgrade FPGA firmware over an emulated JTAG interface, force FPGA re-configuration, reset all logic, etc. Microcontroller I/Os are electrically coupled to rest of the logic of the FEM but transceivers attached to the shared slow control link are opto-isolated to provide galvanic isolation between detector modules. No final decision has been made yet on the slow control protocol. CANbus and RS-485 are the two possible physical layers.

The FEM card requires the following supply voltages: 3.3 V, 2.5 V and 1.5 V. All voltages are produced on-board from a single power input using Low Voltage Drop (LDO) regulators. While LDOs lead to higher dissipation than switching DC/DC converters, they bring considerably less noise. Besides a lower cost, this is a decisive criterion given the proximity of sensitive analog electronics on the FECs. The estimate of the total supply current per FEM is 2.5 A, leading to  $\sim 10$  W dissipation for a 4 V input.

The other elements of the FEM are de-coupling capacitors, several LED indicators, an expansion connector, debug I/O pins, test points, etc. Board length is mainly determined by the spacing between the 6 FECs ( $\sim 30$  cm) while height is estimated to be  $\sim 10$  cm. It is expected that the layout fits on a 10 or 12-layer class 6 printed circuit board. Pre-guidance for easier card insertion, locking screws and card ejectors are needed as well as a cooling plate thermally coupled to the TPC end-plate cooling system.

## **Off-detector Data Concentrator Cards**

As explained above, 6 DCCs will collect the data from the 72 mezzanine cards through optical fiber links and transfer it to the T2K data acquisition after reduction and formatting. They will also distribute the clocks and triggers to the front end electronics.

Each card will be equipped with a Xilinx chip XC4VFX60 from the Virtex4 family. It includes a PowerPC 405, FPGA, memory, RocketIO, and Digital Clock Manager. One big advantage of the Virtex4 is the possibility of synchronising the RocketIO at the hardware rather than the software level. 16 RocketIO are integrated in the Virtex4 chip, which fits nicely with our needs of 12 optical fiber links to one TPC endplate and one link to a master DCC. The availability of a digital clock manager in the FPGA will allow to cope with the different clock and synchronisation signals. The PowerPC 405 (350 MHz) will host a Linux operating system and will perform the data reduction: rather than applying a strict threshold cut for the zero suppression, the algorithm will adjust the cut after checking for signals in the neighbouring pads.

## Synchronization and trigger

The TPC read-out electronics is a synchronous system where all detector pads are sampled using a common reference clock. All front-end ASICs are instructed to start and stop sampling operations simultaneously. The maximum acceptable system wide skew for distributing synchronous control signals shall be limited to one SCA time bucket. Assuming a 50 MHz sampling rate, the tolerable dispersion in time is 20 ns. A tree topology for the clock fanout is proposed, using paths of approximately equal length for all branches. The optical links that connect the DCCs to the FEMs are the central part of the fanout tree. Time alignment shall be fulfilled by design as follows: use optical fibres of equal lengths along all paths, synchronize all DCC transceivers to the common global clock, use the clock recovered from the optical link in the FEMs to derive the sampling clock and the synchronous signals controlling the front-end SCAs. No individual adjustable delay component and calibration is foreseen to compensate for the unavoidable different lengths of copper traces on the various cards: a length mismatch of 20 cm will only contribute  $\sim 1$  ns to the global synchronization dispersion. The latency of the fanout tree shall also be minimized and must be deterministic. A latency of  $2 \mu\text{s}$  for distributing the trigger signal consumes  $\sim 20\%$  of the SCA cells (for the fastest sampling rate).

The primary clock source provided to the DCCs is a 100 MHz clock locked to the GPS. All synchronous signals (beam spill, cosmic trigger, etc.) provided to the DCCs shall be synchronous to that clock (and will be re-synchronized if not). After local distribution, the DCCs make the fanout to all FEMs. All optical links shall be clocked from the primary source at 100 MHz (alternatively 60 MHz may be used after multiplication by  $5/3$  of the primary source). The granularity for distributing synchronous signals is 10 ns (16 ns with a 60 MHz clock). The sampling clock for the pads is derived by division of the link clock by a programmable even factor:  $100 \text{ MHz} / (2.N)$  or  $60 \text{ MHz} / (2.N)$ . Assuming 500 time buckets in the SCA, this translates into drift time ranges of  $10 \mu\text{s}$  ( $16 \mu\text{s}$ ) in increments of  $10 \mu\text{s}$  ( $16 \mu\text{s}$ ) for a 100 MHz (60 MHz) global clock frequency. At each clock period (10 ns or 16 ns), the FEMs receive from the DCCs:

- a trigger signal, indicating (when set) that recording in SCAs must be stopped,
- a 2-bit trigger qualifier indicating the type of event. So far, the TPC can distinguish 4 types of events: Beam spill events, Cosmic triggers, Laser Calibration events, and Test events (for example generated in software to test the system).
- a sampling clock synchronization signal. This is used to phase align the clock generator producing the sampling clock of the SCAs. Hence all SCAs are guaranteed to sample input signals at the same time.
- a resume signal used to force all SCAs to start sampling at the same time. This is not mandatory, but can be used to detect potential synchronization failures.
- clear signals for event counters and the time stamp counter. Each FEM maintains a local counter for each of the 4 types of trigger events, and also counts the number of clock cycles since the last synchronous clear. Each trigger event is tagged locally with a time stamp and event count. This information is embedded by the FEMs in the data stream sent to the DCCs to detect potential synchronization errors.
- a parity bit to protect data integrity.

These synchronous signals make an 8-bit word, which takes half of the 16-bit data path width of a DCC to FEM transmitter. The other half of the DCC to FEM path is used to transport asynchronous messages from the DCCs to the FEMs to configure the various parameters programmable at run-time in the front-end electronics.

## **Slow control, configuration and monitoring**

Various run-time parameters and front-end ASIC programmable registers need to be set-up in the front-end electronics. These operations are performed by the DCCs using the asynchronous part of the optical links to the FEMs. Environmental running conditions and variables that may impact the safe operation of the front-end electronics are controlled and gathered by a dedicated computer via a robust specific path. Two candidate field bus technologies are considered for the slow control network: CANbus, a widespread automotive and industrial standard, and MSCB (Midas Slow Control Bus), a proprietary protocol built on-top of RS-485. Each FEM is attached to the slow control network via opto-isolators. There may be 1 slow control chain per TPC end-plate, or the same slow control daisy chain may be used for 2 to 3 end-plates. The slow control network is used to control power enable switches on the front-end electronics, monitor card supply currents and voltages, the temperature of several component, etc. For safety reasons, it is mandatory that the slow control network is always running when the front-end electronics is powered. However, no critical element in the front-end electronics requires un-interrupted control in case of power outage. The slow control path is also used to upgrade in-situ the FPGA firmware of the FEM cards, to read-out the silicon identification chip used to track the location of each electronic card, and to provide miscellaneous controls. The computer used for monitoring the operation of the front-end electronics may be shared with some of the other items to monitor in the TPC (environmental sensors, gas system, high voltage power supplies...).

## **Low voltage power supplies, power distribution, cabling**

The estimated power consumption of the front-end electronics on each detector module is 40 W, i.e. 500 W per TPC end-plate, and 3 kW in total. This corresponds to a total supply current of 600-750 A for a supply voltage of 4-5 V. Low voltage power for on-detector electronics is supplied from B2 via a set of cables.

The optical fibres between the FEMs and the DCCs run from B1 to B2. Standard 50/125  $\mu\text{m}$  multimode fibre cable assemblies containing 12 fibres are used. Each DCC to FEM fibre is composed of 2 segments: the extra-TPC segment runs from the DCC to the outside of the cover of each TPC, the intra-TPC segment runs from the inside of the cover of each TPC to the transceiver of each FEM card. A gas tight feed through connector is used to link each of the 2 segments. Extra-TPC segments are equipped with 12 standard LC connectors at the DCC end, and either a standard MPO connector or LC connectors at the TPC cover end. Intra-TPC segments are equipped with the opposite gender MPO connector or LC connectors at the TPC cover end, and with 12 standard LC connectors at the FEM extremity. Each fibre optics trunk connects to 6 FEMs, i.e. 2 intra- and 2 extra-TPC trunks are needed per TPC end-plate. For redundancy, a spare trunk is added at each end-plate. Alternatively, each trunk could include spare fibres. The complete TPC system requires 12-18 optical fibre trunks of each type.

Slow control network cables also run from B2 to the front-end electronics of the TPC. Each slow control cable is split into two segments: one runs from the slow control computer at B2 to the outside cover of each TPC, the other segment connects to all FEMs inside the TPC cover. Depending on whether the same chain is used or not for several TPC end-plates, 1 or 2 feed through in the TPC cover are needed. For flexibility, the cover of each TPC end-plate should provide both an input and output connector for the slow control of the front-end electronics. Standard DB9 connectors are foreseen at that level.

## **5.7 Integration**

This section describes how the TPC modules receive the service connections in the ND280 facility and how the modules will be installed into the ND280 detector.

### **5.7.1 TPC Services**

The three TPC modules, forming part of the overall Tracker of the ND280 experiment, are positioned in a supporting basket structure centred approximately five metres above the floor of the experimental hall. During regular operation, the Tracker modules and basket structure are completely enclosed within the magnet yokes, and are surrounded by the ECAL calorimeter. The magnet comprises sixteen 'C' half-yokes formed into eight return yokes split along the central vertical axis of the assembly. Service access to all equipment positioned inside the magnet is made possible via slots located in the lower faces of the magnet yoke interface. Each of the central six yokes have four slots, 105mm in depth when viewed along the magnet axis and 260mm wide, transverse to the magnet axis. A custom designed array of service conduits will be provided to protect cables, optical links, and gas lines as they exit the magnet through this series of slots.

With the exception of the Central Cathode high voltage supply cable, which connects to the TPC at its horizontal mid-point, all other services are connected to the end panels of the module located on each side of the installed assembly. The overall width of the TPC module envelope is 2300 mm, the end panel connector interface is recessed such that all connectors and piping elbows remain within the overall width envelope. It is foreseen to attach cable guides to the basket structure to secure all services in the event the TPC modules are disconnected and removed from the basket for maintenance. Similar cable guides will also be added to the underside of the basket to secure all cables, gas lines, and water pipes making their transition from the side of the basket to the vertical service conduits passing through the magnet yokes.

#### **Cables and optical links**

The approximate volume ratio between regular wire cables and optical links for the TPC installation is 7:1. The space between the outer corners of the TPC and the outer edge of the basket structure is sufficient to allow the safe routing of cables from the horizontal to vertical orientation. Three fibre-optic cables on each side of the TPC are of a larger diameter and of a more rigid material than those optical fibres carrying data. These special fibres will carry the laser light to illuminate the calibration strip pattern inside of each TPC drift volume and must be treated with additional care compared to their more flexible counterparts. It is foreseen to accommodate their larger bend radii within a special restraint to eliminate movement and to provide a protective shield. Available space beneath each TPC for the routing of cables and optical fibres is very generous compared to the cable cross-sections; no installation problems related to space are anticipated.

#### **Gas supply and water cooling**

Plumbing for the gas and water cooling systems will be provided in the form of stainless steel tubes, welded together and leak-tested in convenient lengths to facilitate efficient assembly. Located in strategic positions within each pipe route, O-ring sealed connections will be installed to allow for easy access to other system services and also, to allow the removal of the TPC modules from the basket. The gas system plumbing will originate from a gas supply tank and associated pumping system located on floor B2, directly below the main experiment floor. Water to cool the front-end electronics will be supplied from a chiller located on the main experiment floor. Pipes carrying the cooled water from the chiller to the TPC modules will be insulated to minimize condensation from their immediate environment.

### **5.7.2 TPC Transportation**

Upon completion of manufacture and testing at the TRIUMF site in Vancouver, it is foreseen to ship the TPC and other Tracker modules to Japan using an ISO Intermodal forty-foot shipping container. While the overall transported load is relatively light, and well within the capacity of the shipping

container, the large physical sizes of the various components dictate the use of a special 'high-cube' container which has an additional headroom of 300 mm. The door aperture of 2280 mm wide and 2560 mm high is the limiting factor influencing the design of a suitable TPC module transportation frame.

In order to maintain the lowest possible vertical profile, the transportation trolley will require side mounted castors and a maximum distance of 100mm between the floor and the underside of the TPC module. The resulting 60mm clearance at the door aperture will increase to 150mm once the module is inside the container. Each transportation trolley will be provided with a mechanism to fasten one trolley to another, and also to remove each castor from contact with the floor to provide a stable platform for shipping. A framework will also be provided to constrain module movement with respect to the container floor and walls.

From the time each module passes inspection in Canada, until its re-inspection at ND280 in Japan, each module will be individually wrapped with a waterproof cover, and will be protected against humidity with an appropriate amount of packaged silica-gel. Working within the restrictive height limitations for the TPC modules, it is foreseen to add the maximum possible amount of damping material between the transportation trolley and module to minimize vibrations during shipping.

### **Reception at ND280**

The surface building of the ND280 facility provides a covered reception area, with gantry crane access, measuring approximately  $6.0 \times 14.0 \text{ m}^2$ . This area will be used for the unloading of the TPC/FGD Intermodal container from its transport vehicle. With the container resting on the floor, the modules, on their individual transportation trollies, will be unfastened one from another and removed from the container using their own castor system. Included in the same container will be a custom-designed clean room, previously assembled and tested in Canada, and shipped to Japan in kit form. Dedicated space for the clean room has been assigned on level B3 of the experimental hall, two floors below the experimental floor. Personnel access to the cleanroom is provided by stairs and elevator with equipment access provided by an overhead 10 tonne gantry crane.

There will be a period of time, between unloading the container and the completion of the cleanroom installation, when temporary module storage will be required. Sufficient space will be available for short term storage on level B3 while the cleanroom is being assembled. Each module will retain its protective wrap until such time it can be accommodated in the cleanroom for inspection, testing, and then given approval for installation into the basket structure.

Once all transportation frames and other fixtures have been removed from the shipping container, it will be transferred to a position adjacent the ND280 surface building for use as a part storage and workshop facility. The container will be modified to incorporate suitable doors and windows prior to leaving Canada. Arrangements will be made to provide lighting and power outlets conforming to Japanese building code standards.

### **TPC Installation**

Upon being given approval for installation by the TPC technical group, each module will be provided with a temporary protective cover for its movement to the experimental floor. Mounted on a transportation trolley, each module will be removed from the clean room enclosure and wheeled the 14 metre distance to an area accessible by the overhead crane. After being lifted to the experimental floor, approximately 12 metres above the clean room level, the transportation trolley and protective cover will be removed in readiness for module assembly into the basket.

The vertical centre of the basket is positioned almost 5 m above the floor of the hall. Working platforms will be provided to allow access to all areas of the basket during the installation process. It will be essential to have at least one person on each side of the basket to guide the approach of the TPC module into position and maintain the nominal 10 mm clearance between adjacent features. Securing of the module inside the basket structure is achieved via fasteners inserted from the underside of the

basket into threaded holes in the base of the TPC frame. Alignment will be assured with datum pins and mating holes. Additional restraints will also be incorporated into the upper surface of the TPC modules to restrict movement during periods of seismic activity.

### **5.7.3 ND280 Service routing**

Equipment racks for the TPC and all other sub-detectors are located on the B2 floor immediately below the experimental area. Access from the basket to the B2 floor is provided in the form of six holes cast through the concrete floor of the experimental hall. These holes are located, three on each side of the centreline, in a position coincident with the walls of the lower central support pillar located directly under the basket. The distance from the centreline of the basket to the edge of the hole openings is 500 mm, and the cross-section of each hole will be of sufficient size to accommodate a standard range of cable trays in which to secure the services as they pass from one floor to another. The cooling water chillers are to be mounted on the main experiment floor in a location against the pit wall to the right of the magnet yoke.

#### **Basket Support interface**

An interconnecting steel floor beam of the basket support structure acts as a base for an array of conduits providing guidance for the various services exiting the magnet. There are six individual groups of four conduits, each one having the ability for adjustment to suit the position of mating slots in the central six yokes of the magnet. These conduits will have an approximate internal cross-section of 95 mm X 250 mm and will begin at a point 1125 mm above the floor, continuing through the magnet yokes and coils to terminate 3017 mm above floor level. To assist with segregation of the various service categories, the internal space of the conduits is sub-divided by 6 mm diameter bars, spaced at 200 mm intervals along the length. It is anticipated fourteen of the conduits will be available for sharing between the TPC and FGD modules. Space, between the underside of the service conduits and the floor, provides sufficient room to allow routing of the services into their assigned cable trays, through the floor, and down to level B2.

#### **Service floor interconnections**

Installation of the several hundred service and data interconnections between the TPC modules and the equipment racks on the B2 floor will be a collective effort shared between sub-detector installation teams and site, or contract, personnel. In order to comply with Japanese industrial national standards relating to gas, water, and electrical supplies, it is foreseen most of these services will be installed by qualified Japanese trades people. The many optical fibres for data collection, for laser transmission, and also the regular cables for slow control monitoring will be the responsibility of the TPC group.

## **5.8 Offline software**

The offline software for the TPC subdetector is embedded inside the ND280m software framework that is based on GEANT4 for detector simulation and ROOT for data storage, handling and analysis framework. Refer to software TDR for more details.

The MC geometry description, being similar to that of the ND280m, presents several peculiarities that should be described independently. The ND280m Monte Carlo simulates the transport and interactions of the particles with the detector, but no electron drifting is done inside the TPC. This is provided by an independent package developed by the TPC group.

The reconstruction presents also some differences with respect to other subdetectors. However, we have followed here the principle of using or developing common tools when this was possible.

## 5.8.1 Monte Carlo simulation

The simulation of the TPC, based on GEANT4, is embedded in the ND280 Monte Carlo simulation framework. This section describes the specificities of the TPC, which are the geometry implementation and the simulation of ionization electrons.

### Geometry implementation

The TPC geometry is implemented with GEANT4, and the detail of the implementation (material definition, size and position of the different parts of the TPC, ...) can be found in the software TDR.

During GEANT4 simulation, the tracking information is saved in hits, using the specialized class ND280HitBase. These hits are created when a particle goes through a sensitive detector (detailed information about hits can be found in the software TDR). In the case of the TPC, the sensitive detectors are *voxels*, which are 3D volumes (parallelepiped of tunable size) used to pave the full TPC volume. When a particle goes through one of these voxels, the energy deposited in the voxel is computed and stored, as well as other informations characterizing a hit. Using the voxel ID, the hit position, defined as the voxel center, can later be easily found with the geometry manager.

However, the sampling of the hit position may lead to a bias in the reconstruction, if the voxel size is too large compared to the point resolution (which will be a few 100  $\mu\text{m}$ ). Since the maximum number of voxels is also limited ( $< 2^{32} \simeq 4.3 \times 10^9$  for 32 bits), we used a voxel size of 1 mm<sup>3</sup> in the simulation. The final version of the tracking simulation will be using steps instead of voxels.

### Electron transport

As explained in the previous section, after the tracking simulation, the physics information is available through the time, position and energy loss associated to the voxels which are along the track path. This information is used to create ionization electrons along the track, and then to transport these electrons from their creation point to the detection point.

For a given energy loss  $\Delta E$ , the number  $n_e$  of ionization electrons created in the TPC is given by the formula  $n_e = \Delta E / W_I$ , where  $W_I = 26$  eV is the effective average energy to produce an electron [27]. These electrons are then distributed uniformly along the track path.

These ionization electrons drift from their creation point to the readout plane under the action of the uniform electric field applied in the drift region. The drift velocity  $V_{drift}$  is constant, so the drift time of an electron  $T_{drift}$  is proportional to its distance  $Z$  from the readout plane:  $T_{drift} = Z / V_{drift}$ . During the drift, electrons diffuse, following a Gaussian distribution, with a diffusion  $\sigma_{x,y,z}$  proportional to the square root of the drift length:  $\sigma_{x,y,z} = \sigma * \sqrt{Z}$ . For the transverse diffusion (X,Y),  $\sigma = \mathcal{G}(0, \sigma_T)$  is distributed like a Gaussian with standard deviation  $\sigma_T$ , while for the longitudinal diffusion (Z),  $\sigma = \mathcal{G}(0, \sigma_L)$  follows a Gaussian with standard deviation  $\sigma_L$ .

The values currently used in the simulation for the drift length ( $V_{drift} = 6.5$  cm/s) and the diffusion ( $\sigma_T = 240 \mu\text{m}/\sqrt{\text{cm}}$  and  $\sigma_L = 290 \mu\text{m}/\sqrt{\text{cm}}$ ) are calculated with MagBoltz software [2] for a drift field  $E = 200$  V and a mixture of Ar + 3% CF<sub>4</sub> + 2% iC<sub>4</sub>H<sub>10</sub> in normal conditions. These quantities will be measured with calibration data and read from a data base.

After this step, each individual ionization electron has been created, and its time-position calculated.

### Electronic simulation

For each electron arriving on the readout plane, the electronic simulation looks for the channel that will detect it, simulates the charge produced by this electron and its time distribution, and eventually add this information to an existing signal.

**Readout simulation** This step simply looks for the channel number corresponding to the electron transverse coordinates. The characteristics of the readout plane (module position, pad size and position) will be available from the Root geometry.

The spacing between pads is about  $100 \mu\text{m}$ , for a typical pad size of  $7 * 10 \text{ mm}^2$ , meaning that a very small part readout plane is isolated. Nevertheless, the simulation assumes that the detection efficiency is 100%, because of the configuration of the electrical field lines in these regions.

**Time shaping** The characteristics of the observed signal from a single electron after amplification have 2 distinct origins: the integral of the signal depends on the properties of the amplification region (electric field, gas mixture, ...), while the shape of the signal depends on the characteristics of the electronic (pre-ampli, Analog to Digital Converter, ...).

Thus, for each electron arriving on the readout plane, a function is applied to account for the electronic properties. A typical function is a 4<sup>th</sup> order semi-gaussian filter,

$$f(X) = (Xe^{-X})^4 \quad \text{with} \quad X = \frac{T - T_0}{\tau}$$

where  $T_0$  is the arrival time of the electron and  $\tau$  is the shaping time of the ADC ( $\tau \simeq 200 \text{ ns}$ ).

The digitization is made by Analog to Digital Convertors (ADC), with the sampling frequency given by the ADC clock. In the case of the Alice TPC FEC, the 10 MHz frequency corresponds to 100 ns sampling. In the simulation, the height of the signal in a bin is given by the 4<sup>th</sup> order semi-gaussian function at the rising edge. For each electron, the distribution is calculated in 20 bins and normalized to 1, because the gain is simulated in an independent calculation.

**Gain simulation** In every type of gaseous detector such as Micromegas, for a given channel, the gain has large event by event fluctuations. For Micromegas detector, the gain  $G$  follows a Polya distribution,

$$P_\theta(G) = \frac{\theta (\theta G/G_0)^{\theta-1}}{\Gamma(\theta)} \times e^{-\frac{\theta G}{G_0}}$$

where  $\theta$  is a form factor, characterizing the shape of the distribution, and  $G_0$  is the average gain. The TPC simulation uses the value  $\theta = 1$ , corresponding to an exponential distribution of the gain. The exponential distribution is simulated by  $G = -G_0 \times \log(1 - u_G)$ , where  $u_G$  follows a uniform distribution  $\mathcal{U}_{[0,1]}$ .

The time distribution obtained for one electron in the previous step is then multiplied by this gain  $G$ , and eventually added to a signal from a electron detected on the same pad.

## 5.8.2 Data model

The basic detector unit in the TPC is an electronic channel. In the case of the TPC the information is generated as part of a temporal series that contains the information of the ionization tracks. The basic unit in the TPC reconstruction will not be an ADC digitization of a single channel at a single time but a vector of discrete values in time that represent the charge collected by a pad from the ionization track after diffusion. The series corresponds to a complete readout sequence after any trigger and it might contain several neutrino interactions. This is a consequence of the TPC readout \* It is part of the offline software functionalities to provide a neutrino interaction selection that allows to match slow readouts with fast ones tagging the event time (FGD, POD, ECAL and SMRD)<sup>†</sup>.

\* The Fine Grain Detector (FGD) is adopting the TPC electronics and will show the same readout configuration.

<sup>†</sup> Even in the case of a readout electronics common to that of the TPC, detectors like the FGD will provide always a prompt signal response and a reliable way of tagging the neutrino interaction time.

## TPC software in the ND280m software framework

The TPC reconstruction is a package frame inside the ND280m. The design of the software will be done in a flexible way to accommodate several reconstruction algorithms that can be used for intercalibration or optimization. This way also promotes the collaboration of different programmers in the software development effort. The ND280m software has been designed in such a way that this is naturally implemented. The package segmentation will be done following the algorithms described in Fig.5.40.

### 5.8.3 Reconstruction

The TPC is divided into three different volumes with two Fine Grain Detector (FGD) blocks interleaved. The reconstruction takes into account this layout and distinguished between single TPC block reconstruction and long tracks that matched segments in different volumes and tries to refit the track parameters.

The data flow structure of the reconstruction algorithm can be seen in Fig.5.40. The first step is the application of the gain calibration constants and the removal of dead and noisy channels. This step can be done at the end of the online process, but it has to be possible always to redo it later when updated knowledge of the calibration constants are available. The output of this process is the waveform mentioned before that represents the charge acquired in a single pad along the readout time. The following step is the search for clusters of waveforms in the same row. Clusters are then joined into tracks following a pattern recognition algorithm. The pattern recognition is applied to TPC blocks independently, since there is no information at this level to extrapolate tracks across the more dense material of the Fine Grained Detector. The reconstruction of the track kinematics is done using two different methods: single point reconstruction and likelihood fit. Prior to the track reconstruction, the drift distance has to be reconstructed to be able to predict the size of the electron cloud due to the transverse and longitudinal diffusion. This is achieved by determining the time at which the track was created ( $T_0$  of the track) via a matching with objects in the fast detectors, most probably FGD and ECAL.

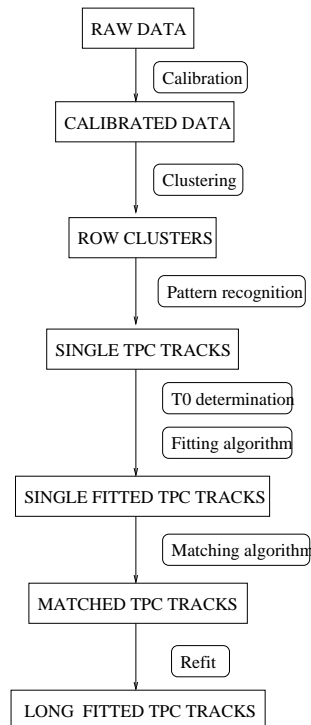


Figure 5.40: Flow diagram of the reconstruction algorithm.

The reconstructed tracks are then matched to tracks in other TPC blocks and refitted to improve the accuracy of the track parameters.

## Clustering

The first step in the TPC reconstruction is the clustering of the wave forms. This is at the moment done following a simple criteria of connectivity: waveforms have to overlap in time and have to be consecutive in space. The clustering is done within TPC vertical detector rows. The clustering in rows is preferred by the main direction of the particles coming out from neutrino interactions. For straight tracks along the beam axis the charge sharing among adjacent pads is due to the transverse electron diffusion. The reconstruction code assumes that this is the case for all tracks becoming a basic assumptions in the point reconstruction methods that are described below.

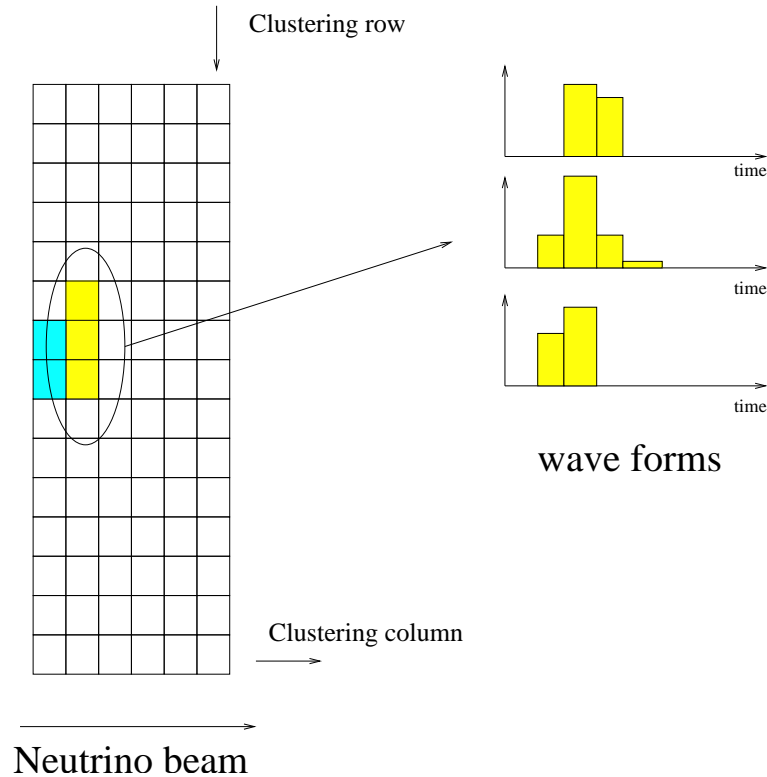


Figure 5.41: Sketch of the clustering method. Clustering in vertical direction is shown but both will be done to allowed for optimal tracking at large angles.

The rows and columns can be clustered independently. This is actually a possibility that will be investigated to improve the momentum resolution when tracks are very inclined and the position of rows and columns can be exchanged from the charge sharing point of view.

More elaborate methods can be developed in the future to account for tracks that are close to each other or for the cases with a hard  $\delta$  electron emission. Similar methods subdividing wide clusters with more than one maximum. The TPC is being designed to have a maximum of 3 PAD per cluster, in most of the cases only one or two. Alternative methods are simply ignoring these clusters. More detailed studies are needed to estimate the impact of both solutions and define the one that optimize the resolution.

## Track pattern recognition

Tracks are characterized as a series of row clusters that follows locally a line. This local approximation is valid even in the presence of magnetic field. The pattern recognition connects the clusters and forms

a track segment. The track segment has to be limited to a single volume inside the TPC block since the  $T_0$  of the track is not defined at this stage and we don't know how to relate segments at both sides of the TPC cathode membrane.

The actual implementation of the track pattern recognition is based in a cellular automaton that is also available for the FGD and POD reconstruction. This code is a adapted of the 2D algorithm implemented for the SciBar detector in K2K and SciBoon to a 3D algorithm. The cellular automaton first creates segments connecting row clusters in contiguous rows. The algorithm is also prepared to jump over a predefined maximum number of empty rows. The segments are then connected if they share a common edge and the three resulting points fulfills a selection criteria, for example that they form a straight line with certain  $\chi^2$  quality criteria. Once the segments are connected, the reconstruction navigates along the list of connected segments and selects the combination that provides the longest reconstructed track segments. The algorithm is sketched at Fig.5.42. The algorithm is also able to find branches corresponding to hard  $\delta$  ray emission or vertexes inside the TPC detector volume. This is done identifying branches that leave the main track and have a minimum number of independent (from the main track) segments.

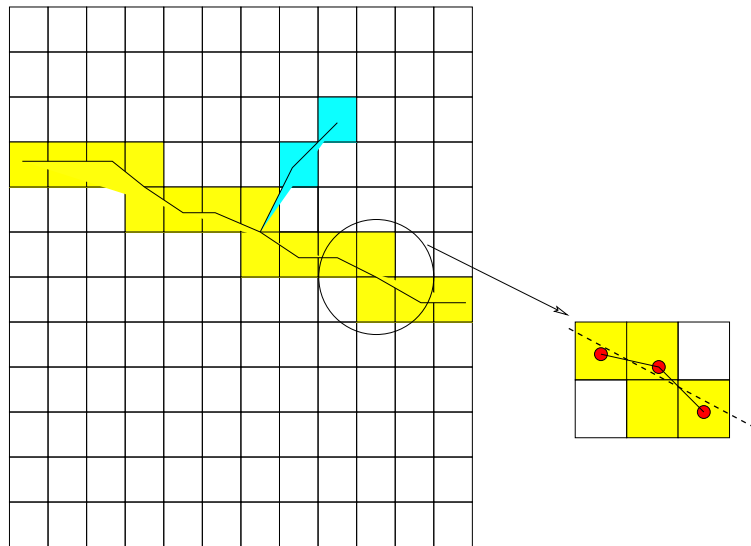


Figure 5.42: Sketch of the pattern recognition algorithm.

At the moment the algorithm is not tuned for tracks that bends back due to the effect of magnetic field. We are however considering several possibilities to fix the problem: adding an additional criteria for segment connection that allows the segment to go back in z direction or to perform a track matching inside a TPC block after the pattern recognition.

### $T_0$ determination

The drifting time of primary electrons from the production point to the readout pad plane is much larger than the beam spill window ( $2.5 \mu s$ ). The position in the direction of drift is computed based on the drift time, but to do so we have first to calculate the time at which the track was created. This is done at ND280m by matching the available TPC tracks to signals in the FGD which provide a time measurement with precision of few nanoseconds. On one hand, the properties of the tracks are not known at this stage and there is a considerable amount of material and distance between the TPC hits and the FGD ones. On the other hand, the occupancy of both the TPC and FGD subdetectors are small, hence it is expected that the determination of the  $T_0$  can be based in a simple algorithm. This algorithm has to be developed based on matching detector signals at the entrance and escape of the track (FGD, ECAL and POD would provide the time reference). Using more than one detector

reference signal, or more than one plane per detector ‡, will overconstrain the determination of the  $T_0$  and will reduce the amount of fake matches. In the case of TPC-FGD we can also try to match the direction of the tracks that can be reconstructed in both subdetector with good precision at this stage of the Reconstruction. Additional information will be provided by the position of escape of the TPC track that has to coincide with the limits of the active volume in the TPC or has to be matched with segments of the TPC volume at the other side of the cathode membrane.

### Single TPC reconstruction

Once the clusters are reconstructed, we should apply a cluster selection criteria to clean up clusters with potential  $\delta$  electron contributions or clusters which are in the vicinity of disabled or noisy pads.

The point and track reconstruction is done with two different methods: in the first one the points are reconstructed independently and then they are fitted to a helix model, in the second a likelihood method is used where the point is not reconstructed but the charge deposition distribution is used to fit the track model. The likelihood method is the default reconstruction method for the TPC since it is able to use the cluster information optimally.

**Point reconstruction method** The charge cloud shape can be represented by a Gaussian:

$$Q(x) = \frac{Q_0}{\sqrt{2\pi}\sigma} e^{-\frac{x^2}{2\sigma^2}} \quad (5.2)$$

where  $\sigma$  is the charge width at the pad plane.  $\sigma(z)$  is function of the drift distance through the transverse diffusion ( $\mathcal{D}$ ):

$$\sigma^2(z) = \sigma_0^2 + \mathcal{D}^2 z$$

The  $\sigma_0$  is the charge cloud smearing at the amplification level§ In the design of the ND280m TPC, the pad width is more than a factor of two larger than the largest transverse diffusion in the gas. The linear centroid, where the pad position is weighted by the fraction of the charge deposited in the pad, is not a good estimator of the point position under these conditions and it has to be corrected by a bias function that can be computed if the angle of the track with respect to the pad row is known. When the track is perpendicular to the pad row, the charge deposited on each pad ( $Q_i$ ) can be computed as follows

$$Q_i = \int_{x_{min}^i}^{x_{max}^i} Q(x - x_{point}) dx = Q_0 \left( erf\left(\frac{x_{max}^i - x_{point}}{\sqrt{2}\sigma}\right) - erf\left(\frac{x_{min}^i - x_{point}}{\sqrt{2}\sigma}\right) \right)$$

where  $Q(x)$  is given by eq.5.2,  $x_{point}$  is the true point of the track in the pad row,  $(x_{min}^i, x_{max}^i)$  are the edge coordinates of the pad  $i$  and  $erf$  is the error function defined as:

$$erf(z) = \frac{2}{\sqrt{\pi}} \int_0^z e^{-t^2} dt$$

The linear centroid ( $x_{cent}$ ) is then calculated as:

$$x_{cent} = \sum_{\forall Q_i \neq 0} Q_i \frac{x_{min}^i + x_{max}^i}{2} = PRF(x_{point})$$

‡ This is mandatory to obtain a two dimensional point in the reference detector

§ This value is assumed to be small in the Micro Mega case and of the order of few hundred micrometers for the GEM system. In any case this value will be measure and used as input to the algorithm.

being a function (denoted as PRF) of the true coordinate  $x_{point}$ . This method assumes that the track is perpendicular to the rows. Under this assumption the track keeps constant the distance to the lateral pads and the charge sharing is only due to the transverse electron diffusion. When the tracks are inclined, the charge sharing depends on the actual distance of the track in the pad and on the longitudinal deposition of charge along the track that is not uniform. Some of this problems can be solved by recomputing the centroid once the track angle is estimated so the distance to the adjacent pads can be computed more precisely.

The dependency of  $x_{cent}$  with the true position  $x_{point}$  is shown in Fig.5.43.

The reconstruction method computes first the linear centroid and inverts the function  $PRF(x)$  to obtain the true value of the track at a given row. For each point, we have to provide the algorithm with the proper value of the transverse diffusion. An estimation of the drift distance is needed before the reconstruction of the track point, see the  $T_0$  determination above for more details. In the point reconstruction method the charge cloud width is always an input to the algorithm and it has to be determined with other methods.

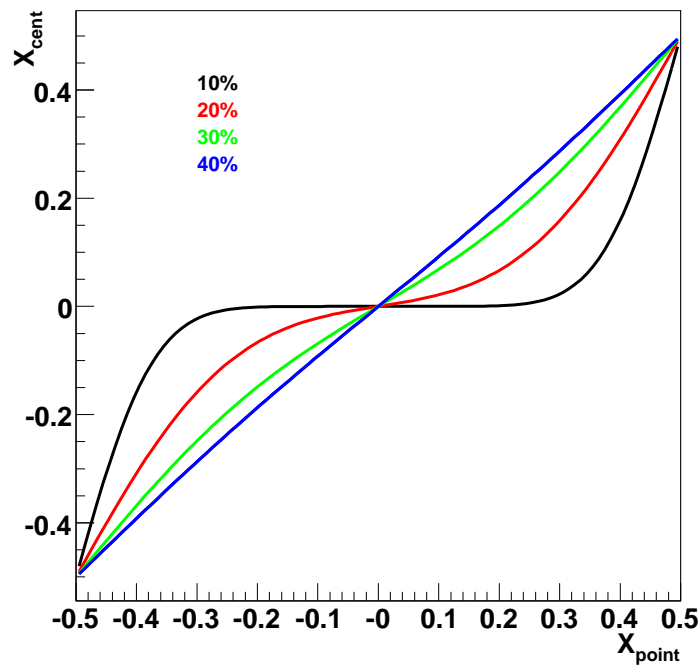


Figure 5.43: Correction function,  $PRF(x_{point})$ , for different values (from 10% to 40%) of the fraction of the charge cloud width to the pad size. The pad size is fixed to one and  $x_{point}$  is represented in the coordinates of the central pad.

Once the points are reconstructed, a fit to a helix is performed using the official Kalman filter software of ND280m.

Results of the performance of this method are shown in the performance chapter for the prototypes that were constructed and operated at CERN during the winter 2005/2006.

**Likelihood method** The likelihood method is based on the same assumptions on charge sharing as the single point reconstruction. The main difference is that points are not reconstructed but instead the observed charge is compared to a prediction assuming the track angle and position.

The likelihood method assumes, like the point reconstruction method, that the charge deposition is constant within a row. When the track angle becomes large we exchange the rows and columns in the clustering such that the above statement is valid for almost any track angle. The exact procedure on how to merge row and column cluster information has been investigated in more detail in the future.

The likelihood method is based in a simple model, see [30] for more details, of the charge deposition and electron drifting. The number of primary electrons released in a row is of the order of 100. These electrons are amplified by the MicroMegas amplification system. The distribution of charge is approximately multi-nomial. This approximation is valid in the MicroMegas where there is no additional charge sharing in the amplification stage. It is also needed that the electronic noise is small compared to that of the primary electron statistics, see the chapter on Electronics.

The number of electrons collected by a pad  $i$  with a pad gain  $g_i$ (ADC value per electron) is defined as:

$$n_i = ADC_i / g_i$$

where  $ADC_i$  is the charge collected in the pad  $i$  in ADC units. These values are non-integer, but a direct continuum extension of the multi-nomial distribution, yields the log likelihood function,

$$\log \mathcal{L}_{row} = \sum_i n_i \log p_i + const$$

where  $p_i$  is the probability of a primary electron from the track to be associated to the pad  $i$ .

$$p_i = Q_i(\vec{x}, \vec{p}, \sigma) / \sum_j Q_j(\vec{x}, \vec{p}, \sigma)$$

where  $Q_i(\vec{x}, \vec{p}, \sigma)$  is the predicted charge deposited in the pad  $i$  for a track with coordinate  $\vec{x}$ , momentum  $\vec{p}$  and the charge cloud width  $\sigma$ .  $j$  runs over all pads in the cluster containing pad  $i$ . The value of  $Q_i(\vec{x}, \vec{p}, \sigma)$  can be computed following the rules explained in the single point reconstruction subsection, modified with the recipes in [30].

A spurious signal in a pad far from the track can cause problems for the likelihood calculation, since the calculated probability for electrons to be present there can be vanishingly small. To make the track fit robust to spurious signals, the probability for a primary electron to be associated with a pad is modified by adding a small constant,  $p_{noise}$ ,

$$p_i \rightarrow \frac{p_i + p_{noise}}{1 + n_{pad} p_{noise}}$$

where  $n_{pad}$  is the number of pads in a cluster. The value of  $p_{noise}$  has to be calculated for the specific characteristics of the electronics, primary electron production and MicroMega amplification.

The likelihood is maximized to obtain the track coordinates and the covariance matrix. The value of the charge cloud width can be fitted during the same procedure or being fixed by other methods. Actually, this parameter is not strongly correlated to the track parameters, so it can be kept free during the fitting without affecting the track resolution.

## Long track reconstruction

Once the segments at the different blocks are found we proceed to match them using a kalman filter algorithm [29], that takes into account the material distribution and track momentum to predict the track coordinates, angle and momentum (state vector) and its covariance matrix at the matching plane. The matching plane is defined at the center of the FGD, but it can be defined at the entrance or exit of any of the two TPCs. The matching is accepted following a quality criteria that can be change. The standard criteria computes the  $\chi^2$  of the matching for the state vector of the tracks at the matching plane.

If several pair of tracks fulfill this requirement, the one with the best quality is selected. The process is repeated several times to allow for matching of three segments in three TPC blocks.

The tracks are refitted after the matching to improve the momentum resolution. This is critical for long tracks that are produced at forward angles and tend to have high momentum. The matching-refit could help in improving the momentum resolution for this kind of tracks that provides information about the kaon production in the T2K beam.

This long track reconstruction can be performed with the single point reconstruction method or the likelihood method. Both methods provide the track coordinates (vector of track state) at a defined point of the track and its corresponding covariance matrix. The state vector is propagated and refitted using the same kalman filter method.

### **Electric and Magnetic fields inhomogeneities**

Although the design of the detector has been done to minimize inhomogeneities in both the drift electric field and the magnetic field, they have to be measured in the final setup. The first version of the reconstruction code will ignore these effects, but they can be taken into account in case they are relevant. This has been done in the past for other TPCs. There are two levels at which the inhomogeneities can affect the measurement:

- Electron drifting. The transverse coordinates can be affected by non uniform electric and magnetic fields. The correction can be done, if the effect is known with enough precision, with a correction matrix that relates measured coordinates and drift distance to provide the correct position.
- Track path. A non uniform magnetic field distorts the helix of a charged particle passing through the TPC. The kalman filter and the likelihood fit methods are able to apply the correct field at each of the track points integrating the inhomogeneities in the reconstruction.

## **5.8.4 Particle Identification**

Following previous methods on particle identification based on  $dE/dx$ , the TPC will measure the average charge deposition per track on a fraction of clusters with the smallest charge collection (truncated mean). Studies in this direction are presented in the performance chapter for the CERN TPC prototypes. The particle identification is performed at the end of the reconstruction chain. At this level the charge attenuation and the particle momentum is already known. We are also foreseeing the possibility of recomputing the track kinematics after the particle identification. The  $dE/dx$  and the multiple scattering are functions of the particle mass and it can affect the precision on the matching determination of the track momentum and position. This particle flavour refit is done with the ND280 kalman filter code.

## **5.8.5 Data Base**

The TPC will need a large number of calibration data. The TPC will be monitored constantly to detect variations in the basic parameters of the TPC: drift velocity, electron amplification, electron attenuation, and transverse diffusion.

All these parameters might vary with the temperature, atmospheric pressure and gas composition and they have a large impact on the performance of the TPC. The amount of data needed to be stored is probably one of the largest among the ND280m subdetectors.

In addition, static parameters like electric and magnetic field maps has to be stored and should be retrieved by the reconstruction and simulation software. Parameters to be stored in the Data Base are of different type, from environment, to detector settings or detector response calibration.

Some of them are derived from the direct monitor parameters (drift velocity and electron attachment) and some others will be derived from the calibration code that is running in parallel to the data acquisition (transverse diffusion, amplification,...). It is either running on true neutrino events or calibration data (cosmic rays and laser).

## 5.9 Calibration

### 5.9.1 Overview

A Time Projection Chamber is a very complex device whose performance strongly depends on good calibration procedures. Many parameters must be measured in order to guarantee an accurate determination of the track parameters and their associated energy deposition. The physics chain in the TPC goes from ionisation energy loss to ADC counts in different electronics channels. The calibration procedure must consider physics processes such as gas ionisation, electron transport in electric and magnetic fields, charge multiplication in the readout chambers, electronics amplification, etc. The following equation summarises all these processes:

$$q_i[ADC] = \sum_j E_{ij} \cdot G_j \cdot \sum_{x,y,z} T_j^{xyz} \cdot q_{xyz}^0[e^-] \quad i, j = 1, \dots, N_{pads} . \quad (5.3)$$

The above equation connects  $q_{xyz}^0$ , the initial ionisation charge produced in a finite volume element centered at  $(x, y, z)$ , and  $q_i$ , the charge measured in pad  $i$ .  $T_j^{xyz}$  is the transport matrix, which represents the fraction of the initial charge that arrives to the region of the micromesh delimited by pad  $j$ . This takes into account transverse diffusion, charge attenuation and spatial distortions.  $G_j$  is the micromegas gain for pad  $j$  and  $E_{ij}$  is the electronics equalisation matrix, which accounts for electronics gain, electrons/ADC conversion and cross-talk. Although the above equation is a simplification <sup>¶</sup>, it permits the reader to understand the several parameters involved in the calibration. Besides the calibration of the charge a time calibration might be needed in order to guaranty a correct measurement of the drift coordinate. This also requires the knowledge of the drift velocity. Finally, once the charge and time calibrations are satisfactory, the TPCs must be aligned, both internally and with the rest of ND280. The following list summarises the calibration procedure:

- Electronics calibration: the ADC and TDC response of all electronic channels to a given input signal must be understood. This includes
  - electronics gain ( $E_{ii}$ ),
  - electronics x-talk ( $E_{ij}$ ),
  - time synchronization,
  - and linearity of the electronic response ( $E_{ij}$  may depend on the input charge).
- Study of the micromegas gain ( $G_j$ ) and absolute energy calibration, that is the relation between the deposited energy by  $dE/dx$  and the number of measured ADC counts.
- Understanding of electron transport ( $T_j^{xyz}$ ):
  - Measurement of the drift velocity.
  - Study of charge attenuation.
  - Measurement of the magnetic field map.
  - Correction of spatial distortions, produced by deviation of the chamber properties with respect to their nominal values: mechanical design, gas properties, magnetic and electric fields, etc.
- Geometrical alignment: between the two halves of one TPC, between different TPCs and with the rest of ND280.

Section 5.9.2 describes briefly the different calibration methods considered. Then, each of the individual measurements is treated separately in section 5.9.3.

<sup>¶</sup> For example, the cross-talk signals have a different time structure than the real signals, what means that the equalisation matrix should have non diagonal time elements,  $E_{ij}(t, t')$ .

## 5.9.2 Calibration methods

The different methods foreseen for the calibration of the ND280 TPCs are briefly described.

### Test bench

The calibration test bench is described in Sec. 5.4.3. Collimated X-rays from  $^{55}\text{Fe}$  with well known energies, are focused into a given pad, allowing precise pad-per-pad study of the micromegas gain, the absolute energy scale, the x-talk, etc. Each of the micromegas modules will be tested and characterised in the test bench. This will be the main quality test in the production chain.

### Pulser

This generic name refers to the two test inputs present in the Front End ASIC, described in Sec. 5.6.3. They allow the injection of calibrated charge via capacitive coupling into the input of the preamplifiers. One of the test inputs operates on individual channels while the other generates the same charge in all channels. The injected charge can be known with a relative precision better than 2%<sup>||</sup> (Sec. 5.6.3), which should be sufficient for a channel per channel gain calibration. Cross-talk studies and time synchronization are also possible.

### Cosmic muons

Cosmic muons provide a very powerful calibration method. They can be used to measure the drift velocity, the attenuation length, the spatial distortions, and also for the geometrical alignment. In addition, this calibration source comes for free and its use only requires the implementation of a cosmic trigger, which on the other hand, is also needed by other subsystems. The cosmic trigger can be given by the SMRD detector.

An event rate of 12 and 9 Hz have been estimated [31] for muons traversing the central cathode and two contiguous TPCs respectively. A minimum transverse track length of 20 cm in each TPC and a positive cosmic trigger have been required.

### Particles in neutrino events

Particles produced in neutrino events can be used for several purposes: study of charge attenuation, absolute energy calibration, correction of spatial distortions and geometrical alignment.

Minimum Ionising Particles (MIP) are of special interest given the fact that their energy deposition depends very little on the actual momentum. Thus, the predicted  $dE/dx$  can be known very precisely once the momentum is measured by curvature, allowing an absolute energy calibration. This will be discussed in Sec. 5.9.3.

### Laser flash over membrane in central cathode

This calibration system, introduced in section 5.2.2, has been previously used in the STAR TPC [32]. It consists of a pattern of aluminised strips implanted in the central cathode. These are illuminated by a UV laser flash located on the pad plane side. Electrons are released via photoelectric effect and drift towards the pad plane producing an image of the strips. A possible pattern of aluminium strips is shown in Fig. 5.44.

This method can be used to continuously measure the drift velocity, which could vary with time due to variations of the gas properties. However, the main motivation for using this method is the study of spatial distortions. Unlike all other spatial measurements (cosmics, MIPs) it permits an absolute position measurement, since the strip pattern is known very precisely.

---

<sup>||</sup> It could go below 1% if the calibration voltage generator is calibrated.

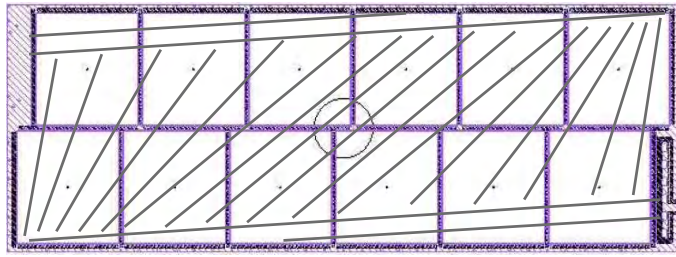


Figure 5.44: Proposed aluminium pattern projected into the pad plane.

The STAR TPC used a 266 gm laser and 3 mm wide aluminium strips. The photoefficiency in STAR was  $10^{-8}$  e/ph for the aluminium strips and  $10^{-10}$  e/ph for the kapton membrane, ensuring a good contrast. A similar system could be used in the ND280 TPCs. The number of photoelectrons produced per unit of length should be close to a MIP, that is  $10 \text{ mm}^{-1}$ . In this case the expected point resolution would be similar to the one expected for MIPs ( $\sim 0.7 \text{ mm}$ ), since diffusion dominates. For 3 mm wide strips the required energy density is  $80 \mu\text{J}/\text{mm}^2$ , which corresponds to a laser power of the order of 1 mJ/pulse to illuminate the entire cathode. Several laser companies have been contacted ensuring that the required product is available in the market.

### Test chambers

A set of small test chambers will be installed in the gas system to directly measure the amplification gain, the drift velocity and the amount of electron attachment. The chambers will be installed at the input of the TPCs as well as in the mixing station. A detailed description of the test chambers can be found in chapter 5.3.

### 5.9.3 Calibration procedure

The sequence of steps leading to a good knowledge of the unknown parameters is described. The strategy of the alignment procedure is such that the redundancy of various calibration methods to obtain the same quantities is used whenever is possible. This allows to cross-check the results and to reduce the systematic uncertainties. The presented calibration scheme ensures a good calibration for a wide range of data quality. The details of the calibration procedure will be only defined once real data are available.

#### Electronics calibration

The first step in the calibration procedure is the calibration of the full electronic chain. Apart from general operation tests and the usual analysis of pedestals, noise and common mode noise, the following aspects must be covered:

- equalisation of electronic gain of all channels,
- cross-talk measurements,
- synchronization of readout timing,
- and linearity of the electronic response.

These items are treated now separately.

**Equalisation of electronic gain** The electronic gain of individual readout channels can be computed by injecting a known amount of charge at the input of each preamplifier. This can be done once the electronics is mounted in its final location by using the pulser, described previously. This operation is usually called equalisation. The result of the equalisation procedure is a set of constants  $E_i$ , such that

$$q_i[ADC] = E_i \cdot q_i^0[e^-] \quad i = 1, \dots, N_{pads} , \quad (5.4)$$

where  $q_i^0$  and  $q_i$  are the injected and measured charge respectively in the same channel  $i$ . Notice that  $E_i$  includes the electron amplification factor and the  $e^-/ADC$  conversion factor.

The equalisation procedure must be also applied to the electronics used in the test bench in order to deconvolve the micromegas gain of the module under test from the total gain, which includes the electronics.

**Cross-talk** A single pad receiving charge may share it with other pads by capacitive coupling between the output of its preamplifier and the input of other preamplifiers. This effect, usually called cross-talk (x-talk), is due to the physical proximity of the vias carrying the signal before and after amplification. Although the design of the ASIC FE card suggests a negligible x-talk level, this must be measured experimentally. The coupling between individual channels is studied by injecting charge (with the pulser) in only one channel at the time and recording the fraction of the initial charge measured by its electronics neighbourhood. X-talk can be also studied in the test bench. It is worth noting that the time structure of real signals is in general different from the one of the x-talk signals. Thus, not only the total amount of charge shared must be studied but also its time distribution.

**Time synchronization** The determination of the drift coordinate requires a relative precision of the time measurement between different channels to be within 20 ns. Variations in the timing are caused mainly by varying cable lengths in the distribution of the trigger signal over the readout plane and by variations in the shaping time of the preamplifier/shaper chips. Although no measurable effect is expected, the pulser can be use to estimate possible time shifts that would be subtracted from the measured time.

**Linearity of electronic response** The pulser can be used to determine the linearity of the electronics by generating a sequence of increasing amplitudes, ranging from 120 fC to 600 fC. This is possible thanks to the four capacitors used for signal injection (see Sec. 5.6.3).

### Micromegas gain and absolute energy calibration

The next step in the calibration procedure is the measurement of the micromegas gain – or gas gain –, that is the amplification factor between the charge arriving to the micromesh and the charge arriving to the pad plane ( $G_j$  in Eq. 5.3). The micromegas gain depends on the distance between the micromesh and the pad plane, on the micromesh geometry, on the gas and on the micromegas voltage ( $V_{MM}$ ). The first could vary from pad to pad in a single module. Imperfections on the geometry could also affect the gain. As discussed in chapter 5.4, micromegas gains of several thousands are expected.

Given the difficulty of injecting calibrated charge into the micromesh, the input charge must be inferred from the knowledge of the energy of the ionisation source and the energy required for the creation of an ion-electron pair in the gas. Therefore micromegas gain and absolute energy calibration are strongly related. Two types of sources are usually considered: radioactive sources and MIPs in neutrino events.

To measure the micromegas gain electronics gain, x-talk and charge attenuation must be deconvolved from the total gain. The equalisation matrix has been previously measured using a pulser calibration. On the other hand, charge attenuation, diffusion and spatial distortions can be avoided by selecting small drift distances. Thus, the micromegas gain can be extracted from equation 5.3 once the equalisation matrix has been applied.

In practise, the micromegas gain of individual modules will be measured first in the test bench, taking advantage of the fixed small drift distance and of the perfectly known energy of the ionising photons from the radioactive  $^{55}\text{Fe}$ . This will be the main quality check in the production chain and will serve as a starting point for the absolute energy calibration in the final chamber. The micromegas gain of each of the modules can be cross checked once those are mounted in the final chambers by using MIPs with good momentum resolution and small drift distances. In this case, the initial charge,  $q_j^0$ , is the mean number of ionisation electrons over the pad, calculated using the most probable  $dE/dx$  for the measured momentum, and the energy required for the creation of an ion-electron pair in the gas. Eventually, tracks with larger drift distances could be used as well provided that the attenuation length is well known and spatial distortions and diffusion are small. The possibility of implanting small dots of  $^{55}\text{Fe}$  in the central cathode is also being investigated.

## Electron transport

The transport of electrons from the production point to the micromesh is considered. The spatial properties of the charge cloud are mainly affected by diffusion and spatial distortions in the transverse plane, and by the drift velocity in the drift direction. On the other hand, the absolute amount of charge may be attenuated due to electron attachment.

**Drift velocity** The drift coordinate of individual hits is obtained by multiplying the corrected time (after synchronization of all channels) by the drift velocity ( $v_{drift}$ ). This can be approximately known from simulations [2], since it depends mainly on the gas properties and the drift field. However an empirical measurement is required.

To measure the drift velocity the time difference between the ionisation process and the electronics measurement, and some reference points on the path of the ionising particle must be known. The aim is to reach a precision such that the error on the drift coordinate is dominated by the resolution on the time measurement. Possible variations with time and position must be considered.

In general, the chamber performance is insensitive to small drift velocity variations along the transverse coordinates. Thus, the drift velocity could be measured in the test chambers under similar conditions. Another way of measuring the drift velocity is with cosmic muons traversing the central cathode, since the position of the intersection point is well known. Finally, the laser flash will provide a continuous ( $\sim 1$  Hz) monitoring of the drift velocity.

**Charge attenuation** In a perfect TPC the charge arriving to the micromesh would equal the one produced initially by the ionising particle. However, due mainly to gas impurities electron attachment might produce a strong charge attenuation, given by the law

$$q = q^0 e^{-x/\lambda} , \quad (5.5)$$

where  $x$  is the drift coordinate and  $\lambda$  is the attenuation length. The transport matrix of Eq. 5.3 can be factorised in two terms, the exponential attenuation factor of the above equation and a migration matrix accounting for spatial distortions and transverse diffusion.

As deduced from Eq. 5.5, the attenuation length can be extracted from an exponential fit to the graphic charge measured versus drift coordinate. Attenuation will be studied in the test chambers. Cosmic muons or MIPs in neutrino events can be also used for this purpose given the fact that the drift coordinate of all charge clusters produced by the particle is known. This method has been used for the prototype described in chapter 5.10, giving very good results. For example, the attenuation length for the Ar-CF4-Isobutane gas mixture was found to be larger than 30 m. This method allows the study of possible variations of the attenuation length with the transverse coordinates.

**Transverse diffusion** A localized distribution of charges diffuses by multiple collisions following a Gaussian law. Longitudinal diffusion may affect slightly the resolution on the drift coordinate. More important is the effect of transverse diffusion, which enlarges the transverse dimensions of the charge cloud. Thus, a point like source will produce a circular charge cloud on the pad plane. The knowledge of the transverse diffusion coefficient ( $D_T$ ) is important for an accurate determination of the track parameters.

$D_T$  can be obtained from simulations [2] and a detailed study of tracks allows an empirical measurement. For example, the track fitting likelihood method, described in section 5.8.3, provides the width of the charge cloud as a result of the fit.  $D_T$  can be directly extracted from the comparison of this width for different values of the drift coordinate. This method was applied to the prototypes (see chapter 5.10).

**Spatial distortions** Spatial distortions may affect the average trajectory of the drifting electrons in the gas, such that they do not follow a perfect straight line parallel to the  $x$  axis. In this case the transport matrix,  $T_j^{xyz}$ , must account for a systematic transfer of charge to a pad  $j$  from a volume element ( $xyz$ ) whose transverse coordinates are beyond the limits of that pad. Spatial distortions are due to local variations of the chamber properties with respect to their nominal values. Some of these properties are: magnetic and electric fields, gas properties and mechanical design.

A precise knowledge of the electric and magnetic fields is crucial for a good understanding of the electron transport. The electric field map cannot be measured experimentally. Thus, one must rely on simulations (Maxwell [35]), as the ones shown in Fig. 5.14. The magnetic field map can be measured experimentally with Hall probes, as explained below. Measurements with no magnetic field can be taken in order to study all other effects, however the increase in transverse diffusion may complicate the analysis. A rather conventional way of measuring spatial distortions is with laser tracks [32, 33], which have a well defined straight trajectory even inside the operation magnetic field. However, this system is very complicated since it requires mirrors inside the field cage, and has been discarded. Spatial distortions other than the ones due to the magnetic field will be studied using the measured magnetic field map.

A misalignment between the magnetic and electric fields results in spatial distortions (known as  $\vec{E} \times \vec{B}$  effect). In some cases this misalignment can be understood and introduced in the Monte Carlo simulation, what permits the calculation of this particular contribution to the transport matrix.

Spatial distortions will be addressed using two different methods: particle tracks and laser flash. Energetic tracks (cosmics or MIPs in neutrino events) can be used to observe deviations from the predicted trajectory beyond the point resolution. This will allow only a partial understanding of the problem since the absolute position of these tracks is not known. On the contrary, the laser flash system, which projects the strip pattern of the central cathode into the pad plane, will allow the absolute determination of the transport matrix for  $x = x_{cathode}$ . The combination of both methods brings the possibility of a full understanding of the transport matrix for all values of the drift coordinate.

In practise, spatial distortions can be accounted for in several ways. A concrete mathematical treatment needs still to be defined.

**Magnetic field map** The nominal magnetic field map can be simulated with Maxwell [35] using the design specifications of the magnet. However, deviations from the nominal value must be measured experimentally.

The field map used by the NOMAD experiment can be used as the nominal field \*\*. Figure 5.45 shows the deviations with respect to the field in the center of the magnet for the different field components, for the entire magnet (on the left) and for the region interesting for the TPCs (on the right). It can be shown that there are important inhomogeneities mainly in the regions near the magnet walls.

---

\*\*The UA1 magnet was used by the NOMAD experiment

The plots in Fig. 5.46 show the corresponding one-dimensional projections. The x component diminishes by 2% in the laterals while it falls drastically at the downstream end of the magnet, where the z component becomes important. Fortunately, this dramatic effect is reduced to 2 – 3% (in both components) in the TPC region ( $|x|, |y| < 105$  cm,  $280 < z < 619$  cm). The y component has a sinusoidal variation with x and might be relevant ( $\sim 1\%$ ) at the top and bottom of the TPCs. This suggests that special care has to be taken when measuring and modeling the field in those regions.

The BaBar [36] case can be taken as an example. The dimensions are similar (3.8 m long by 3 m diameter), but the field is different, a solenoid of 1.5 Tesla. The relative momentum resolution obtained by the measurement of the curvature is 0.3% at 1 GeV/c. To ensure that the magnetic field knowledge does not affect the momentum resolution it was measured with a precision of the order of 0.1%, since  $(\sigma_p/p) = (\sigma_R/R) \oplus (\sigma_B/B)$ . The measurements were carried out by means of a transport mechanism that could move a set of Hall probes throughout the inside volume of the solenoid. A total of 12 probes were used to take measurements over a 3D grid of about 10 cm pitch. The measurements took about a month. These data were used to model the field in the entire magnetic volume with a systematic uncertainty smaller than 0.01%, which was the upper limit established by the momentum resolution requirements.

A similar strategy has been foreseen for ND280. In principle, the required precision should not be that good, since for ND280 the aim is 10% momentum resolution at 1 GeV/c. However, in this case there are extra problems associated to the spatial distortions produced by the  $\vec{E} \times \vec{B}$  effect. In the absence of these distortions a point to point precision on the field measurement of a few per cent, and a systematic error in the modelling below 1% would be sufficient <sup>††</sup>. However, small magnetic field components in the transverse coordinates could produce important distortions leading to undesired momentum biases. These distortions can be accounted for in the transport matrix if the field is known with sufficient precision. The required accuracy needs still to be understood. At the moment, three to four weeks have been foreseen for such a measurements and the possibility of using existing material is being investigated.

## Geometrical alignment

Although a detailed alignment strategy has still to be defined, some ideas can be introduced at this stage. The alignment between TPC halves, different TPCs and with the rest of ND280 must be considered. The starting point will be the result of the mechanical survey. A precision of better than 1 mm is expected. This will be followed by an alignment with tracks. Useful cosmic muons will traverse the central cathode at a rate of 12 Hz, providing sufficient statistics for a precise alignment between TPC halves. Cosmic muons can be also used for the alignment between contiguous TPCs, since the rate is the 9 Hz per TPC halve. Tracks in neutrino events will complement this data sample, ensuring that the accuracy of the geometrical alignment will not be limited by statistical errors. The only limitation could come from spatial distortions.

## 5.10 Prototype results

This section describes the tests performed by the Canadian groups using the prototype field cage and a GEM readout, and the tests performed by the European groups using the Harp field cage at CERN and with both GEM and Micromegas readout.

### 5.10.1 Prototype field cage with GEM readout

To test the design concept of the T2K field cage, a prototype TPC was built at TRIUMF having a drift volume that was the full drift length and space for two large readout modules, based on  $31 \times 31$  cm<sup>2</sup>

<sup>††</sup> The muon momentum scale is required to be understood at the 2% level

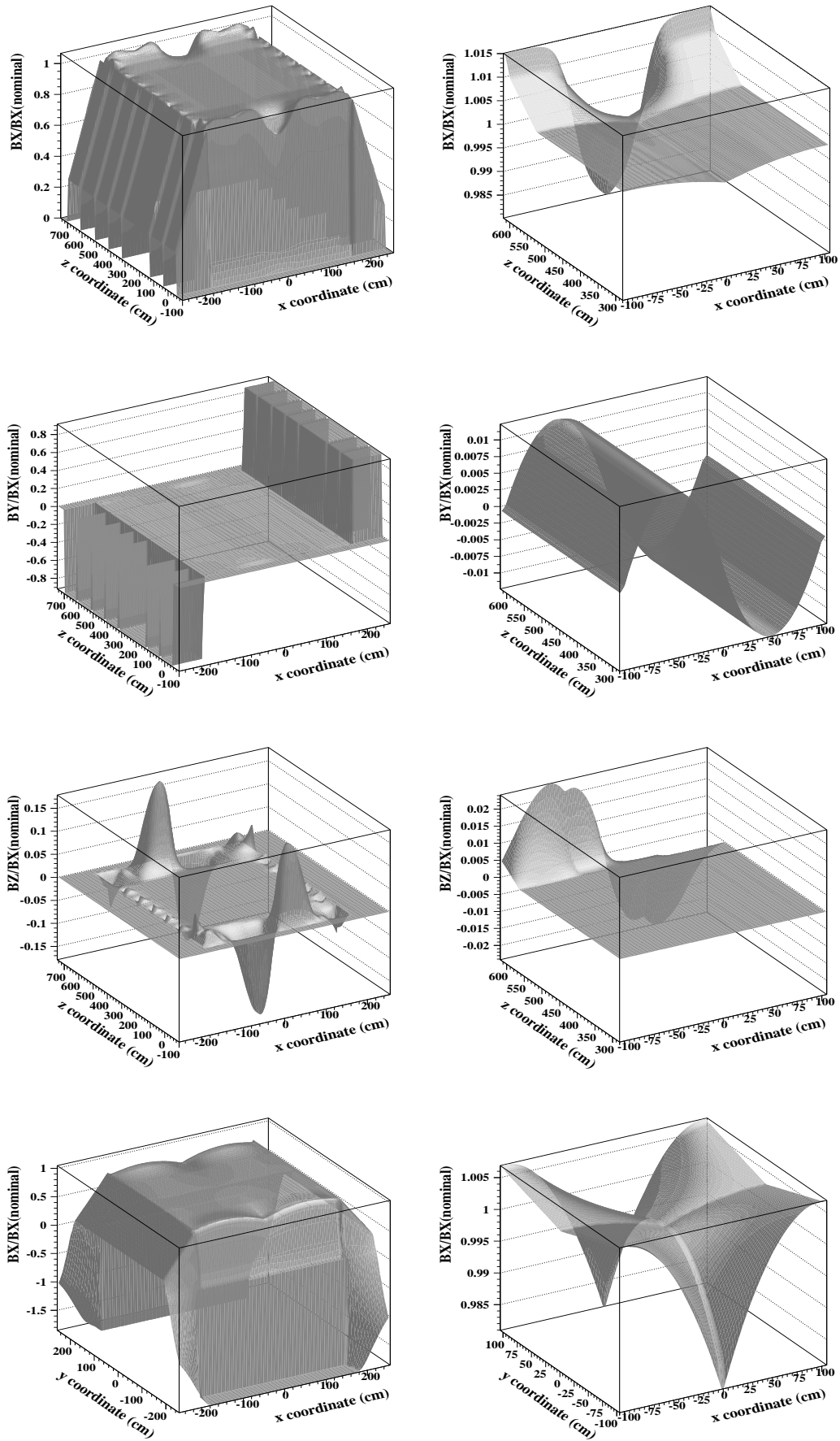


Figure 5.45: Magnetic field map in the NOMAD experiment. On the left panels for the entire magnetic volume and on the right for the region of the TPCs.

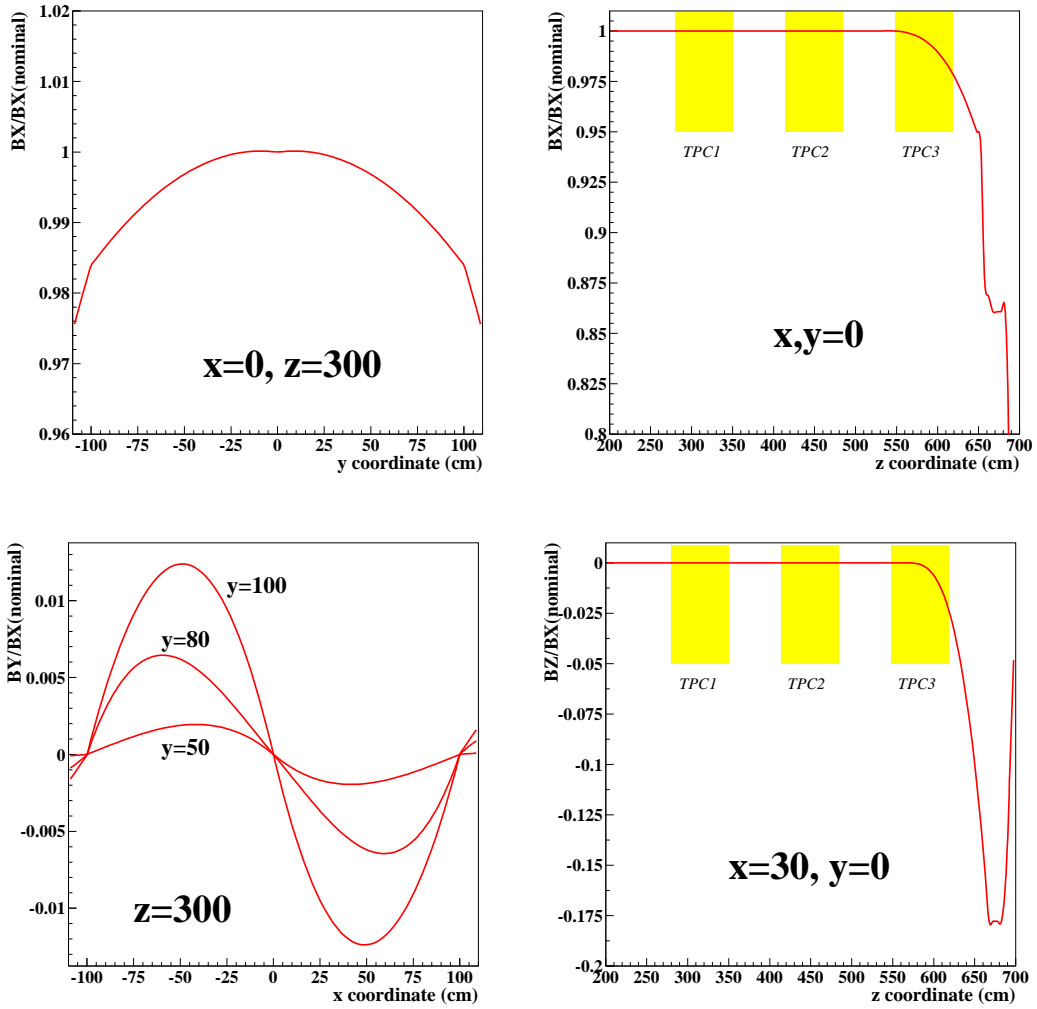


Figure 5.46: Magnetic field map in the NOMAD experiment. The right pannels also show the regions corresponding to the different TPCs.

GEM foils. Figure 5.47 shows the side view drawing with dimensions.

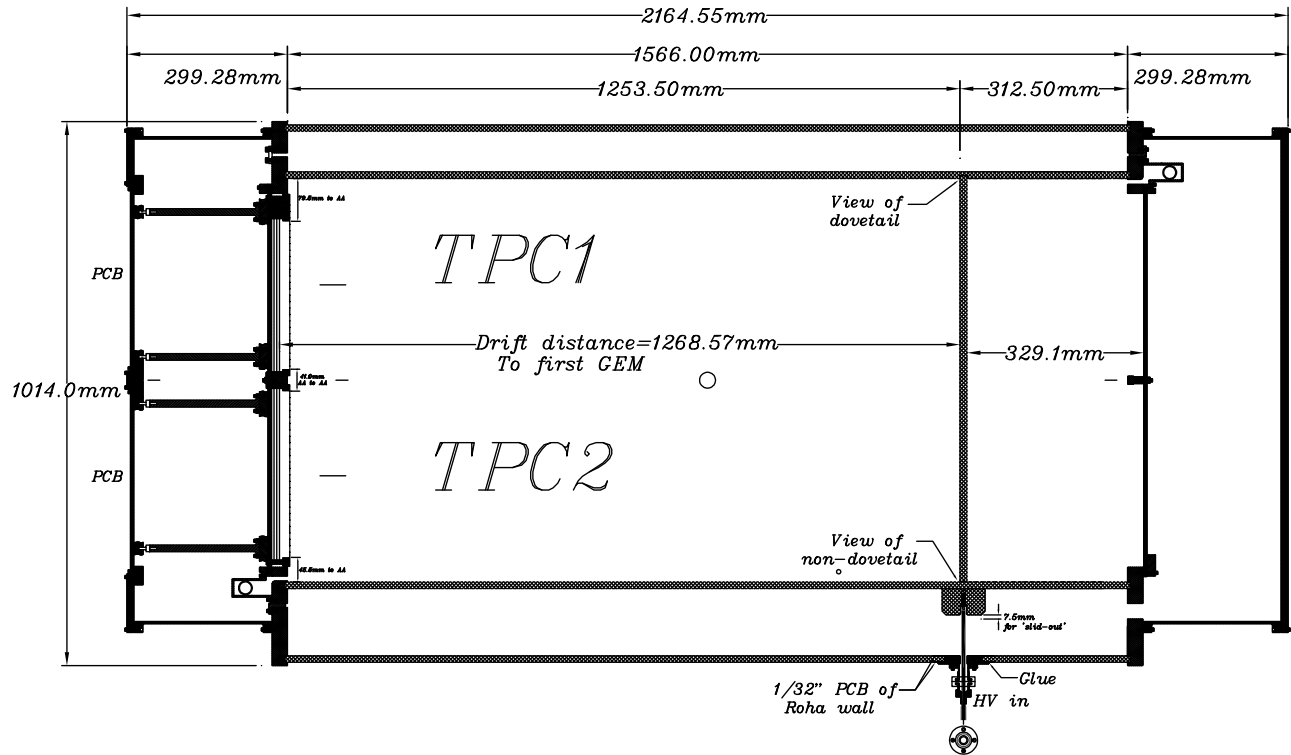


Figure 5.47: The prototype fieldcage design. The cathode is not central, as only the drift volume on the left is designed for readout.

A portion of the outer surface of the lower panel of the inner field cage is shown in Fig. 5.48. It shows the copper strip pattern, the jumpers through the wall, and the paired surface mount resistors that define a uniform gradient within the field volume. The figure also shows the completed prototype TPC with scintillators arranged to provide a cosmic trigger. For most studies, the scintillators were placed to emphasize tracks at relatively large angles  $0 < \phi < 0.4$  rad.

One of the GEM amplification modules in final stage of construction is shown in Fig. 5.49. A triple GEM structure was built, with power distributed to the GEM sectors through current limiting resistors on small PCBs mounted with the G10 frames that is seen in this figure. The figure also shows a view inside the TPC field cage.

ALICE electronics front end cards were used to readout out signals on approximately 1600 pads. As described below, special signal inverter cards were constructed to convert the negative going GEM signals into positive pulses that the ALICE electronics were designed for.

A novel HV system using inexpensive DC converters was built. This allowed the upper surfaces of the GEMs to be at identical voltage, while maintain full flexibility to define the potential difference across any GEM in a very safe manner.

The TPC has been operated with Ar CO<sub>2</sub> and Ar CO<sub>2</sub> CH<sub>4</sub> mixtures. The central cathode operated at about 25 kV during the tests providing a drift field of about 180 V/cm, giving a maximum drift time of about 100  $\mu$ m for Ar CO<sub>2</sub> (90:10).

## Gas properties

The drift velocity was determined by using cosmics that cross the cathode, thereby leaving an incomplete track segment in the active tpc volume. The drift time at the edge of the track segment represents the longest possible drift time, which is easily converted into the drift velocity

Track fitting is performed using the likelihood technique as described in reference [30]. This allows a proper treatment of the spread of ionization amongst the pads, and allows for the width of

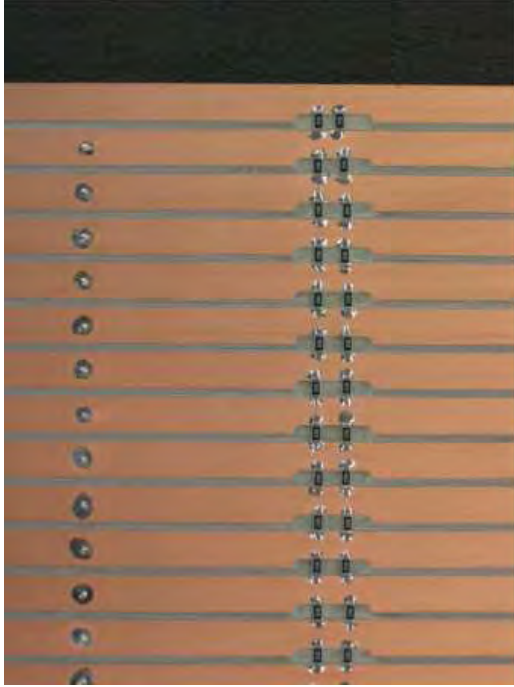


Figure 5.48: (a) The outer surface of the lower panel for the prototype. (b) the completed TPC with cosmic telescope for triggering.

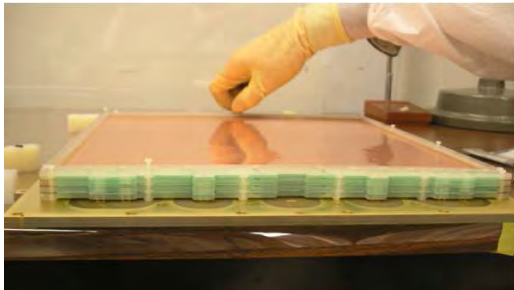


Figure 5.49: (a) A triple GEM structure being attached to the pad board. (b) a view inside the TPC through the hole intended for a GEM amplification module.

the charge cloud to be measured. In general, the observed gas properties (drift velocity and diffusion constants) agree within about 10% with the values calculated by Magboltz [2].

**Attachment** For Ar CO<sub>2</sub> (90:10) studies, a reduction in signal amplitude for long drift distances was observed. A fit to the electron lifetime yields roughly 200  $\mu$ s. The amount of oxygen was monitored at the output of the drift volume, and was found to be contain only a few ppm, much less than the amount that would be required to explain the observed attachment, roughly 25 ppm. Studies are underway with the test cell built for the STAR TPC to see if any of the construction materials could be responsible.

### Position resolution

The transverse coordinate resolution of the system was studied by examining single row residuals to full track fits. As expected, the resolution depends on the number of pads hit in a row. For those rows with only one pad hit, the track passed relatively close through the center of the pad, and the resolution is roughly 1.1 - 1.3 mm. For the majority of rows two pads are hit, yielding a resolution of typically 0.6 - 0.7 mm. Those with more than 2 pads hit typically have slightly worse resolution, typically 0.8 mm. Results from some of the data collected with Ar CO<sub>2</sub> (90:10) are summarized in Table 5.3 and Fig. 5.50. Overall, it appears that the resolution as predicted by the Monte Carlo simulation, roughly 0.7 mm per row, is achieved.

Table 5.3: Single row resolutions are shown for Monte Carlo simulation (MC) and various data samples collected with Ar CO<sub>2</sub> (90:10). The columns show the fractions of rows with 1 or 2 pads hit, and the resolutions for those rows.

Sample	transfer field (V/cm)	frac $n = 1$	frac $n = 2$	res $n = 1$ (mm)	res $n = 2$ (mm)
MC		0.36	0.63	1.44	0.55
2a	800	0.21	0.74	1.13	0.64
3b	600	0.27	0.71	1.28	0.65
3e	800	0.18	0.78	1.09	0.64
3d	1000	0.11	0.79	1.22	0.60

### Sensitivity to atmospheric contamination

A study was performed with the prototype field cage on the sensitivity to contamination of nitrogen, which cannot be removed by filters. A leak that brings in air into the TPC volume will result in a level of N<sub>2</sub> that depends on the leak rate and the rate of fresh gas injection. The drift velocity and diffusion were not seen to be affected by an addition of 1% N<sub>2</sub> to Ar CO<sub>2</sub> (90:10), but the gain was found to be reduced by about 50%. In order that the  $dE/dx$  resolution not be affected by N<sub>2</sub> concentration, this sets a target for the N<sub>2</sub> concentration of less than 0.1%.

### 5.10.2 Prototype Micromegas and GEM studies with HARP field cage

The TPC experimental setup at CERN consists of the HARP TPC field cage inside a solenoidal magnet and its gas system. The TPC field cage consists of a large cylindrical vessel, 80 cm of inner diameter and 154.1 cm in drift length, where a series of strips connected by a resistor chain creates an axial electric field. The cathode was set at a potential corresponding to an electric field of 160 V/cm. The TPC field cage is mounted inside a solenoidal magnet of 90 cm inner diameter and 225 cm length.

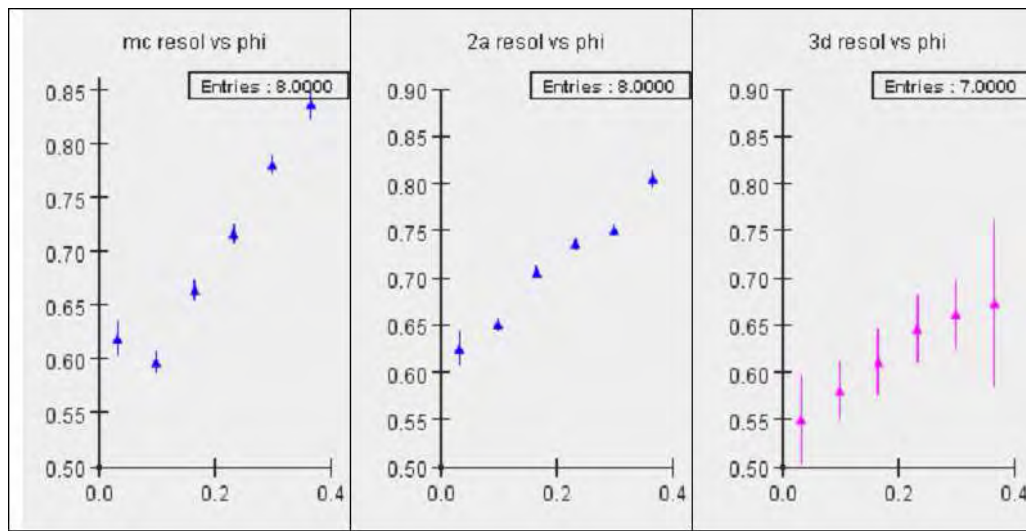


Figure 5.50: The single row resolution is shown as a function of azimuthal angle. The degradation in resolution for larger angles is a result of the non-uniform ionization along the length of a track. All rows are used for this plot: 1, 2, or more pads hit per row. The left figure shows the result for a Monte Carlo simulation, the right two are for two data sets.

A system of seven scintillators, above and below the magnet, equipped with PMT, provided the trigger signal. The electronics consists of 12 inverter boards and 12 Alice TPC FEC cards for a total of 1536 channels. The cards instrumented the central part of the active region of the two detectors, for a total vertical length of 38.4 cm over 48 rows of pads. The input noise level was 2000  $e$  RMS for a sampling frequency of 10 MHz, a shaping time of 190 ns and an overall gain of 1000  $e$  per ADC.

### Micromegas prototype

**The Micromegas endplate** The end-plate hosting two Micromegas modules (fig. 5.51, 5.52 and 5.53) consists of an aluminum support structure covered on its inner surface by a large PCB with copper coating for an uniform termination of the drift electric field. The total inactive region between the two Micromegas sensitive regions is 12 mm.

The Micromegas modules have been built with the procedure and materials described previously. Their active dimensions are 26.76x26.35 cm<sup>2</sup>, with square pads of 8x8 mm<sup>2</sup> arranged in 32 rows of 32 pads each.

Before mounting the Micromegas module on the endplate, they were tested in a small test box. This gas box provided an easy way to test the detector in a specific gas mixture with a <sup>55</sup>Fe source. The box was provided with a mylar window and an electrode to create a drift electric field pushing electrons toward the Micromegas mesh. The energy resolution was measured to be 10 % from the width of the Fe line (fig. 5.54). Several gas mixtures were tested with maximum gains ranging from a few thousand (Ar-CO<sub>2</sub>, Ar-CF<sub>4</sub>) to a few 10<sup>4</sup> in Ar-CF<sub>4</sub>-iC<sub>4</sub>H<sub>10</sub> (fig. 5.55).

The HARP tests have been performed with the non flammable gas mixture Ar-CF<sub>4</sub> (3%)-iC<sub>4</sub>H<sub>10</sub> (2%). It offers a fairly large drift velocity (6.5 cm/ $\mu$ s) close to its maximum at an electric field of 160 V/cm, low diffusion coefficient at small magnetic field (247  $\mu$ m for B=0.2 T) and allows operation of Micromegas with a gain larger than 10000.

**Track reconstruction** We have taken cosmic ray data with this setup for almost one month. Typical Micromegas voltages were 330-360 V corresponding to gains of 2000 to 10000. The magnetic field varied from 0 to 0.4 T. The detector operated smoothly, the typical current drawn from the power supply being 1 nA. We observed sporadic sparks, triggering the current limit of the detector high voltage power supply (500 nA), without consequence neither for the detector nor for the electronics.

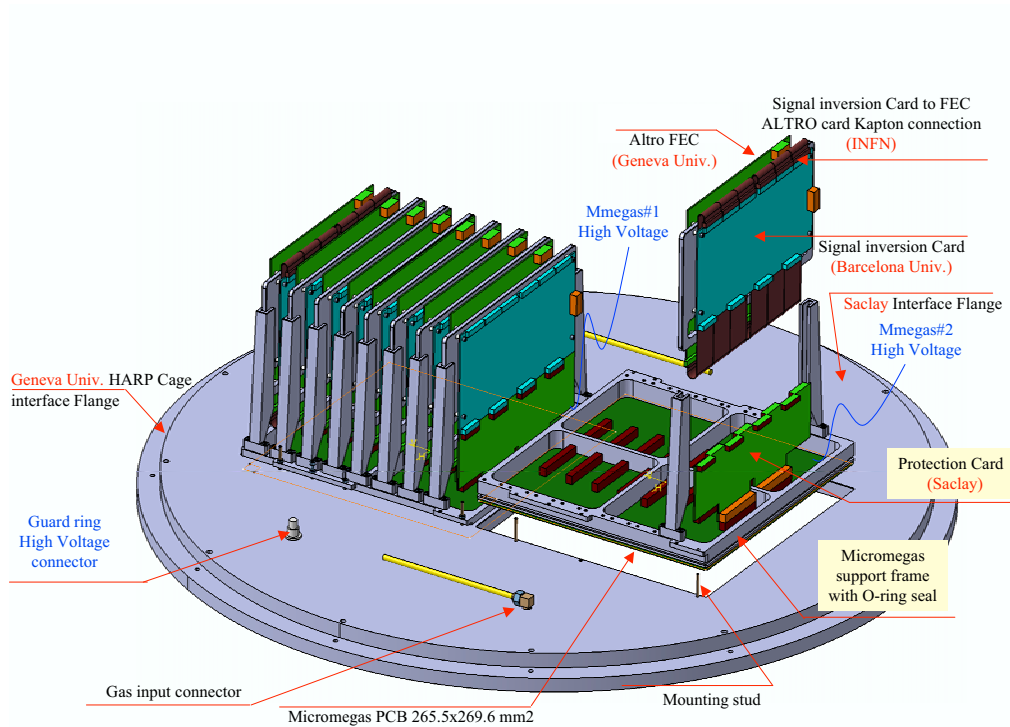


Figure 5.51: The Saclay Micromegas endplate for the cosmic ray tests at CERN.

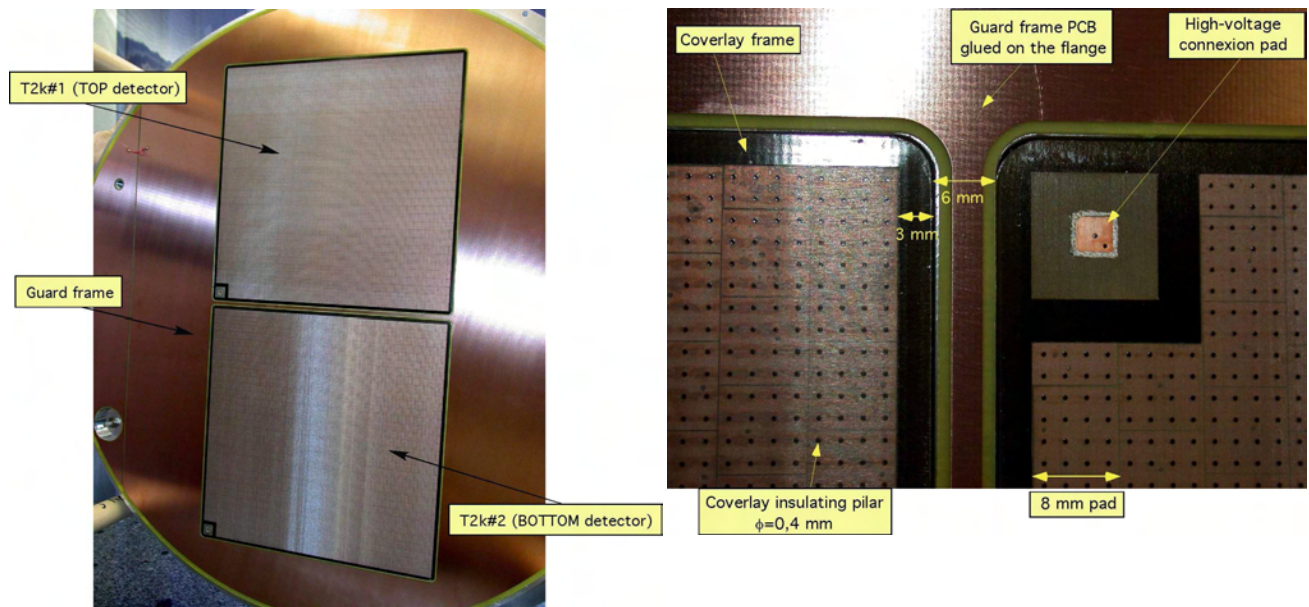


Figure 5.52: The two Micromegas detectors mounted on the end plate (left) and close up of the region between two detectors and the HV corner.) (right).

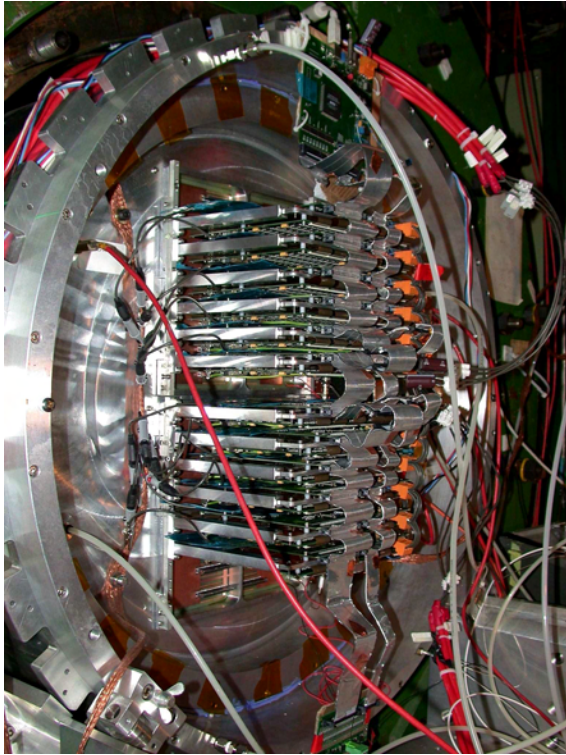


Figure 5.53: Final setup of the Harp end plate with the electronics readout chain mounted.

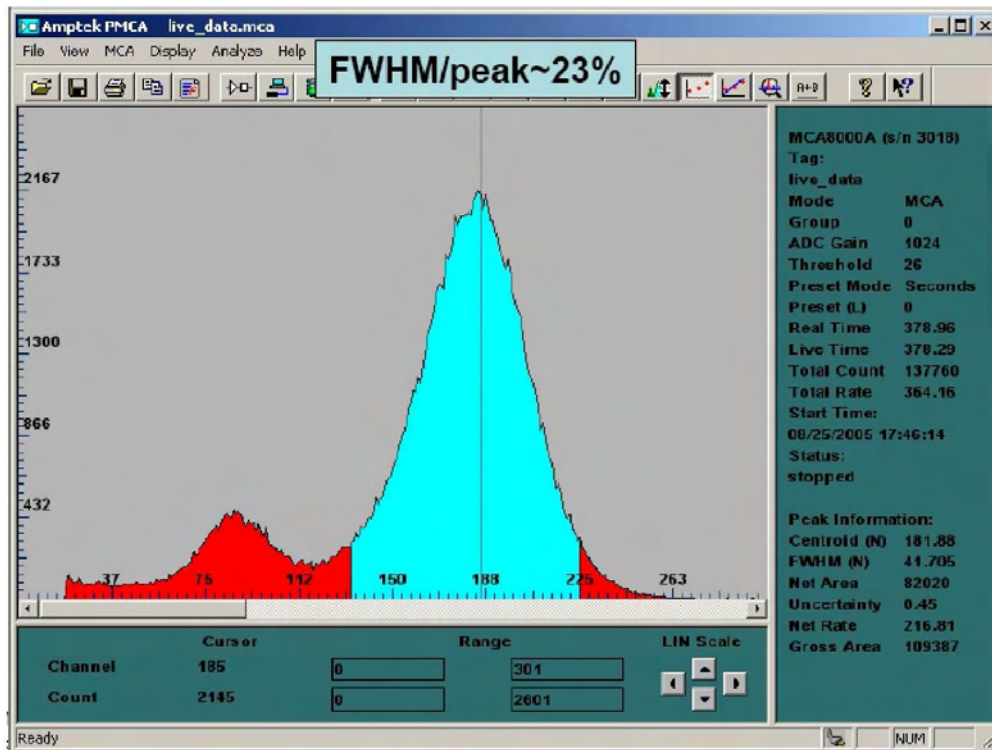


Figure 5.54: Left: charge spectrum obtained with a Fe55 X ray source showing a resolution of 10 %.

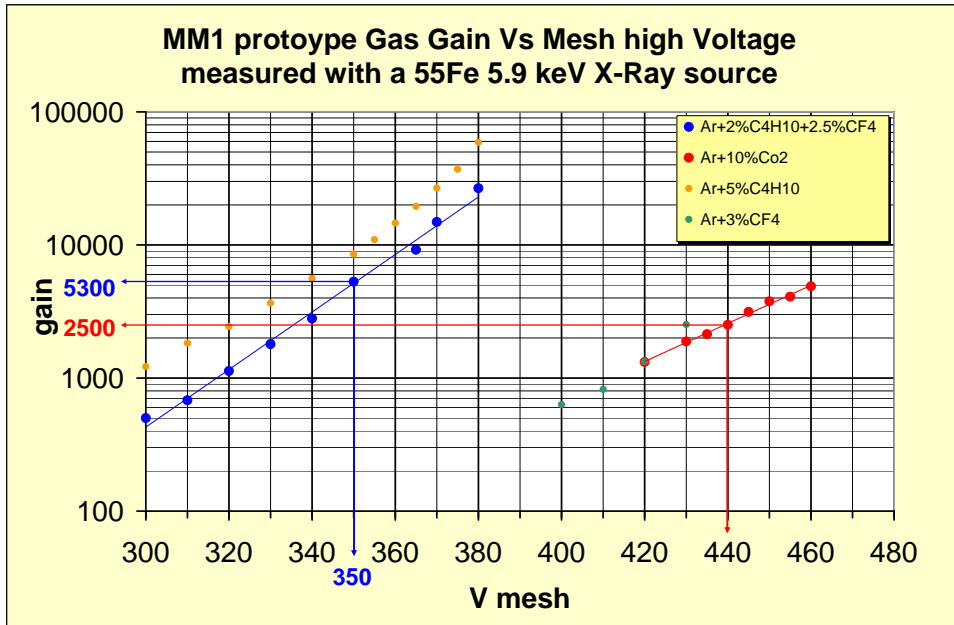


Figure 5.55: Gain versus micromesh high voltage in Ar-CF<sub>4</sub>(2.5%)-iC<sub>4</sub>H<sub>10</sub>(2%) (left curve) and in Ar-CO<sub>2</sub>(10%) (right curve)

Data taken with cosmic rays have been analyzed using a complete analysis chain including an event display, a reconstruction program and a full simulation based on the Geant4 package. A threshold equal to 3.5 times the RMS of the pedestal (typically 2 ADC) is applied to the raw data.

Hits in the same row are associated in a cluster. In the case of clusters with two pads, the position cannot be reliably estimated using a simple barycenter as the pad width is much larger than the electron cloud size, introducing large non-linearities. Instead, using numerical methods, the gaussian function is found whose integrals on the two pads reproduce the observed charge ratio. The gaussian width  $w$  is estimated from  $w = C_T \sqrt{l_d}$ , where  $C_T$  is the transverse diffusion coefficient computed using the Magboltz program [2] and  $l_d$  is the drift length.

For clusters with three hits, the position is estimated in a similar way, fitting the gaussian distribution to the two measured charge ratios. We have associated an uncertainty equal to  $l_p / \sqrt{12}$  to clusters with only one hit, where  $l_p$  is the pad width.

The space point uncertainty is estimated taking into account both the binomial fluctuations of the number of electrons collected by the two pads and the electronic noise. Gain fluctuations due to the stochastic nature of the avalanche process reduce the number of effective primary electrons to be considered in the uncertainty evaluation. The pull distribution of the cluster position with respect to the fit position of the track has a width of approximately 1 assuming that the number of effective electrons is one half of the electrons in the cloud. This reduction factor is in fair agreement with expectations from numerical simulations.

**Point resolution** Tracks close to the vertical axis and crossing the two Micromegas modules are reconstructed and fitted separately in the two projections with a least square fit. The space point resolution for each cluster has been studied considering the residual between its position and the extrapolated track position without using this cluster. Figure 5.56 show the gaussian widths of these residuals for B=0.2 T. To estimate the momentum resolution capabilities of this device it is necessary to consider the fraction of rows with one, two or more pad hit (fig. 5.56): approximately 75 % of the clusters have two or more hits at one meter drift length for B=0.2 T. This is the experimental situation

corresponding to the T2K TPC. The momentum resolution of a TPC equipped with these detectors and measuring a track length of 70 cm in a 0.2 T magnetic field is expected to be 8% at 1 GeV/c, slightly better than the required performance of 10% for the T2K tracker.

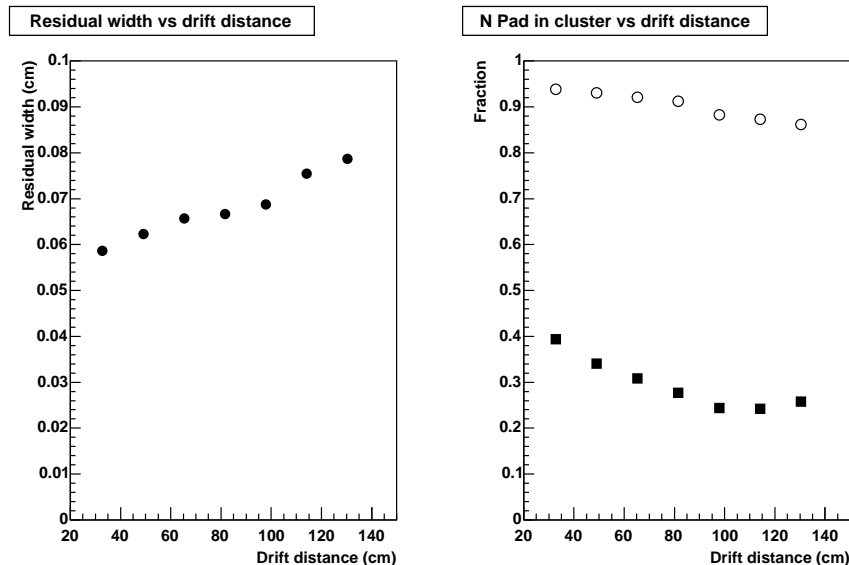


Figure 5.56: Left plot: the gaussian width as a function of the drift distance for the two pad cluster track residual for  $B=0.2T$ . Right plot: the cumulative fraction of clusters with one pad (squares) and two pads (open circles).

**Gas properties** A first study of the gas properties has been done during the data taking by studying tracks that cross the field cage cathode. These tracks give a very precise measurement of the drift velocity that is in agreement with Magboltz predictions (Table 5.4). Clusters with two pads can be used to study the width of the electron cloud if the position given by the track fit is assumed. This is shown in figure 5.57. The mean value of this distribution as a function of the drift length  $l_d$  has been fit with the function  $\sqrt{s_0^2 + C_T l_d}$ . The first term models the uncertainty due to the track position. The values for the transverse diffusion coefficient  $C_T$  are in reasonable agreement with the Magboltz predictions (table 5.4). The attenuation in the Ar-CF<sub>4</sub>-Isobutane mixture was found to be negligible after a few days of gas flow with a lower limit on the attenuation length of 30 m.

Table 5.4: Expected and measured (last two columns) gas properties (drift velocity  $v_d$  (cm/ $\mu$ s) and transverse diffusion coefficient  $C_T$  ( $\mu$ m/ $\sqrt$ cm)) for different experimental conditions.

Field	$v_d$ (exp)	$C_T$ (exp)	$v_d$ (meas)	$C_T$ (meas)
B=0 T E=160 V/cm	6.50	309	$6.26 \pm 0.05$	$302 \pm 15$
B=0.2 T E=160 V/cm	6.50	237	$6.27 \pm 0.05$	$253 \pm 15$
B=0.4 T E=160 V/cm	6.50	157	$6.30 \pm 0.05$	$173 \pm 15$
B=0.4 T E=100 V/cm	4.46	157	$4.23 \pm 0.02$	$176 \pm 15$

### First study of $dE/dx$

A first study of the measurement of  $dE/dx$ , the energy loss per unit length, has been performed considering for each track the total charge in each cluster. A truncated mean retaining only 80% samples

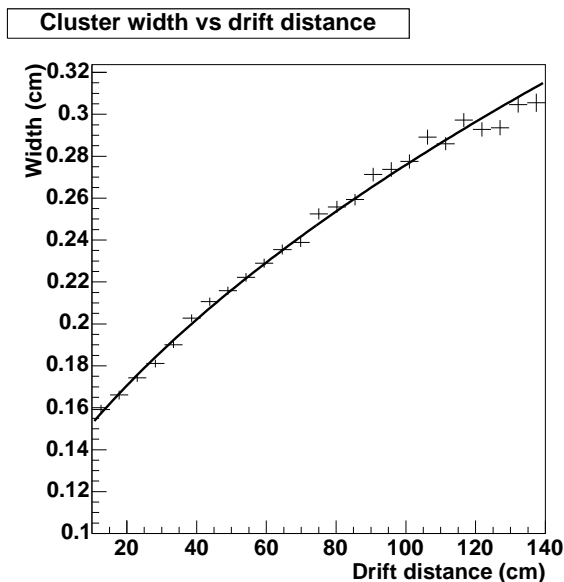


Figure 5.57: Gaussian width of the electron cloud measured using the track position and the charge ratio in clusters with two pads as a function of the drift distance for  $B=0.2T$ . The curve shows the result of the fit to the function  $\sqrt{s_0^2 + C_T l_{drift}}$  where the transverse diffusion coefficient  $C_T$  has been found  $253 \mu\text{m}/\sqrt{\text{cm}}$ .

with lower measured charge has been used. This mean has been corrected for the track length in the active volume of the TPC. The result are shown in figure 5.58. A resolution on the  $dE/dx$  of  $12.2 \pm 0.4\%$  (Fig. 5.58) has been obtained for a nominal track length of 38.4 cm and 48 samples. Using the PDG formula, a resolution around 10 % is expected.

## 5.11 TPC performance

In this section, preliminary results obtained with the full chain of simulation and reconstruction are presented.

### 5.11.1 Simulation and reconstruction

The simulation program used in these studies has already been described. We have used here a standalone version of the reconstruction program. This reconstruction package, written in C++, provides a simple and flexible framework for generic TPC data analysis. Few basic classes represent the data structures used and implement in a classic object-oriented approach the methods needed to treat the raw information. This program uses the point reconstruction method described previously. The likelihood method will in principle make a more effective use of all the available information and therefore offer an improved performance.

The main classes used in the reconstruction package are the following:

**Pad** Class OoPad is a static object representing the geometrical information related to a Pad

**Hit** A Hit, stored in a OoHit instance, represent a series of charge measurements above threshold in a pad. A pointer to this pad is a data member of the class.

**Cluster** A cluster (class OoCluster) is a list of hits in a row close in space and time. Various methods allow to compute the total charge, x position, and time coordinate of the hit.

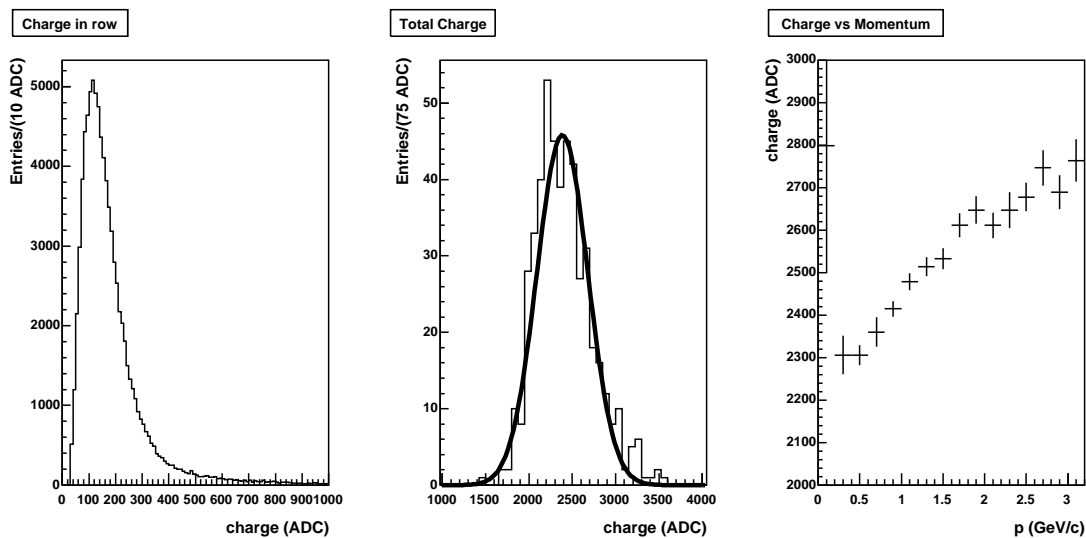


Figure 5.58: Left plot: the charge per pad row. Middle plot: the 80% truncated mean for the sum of the charge in the two detectors. A resolution of 12.2% has been obtained. Right Plot: the measured charge versus the track momentum.

**Track** A track (class `OoTrack`) is a list of clusters. Methods allow to fit the track in its x-y and y-t projections. This fit is done using the least-square method.

Other classes were used to implement the data input, the geometry definition, the management of the program, the input of the various parameters and switches.

At a lower level, these classes use the standard C++ STL library for managing lists and vectors of objects. The fits are done using the Minuit package through its ROOT encapsulation. The summary of the output is stored with the ROOT package as histograms and a TTree for the tracks.

The program has been debugged and exercised using LC TPC prototype data taken in Saclay using cosmic rays.

## Hits and clusters

A hit is created when a sample exceeds the threshold and contains all the samples above it and two samples before and four samples after the threshold crossing. The charge of the hit is computed as the sum of the charge of the samples. The time coordinate of the hit correspond to the charge peak. A cluster is created for hits in adjacent pads distant less than 15 time ticks.

## Space point reconstruction

The precision of the space point depends strongly on the number of hits in the cluster. In fact, when the diffusion coefficient of gas mixture is small, the track width is typically 2-3 mm even after 1 m of drift. The pad response function of Micromegas is very narrow, no more than few tens of  $\mu m$ . Track at small drift distance or passing close to the center of a pad can therefore produce a cluster with only one pad hit. In this case the resolution is rather poor, of the order of  $l_{pad}/\sqrt{12} = 2.2mm$ , where  $l_{pad}$  is the full pad width.

Clusters with two pads allow to estimate the position from the ratio of the two charges registered on the pads. A linear estimation is not appropriate since the large pad width implies large non-linearities. In fact the total charge registered on a pad is more aptly modeled by the integral over the pad of a gaussian with width equal to the track width. To implement this estimator, we assume the width given by  $w = C_T \sqrt{l_{drift}}$  where  $C_T$  is the trasverse diffusion coefficient computed with the Magboltz program and  $l_{drift}$  is the drift distance. In this way, a relation between the track position

and the charge ratio is established. The position of the cluster is then computed with a numerical method. Clusters with three pads hit are treated in the same way.

### Track fitting

Track fitting is performed using the least-square method. The track is modeled as a circle in the y-z plane and a line in the y-t projection. For the y-z projection, a first fit is performed using all the space points selected by the track finding algorithm. Then all the points contributing more than 50 to the  $\chi^2$  were rejected and the track refitted. Finally, the track was refitted without each space point in turn and the residual (difference between the space point and the track position in the row) was stored for further analysis.

The parameters used for the y-z fit are :

$y_0$  The y position of the track on a z plane at equal distance from the two Micromegas columns;

$\phi$  The angle of the track with the z axis at  $y = y_0$

$R_c$  The inverse of the curvature radius.

and for the the y-t fit are

$t_0$  The time of the track at  $y=0$ ;

$dt/dy$  The slope of the track in the y-t plane.

### 5.11.2 TPC tracking capability

We show here some event displays (projection on the Y-Z detection plane) of neutrino interactions generating multi-tracks events to illustrate the tracking capabilities of the TPC detector (fig.5.59 to 5.61). The color code is related to the integrated charge deposited in each pad, blue and green representing a lower charge while yellow and red represent larger ionizations.

### 5.11.3 Space point resolution

The space point resolution has been studied by comparing the measured position of the track in the cluster with the fitted position given by the track. Typical resolution are 600  $\mu\text{m}$  at 100 cm drift distance (fig. 5.62), somewhat better than what has been obtained in the prototype test. A detailed tuning is underway to improve the data-MC comparison on several basic variables and this will affect this distribution.

### 5.11.4 Momentum resolution

We have studied a sample of CCQE interaction in the FGD. In these events only the muon track has been tracked in the TPC and has been reconstructed. Figures 5.63 to 5.65 show event displays where the curve show the reconstructed track position.

The momentum resolution has been studied comparing the reconstructed and the generated transverse momentum of the muon. As shown on fig.5.66, the momentum resolution is at the 5 % level for most of the muons (momenta around 600 MeV) while it is still below 10 % at 1 GeV/c, thereby satisfying the requested physics performance if a gas with low transverse diffusion coefficient is used ( $CT < 450 \mu\text{m}/\sqrt{\text{cm}}$ ). Tracks traversing several TPC can be fitted with a Kalman filter technique thereby improving the momentum resolution at large momenta.

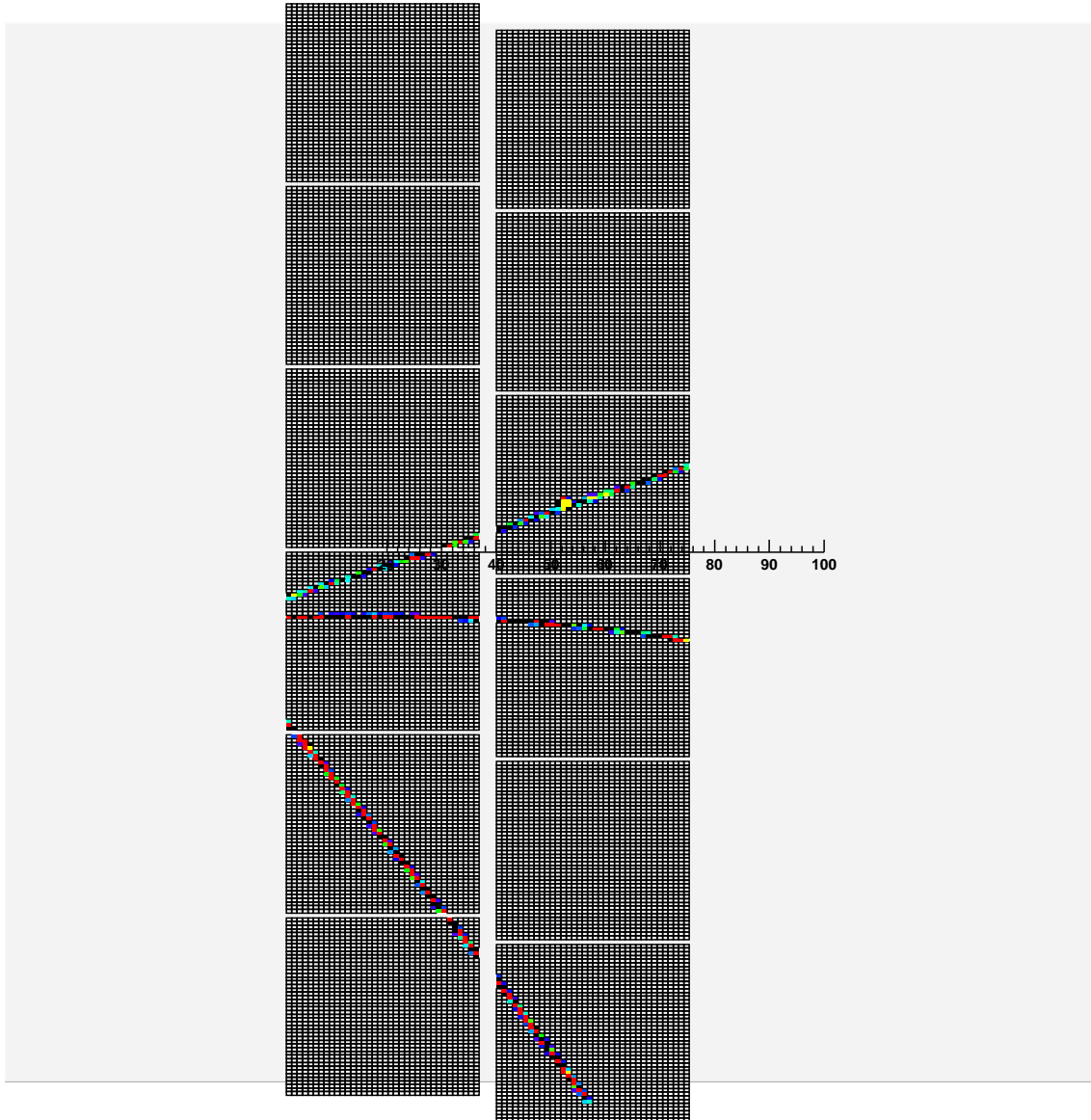


Figure 5.59: Event display (projection on the Y-Z plane) of a NC1 $\pi$  interaction by a  $\nu_\mu$  in the FGD producing several tracks in the TPC.

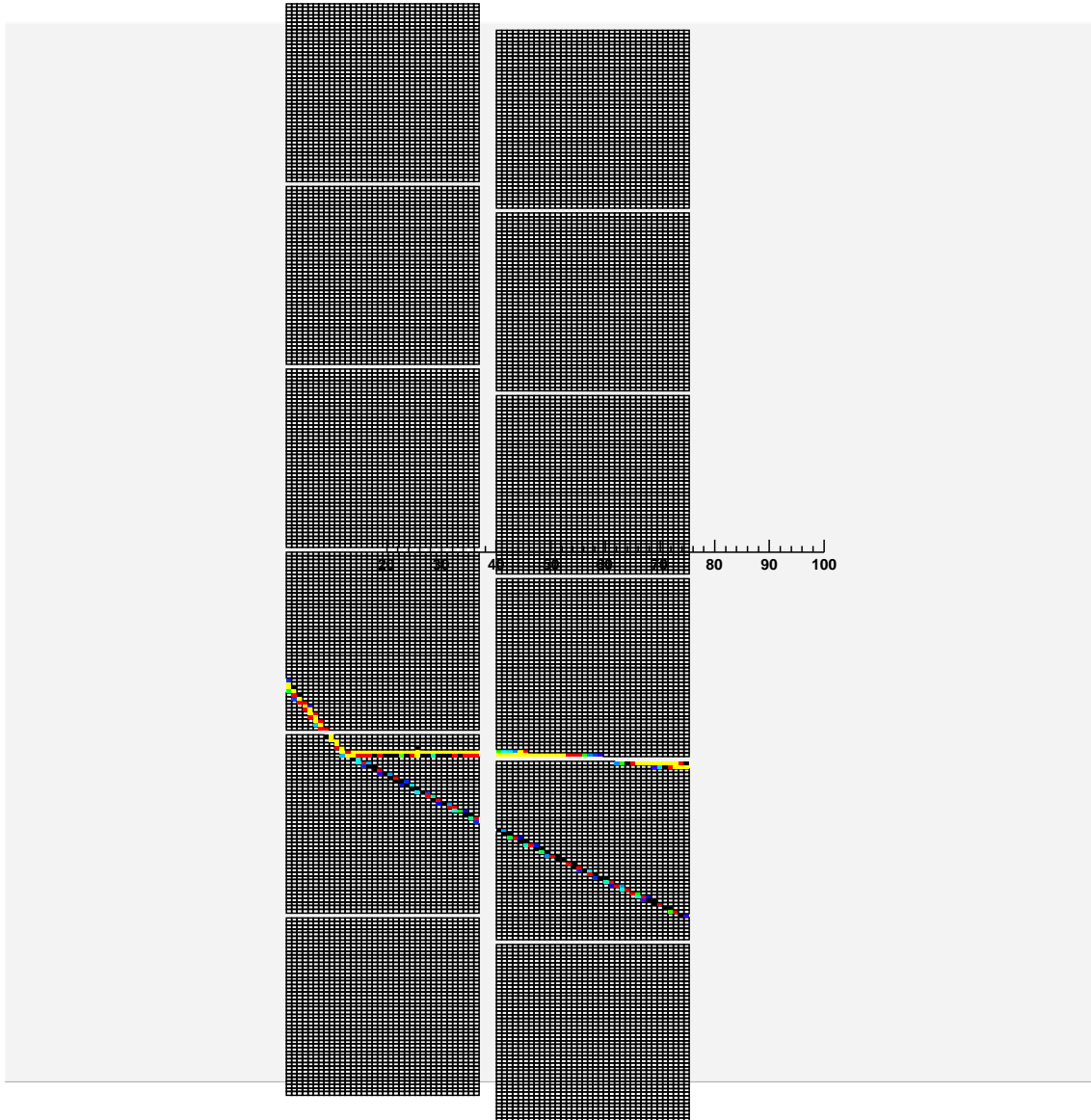


Figure 5.60: Event display (projection on the Y-Z plane) of a CCQE interaction by a  $\nu_\mu$  in the TPC gas producing several tracks in the TPC.

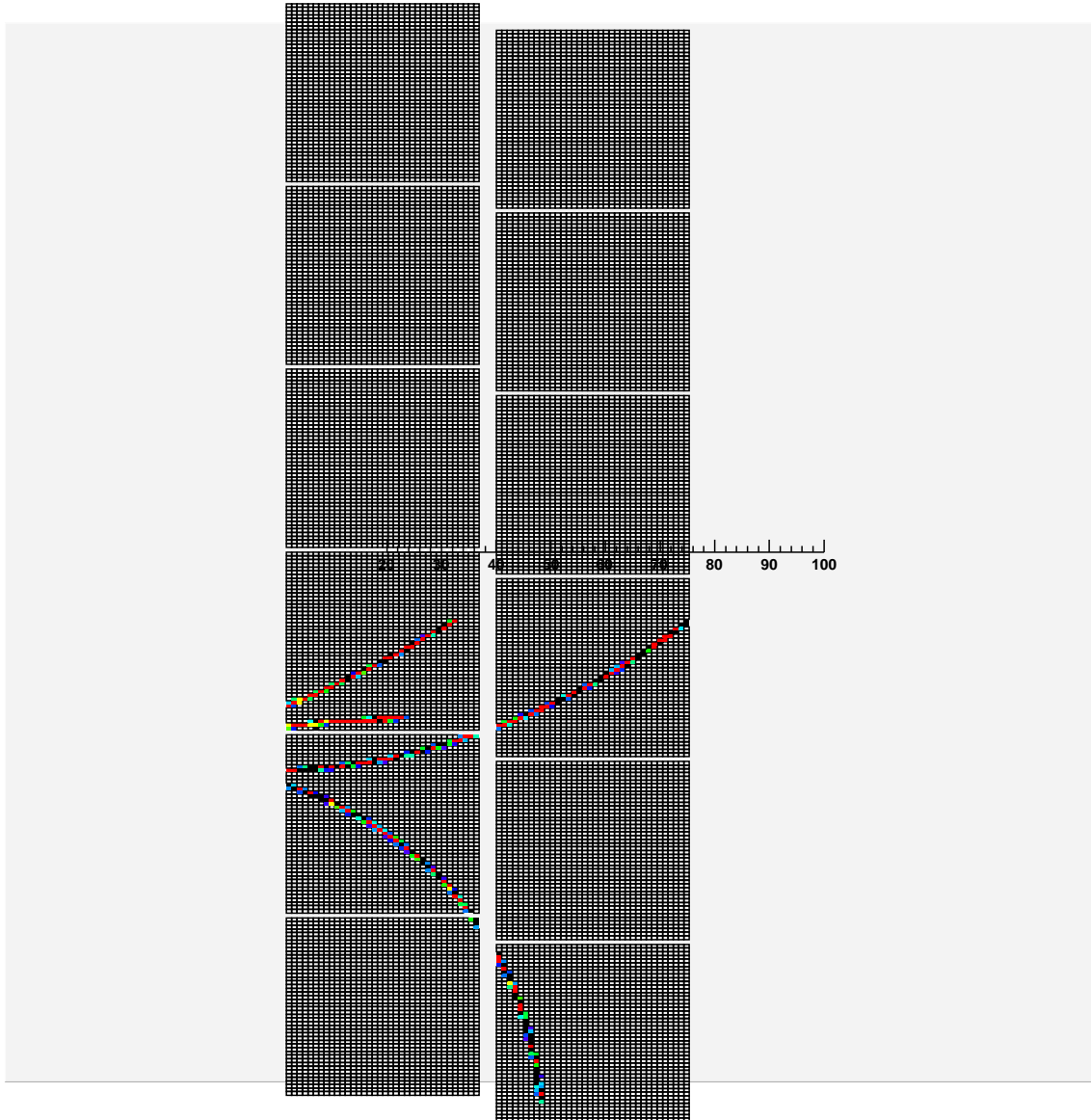


Figure 5.61: Event display (projection on the Y-Z plane) of a  $\text{NC}1\pi^0$  interaction by a  $\nu_\mu$  in the FGD followed by gamma conversion .

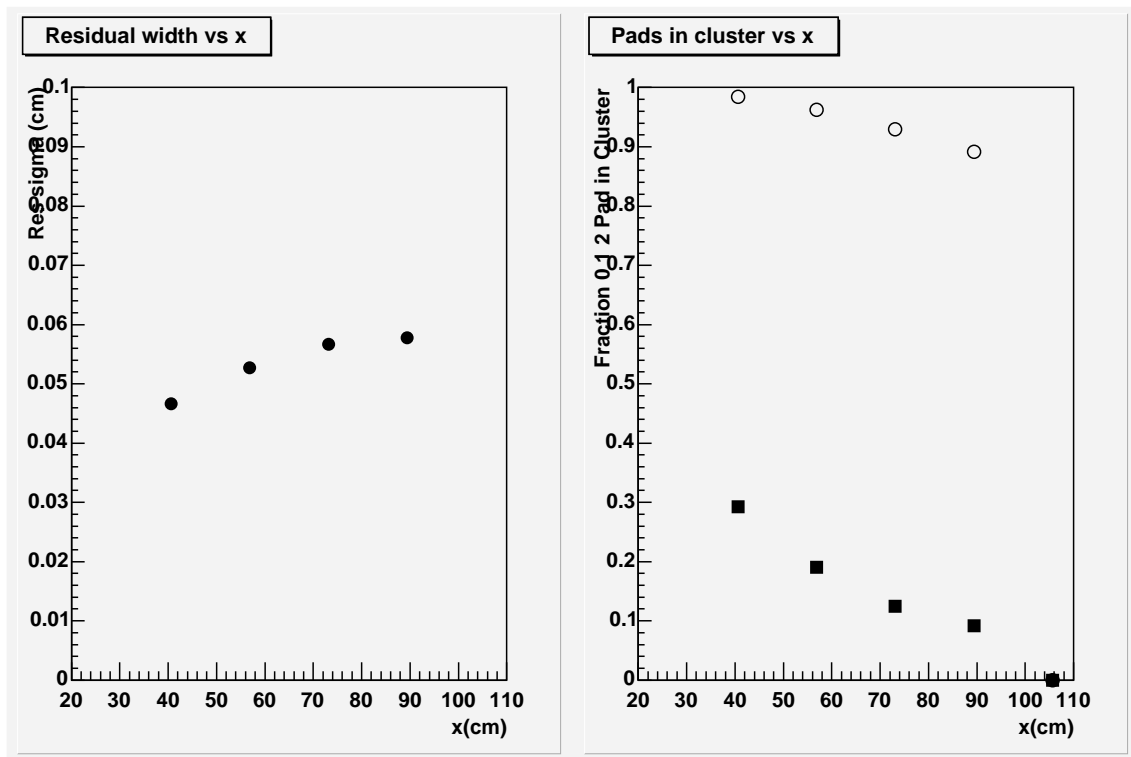


Figure 5.62: Space point resolution as a function of the drift distance (left) and cumulative fraction of clusters with one(squares) and two (circles) pads hit (right).

### 5.11.5 Further studies

We plan to use the full simulation and reconstruction chain for the following studies:

- track finding efficiencies in generic multi-track events;
- position, angular and momentum resolution;
- acceptance and tracking efficiency for CCQE (muon and proton tracks);
- $dE/dx$  resolution studies and  $e-\mu$  separation as a function of momentum.

## 5.12 Schedule

### 5.12.1 Schedule for construction

The TPCs are to ready for initial commissioning of the neutrino beamline in April 2009. A full size pre-production TPC, called Module 0, will be built at TRIUMF in 2007 to verify the complete design and assembly procedures. At the same time, several pre-production micromegas modules will be constructed for standalone tests in Europe and tests in Module 0 at TRIUMF. For these tests, front end electronics cards will be produced from the first production sample of the AFTER ASIC. Xilinx FPGA evaluation boards will serve the function of the data collectors, the backend electronics. A simplified gas recirculation system will be setup for tests with module 0.

After gaining some experience with Module 0, the production of the TPCs will begin later in 2007 and finish in the fall of 2008. As micromegas modules are completed, they will be thoroughly tested prior to insertion and tests in the TPC modules at TRIUMF. As the electronics become available, they will be used in large integration tests at TRIUMF, prior to shipping the TPC modules to Japan in early 2009.

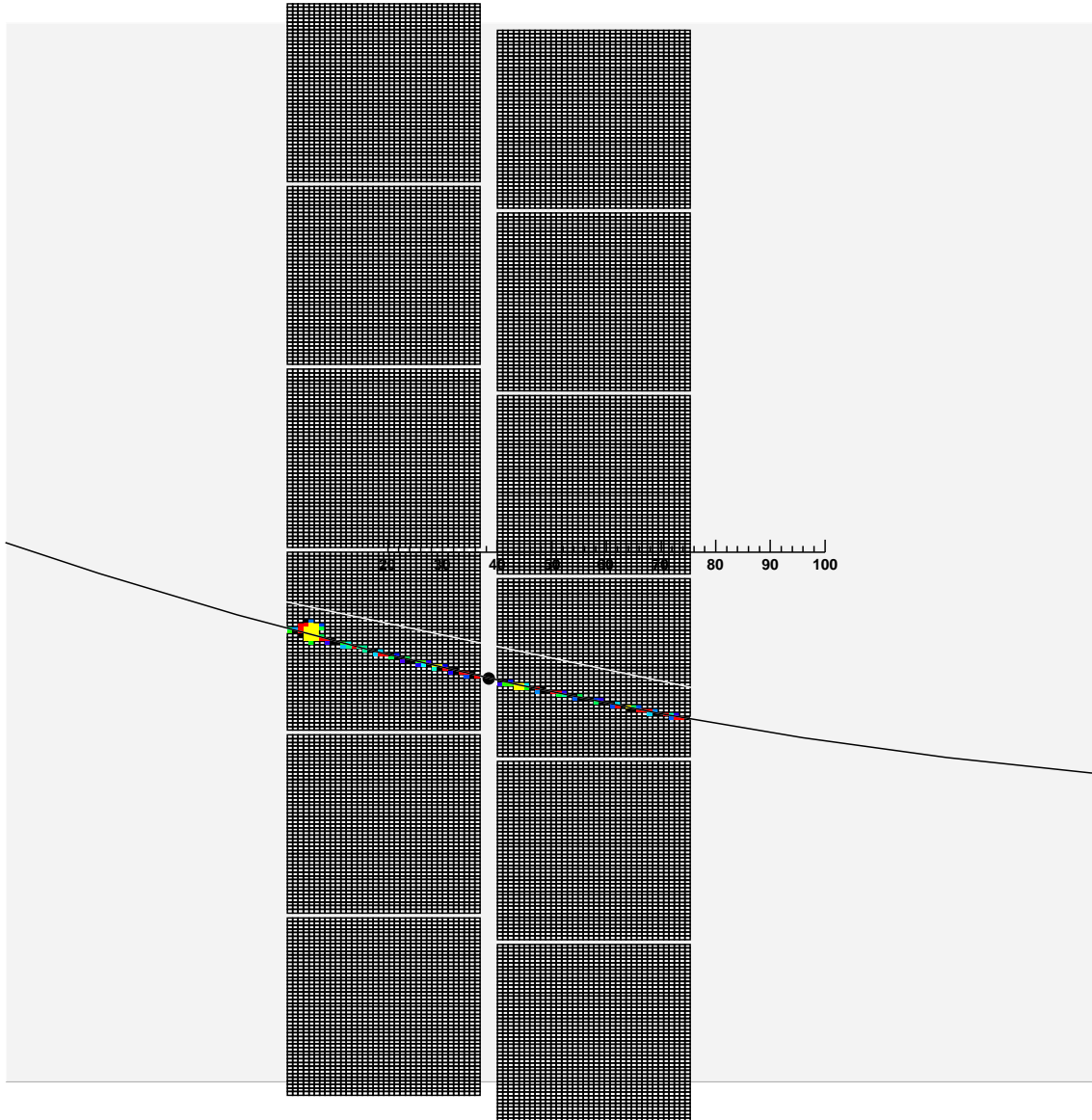


Figure 5.63: Event display (projection on the Y-Z plane) of a CCQE interaction by a  $\nu_\mu$  in the FGD producing a muon track in the TPC. The curve shows the fitted track.

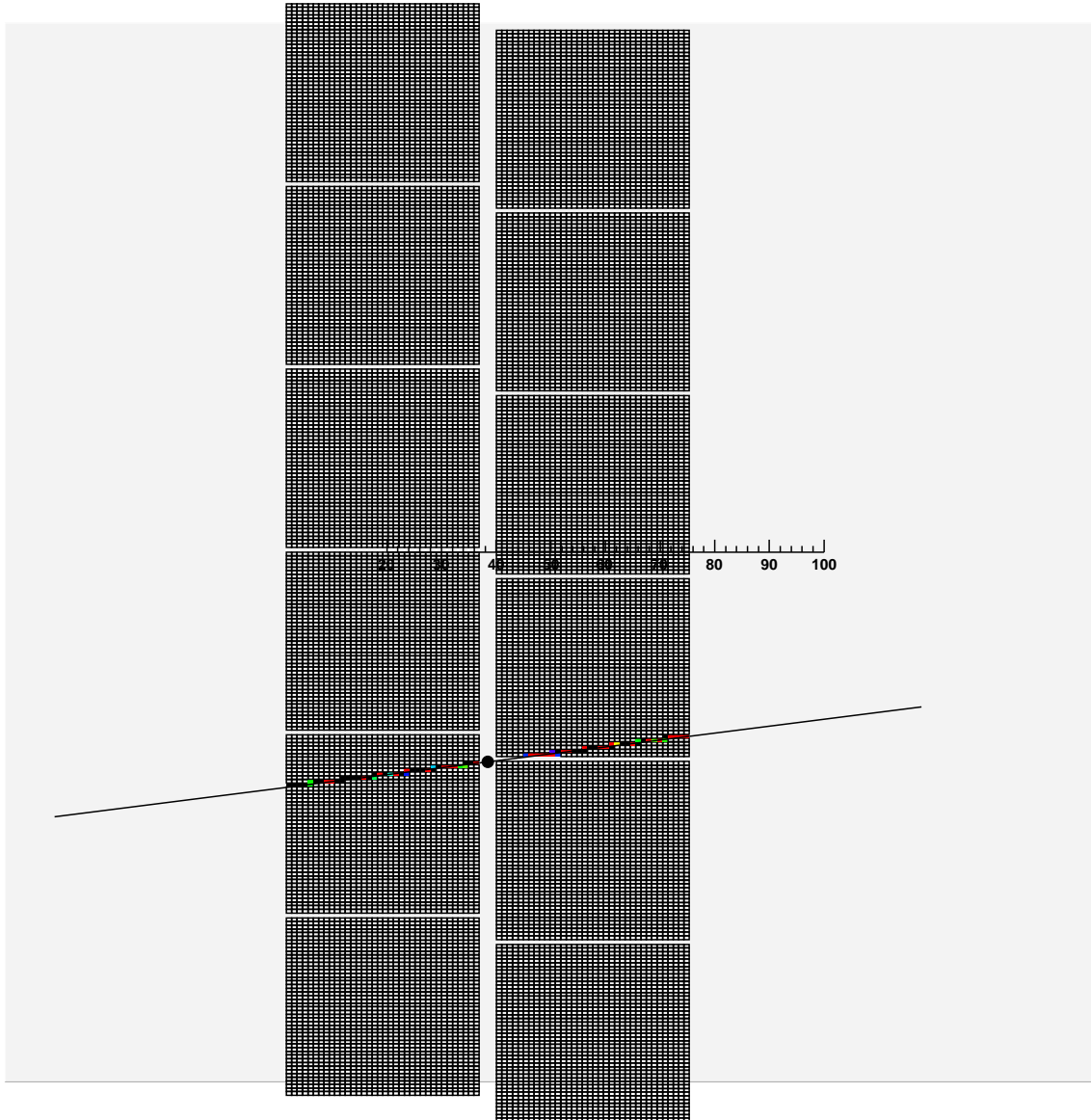


Figure 5.64: Event display (projection on the Y-Z plane) of a CCQE interaction by a  $\nu_\mu$  in the FGD producing a muon track in the TPC. The curve shows the fitted track.

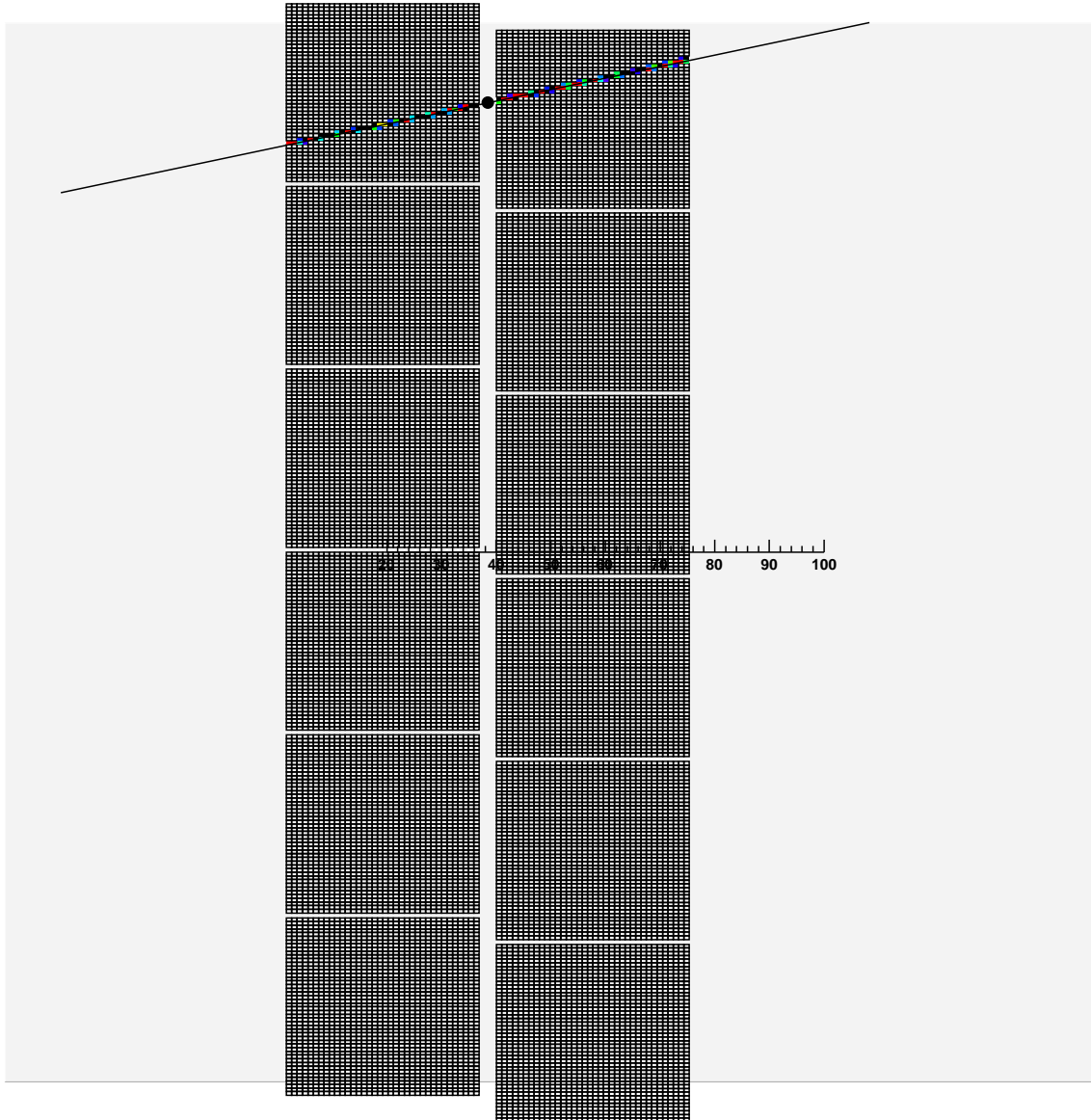


Figure 5.65: Event display (projection on the Y-Z plane) of a CCQE interaction by a  $\nu_\mu$  in the FGD producing a muon track in the TPC. The curve shows the fitted track.

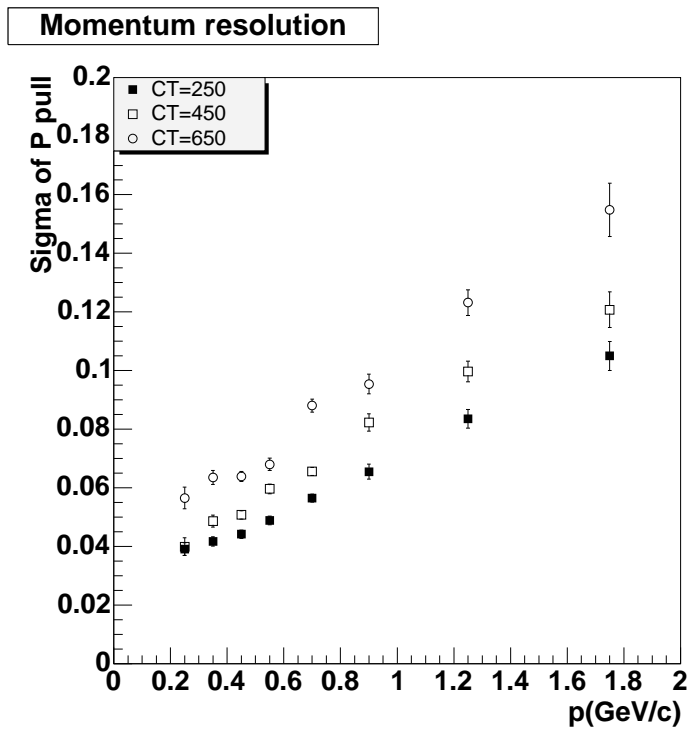


Figure 5.66: Momentum resolution as a function of momentum for CCQE events for several values of the transverse diffusion coefficient CT (from bottom set of points to top CT =250, 450 and 650  $\mu\text{m}/\sqrt{\text{cm}}$ ).

Two to three months are foreseen for the installation of the TPCs in the ND280 hall. The milestones of the project are summarized in Fig. 5.67.

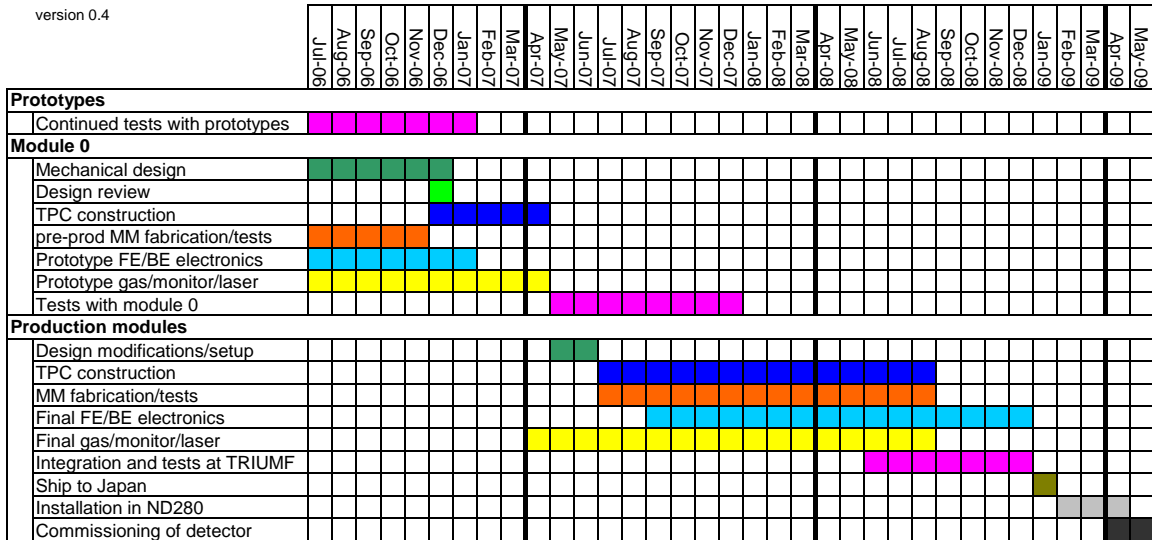


Figure 5.67: Summary of the milestones for the TPC project.

### 5.12.2 Workpackages for the TPC project

The TPC project is structured on the basis of the following workpackages:

- Workpackage 1 - TPC mechanical : includes gas containment, fieldcage, cooling, connections.
- Workpackage 2 - Gas system : includes the monitoring systems

- Workpackage 3 - ND280 Integration : integration with ND280 hall, FGD, basket
- Workpackage 4 - Micromegas detectors : includes HV system and cables
- Workpackage 5 - Micromegas mechanics : includes gas seal, cooling connections, front end electronics mechanics
- Workpackage 6 - Readout electronics
- Workpackage 7 - Online Software: includes DAQ and slow control
- Workpackage 8 - Offline Software
- Workpackage 9 - Calibration: includes laser, cosmic trigger, sources, magnetic field mapping.

# Bibliography

- [1] M. Anderson *et al.*, *The STAR time projection chamber: A unique tool for studying high multiplicity events at RHIC*, Nucl. Instrum. Meth. A **499**, 659 (2003) [arXiv:nucl-ex/0301015].
- [2] S. Biagi, *Monte Carlo simulation of electron drift and diffusion in counting gases under the influence of electric and magnetic fields*, Nucl. Instrum. Methods A, 421 (1999)234.
- [3] R. Veenhof, *Garfield, a drift chamber simulation program*, Prepared for International Conference on Programming and Mathematical Methods for Solving Physical Problems, Dubna, Russia, 14-19 Jun 1993
- [4] Georg Altenhöfer, "Development of a Drift Chamber for Drift Velocity Monitoring in the CMS Barrel Muon System", Diploma thesis Aachen (2006).
- [5] P. Colas *et al.*, "Electron drift velocity measurements at high electric fields", Nucl. Instr. and Meth. A **478**, 215 (2002).
- [6] M. Killenberg *et al.*, "Modelling and Measurement of Charge Transfer in Multiple GEM Structures", Nucl. Instr. and Meth. A **498**, 369 (2003).
- [7] G. Charpak, I. Giomataris, Ph. Rebougeard and J.P. Robert, Nucl. Instrum. Methods A376, 29 (1996).
- [8] P. Colas, I. Giomataris and V. Lepeltier, 'Ion Backflow in the Micromegas TPC for the future Linear Collider', Nucl. Instr and Methods A535, 226 (2004).
- [9] S. Andriamonje *et al.*, Nucl. Instr and Methods A535, 309 (2004).
- [10] B. Peyaud *et al.*, 'KABES, a novel beam spectrometer for NA48', Nucl. Instr and Methods A535, 247 (2004).
- [11] P. Colas, I. Giomataris, V. Lepeltier and M. Ronan, 'First tests of a Micromegas TPC in a Magnetic Field', Nucl. Instr and Methods A535, 181 (2004).
- [12] M.S. Dixit *et al.*, Nucl. Instr and Methods A518, 721 (2004).
- [13] A. Bellerive *et al.*, Proc. of LCWS05, Stanford 2005.
- [14] I. Giomataris *et al.*, 'Micromegas in a bulk', DAPNIA 04-80 (March 2004), to appear in Nucl. Instrum. Methods A.
- [15] The T2K 280m collaboration, "The T2K 280m detector conceptual design report", september 2005, unpublished.
- [16] Technical Support (TS) Department - Development of Electronic Modules (DEM) Group, CERN, CH-1211 Geneva 23, SWITZERLAND.
- [17] Gantois, B.P. 307, F-88105 Saint Die des Vosges cedex, FRANCE.

- [18] DuPont de Nemours (Europe) Rue General Patton, Contern L-2984 Luxembourg.
- [19] S. Beole et al., CERN/LHCC 98-19 (1998).
- [20] A Micromegas based TPC for the T2K ND280m detector, The TPC Micromegas Collaboration, internal T2K/TPC note, 01/16/2006.
- [21] A. Delbart, R. De Oliveira and J-L. Ritou, "Production process of a "bulk" micromegas for the T2K-TPC", CEA-Saclay/DAPNIA/T2K-TPC internal note EDMS6234, 12/16/2005.
- [22] A. Delbart and J-L. Ritou, "Gluing and cutting procedure of the T2K/TPC "bulk" micromegas detector on its aluminum support frame", CEA-Saclay/DAPNIA/T2K-TPC internal note EDMS6883, 06/14/2005.
- [23] A. Delbart and J-L. Ritou, "Mounting procedure of the T2K-TPC micromegas modules on the HARP cage endplate", CEA-Saclay/DAPNIA/T2K-TPC internal note EDMS6851, 10/19/2005.
- [24] N.Abgrall and P.Bene and A.Blondel and M.Di Marco and D.Ferrere and F.Masciocchi and E.Perrin, "Micromegas Calibration Test Bench and GEM Prototype Study", T2K-TPC internal note T2K-TPC Note-006, sept. 2006.
- [25] Eckert & Ziegler, Isotope Products Europe GmbH, Robert-Roessle-Strasse 10, D-13125 Berlin, [www.isotopes.com](http://www.isotopes.com).
- [26] N.Abgrall, "Construction and Performance of a Triple GEM as Amplification Device for the ND280m TPC Detector at the T2K Experiment", Master Thesis, University of Geneva, 2006.
- [27] F. Sauli, *Principle of operation of multiwire proportional and drift chambers*, CERN Report 77-09 (1977).
- [28] S. Biagi, Nucl. Instrum. Methods **A**, 421 (1999)234.
- [29] A.Cervera-Villanueva, J.J.Gomez-Cadenas, J.A.Hernando, "RecPack", a general reconstruction toolkit, Nuclear Science Symposium Conference Record, 2003 IEEE Publication Date: 19-25 Oct. 2003, Volume: 3.
- [30] D. Karlen, P. Poffenberger and G. Rosenbaum, *TPC performance in magnetic fields with GEM and pad readout*, accepted by Nucl. Instr. Meth. A, arXiv:physics/0509051.
- [31] [http://phys01.comp.uvic.ca:8080/t2k/projects/tpc/Calibration/pof\\_050525.pdf](http://phys01.comp.uvic.ca:8080/t2k/projects/tpc/Calibration/pof_050525.pdf)
- [32] J. Abele et al., *The Laser System for the STAR Time Projection Chamber*, Nucl. Instrum. Methods **A**, 499 (2003)692.
- [33] G. Renault et al., *The Laser calibration system of the ALICE time projection chamber*, Czech.J.Phys. **A**, 55 (2005)1671. e-Print Archive: nucl-ex/0511014
- [34] V. Eckardt et al., Jan 2001. 13pp. *Calibration of the STAR forward time projection chamber with krypton-83m*, e-Print Archive: nucl-ex/0101013
- [35] *Electromagnetic field simulation software for Signal Integrity and detector design applications*, <http://wwwce.web.cern.ch/wwwce/ae/Maxwell/index.html>
- [36] E. Antokhin et al., *Field Measurements in the BaBar Solenoid*, BaBar note #514 Jan,20,2000.

# Chapter 6

## P0D ( $\pi^0$ Detector)

### 6.1 Introduction

The primary physics goal of the P0D is to measure neutral current  $\pi^0$  events produced in a water target within the expected momentum T2K  $\nu_e$  appearance signal. At Super-Kamiokande, the  $\nu_e$  appearance measurement backgrounds will be dominated by misidentified neutral current single- $\pi^0$  interactions (40%) and intrinsic  $\nu_e$  in the neutrino beam flux (60%). Single  $\pi^0$  NC interactions on water have been measured only at  $\sim E_\nu = 1.3$  GeV. The measured rate was found to be  $6.4 \pm 0.1(\text{stat.}) \pm 0.7(\text{syst.})\%$  of the CC neutrino rate in agreement with expectation, but significant disagreement was found between the observed and expected  $\pi^0$  momentum distributions[1]. Since this interaction is poorly studied at the T2K neutrino energies, it must be measured at the T2K neutrino energy range on a water target so an accurate background subtraction can be performed at Super-Kamiokande. The P0D will measure the  $\pi^0$  production through exclusive channels;  $\nu_\mu n \rightarrow \nu_\mu n \pi^0$ ,  $\nu_\mu p \rightarrow \nu_\mu p \pi^0$ , and  $\nu_\mu n \rightarrow \mu^- - p \pi^0$ . The P0D will also make inclusive neutral current and charged current  $\pi^0$  production measurements, and provide a measurement of the intrinsic  $\nu_e$  flux using quasi-elastic events to complement a similar measurement in the FGD and TPC.

The impact of the P0D measurement can be understood by considering how the uncertainty on NC single- $\pi^0$  background rate affects the search for  $\nu_e$  appearance. Simulations estimate that during a  $5 \times 10^{21}$  p.o.t. exposure, there will be 9 events from the single  $\pi^0$  NC events and 12 events from the intrinsic beam  $\nu_e$  flux reconstructed as  $\nu_e$  charged current quasi-elastic event candidates in Super-Kamiokande. Since the fractional statistical error on the estimated background will be 22%, maintaining the total systematic error on the estimated background to a level of 10% will insure that the  $\nu_e$  appearance search is statistically limited. If the total background systematic increases to 15% the  $\nu_e$  appearance sensitivity will decrease by 20% relative the statistical sensitivity. Since each of the dominant components contribute about half of the background events, we seek to maintain a systematic error of less than 14% error on each so that when combined in quadrature the total background systematic will be 10% (See Chapter 1).

The major contributions to the NC single  $\pi^0$  background uncertainty are: The P0D total single- $\pi^0$  production rate statistics, the P0D total single- $\pi^0$  rate systematics, the P0D non NC single- $\pi^0$  background subtraction uncertainty, the extrapolation from the ND280 measurement to the Super-Kamiokande expectation, and the Super-Kamiokande reconstruction uncertainty (estimated to be  $\sim 7\%$ ). To maintain total NC single- $\pi^0$  background uncertainty of 14% we set a goal of maintaining a P0D statistical error of  $< 5\%$ , a P0D rate systematic of  $< 5\%$ , a P0D background subtraction uncertainty of  $< 7\%$  for a total P0D systematic error of 10%. In addition, we set the goal to maintain the near to far NC single- $\pi^0$  rate extrapolation uncertainty to below 8%. In the event that an excess of  $\nu_e$  events are observed the P0D measurement of the NC single- $\pi^0$  rate will eliminate a standard, but poorly known cross section as the cause.

In the baseline design, cross section measurements on an oxygen target are achieved by configuring the P0D into three separate analysis regions (see Figure 6.7). The upstream and downstream

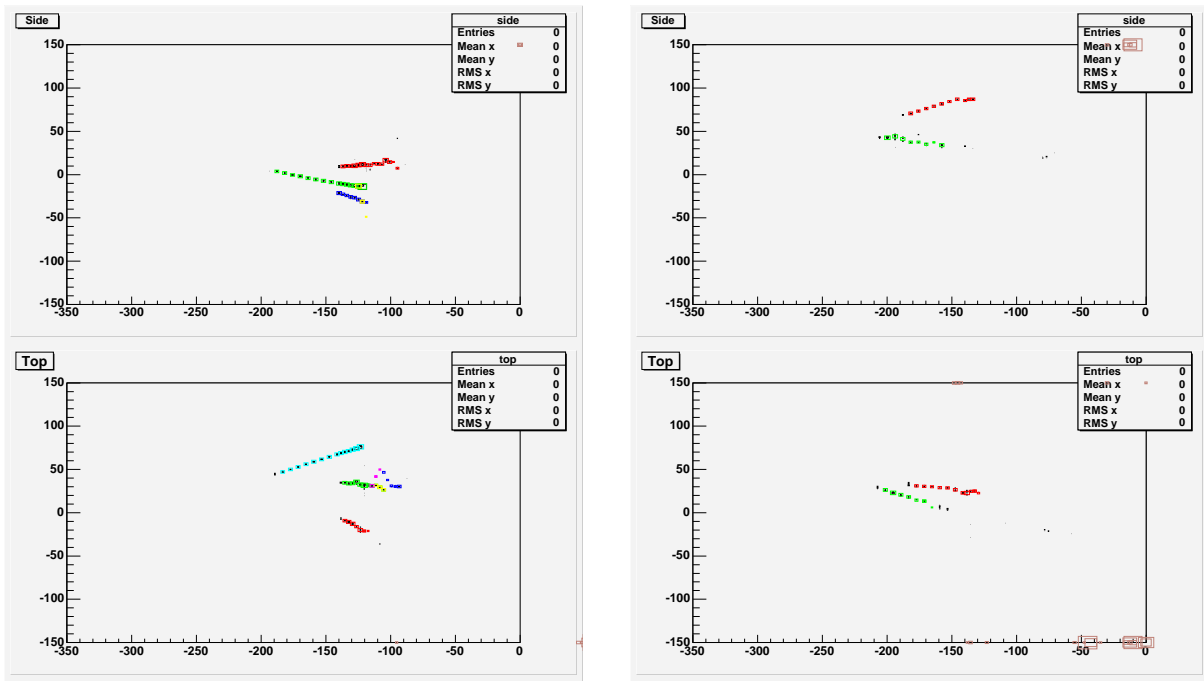


Figure 6.1: Typical neutral current single  $\pi^0$  production events. The left panels show a 983 MeV/c proton and a 495 MeV/c  $\pi^0$ . The right panels shows a single 473 MeV/c  $\pi^0$  that was accompanied by a neutron. The upper (lower) panels show the Y-Z (X-Z) hits. The various colors (red, green, etc.) show the results of a track reconstruction applied to these events. In the left panels a long track is the proton and two short tracks are  $\gamma$ s from the  $\pi^0$ . The axes are labeled in centimeters.

regions are configured as EM calorimeters providing energy containment and active shielding. The central region of the POD provides the fiducial mass for the  $\pi^0$  measurement and has alternating water target planes ( $\sim 3$  cm thick) and X-Y scintillator tracking layers (also  $\sim 3$  cm thick). A thin sheet of lead ( $\sim 0.6$  mm thick) is sandwiched in the X-Y tracking layer. Oxygen cross section measurements will be made by comparing the interaction rate of events collected with water in the target region (target in) versus similar running periods with water removed from the target region (target out). The baseline detector design has a total mass of approximately 15 tons with a fiducial mass of 2 tons of water, and 3 tons of other material.

### 6.1.1 POD Event Reconstruction Capabilities

The capabilities of the POD have been studied using the ND280 hit level detector simulation. This includes a simulation of the behavior of the scintillator, WLS fiber, and photo-sensor which is tuned to match light-yield measurements described in Section 6.3.2 and corresponds to approximately 5 pe/MeV of deposited energy. Neutrino interactions have been simulated using the NEUT event generator. The generated events are reconstructed using pattern recognition and track reconstruction to determine event characteristics.

Figure 6.1 shows two examples of  $\pi^0$  events as simulated in the POD. The left figure shows an X and Y projection of a neutral current  $\nu_\mu p \rightarrow p\pi^0$ . The proton track, and the  $\gamma$ -rays from the  $\pi^0$  are clearly visible in both projections. The proton can be identified based on the charge deposition as a function of length, while the  $\gamma$ -ray tracks show a clear E&M shower signature. All tracks can be projected back to a single vertex within the detector which corresponds to the start of the proton track. The right figure shows an X and Y projection of a  $\nu_\mu n \rightarrow n\pi^0$  event where the  $\gamma$ -rays from the  $\pi^0$  are clearly visible. The  $\gamma$ -ray tracks can be projected back to a single position along the Z axis, and show a clear E&M shower signature.

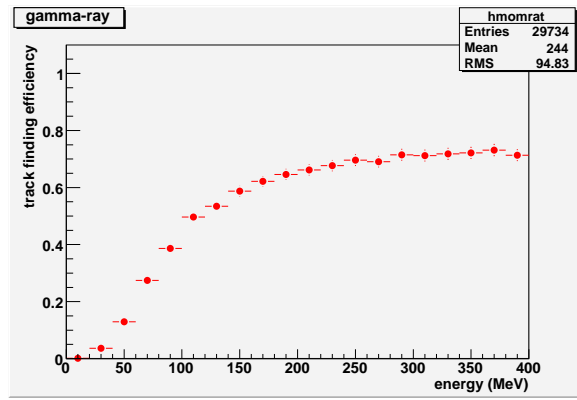


Figure 6.2: The efficiency to reconstruct a gamma ray generated in the fiducial volume as a function of momentum using the current reconstruction algorithms.

The primary goal for the POD active target is to measure neutral current single  $\pi^0$  production where in the typical case all particles traveling further than a few centimeters from the interaction vertex without a hit will be neutral. The  $\pi^0$  will be identified by reconstructing the gamma-rays from the decay. For this reason, it is quite important that the POD have high efficiency to detect gamma rays generated in the fiducial volume. Figure 6.2 shows the efficiency to reconstruct isotropic gamma-rays in a single projection as a function energy using current reconstruction algorithms. Gamma rays which leave the target without depositing energy are likely to be detected in the POD EM calorimeter which is discussed elsewhere.

Without accounting for photon-counting statistics of the light collected from the scintillating bars, the energy resolution for events fully contained in the active target is approximately  $\sigma_E = 10\% + 3.5\%/\sqrt{\text{GeV}}$ . Including the effect of real light detectors worsens the statistical component of the energy resolution to approximately 5%.

### Neutral current single- $\pi^0$ event rates and backgrounds

The ability of the POD to reconstruct events containing  $\pi^0$  particles has been studied using the ND280 detector simulation and event reconstruction. The reconstruction cuts are optimized to find neutral current single- $\pi^0$  candidates. In this study, monte carlo events samples were generated for the detector with the water target filled (water-in) and with the water target empty (water-out). The monte carlo events were then reconstructed with the same cuts and the surviving number of events have been divided into four categories using monte carlo truth information about their origin. The four categories are:

1. NC events containing a single  $\pi^0$  with momentum greater than 200 MeV/c, and possibly one or more protons and neutrons. These are the events which contribute to the Super-Kamiokande electron neutrino appearance background.
2. NC events with a single  $\pi^0$  which has a momentum less than 200 MeV/c.
3. Other NC events which contain at least one  $\pi^0$ . These events may contain multiple  $\pi^0$ s, or charged pions.
4. All other events are labeled as background (e.g. the misidentified NC and CC events, and external background).

Table 6.1 gives the estimated number of events of each type for an exposure of  $5 \times 10^{20}$  pot which corresponds to half of a nominal T2K year. The uncertainty is given as the statistical uncertainty in the simulation, and does not include any systematic effects. These estimates include the effect of fiducial

Table 6.1: Summary of POD neutral current signals and backgrounds from an exposure of  $5 \times 10^{20}$  pot (half of a nominal year) with the water target filled (first column), and empty (second column). The rates with an empty water target have been estimated from a slightly different granularity, and then rescaled based on target mass.

	Water-In	Water-Out
NC Single $\pi^0$ ( $P_{\pi^0} > 200$ MeV/c)	$2517 \pm 121$	$1725 \pm 134$
NC Single $\pi^0$ ( $P_{\pi^0} < 200$ MeV/c)	$262 \pm 39$	$199 \pm 46$
NC Multi $\pi^0$	$1148 \pm 82$	$575 \pm 78$
Neutrino Background	$1381 \pm 90$	$952 \pm 102$
External Background	$74 \pm 37$	$44 \pm 22$
Total Events	$5382 \pm 180$	$3495 \pm 191$

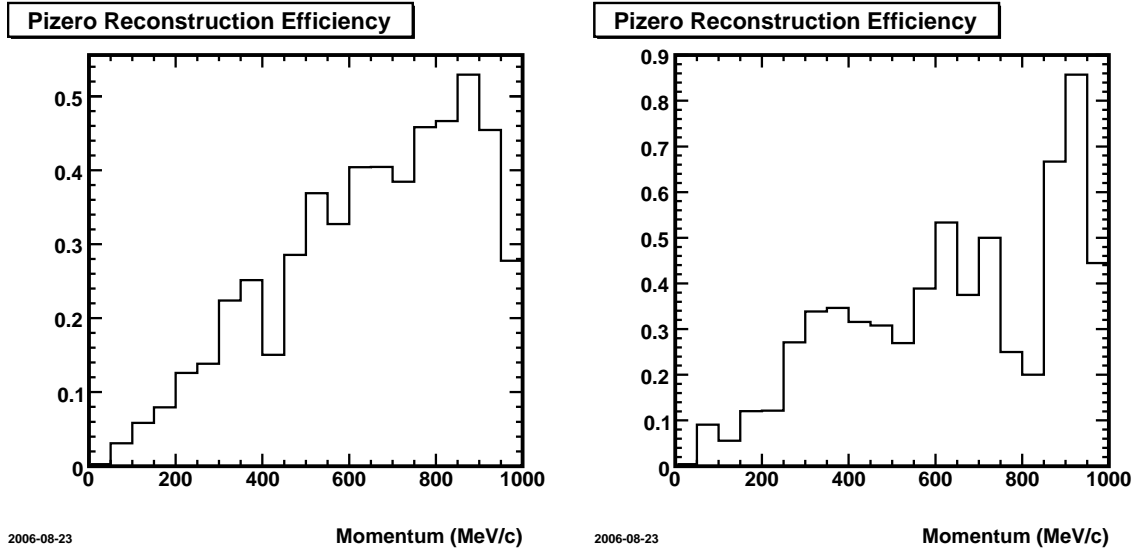


Figure 6.3: Efficiency to reconstruct neutral current single  $\pi^0$  event as a function of the  $\pi^0$  momentum. The left figure shows the efficiency when the target module contains water. The right figure shows the efficiency when target module contains air.

mass, and reconstruction efficiency. The NC single  $\pi^0$  background ratio is  $1.73 \pm 0.23$  (water-in), and  $1.73 \pm 0.37$  (water-out). A decay electron cut has been studied as a method of identifying untracked muons and pions, and found to be effective. If applied, the signal to noise will increase to approximately 2.5.

Figure 6.3 gives the efficiency to save a neutral current single  $\pi^0$  production event as a function of the  $\pi^0$  momentum for two different detector configurations. The left (right) plot shows the efficiency when the target module is filled with water (air). The efficiency grows roughly linearly with momentum. The distribution for air is presented with very limited statistics. The efficiency to reconstruct a  $\pi^0$  with momentum greater than 200 MeV/c is approximately 30% ( $27\% \pm 1\%$  w/ water,  $33\% \pm 2\%$  w/o water). Work is continuing to understand the differences between the two configurations.

Based on the results presented in Table 6.1 and the systematic estimates below, the error on the raw  $\pi^0$  rate can be estimated. Taking the conservative assumption that all NC multi- $\pi^0$  events are incorrectly reconstructed as having a single  $\pi^0$ , correcting for the efficiency differences between water-in and water-out and subtracting the number of events from non NC single- $\pi^0$  production, we expect a fractional statistical uncertainty of approximately 6%, and a crudely estimated systematic uncertainty of  $\sim 8\%$ . If NC multi- $\pi^0$  events are correctly reconstructed the statistical uncertainty remains approx-

imately constant, however the systematic uncertainty will be reduced to  $\sim 7\%$ . Work is continuing to demonstrate a complete single- $\pi^0$  analysis.

**Backgrounds to the neutral current  $\pi^0$  sample** As can be seen in Table 6.1, the POD neutral current  $\pi^0$  sample contains a significant background. Background is dominated by misclassified charged current, and neutral current neutrino interactions. These backgrounds have been fully simulated. This background includes secondary  $\pi^0$  production where a neutrino interactions occur within the POD, and a charged pion, neutron, or other particle produces a  $\pi^0$ .

The external background comes from neutrino interactions which occur within the material outside of the POD. Two significant external sources of background have been identified: Neutrons from the surrounding off-axis detector, dominated by neutrons from the up-stream coils and neutrons from the surrounding detector hall. These results are for a slightly different detector geometry and are being updated for the current design.

The background coming from neutrons generated outside of the off-axis detector were simulated by generating a sample of neutrons with the correct momentum and direction distribution on a  $100\text{ m}^2$  located 50 cm outside of the off-axis detector. The sample contains  $100\text{ neutron/m}^2$  and is estimated to represent approximately  $3 \times 10^{19}$  pot. After reconstruction using the procedure described above one event was found to pass all cuts.

The background from the surrounding off-axis detector has been studied with special simulation runs with events generated through-out the entire detector. A run equivalent to  $4.6 \times 10^{17}$  pot was simulated. One event was reconstructed as coming from the fiducial volume. Since this event originated in the upstream coil, and practical considerations prevented the simulation of significantly larger samples from the entire magnet, a special high statistics run has been made simulating events in the upstream portion of the Magnet.

The background from the upstream portion of the magnet was simulated in a  $2.5 \times 10^{19}$  pot exposure with events generated in the upstream coil, and in the upstream portion of the ECAL and basket. This corresponds to approximately 25 t of material.

The external background from all sources is estimated to be  $36 \pm 18\text{ ev}/(10^{21}\text{ pot})/\text{t}$ .

A crude estimate of the systematic error contribution to the POD pizero rate measurement from background subtraction can be made based on the results in this report. As noted above, the background is composed of two main components: neutral current events which contribute about  $\sim 40\%$  of the background, and charged current events which make up the remaining  $\sim 60\%$  of the background. Most of the charged current events in the background sample have an associated  $\pi^0$ . The uncertainty in this production rate can be reduced by studying events where the muon has been reconstructed and then extrapolating to determine the number of events where the muon has been missed. This extrapolation will probably be dominated by the statistics, and by combining information from the POD and tracker may have an uncertainty as low as 15%. The neutral current events in the background sample are evenly divided between neutral current elastic, and neutral current charged pion production events. The prior uncertainty on the ratio of neutral current elastic to charged current quasi-elastic is 12% [2], and can be measured in the POD. Neutral current charged pion production will be measured in the tracker by looking for single track events with a “wrong-sign muon”, in other words events with a  $\pi^+$ , and no  $\mu^-$ . We assume that the systematic uncertainty on the number of neutral current elastic and neutral current charged pion production events will be approximately 20% and 15%, respectively.

Combining the systematic error guesses for the various background channels predicts a background subtraction systematic for the single  $\pi^0$  rate of 7–8%. If a decay electron cut is successfully applied, the background subtraction systematic will become  $\sim 4\%$ .

## 6.1.2 Predicting the $\nu_e$ Appearance Background

Predicting the background to  $\nu_e$  appearance from  $\pi^0$  production at Super-Kamiokande is the most important role of the POD. This background is dominated by  $\nu_\mu X \rightarrow \nu_\mu \pi^0 X$ , with less than  $\sim 15\%$

coming from other processes, but with rather different neutrino spectra at the two locations. To compensate, the  $\pi^0$  rate at Super-Kamiokande must be determined using event rate and neutrino spectrum measurements at the ND280 detector and corrected for the differences in flux. Explicitly, the POD will measure

$$\left. \frac{dN_{\pi^0}}{dp_{\pi^0}} \right|_{280} = \int dE_\nu \Phi_{280}(E_\nu) \frac{d\sigma(\nu_\mu N \rightarrow \pi^0 \nu_\mu N)}{dp_{\pi^0} dE_\nu} \quad (6.1)$$

which is then used to predict

$$\left. \frac{dN_{\pi^0}}{dp_{\pi^0}} \right|_{sk} = \int dE_\nu \Phi_{sk}(E_\nu) \frac{d\sigma(\nu_\mu N \rightarrow \pi^0 \nu_\mu N)}{dp_{\pi^0} dE_\nu} \quad (6.2)$$

at Super-Kamiokande. This requires an unfolding between  $\frac{d\sigma}{dp_{\pi^0} dE_\nu}$ , the near and the far spectrum (also required for the disappearance measurement). This is further complicated since the momentum of the incoming and outgoing neutrino is not measured in neutral current interactions. However, the  $\pi^0$  production rate can be converted into a differential cross-section by assuming

$$\left. \frac{d\sigma(\nu_\mu N \rightarrow \pi^0 \nu_\mu N)}{dp_{\pi^0}} \right|_{Q^2} \sim \left. \frac{d\sigma(\nu_\mu n \rightarrow \pi^0 \mu^- p)}{dp_{\pi^0}} \right|_{Q^2} \sim \left. \frac{d\sigma(\nu_\mu N \rightarrow \pi^+ \mu^- N)}{dp_{\pi^+}} \right|_{Q^2} \quad (6.3)$$

and understanding the neutrino cross section as a function of  $Q^2$ . In simple terms, relationship between  $Q^2$  and the  $\pi^0$  momentum is assumed to be approximately the same for neutral current and charged current interactions, and unchanged under isospin rotations. Under these assumptions, the measurements that must be done at the ND280 off-axis detector are:

1. Measure  $\pi^0$  production rate as a function of momentum.
2. Measure the exclusive cross sections  $\frac{d\sigma(\nu_\mu n \rightarrow \pi^0 \mu^- p)}{dp_{\pi^0} dQ^2}$ ,  $\frac{d\sigma(\nu_\mu X \rightarrow \pi^+ \mu^- X)}{dp_{\pi^+} dQ^2}$  and  $\frac{d\sigma(\nu_\mu p \rightarrow \pi^+ \mu^- p)}{dp_{\pi^+} dQ^2}$ .
3. Measure the  $\nu_\mu$  flux,  $\Phi_{280}$ , as a function of neutrino energy.
4. Determine the far/near ratio,  $\Phi_{sk}(E_\nu)/\Phi_{280}(E_\nu)$ .

The POD is vital to the first two goals and will allow the  $\pi^0$  production rate as a function of momentum to be predicted at the Super-Kamiokande detector.

The assumptions can be validated using the reconstructed SK  $\pi^0$  sample. Model uncertainties can be further controlled by a cross comparison of the measured rates for the exclusive charged interactions. The assumptions used to predict the event rates can be further validated by repeating a similar analysis for  $\nu n \rightarrow \mu^- \pi^0 p$ , where the near and far spectra will be dramatically altered by neutrino oscillations and hence, will severely test the model dependencies of this extrapolation method.

As shown elsewhere, the far/near ratio of the neutrino energy spectrum varies by more than 50%, especially in the energy region between 400 MeV and 700 MeV; however, the expected far/near ratio of the  $\pi^0$  momentum, on the other hand, is quite flat. This is seen in Figure 6.4 which shows the NEUT neutrino interaction simulation prediction for the ratio of  $\pi^0$  yield at Super-Kamiokande to that at 280 m as a function of the  $\pi^0$  momentum (far/near ratio of  $\pi^0$  momentum) where scale is arbitrary to allow comparison of the shape. Within the statistical errors this ratio does not depend on the  $\pi^0$  momentum. Based on current knowledge, the  $\pi^0$  momentum spectrum from neutral current inclusive  $\pi^0$  production does not depend very much on the neutrino energy spectrum.

### Effect of systematic error on extrapolation to Super-Kamiokande

In the following we will consider sources of systematic error for the prediction of inclusive neutral current  $\pi^0$  events produced at Super-Kamiokande using the measurement on the same neutral current inclusive  $\pi^0$  events at the POD. These sources come from:

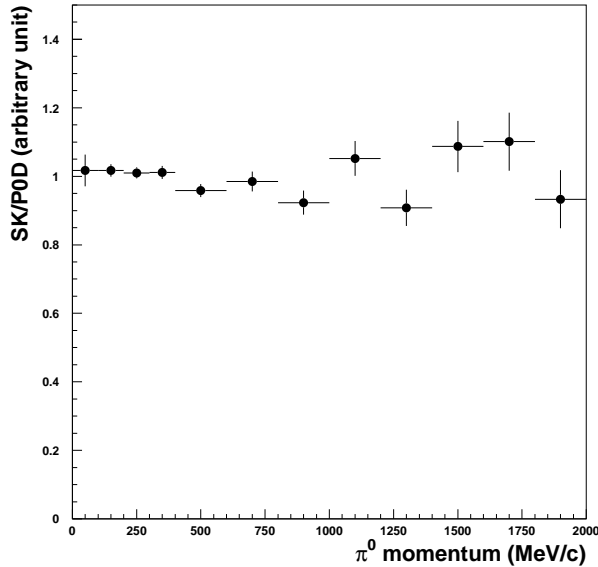


Figure 6.4: The NEUT prediction for the ratio of  $\pi^0$  momentum spectrum at Super-Kamiokande to that at 280 m in arbitrary scale. The total numbers of  $\pi^0$  inclusive events at 280 m and at Super-Kamiokande were normalized to be the same.

- Uncertainty arising from the statistical errors on the measurement at the POD.
- Uncertainty arising from the detection efficiency for the neutral current inclusive  $\pi^0$  events (signal events).
- Uncertainty arising from the detection efficiency from non neutral current events (background events).

Here the uncertainty in the detection efficiency should be understood in a broader sense than usual. It includes uncertainties in the estimate of the number of target nucleons and in the knowledge of event migration due to  $\pi^0$  energy resolution. Further, the detection efficiency uncertainty includes systematic uncertainty associated with the subtraction that is required to obtain the event rate on oxygen which is estimated to be 8%. A particularly important component will come from the uncertainty in the relative efficiency of different portions of the POD.

Using the number of neutral current inclusive  $\pi^0$  events observed by the POD, we can estimate how many  $\pi^0$ s will be produced at Super-Kamiokande. Based on the  $\pi^0$  reconstruction efficiency and sample size (Table 6.1 and Figure 6.3), Figure 6.5 summarizes the statistical errors for several  $\pi^0$  momentum ranges assuming a 2 ton fiducial mass of the POD.

The systematic error on the number of NC inclusive  $\pi^0$  events produced arises from uncertainties in the estimation of the signal and background detection efficiency, and in the estimation of the cross section ratio for the background to the signal. For simplicity, the neutrino flux is assumed to be exactly known, but will also contribute to the systematic error if that is not the case.

The  $\pi^0$  flux uncertainty is dominated by the statistical error and the error on signal detection efficiency (in the broad sense as explained above). Since we aim to control this systematic error to about 10%, we need to control the detection efficiency error to approximately 9%, considering the maximum statistical error of 5% for  $\pi^0$  momentum of up to 1.0 GeV/c. Although the uncertainty in the relative cross section of the background to the signal can be quite large, we can maintain the total error on estimation of the  $\pi^0$  production rate at a level of <10% below the  $\pi^0$  momentum of 1.0 GeV/c for  $1 \times 10^{21}$  pot ( $5 \times 10^{20}$  pot with the water target and  $5 \times 10^{20}$  pot without the water target) as long as we control the systematic uncertainty in the signal and background “efficiency” (in the broad sense as

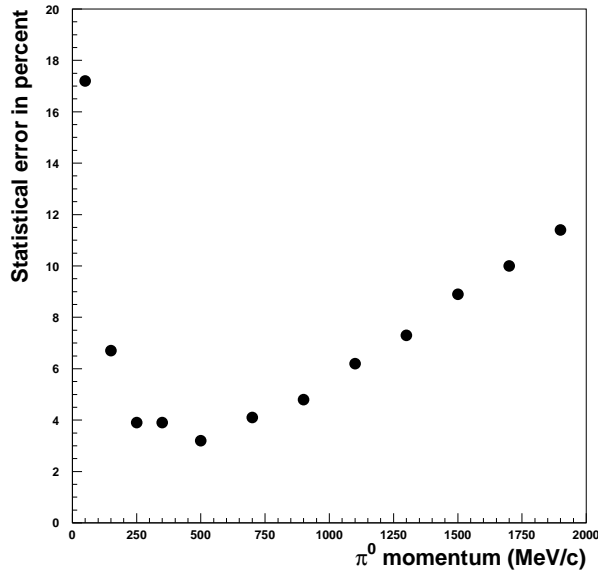


Figure 6.5: The percent statistical error as a function of  $\pi^0$  momentum after one accelerator year of a 1.9 ton of fiducial volume.

described) at a level of up to 12%. Since the systematic error from the subtraction to obtain the event rate by oxygen target is estimated to be 8%, we can still afford an error on the efficiency from other sources (such as the uncertainty on the number of target oxygen) up to 8.9%, which is achievable.

## 6.2 Detector Design, Specification and Assembly

The P0D is a solid scintillator strip detector using water to provide a large oxygen content and is based on the K2K SciBar experience and the MINERvA design. The P0D target is constructed of water layers between X-Y scintillator modules which provide the charged particle tracking. The scintillator modules are constructed with  $\sim 10\%$  lead by mass so that  $\gamma$ s have a high probability of creating an electromagnetic shower. The P0D has a total target mass of approximately 15 tons and a fiducial mass of approximately 5 tons.

Figure 6.6 shows the schematic view of a P0D layer. The tracking layers consist of X and Y extruded scintillator planes (white) with a 0.6 mm foil (red) sandwiched between them. The scintillator planes are made light tight with layers of polystyrene on the large faces (not shown), and end caps (dark green). The end caps serve the dual purposes of providing a manifold to bring WLS fibers (cyan) out of the scintillating bars, and keeping the ends of the scintillator light tight. A water cell is placed between the scintillator modules to provide an oxygen target. Read-out is performed using a single SiPM for each WLS fiber.

The water cells consist of semi-flexible pillow bladders, nominal dimensions 30 mm  $\times$  2100 mm  $\times$  2230 mm, holding about 140 kg of water each. The cells are filled and drained at the top to prevent leaks.

Figure 6.7 shows the P0D detector as viewed from the upstream end. The P0D is composed of three super modules (dubbed Super-PØDules) distributed along the beam axis. The upstream and downstream Super-PØDules are EM calorimeters providing containment for EM showers and improving the P0D energy resolution. The central Super-PØDule provides the primary target mass for the P0D. Each Super-PØDule is constructed of sub-modules (dubbed PØDules). The PØDules are constructed of triangular scintillator bars and read out using wave length shifting fibers instrumented with multi-pixel Geiger-mode APDs. The details of the detector are discussed below. The sub-

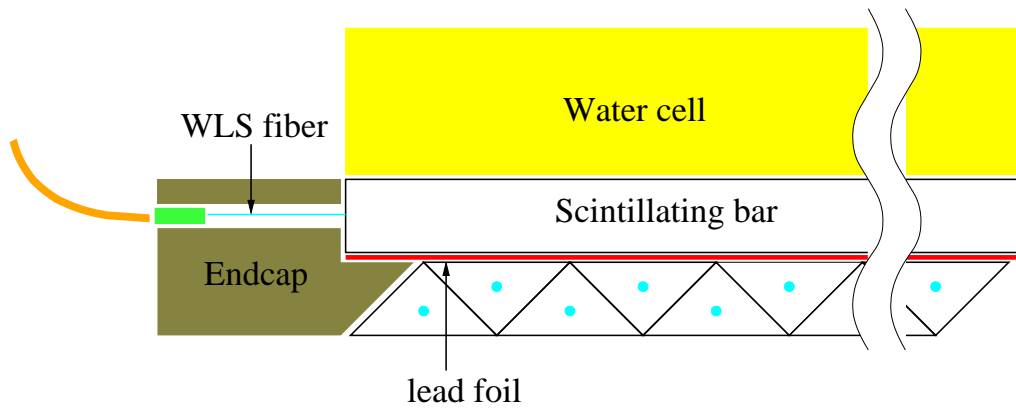


Figure 6.6: The schematic view of a POD layer.

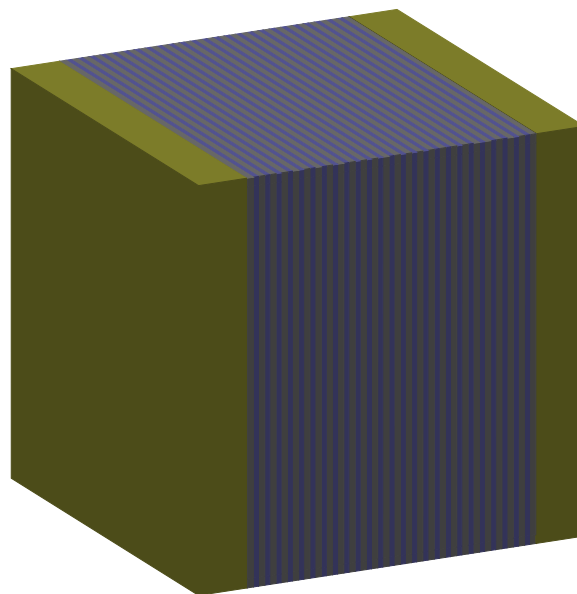


Figure 6.7: The POD detector viewed from the upstream end. The central region of the POD is constructed of alternating water target and scintillator tracking layers. The upstream and downstream regions are composed of lead radiator and scintillator tracking layers.

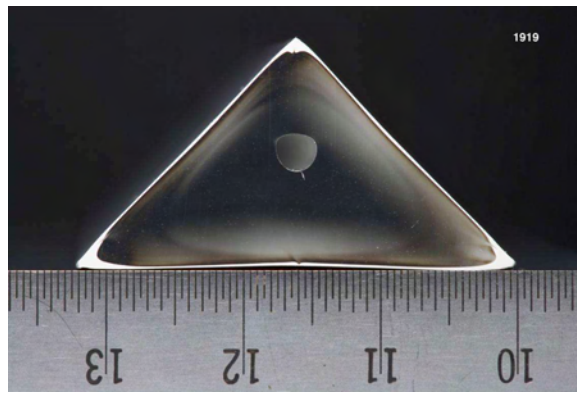


Figure 6.8: Prototype scintillator bar for use in the POD. The bar is 32.5 mm in base and 17 mm in height.

detector envelope is 2320 mm  $\times$  2400 mm  $\times$  2448 mm. Allowing space for the electronics and cable routing, the POD target mass and frames will occupy approximately 2200 mm  $\times$  2330 mm  $\times$  2415 mm.

Particle tracking is done using extruded scintillators similar to that used in the K2K SciBar detector. The POD design calls for triangular scintillator bars that are 17 mm in height and 32.5 mm in base co-extruded with a  $\text{TiO}_2$  surface treatment (see Figure 6.8). Each scintillator module is constructed from 128 (136) bars oriented in the X (Y) direction and there are a total of 40 scintillator planes in the baseline design.

### 6.2.1 The Water Target Design

The POD uses water to match the nuclear composition of the far detector, and to provide interactions primarily on oxygen target nuclei for comparison with the plastic (C, H, O) materials comprising the scintillator planes. Water cells are placed between half of the scintillator modules to provide oxygen target nuclei. Based on K2K experience, we chose to avoid rigid containers, where container mass would necessarily rival water mass. Instead, the water cells consist of semi-flexible pillow bladders, nominal dimensions 3 cm  $\times$  1.8 m  $\times$  2.1 m, holding about 100 kg of water each. They are provided with fill tubes and drain tubes at the top, with internal semirigid tubing carrying the drain inlet to the bottom of each bag. Figure 6.9 shows a schematic view of the POD water target arrangement.

The bladders are made from rubberized cloth or polyethylene-coated EVAL plastic. Similar in construction to inflatable boats or industrial fluid storage bladders, such bags have a well-established engineering history of toughness and long-term reliability. (Similar bags have been used for decades to waterproof balloon flight packages in Japan, where scientific balloon flights typically land in the sea.) We will use double bags (not just double walls, but one bag contained within another, each fully waterproof) to minimize the chance for leaks while adding negligible non-water mass. Figure 6.10 shows the design of the prototype water bladder. Water bags will be supported from the bottom and top, and retained in the transverse dimensions by gasketed frames, which make each water target section of the POD an independently watertight cell.

External pumps will allow fill and drainage upon demand. Pump capacity and tubing will be sized to allow expeditious fill and drain operations, taking less than about one hour. Figure 6.11 shows a schematic view of the POD water pump system. Load cells and leak detectors will be located in Al support channels underneath the water bags, allowing continuous monitoring of target contents and prompt identification of leaks. The support channels will be shaped to direct water into drain channels external to the basket.

All water systems leak at some level, and our goal is to make leakage effects negligible. The main concern when using bladder targets is the possibility of one layer leaking catastrophically and thus

Figure 6.9: Schematic view of the POD water target bladders, and associated support and monitoring system components.

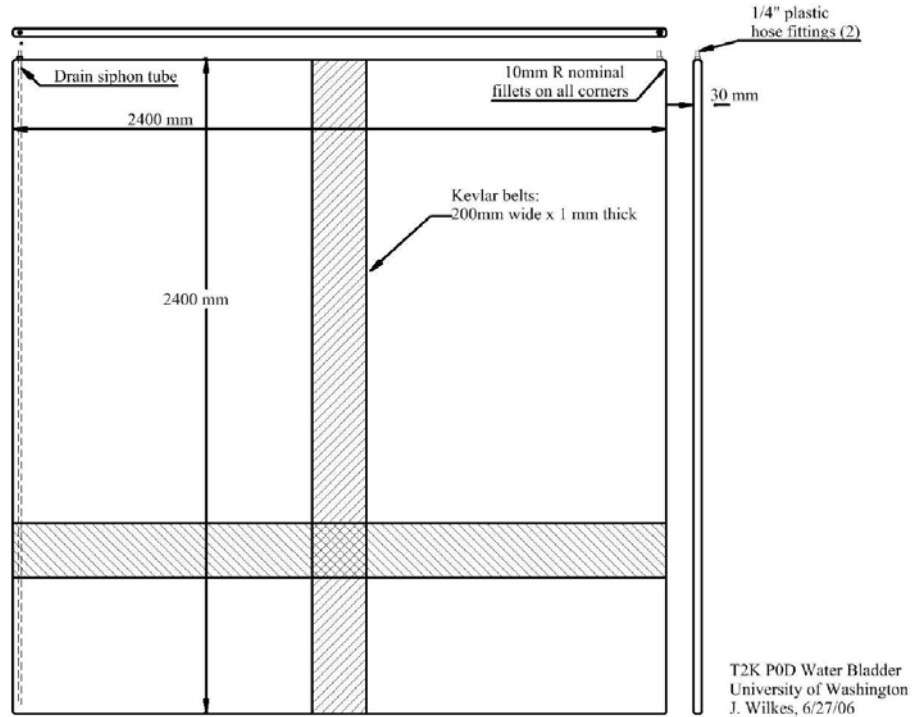


Figure 6.10: Prototype design of the POD water target bladders.

emptying rapidly. The gasket and channel system will greatly constrain the leakage rate in case of bladder failure, and prevent splashing of electronics in the basket. However, an empty target layer presents a mechanical problem. With all bladders approximately filled, the POD is self-supporting in the beam direction, and scintillator layers have no unbalanced forces in that direction. With one bladder empty, the adjacent scintillator layers must provide mechanical support for the bladders on their opposite sides, since the bladders are not self-supporting. Our prototype tests are intended in part to confirm analytic and finite-element estimations that in this worst-case situation, the scintillator bars will be stressed by an amount that can be tolerated without permanently affecting bar performance.

We expect to finish testing an initial prototype bladder, purchased from a commercial supplier of bladder tanks, by early 2007. Tests, using the full scale PØDule prototype assembly at SBU, will include checking bladder integrity (at UW, before shipping to SBU), piping, pumping and long-term leakage tests, and engineering tests to determine stresses and deflections imposed on adjoining scintillator bar layers in case of bag failure. A second prototype will be designed and subjected to similar tests in mid 2007. At that time we will decide whether to purchase bags from a supplier or construct our own using facilities developed at CSU for Auger water Cherenkov detector bags. A final design will be ready for production in early 2008. Production bags will be long-term tested under full water loads as long as possible before shipment to Japan in late 2008. We have budgeted \$28K for bag construction (including prototypes), \$17K for construction of frames and mounting hardware, \$15K for the water distribution system (pumps and plumbing), and \$2K for construction of the catchment basins to be installed under the PØDules to collect and safely drain away any leakage. The total of \$61K for the water target system construction has been assigned 50% contingency allowance, due to the unique character of the target design.

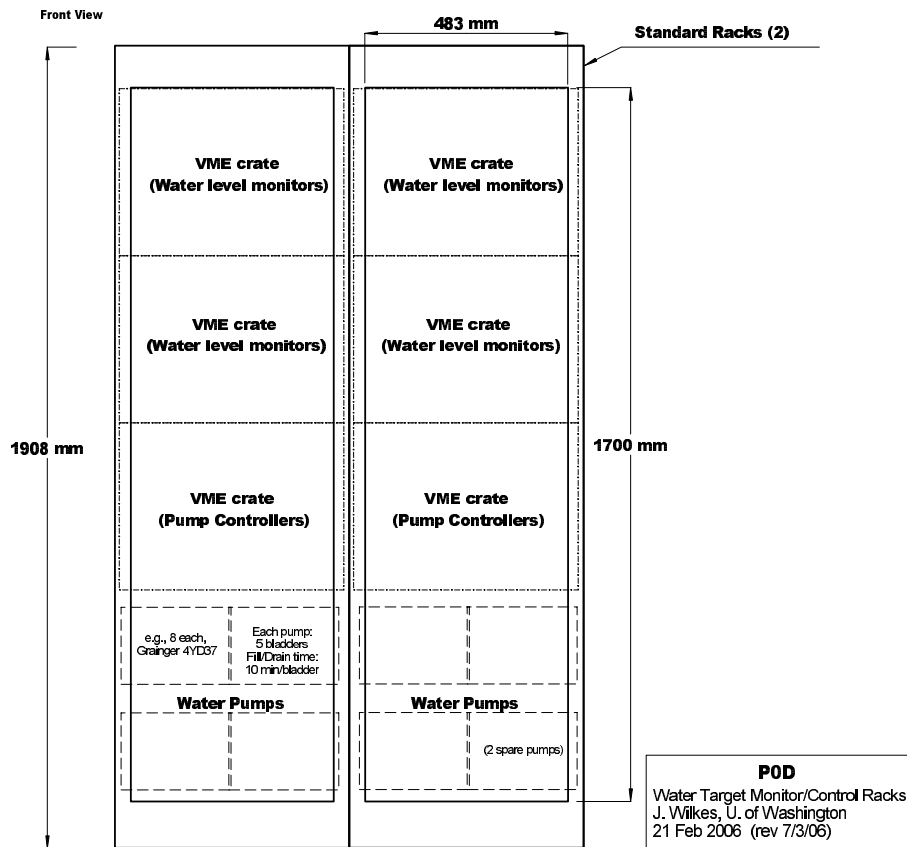


Figure 6.11: The schematic view of the POD water system. Pumps and network interfaces for leak and level monitors will be mounted in racks located in the B280 electronics room.

### Water target frame

The water target liners will be supported inside of a PVC frame. The frame, 29 mm thick with 40 mm wide walls, will be made of four machined strips adhesively bonded and pinned in the corners. The bottom frame member will slope slightly towards the central axis of the PØDule, where a drain line will remove any water escaping from the liner and caught within the frame.

The frame will be sealed to the outer HIPS skins on neighboring target PØDules with 3 mm thick by 20 mm wide polyethylene closed-cell foam gaskets, which provide the secondary line of defense against water leakage (See Figure 6.12). The PVC frames will be assembled into the target Super-PØDule using the same M-8 bolts used to assemble the target PØDules, also through stainless steel bushings.

The entire final layer of leak protection will be provided by a "drip pan" of stainless steel sheet covering the entire underside of the target Super-PØDule. This drip pan will be large enough to contain the volume of an entire failed water target section, and will be drained through an 80 mm drain line to allow for rapid removal of water in case of a catastrophic failure of the water target Super-PØDule.

## 6.2.2 PØDule Design and Assembly

The POD detector is composed of 40 individual sections or modules called PØDules. Each PØDule is an array of triangular polystyrene scintillator bars, arranged in perpendicular X-Y layers separated by a lead sheet (See the schematic side view in Figure 6.6), enclosed in a PVC frame, and shielded from external light by black polystyrene skins.

There are two types of PØDule: ECAL PØDules and Target PØDules. The ECAL PØDules have two lead moderator sheets each 2 mm thick and the target PØDules have one moderator sheet 0.6 mm

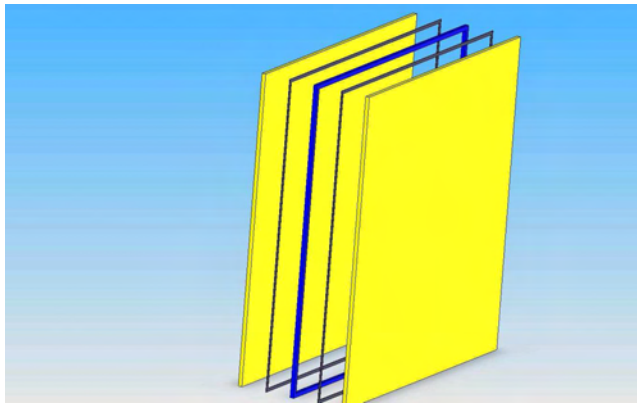


Figure 6.12: Exploded view of a PVC water target frame sandwiched between target PØDules and sealed with foam gaskets. A drip pan will be installed to shield the entire bottom of each water target.

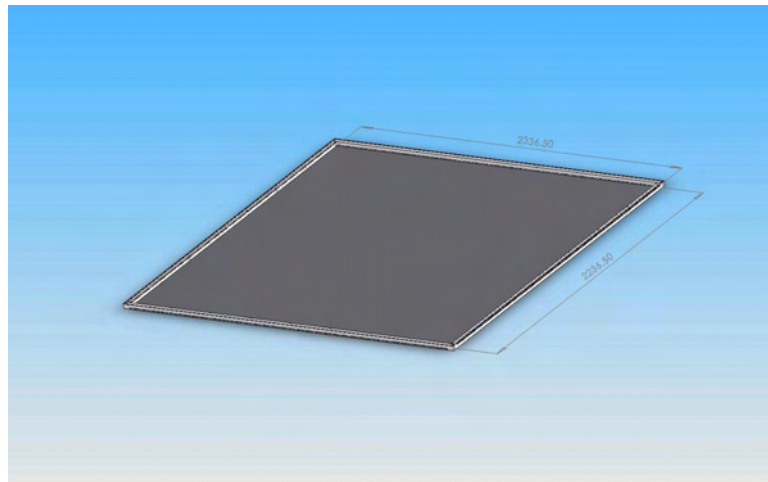


Figure 6.13: The PØDule showing the bottom polystyrene skin and the PVC frame.

thick. The finished PØDules are 2200 mm wide, 2330 mm tall, and approximately 40 mm thick, weighing approximately 230 kg (target PØDule) or 350 kg (ECAL PØDule). We next describe the scintillator bars, the PVC frame, and the lead moderators sheets.

The scintillator bars are assembled into planes oriented in alternate X-Y directions (see Figure 6.14). The scintillator bars have a triangular cross-section, 17 mm across the base and 17 mm tall. There are 136 bars each 2137 mm long in each X-plane (oriented horizontally in the detector) and 128 bars each 2268 mm long in each Y-plane (vertical), for a total of 264 bars per PØDule.

The scintillator bars are made from extruded Dow Styron 663 with POPOP scintillating additive. The bars are coated with a  $\text{TiO}_2$ /Polystyrene blended outer layer to act as a reflector. Each scintillator bar has a 1.8 mm diameter hole extruded axially along the length of the bar. A 1 mm diameter Kuraray Y-11 fiber is inserted through the extruded hole for readout of the scintillating bar. The fibers penetrate one end of the PØDule frame, and are read out by a Geiger-mode Avalanche Photodiode array. The photosensors are attached to the Y-11 fiber using a custom-molded plastic optical coupler (See Figure 6.15).

The PVC PØDule frame pieces are machined from grey Type 1 PVC sheet. The frame pieces are designed to interleave in the corners to provide for a light seal. Two of the frame pieces have precision-machined holes through them to align the scintillator bars in PØDule during assembly and to allow for the optical readout of the WLS fibers. The other two frame elements have smaller holes for allowing the optical calibration fibers to penetrate to the scintillator bars (see Section 6.6.2).

The lead moderator sheets are made up from four sheets each approximately 1.2 m square with

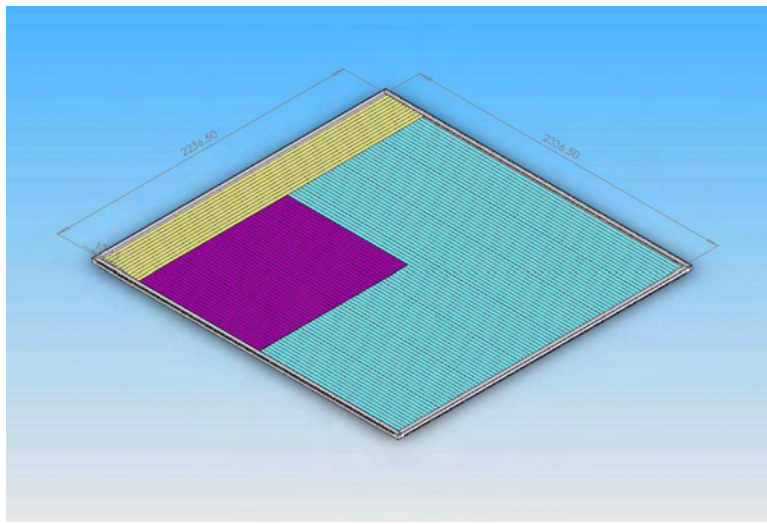


Figure 6.14: A cutaway view of the target PØDule showing the frame scintillating bar orientation, and lead sheet.

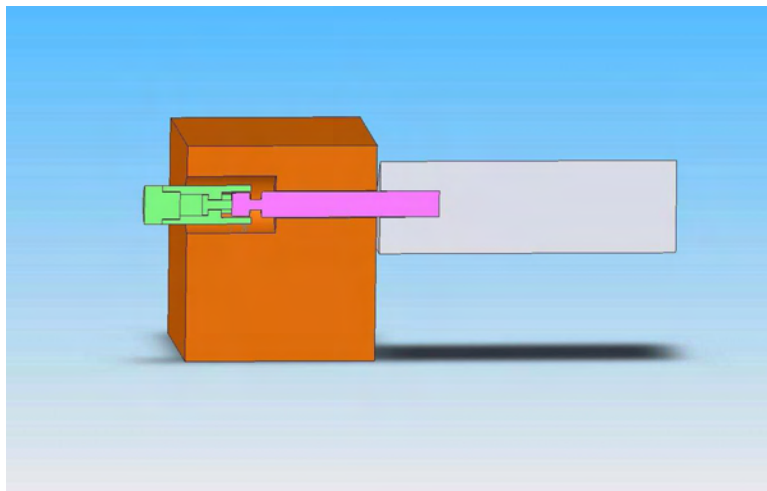


Figure 6.15: The concept of the bar read-out through a ferrule and optical connector.

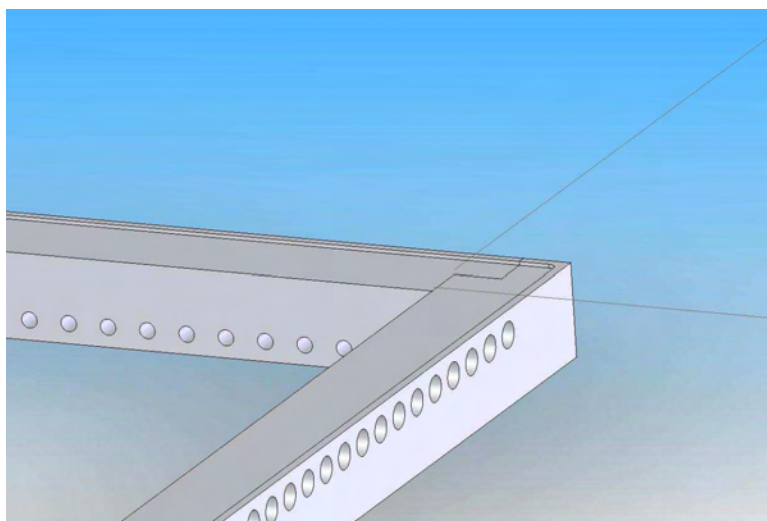


Figure 6.16: A detail of the PØD frame showing the optical connection holes.

0.6 mm or 2 mm thickness. The sheets are joined with high bond strength tape and cut to size before installation in a PØDule. This technique has been tested and found to work well in preliminary prototype PØDule assembly at SBU.

## Material choices

PØDules are large flat planes, extremely susceptible to effects of thermal expansion and stresses due to force concentrations caused by differences in mechanical properties from dissimilar materials. The PØDules will experience a range of ambient temperatures through a range of as much as 50°C during shipping, and must not fail due to thermal effects. Care was taken in the selection of frame and skin materials to ensure that the thermal and mechanical properties of the selected materials matched those of the scintillator bars, while remaining strong enough to allow for handling and supporting the PØDules in the ND-280 basket.

Engineering tests of tensile strength and flexural modulus were made at CSU to optimize the selection of similar materials for PØDule frame elements. Adhesives were selected to ensure sufficient bond strength and flexibility combined with a long working life to allow for PØDule assembly.

## Fiber preparation

Wavelength shifting (WLS) fiber is inserted into the hole of each scintillator strip. We have chosen a fiber based on qualification tests performed for previous experiments (CDF, CMS, MINERvA): Kuraray multi-clad, J-type fiber with S-35 core. The WLS dopant will be Y-11 at a concentration of 175 ppm. The fiber diameter is chosen to be 1.0 mm to match the available photosensor size. Fiber shipped from Kuraray will be batch tested in a source scanner to ensure that its relative light yield compared to prototypes and its attenuation length (> 5 meters) meets our specification.

For the POD, light will be read out from only one end of each fiber. To increase the light collection and uniformity, the unread end of each fiber is mirrored. Mirroring consists of polishing the end to be mirrored, depositing a 99.999% chemically pure aluminum reflective surface on the fiber, and covering with a coat of epoxy. This procedure, to be done by Eileen Hahn's group at Fermilab has been shown to result in high  $\approx 80\%$  reflectivity and to be very reproducible.

Finally, the fiber ferrule part of the optical connector will be placed on the non-mirrored end of the fiber and the assembly will be polished. Again, source scanner batch quality-control checks will be used to quality during production. This entire completed assembly, mirrored fiber terminated in a polished ferrule, will be installed and glued into the bar at the ferrule.

## Scintillator production

The POD design calls for triangular scintillator bars that are 17 mm in height and 32.5 mm in base (see Figure 6.8). The scintillator strips are made of polystyrene doped with PPO (1% by weight) and POPOP (0.03% by weight) and co-extruded with a reflective coating of TiO<sub>2</sub>.

A scintillator extrusion meeting the POD specifications has already been developed for the MINERvA collaboration through a collaboration between the Fermilab Scintillator Detector Development Laboratory (FSDDL) and the northern Illinois Center for Accelerator and Detector Development (NICADD) at Northern Illinois University (NIU). Small prototype runs of the proposed extrusion have been completed and been used to measure light output of a scintillator and fiber assembly using these extrusions (see Sect. 6.3.2). A lengthy prototyping run producing 5 – 7 km of scintillator bars is planned for late 2006, and POD prototypes will be constructed from some quantity of these bars. The POD construction projects benefits significantly from the use of the MINERvA-developed scintillator extrusions because it avoids development costs and time required for a new die and because there is little uncertainty in the production schedule with R&D on the sub-project largely already completed.

The total 6.6 tons of extruded scintillators included in the full POD design will require a production run of approximately six weeks.

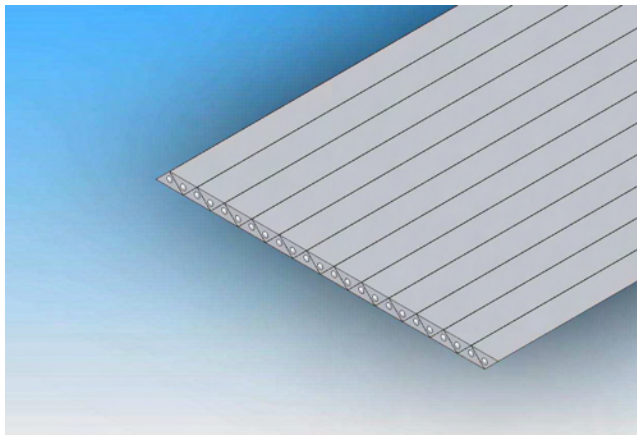


Figure 6.17: The PØD plank showing the alternating bars.

### **Scintillator plank assembly**

Scintillator bars will be pre-assembled and glued into groups of bars into precision-aligned assemblies called “planks.” The final assembly of the PØDule is simplified by assembling groups of 5-6 planks of scintillator bars per layer instead 130 scintillator bars per layer. Planks will be assembled with 2 different numbers of bars to meet the requirements of the different width and height of PØDules.

Prior to assembling a plank, the scintillator bars will be prepared by cutting them to length with a +/- 2 mm tolerance, and by boring a 5 mm diameter hole 1cm deep in each end of the bar concentric with the fiber hole. This hole will be used to align the bar ends during assembly into planks, and later it will accept the optical connector ferrule which aligns and protects the WLS fiber.

Scintillator bars are arranged in a close packed arrangement (See Figure 6.17) in a plank. Planks are assembled by first laying down the bottom layer of bars (wide flat side down) into fixture bars mounted on an optical table. The bars are positioned by inserting 4.9 mm diameter Teflon-coated brass pins through alignment fixtures at each end of the plank into the 5 mm holes in the bars. Next epoxy (Stycast) is applied to the bars, and the top row of scintillator bars (wide flat side up) is inserted and aligned with Teflon-coated brass pins through the fixture plates at each end.

Following assembly into the fixture, the plank is compressed into the fixture by vacuum bagging it to the optical table. A thin polymer sheet is taped to the surface of the optical table over the plank under assembly. The air is then evacuated from under the sheet to a pressure of about 2 PSI gauge, resulting in a uniform pressure over the entire plank while the epoxy sets. The epoxy is allowed to set for 6 hours, and the plank is removed from the fixture.

This procedure has been tested at CSU as part of the mechanical prototype we developed in June of 2006. It appears to work well. Our initial estimates of 1.5 man-hours of assembly time per plank was validated by the test assembly.

### **PØDule assembly**

The assembled PØDule exhibits mechanical properties similar to a solid block of Polystyrene when properly assembled. Mechanical tests of the properties of bonded scintillator bars and frames demonstrate that the adhesion strengths developed between these bars is extremely strong and comparable to the strength of the material itself. Achieving solid adhesive bonds is a critical part of PØDule assembly, and ensuring the reliability of these bonds is the main focus of our assembly plan design and testing.

Assembling a PØDule requires many assembly steps. While every attempt has been made to minimize the assembly time required, we still require an adhesive with a long cure time. We have selected Hysol 3145/3163 adhesive for our application. This adhesive has a very long work life (more

than three hours), is black to help insure a light-tight assembly, and has sufficiently high viscosity to facilitate assembly.

PØDules are assembled on a special full-sized fixture table constructed to align the frame members to their correct positions while the entire structure is assembled. This fixture table is the “template” for aligning all the components during assembly, ensuring that the PØDules can be easily assembled into Super-PØDules later. The polystyrene outer skins are cut and drilled on a fixture attached to this table, and the lead sheets are also assembled and cut on this table. In this way, all the assembly tolerances are maintained by the fixture table, ensuring that the PØDule assembles correctly while minimizing the precision machining of components required for assembling a PØDule.

Before assembling a PØDule we use the fixture table for component preparation. The PVC frame elements are prepared by positioning them on the table and installing (adhesively) 1.5 cm diameter stainless steel bushings in the PØDule assembly bolt holes aligning them to positioning bushings in the table (thus ensuring a large precision aligned bearing surface for Super-PØDule assembly). The polystyrene outer skins are cut to size and the assembly alignment holes drilled through bushings in the table, following which the skins are set aside for later use. Also, the lead sheets are rolled out, taped together, and cut to size. The lead sheets are then rolled up and set aside for later use.

Assembly of a PØDule proceeds as follows: First, one of the polystyrene outer skins is laid on the fixture table and pinned in place to the table using plastic pins. Next, a layer of Hysol adhesive is applied to the entire surface of the outer skin, and the frame pieces are placed onto the skin, over the same plastic pins. Next, a layer of planks is positioned into the frame, and Teflon-coated brass pins are pressed through the holes in the frame to align them in the PØDule. A second layer of Hysol is applied, and a lead skin is rolled out onto the layer of planks. A third layer of Hysol is applied, and another layer of scintillator bar planks is positioned on top of the lead sheet, in the perpendicular orientation from the lower layer, and once again Teflon-coated brass pins are inserted into the holes. A fourth and final coat of Hysol is applied, and the top skin of polystyrene is positioned over the same plastic alignment pins used to align the frame and lower polystyrene skin. Following assembly, the entire structure is vacuum-bagged to the fixture table and allowed to cure for 12 hours.

Following curing, the vacuum bag is removed, the PØDule is lifted off the table, and the plastic pins are cut flush with the surface of the polystyrene skin. The joints between the polystyrene skins and the frame are taped over with an ultra high bond strength adhesive tape to prevent them from mechanically peeling during handling. Three 10 mm diameter mechanical support pin holes are drilled into each corner of the frame, and aluminum pins pressed into place for additional mechanical support at the corners.

### 6.2.3 Super-PØDule Assembly

The final POD detector is composed of three sections called Super-PØDules. There are two ECAL Super-PØDules each made of seven ECAL PØDules, and a target Super-PØDule composed of 26 target PØDules interspaced with 25 water target frames. The ECAL Super-PØDules each have an approximate mass of 3050 kg, and the target Super-PØDule has a mass of 6850 kg empty and 10,450 kg filled with water. The three Super-PØDules will be completely assembled at SBU and shipped to J-PARC where they will be installed and aligned in the support basket separately.

The proper alignment of the PØDules into the Super-PØDules will be achieved using the stainless steel bushings pre-installed into the frames as part of the PØDule assembly process. There are 36 bushings spaced approximately 10 cm apart around the frame (See Figure 6.23). The PØDules to be installed are located on an assembly fixture, holding them roughly in position. Tapered rods are inserted through the four corner bushings to align the PØDules. The PØDules are then assembled using M8 bolts through the remaining bushings. Following installation of the initial 32 bolts, the four tapered rods at the corners are removed and replaced with M8 bolts. Using this alignment method, we expect to align the individual PØDules within a Super-PØDule to within  $\pm 1$  mm along all three linear axes.

The outermost two PØDules in a Super-PØDule have special bushings: Those in the last frame in each PØDule are threaded, and those in the first PØDule are countersunk, to allow the M8 socket head cap screws used to hold the Super-PØDule together to be buried completely within the frame.

## 6.2.4 Electronics and Photosensors

Following the collaboration wide effort to select a photosensor and design front end electronics, the US-B280 group will take responsibility for procurement and quality control for the POD.

### Photosensors

A significant development since the original US-B280 proposal is the change of photosensor from micro-channel multi-anode photomultiplier tubes (MCMAPMT) to highly-pixelated avalanche photodiodes operated in Geiger mode. These devices, referred to as "silicon-photomultipliers" (SiPM), have been adopted by all of the scintillator-based B280 detector elements (POD, SMRD and FGD). Primary advantages of the SiPMs are that they are insensitive to magnetic fields and small enough to be mounted directly onto individual WLS fibers. Their use removes the need for the substantial optical fiber plant required for the MCMAPMT readout and results in a substantially lower system cost. Other advantages include low cost per channel and low voltage operation (50-70V).

Two SiPM implementations are being considered currently: the Multi-Pixel Photon Counter (MPPC) by Hamamatsu Photonics (HPK), Japan; and the Metal-Resistor Avalanche Photodiode (MRS-APD) by the Center of Perspective Technology and Apparatus (CPTA), Russia. Substantial quantities will be available in fall 2006 and a substantial effort to investigate these devices is already underway at numerous T2K collaborating institutions. There will be three such efforts in the US B280 group: scintillator light yield measurements at Rochester, prototype POD fabrication and readout at Stony Brook, and design of the production QA testing apparatus and optical calibration system at Colorado State.

A decision on the choice of photosensor for the POD will be made during CY2007.

### Readout electronics

The development (design and firmware) of the readout electronics is the responsibility of the UK-T2K group (See Chapter 10). The US-B280 group will be responsible for production, testing, calibration, installation and maintenance for the POD TFBs (Trip-t Front-end Boards), as well as the cabling required to connect the TFBs to the RMMs (Read-out Merger Modules). The remainder of the electronics, including the RMMs, is provided by the UK group.

According to the present schedule, the UK group will produce a final TFB prototype in April 2008 and start production in the summer of 2008. The manufacturer will perform initial tests to verify that the boards are working prior to delivery. The 198 POD and 180 SMRD TFBs (includes 20% spares) would then be shipped to Pittsburgh for burn-in testing, QA, and board characterization. It is therefore imperative that the University of Pittsburgh has a working TFB teststand by the beginning of summer 2008.

A first TFB prototype will be available by the end of 2006 from the UK. Starting in spring 2007 the UK will commence, with involvement of the Pittsburgh group, the development of a teststand for board QA and calibration. A working teststand will be in place at Pittsburgh by early summer 2008. Production testing of the boards will begin in summer 2008. All board testing will be completed by early 2009 for installation onto the POD. After testing, the boards will be installed on the POD before shipping to Japan. The work of testing, installation and maintenance will be carried out by members of the Pittsburgh group.

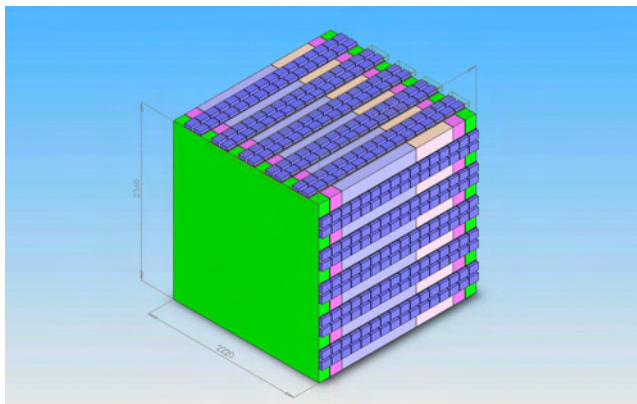


Figure 6.18: The electronics mounted on the P0D.

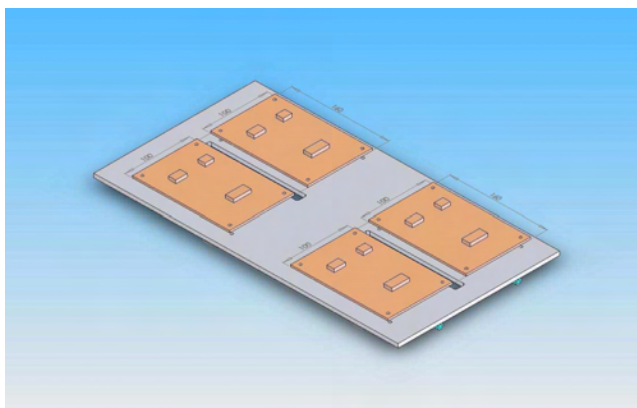


Figure 6.19: The “ladder” that provides a mounting surface for the front-end electronics, and provides thermal coupling to cooling.

### Electronics mounting

The P0D electronics to be mounted in the detector includes the photosensors, the TFB boards, and the Readout Merger Modules (RMMs).

The photosensors mounting was described in the PØDule design and assembly section and a drawing is shown in Figure 6.15. They are installed into the PØDules as they are tested, and are not removed again.

The TFB boards are attached to aluminum support bars called “Ladders”, which are mounted directly to the Super-PØDules during their assembly, before shipping to J-PARC (See Figure 6.18). The ladders (Figure 6.19) provide cooling for the front-end boards, and also a conduit for routing the signals from the TFBs to the Readout Merger Modules (RMMs), the next level of readout. The electronics are connected to the photosensors, tested at SBU, and re-tested on the Super-PØDule at the ND280 site before the Super-PØDule is lowered into the basket.

The RMMs are mounted in the spaces between the basket support members, and are installed after the Super-PØDules have been lowered into the basket.

### Slow control electronics

The slow control electronics will be provided by the UW Group working with the ND280 slow control working group. One particularly important aspect of the P0D slow control will be water level and leak monitoring. In each target layer’s support beam, which also functions as a drain channel, the UW group will provide load cells to monitor the water mass, and leak detectors to signal the presence

of water.

The UW group is working closely with colleagues in Japan on the design and development of a low-cost custom DAQ board to be used for digitizing beam monitor raw signals and interfacing them to the T2K online DAQ system. This board will also be used for the less-challenging task of interfacing water target monitors and other slow-control signals from the P0D. These boards, as currently under development, are based on the Texas Instruments ADS5410 (12-bit, 80 MSPS) A/D chip, although higher-performance chips may be substituted later. FPGA techniques will be used for DAQ control, processing, and interfacing. An onboard MCU will allow all control functions to be downloadable, so the board can be readily adapted to different specific functional requirements as and if needed (Figure 6.20).

Monitor DAQ boards will be housed in standard VME crates, interfaced to the overall beamline data system via commercially available memory-mapping VME-PCI adaptor cards. The recorded data will be pre-processed by PC-based workstations and sent to the ND280 control network. In addition to the sensors associated with the water targets, the UW group will also interface several hundred temperature sensors to monitor the SiPM temperature. A Linux PC workstation will be provided with a memory-mapping interface to the VME crates. The workstation will organize and preprocess sensor data, and interface P0D slow control via ethernet to the overall T2K online data and control system network.

The UW group's direct experience with DAQ system integration from Super-Kamiokande and K2K will be used to design an improved and highly functional system for the T2K subsystems the group is handling. The group is working closely with the groups at KEK, SBU, and Rochester on this effort.

In addition, the UW group has extensive experience from Super-Kamiokande and K2K in preparing, documenting, and operating web-based monitor systems for critical detector elements. These consist of running quality-control graphs, showing history as well as minimum/maximum limits of the displayed parameter, linked to documentation and clear instructions on when to summon expert help. The goal is to allow new collaboration members to quickly be able to safely (in terms of data quality) take detector monitoring shifts without extensive training. In this role, the UW group will work closely with members of the TRIUMF group who are preparing the complex monitoring and control database system, based on the MIDAS data acquisition software package, for the entire near detector suite.

The UW group will have prototype DAQ front end boards ready by the end of 2007. The group will use the full-scale PØDule prototype setup at SBU to select and test sensors for water mass, leakage, temperature, and other environmental parameters. The software required to test and monitor the sensor system, and interface its data to the ND280 slow-control system, will be prototyped by the end of 2007 and integrated into the MIDAS online system by mid-2008.

### **6.2.5 Mounting in the Basket**

The P0D mass will be supported at the bottom of the basket, with additional stabilization mounting points at the basket midpoint rail and at the top. The base supports will allow adjustment both vertically and along the detector axis to facilitate placing the P0D in the basket and adjusting its position to compensate for the expected approximately 15 mm vertical deflection as the basket takes up the P0D mass.

Each Super-PØDule will be installed and aligned in the basket separately. Since the individual PØDules are constrained in the Super-PØDule assembly, the problem of locating the P0D in the basket is reduced to surveying the positions of the three Super-PØDules.

Initially, the Super-PØDules will be located roughly in the basket by measuring their position relative to the basket with rulers. Next, higher accuracy positioning will be accomplished by optically surveying four reference points on top of each Super-PØDule, allowing positioning of the assemblies to the desired position tolerances of  $\pm 3$  mm in all three directions.



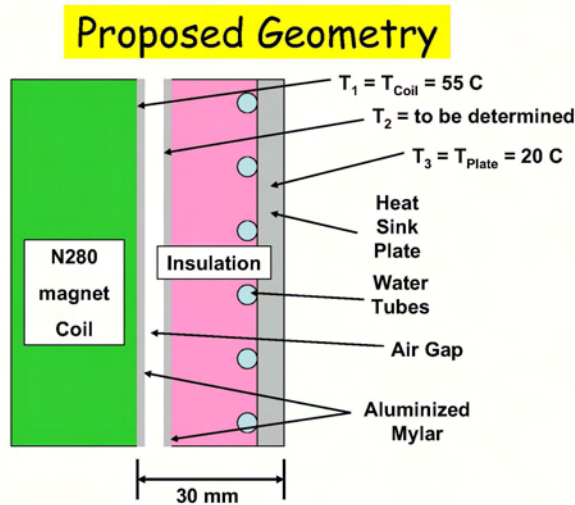


Figure 6.21: Schematic layout of heat shield.

### 6.2.6 POD Heat Shield

The T2K inner sub-detectors, POD, FDG, and TPC, are placed inside the ECAL sub-detector, which is mounted inside the magnet coils. The magnet coils are expected to operate at a nominal temperature of 50°C. The inner sub-detectors need to be temperature insulated from the magnet coils. The ECAL is planned to be cooled to reduce the temperature to 20°C. However, the ECAL does not cover the front region and the first layer of the POD is exposed to the magnet coil. Currently, the ECAL is being planned to be installed after the start of the T2K run in 2009, so there is need for a (1) permanent protective heat shield in the front area between the front coil and the first layer of the POD and (2) a temporary heat shield in the region where the ECAL will be installed at a later time.

The CSU group was asked to investigate the heat shield requirements for these two items. To study and test a design, the CSU group has subcontracted a thermal engineering consultant, Prof. P. Burns, a CSU thermal Engineering Professor, who formerly worked on thermal codes on projects at Lawrence Livermore Labs. Using his proposed schematic design shown in Figure 6.21, the CSU group has built and tested a 4×4 ft. prototype to measure the cooling rate (water flow and temperatures) and to compare to Burn's calculations. Demonstrating agreement between these calculations and prototype measurements would prove that scaling to a larger design would be successful.

In the proposed geometry, there is a cooling aluminum plate, copper cooling pipes and polyurethane insulation. Between the polyurethane and the coil is an air gap that has aluminized mylar on both the coil and the polyurethane surfaces. This design minimizes both radiation and conduction heat transfer. To test this design, a horizontal prototype was built with 4×4 foot high purity 1/2 inch thick aluminum plate (#1011) which was cooled with eight 1/4 inch I.D. copper pipes which were covered with a 1 inch polyurethane insulation with an aluminized mylar. This represented the proposed heat shield. To reproduce the heat from the magnet coils, a 2nd layer 4×4 foot of inexpensive 1/4 inch thick aluminum pate (#6061) covered with electric heating mats was mounted on top separated by a 1 inch air gap and wood spacers. See Figure 6.21 for the schematic layout.

The prototype was operated for several hours to stabilized the temperatures. The heating plate was at 55.6°C and the cooling water was flowed at 3.5 cc/s at 17.2°C from a NESLAB recirculating water chiller. The measured surface temperature of the polyurethane was 30.6°C. Burns calculation predicted 32.6°C (no wood spacers) and 34.2°C (with wood spacers). The measurements and predictions shown in Figure 6.22 were in very good agreement.

The proposed design for the heat shield an arrangement of Al plate + cooling pipes + insulation with aluminized mylar on the coil and insulation surfaces. The final layout should be optimized to reduce costs and to simplify the installation, handling, and maintenance. The inner detector is

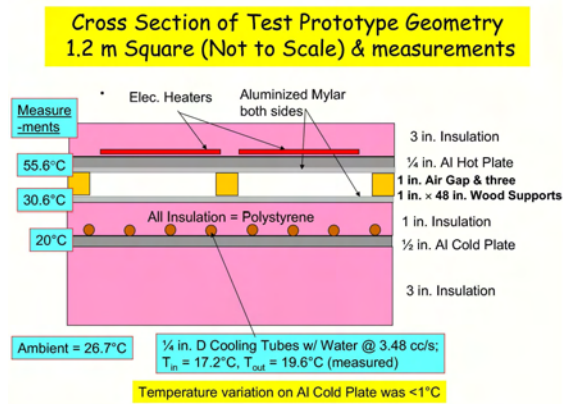


Figure 6.22: Results of the prototype heat shield measurements.

planned to be mounted inside the basket and the heat shield plates are proposed to be mounted from the basket in roughly 4×4 foot sections. The 4×4 foot size should provide easy handling by two people at the detector site. The permanent protective heat shield in the front POD region (roughly 8×8 foot) requires four heat shield sections. The temporary exposed ECAL region covering the top/bottom/sides/rear regions would require 28 additional sections and is about 7 times larger. In this scheme, we propose to modularize the design into 32 heat shield sections which are very similar to the first prototype describe above. The cost estimates of this include the aluminum plates (purchased in 4×4 foot sections), copper pipes, hoses and connectors, G10 fabricated mounting supports between the heat shield and basket, aluminized mylar, temperature probes, water pressure probes, engineering, design, oversight, technician time, and shipping. The costs do not include the slow control readout of the temperatures and water pressures and the water chiller.

## 6.3 Detector Technology R&D

The POD is based on well understood detector technology and is leveraging the US-B280 experience with scintillator bar tracking detectors, but there are several details specific to the current design that require development before construction can proceed.

### 6.3.1 PØDule Mechanical Prototypes

PØDule assembly techniques were extensively tested during the mechanical prototype assembly tests at SBU in June of 2006. Most of the steps described in the PØDule assembly above, and found to be successful. Our assembly rate assumptions were also validated, and we expect to be able to assemble one PØDule per day per assembly table. We currently plan for only one assembly table for POD production, but this could be increased if necessary to accelerate the production rate.

The current mechanical prototype has been constructed using PVC as a replacement for the scintillating bars and the dimensions as slightly different than in the proposed final design. Specifically, the dimensions of the mechanical prototype were limited to size of PVC stock that is readily available. The most significant deviation from the baseline design described in this document is that the simulated scintillating bars are 26 mm in base, and 13 mm in height (e.g. the maximum dimension that can be fabricated from a 1/2 inch sheet of PVC). We feel this has very little effect on the assembly technique, and will be corrected as new prototypes are constructed using the extruded scintillator bar stock.

Figure 6.23 shows various stages of the prototype assembly. The upper left image shows how the position of the pre-assembled scintillator planks will be maintained during PØDule assembly. Each scintillating bar will be pre-drilled to accept an alignment pin. The upper right image shows the lead



Figure 6.23: (upper left) Brass pins holding a dummy scintillator bar plank into the frame. (upper right) The lead radiator sheet installed into the PØDule during construction. (lower left) A PØDule vacuum-bagged for curing. (lower right) The completed PØDule.

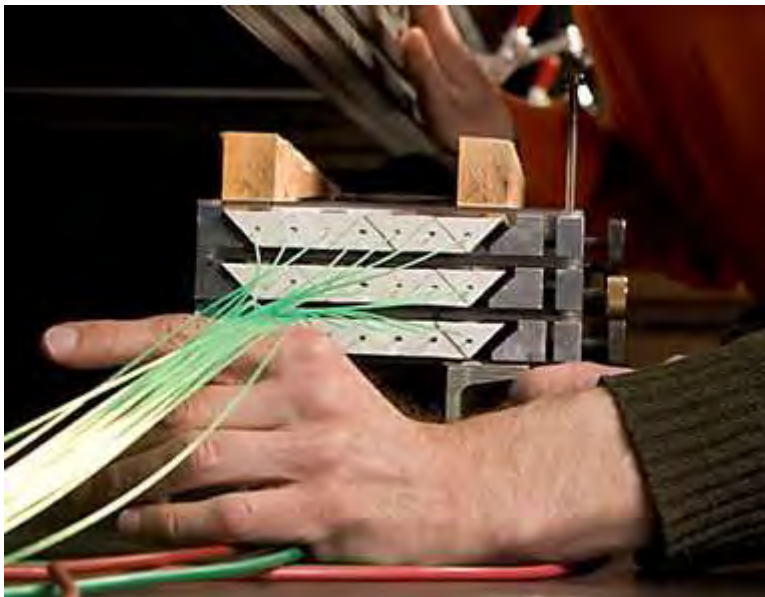


Figure 6.24: The scintillator of the POD light yield test with the exiting WLS fibers shown.

radiator as it is being smoothed against the lower scintillator layer. The lower left image shows the assembled PØDule under vacuum pressure to allow the epoxy to cure. The lower right image shows the assembled PØDule. Epoxy was not used during the assembly tests shown in these images to allow the parts to be disassembled and studied. Full assembly tests including the bonding of the parts using epoxy will be done during the Fall of 2006.

Water bladders will be pre-tested for leaks and general integrity in Seattle, using a support frame setup in the UW Physics Machine Shop equipped with strain gauges and load cells to measure forces on support members. They will then be shipped to SBU where they will be used in the full-scale prototype test.

The completed mechanical prototypes will be tested to verify the deflections under various loads as predicted by FEM analysis. The critical test will be the deflection of the PØDule when it must support a full water target. Test will also be performed to verify the peel and shear properties of the glue as the PØDule flexes under various loads.

### 6.3.2 Functional Prototypes

Light output of the POD detector will be demonstrated in two phases. The first phase will be completed with tests of detector components or related stand-in components; these tests are largely completed and were used in verifying the performance of components chosen for the detector. In the second phase, we will build full prototype PØDules and characterize their performance.

#### Component Prototypes

The key detector performance test is the verification of the simulation estimates of light yield in the scintillator. The measurement was completed in a partial vertical slice of three parallel layers of the detector with a cosmic ray telescope trigger. The 21 scintillator bars are short (50 cm) prototypes which are extruded in exactly the way planned for the production scintillator bars. The WLS fiber, however, is a larger diameter (1.2 mm) than the 1.0 mm fiber planned for the current detector, but otherwise uses the same core, cladding and dopant concentrations and is mirrored in the planned procedure. As shown in Figure 6.24, the WLS fiber exits the short scintillator but has a total length of

Table 6.2: Corrections from the light yield measured in the test detector to the extrapolated yield of the POD.

Correction	Multiplicative Factor
Fiber attenuation	$1.32 \pm 0.05$
PMT Box Connector and Fiber	$1.18 \pm 0.04$
Photosensor Efficiency	$1.4 \pm 0.2$
Fiber Diameter	$0.83 \pm 0.3$
Total	$1.8 \pm 0.3$

350 cm, chosen to be longer\* than the longest POD fiber. This fiber travels to a dark box containing a multi-anode PMT (a testbeam detector box from the MINOS experiment) of a known quantum efficiency and gain. The WLS fiber meets the dark box at a MINOS fiber connector, and there are short clear fibers inside the box to route the light to the PMT pixels. The multi-anode PMT is used for this test because a sufficient quantity of SiPM photosensors were not available. The readout electronics is based on the TriP ASIC, but uses the MINERvA front-end design rather than the T2K design, again because of component availability.

Cosmic rays at normal incidence in this test detector produce a charge measured in the electronics which can be related to the charge from single photoelectrons as determined from a low-level light injection system to excite the WLS fibers. The ratio of the sum of the charge measured in two adjacent scintillator bars struck by the same cosmic ray to the charge of a single photoelectron is measured to be  $13.9 \pm 0.6$ . To get the light expected from a muon in the center of the POD, a series of correction factors shown in Table 6.2 is applied resulting in a predicted light level of  $25 \pm 4$  photoelectrons in two scintillators for a cosmic ray muon. This convert to an expectation of  $7.6 \pm 1.2$  photoelectrons per MeV of energy deposited. The uncertainty is dominated by uncertainty in the SiPM photon detection efficiency.

Our fiber dopant choice was evaluated using measurements with rectangular extruded scintillator bars from MINOS which have the same composition as our proposed scintillator bars. The fibers used were identical 1.2 mm S-35 core Kuraray multi-clad fiber, doped with 175ppm Y-11 or Y-7, and fibers were read out with a CPTA MRS photosensor. The use of the MRS photosensor is key because the spectral response is different than the MA-PMT used for the MINERvA test. At short distances from the photosensor (less than 15cm), the measurements carried out with cosmic ray muons resulted in the light yield of  $\sim 22.0$  photoelectrons for rectangular scintillator. The same measurement for rectangular scintillator using 1.2 mm outer diameter Y7 WLS Kuraray 175 ppm doped fiber yields  $\sim 19.5$  photoelectrons. Because the Y-7 fiber also is observed to have a significantly shorter attenuation length than Y-11, 2.9 m compared to 4.6 m, the Y-11 performance will be significantly better in a  $\sim 2$  m bar.

## Future Prototypes

After the completion of the mechanical prototypes and light yield measurements, we will construct two fully functional PØDule prototypes using the materials called for in the final design. These prototypes will be tested for mechanical properties such as flexure under load, as well as for optical properties. As part of this effort, a data acquisition setup is being finalized at Stony Brook University for the testing of the POD functioning module prototypes and finalized-design modules during production. This setup will include adjustable number of fast ADC channels (up to 54 available) read out to computer via CAMAC crate interface. Additional electronics for providing the gate-generating logic for various trigger configurations is available for the tests of modules using cosmic ray.

\* In fact, this choice was made at a time when the WLS fibers were envisaged to exit the POD and travel some distance to be ganged together into multi-anode photomultiplier sensors.

Task	Beg.	End	2007	2008	2009
Design and Engineering	9/06	10/06	■		
PØDule Prototypes	10/06	5/07	■		
Water Target Prototypes	11/06	2/07	■		
Optical Calibration Prototype	12/06	4/07	■		
Prototype Photosensor Testing	1/07	2/07	■		
Slow Control Prototype	3/06	4/06	■		
POD Critical Design Review		5/07	●		
Initial Scintillator Prod.	5/07	2/08		■	
Optical Connectors	5/07	1/08		■	
Fiber Mirror and Polish	7/07	4/08		■	
Photosensor Testing	5/07	12/08		■	
Water Target Fab.	8/07	1/08		■	
PØDule Components	9/07	1/08		■	
Scintillating Plank Fab.	2/08	6/08		■	
PØDule Fab. and Q. C.	3/08	8/08		■	
POD Integration	9/08	1/09			■
Shipping To Japan	1/09	6/09			■
Installation	6/09	7/09			■
Commissioning	7/09	8/09			■
Neutrino Beam					■

Figure 6.25: The preliminary construction and installation schedule for the ND280 POD. This detector will be installed during the 2009 summer shutdown. Needs to be synchronized with the more detailed WBS based schedule.

## 6.4 Detector Construction Schedule

The current preliminary POD construction schedule is shown in Table 6.25. This schedule a summary based on a bottom up approach. We summarize several key dates below:

- Spring 2007, Critical Design Review
- January 1, 2009, POD shipped from SBU
- July 1, 2009, POD installation begins at ND280 hall, J-PARC
- August 28, 2009, commissioning completed.

The most significant milestone is the “Critical Design” review which takes place in Spring 2007, and is expected to be immediately followed by a DOE progress review.

## 6.5 Detector Installation/Commissioning

The full POD subsystem will be assembled before shipment to Japan. During this final assembly, the optical calibration system, front-end electronics, and Super-PØDule assemblies will be integrated into three units (the Upstream-ECal, the POD target module, and the Central ECal). During this period, we will perform initial detector commission tests, and verify that all subsystems are functioning correctly.

### 6.5.1 Detector Integration and Shake-Down Tests

As part of the POD integration, the full subsystem up to and including the back end electronics will be tested for an extended period before shipment to Japan for installation into the ND280 off-axis

detector. This “shake-down” test is expected to involve approximately one month of cosmic ray data. This will allow us to perform the initial pre-commissioning tests in a convenient laboratory environment and allow problems to be corrected. During this period, we will perform basic electronics commissioning tests, collect sufficient cosmic ray exposures to allow geometric alignment of the PØDules within each Super-PØDule, do a final verification of the light yield for each bar and WLS fiber, and do a preliminary energy calibration using cosmic ray data.

At the completion of the shake-down tests, the completed Super-PØDules will be packed fully assembled into a container for shipment to Japan.

## 6.5.2 Detector Installation and Commissioning

Detector installation will be divided into two phases. During the first phase, the various external support utilities will be installed in preparation for sub-detector installation. This phase is closely linked to the facility construction schedule and is being developed in conjunction with the ND280 Technical Board. The second phase is the installation of the fully assembled POD Super-PØDules into the ND280 Basket. The schedule for both of these phases is determined by the completion of the ND280 facility and the T2K neutrino beam schedule.

We expect that the assembled POD components will arrive at the T2K pre-installation site approximately three months before the scheduled installation.<sup>†</sup> While at the pre-installation site, we will run a full set of diagnostics to verify the equipment condition following shipping for the U.S. assembly site. In addition to specific tests of the optical calibration system and the electronics, these diagnostics will include a full energy calibration using cosmic ray data. Problems identified during this phase will be corrected before installation into the ND280 off-axis detector.

The POD design allows the detector to be lowered into the ND280 off-axis detector basket as three complete Super-PØDules. The individual Super-PØDules have total masses of significantly less than 10 t and will be lifted directly into the location within the off-axis detector. After preliminary installation, the precise location of the Super-PØDule will be set with respect to the basket using fine-tuning adjustments built into the detector mounts. Finally, the Super-PØDule locations will be optically surveyed. We expect to maintain 3 mm position tolerance in all three dimensions with respect to the ND280 detector coordinate system.

Following the mechanical installation of the POD, it will be connected to the various detector services, and the electronics will be connected to the RMM boards. During this phase, the detector will undergo final electronics commissioning, the water target will be filled with water, and the initial cosmic ray calibration data will be take.

## 6.6 Detector Calibration

Several calibrations are planned for the POD, beginning with pre-assembly calibration done before shipping components to Japan, and leading up to a program of in situ calibrations that will be performed on a regular basis during normal data collection.

### 6.6.1 Preinstallation Detector Calibrations

After the modules have been fully assembled, the energy response as a function of position will be scanned using a  $^{137}\text{Cs}$  source mounted on a moving scanning head. Measurements will be taken along each fiber so that the attenuation or any non-uniformity of scintillator-fiber coupling can be accurately determined. In addition, the scanner will make multiple measurements of the transverse position of

---

<sup>†</sup> A specific installation preparation site has not been identified. It will be preferable if this site is located at J-PARC in Tokai; however, much of the preparation could also take place at KEK

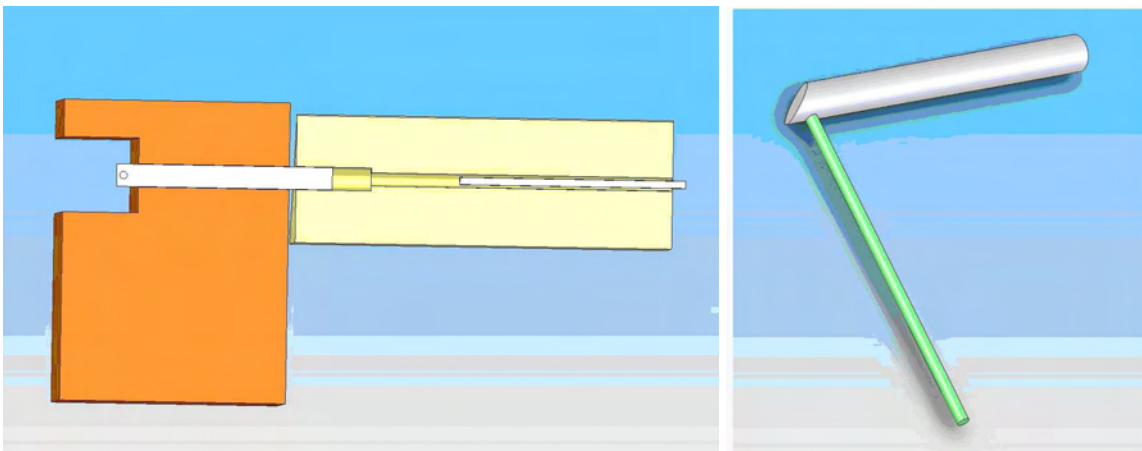


Figure 6.26: A cutaway view of the 3-mm diameter molded acrylic light-guide passing through the PØDule frame into the scintillator bar (left); and the optical fiber glued into the light-guide which is mirrored on the outside (right).

each bar. These measurements in turn will provide a precise determination of the position of each bar in the assembled PØDule.

### 6.6.2 Optical Calibration System

The primary purpose of the optical calibration system is to map and monitor the silicon photosensor gain. The response of the silicon photosensors becomes non-linear at light levels that approach the total number of sub-pixels (which has not yet been determined) so a gain curve for each sensor should be determined and checked periodically. The photosensors can also experience short-term gain drifts due to their sensitivity to small changes in temperature and bias voltage. The light injection system will also provide a quick and thorough check to ensure that no fibers or interfaces are broken.

The modest energy resolution requirements for POD and the stable temperature conditions enable us to use a relatively simple optical calibration system to calibrate and monitor the stability of the detector. We have chosen a scheme based on that developed for the MINOS experiment calibration system [3] A pulsed ultraviolet (UV) LED light source is used to excite the WLS fiber; the LED intensity is monitored by a PIN diode [4]. This scheme is a cost effective solution that provides the necessary dynamic range and stability for our application.

Since the POD scintillator is read out only at one end, a relatively simple optical fiber distribution system can be used to deliver the light pulse to each bar. We envision using one LED to illuminate a bundle of 32 clear optical fibers: one fiber is routed to a PIN photodiode to monitor the LED output on a pulse-by-pulse basis, the remaining 31 are distributed to molded light-guides that penetrate the PØDule frame to deliver the pulse to individual bars, as shown in Figure 6.26. The light intensity uniformity in each fiber will be investigated during the development stage of this system. There will be four such bundles for each PØDule plane (eight per PØDule). The routing of the fibers will ensure that for each calibration pulse no more than one-quarter of the front-end board channels will be energized. For each 40-plane PØDule there will be eight fiber bundles per PØDule (four per side) for a total of 320 LED/fiber bundles.

### 6.6.3 Cosmic Ray Calibrations

The energy responses of the scintillator bars are calibrated by cosmic ray muons. This is directly based on the K2K SciBar experience. There are several hundred of cosmic muons per second which cross the POD detector. We take cosmic muon data in between beam spills for calibrations. From

this sample, we select a well-tracked horizontal muon sample. The light yield measured by SiPMs is corrected for path length in each scintillator bar and light attenuation in the WLS fiber. We then obtain the calibration constant which converts the light yield (PE) to the energy deposited (MeV) of a minimum ionization particle. The stability of the light yield is also monitored by cosmic muons. In order to monitor a 1% level stability, we need 100,000 events per channel. We monitor this level stability week by week. The relative timing information is also calibrated. The timing information is critical to distinguish the signal from the incoming background particles.

The scintillator bar alignment is necessary for the correct track reconstruction. Using cosmic muons, the actual placement is determined. The accuracy of the scintillator positions is a combination of the accuracy at assembly and the stability of their locations. We measure the alignment continuously during the experiment.

# Bibliography

- [1] Nakayama, S. *et al.*, Measurement of single  $\pi^0$  production in neutral current neutrino interactions with water by a 1.3-GeV wide band muon neutrino beam, *Phys. Lett.*, B619:255-262,2005
- [2] L. A. Ahrens *et al.* Measurement of neutrino-proton and antineutrino-proton elastic scattering *Phys. Rev D* **35**:785, 1987
- [3] P. Adamson and others, Unknown Title, *Nucl. Instr. Meth.*, a492:325,2002. Design later modified to use an ultraviolet LED to improve the linearity
- [4] Hamamatsu S5971

# Chapter 7

## SMRD(Side Muon Range Detector)

### 7.1 Introduction

The principal tasks for the side muon range detector (SMRD) are to (1) measure muon momenta and angle for CC-QE reactions to help determine the neutrino energy, (2) identify backgrounds from beam neutrino interactions in the iron yokes, and in the cavity walls surrounding the detector, and (3) trigger on through going cosmic ray muons for calibration purposes of the inner detector components.

One of the main goals of the ND280 detector is the measurement of the neutrino energy spectrum. For charged current quasi-elastic (CC-QE) processes the neutrino energy is closely related to the muon energy. The neutrino energy can be reconstructed for CC-QE events using the muon momentum and its scattering angle if the Fermi motion is ignored. A full spectral measurement of the neutrino beam must include muons with large angles relative to the neutrino beam direction. The ND280 detector (see Figure 1.1) will serve to measure CC-QE interactions. The active target mass is largely concentrated in the FGD and the POD, and the TPC will serve to measure muon momenta for forward muons. Muons which escape at large angles with respect to the beam cannot be measured by the TPC. However, these muons will intersect the iron yoke surrounding the entire detector, and therefore muon momenta can be inferred from the range by instrumenting the iron at various depths. A high detection efficiency of the SMRD emerges as a natural requirement. In addition, the direction of muons can be determined if the SMRD modules are capable to provide position information. We have performed a MC study to show the muon distributions across the various detector components. Muon vertices for muons originating from CC reactions are distributed throughout the FGD and POD regions. Although precise numerical results depend on the precise assumptions about detector dimensions and fiducial volume, the following results can safely be used to define the average required SMRD performance.

The total fraction of muons from CC-QE reactions that is expected to intersect the SMRD amounts to about 40%. For CC non-QE reactions about 15% of all muons are expected to intersect the SMRD.

In addition to measuring muons which would otherwise escape unseen from the inner detectors the SMRD will also help to reduce the systematic uncertainties in the muon detection efficiency in the momentum range around 500 MeV/c. Monte Carlo studies indicate that the mean momentum of the muons that would have to be ranged out in the SMRD is on the order of 400 MeV/c. The muon momentum distribution for CC-QE interactions that hit the SMRD is shown in Figure 7.1. The muon momenta are shown for the vertex. The vast majority of large angle muons, namely 91% of all muons not escaping in the forward direction (e.g.  $\cos\theta < 0.8$ ) have momenta of less than 600 MeV/c. Figure 7.2 shows an average energy slant depth relation for muons which were sampled from a flat angular distribution and an energy spectrum from 0 to 1 GeV which has been weighted according to figure 7.1 in order to account for a more realistic energy and angular distribution. The slight rollover at muon energies around 1 GeV is due to the low flux for energies above 1 GeV. As can be seen in Figure 7.2 muons with energies less than 600 MeV will range out within less than 35 cm of iron. Since

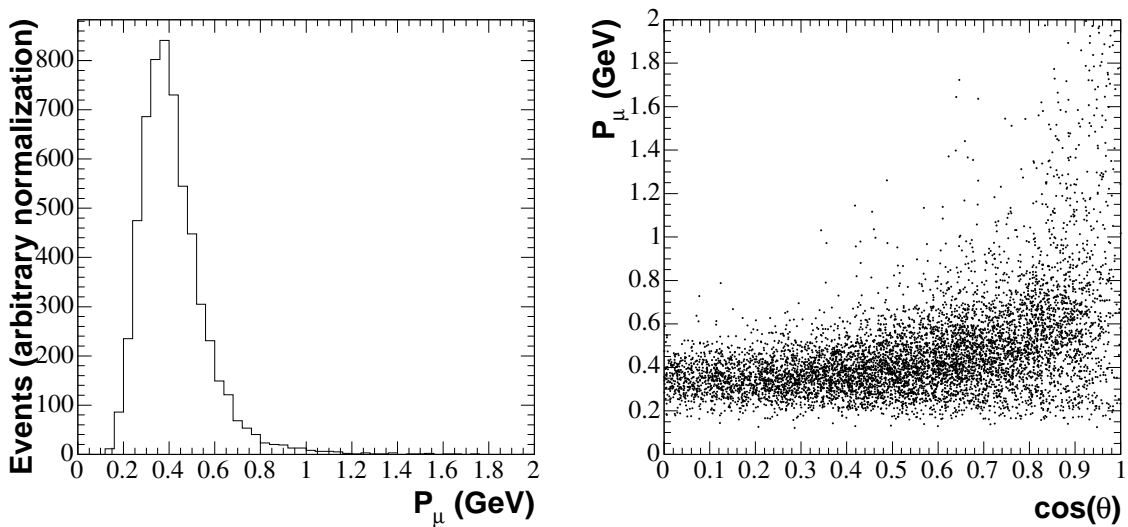


Figure 7.1: Left plot: muon momentum at vertex for CC-QE muons reaching the SMRD with  $\cos \theta < 0.8$ . Right plot: muon momentum at vertex for CC-QE muons reaching the SMRD versus  $|\cos \theta|$ .

$P_{\mu}^{max}$ (GeV)	$f$ (%)	Range (cm)	Layer
0.5	79	24	5
0.6	91	31	6
0.7	96	37	7
0.8	98	44	9
0.9	99	51	10
1.0	99	57	12
1.1	100	65	13

Table 7.1: Maximum detected muon momentum and corresponding fraction  $f$  of ranged out muons originating from CC-QE reactions with  $|\cos \theta| < 0.8$ . The penetration depth in iron and the corresponding number of layers in the SMRD are specified in the two right-hand columns. A realistic angular and energy distribution was used to calculate the fraction.

the iron plates in the MAGNET yokes (Section 3) are 4.8 cm thick it would be sufficient to instrument 6 to 7 radial layers in order to completely range out 95% of all muons that are not escaping in the forward direction (e.g. 95% of muons with  $\cos \theta < 0.8$ ). Table 7.1 lists the range of muons in iron and the corresponding number of layers as functions of energy, along with the fraction of muons that is represented. First energy resolution estimates from a crude GEANT 3 based Monte Carlo study are shown in Figure 7.3. This Monte Carlo assumed a set of 5 cm thick parallel iron plates onto which a sample of 200 MeV to 1 GeV muons impinge at angles in the range from 0 to 90°. The study indicates that a muon energy resolution of less than 10% can be achieved. As expected, the energy resolution is best for muons emitted at large angles (e.g. perpendicular to the beam direction) and worsens for muons emitted at smaller angles with respect to the beam direction.

In order for the ND280 detector to reliably identify CC-QE interactions and identify background events originating from the cavity and the iron yokes themselves, the SMRD is required to identify minimum ionizing particles (MIP) with very good efficiency. Hence, the active detector medium has to enclose the inner detectors hermetically and the medium has to provide high light yield across the entire sensitive area.

The SMRD will also serve to identify backgrounds entering the detector from outside, and secondary particles from beam neutrino interactions in the iron of the magnet yokes.

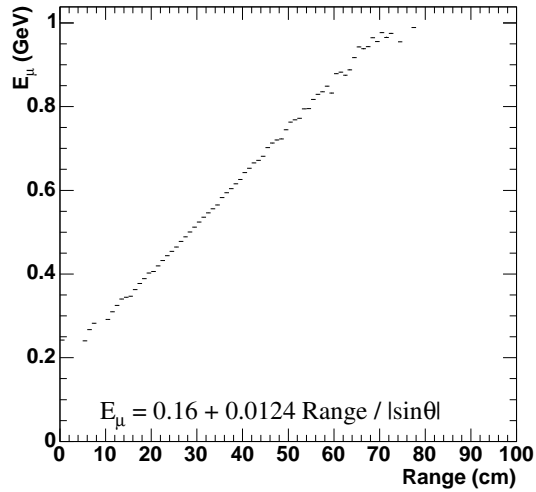


Figure 7.2: Relation between muon energy and range in iron as seen in data from Monte Carlo study [1].

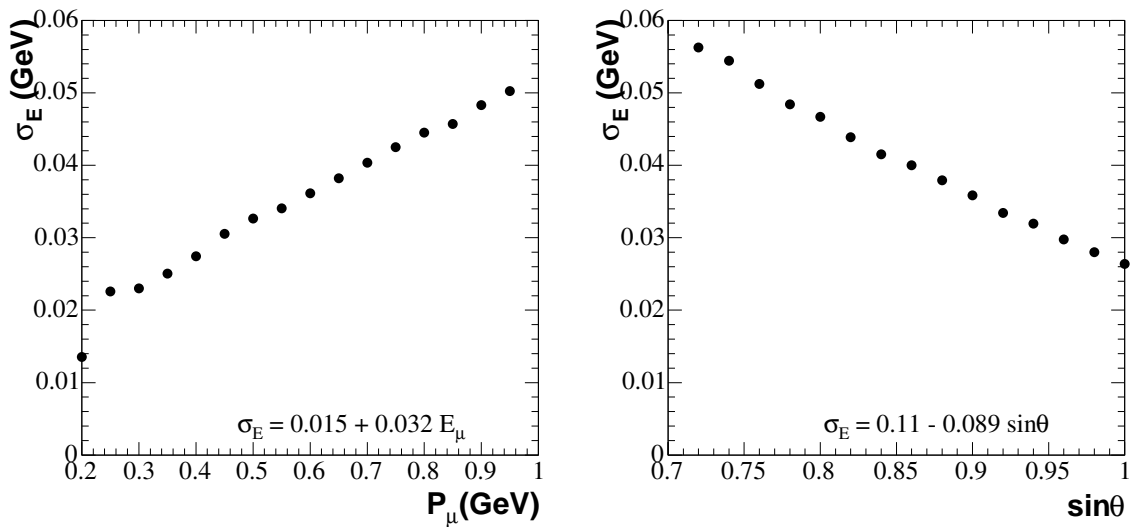


Figure 7.3: The muon energy resolution as function of muon momentum (left) and as a function of angle with respect to the beam (right) [1].

Last but not least the SMRD will provide a trigger signal in response to through going vertical and inclined cosmic ray muons. These muons are an invaluable calibration source for the inner detectors as they provide sample tracks that are very similar in nature to muons that are created in beam neutrino interactions.

Work on more refined Monte Carlo simulations is in progress. The current studies include a more accurate implementation of all the ND280 detector components, in terms of geometry and materials, as well as the magnetic field. Modifications to the current baseline distribution of detector modules in the gaps of the yokes is conceivable and will depend on the results of this more comprehensive simulation study.

## 7.2 Detector design and specification

The iron yoke consists of 16 C-shaped elements. One of these C-elements is shown in Figure 3.2. Each C is made of sixteen 48 mm thick iron plates, with 17 mm air gaps between the plates, and is segmented in 12 azimuthal sections. To build the SMRD, the air gaps will be equipped with particle detectors. The horizontally and vertically oriented gaps have slightly different dimensions;  $876 \times 700 \times 17 \text{ mm}^3$  and  $876 \times 910 \times 17 \text{ mm}^3$  for horizontal and vertical gaps, respectively. The corner gaps have a variety of different sizes with the smallest gaps closest to the beam and the largest gaps furthest away from the beam. In the following description of the SMRD the corner gaps will be neglected since we do not anticipate to instrument them.

### 7.2.1 Layout

The detector layout description is divided into two categories. The first describes the distribution of the individual SMRD modules amongst the available gaps in all of the 16 yokes. Secondly the layout of the individual SMRD modules which populate the gaps in the yokes is described. The detector layout optimization is accordingly split into two tasks which are pursued in parallel. These tasks are the design of individual SMRD modules which will occupy the gaps in the magnet yokes, and the question of how to best distribute the SMRD modules in the available magnet gaps under consideration of physics capability and cost of the SMRD.

#### SMRD Module Distribution

Based on an early simulation study 6 radial layers of active material in successive gaps starting from the inside out would be required to range out 95% of all CC-QE muons. In order to range out the remaining 5% of CC-QE muons with equal sensitivity in energy resolution an additional 5 radial layers would be required. Since the associated increase in cost for these additional layers cannot be justified 6 radial layers along the entire length of the detector have been adopted as a baseline design for the SMRD. More detailed simulation studies are currently in progress to optimize the layout of the SMRD detector.

#### SMRD Module Design

Individual modules have been optimized for high detection efficiency, good light yield, stability, and reliability. At the same time a design was chosen to minimize the number of photon sensors and electrical channels.

The size of a basic SMRD module is determined by the size of the gaps in the yoke. In order to achieve good coverage and increase the detection efficiency of laterally escaping muons it is desirable to make the active area in each gap as large as possible. Each SMRD module will consist of 4 extruded slabs of scintillators for horizontal gaps, and 5 slabs for vertical ones. The dimensions of each scintillator slab are  $870 \times 170 \times 10 \text{ mm}^3$  and  $870 \times 180 \times 10 \text{ mm}^3$  for the horizontal

and vertical gaps, respectively. The scintillators which will have an immersed S-shaped wavelength shifting (WLS) fiber will be described in detail in section 7.2.2. In this section an overview of the modules is provided. The scintillators are surrounded by a robust aluminium frame which will provide mechanical stability, and represents the medium into which optical connectors and photo-sensors can be implemented to read out the WLS fibers. Figure 7.4 shows the design of the frame along with 4 scintillator slabs. The large faces of each module will be covered with a thin aluminium sheet such

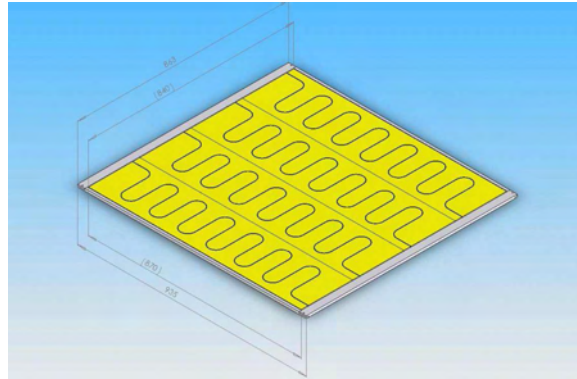


Figure 7.4: Four scintillator bars with immersed S-shaped WLS fiber are grouped together to form one SMRD module. The scintillators are surrounded by a frame which forms the back bone of a light tight box.

that a light tight dark box is formed that also protects the scintillators from humidity. Each WLS fiber will be coupled to and read out by two MRS APDs by means of optical connectors at both ends.

### SMRD Module Distribution

Based on the previously described simulations 6 radial layers of active material in successive gaps starting from the inside out would be sufficient to range out 95% of all CC-QE muons. In order to range out the remaining 5% of CC-QE muons with equal sensitivity in energy resolution would require an additional 5 radial layers and constitute a large cost. Hence, 6 radial layers along the entire length of the detector have been adopted as a baseline design for the SMRD.

More simulation studies are currently in progress to optimize the layout of the SMRD detector. Optimization studies need to be performed how to best distribute individual SMRD modules amongst the available gaps and what the total number of required SMRD modules should be.

## 7.2.2 Scintillator and WLS fiber detectors

The active component of the SMRD will consist of slabs of 7 mm thick extruded plastic scintillator with a white chemical reflector etched to all outer surfaces. The purpose of the chemical reflector is to enhance the light yield. A 4 mm deep S-shape groove will be machined into each scintillator slab to allow the insertion of a WLS fiber of 1mm diameter. Figure 7.5 shows a prototype scintillator slab with a S-shaped WLS fiber.

### Scintillator Production

It is planned that Uniplast, a company in Vladimir, Russia will provide the scintillator for the SMRD. This company has a good track record in that it has previously manufactured extruded scintillators for particle physics experiments. In particular, the scintillators for calorimeters in PHENIX, HERA-B, LHCb [4], and E949 at BNL [3] were produced by the same company. Figure 7.6 shows the scintillator response as function of time for a three year period. Less than 4% degradation in light yield was observed for the measurement period.

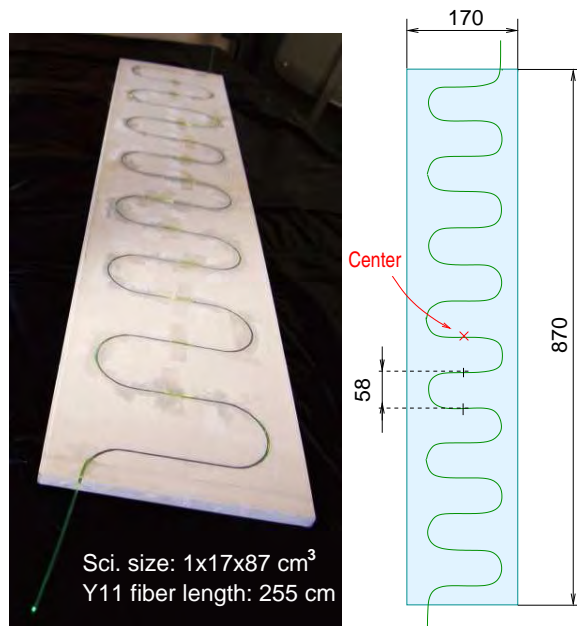


Figure 7.5: Prototype scintillator with chemical reflector and machined S-shape groove with an immersed WLS fiber. Left panel: photograph; right panel: schematic view.

The attenuation length of extruded polystyrene scintillator for light was measured to be about 10 cm. Hence, WLS fibers are required to efficiently transport the light out of the scintillator and into the photo-sensors.

The WLS fiber serves to guide the light out of the scintillator into the photon sensors. The absorption length of scintillation light inside 7 mm thick extruded scintillator is on the order of several centimeters which determines the maximum distance between the WLS fiber and any location on the scintillator slab. The light yield can be enhanced if the scintillator surface is etched by a chemical agent that produces a micropore deposit over the plastic surface. Following this procedure a diffuse film is fixed to the scintillator surface using a settling tank. The thickness of the deposit (30-100  $\mu\text{m}$ ) depends on the etching time. The advantage of this approach over the commonly used white diffuse papers is an almost ideal contact of the reflector with the scintillator. Details can be found in Ref. [12].

We anticipate to employ a single WLS fiber embedded in a serpentine shaped (S-shape) groove. Such a shape allows the fiber to collect the scintillation light over the whole surface of a scintillator slab keeping the maximum distance between fiber and any given position on the scintillator short. At the same time the number of required readout channels is kept to an absolute minimum. We plan to use 1 mm diameter Kuraray Y11, double clad, S-type fiber which is relatively flexible and hence suitable for insertion into the S-shaped groove. According to the manufacturer and our own experimental experience bending radii larger than 10 mm do not represent a problem for this type of fiber. Hence, the anticipated bending radius of 29 mm represents a safe bending range. A single fiber has the great advantage of requiring fewer readout sensors when compared to a multi-fiber design. Each fiber will be read out on both sides to provide higher light yield and also to allow relative signal arriving time measurements. The latter can be translated into a position measurement of the through going particle in the direction along the fiber.

The detector prototypes were manufactured using an extrusion technique developed at the Uniplast Factory, Vladimir, Russia. A few scintillator slabs of  $1 \times 17 \times 87 \text{ cm}^3$  with a S-shaped groove of 3 mm depth were manufactured. The width of a groove is about 1.1-1.2 mm to allow the insertion of a WLS fiber of 1mm diameter. The half-period of the S-shape groove is 58 mm, as shown in Figure 7.5. A 2.55 m long multi-clad S-type Kuraray Y11(200) WLS fiber of 1 mm diameter was embedded into the groove with optical grease and both ends are attached to MRS photodiodes.

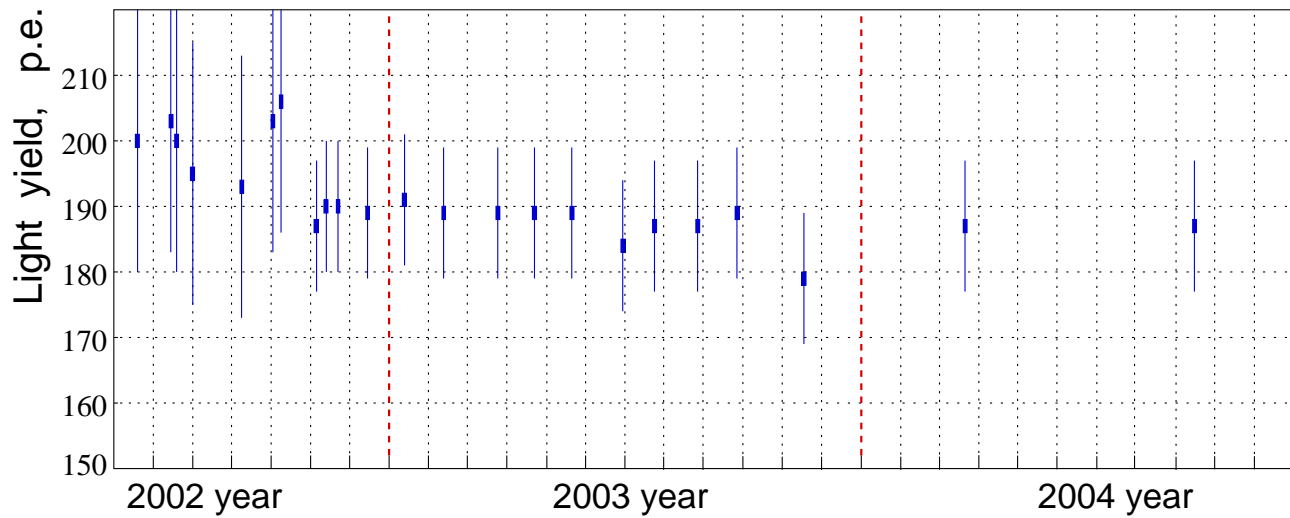


Figure 7.6: The MIP light yield as a function of calendar year for a prototype made of 10 extruded scintillator slabs with embedded WLS fibers. The prototype for this test measurement has parallel WLS fibers.

### Scintillator Performance

The assembled module was tested with cosmic muons. A light yield (l.y.) of 16.4 p.e. was obtained for MIP's in the center and for summed signal from both photodiodes. A time resolution of  $\sigma = 1.75$  ns was obtained for MIP's which passed through the central part of the slab.

### Beam tests of the SMRD prototype

The response of a single prototype scintillator slab with an immersed S-shape wavelength shifting fiber was tested at the KEK PS facility with a 1.4 GeV/c proton and positive pion beam [13]. Only pions were selected for analysis as their response is close to that expected from MIP's in the T2K experiment. The ambient temperature drifted between 15–18°C during the beam test. Table 7.2 displays results of the light yield measurements for a prototype scintillator with an embedded S-shaped WLS fiber in response to traversing MIPs. The beam spot spreads beyond the scintillator area near the edges at  $y = \pm 80$  mm causing the small l.y. values. If the edges are ignored, the light output over the S-counter (sum of both end signals) varies from 12 to 20 p.e./MIP. The largest l.y. is measured at the ends, close to either of the two MRS photodiodes. Light yield measurements with a reduced beam size of  $0.5 \times 0.5$  cm<sup>2</sup> across the scintillator slab indicate light yield variations of order 20% with a maximum l.y. observed in points where the beam crosses the fiber.

**Detection Efficiency:** Table 7.3 shows the detection efficiency of the same prototype scintillator in response to throughgoing MIPs. The average statistics in each location is about 2000 events. The signal detection threshold for each of the two photon sensors was set to 2.5 p.e. The detection efficiency is close to 100 % except for the edge area where a part of the beam missed the counter due to some misalignment between the beam counters and the tested detector. For a higher threshold of 4.5 p.e. the MIP detection efficiency is still greater than 98%. We can conclude that the l.y. of more than 12 p.e. (sum of both ends) satisfies the requirement for the SMRD counter to provide a detection efficiency better than 99% for a MIP. If we require each MRS photodiode signal at both ends to exceed 0.5 p.e. (coincidence criterion), the MIP detection efficiency is found to be about 99.5%.

In summary, the light yield was found to be  $15 \pm 2$  photo electrons /MIP and the average detection efficiency at a threshold of 0.5 photo electrons was found to be 99.5%. At a higher threshold of 5 photo electrons the average detection efficiency decreases to  $\sim 98\%$ .

$y$ , mm	-80	-60	-40	-20	0	20	40	60	80
$x$ , mm									
-406	6.3	11.9	13.2	16.0	17.8	18.6	18.7	18.8	13.8
-319	10.2	11.6	14.7	15.7	15.9	16.4	17.3	16.7	13.2
-200	10.2	12.7	14.3	16.0	15.5	16.6	18.2	18.7	15.0
-87	10.4	11.7	13.0	15.0	15.0	15.4	16.3	14.5	11.0
-30	8.8	14.4	16.4	16.2	15.3	14.6	13.8	12.9	10.9
0	11.0	12.9	14.8	14.3	15.3	16.2	14.9	13.9	11.7
30	9.3	11.8	12.6	14.4	14.8	15.8	16.8	16.0	13.0
87	12.3	14.4	15.1	14.6	14.2	14.7	14.2	12.9	11.8
200	11.0	15.2	16.0	15.9	15.6	15.5	13.7	12.9	11.3
319	12.6	16.1	17.4	16.3	15.5	15.2	14.5	12.3	10.4
406	11.8	12.9	17.9	19.9	20.0	19.1	19.1	16.2	11.9

Table 7.2: Light yield in photo electrons for a MIP (p.e./MIP) as function of position on the scintillator and for a detection threshold of 0.5 p.e. The light yield is the sum of the signals from both ends of the WLS fiber.

$y$ , mm	-80	-60	-40	-20	0	20	40	60	80
$x$ , mm									
-406	0.660	0.995	0.999	1.000	1.000	0.999	1.000	1.000	0.999
-319	0.750	0.999	0.999	0.999	0.999	0.999	0.999	0.998	1.000
-200	0.788	0.998	0.999	0.999	1.000	1.000	0.999	0.999	1.000
-87	0.839	0.996	0.998	0.999	1.000	0.999	1.000	0.999	0.995
-30	0.886	0.999	0.999	1.000	1.000	0.999	1.000	0.997	0.998
0	0.985	0.998	0.997	0.998	0.996	0.998	0.999	0.999	0.998
30	0.918	0.996	0.998	0.999	1.000	1.000	1.000	0.999	0.998
87	0.989	0.997	1.000	0.999	0.999	1.000	0.998	0.999	0.996
200	0.995	0.998	1.000	0.999	1.000	1.000	1.000	0.999	0.994
319	0.999	0.998	1.000	1.000	1.000	1.000	1.000	0.998	0.994
406	0.998	0.999	1.000	1.000	1.000	0.999	1.000	1.000	0.984

Table 7.3: Detection efficiency as function of position on the S-counter/scintillator and for a detection threshold of 2.5 p.e.

**Time and spatial resolution of the S-counter:** Double ended readout of the WLS fiber does not only provide a higher light yield but also provides the opportunity to perform signal timing studies based on the relative arrival times of the two signals.

The time resolution was measured with the discriminator thresholds set to a level of 0.5 p.e. for each MRS photodiode. The dependence of the time resolution on the light yield is presented in Fig. 7.7. The time resolution depends on photon statistics and is proportional to  $1/\sqrt{N_{p.e.}}$ . At a typical l.y. of 15 p.e./MIP  $\sigma_t = 1.75$  ns is obtained. The time resolution of the S-counter is mainly determined by the slow decay time of the Y11 fiber which amounts to  $\sim 7$  ns.

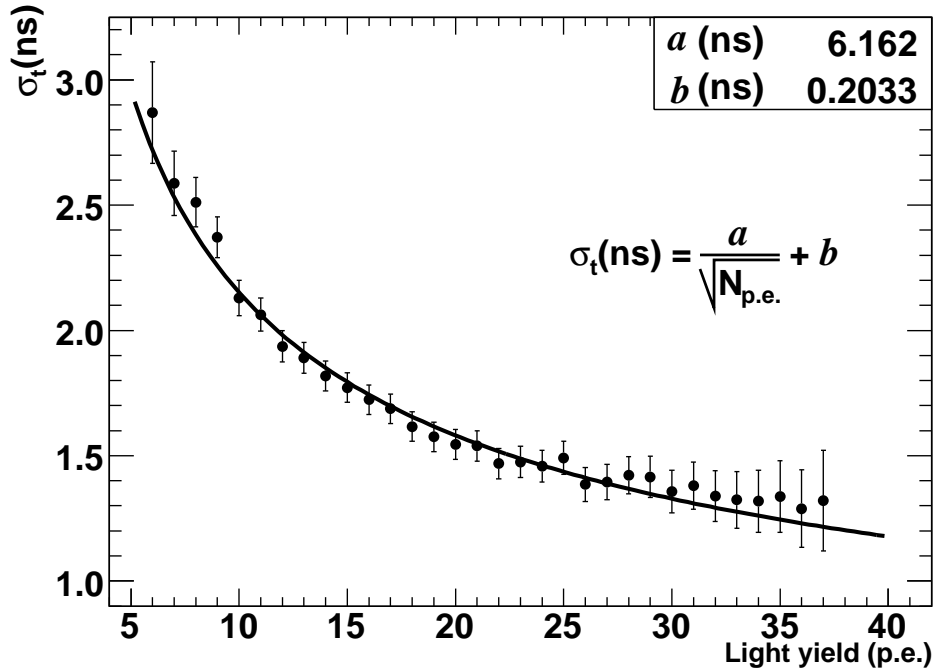


Figure 7.7: Time resolution vs the light yield in a center of the S-counter.

Green light travels along a WLS fiber at a speed of 17 cm/ns while the signal propagates along the counter at a smaller speed of 7.4 cm/ns because of the fiber routing. The time difference between signals from the left and right end allows to extract the coordinate of the light generating particle. A spatial resolution of  $\sigma_x = 13.4$  cm and 10.4 cm was obtained in the center and near both ends, respectively.

The spatial resolution can be improved by taking into account the light attenuation along a fiber. The asymmetry between the signal sizes from the left and right MRS photodiodes is sensitive to the hit position. The spatial resolution based on pulse sizes alone is poor due to large fluctuations in the light yield but the combination of both methods improves the spatial resolution by about 5%. Fig. 7.8 shows the spatial resolution obtained from timing, amplitude asymmetry and the combination of both. The spatial resolution is obtained to be 12.4 cm in the center and 9.9 cm at both ends.

### 7.2.3 Optical Connectors and Mechanical Module

Each fiber end will be coupled to a single photon sensor whose sensitive area matches the 1 mm diameter of the fiber closely. An accurate alignment of a fiber end and the photon sensor active area are crucial in order not to lose any light. Excellent and reliable optical couplings between the fiber

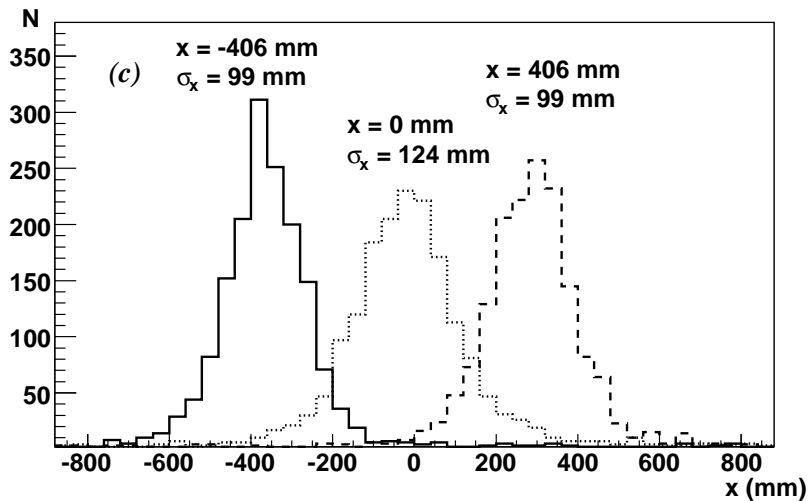
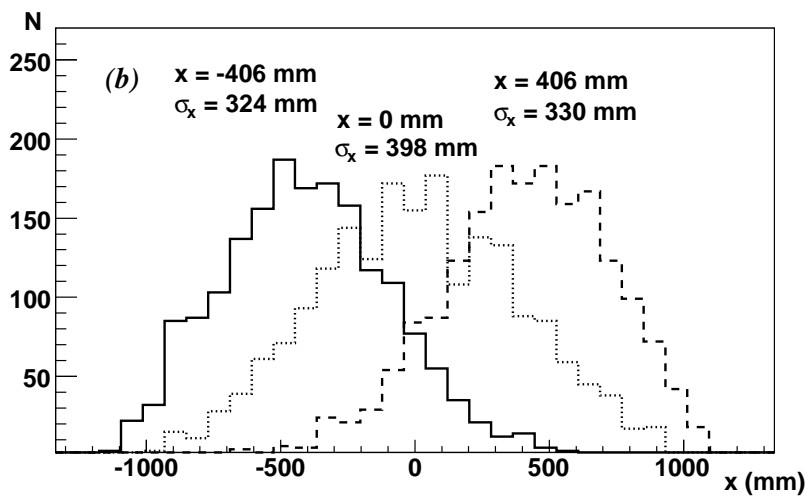
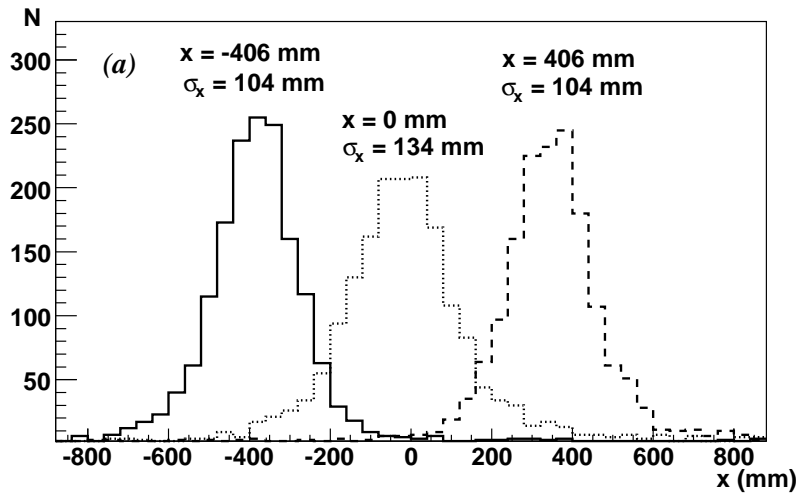


Figure 7.8: The spatial resolution along the S-counter at 3 beam positions: (a) the coordinate  $x$  is obtained from timing; (b) the coordinate  $x$  is obtained from the asymmetry between light yields at the two counter ends; (c) the combined position resolution.

ends and the photon sensors are mandatory. The connection must be shielded from any external light and allow faulty photon sensors to be replaced without causing damage to the fiber. Custom made optical connectors have been designed and a conceptual prototype has been produced. Figure 7.9 shows the design of the optical connector for the SMRD. The connector consists of a 3.5 mm diameter ferrule and a snap-on housing with a 6 mm outer diameter. The housing is designed to fit the photo-sensor package and contains a foam spring to ensure good contact between the fiber end and the epoxy layer on the front-face of the photo-sensor.

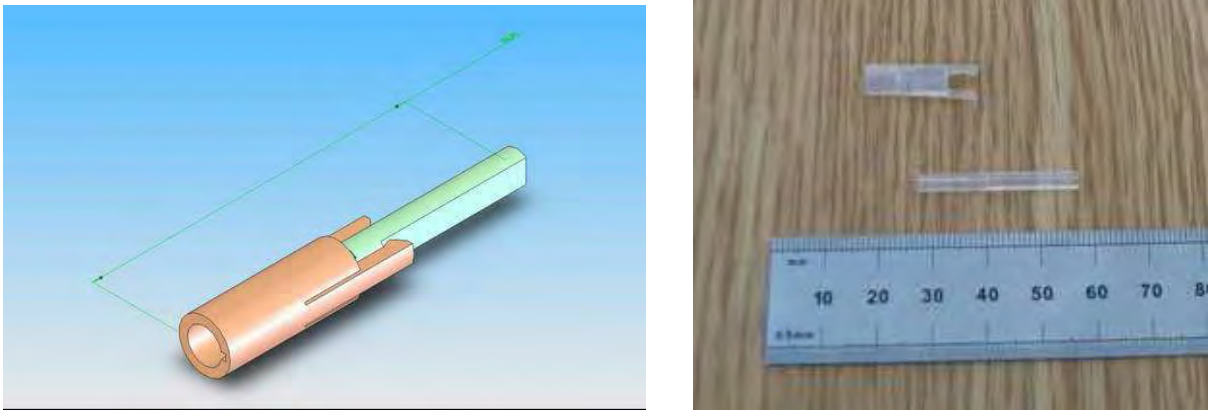


Figure 7.9: Prototype design of the optical connector for the SMRD modules.

**Mechanical Module:** Four (five for vertical modules) scintillator slabs will be grouped together side by side to form one SMRD module. The scintillators will be surrounded by an aluminium frame which consists of 4 bars of about 20 mm depth. The large faces of the 4-scintillator will be covered with a thin aluminium sheet which is slightly recessed into the frame in order to prevent peeling of the aluminium skin during installation of the modules into the magnet gaps. The scintillators and the frame are glued together to form a structurally sound unit. Hysol 3145 (cat 3163) has been chosen as the adhesive because of its compatibility with the scintillator plastics and long work time. Hysol 3145 has been used successfully to glue prototype modules and no adverse effects have been observed to date.

The previously described optical connectors will be embedded into the front panels of the aluminium frame. Figure 7.10 shows a cut-out view of the front bar with a recess for the optical connector. The ferrule is embedded into the scintillator and the front bar and thereby protects the fiber

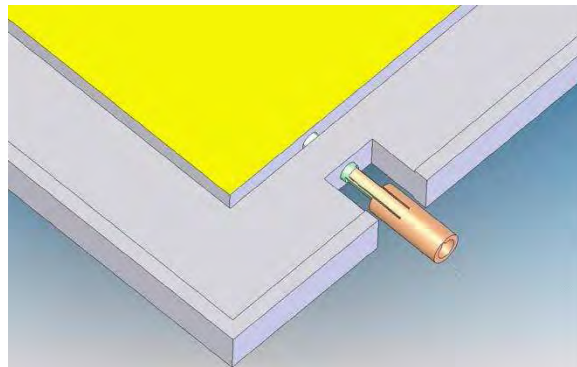


Figure 7.10: Shown is a corner of an SMRD module with the scintillator in yellow and the module frame in grey. The ferrule links the scintillator with the front bar and is barely visible. The snap on housing which will contain the photo-sensor is recessed into the front bar.

as it exits the scintillator and penetrates the module front bar. The ferrule also serves to align the scintillator slabs within the frame and in particular relative to the front bar.

## 7.2.4 Photon Sensor + Electronics

The photon sensors for the SMRD are described in detail in section 9. For the SMRD a total of about 7000 photon sensors, including spares is needed. It is planned to use MRS-APDs from CPTA, Moscow, Russia.

Similar to the photon sensors the electronics of the SMRD will be the same as the one used for the POD, the ECal, and INGRID. It is described in section 10. All the boards will have the functionality to provide a cosmic ray trigger based on coincidences between channels on one card and coincidences between multiple cards serving detector modules located across the detector. Such a cosmic ray trigger will be used to provide a well defined muon track to serve as calibration signal for the inner detectors.

## 7.3 Detector Technology R&D

The SMRD uses well established technology which has been proven to work in numerous experiments. Only exception is the technology choice for the photon sensors which are a new device. The photon sensors and the R&D status of these devices is described in section 9.

Full scale SMRD prototype modules have been built and tested. The performance was found to satisfy the design criteria and only minor modifications of the design are required. In addition, a set of passive prototype modules has been build to test the assembly procedure and the mechanical staility of the module. This passive prototype module has also been used for installation scheme testing in a yoke mock-up test stand which simulates distorted gap dimensions and misalignments.

**WLS fiber** Measurements are on-going to study and compare the aging characteristics of thermally bent fibers with fibers which are formed into a S-shape at room temperature. Tests are being performed on 1 mm diameter Kurary Y11, double clad, S type fiber. Thermally bend fibers show an initial 15% drop in light yield measurements compared to a straight fiber but no further decrease has been observed to date. Thermally pre-bend fibers would facilitate easier module assembly.

### 7.3.1 Performance of SMRD Prototype modules

Three active and full-size SMRD prototype modules were built. One was constructed at LSU while the other two fully active prototypes were manufactured and tested at INR. Each module comprises 4 scintillator counters of the same design as the one characterized in the KEK beam. One of the prototype modules is shown in Figure 7.11. Fibers are fed out through ferrules which are glued into the scintillator slabs. The readout is implemented with MRS APD's. The assembled prototype module were tested for light tightness and no light leaks were observed. Successively, the module response to cosmic ray muons was studied. The light yield observed per cosmic mip was 14 p.e. , 19 p.e. and 21 p.e. in the first, second, and third module, respectively. The higher light yield in the second and third modules can be attributed to additional Tyvek wrapping of the scintillator modules.

## 7.4 Detector construction schedule

### 7.4.1 Schedule

On overview of the SMRD schedule is shown in Figure 7.12.



A more detailed schedule with start and ending dates of all sub-tasks is available online to all SMRD group members.

## 7.4.2 Quality Control

All detector components will be carefully tested before detector assembly, at intermediary assembly stages, after the module assembly is complete, and after arrival of the modules in Tokai before installation into the yokes. The tests include light injection into the WLS fibers with successive light leak monitoring, scanning of the scintillator slabs with a radioactive source, characterization of photosensors, light leak tests of the assembled modules, and a final x-y scanning of the module in response to a radioactive source. The required quality monitoring tools either exist already or are in preparation at this time.

## 7.5 Detector installation/commissioning

The SMRD installation scheme foresees to slide the individual modules into the gaps of the yokes after all 16 yokes have been installed in the detector pit and the surface building has been constructed. Insertion is anticipated from both, the up- and downstream sides. A pushrod which can be attached to individual modules has been designed and successfully tested on a yoke mock-up setup. The method requires good alignment of neighbouring gaps. Detailed measurements on all 16 steel yokes have been performed and an analysis of the collected data has been reported [14]. The measurements were performed with the yokes in a position rotated by 90deg with respect to their final orientation. A finite element calculation was performed to estimate additional sag of the yokes, which is planned to be confirmed with additional measurements in January 2007. Table 7.4 shows the number of problem slots for various assumed module thicknesses. A gap is labelled as problem slot if it cannot be populated with a SMRD module. Insertion of modules from the up- and downstream sides have been taken into account. The third column specifies the fraction of problem slots relative to the total number of slots in the six innermost layers of all 16 yokes. The analysis assumes that all 16 yokes

thickness (mm)	no. of problem gaps	fraction (%)
8	3	0.4
9	6	0.8
10	10	1.4
11	51	7
12	130	17

Table 7.4: Column two lists the number of problem slots for the module thicknesses indicated in column one. A gap is labelled as a problem slot if it cannot be populated with a module. Insertion from the up- and downstream sides were assumed. Column three specifies the fraction of problem slots relative to the six innermost layers in all 16 yokes.

are perfectly aligned with respect to reference planes A and B (see figure 7.13). An engineering evaluation of the achievable accuracy of the yoke setup at Tokai is anticipated. The above analysis assumes perfectly rigid SMRD modules. However, tests with the prototype module indicate some flex in the module. The flex is on the order of several millimeters and will help to bridge neighbouring gaps with poor alignment. Misalignments of up to 6 mm in opposite directions for the top and bottom sides of the gap transition did not present a problem for sliding the module through the transition in the test set-up. Figure 7.14 illustrates the installation scheme.

The drawer installation of the SMRD will allow access to each scintillator slab even after the start of the experiment, so that repairs and adjustments can be accomplished. A jamming device will assure

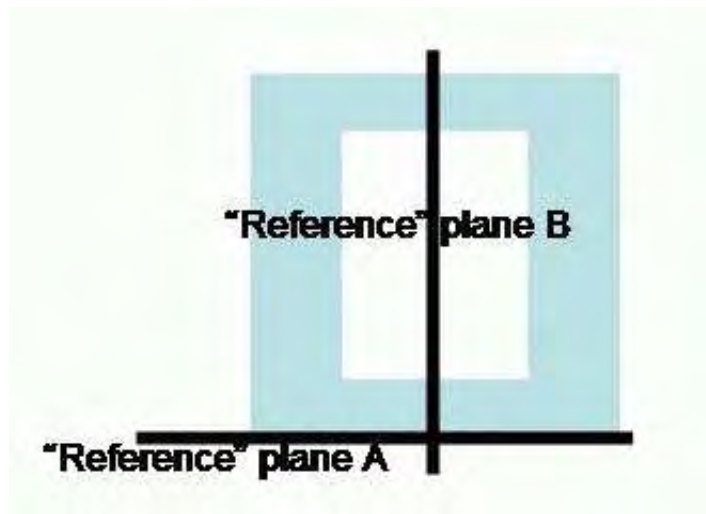


Figure 7.13: Shown are reference planes A and B with respect to which yoke measurements have been performed.

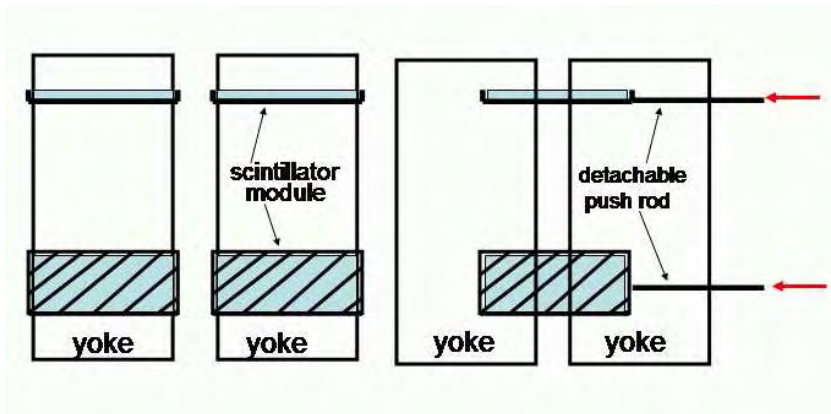


Figure 7.14: Illustration of the installation scheme which will allow deployment and retrieval of the scintillator slabs.

secure placement of the modules inside the gaps of the yokes. The signal and high voltage cables will be routed through the gaps between yokes to the front-end electronics which will be mounted on the back of each yoke.

## 7.6 Detector calibration

The primary purpose of the SMRD is to detect and range out laterally escaping muons. Since the energy loss of these muons is dominated by the iron layers an accurate measurement of the deposited energy within the SMRD scintillator modules is not required. Hence, the calibration requirements for the SMRD are rather loose.

A self calibration system is foreseen for the SMRD. The excellent photo electron resolution of the photon sensors allows to accurately determine the peak positions of the various photo electron peaks in any given ADC charge spectrum. Additionally, the separation between neighbouring photo electron peaks can be exploited for calibration purposes. Trigger on cosmic ray muons as well as random triggers outside of the beam spill window will provide the required ADC charge spectra at sufficiently high rate to allow frequent calibration of the detector and monitoring of the photo-sensor gain.

We estimate the rate of cosmic ray muons based on the intensity of vertical muons above 1 GeV

at sea level which is  $I \approx 1\text{cm}^2/\text{min}$  [11]. Given an active detector surface in the horizontal plane of  $87 \times 70 \times 8 \times 4\text{cm}^2$ , a total of 195,000 muons per minute, or 3,250 muons per second hit the detector. This constant flux of MIPs can be used to continuously monitor the response of the horizontally oriented scintillator slabs. If the position of individual cosmic muons can be derived accurately with the inner detector components, the attenuation of the WLS fibers can be measured and compared to measurements before installation. For the ECal a position resolution of a few centimeters is expected and should provide such a set of cosmic ray muons.

# Bibliography

- [1] F. Sanchez, Talk at the T2K280m meeting, October 7, 2004
- [2] N.Yershov *et al.* arXiv: physics/0410080
- [3] O. Mineev *et al.* arXiv: physics/0207033
- [4] Kudenko *et al.*, NIM A469 (2001) 340
- [5] Yu. Kudenko, private communication, Feb. 2005
- [6] ZEUS Experiment
- [7] Proceedings of the Symposium on 'Detector Research and Development for the Superconducting Super Collider', October 1990 ; editors: T. Dombeck, V. Kelly, G.P. Yost; World Scientific Publishing
- [8] P.Adamson *et al.*, hep-ex/0204021.
- [9] BaBar Collaboration, B. Aubert *et al.*, Nucl.Instrum.Meth.A 479 1, 2002.
- [10] The MINOS Technical Design Report
- [11] Particle Data Group, S. Eidelman *et al.*, Phys. Lett. B **592**, 1 (2004)
- [12] Yu.G. Kudenko *et al.*, Nucl. Instr. Meth. **A469** (2001) 340; O. Mineev *et al.*, Nucl. Instr. Meth. **A494** (2002) 362; N. Yershov *et al.*, Nucl. Instr. Meth. **A543** (2005) 454.
- [13] O. Mineev *et al.*, physics/0606037.
- [14] [www.nd280.org/SMRD/...](http://www.nd280.org/SMRD/)
- [15] NUANCE Neutrino Generator; <http://nuint.ps.uci.edu/nuance/>
- [16] GEANT 4; <http://geant4.web.cern.ch/geant4/>

# Chapter 8

## ECAL

### 8.1 Introduction

#### 8.1.1 Overview of ECAL Physics

The Electromagnetic Calorimeter comprises two sections. The Tracker ECAL (TECAL) surrounds the FGDs and TPCs. It detects, reconstructs, and identifies particles leaving the tracking volume. The POD ECAL (gamma / muon tagger) is a simpler device which helps to positively identify photons and muons escaping the POD.

Both ECAL sections tag interactions occurring outside the inner detectors, which produce event signatures that can resemble those of signal neutrino interactions in the fiducial volumes of the inner detectors.

In general, when considering neutrino interactions in the entire off-axis detector, a non-MIP energy deposit of a few hundred MeV can be expected to occur approximately every 4 beam bunches or so. This indicates that the number of background clusters that need to be disentangled from any one signal interaction will typically be less than two. The good cluster and MIP reconstruction capabilities of the ECALs, described in the following sections, will allow satisfactory background rejection to be performed.

#### 8.1.2 The Tracker ECAL

The main purpose of the Tracker ECAL is to aid the Tracker in fully reconstructing neutrino interactions in the FGDs. Fig. 8.1a shows that muon detection probability (combined geometrical acceptance and reconstruction efficiency) in the Tracker varies significantly around the peak beam momentum region, or equivalently the neutrino oscillation maximum. The TECAL geometrical coverage and its particle identification capability improve the reconstruction efficiency for CC-QE interactions, which is essential for the accurate measurement of the off-axis neutrino beam flux. In these plots, the momentum resolutions of tracks in the TPC are estimated using the approximate number of measurement points in the bending plane and the measurement resolution, according to the current design. Muons with track lengths of greater than 60cm, whose identity can be positively determined from their charge deposits in the TPC (see TPC chapter), and electrons with a relative momentum error of less than 10% are included in the “TPC” category. For much of the momentum range, the TECAL is able to positively identify muons and improve the energy measurement of electrons which do not satisfy these criteria.

The TECAL is also important for the energy measurement of electrons from beam  $\nu_e$ , especially for momenta above 1 GeV/c, where TPC momentum resolution deteriorates (Fig. 8.1c). The photon shower reconstruction capabilities of the Tracker ECAL have been chosen to allow it to point back from photons created from  $\pi^0$  decays, to measure their invariant mass and determine if they were produced in the FGDs. This method of observing  $\pi^0$  production is less efficient than that in the dedicated

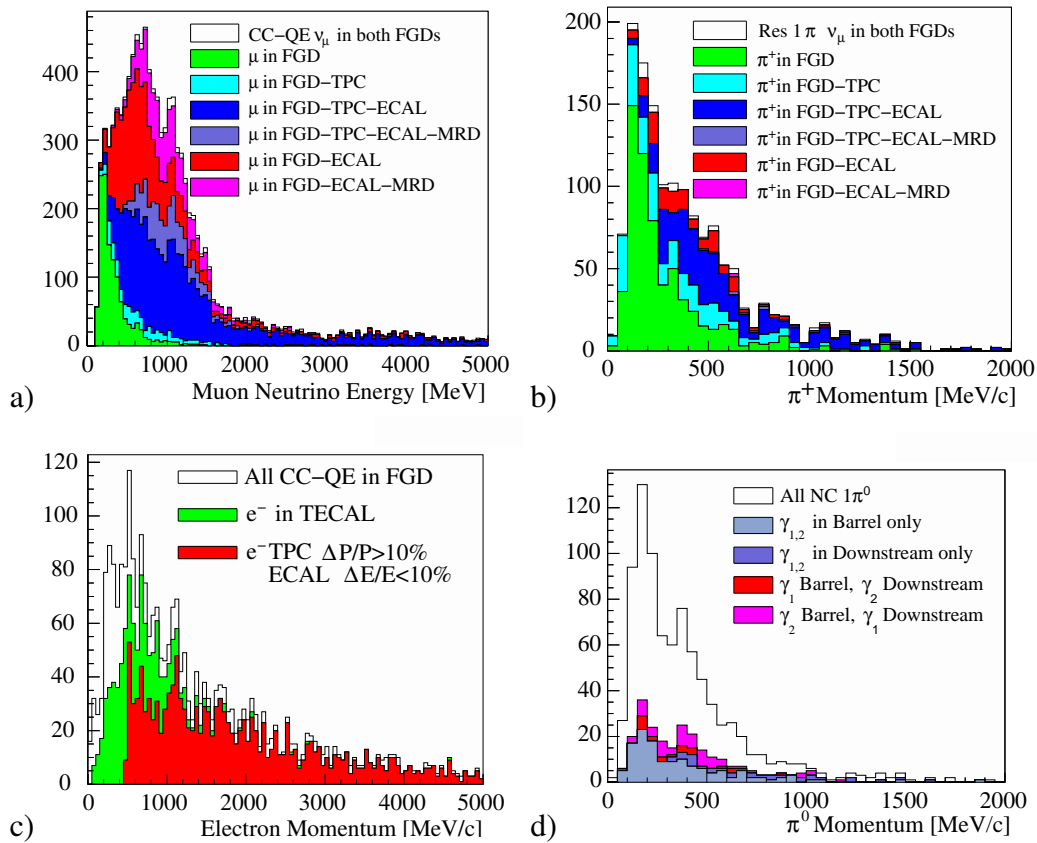


Figure 8.1: a) True neutrino energy distributions for CC-QE interactions for different outgoing muon path categories through the sub-detectors. Muon tracks shorter than 60cm in the active TPC regions are excluded from the “TPC” category, as they are difficult to positively identify. The TECAL will have good particle identification capabilities for many of these tracks. b) Similar to a), but for CC- $1\pi^+$  pion momentum distributions. c) True electron energy distributions from CC-QE  $\nu_e$  events for electrons detected in the Barrel and Downstream ECALs. The shaded regions indicate tracks which are expected to have relative momentum resolutions of worse than 10% (see text for details) in the TPCs, and for which the energy resolution in the ECAL is better than 10%. d)  $\pi^0$  momentum distributions from NC- $1\pi^0$  and coherent production, for different event reconstruction categories.

P0D, but the systematics are very different and it will provide a complementary means of making this difficult measurement of what is the most important background channel for the observation of  $\nu_e$  appearance at Super-K.

Table 8.1 summarises the statistics for neutrino interaction products entering the TECAL, as well as the fractions of muons, protons, and charged pions that stop inside its active volume.

Another physics role for the TECAL will be the measurement of CC-QE muon interactions in the detector itself. The ECALs have the widest lateral span of all the highly granular detectors, stretching almost twice the width and height of the FGD fiducial volumes. The large mass of the ECALs results in a high rate of interactions, and by positively identifying the outgoing muons (and high energy protons), this is expected to provide an additional handle which will help us understand the properties of the J-PARC neutrino beam. The effectiveness of the ECAL in making this measurement is currently under study.

### 8.1.3 Gamma/Muon Tagger (P0D ECAL)

The P0D functions by having layers of active scintillator detectors interspersed with thin sheets of lead which act to convert photons quickly, allowing the characteristic two-shower signature of  $\pi^0$

	Int./10 <sup>21</sup> POT/ton	TECAL	Reconstruction method
CC-QE $\nu_\mu$	65038 (0.38)		
CC-QE $\nu_\mu \mu^-$		0.82(0.21)	PID/(Range)
CC-QE $\nu_\mu$ proton		0.28(0.25)	PID
CC-Res1 $\pi$	30029		
CC-Res1 $\pi \mu^-$		0.79(0.37)	PID/(Range)
CC-Res1 $\pi \pi^+$		0.37(0.29)	(PID)
NC-Res1 $\pi^0$	7455	0.22	
NC-Res1 $\pi^0 \gamma_1$		0.55	Dir/PID/E
NC-Res1 $\pi^0 \gamma_2$		0.54	Dir/PID/E
CC-QE $\nu_e$	500		
CC-QE $\nu_e e^-$		0.78	PID/E
CC-QE $\nu_e$ proton		0.33(0.28)	PID

Table 8.1: ‘‘TECAL’’ column: Fractions of particles crossing (stopping in) the TECAL for various neutrino processes occurring in the FGD. Neutrino interactions are as given by the NEUT generator. Event reconstruction methods are : PID = cluster shape particle identification, Dir = direction reconstruction, Range = muon ranging, E = energy measurement.

decays to be reconstructed. These layers are perpendicular to the beam, to increase photon detection efficiency in the forward direction. This design leads to variations in photon showering behaviour in the direction transverse to the beam, and it is the role of the GM to tag photons which escape the sides of the POD. These POD photon showering efficiencies are shown in Figs. 8.2a and b, in which a large fraction of  $\pi^0$ s with one or both of the photons escaping the POD completely (peaks at (1,0), (0,1), and (1,1)). The first figure is of photons from  $\pi^0$ s from an inner region of the POD defined by  $|x|$  and  $|y| < 0.6\text{m}$ , while the second figure is for an outer region with  $|x|$  or  $|y| > 0.9\text{m}$ .

Counting over all  $\pi^0$ s produced in the ‘‘carbon’’ and ‘‘water’’ regions of the POD and without any further fiducial cut, we find that the probability that more than half of a photon’s energy escapes the POD is 34% per photon and the probability that a photon escapes completely the POD is 22% per photon. Losses are correlated for  $\pi^0$ s produced near the edges of the POD, leading to 7.5% of events where both photons escape completely (resonant single pion production, Nuance codes 6-8). This number is 5.6% for NC coherent and diffractive pion production (Nuance code 96).

These events constitute a significant fraction of the  $\pi^0$ s created in the POD, and the POD ECAL helps these to be identified, enhancing the determination of the fiducial volume and the counting of the  $\pi^0$ s originating in it.

The design of the POD with layers perpendicular to the neutrino beam also results in a significant fraction of muons from CC-QE interactions that escape laterally. The POD ECAL is designed to identify MIPs escaping the POD to allow these background events to be tagged.

## 8.2 Detector design and specification

The ECAL consists of lead-scintillator sandwich sampling calorimeter modules located around the ND280 inner detectors on all four sides and at the downstream end of the magnet.

The tracking detectors (FGDs, TPCs) are surrounded on four sides by Tracker ECAL modules, made of 4cm-wide, 1cm-thick plastic scintillator bars arranged in 32 layers and separated by 31 layers of 1.75mm-thick lead sheets. The scintillator bars of the innermost layer are perpendicular to the longitudinal axis of the magnet. The orientation of the bars alternates between layers so that the bars in any layer are perpendicular to the bars in the two adjacent ones. The segmentation of the active material (scintillator) provides the spatial resolution required for reconstruction of the direction of incoming photons. This in turn allows to reconstruct  $\pi^0$  decay points and match them to candidate

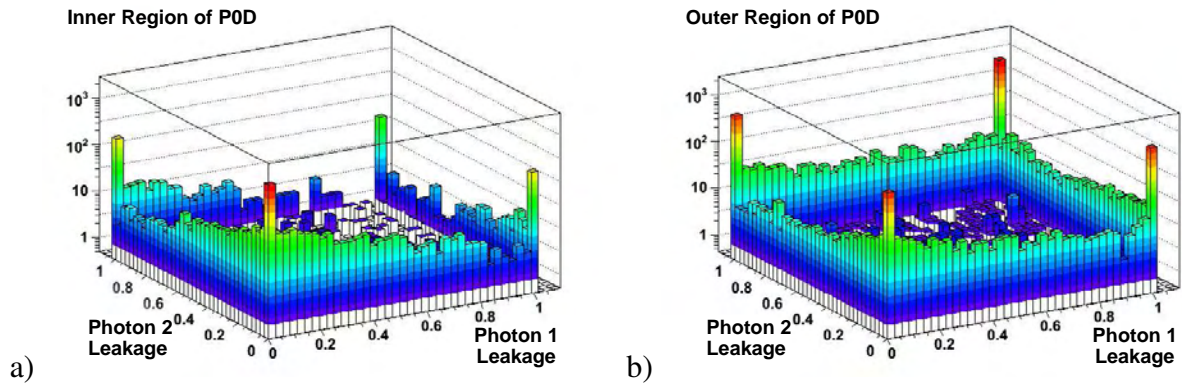


Figure 8.2: Distributions of photon pairs from decays of NC  $\pi^0$ s in the POD as a function of the fraction of the energy of each photon that escapes the POD, for the a) inner and b) outer parts of the POD. See the text for the definitions of the detector parts. A significant fraction of  $\pi^0$ s from the centre of the detector have one or two photons which escape the POD, either completely, or partially. Many of these events will be indistinguishable, in the POD, from similar events originating in the outer POD. The Gamma / Muon tagger allows photons from all these event categories to be tagged.

interaction vertices inside the fiducial volume. The bar width was set to 4cm as this allows good  $\pi^0$  reconstruction efficiency with a reasonable number of channels. This segmentation allows the use of shower shape variables for charged particle identification (muon-pion-electron separation). Details of the relevant full-simulation studies are given in the following sections.

Considering the internal dimensions of the UA1 magnet and the need for large fiducial volume, we have decided to limit the total depth of the ECAL to 50cm. Allowing for module frames, cooling, mounting mechanisms, and component and assembly tolerances, and optimising the sampling fraction for  $\pi^0$  reconstruction efficiency, we have arrived at the current design of 32 active layers of 1cm-thick scintillator and 31 layers of 1.75mm-thick lead sheet converter. This gives the Tracker ECAL an effective depth of  $10.5X_0$  (including the scintillator material). Each module is located outside the Basket and is fixed independently to the iron of the magnet yokes.

The active length of the Tracker ECAL (i.e. the length of the longitudinal bars) is 3840mm, allowing for structural elements of the module boxes and space for photosensors, Front End electronics, cables and cooling pipes routing, and access for assembly and repair work.

The top and bottom Tracker ECAL modules are split in two (left and right) so that each module is mounted to the magnet iron yoke and can move with it when the magnet opens (see Fig. 8.3). The active width of each module (i.e. the length of the shorter bars running perpendicular to the beam direction) is 1520mm. Each of the four identical modules has 16 layers with 38 3840mm-long bars per layer, and 16 layers with 96 1520mm-long bars per layer. The combined weight of lead and scintillator in each module is 5.6tons.

There are two side modules, one on each side of the magnet iron yokes. The active width of each module is 2360mm. Each of the two identical modules has 16 layers with 59 3840mm-long bars per layer, and 16 layers with 96 2360mm-long bars per layer. The combined weight of lead and scintillator in each module is 8.6tons. Each module will be built physically as two sub-modules which will be lowered separately into the ND280 pit and will be assembled together before fixing to their mounting points on the magnet.

All scintillator bars have a hole in the center with a 1mm wavelength-shifting fibre running in it (as in SciBar). The diameter of the hole will be determined during the production setup phase, and will depend on extrusion tolerances and reproducibility. It is envisaged that a nominal diameter of up to 2mm will be specified to ensure that fibres can be thread through all of the long bars. All 3840mm-long bars are read out by one photosensor at each end (double-end readout), while all shorter bars are mirrored at one end and read out by a photosensor at the other (single-end readout). The mirrored

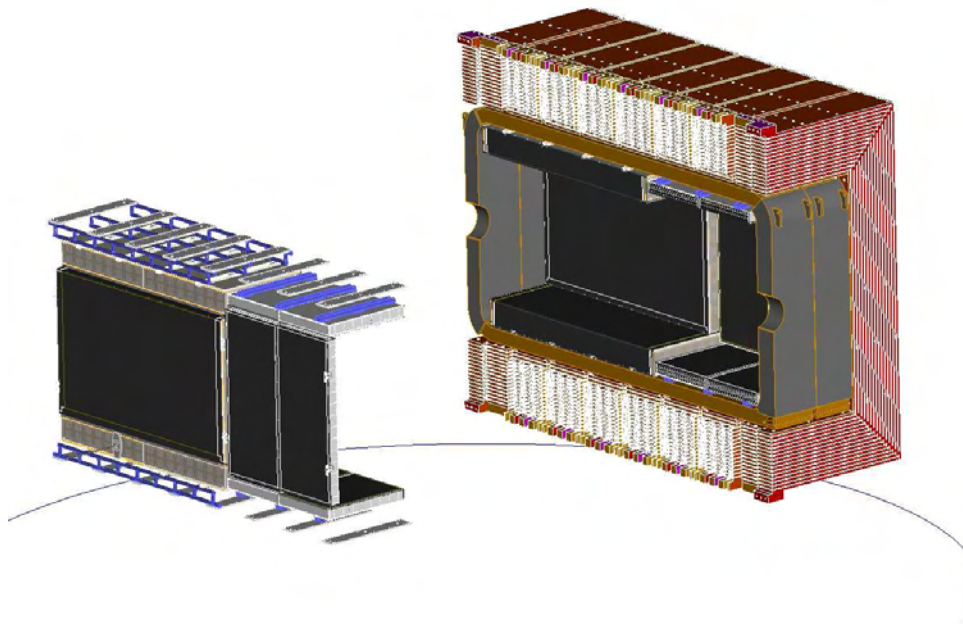


Figure 8.3: ND280 ECAL modules: On the right the modules are shown inside the magnet yokes and coils. The longer and thicker Tracker ECAL modules are located downstream of the POD ECAL modules. On the left the other half of the ECAL modules are shown, together with their mounting structures, but without any magnet elements. The neutrino beam travels along the magnet iron axis, entering from the right in this drawing.

ends are located in such a way as to maximise the geometrical coverage of the ECAL.

The Downstream ECAL is a single module with the same granularity and similar construction as the Tracker ECAL modules. It is located inside the Basket, taking up the last 50cm at its downstream end, at the “exit” of the tracking volume. Its overall dimensions are dictated by the Basket, and its active surface transverse to the beam direction is 2040mm by 2040mm. It has 34 active layers (compared to 32 in the Tracker ECAL modules) and 33 lead sheet converter layers. Bar orientation alternates between layers as in the Tracker ECAL. The length of each bar is 2040mm, giving a square active cross-section. All bars have double-end readout to compensate for the higher multiplicity of particles moving forward, and with higher average energies due to the boost. There are 51 scintillator bars in each layer. The combined weight of lead and scintillator in the Downstream module is 4.2tons. It has an effective depth of  $11.0X_0$ . This is motivated by the higher energies of forward-moving particles, and is made possible by the thinner structural elements allowed by the different suspension method.

Bar length	Number of bars	Readout	Number of channels
3840 mm	4320	Double end	8640
2040 mm	1734	Double end	3468
1520 mm	6144	Single end	6144
2360 mm	3072	Single end	3072
Total	15270		21324

Table 8.2: Statistics for the Tracker and Downstream ECAL modules. All scintillator bars are 4cm wide by 1cm thick. The total length of the bars is 36.7km and their weight is 15.5tons. The corresponding number of wavelength-shifting fibres is 6054 pieces with connectors at both ends and 9216 pieces with one side mirrored and one side fitted with a connector. The total lead weight is 28.3tons. There are 226 single layers in all the fine segmentation ECAL modules.

The POD is surrounded by ECAL modules with coarser segmentation and less total radiation length. The POD ECAL does not have the energy or spatial resolution required for full  $\pi^0$  reconstruction. However its presence is necessary to detect photons that do not convert in the active POD volume or their showers are only partially contained in it. It can also confirm the passage of charged tracks, identify MIPs, and act as veto for incoming backgrounds. The POD ECAL modules consist of 6 active scintillator layers separated by 5 layers of 5mm-thick lead converter. Each module has an effective depth of  $4.5X_0$ . All scintillator layers are made of 20cm-wide, 2cm-thick slabs. Light is collected in a wavelength-shifting fibre running in an S-shaped groove in one of the large surfaces of each slab, and readout is by one photosensor at each end of the fibre (double end readout). The fibre-equipped scintillator slabs are similar to the ones described in arXiv:physics/0606037, which will be used in ND280 as the active elements of the SMRD. All slabs in all layers are oriented with their long axis in the direction of the beam. As the total POD length of 2.5m would give very low light output in this type of design, we have decided to make all POD ECAL modules half length. This keeps the length of each slab to 1150mm, inside the region where adequate light output and dependable manufacturing have been demonstrated. However the number of slabs to be handled and the number of modules to be assembled and installed doubles. This is partially offset by the easier handling thanks to smaller dimensions and less weight.

The POD modules are shown in Fig. 8.3. In total there are four side modules (two left, two right) and eight top/bottom modules (upper right and left, lower right and left, repeated twice along the beam axis). Each of the eight top and bottom modules has active width of 1600mm and has 6 active layers of 8 scintillator slabs each. The weight of lead plus scintillator in each module is 0.75tons. Each of the four side modules has active width of 2800mm and has 6 active layers of 14 bars each. The weight of lead plus scintillator in each module is 1.32tons. In total the POD ECAL is made of 720 scintillator slabs that weigh 3.5tons, while the total lead weight is 7.8tons. It has 1440 readout channels. Each slab has about 3.3m of wavelength-shifting fibre, leading to 2.5km of fibre for the whole POD ECAL.

The scintillator used in all ECAL modules is the same as for all other scintillator detectors in ND280: extruded polystyrene with 1% PPO and 0.03% POPOP. A 0.25mm-thick layer of  $\text{TiO}_2$  is co-extruded at the surface of the bars as light reflector. The 4cm-wide bars for the Tracker and Downstream modules will be produced at FNAL, while the POD slabs will be produced in Russia (same supplier as for the SMRD). The fibre will be 1mm-diameter Kuraray multiclاد Y11(200)S-35, as for the POD and the FGDs.

The absorber sheets will be made of low activity Pb-Ca (0.03%). This material has enough stiffness to allow precise machining, cutting, and handling. It was developed by the German company JL Goslar for use in the OPERA emulsion detector. JL Goslar is one of the best known companies in the area of lead products, radiation shielding, and special research constructions using lead. They use freshly-mined lead to avoid contamination from recycling, and they can guarantee good control of admixtures and radiation levels. Engineers in the UK are using sheets bought from them for gluing tests and prototype sandwich construction.

Each module is contained inside its own light-tight box, as shown in Fig. 8.4. The box sides are made of Aluminium bars, precision-machined to our specifications at a UK manufacturer. The “rear” side of each module box is strengthened by Aluminium cross-members which incorporate the mechanisms (sliders or attachment points) that fix the module on the magnet yokes. They also carry extruded cooling tubes. Water from dedicated chillers is circulated in order to remove heat coming from the magnet coils (upper and lower modules as well as downstream) and from the inside of each module (photosensors and front end readout cards). The ECAL module frames must act as thermal shield between the magnet and the active ECAL, and obviously all the other detectors in the centre of ND280. The cooling circuits extend to the interior of each module and in particular the regions where the photosensors and electronics are located.

The front of each module is made of a purpose-built carbon fibre skin that provides the necessary mechanical rigidity and support, as well as ensure that the modules are light-tight. At the back,

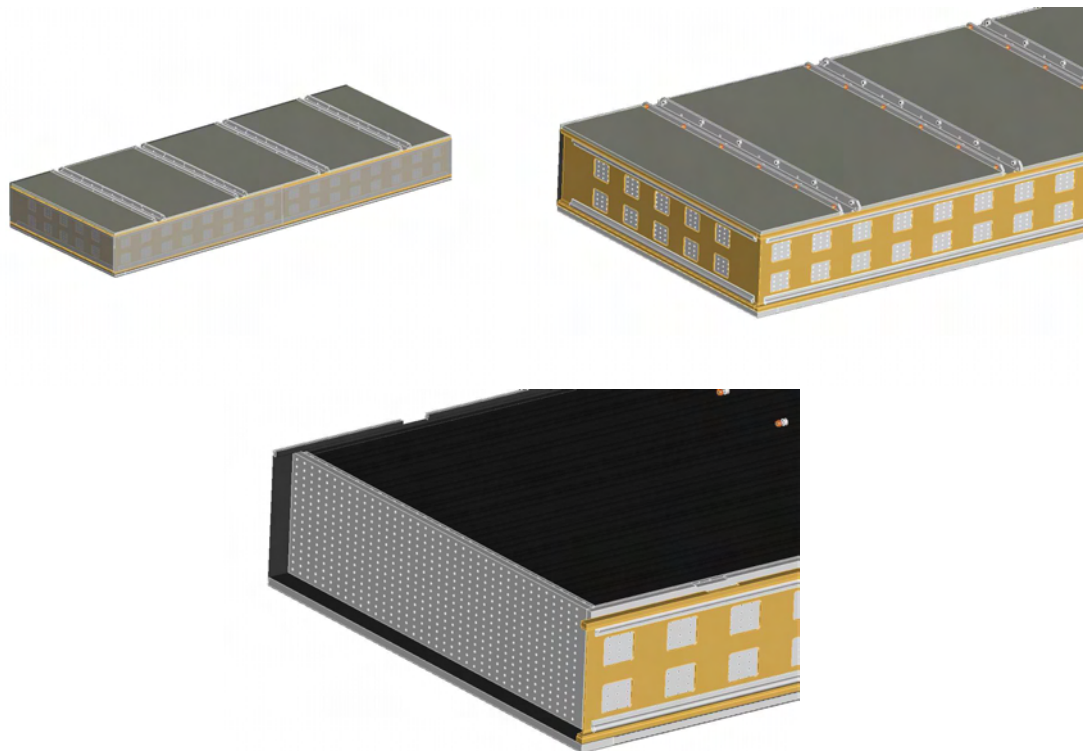


Figure 8.4: One of the Tracker ECAL modules: Complete module with mounting sliders on the backframe, followed by detail of the same module after the side light-tightening covers have been removed, showing the main aluminium frame of the module (dark yellow). The Front End Readout cards (not shown) are mounted flat at each window in the frame. Cooling pipes are shown running along the frame elements. *bottom*: one side of the frame has been removed showing the aluminium bulkhead underneath. Each hole in the bulkhead lines up with a fibre coming out of a scintillator bar.

where the Aluminium frame has a ladder-like layout, smaller size carbon fibre panels are used to close the modules. Each module is attached to the magnet iron at a number of locations along its back, ensuring that deflections are kept within the overall tolerances required for ND280 integration. Special carrier frames will be constructed and used to provide rigidity to each module during transport and installation. ECAL modules will be attached to their frames at all times other than when they are mounted inside the magnet.

Inside each module, and on sides where there is no optical readout, the lead-scintillator sandwich will be supported in place directly by the aluminium module frame. On sides where there is optical readout, the sandwich is held in place by a special aluminium bulkhead (see Fig. 8.4) which has precision-drilled 2mm-diameter holes which align with the scintillator bar holes, allowing the fibre to be pushed in and then locked in place using the optical connector at its end.

The aluminium bars at the end of each layer are kept at a distance of 1cm from the bulkhead with special standoff buttons. In this area the fibres are running free between the bar and the bulkhead. This area will be equipped with a diagnostics light pulsing system. This will be an LED-based system able to illuminate a large number of fibres simultaneously. It will be used to identify dead/faulty channels and not as a precision calibration tool. Hence its design is aimed at robustness and low cost. The preferred option at this time is to illuminate directly the fibres by a large number of LEDs. The exact specification and layout of the system is still under study.

There is free space between the bulkhead and the outside module wall, where the front end readout cards are located. The readout cards can be reached from the outside through openings that are covered by carbon fibre panels for light tightness. These panels are in place in the first picture in Fig. 8.4 where they appear semi-transparent, and have been removed in the second picture. The area

of each module where the electronics are located is cooled by chilled water circulating in extruded metal pipes. This volume is constantly flushed with dry nitrogen to remove any water vapour and protect from condensation.

### 8.2.1 ECAL cluster reconstruction

The reconstruction of particles in the Tracker ECAL is outlined here. The P0D ECAL is of a simpler design and hence cluster reconstruction is simpler than with the TECAL. A software framework for ECAL reconstruction has been built, and is currently being refined and the ECAL designs evaluated using the full ND280 simulation.

In the first reconstruction phase, hits in adjacent ECAL scintillator bars are grouped into clusters. The position of a cluster in three dimensions is estimated using information from the two projections, pulse height comparison for double-end readout bars, and timing. Clusters are then matched with charged tracks reconstructed in the other subsystems. Clusters which appear to be unrelated to the charged tracks are considered to be photon candidates.

As an indication of E.M. cluster sizes we give here the number of scintillator bars with a hit for electrons of 300(500)MeV entering the DS ECAL at 90 degrees. The mean number of hits is 34.8(49.4) and the FWHM of the hit distribution is 12(14).

### 8.2.2 Electron and photon energy measurement

At this time, the basic energy measurement of electromagnetic showers in the simulation is performed as a simple weighted sum of the energy deposited in the TECAL scintillator bars of a cluster:

$$E_{rec} = \sum_i \frac{\rho_{bar}d_{bar} + \rho_{Pb}d_{Pb}}{\rho_{Pb}d_{Pb}} E_i \quad (8.1)$$

with  $\rho_{bar}$  and  $d_{bar}$  being the density of plastic scintillator and thickness of the bar,  $\rho_{Pb}$  and  $d_{Pb}$  respectively the density and thickness of the lead layer and  $E_i$  the individual bar hit energy in MeV. This formula assumes that the energy loss in the bar comes solely from ionisation. To properly reconstruct the shower energy, the so-called  $e/mip$  and  $\gamma/mip$  ratio respectively for electron and  $\gamma$  shower is applied on  $E_{rec}$ .

The TECAL energy resolutions for electron and photons is shown in Fig. 8.5. The Tracker ECAL intrinsic sampling fluctuation obtained from the figure is about  $7.5\%/\sqrt{E}$  up to 5GeV, which meets the requirement for photon and electron energy measurement to 10% or better. Our studies indicate that photosensor saturation at very large signals due to multiple photons in individual pixels affect the energy resolution by only few percent for devices with 400 pixels or more.

### 8.2.3 Energy measurement using shower shape information

Due to the nature of electromagnetic showers in the ECAL, there is more information on the shower energy than just the total energy deposit. Additional information on the shower energy can be found in the distribution of the energy deposited in each scintillator bar and the geometrical distribution of the energy deposit. We are developing an electromagnetic shower energy fitter that uses this additional information. Currently only the shape of the energy distribution is used. The fitter will be extended to include more shape variables.

The energy deposit in each bar is extracted from the photosensor signal through a position-dependent calibration, specific for each channel. This takes into account all effects of light emission and transmission in the scintillator bar, the fibre, its optical connection to the photosensor, and the quantum efficiency and gain of this sensor.

There is one photosensor property that would not be corrected in this step: the non-linearity that arises from multiple photon hits in single pixels which happens for very high signals. This depends

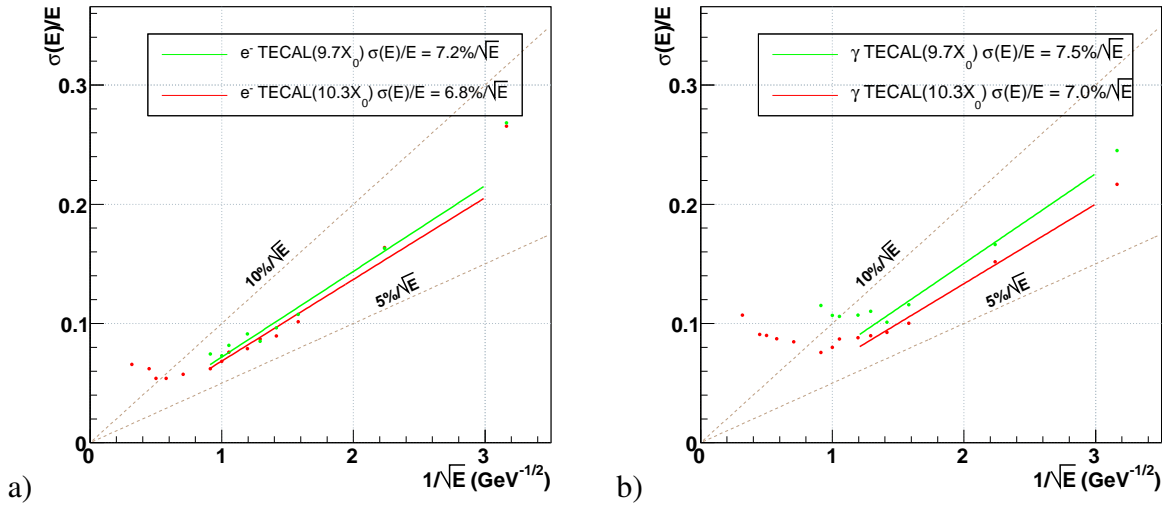


Figure 8.5: Energy resolutions for a) electrons and b) photons in the Tracker ECAL. The Barrel ECAL points lie slightly above those for the thicker Downstream ECAL. Linear fits are made to the region from 0.2 to 1.2 GeV in energy. The increases in resolution in the higher energy regions, due to energy leakage, will be reduced with more optimised algorithms and full detector calibration. The albedo effect can be seen at the very lowest energy points.

on the effective number of pixels available on the photosensor and we present here the study we did to understand the impact of this effect on the energy extraction method presented here. Fig. 8.6 shows the energy deposit in each bar from 500MeV electrons and muons. As the units are set as the mean response from a minimum ionising particle, thus the mean response from the muons is one MIP, and there is a peak at this point for the electrons. One way to characterise the electron distribution is to use moments. Each of the first three moments, the mean, RMS and skew, of the distribution are functions of energy and along with the total energy deposit and the maximum energy deposit in a single bar, are used in the energy fit. Each of these distributions is fit to a Gaussian at a series of energies between 50 MeV and 5.5 GeV; the expected mean and width of a Gaussian distribution can then be calculated for any trial energy in this range by interpolation. These values are used to calculate the probability of observing the given value of each of the five parameters at current trial energy, and are used to construct a likelihood. By maximising this likelihood, the most likely energy of the shower can be fit.

In order to test sensitivity to the non-linearity of the photosensors a series of fits have been carried out with progressively bigger mistakes in the number of operational channels. The default sensor in these studies has 556 pixels, the same number as the current Russian sensor. In the real detector mis-calibrated channels would in fact have fewer operational pixels. To mimic the effect of this mis-calibration the number of pixels can be increased in the energy fit, allowing us to study the impact of uncertainties in the non-linearity of the photosensors. Fig. 8.7 shows the results from fitting 1000 2 GeV electrons while varying the number of pixels in the photosensor calibration step. This shows that the fitter is performing well at 2 GeV, and that for deviations the linearity calibration have only a small effect at this energy. This is an encouraging result.

The sensitivity of the fitter to the calibration of the non-linearity is found to be small and suggests that this will be only a small contribution to the TECAL energy resolution.

## 8.2.4 Reconstruction of $\pi^0$ in the Tracker ECAL

The neutral current single  $\pi^0$  (NC-1 $\pi^0$ ) production rate will be measured in the dedicated POD. This will be a complicated measurement, and therefore a complementary observation will be made in the Tracker, where the method used will have systematic errors of a very different nature to the POD.

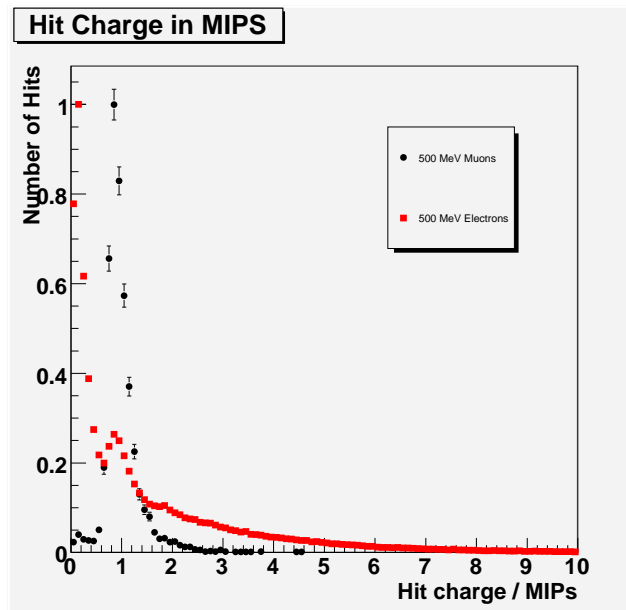


Figure 8.6: The distribution of energy deposit in the scintillator bars for 500 MeV electrons and muons, in units of the mean energy deposit of a minimum ionising particle.

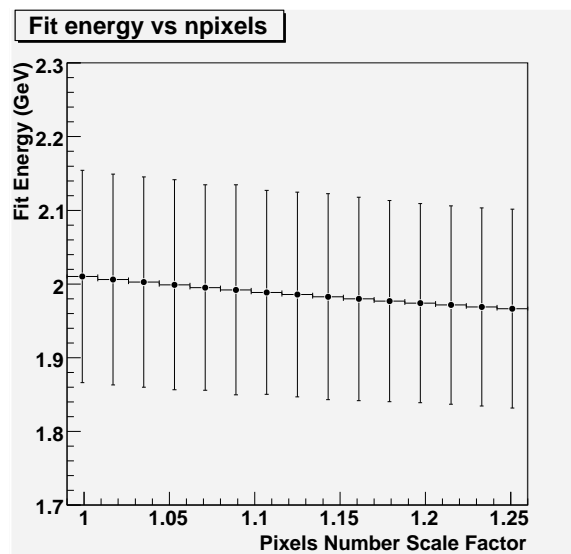


Figure 8.7: The result of the energy fit for 2 GeV electrons as the number of pixels in the calibration is varied by a scale factor. The error bars are representative of the resolution of the fitter at 2 GeV.

This measurement takes advantage of the high sampling fraction and granularity of the Tracker ECAL (TECAL) to identify  $\gamma$ -cluster partners and to extrapolate back to the decay point of the  $\pi^0$  in the FGD block. The TPCs are used as vetoes for charged particles. In the  $\pi^0$  momentum range of particular interest ( $200 < p_{\pi^0} < 800$  MeV/c), approximately one third of the FGD NC-1 $\pi^0$  events have both decay photons converting in the TECAL.

A reconstruction algorithm has been developed in the simulation based on preliminary studies (I. Kato, nd280m-note 001). Here we focus on  $\pi^0$ s originating in the downstream FGD2, whose reconstruction involves the Barrel and Downstream ECALs. A proportion of events from FGD1 have one or both photons converting in FGD2, creating a shower in the TPC further downstream. These events go beyond the scope of the present ECAL discussion, but should be recoverable by reconstructing the tracks within the Tracker.

In this preliminary study, a  $\pi^0$  candidate is selected using the following requirements:

- low activity in the Tracker region
- identification of  $\gamma$ -like clusters
- good reconstruction of direction of incidence of one  $\gamma$  using a thrust analysis
- intersection of  $\gamma$  direction with FGD fiducial volume
- consistency of invariant mass formed with second  $\gamma$  with  $\pi^0$

The first three requirements constitute a pre-selection, and their efficiency depends mostly on the geometry of the Tracker and ECAL, and basic ECAL properties. The remaining events are then studied for their consistency with being from a  $\pi^0$  decaying in the FGD, from both the direction of the principle photon and the invariant mass. This step is highly dependent on the reconstruction capabilities of the ECAL.

Fig. 8.8a shows the effect of two pre-selection algorithms of differing tightness. The efficiencies are calculated with respect to the total rate of NC- $\pi^0$  events in the FGD. The current estimate for the efficiency of the final step after pre-selection is plotted in Fig. 8.8b.

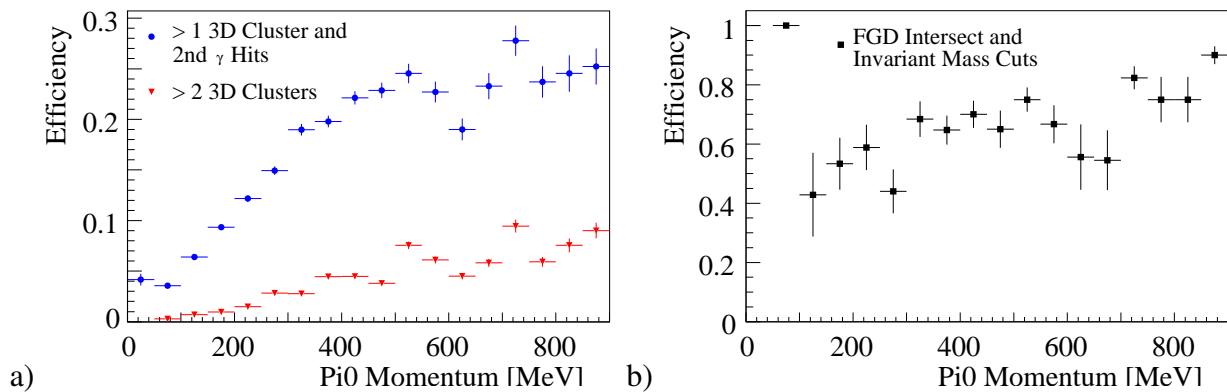


Figure 8.8: a) Pre-selection efficiencies for  $\pi^0$  events in FGD2 which can be reconstructed in the TECAL. The upper points indicate the case where one well-reconstructed cluster is found, and another smaller cluster also exists in the ECALs. The lower distribution is for events where the two clusters are both reconstructed well in both “views” of the ECALs. The two distributions represent loose and tight pre-selection cuts. In a final analysis, the efficiencies are expected to lie somewhere between the two curves. b) Estimated efficiencies for the cuts which are most dependent on the direction pointing and energy measuring capabilities of the TECAL, the requirement that the photons combine to form a  $\pi^0$  candidate which lies in the correct FGD and has the correct mass. These cuts would be applied after the pre-selection cuts in the plot on the left.

The  $\gamma$ -cluster direction reconstruction and thus the  $\pi^0$  efficiency is highly dependent on the Tracker ECAL design. To study the impact of the TECAL design parameters on the  $\pi^0$  reconstruction efficiency, a range of values of the TECAL sampling fraction, granularity, and total thickness have been explored. The relative change in the  $\pi^0$  efficiency with these parameters is illustrated in Fig. 8.9. Potential background rates and the NC- $1\pi^0$  interaction rate are listed in Table 8.3

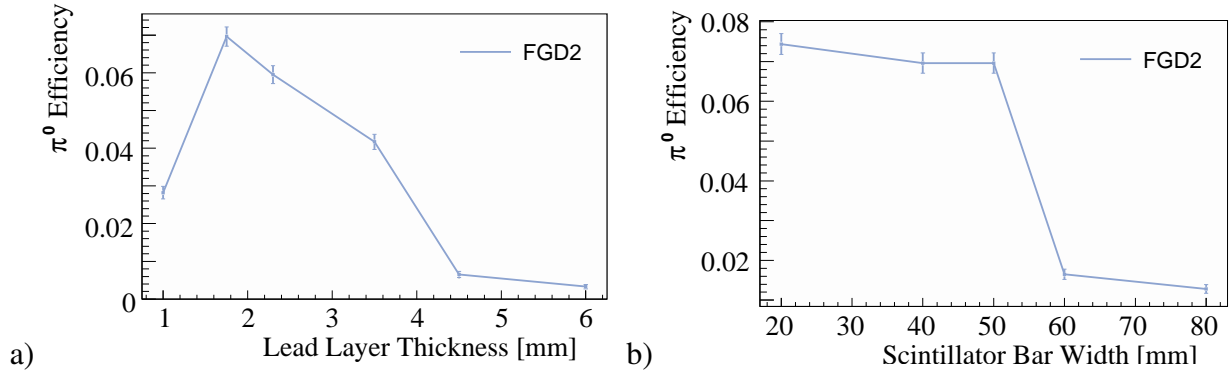


Figure 8.9: Total reconstruction efficiencies of  $\pi^0$ s from FGD2, as functions of two TECAL design parameters. A tight pre-selection algorithm is used for this study. The a) thickness of the lead layers and the b) width of the scintillator bars both affect the reconstruction directly. Thick lead layers worsen the energy resolution, and reduce the number of active layers in which the shower direction is reconstructed. Narrower scintillator bars do not help reconstruct shower direction once they are below a certain width, due to the Moliere radius. In the present design, a bar width of 4cm is chosen, which also ensures good light collection efficiency for the longest bars. The efficiency drops rapidly above bar width of 5cm. This is due to the loss of MIP-EM shower discrimination and loss of resolution in the reconstruction of photon direction, hence also in  $\pi^0$  invariant mass.

	FGD
Total Interaction rate (per bunch)	$7.7 \times 10^{-3}$
NC- $1\pi^0$ rate (per bunch)	$3.7 \times 10^{-4}$
Magnet neutron background induced $\pi^0$ rate (per bunch)	$5.0 \times 10^{-6}$
Cavern neutron background induced $\pi^0$ rate (per bunch)	$< 1.0 \times 10^{-6}$

Table 8.3: Expected process rates per beam bunch in a 1.2ton FGD module. Background rates from  $\pi^0$  produced by neutrons from neutrino interaction in the cavern and in the magnet are estimations using GEANT4. Rate variations are expected to be large due to uncertainties in hadron production models.

## 8.2.5 Particle identification: muon-electron separation

The TECAL plays an important role in identifying charged particles. This section is concerned with matched clusters, and in particular how the clusters are used to distinguish between different particle hypotheses for each track. The finely segmented ECAL modules surrounding FGDs and TPCs allow shower characteristics to be used for the separation between hadrons (pions, protons), electrons, and muons over a large range of particle momenta ( $0.5 < p < 10$  GeV/c).

Matched clusters are first categorised as track-like or shower-like. This is essential in order to resolve mis-identification of muons as electrons in the small CC-QE beam  $\nu_e$  sample. The PID selection cuts are based on the shape and energy deposition characteristics of the cluster : (i) The ratio between cluster view axis eigenvalues in a principal components analysis (Axis Maximum Ratio); (ii)

The variation of energy deposits within the cluster; (iii) The variation and spatial distribution of the number of hits in the cluster.

The PID algorithm has been run on samples of muons and electrons from CC-QE  $\nu_\mu$  and  $\nu_e$  interactions using a 200:1 weighting factor, which reflects the ratio in the beam, in order to estimate the cluster identification efficiencies and purities of the TECAL. These numbers are shown in table 8.4. Using solely the particle identification capability of the TECAL, it is possible to discriminate

Sample category	ECAL Barrel		ECAL Downstream	
	efficiency	purity	efficiency	purity
Shower-like electrons	0.43	0.78	0.84	0.86
Track-like muons	0.97	0.92	0.99	0.90

Table 8.4: Efficiencies and purities of shower and track type cluster selection in muon and electron samples from CC-QE interactions in the FGD. Each sample is normalised to the expected interaction rate. It can be seen that the finite spatial resolution in the shape of clusters for low energy particles limits the recognition of shower-like cluster in the barrel region.

electrons from muons with very high efficiency. It should be noted that a more elaborate identification strategy using timing information and Michel electron signature will improve the separation between muons and electrons in the low momentum region ( $p < 500 \text{ MeV}/c$ ).

## 8.2.6 Particle identification: electron-pion separation

The Tracker ECAL will be required to separate showers from electrons and charged pions over a range of energies. We currently do this using Neural Nets and we present briefly the performance achieved in simulation. Two different nets are used: in the first one truth information about the incoming particle (momentum, direction, position of intercept with the front of the calorimeter) is used to mimic clusters matched to charged tracks; in the second one we do not use any such information, hence we simulate the PID capabilities of the ECAL in the absence of any tracking information from other subsystems.

The neural net inputs are the (0,0)th to (3,3)rd 2-dimensional Legendre moments of the distribution of energy through the ECAL. Separate sets of moments are used for horizontal and vertical bars, for a total of 32 variables. The positions of each deposit of energy are rotated to the frame of the incoming particle - for the “track matched” net truth information is used for this rotation, otherwise it is estimated from ECAL information only. In addition, we use the following inputs: momentum (“track match” only), direction and point of intercept of the incident particle (from truth for “track match”, estimated otherwise). This gives 38 inputs for the “track match” net, 37 for the “ECAL only” net.

We use large sets of GEANT4 simulated single-particle samples of electrons and pions with energies up to  $6\text{GeV}$  and over the full angular range. 200,000 events are used in the training set, another 200,000 as a comparison set to avoid over-training and 600,000 are used for evaluation. Events must have an identifiable cluster which passes the MIP/Shower separation described above. The neural net is trained through 1000 epochs.

A multilayer perceptron is used. Many different configurations were tested. When there was no significant difference in performance, the simplest configuration was chosen. The “track match” net used a 38-25-13-1 configuration (38 inputs, two hidden layers of 25 and 13 nodes and one output) and the “ECAL only” net used 37-26-9-1. An efficiency-purity plot of the NN performance is shown in Fig. 8.10

## 8.3 Detector technology R&D

The scintillator and wavelength-shifting fibre techniques and materials used in the ECAL are well established, robust, and relatively simple. The same is true for the module construction materials and

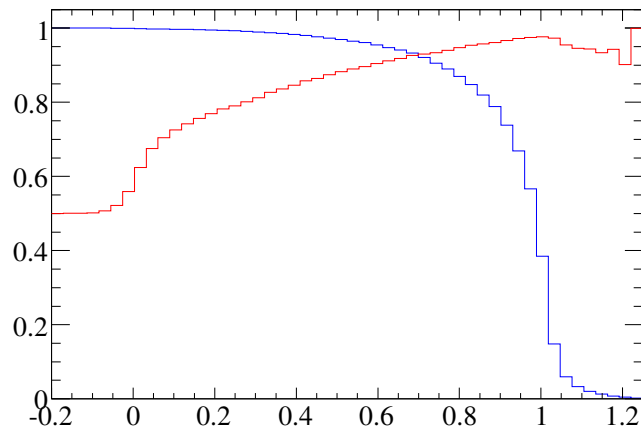


Figure 8.10: Electron identification efficiency (rising red curve) and purity (falling blue curve) achieved with the NN electron-pion selector as function of the cut at the NN output value. The samples are 1GeV electrons and pions with identical initial distributions, reconstructed in the downstream ECAL, and with valid tracking information from the TPC. An efficiency of 90% for electrons can be achieved with 95% pion rejection.

procedures. The photosensor is the only novel component, and this is covered in its own section in this document. We are performing light-yield measurements using combinations of bars, fibres, and prototype photosensors, with cosmic muons, radioactive sources, and light pulsers. We are doing these measurements to validate details of our design (e.g. fibre mirroring method) and we don't anticipate any major modifications as result of these.

## 8.4 Detector construction schedule

### 8.4.1 Facilities used in ECAL construction

The ECAL is fully-UK funded and will be constructed by the T2K-UK collaboration. The centre of the activity will be Daresbury Laboratory (25 miles from Liverpool). A large construction hall has been earmarked for our operations. It is 70m long and is equipped with a 30-ton crane and reconfigurable clean rooms. We will use this space for most of the assembly and tests operations, as well as storage. In addition we will use workshop and laboratory facilities at the Universities of Lancaster, Liverpool, QMUL, Sheffield, and Warwick (mentioned as "university centres" in the rest of this chapter). Daresbury and Liverpool have large mechanical workshops with a variety of modern computer-controlled machines, where we will make prototypes and production parts for the ECAL.

### 8.4.2 Timescales and notation

Funding for the ECAL from PPARC in the UK is in the final approval stages, and we expect to have funds available in early 2007, at which point we will be in position to launch orders and calls for tenders, and sign contracts. We expect bulk deliveries starting in summer 2007, which gives us two years before summer 2009, our target for having all ECAL modules assembled. In the rest of this section we speak of *first year of production* and *second year of production*. All steps of the construction procedure have been optimised for minimal dependencies so that multiple operations can go on in parallel. The long production stages (layer and module assembly) can be rearranged between production centres to absorb eventual delays in deliveries. The distribution of construction work mentioned in the following paragraphs is tentative at this point in time. The majority of construction

will definitely be done at Daresbury, however the allocation of smaller parts may be re-assigned to ensure timely completion if unexpected problems arise.

### **8.4.3 Design**

Design engineers at Daresbury and Liverpool are working on the detailed drawings of the ECAL modules and related structures on ProEngineer, and Finite Elements Analysis using ANSYS. At present the design focus is on cables and cooling pipes routing inside and outside the modules. Other centres are contributing in the design of components like the fibre-photosensor connectors (Warwick), light injection system (Sheffield), module scanners (Warwick, QMUL), etc. Design is already ongoing, and we expect to have final drawings ready for orders by the end of calendar year 2006.

### **8.4.4 Major procurements**

We have identified possible suppliers for scintillator bars (FNAL, Russian companies), fibre (Kuraray) and lead (JL Goslar). We are in contact with companies in the UK who specialise in large constructions using carbon fibre and Aluminium for the module box elements, and steel frames for the module carrying and installation structures.

Procurement formalities for the more expensive items are regulated by UK and EU rules. Orders will be placed through the CCLRC/RAL office which has large experience in handling such procedures in a timely fashion. At this moment we have identified at least one dependable source for each of our main procurements. We aim to sign all major contracts as early as possible in the first half of calendar year 2007, allowing start of "first year of construction" in late summer 2007. Electronics production and photosensor procurement are covered in other sections in this document. We expect them to be available at the appropriate times for timely completion of the ECAL as described here.

### **8.4.5 Fibre preparation**

Fibres will be delivered in canes, cut slightly longer than their nominal length. The ones for single end readout bars will be cut at one end, polished, and mirrored. The rest will be fitted with optical connectors at both ends, cut to length, and polished. We are currently performing tests to decide if mirroring will be done at FNAL. Their vacuum deposition method gives excellent reflectivity and reproducibility. However this option adds a step of transport (manufacturer to FNAL, then to the UK) and cost. We are evaluating the option to set up a mirroring facility using simpler technology in one of the university centres.

Fitting connectors on one end of all fibres will be done in one or two production centres. Fitting the fibre, cutting, and polishing the other end for double-end readout channels will be done at Daresbury or any other place where final module assembly will take place.

### **8.4.6 Layer preparation for the Tracking and Downstream ECAL modules**

There are 226 such layers to prepare, taking one full year at the rate of one per working day. For each layer the lead sheet(s) will be placed on a large aluminium machined table and will be covered with slow-curing glue. Then the scintillator bars will be positioned on the glue. Thin aluminium bars will be placed around the layer to ensure its alignment and rigidity (see Fig. 8.11). The layer will be covered with plastic and vacuum pumps will evacuate the air, minimising gaps and tolerances in the layers. Each layer will then be moved using a special suction system and will be stored. We are currently validating this procedure in small-size tests using the proper materials. Layers will be prepared mainly at Daresbury during the first year of production. A number of layers for the side-TEACL modules will be prepared at Liverpool. The downstream layers are smaller and will be prepared at Lancaster.

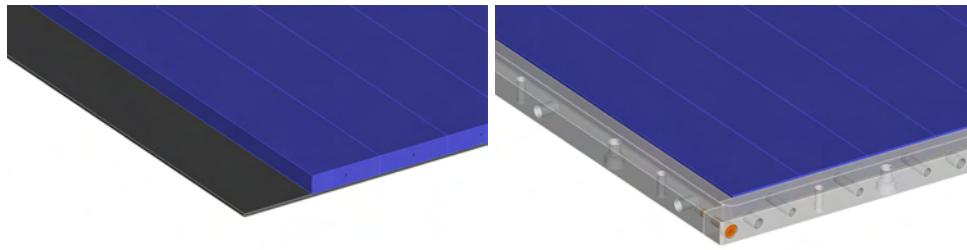


Figure 8.11: Scintillator bars glued on lead sheet, and complete layer with its aluminium bar border. The border bar has holes for fibre routing and for assembly with the other layers in the module.

### 8.4.7 Module assembly for the Tracking and Downstream ECAL

Once the layers, fibres, and photosensors are ready, we will start module assembly. At that point we will have 226 layers to be assembled in 7 modules. We plan to do one layer per day, during the second year of production. The module box will be positioned on one of the large flat tables used in the previous step. A layer will be lowered in with special care for alignment. This will be ensured by a system of pins and holes in the aluminium bars surrounding each layer. At this point the aluminium bulkheads will be in position in the modules, but not the module sides that surround them. Fibres will then be pushed through each bulkhead hole and the corresponding scintillator bar. When the fibre is fully inserted the connector will be secured to the bulkhead. For single readout fibres this is the end of this step. For double end readout bars, the fibre will come out of a hole in the bulkhead on the far side of the module. Then the connector will be fitted and the fiber cut and polished in-situ. We are currently developing the details of this procedure. The final step is to attach the photosensors to all fibres and connect them to readout electronics for testing. After a layer is finished, it will be inspected optically and then it will be scanned with a radioactive source. In case some channels are defective (e.g. cracked fibre), the fibres and photosensors will be replaced after the test cycle is over. These channels will be scanned again. The downstream module is smaller and will be assembled at Lancaster.

### 8.4.8 POD ECAL modules

We plan to order the scintillator slabs fitted with the S-shaped fibre to the same Russian suppliers as for the SMRD. They will produce the scintillator, fit the fibre and the connectors, test the slabs, and ship them to the UK. We will then assemble them into modules at Warwick and Sheffield. The procedure will be the same as described above, with the exception of fibre threading which is obviously not applicable. There are 720 scintillator slabs to be assembled in 12 modules (72 individual layers). We plan to do this during the second year of production.

### 8.4.9 QA and initial calibration

Upon delivery of the components (scintillator bars, fibres, POD slabs), they will be inspected for any obvious damage and tagged with serial numbers that will be entered in our production database. Samples will be scanned (with radioactive source for scintillators and with light source for fibres). The sampling frequency for each component will be decided based on existing experience in other projects and our initial experience with our suppliers. The initial batches will undergo full testing.

Once a layer has been installed in its module, it will be scanned with an automated x-y scanner carrying a radioactive source. Many data points will be taken along each individual bar and will be stored as the initial calibration of the bars.

The Downstream ECAL module is the first one to be assembled, as it will be used for beam tests at CERN in 2008. We will use this and some of the other modules to collect cosmic data. We will correlate the scans, beam test, and cosmics, to validate the ECAL simulation and calibration procedure.

## 8.5 Detector installation/commissioning

The ECAL modules and all installation equipment will be shipped to Japan in the fourth quarter of 2009, for installation at the end of December. The first step will be to open the magnet. Then the installation platforms, structures, and jigs will be lowered at one side of the basket. Then the two parts of the Side Tracker ECAL module will be lowered from the surface to the platform between the magnet and the basket. The two parts of the module will be assembled together. Then the module in its carrying structure will be aligned to the mounting points on the magnet, by means of adjustment motors and jacks that are built into the equipment. The module will then be pushed back to the magnet yokes and fixed to its mounting points. Electrical, cooling, and gas connections will be done and tested. Some basic functionality test will be done using the LEDs in the modules. At this point the module is considered operational, and the process goes on with the Bottom Tracker ECAL module and then the Top Tracker ECAL module. Test installations will have been performed at Daresbury before shipment, in order to validate the equipment and procedure, so as to avoid delays at J-PARC. We estimate one week per Tracker ECAL module installation. The POD ECAL modules on the same side of the magnet will be done next. Due to their smaller size and number of channels we expect to do all of them in two weeks. At this point (five weeks from start) the platforms and other installation structures will be lifted above the basket and installed on the other side of it. The same sequence will be repeated for the other half of the ECAL. The Downstream ECAL module will be lowered from the surface straight into the basket, fixed, connected, and tested as for the other modules.

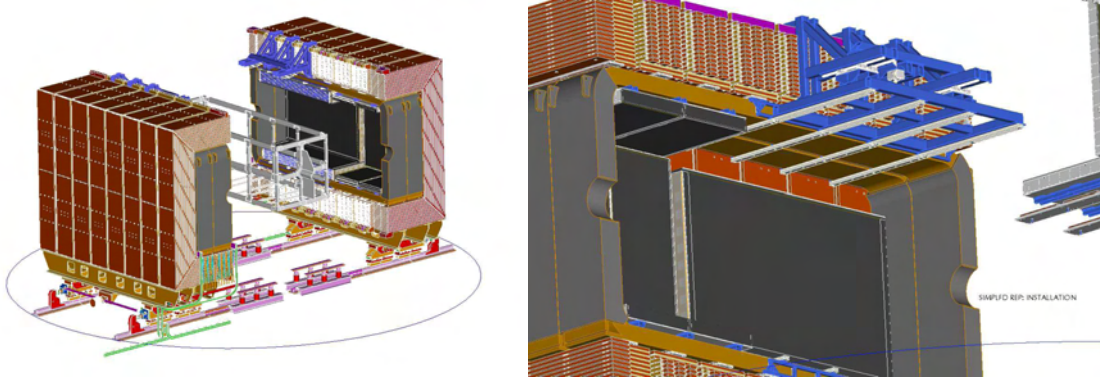


Figure 8.12: *left*: The UA1 magnet in open position, with ECAL modules visible inside the right hand magnet half. The blue structure hanging from the top of the magnet is part of the ECAL installation equipment. The Downstream ECAL (not shown) would be installed inside the far end of the basket. *right*: top Tracker ECAL module not shown. The blue structure hanging from the magnet is the same one as before, with the module carrier frame hanging from it. The module carrier frame has sliders that line up with the ones in the magnet, allowing to transfer the ECAL module from one to the other by simple pushing or pulling.

Details of the installation are evolving as the design of the ECAL and the relevant frames and structures converges to its final stage. Special points of concern that are being addressed in the ND280 Technical Board are services (cooling, dry gas, electricity), survey system and alignment points on the modules, and earthquake protection after each module leaves the surface and before it is secured to its final attachment points on the magnet. It is clear that this time period is critical and every effort will be done to keep it to a minimum.

Commissioning will consist of close monitoring of the operation of all sensors and control systems (photosensor voltage supply, cooling, dry air circulation) and accumulation of cosmic muons data which will provide reference points and together with the production time measurements will yield the first full set of calibration constants. The integrity and correctness of all connections inside the modules will have been done in the UK, so we don't envisage taking modules off the magnet for repairs or maintenance.

## 8.6 Detector calibration

The electromagnetic calorimeter in the T2K near detector must fulfil the requirements for a variety of tasks. The major tasks, such as the detection of photons from  $\pi^0$  decay or the contribution of information to the particle identification capability of the detector, require that the calorimeter be both well understood and monitored continuously.

The calibration of the ECAL is a multiple stage procedure with the goal of converting an observed ADC count in the front-end electronics into an energy deposition from a particle or shower passing through the ECAL. The process requires knowledge of the linearity of the electronics and photosensors, monitoring of the response of the scintillator and wavelength shifting fibre and conversion of energy observed in the ADC to energy of the initial particle.

It is important to have quality control procedures in place during the layer production and after assembly of each layer in the modules. Once assembled, an understanding of the relative response of each scintillator bar, and an absolute calibration of the ECAL energy scales is required.

### 8.6.1 Fibre and Scintillator characterisation and quality control

The quality of the ECAL components will be monitored as they arrive at the production centers. Although initially a large fraction of the material will require checking, it is expected that the checking frequency will decrease as more confidence is attributed to the production process.

To control the quality of the assembly procedure a bar scanner will be used for each of the institutes participating in the module production - either production of the TECAL at the Daresbury center or the production of the POD ECAL, which will take place at a number of the university centers. The scanner will position a radioactive source at selected points down the length of the scintillator bar on delivery and the light output of the scintillator will be measured using a photomultiplier. The radioactive source is currently expected to be a 5 mCi  $^{137}\text{Cs}$  source. A preliminary engineering design of the bar scanner to be used at Daresbury is shown in Figure 8.13. The scanners used at the university centers will be slightly different in design, due to the larger size of the POD ECAL scintillators.

Once the scintillator bars have been assembled into modules at Daresbury, a larger automated source scanner will be used to check the assembly and determine the attenuation lengths of each scintillator bar in the module. Such a scanning machine already exists at Daresbury Laboratory and can be used with minimal modification.

### 8.6.2 Electronics Calibration

The main goal of the electronics calibration is to linearise the response of the front-end electronics so the non-linearities in other components (e.g. photosensors) may be addressed. This will be done using a charge injection system that will inject known quantities of charge into each channel in the readout electronics chain. Scanning the amount of charge over the dynamic range of the ADC will allow the relation between input charge and channel to be determined and will provide monitoring of the performance of the electronics that is independent of the scintillator or photosensor response.

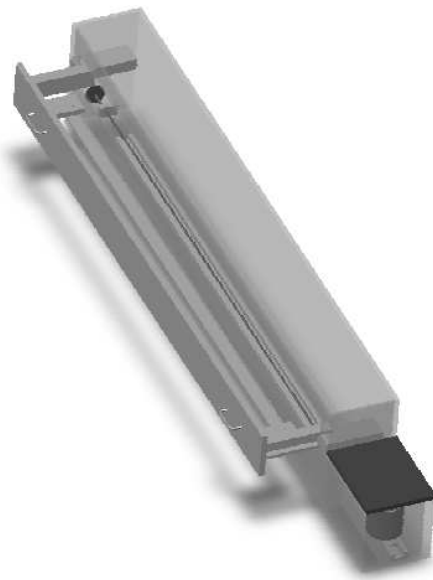


Figure 8.13: Engineering drawing of bar scanners which will be used in the scintillator bar assembly quality control procedure at Daresbury. Shown is the central light-tight drawer, which will contain the scintillator bar, the lead roofed garage in which the source resides and a thick lead screw along which the platform supporting the source travels.

### 8.6.3 Photosensor Linearity and Monitoring

The aim of monitoring the gain and linearity of the photosensors, usually photomultipliers, has been traditionally fulfilled by a light injection (LI) system. Due to cost and space limitations the present design does not include such a system. The photosensor is “self-calibrating” because of the excellent photoelectron resolution. The photosensor gain can be monitored by observing the pulse spectra obtained from the passage of cosmic ray muons, whose single photoelectron peak position can be fitted, and the corresponding photosensor gain extracted. Simulation has also shown that, for the maximum size of signals of interest, the photosensor will always be operating in the linear regime of the photosensors. With careful design of the photosensor connector, it is expected that the linearity will be stable enough not to require constant measurement.

### 8.6.4 Relative response correction

Having calibrated the electronics and photosensors, corrected for non-linearities and attenuation effects, the light output of the scintillator and wavelength shifting fibres must be considered. For a given energy deposition by a charged particle, the size of the signal detected from different scintillator bars will be slightly different. Small variations in the concentration of fluor, in the optical coupling of the fibre to the scintillator and the fibre to the photosensor, in the photosensor gain and quantum efficiency, and environmental reasons give rise to a different response from each scintillator.

All these effects can be compensated for by using cosmic ray muons and muons from neutrino interactions both in the detector and in the material surrounding the detector. Such muons provide a continuous, well-understood source that can be used to monitor the scintillator response over the life time of the experiment. The general procedure will be to collect a number of muon hits in each bar and then fit the energy deposition profile with a functional form based on known muon  $dE/dx$  behaviour. A standard energy deposition from a minimum ionising particle (m.i.p) is then defined to be some statistic based on this distribution, such as the position of the peak in the energy loss spectrum or the truncated mean of the distribution. The exact statistic that will be used will be determined by investigating the stability of different options in the working system. The rate of external muons going

through the ECAL is of the order of 100Hz, whilst the rate of muons from interactions in the cavern walls is of the order of 1 Hz. This provides sufficient statistics to perform this relative correction daily.

### **8.6.5 Determination of the absolute energy scale**

To fulfil the main function of calorimetry it is important that the conversion factor between deposited energy and ADC counts be known. The calibration tasks described in the previous sections have established the conversion from ADC counts to deposited energy measured in units of a m.i.p. The last part of the puzzle is to determine the conversion from these arbitrary units to units of GeV. This requires *a priori* knowledge of the energy of particles that enter the calorimeter and hence a beam test will be used to derive the absolute energy scale.

The requirements of the beam test are clear. The calorimeter must be capable of studying electromagnetic particles and hadrons with energies ranging from 200 MeV to 5 GeV. There are, then, requirements for an electron beam and a pion beam. Since muons will be used extensively in the relative calibration, they should also be present. Clearly the beams must be able to be set to several intermediate energies as well in order to fully map the response function. Since the calorimeter will be used to study neutrino interactions, with particles entering from all angles, the capability of rotating the ECAL module to present different angles of incidence is necessary. The capability to trigger on particle type is also a requirement, if a mixed beam is used.

Comparison of all test-beams that are expected to be operating around 2008/2009 shows that the secondary beam lines in the CERN East area match the requirements most closely. It is expected that both the downstream ECAL module, and one of the POD ECAL modules will be inserted into the beam.

# Chapter 9

## Photo-sensor

### 9.1 Introduction

In the ND280 detector complex, all the sub-detectors except for TPC's will use scintillators read out with wavelength shifting (WLS) fibers as active components. This readout technique is now well-established in particle detectors. However, there are several constraints that are to be taken into account for the T2K-ND280 detectors:

- Existence of magnetic field in off-axis detector. This sets severe limitation on the use of traditional multi-anode photomultipliers.
- Limited space available, both in on-axis and off-axis detectors.

After investigating several candidates that include multi-channel plate (MCP)-PMT's and avalanche photodiodes (APD's), we have chosen semiconductor-based photosensors: metal-resistor-semiconductor (MRS) APD developed in Russia by the Center of Perspective Technologies and Apparatus (CPTA) and multi-pixel photon counter (MPPC) developed in Japan by Hamamatsu Photonics, as our baseline candidates. Fig. 9.1 shows pictures of these devices. Detailed description of MRS-APD and operation

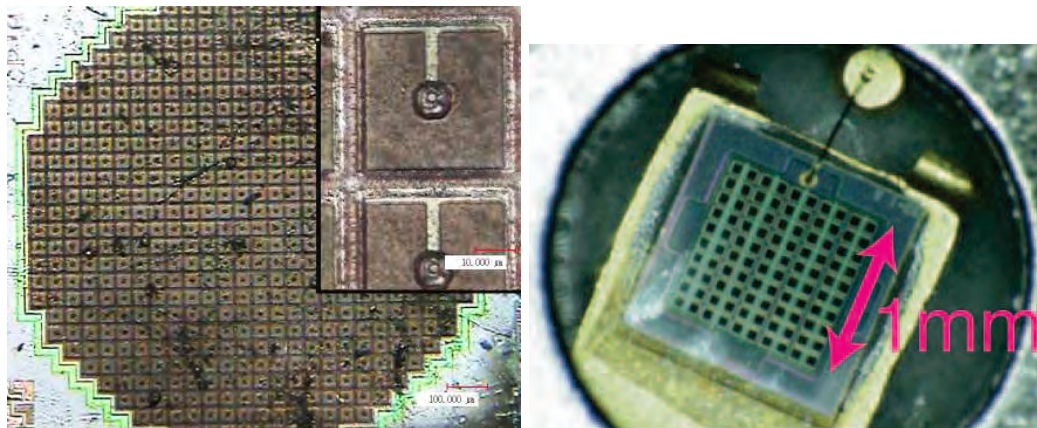


Figure 9.1: Pictures of MRS-APD (left) and MPPC (right). Face view of a MRS APD with 556 pixels magnified  $\times 200$  and  $\times 2000$  in the inset. The sensitive area of MRS has an octagonal shape with an 1.2 mm side-to-side distance. Sensitive pixels of  $35 \times 35 \mu\text{m}^2$  size are separated by  $7 \mu\text{m}$  wide grooves.

principles can be found in [1, 2, 3, 4]. Descriptions of MPPC are presented in [5, 6].

## 9.2 Operation principle

Both MRS-APD and MPPC are multi-pixel semiconductor photodiodes which operate in the limited Geiger mode and consist of many small pixels on common silicon substrate. Typically 100 – 1000 pixels are integrated on about 1 mm<sup>2</sup> of substrate. Each pixel operates as an independent Geiger micro-counter with a gain of the same order as a vacuum photomultiplier. Geiger discharge is initiated by a photoelectron in a high electric field locally created in a very thin layer ( $\mathcal{O}(1)$   $\mu\text{m}$  p-n junction) by the applied bias voltage above the breakdown voltage so that the electric field can sustain the carriers avalanche, however no current is going through the depletion layer until the first carrier is generated. The avalanche current in each pixel produces a voltage drop at individual resistors. As a result, the electric field density becomes small and can no longer support the discharge quenched in such a way. Then, the bias circuit restores the high electric field in the fired pixel in a short time interval, and this pixel is again able to detect another photon.

The gain is determined by the charge accumulated in a pixel capacitance:

$$Q_{\text{pixel}} = C_{\text{pixel}} \cdot \Delta V, \quad (9.1)$$

where  $\Delta V$  is a difference between the applied bias voltage and the breakdown voltage of the diode (overvoltage). Since  $\Delta V$  is about a few volts and  $C_{\text{pixel}} \simeq 50$  fF, then typical  $Q_{\text{pixel}} \simeq 150$  fC, that corresponds to  $10^6$  electrons. For MRS-APD/MPPC's the operational bias voltage  $V_{\text{bias}}$  is well below 100 V. A single incident photon can fire more than one pixel due to cross-talk. Thus, the more accurate gain value of a photodiode is equal to the charge of a pixel multiplied by the average number of pixels fired by a single photon.

The amplitude of a single pixel signal does not depend on the triggered number of carriers in this pixel. In such a way, the photodiode signal is a sum of fired pixels. Each pixel operates as a binary device, but the multi-pixel photodiode as a whole unit is an analogue detector with a dynamic range limited by the finite number of pixels. The pixel size can be  $15 \times 15$  to  $100 \times 100$   $\mu\text{m}^2$ , and the total number of pixels is 100–4000 per mm<sup>2</sup>. In addition, because the thickness of the amplification region is a few  $\mu\text{m}$ , the devices are insensitive to applied magnetic field. These features make MRS-APD/MPPC the best photosensor candidates for T2K-ND280.

There are several parameters that are important for the evaluation of these devices. The **gain** of a device is defined as the output charge corresponding to single Geiger discharge, often called one “photo-electron (p.e.)” signal, divided by the electron charge. The **dark noise rate** is the counting rate for a given threshold (for example, 0.5 p.e., 1.5 p.e.) when no light illuminates a device. The **photon detection efficiency (PDE)** is defined as the probability that a signal is observed when a photon hits a device. The **cross-talk rate** is the probability that Geiger avalanche is triggered in the neighboring channel(s) when a pixel is fired.

## 9.3 Requirements from detectors

Table 9.1 summarizes the requirements from each sub-detector. Fortunately, the required parameters are rather similar in all subdetectors. All the subdetectors will use WLS fibers of 1 mm diameter. Photosensors are required to provide high enough light signals viewing these fibers. Therefore it must have good photon detection efficiency (PDE) for green light and match to a 1 mm diameter of WLS fibers. Light signals from a minimum ionizing particle in T2K detectors are estimated to be in the range from a few to a few ten photoelectrons from each fiber end. To obtain such signals the minimum PDE of the photosensors is required to be at the level of a green-extended PMT.

The number of pixels is also an important parameter that limits the linearity of the response and the dynamic range of a device. On the other hand, each pixel needs to be isolated from adjacent pixels that reduces the active sensitive area due to the dead region between pixels. Large number of pixels reduces the active area. Thus, there is a trade-off between the linearity and the photon detection

Table 9.1: Requirements on photo-sensor from each sub-detector.

Item	FGD	POD	SMRD	ECAL	IN-GRID
Number of sensors	9216	10K	8-10K	~21K	7K
Pixels per sensor	> 400	> 400	> 400	> 400	~ 100
Efficiency for green light, %	> 10	> 10	> 10	> 10	> 15
Dark rate, MHz (0.5 p.e. threshold)	< 1.5	< 1.5	< 1.5	< 1.5	< 1.5
Gain, $\times 10^6$	0.5 – 1	0.5 – 1	0.5 – 1	0.5 – 1	> 0.5

efficiency of a device. For off-axis detectors, the number of pixels is required to be  $\geq 400$  to keep response linearity up to 100 photoelectrons. The IN-GRID detector does not need a wide dynamic range and linearity, but requires high PDE.

Dark rate is an intrinsic feature of MRS-APD/MPPC sensors. High dark rate deteriorates the detector performance and reduces the particle detection efficiency for low energy deposits. We require that the rate of dark pulses has to be not higher than 1-1.5 MHz at operating conditions. Gain of MRS-APD/MPPC is not a critical parameter. However, it is desirable to have it around  $(0.5-1.0) \times 10^6$  to match the unified front-end electronics.

Taking into account the total number of photosensors the cost issue can be decisive. In total, we need about 60K sensors. The choice between MRS-APD and MPPC is subject to decision by each sub-detector group, but it is expected that each sub-detector will use only one type of photosensor.

## 9.4 R&D status of the MRS-APD's

A simplified topology of a MRS photodiode is shown in Fig. 9.2. Small pixels are separated by

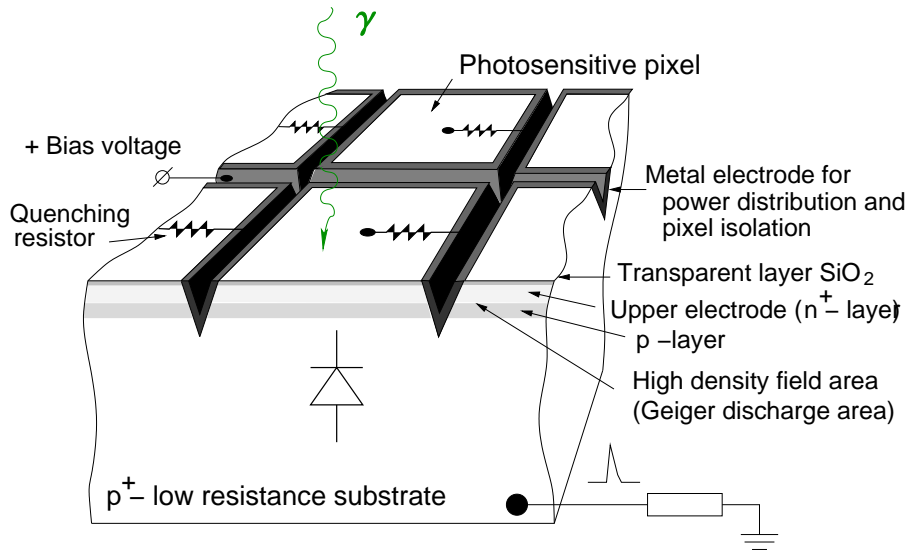


Figure 9.2: The schematic view of the MRS photodiode structure.

grooves filled with an optically non-transparent material to suppress cross-talk.

The main parameters of the MRS photodiodes such as the gain, photon detection efficiency (PDE), intrinsic noise, cross-talk depend on the applied bias voltage or overvoltage  $\Delta V$ . Tests were done using a signal from a green light emitting diode (LED). The MRS signal was amplified and split into

two signals: one was fed to a discriminator, another was measured by an ADC with a gate of about 100 ns.

### 9.4.1 Tested samples

The number of tested MRS-APD is about 300, they were delivered in 2003–2006. Common feature of these devices was the sensitive area size with 1.2 mm side-to-side distance and octagonal shape as shown in Fig. 9.1. The number of pixels is 556, and size of an individual pixel is  $35 \times 35 \mu\text{m}^2$ . Another parameters such as bias voltage, dark rate, gain, PDE varied for different types with changed inner topology. R&D results are presented for the last type which was manufactured and tested in the large quantity of 200 samples. Some details of the tests and obtained parameters can be found in Ref. [7].

### 9.4.2 Gain

A typical operating voltage is around 40 V for the tested MRS photodiodes, although the voltage can differ by a few volts to equalize the gain of photodiodes. The MRS photodiode has an excellent single photoelectron (p.e.) resolution determined mainly by electronics noise even at room temperature. It means that there are only small pixel to pixel gain variations as well as small fluctuations in Geiger discharge development. Scintillator signal spectra obtained with a MRS-APD are shown in Fig. 9.3. The light signal was obtained at two bias voltages. Fig. 9.3 demonstrates that the PDE increases for

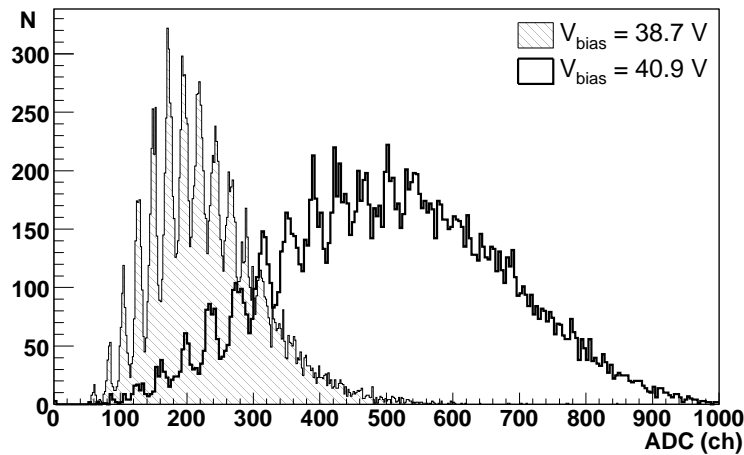


Figure 9.3: Spectra of scintillator signal obtained with a MRS-APD in a beam for two bias voltages. Higher voltage increases the gain and PDE but degrades p.e. resolution because of higher dark rate.

higher bias voltage, but worsens the p.e. resolution at the same time.

The gain depends on the photodiode topology, bias voltage and temperature. The voltage and temperature sensitivities of the MRS APD gain are rather weak as will be demonstrated below. A 0.1 V change in bias voltage corresponds to a 2–3% variation in gain. The charge of a single p.e. signal in a calibrated ADC was used to determine the MRS APD gain. The typical gain value was measured to be about  $0.5 \times 10^6$  at room temperature (22°C).

### 9.4.3 Photon detection efficiency

The photon detection efficiency (PDE) of a multi-pixel avalanche photodiode operated in the limited Geiger mode is a product of 3 factors:

$$\text{PDE} = \text{QE} \cdot \varepsilon_{\text{Geiger}} \cdot \varepsilon_{\text{pixel}}, \quad (9.2)$$

The meaning of each parameter is as follows.

- QE is the wavelength dependent quantum efficiency
- $\varepsilon_{\text{Geiger}}$  is the probability to initiate the Geiger discharge by a photoelectron
- $\varepsilon_{\text{pixel}}$  is a fraction of the total photodiode area occupied by sensitive pixels

The bias voltage affects one parameter in expression (9.2),  $\varepsilon_{\text{Geiger}}$ . The geometrical factor  $\varepsilon_{\text{pixel}}$  is completely determined by the photodiode topology. Its value is estimated to be close to 70% in a MRS-APD. The absolute value of the PDE was measured using small pulses from a green LED (525 nm) which illuminated a MRS photodiode through a 0.5 mm diameter collimator. The number of emitted photons was obtained using a calibrated PMT XP2020. The PDE values at 525 nm at different bias voltages are presented in Fig. 9.4. The cross-talk contribution was subtracted from the

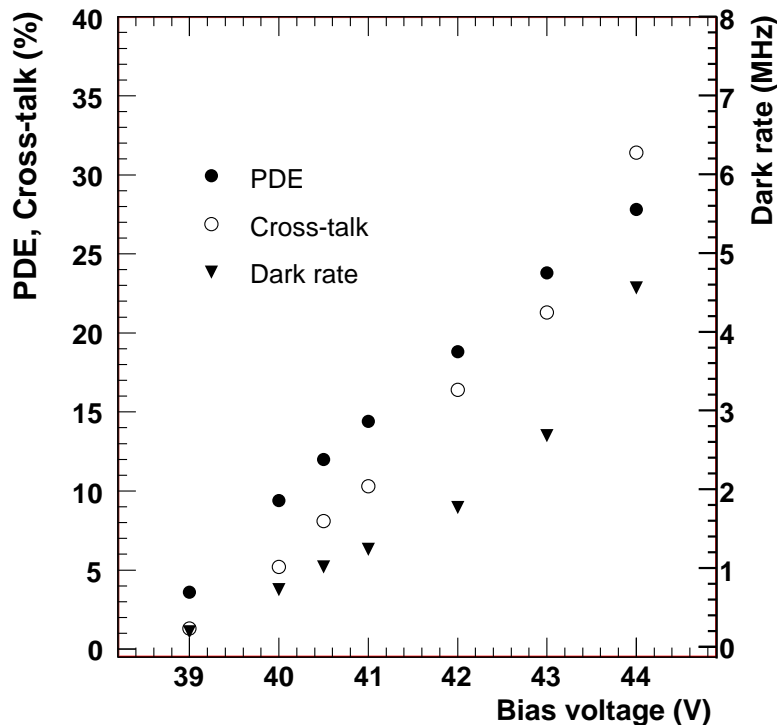


Figure 9.4: The photon detection efficiency (PDE), cross-talk and dark rate as a function of the applied bias voltage for a MRS-APD.

signal to obtain the correct value of the PDE, the accuracy of which is estimated to be  $\pm 10\%$ . As seen in Fig. 9.4, the PDE is about 12% at a dark rate of 1 MHz. The PDE can be increased up to almost 30% at the expense of much higher dark rate. The PDE dependence on the wavelength of the detected light, as well as the emission spectrum of the WLS fiber Y11 are shown in Fig. 9.5. The spectrum of light transported through a fiber depends on the fiber length since short wavelengths are attenuated more strongly than long wavelengths. The spectral response of a MRS photodiode was measured in a spectrophotometer calibrated with a PIN-diode [8]. The PDE was measured at higher  $V_{\text{bias}}$  and, therefore, the dark rate was higher (about 2.3 MHz for a discriminator threshold of 0.5 p.e.). The PDE decreases by about 50% when  $V_{\text{bias}}$  is lowered such that the dark rate is  $\sim 1$  MHz.

#### 9.4.4 Dark rate

The limiting factor for a wide application of multi-pixel avalanche photodiodes in the readout of scintillators is the dark noise rate which originates from thermally created carriers in the depletion

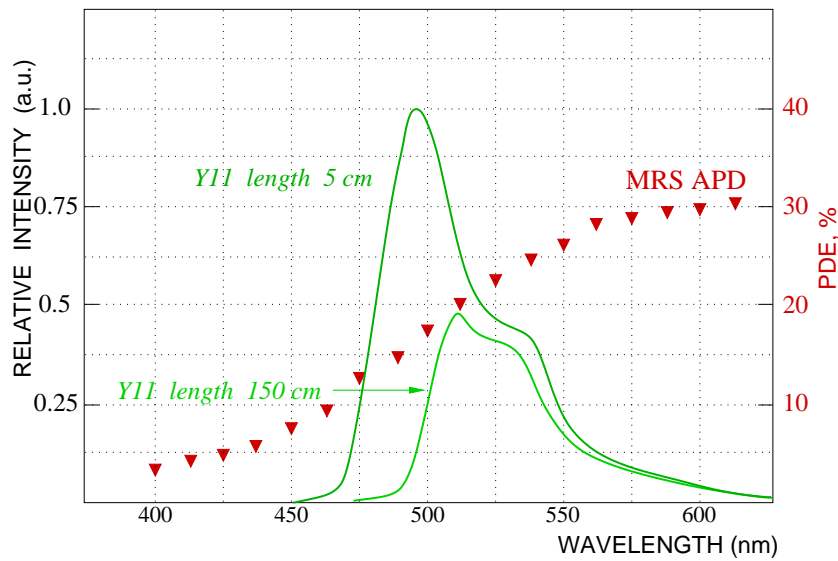


Figure 9.5: Light emission spectra of the Y11(150) fiber at lengths of 5cm and 150 cm (from Kuraray plots). The PDE of a MRS-APD as a function of the wavelength at high bias voltage.

region under high electric fields. The dark rate mainly consists of single p.e. pulses. Larger amplitude pulses also contribute to the dark rate, as shown in Fig. 9.6. However, the intensity of the pulses with 2

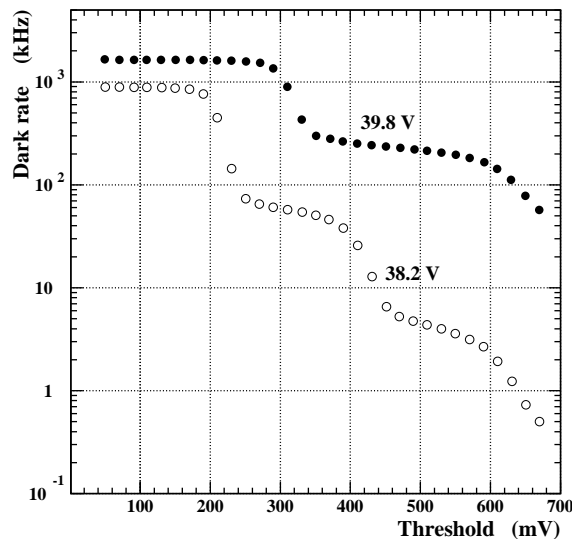


Figure 9.6: Dark rate vs the discriminator threshold for two bias voltages. The discriminator threshold values of 100, 300, and 500 mV correspond to 0.5 p.e., 1.5 p.e., and 2.5 p.e., respectively, for  $V_{\text{bias}} = 38.2$  V.

p.e. amplitudes is about 10-15 times less than the intensity of the single p.e. pulses. Large amplitudes ( $> 1$  p.e.) are generated by the optical cross-talk as well as by accidental pile-ups between the independent pixels, though the second effect is relatively small. The dark rate decreases to a few kHz at a threshold of 2.5 p.e. The intensity of 1 p.e. pulses as well as 2 p.e. pulses is significantly higher for higher bias voltage, as can be seen from Fig. 9.6. Dark pulses and mostly leakage currents create the dark current through a MRS photodiode in a typical range of  $0.3 - 1.0 \mu\text{A}$

## 9.4.5 Optical cross-talk

A single incident photon can fire more than a single pixel due to optical cross-talk. The mechanism of this effect is not quite clear. Models predict that infrared and even visible photons are emitted during the Geiger discharge and recombination of carriers. In Ref. [9] the emission probability was estimated in  $10^{-5}$  photons per carrier at a junction, and the most effective photons have an absorption coefficient of  $\sim 1$  mm. These photons penetrate into the adjacent pixels and fire them. Optical cross-talk leads to a higher than expected signal as Geiger discharge occur in additional pixels. An adverse effect comes from the correlated nature of cross-talk signal which can produce large amplitudes from dark noise.

The absolute value of the cross-talk can be calculated by assuming a Poisson distribution for the number of photoelectrons observed in response to the light from a LED. When the MRS APD noise is small, the measured mean number of fired pixels by the LED photons,  $\bar{N}_{\text{LED}}$ , is compared with the calculated value  $\bar{N}_{\text{pe}}$  given by

$$\bar{N}_{\text{pe}} = -\ln P(0), \quad (9.3)$$

where  $P(0)$  is the fraction of 0 p.e., or “pedestal” events. Then the deviation of the ratio  $\bar{N}_{\text{LED}}/\bar{N}_{\text{pe}}$  from 1 gives the cross-talk value. These values measured at several bias voltages are presented in Fig. 9.4.

A cross-talk value of about 5% was obtained at a bias voltage that provides a dark noise rate of  $\leq 1$  MHz at a discriminator threshold of 0.5 p.e. The cross-talk is larger for higher bias voltage. The sharp decrease of the dark rate shown in Fig. 9.6 is a good demonstration of the low optical cross-talk. It should be noted that the signal amplitude expressed in p.e. is smaller than the measured amplitude obtained from the average number of fired pixels by the cross-talk value, i.e. by a few per cent.

## 9.4.6 Temperature dependence

The PDE and gain of MRS photodiodes (as well as the signal amplitude) are expected to be sensitive to temperature because the breakdown voltage depends on temperature. The MRS signal amplitude (light yield) is proportional to  $N_{\text{photons}} \times \text{PDE} \times \text{gain}$ , where  $N_{\text{photons}}$  is the number of photons from the LED which illuminates the photodiode. The parameters of the MRS photodiodes were measured over temperatures from  $15^\circ$  to  $33^\circ\text{C}$ . The temperature variation of the MRS signal (a green LED was used as a light source) is presented in Fig. 9.7. The MRS signal dependency of  $-1.5\%/^\circ\text{C}$  is

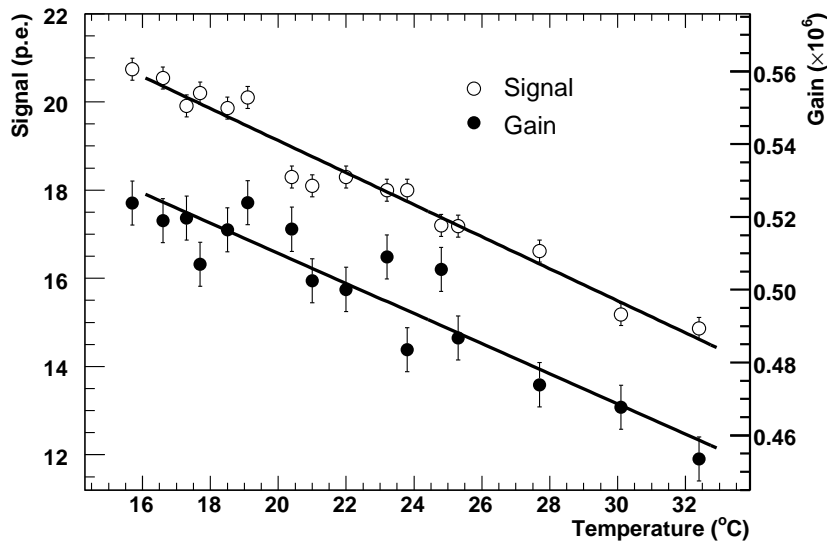


Figure 9.7: The MRS signal from a green LED and gain as a function of the ambient air temperature. The MRS signal itself decreases with temperature as  $-1.5\%/^\circ\text{C}$  obtained for increasing temperature. The MRS gain itself decreases with temperature as  $-1.2\%/^\circ\text{C}$

(see Fig. 9.7), while the PDE varies with temperature as  $-0.3 \text{ \%}/^\circ\text{C}$ . In a limited temperature interval around room temperature, the dark rate depends on temperature with a coefficient of  $62 \text{ kHz}/^\circ\text{C}$ , as shown in Fig. 9.8. The discriminator threshold was kept at the constant level in these tests. Decreasing

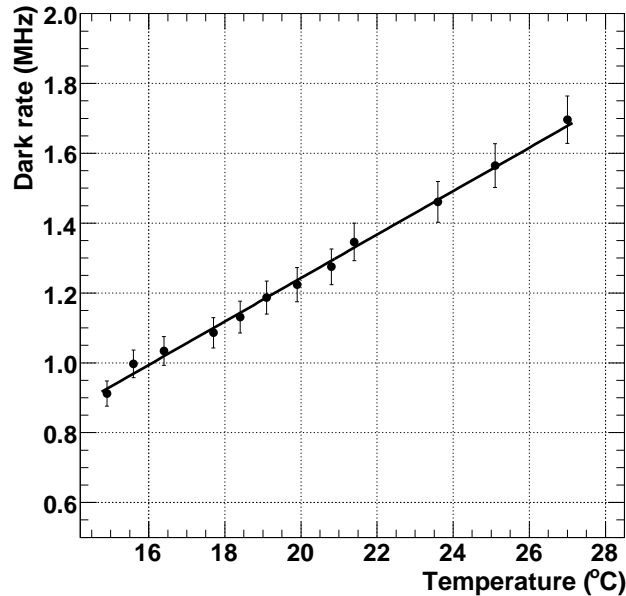


Figure 9.8: Dark rate of MRS-APD at a threshold of 0.5 p.e. vs the temperature.

the temperature below  $0^\circ\text{C}$  greatly reduces the noise and increases the PDE, as shown in Ref. [8].

#### 9.4.7 Recovery time

The ability of MRS photodiodes to operate at high counting rates was tested using two LED signals. The first signal is employed to activate the pixels, and the second one is to check their response. We measured the amplitude of the second signal  $A_2(t)$  as a function of the time difference  $t$  between the first and second signals. Fig. 9.9 shows the ratio  $A_2(t)/A_2(0)$ , where  $A_2(0)$  is the amplitude of the second signal when the first LED signal is off. As seen from Fig. 9.9, a minimum time interval between the first and second pulse of about  $5 \mu\text{s}$  is needed to recover about 95% of the full amplitude of the second signal. This long recovery time is due to the fact that the individual resistor of each pixel,  $R_{\text{pixel}}$ , has the value of about  $20 \text{ M}\Omega$ , the pixel capacitance  $C_{\text{pixel}}$  is typically  $50 \text{ fF}$  that gives  $\tau = R_{\text{pixel}} \cdot C_{\text{pixel}} \sim 1 \mu\text{s}$ . This parameter defines the dead time for an individual pixel but not for the whole device.

#### 9.4.8 Dynamic range and linearity

The dynamic range of the MRS photodiode is limited by the finite number of pixels. The saturation of the MRS photodiode in response to large light signals is shown in Fig. 9.10. In this test, the LED signal was adjusted to obtain similar response for both PMT and MRS photodiode at the light yield below 150 p.e. The photodiode signal is linear at low LED amplitudes. A nonlinearity of about 10% is already seen for signals of 150-200 p.e. For the PMT signal of 500 p.e., the MRS APD produces a 30% smaller value than that of the PMT. Full saturation of all 556 pixels begins when the PMT signal from LED is greater than 2000 p.e.

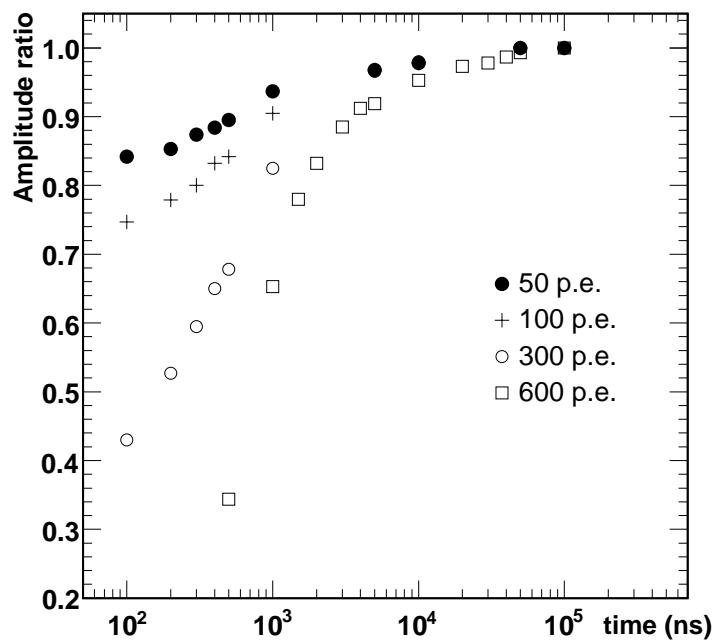


Figure 9.9: The relative amplitude of the MRS delayed signal from a LED as a function of the time difference between 1-st LED pulse and 2-nd one. The amplitude is 100% when the 1-st LED signal is off. The amplitudes of the 1-st signal are 50, 100, 300, 600 p.e.

### 9.4.9 Timing

The development of the Geiger discharge over the whole active area of a pixel takes a few hundred picoseconds. The avalanche spreads over the pixel volume from a seed point where the first carrier was created. For a pixel size of 35  $\mu\text{m}$  the dominant process is the lateral diffusion of free carriers assisted by the avalanche multiplication [9]. The typical rise time of the pulse is 1 ns, the decay time is determined by the pixel capacitance as well as the quenching circuit of a device.

A laser with a wavelength of 635 nm and a pulse width of 35 ps (FWHM) was used to measure the intrinsic time resolution of 1 p.e. pulses. Very weak laser light created only 1 p.e. signals in a MRS photodiode. Fig. 9.11 shows the time resolution obtained at a threshold of 0.2 p.e. at 22°C .

### 9.4.10 Life time

The failure rate of the MRS photodiodes is an important figure of merit for the overall detector performance, because most photodiodes can not be replaced without significant disassembly of the ND280 detector. Exposure to elevated temperature is used to evaluate the expected life time of semiconductor devices. We have placed 19 MRS photodiodes in an oven at 80°C for 30 days. All photodiodes were kept under operating bias voltages. One of the devices started to conduct a large current after a week of heating. The failed device had the worst PDE among of the tested devices. This points to a possible defect in its structure. All other devices passed the test without residual effects. The signals of the tested photodiodes in response to a LED were measured before heating and for a period of about 260 days after heating. The results for two devices are presented in Fig. 9.12. The accuracy of these measurements is about  $\pm 2.0$  p.e. (rms) due to misalignments between the light aperture and the MRS-APD sensitive area. No degradation in the light signal was observed for more than 7 months after heating.

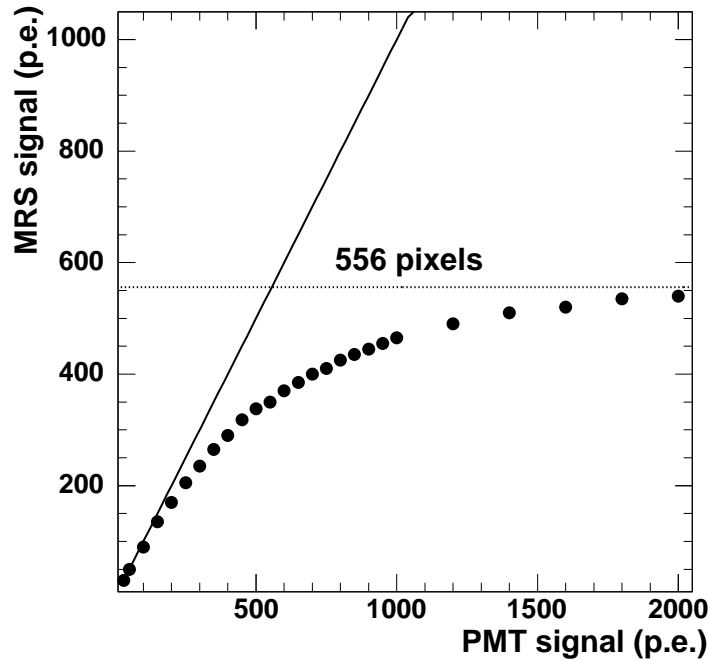


Figure 9.10: The MRS-APD response vs the PMT signal. The signal of the MRS-APD is saturated at the level of the maximum number of 556 pixels.

#### 9.4.11 Dispersion of parameters

Two hundred MRS photodiodes fabricated from a few different wafers were tested. In order to meet the requirements of the experiment, the bias voltages were set so that dark rate of each device was close to a reference value of 1 MHz at 22°C at a discriminator threshold of 0.5 p.e. The bias voltages were 38-42 V, which resulted in a wide range of 8.9–18.8% for the PDE values, and the gains of these 200 MRS-APD were found to be between  $0.34 \times 10^6$  and  $0.69 \times 10^6$ .

#### 9.4.12 Summary and prospects

The studied MRS photodiodes demonstrate good performance: a low cross-talk value of a few per cent, and photon detection efficiency for green light ( $\sim 525$  nm) of about 12% at dark rate of around 1 MHz. Long term stability was observed in several monitored devices over 260 days. Gain value of  $0.5 \times 10^6$  is acceptable for the front-end electronics which is under development.

Their calibration and stability control can be provided by means of the excellent p.e. peak resolution. The linearity range of the tested MRS APD is less than 200 p.e. and the recovery time is about 5  $\mu$ s. Although these parameters might be critical for some applications, the performance is acceptable for many detectors of the ND280 complex of the T2K experiment.

Tests of 200 samples show that the selection procedure is required to reject the devices with low PDE at operating bias voltage. Operating bias voltage is set so that to keep dark rate below 1 MHz.

In the fall 2006 we have to complete the development of a new compact package for MRS-APD's. The mass production of MRS-APD then can be started in the end 2006 - beginning 2007.

It should be noted that new devices operating at bias voltage of about 23 V were developed by CPTA in August 2006. The new MRS photodiodes have higher PDE for green light. First tests demonstrated that their sensitivity to green light is improved by a factor 2. Detailed study of these devices is under way.

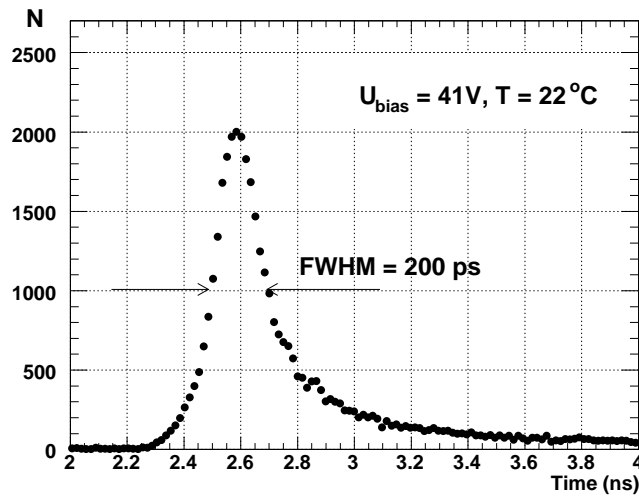


Figure 9.11: Time spectrum of single photoelectron signals obtained by a MRS-APD at 22°C.

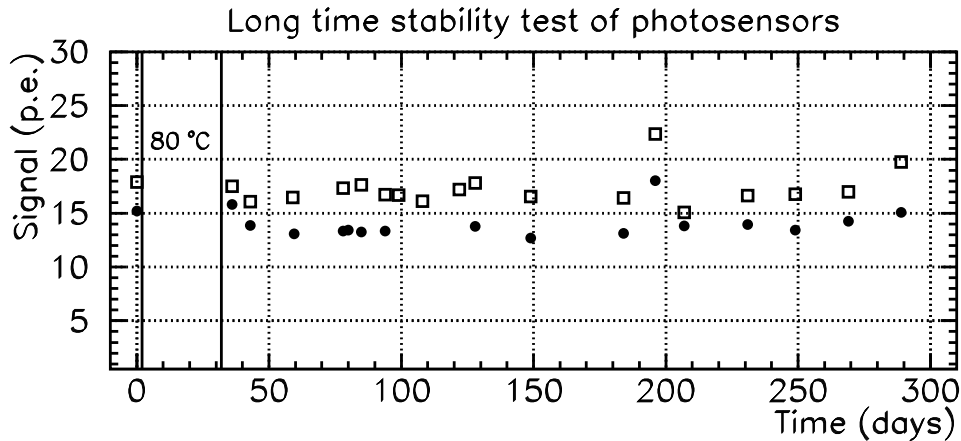


Figure 9.12: Light yields of two MRS photodiodes measured with a green LED before and after the heating test. The heat exposure at 80°C lasted for 30 days. Successively, the photodiodes were monitored for 260 days. The signals were corrected for temperature changes in the range from 18 – 27°C. Each point has an error of  $\pm 2.0$  p.e.

## 9.5 R&D status of MPPC

### 9.5.1 Tested samples

We have tested more than 30 samples from three test production in two years since we started this R&D. The performance of the device improved in each production cycle. Here, we report the performance obtained with samples delivered in Jan. 2006\*. Three 100 pixel devices and three 400 pixel samples were available for tests. Both types have the same active area of  $1 \times 1 \text{ mm}^2$ . The main topology parameters of the tested samples are listed in Table 9.2. The device-by-device variation of each type of MPPC was also tested.

\* New samples were delivered in October 2006 and are being evaluated.

Product number	Num. of pixels	Pitch( $\mu\text{m}$ )	Op. voltage (V)	Signal width (ns)
311-53-1A-002	100	100	70V	40
311-32A-002	400	50	70V	10

Table 9.2: Summary of test samples. Both types have  $1 \times 1 \text{ mm}^2$  active area.

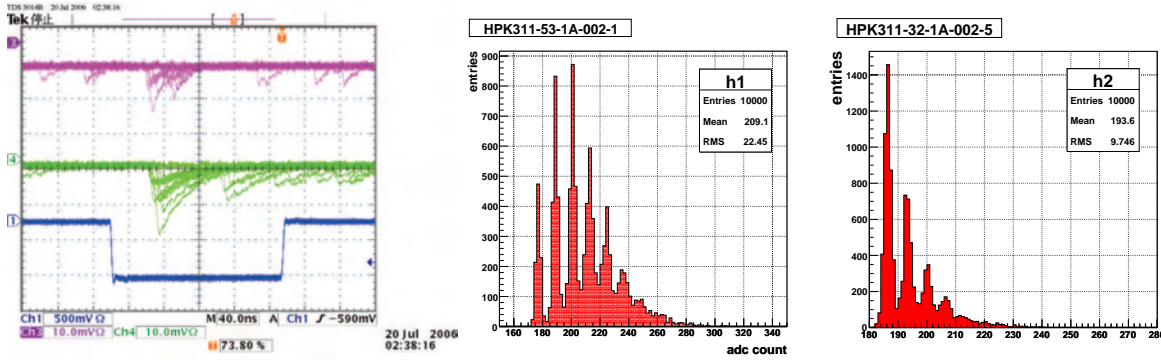


Figure 9.13: Left: Signal of the 400 (pink, top) and 100 (green, middle) pixel device taken with oscilloscope. Middle and right: Signal of the 100 (middle) and 400 (right) pixel device taken with ADC. The leftmost peaks in these figures correspond to the pedestal.

## 9.5.2 Raw signal

Figure 9.13 shows the raw signal of two devices (100 and 400 pixels) taken with an oscilloscope and output charge read out by an ADC. The MPPC is illuminated by a low intensity pulsed light from a LED. The responses for multiple triggers are overlaid in Fig. 9.13. One can see well separated signals corresponding to one, two, and three fired pixels. These observations demonstrate the excellent photon counting capability of the MPPC.

## 9.5.3 Gain

The gain is measured by illuminating a MPPC with light from a LED. From the number of ADC counts between a pedestal and 1p.e. peak, we calculate the charge of a single fired pixel,  $Q$ . The gain is defined as  $Q$  divided by the charge of an electron. Figure 9.14 shows the measured gain of a 100 (left) and 400 (right) pixel device as a function of the applied voltage. The measurement is performed inside a temperature-controlled chamber and the data at 15, 20, and 25°C are shown.

The measured gain is  $3.0 \times 10^5 - 1.2 \times 10^6$  for a 400 pixel device and  $1.0 \times 10^6 - 3.0 \times 10^6$  for a 100 pixel device. The gain linearly depends on the applied voltage as expected from Eq. 9.1. The breakdown voltage decreases with lower temperature, resulting in larger gain at a fixed applied voltage. The breakdown voltage is derived by linearly extrapolating the gain-voltage curve in Fig. 9.14 to the point where gain becomes zero. The temperature coefficient is about  $-3\%/^\circ\text{C}$  at 69.2 V for both types of MPPC.

The device-by-device gain variation is also measured for both types of MPPC at 15°C. The results are shown in Fig. 9.15. The device-by-device variation is about 10% for both types of MPPC. Because the number of tested samples is limited to three, we plan to test much larger numbers of devices in the near future.

Figure 9.16 shows the measured gain for a 100 and 400 pixel device as a function of the difference between applied voltage and the breakdown voltage,  $V_{\text{bias}} - V_{\text{bd}} (\equiv \Delta V)$ . One can see from this figure the gain value is independent on the temperature at the same  $\Delta V$ , so that the gain is a function of only  $\Delta V$ . The breakdown voltage  $V_{\text{bd}}$  for a 100 pixel device as a function of the temperature is shown in

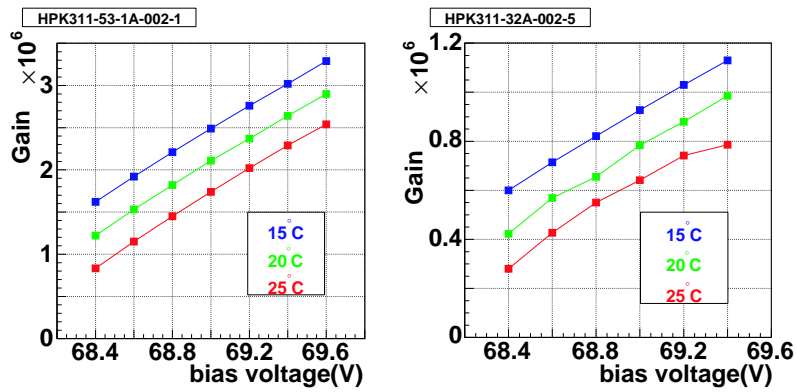


Figure 9.14: Measured gain for a 100 (left) and 400 (right) pixel device as a function of the applied voltage. Blue, green, and red points correspond to data at 15, 20, 25°C, respectively.

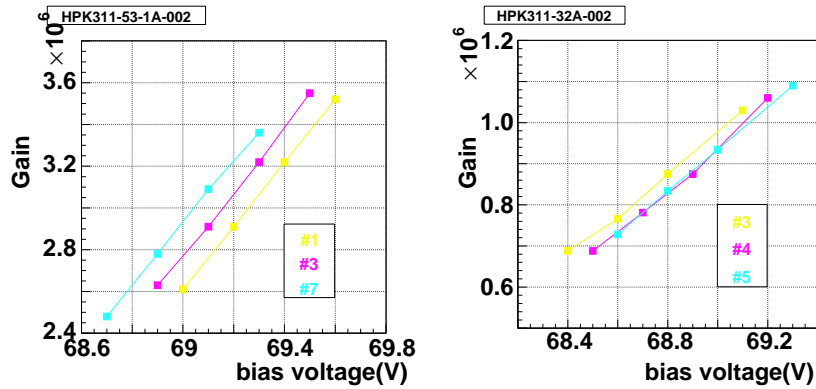


Figure 9.15: Device-by-device gain variation for 100 (left) and 400 (right) pixel devices at 15°C. Yellow, pink, and sky blue points correspond to data of different samples of the same type of MPPCs.

Fig. 9.17. One can see from this figure  $V_{bd}$  increases linearly with the temperature, which is consistent with the description in [10].

### 9.5.4 Dark noise rate

The dark noise rate is measured by counting the rate above 0.5 and 1.5 p.e. threshold without external light input. The results at 15, 20, 25°C are shown in Fig. 9.18. With a threshold of 0.5 p.e., the noise rate is 0.5-1 MHz. However, it decreases by about an order of magnitude if the threshold is set to 1.5 p.e. The noise rate measured at the 0.5 p.e. threshold decreases as the temperature becomes lower, while the noise rate measured at the 1.5 p.e. threshold shows the opposite behavior. This is because the cross-talk rate at the same bias voltage increases as the temperature becomes lower, as shown below.

The device-by-device variation of the noise rate at the 0.5 p.e. threshold for both types of MPPC is also shown in Fig. 9.19. This is measured at 15°C. The maximum difference among three samples for 100 (400) pixel devices is about 13% (30%). It is necessary to test much larger number of devices.

The device-by-device variation of noise rate for 100 and 400 pixel devices as a function of  $\Delta V$  at 15°C is shown in Fig. 9.20.  $V_{bd}$  for each device is calculated from Fig. 9.15. The device-by-device variation of the noise rate at the same  $\Delta V$  becomes about a few percent for both type. The device-by-device variation of noise rate is mainly due to the variation of the breakdown voltage.

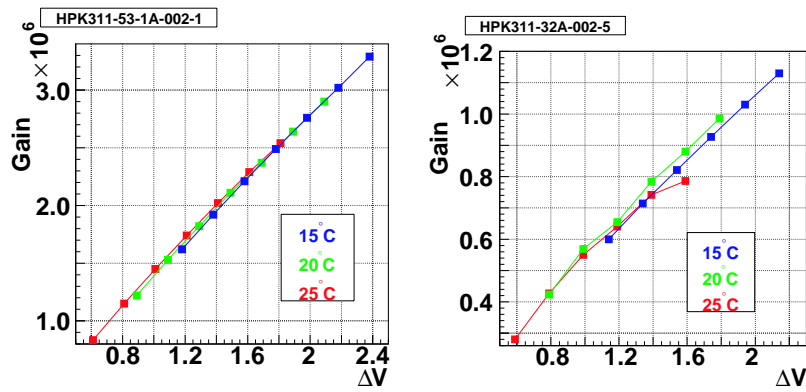


Figure 9.16: Measured gain for a 100 (left) and 400 (right) pixel device as a function of  $\Delta V$ . Blue, green and red points correspond to data at 15, 20, and 25°C, respectively.

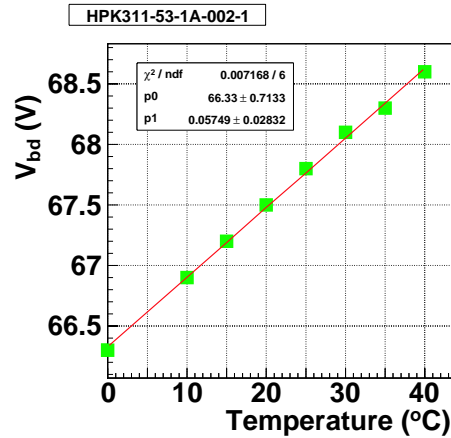


Figure 9.17: Breakdown voltage for a 100 pixel device as a function of the temperature. The linear fitting line is also showed.

### 9.5.5 Photon detection efficiency (PDE)

Because it is difficult to know the absolute light intensity which is injected to an MPPC, we have measured the PDE of an MPPC relative to that of a half-inch PMT, Hamamatsu H3165-10 (Bialkali, QE=15% at  $\lambda = 450$  nm from catalog).

With the current package shown in Fig. 9.1, there is a space of about 0.8 mm between the surface of the cover and the surface of an MPPC. Because the light from a fiber spreads with as large angle as  $40^\circ$ , some light from a fiber may be lost with the current package. In order to study this effect, we have measured the PDE of an MPPC with two setups shown in Fig. 9.21 (setup 1) and Fig. 9.22 (setup 2). With setup 1, an MPPC and a PMT are illuminated with green light from a fiber, Kuraray Y11, through a slit with 1 mm diameter. Because the active area of an MPPC is  $1\text{mm} \times 1\text{mm}$ , all the light from the slit is injected to the MPPC and we can measure the PDE of the MPPC. With setup 2, on the other hand, an MPPC and a PMT are directly connected to a fiber. With this setup, we measure the *effective* PDE including the loss of light from the fiber. Comparing the PDE measured with setup 1 to that with setup 2, we can evaluate how much light is lost due to the current package of an MPPC.

The PDE for both types of MPPCs measured with setup 1 and setup 2 at 15°C is shown in Fig. 9.23. In order to avoid the effect of cross-talk, the number of photoelectrons for the MPPC is derived from the fraction of pedestal (=0 p.e.) events to the total number of trigger, assuming a Poisson distribution. For the PMT, the number of photoelectrons is calculated by dividing the mean output charge by the charge corresponding to 1 p.e. The PDE of the MPPC, measured with setup 1,

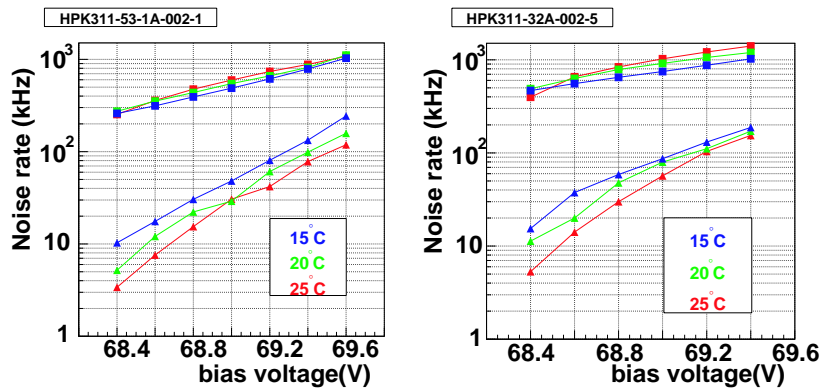


Figure 9.18: Measured dark noise rate for a 100 (left) and 400 (right) pixel device as a function of the applied voltage. Blue, green, and red points correspond to data at 15, 20, 25°C, respectively. Rectangular and triangle points represent the rate with thresholds of 0.5 and 1.5 p.e., respectively.

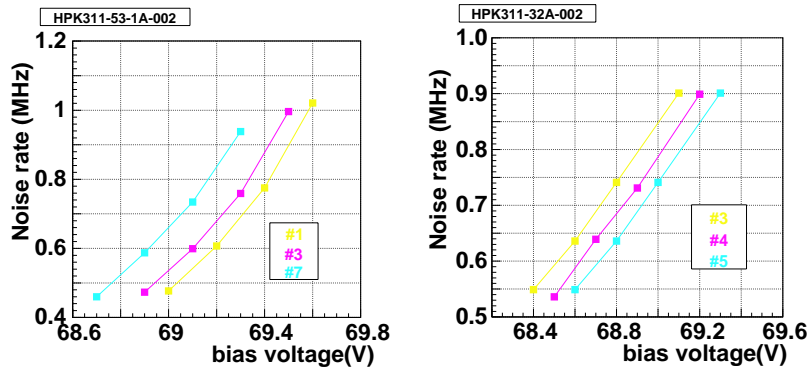


Figure 9.19: Device-by-device variation of the dark noise rate at 0.5 p.e. threshold for 100 (left) and 400 (right) pixel devices. Yellow, pink, and sky blue points correspond to data of different samples of the same type of the MPPCs. This is measured at 15°C.

is about or more than twice of the QE of the PMT. Although about 50% of the light is lost with the current package as seen from the comparison of setup 1 and 2, this will be improved by new package now being designed.

The temperature dependence of the PDE for a 100 and 400 pixel device measured with setup 1 is shown in Fig. 9.24. The PDE becomes lower as the temperature becomes higher. This is also explained by the fact that the breakdown voltage becomes higher as the temperature becomes higher. The measured PDE of a 100 and 400 pixel device as a function of  $\Delta V$  is shown in Fig. 9.25. From these figures, one can see the PDE is independent of the temperature and a function of only  $\Delta V$ .

The device-by-device variation of the PDE measured with setup 1 at 15°C for 100 and 400 pixel devices is shown in Fig. 9.26. The device-by-device variation of the PDE is found to be about 10 - 20%.

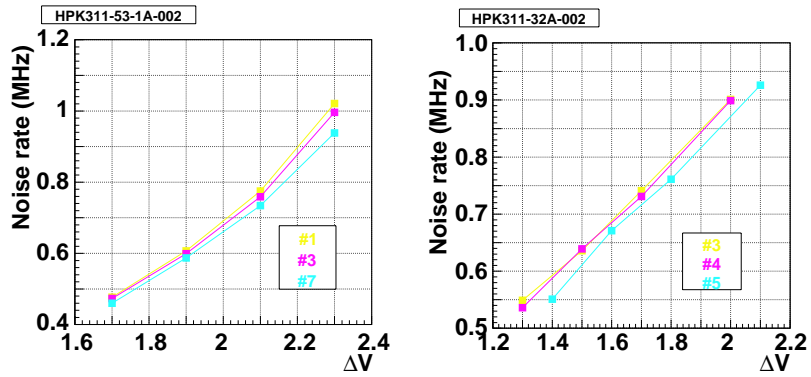


Figure 9.20: Device-by-device variation of the noise rate for 100 (left) and 400 (right) pixel devices as a function of  $\Delta V$  at 15°C. Yellow, pink and sky blue points correspond to data of different samples of the same type of MPPCs.

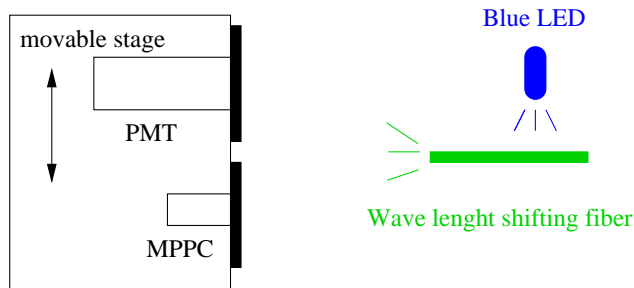


Figure 9.21: Setup for measuring the PDE (setup 1).

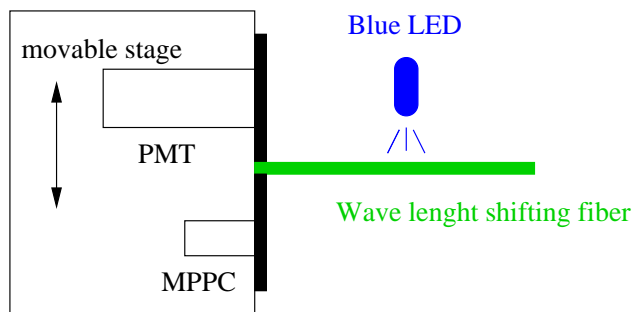


Figure 9.22: Setup for measuring the *effective* PDE including the loss of the light due to the current package (setup 2).

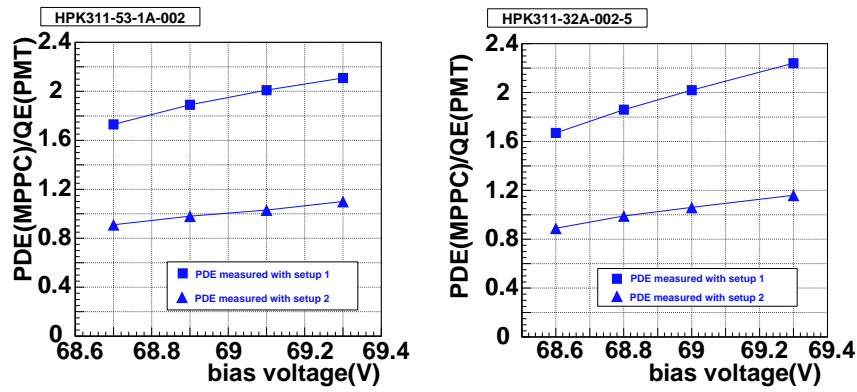


Figure 9.23: PDE of a 100 (left) and 400 (right) pixel device as a function of the applied voltage at 15°C. Rectangular and triangle points represent the PDE measured with a setup 1 and *effective* PDE with setup 2, respectively.

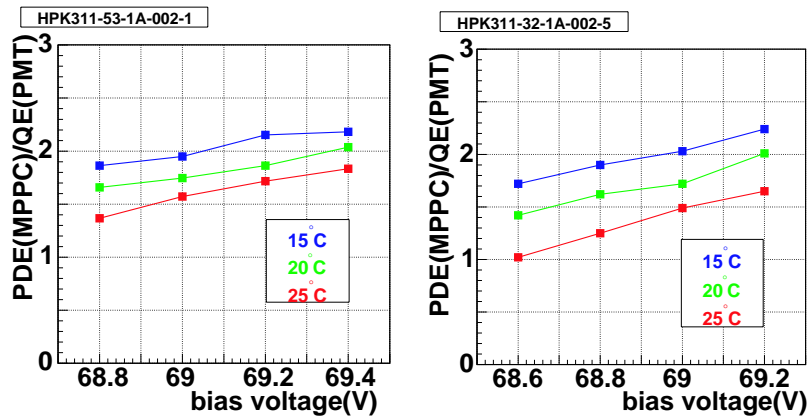


Figure 9.24: Temperature dependence of the PDE for a 100 (left) and 400 (right) pixel device. Blue, green, and red points correspond to data at 15, 20, 25°C, respectively.

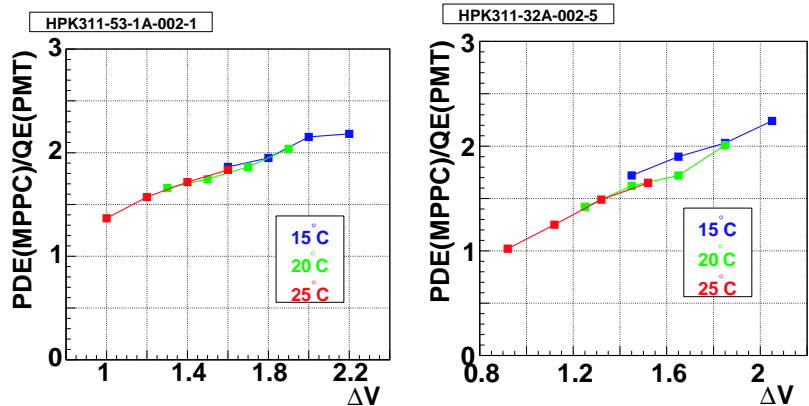


Figure 9.25: The PDE of a 100 (left) and 400 (right) pixel device as a function of  $\Delta V$ . Blue, green and red points correspond to data at 15, 20, and 25°C, respectively.

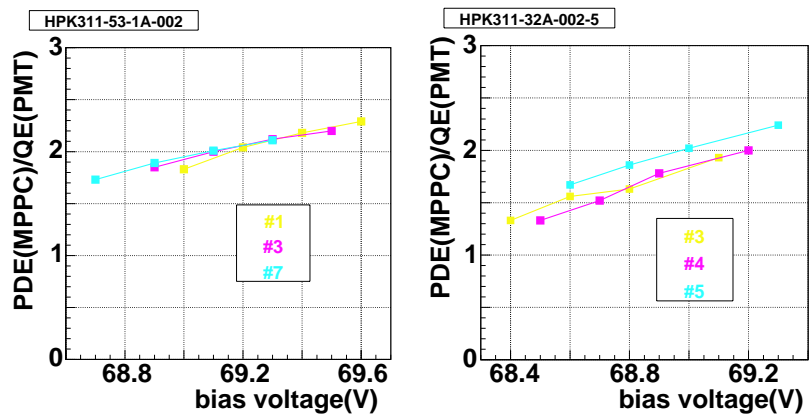


Figure 9.26: Device-by-device variation of the PDE at 15°C for 100 (left) and 400 (right) pixel devices.

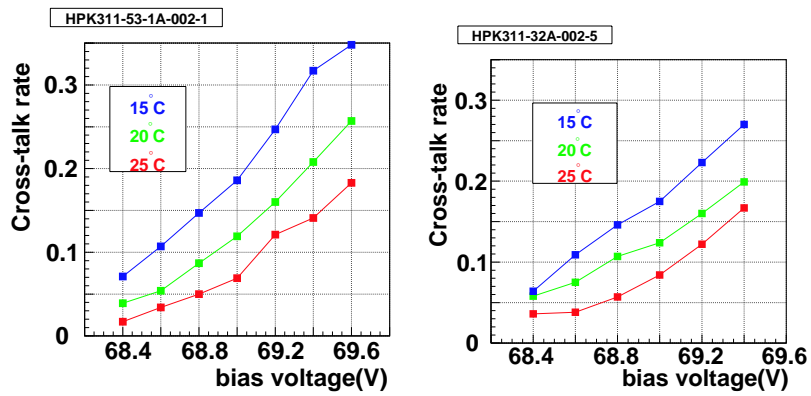


Figure 9.27: Cross-talk rate of a 100 (left) and 400 (right) pixel device as a function of the applied voltage. Blue, green, and red points correspond to data with 15, 20, and 25°C, respectively.

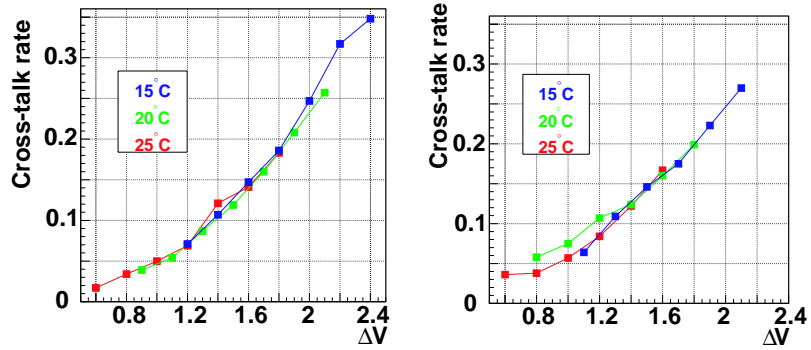


Figure 9.28: Cross-talk rate of a 100 (left) and 400(right) pixel device as a function of  $\Delta V$ . Blue, green, and red points correspond to data with 15, 20, 25°C, respectively.

### 9.5.6 Cross-talk rate

The cross-talk between neighboring pixels has been observed with the MPPC. The origin of the cross-talk is presumed to be optical photons emitted during avalanche which enter neighboring pixels and trigger another Geiger discharge. The probability of cross-talk is estimated from the fraction of events with more than 1.5 p.e. to that with 0.5 p.e. in randomly triggered events. We assume that the events with more than 1.5 p.e. are caused by the cross-talk from the original Geiger discharge in a single pixel due to thermal noise. The effect from accidental coincidence of two independent discharges has been subtracted.

Figure 9.27 shows the cross-talk rate as a function of the applied voltage. The cross-talk rate at the same bias voltage seems to be higher as the temperature becomes lower. This is explained by the fact that the breakdown voltage becomes lower as the temperature becomes lower.

Fig. 9.28 shows the measured cross-talk rate of a 100 (left) and 400 (right) device as a function of  $\Delta V$ . From these figures, one can see the cross-talk rate is independent from the temperature and a function of only  $\Delta V$ .

### 9.5.7 Linearity

The linearity of the MPPC response to a large amount of light is intrinsically limited by the finite number of micropixels. Figure 9.29 shows the number of fired pixels of a 100 and 400 pixel device as a function of light intensity at 20°C. The number of injected photoelectrons is estimated by the p.e. detected by a monitor PMT. We guarantee the linearity of PMT by changing the applied voltage of PMT and repeating the same measurement. The red curve shows the expected response calculated

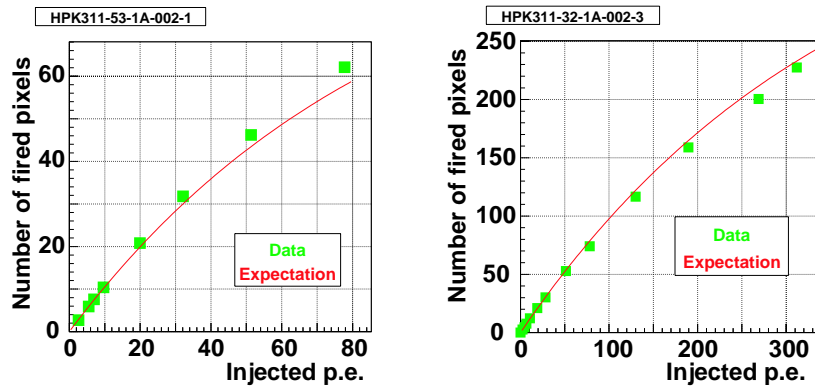


Figure 9.29: Response of a 100 (left) and 400 (right) pixel device as a function of light intensity at 20°C.

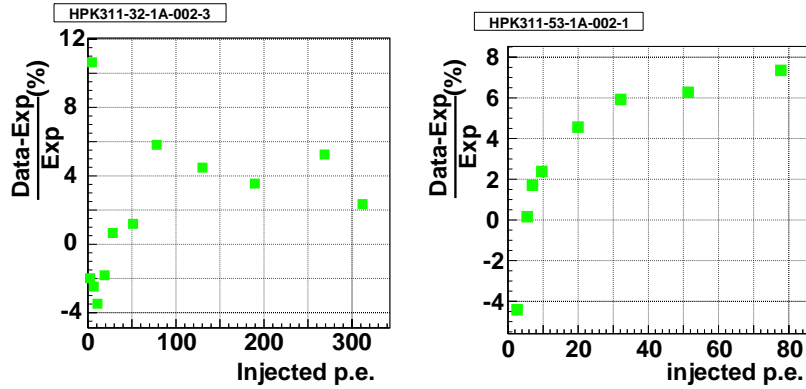


Figure 9.30: Deviation from the expected linearity curve for a 400(left) and 100(right) pixel device at 20°C.

from the number of pixels and separately measured cross-talk rate, and described by the following equation:

$$N_{\text{fired}} = N_0 \times \left(1 - \exp\left(-\frac{x(1+k)}{N_0}\right)\right), \quad (9.4)$$

where  $N_{\text{fired}}$ ,  $N_0$ ,  $x$ , and  $k$  are the number of fired pixels, the total number of pixels, number of injected photoelectrons, and cross-talk rate, respectively. The deviation from the expected curve is shown in Fig. 9.30. It is found to be within 8 (6)% for a 100 (400) pixel device, thus the response of the MPPC to a large amount of light is well understood.

### 9.5.8 Recovery time

The use of MPPCs with high counting rate is limited due to the finite time taken to quench the avalanche and then reset the applied voltage to its initial value. In order to study this recovery time, we fire all pixels of MPPC by illuminating one LED (LED1) with large intensity and check the response to the light from another LED (LED2) at 20° C with changing the time difference between LED1 and LED2 signals. The result is shown in Fig. 9.31. We change the time difference from 1  $\mu\text{s}$  to 120 ns, but the size of signal for LED2 does not change. From this we can see that the recovery time of a 400 pixel device is <120 ns. The recovery time for a 100 pixel device is measured to be also <120 ns. The recovery time is much shorter than MRS-APD because the quenching resistor is order of 100 k $\Omega$  for MPPC.

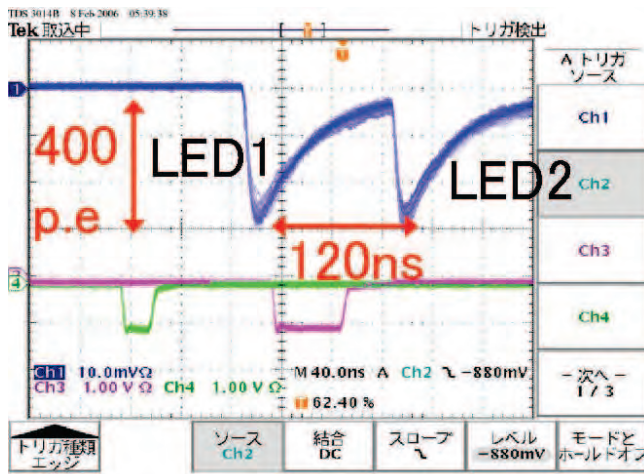


Figure 9.31: Response of a 400 pixel device to the light from an LED2 when all pixels are fired by illuminating LED1 with large intensity at 20°C. The time difference between LED1 and LED2 is 120ns.

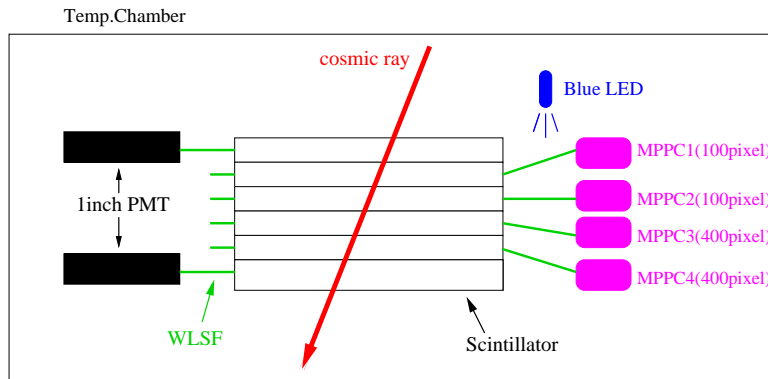


Figure 9.32: Setup for the test of the calibration system.

## 9.5.9 Calibration

The basic parameters of MPPC, gain, PDE and cross-talk rate are all sensitive to the temperature and applied voltage as described above. For the test of calibration scheme, we have traced the MPPC signal for MIP<sup>†</sup> intentionally changing the temperature.

We have tested two calibration schemes described below.

**A: Monitoring gain by 1 p.e. peak** In this calibration method, gain ( $\equiv 1\text{p.e. ADC count}$ ) is monitored by illuminating an LED with low intensity. All of the gain, PDE and cross-talk rate depend only on  $\Delta V$  as discussed before. Because we can calculate the variation of  $\Delta V$  by monitoring only gain, it is possible to derive the PDE and cross-talk rate using the  $\Delta V$  dependence measured beforehand as shown in Fig. 9.25 and 9.28.

**B: Monitoring overall response using LED** In this calibration method, MPPCs are illuminated by LED with the same intensity as the MIP light yield. Because the response to LED light also depends on gain, PDE, and cross-talk rate, we can correct those factors at once by taking the ratio of ADC counts for MIP to ADC count for LED.

The setup of the test of the calibration system is shown in Fig. 9.32. Extruded plastic scintillators developed for K2K SciBar detector,  $1.3 \times 2.5 \times 20\text{cm}^3$  in size, are put in four layers. Kuraray

<sup>†</sup> cosmic-ray muons

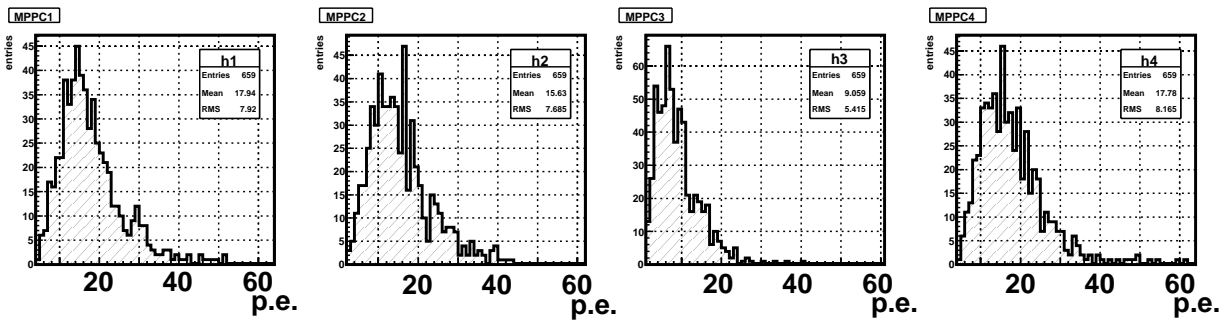


Figure 9.33: Light yield distribution of four scintillators for MIP at 20°C. Left (right) two figures correspond to 100 (400) pixel devices.

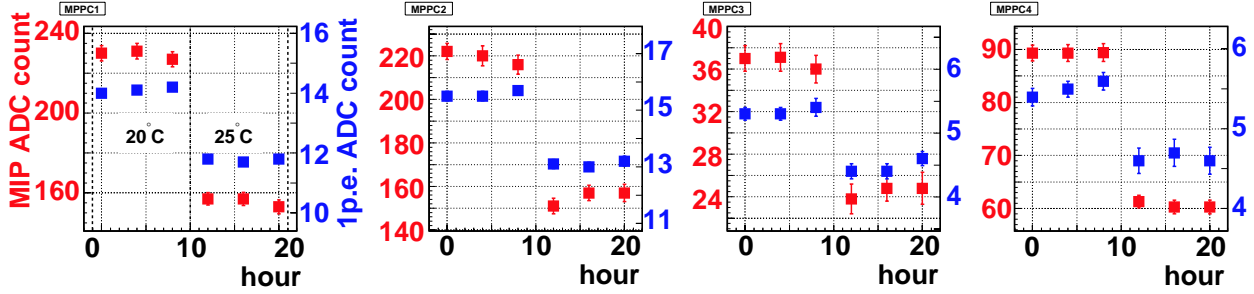


Figure 9.34: Variation of the 1p.e. ADC count (blue points) and ADC counts for MIP (red points). Left (right) two figures correspond to 100 (400) pixel devices.

Y11 wave length shifting fibers of 1mm diameter are inserted into holes at the center of scintillators. The fibers are connected to four MPPCs (two are 400 and two are 100 pixel devices). The MPPC1 (100pixel) and MPPC3 (400 pixel) are the devices whose temperature dependence of gain, PDE, and cross-talk rate are measured before. The size of the trigger counters are the same as that of the tested scintillator, but the WLS fibers have 1.5 mm diameter and are connected to 1-inch PMTs. This setup is put in the temperature-controlled chamber and the temperature is changed between 20°C and 25°C.

Figure 9.33 shows the light yield distribution of four MPPCs for MIP at 20 °C. The top (bottom) two figures correspond to 100 (400) pixel devices. The light yield of an MPPC3 is much smaller than that of others. Because the PDE of MPPC3 is about the same as that of others from Fig. 9.26, the low light yield of a MPPC3 is presumed to be due to misalignment of the fiber and the MPPC.

The variations of 1p.e. ADC count and ADC counts for MIP are shown in Fig. 9.34. For method A, correction factors are calculated from measurements shown in Fig. 9.16, Fig. 9.25, and Fig. 9.28. The same correction functions for the PDE and cross-talk rate as MPPC1 and MPPC3 are applied to MPPC2 and MPPC4, respectively. The variation of the light yield after correction is shown in Fig. 9.35. Lines corresponding to  $\pm 3\%$  deviation from the mean are also shown. The detector response is calibrated with about 3% precision after correction for gain, PDE, and cross-talk rate with method A.

The test of calibration method B is done in different period from that of calibration method A. The variation of ADC counts for MIP and LED are shown in Fig. 9.36 and Fig. 9.37, respectively. The corrected light yield is shown in Fig. 9.38. Lines corresponding to  $\pm 3\%$  deviation from the mean are also shown. The device response is also well calibrated with about 3% precision with method B.

Table 9.3 shows the calibration precision for each device. The calibration precision is found to be within about  $\pm 3\%$  for all four MPPCs even if the temperature changes by 5°C. The precision of calibration is better for method B.

For method A, it is necessary to measure the  $\Delta V$  dependence of PDE and cross-talk rate before

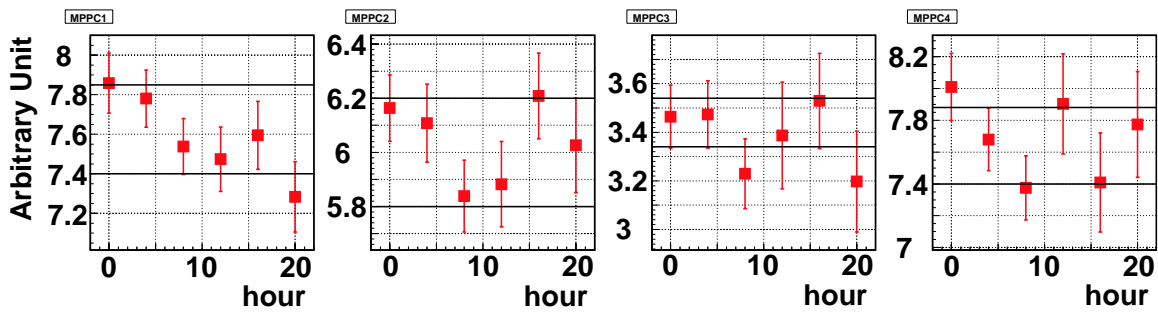


Figure 9.35: Variation of the corrected light yield. The correction factor is calculated from measured 1p.e. ADC count shown in Fig. 9.34 and measured  $\Delta V$  dependence for PDE and cross-talk rate. Left (right) two figures correspond to 100 (400) pixel devices. Lines corresponding to  $\pm 3\%$  deviation from the mean are also shown.

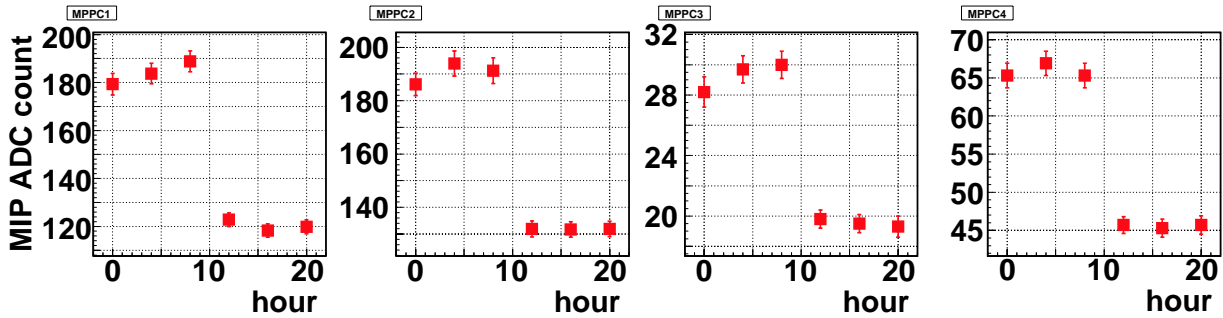


Figure 9.36: Variation of the ADC counts for MIP. Left (right) two figures correspond to 100 (400) pixel devices.

installation of MPPCs. We have found that we can apply the same correction function for PDE and cross-talk rate to the same type of MPPCs. Sampling measurement may be enough for the same type of MPPCs before installation of MPPCs if their characteristics are uniform. We have monitored the gain with LED in this time, but it is possible to monitor the gain with the noise distribution taken by self-trigger (In that case the construction of calibration system will be simpler).

For method B, we need to assure the stability of LED light intensity and distribute the light from LED to MPPCs.

### 9.5.10 Summary and prospects

We have shown that the basic performance of the MPPC is promising and actually already satisfactory for use in T2K:

- Gain of  $10^6$  is achieved with noise rate less than 1 MHz with 0.5p.e. threshold.
- Photon detection efficiency for green light is about twice than that of a photomultiplier tube.

Calibration method	MPPC1(100)	MPPC2(100)	MPPC3(400)	MPPC4(400)
Method A	2.5%	2.3%	3.8%	3.1%
Method B	2.5%	1.3%	2.4%	1.4%

Table 9.3: Calibration precision for each device in RMS/mean.

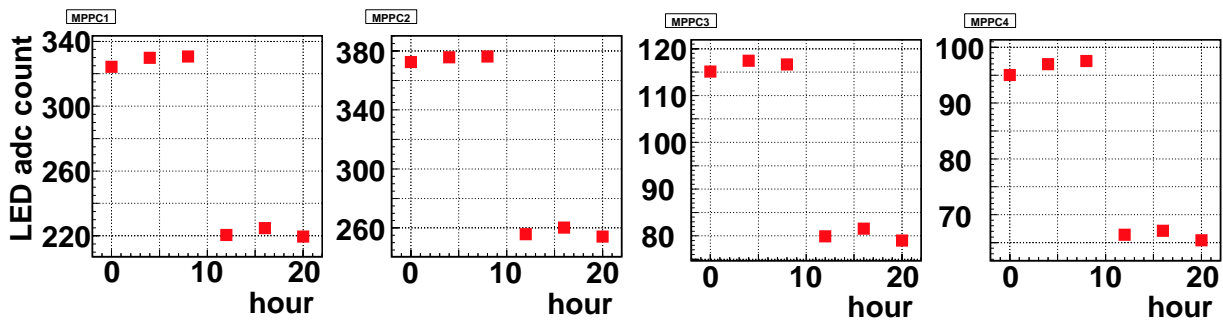


Figure 9.37: Variation of the ADC counts for LED. Left (right) two figures correspond to 100(400) pixel devices.

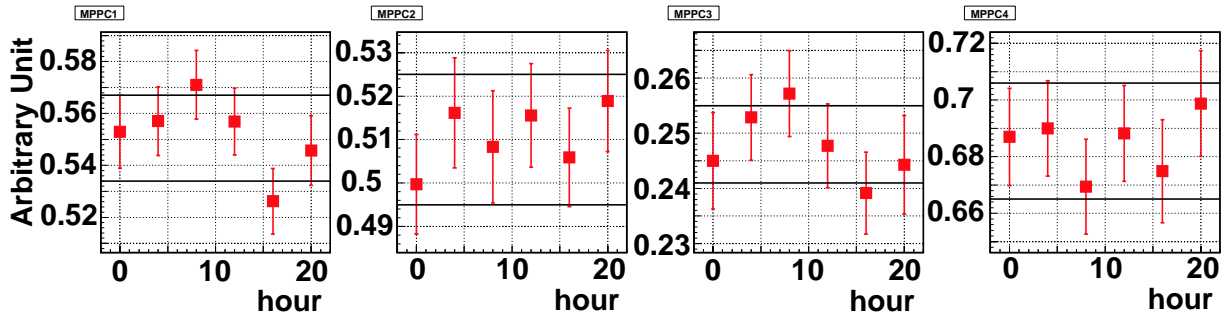


Figure 9.38: Variation of corrected light yield calculated from the variation of ADC counts for MIP and ADC counts for LED. Left (right) two figures correspond to 100(400) pixel devices.

- Cross-talk probability is less than 30%.
- Nonlinearity is about 15% at 50 (200) injected photoelectrons for a 100 (400) pixel device.
- Recovery time is  $< 120$  ns.

However, the number of tested sample is limited. In order to understand device by device dependence in the mass production, we are going to test  $\sim 1000$  of samples in JFY 2006. In the same time, we are developing a package and optical connector to avoid loss of light at the connection to WLS fibers.

The mass production of MPPC is expected to start in the middle of 2007. The delivery rate will be limited by the complexity of the test procedure we request, which will be developed after the test of large number of samples mentioned above. However, past experience with the manufacturer indicates there would be little concern about delivery rate and quality of the device.

## 9.6 Summary of device performance

Figure 9.4 summarizes the typical performance of MRS-APD and MPPC at dark noise rate of about 1 MHz and room temperature. While there is difference in some of parameters, both devices satisfy requirements from detectors. Although efforts to improve device performance will continue for some time, they are considered to be close to production prototype. Based on the results of tests presented in this document, we believe the parameters of currently available devices already satisfy our requirements. and we do not consider a fallback option for photo-sensor. As noted earlier, the choice of photodetector between MRS-APD and MPPC is subject to decision by each sub-detector group.

Table 9.4: Summary of MRS-APD and MPPC parameters at dark noise rate of about 1 MHz and room temperature.

Item	MRS-APD	MPPC
Number of pixels	556	400
Sensitive area (mm <sup>2</sup> )	1.1	1.0
Gain (10 <sup>6</sup> )	0.5 - 0.7	1
PDE for green light (%)	>12	>15
Cross-talk rate (%)	8	20
Recovery time	~5μsec	<120 ns

# Bibliography

- [1] G. Bondarenko *et al.*, Nucl. Phys. Proc. Suppl., **61B** (1998) 347.
- [2] A. Akindinov *et al.*, Nucl. Instr. Meth. **A494** (2002) 474.
- [3] G. Bondarenko *et al.*, Nucl. Instr. Meth. **A442** (2000) 187.
- [4] V. Golovin, V.Saveliev, Nucl. Instr. Meth. **A518** (2004) 560.
- [5] M. Yokoyama *et al.*, arXiv:physics/0605241.
- [6] M. Taguchi *et al.*, “Development of multi-pixel photon counters,” available online from <http://www-he.scphys.kyoto-u.ac.jp/member/mtaguchi/MPPC/note.pdf>
- [7] O. Mineev *et al.*, arXiv:physics/0606037.
- [8] E. Gushchin *et al.*, Nucl. Instr. Meth. **A567** (2006) 250.
- [9] A. Lacaita *et al.*, Nucl. Instr. Meth. **A326** (1993) 290.
- [10] H. Kressel, Semiconductor devices for optical communication, Topics in applied physics vol.39, Springer (1982).

# Chapter 10

## POD/ECAL/SMRD/INGRID Electronics

### 10.1 Introduction

The electronics for the scintillator detectors has several functions:

- Receive signals from photosensors
- Digitise and (zero) suppress the data from the photosensor
- Assemble the scintillator data and transmit it to the DAQ system
- Generate and transmit cosmic triggers

It also controls the voltage of the photosensors and monitors the basic performance of all detectors. It obviously has to ensure that all the data during the  $5 \mu s$  neutrino spills is collected, but it should also be sensitive to through-going and stopping cosmic muon interactions out of spill.

The main features governing the design of the electronics are the following:

- Photosensor gain larger than  $5 \times 10^5$  per photon electron (PE)
- 1-500 PE dynamic range
- 0.1 MHz photosensor dark noise rate at 1.5 PE thresholds
- Spill structure
  - 0.3 -0.5 Hz
  - 15 bunches (length 60 ns, separated by around 280 ns)

There are around 70k channels to be read out (see table 10.1 for details).

The requirements for the all different scintillator detectors are quite similar and the most cost effective choice is to use an identical electronics/DAQ system for all of them. This will also make the design, production, commissioning and maintenance of the system much easier and cheaper. We will therefore build the functionally identical electronics for all the scintillator detectors as described below.

detector	granularity	channels/unit	channels
ECAL			22k
POD	60 planes	320	11k
SMRD	160 towers	48	8k
INGRID	16 modules	560	9k
total			50k

Table 10.1: Channel count for the scintillator detectors.

## 10.2 Electronics design and specification

We have designed this electronics around an existing ASIC, which was developed by Fermilab to be used with VLPCs in DO. The MINERVA experiment[1] is also using this ASIC to read out MA-PMTs. Using this TRIP-t ASIC significantly reduces the cost, risk and development cycle. An overview of the proposed electronics is illustrated in Fig. 10.1.

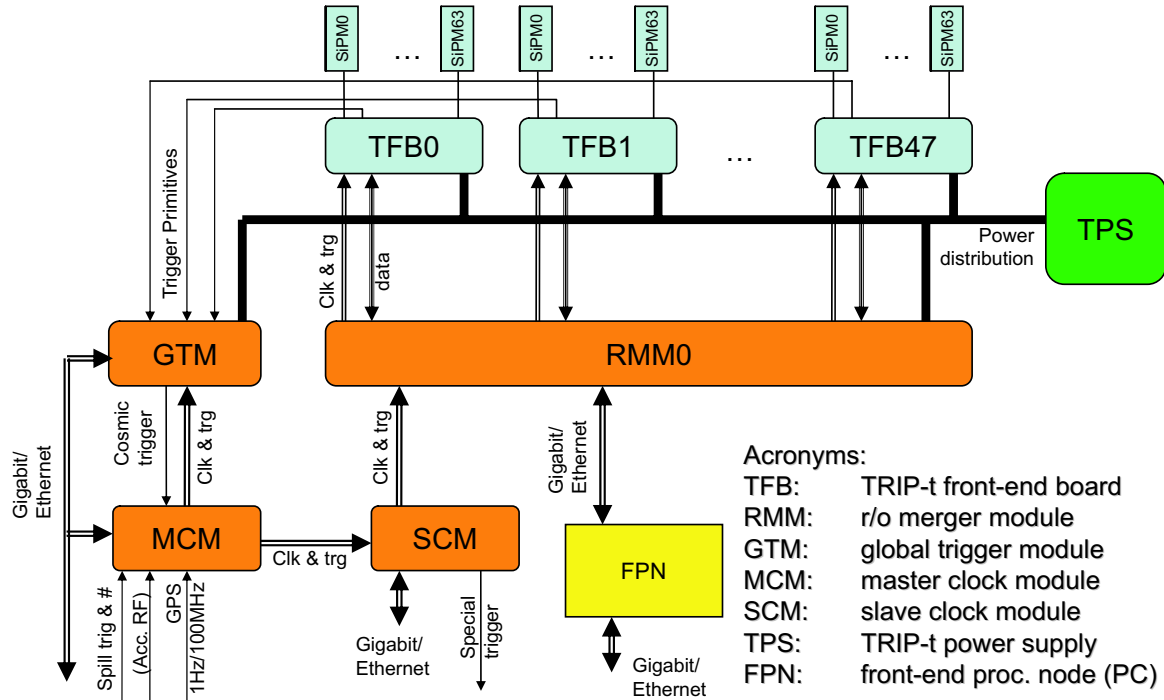


Figure 10.1: Schematic overview of the scintillator electronics

### 10.2.1 TRIP-t ASIC

The TRIP-t ASIC is a 32 channel device that integrates and stores signals in a 48 channel deep analogue pipeline. Due to technical reasons, we will use 23 out of the 48 slices well in excess of the number of bunches in the T2K spill. Simplified schematics taken from [2] can be seen in Figs. 10.2 and 10.3. Each channel has its own discriminator (with a global programmable threshold), but only the outputs from 16 channels (in parallel) can be selected for output at any one time. More details can be found in [2].

The gain of the TRIP-t ASIC is programmable, but the large range of photosensor input signals (up to 500 PE) cannot be accommodated while simultaneously allowing a discriminator threshold of 1.5 PE. to be set with precision. We therefore intend to capacitively divide the photosensor signals into low and high gain paths, using two TRIP-t channels per photosensor. The discriminator setting will apply to the 16 high gain channels, and the discriminator outputs of these will be the ones selected for output, and from which the precision time-stamps for the hits will be derived.

During the T2K spill period the TRIP-t preamplifiers are cycled between the integration and reset phases. At the end of each integration phase the integrated charge in all preamplifiers is stored in one of the pipeline time-slices, before the preamplifiers are reset. This operation will be synchronised to the accelerator clock which runs at approximately 3 MHz.

The TRIP-t ASIC also has a charge injection circuitry included. This will be used as a relative gain and linearity calibration for the different channels.

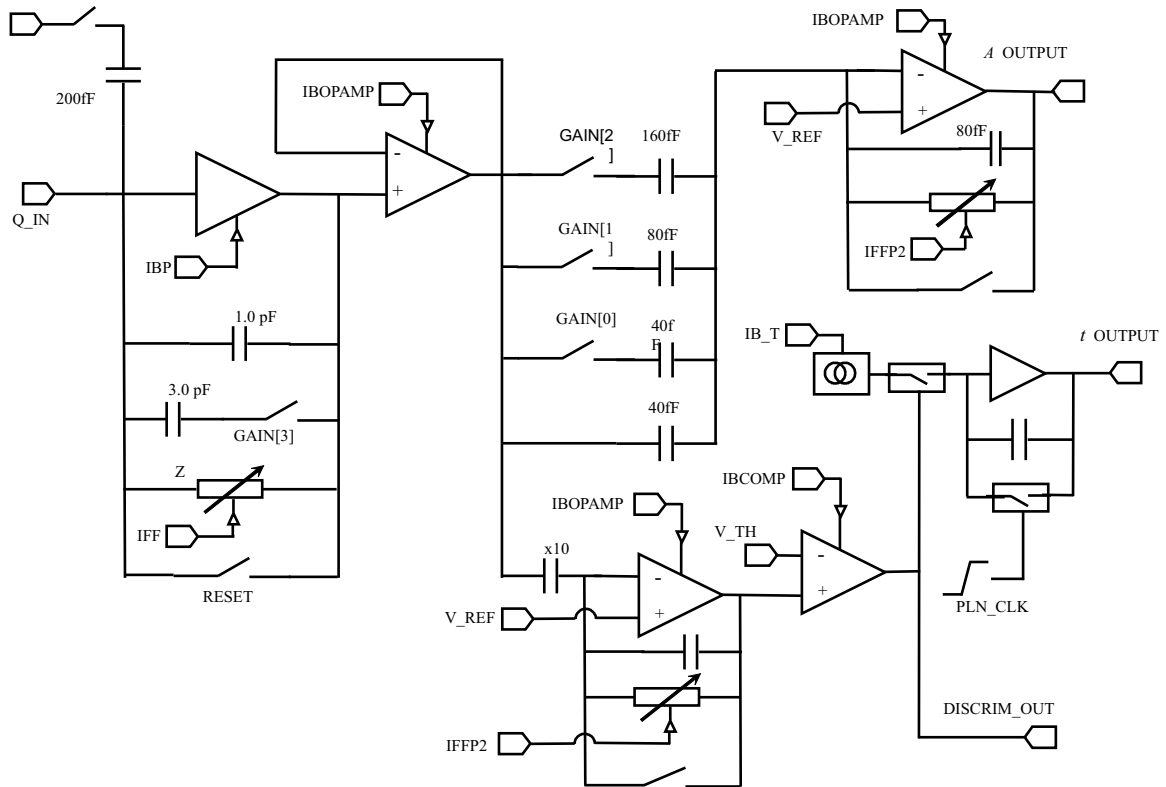


Figure 10.2: Schematics of the front end of the TRIP-t ASIC

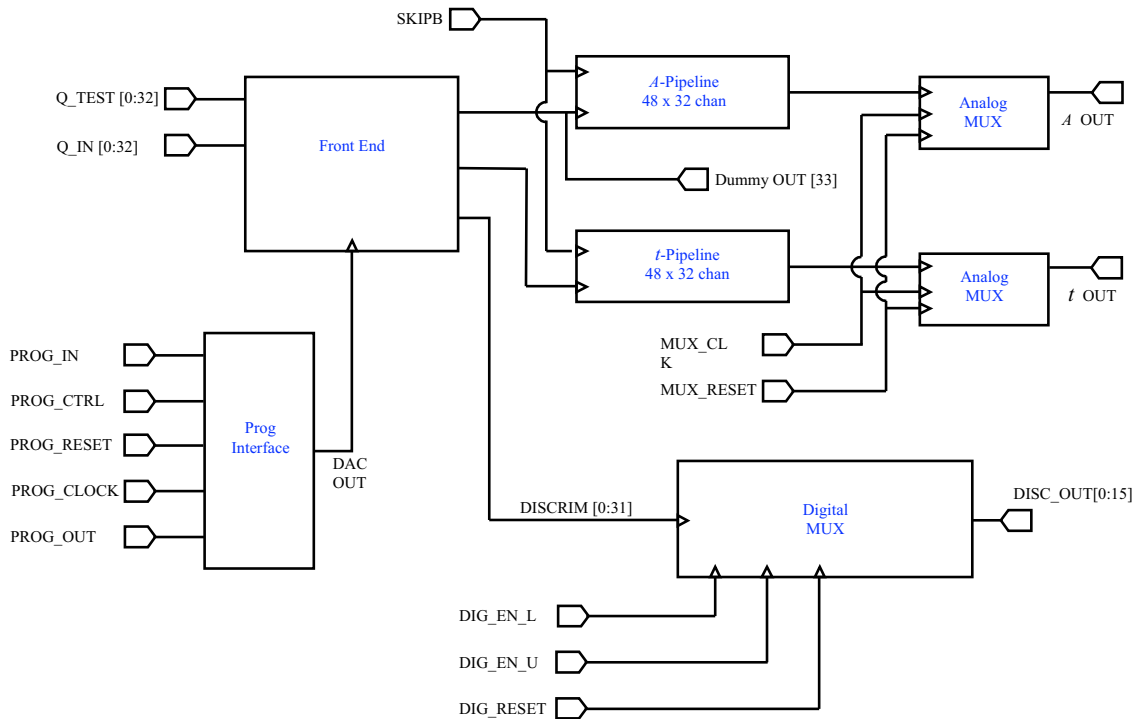


Figure 10.3: Block diagram of the basic functions of the TRIP-t ASIC

## 10.2.2 TRIP-t Front-end Board (TFB)

A total of 4 TRIP-t ASICs will be mounted on each front-end board. The TFB will thus read out 64 photosensors. We envisage that the photosensors will be connected with short (either miniature coax or twisted pair) cables to the TFB; this allows the maximum flexibility in connecting the scintillator/photosensors to the electronics. The maximum allowed cable length will depend on the readout chain noise, which depends on the final photosensor gain and cable capacitance. Preliminary studies indicate coaxial cable lengths of up to 200 cm are tolerable. A schematics of the cabling scheme can be found in Fig. 10.4.

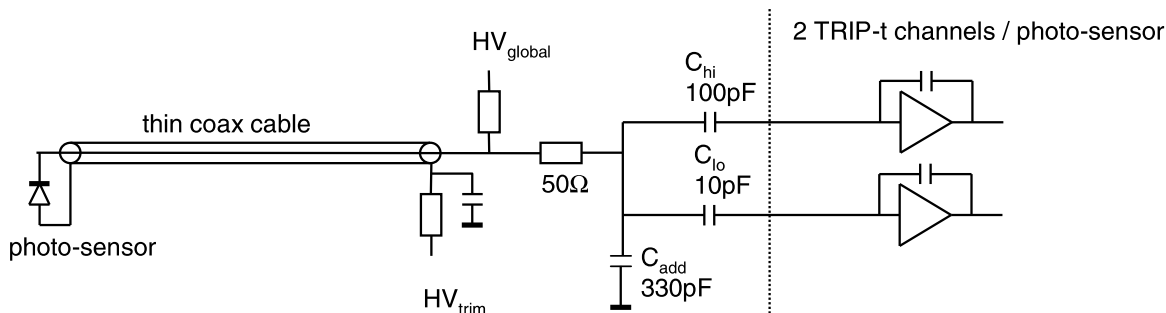


Figure 10.4: Cabling schematics for the photo-sensor TRIP-t connection. The photo-sensor is connected with a long thin coax cable to the TFB. The global HC is supplied via the signal pass to the sensor. An individual HV trim is achieved by changing the ground potential via a 5V DAC.

The TRIP-t chips are controlled by a Field Programmable Gate Array (FPGA), which runs at a centrally synchronised 100 MHz clock. It will also receive a pulse-per-second signal to reset its internal clock counters, a signal synchronised to the accelerator clock and an external trigger signal.

Using its internal clock managers, the FPGA will be able to time stamp all TRIP-t discriminator signals with a 2.5 ns resolution (least significant bit). It will also control the TRIP-t to integrate the photosensor signals. At the end of the spill, the analogue pipeline is stopped and all integrated charges in the analogue pipeline will be multiplexed to a 10 bit ADC. All the charges and discriminator timestamps will be stored and sent to the Readout Merger Module (RMM, see below). We foresee that all charges, independent of the discriminator signal, will be histogrammed in the downstream DAQ. This data can be used to study the photosensor dark spectrum and to monitor the photosensor and electronics gain.

The TFB has two other main functions. It will provide the bias voltages for the photosensors and generate trigger primitives for a cosmic trigger.

The HV for the photosensors will be somewhere between 25 and 70 V, depending on the device chosen. However, individual devices will have slightly different gains, which can be equalised by individually adjusting the HV of that channel. The TFB will distribute the HV from an external power supply to all the channels. The HV will be adjusted by floating the photosensor ground to a potential set by individual 5V DAC channels.

The TFB can also be used to generate triggers primitives. However, we only foresee this function to be used in the TFBs connected to the SMRD. Each SMRD will read out one tower in the SMRD. By looking for patterns in the discriminated photosensor signals one can determine whether there was a track or track segment in each of the towers. This information can easily be used to determine whether a cosmic muon traversed the detector, as the towers cylindrically surround the entire detector. The FPGA would look for these patterns and transmit a signal on a separate LVDS link to the Global Trigger Module (GTM, see below) to indicate whether there was a track segment in a tower. These trigger primitives will be used to calculate a global trigger decision.

### **10.2.3 Readout Merger Module (RMM)**

The RMM controls the TFB. It will transmit, set-up and run specific parameters to the TFB and will also be able to re-program the firmware of the TFB FPGA. It receives the timing and trigger signal from the Master Clock Module (MCM, see below) and redistributes these signals to the TFB. After each trigger the TFB will send its data to the RMM. The RMM will collect the data from up to 48 TFBs and send them to the DAQ via a commercial optical Gigabit/Ethernet link. The RMM is not much more than a massive I/O module, which is implemented with a high end FPGA. It will have 48 times 4 LVDS links to the TFB and two high speed optical links, one for data transfer to a DAQ PC and another to receive the clock and trigger signals. Control of the RMM and TFB will be via the Gigabit/Ethernet interface on the RMM.

### **10.2.4 TRIP-t Power Supply (TPS)**

The final design of the power distribution system is currently under review. We will use commercial units. Powersupplies (from Wiener and Lambda are well suited for our application. Due to space constraints it is unpractical to supply each TFB with its individual power line. The power shall therefore be fed via a multi-core power-bus to the different detector components. Special care will be taken to avoid ground loops and minimise the total cabling. The power consumption of the TFB totals 17 W (35 W Including cable losses and TPS inefficiencies).

### **10.2.5 Timing and Trigger System**

The timing and trigger system for the detector consists of several functionally different modules. However, the hardware of those modules is largely identical to the RMM, with the only modification being the I/O connectors. All timing modules will have an Ethernet connection and will be controlled and programmed via the network.

#### **Global Trigger Module (GTM)**

The GTM will receive the trigger primitives from all SMRD TFBs modulated on a 100 MHz LVDS link (see above). It will look for coincidences between different SMRD towers and generate a cosmic trigger decision. As this system is implemented in an FPGA it is quite flexible and trigger conditions and pre-scaling factors can easily be changed. The trigger will be transmitted to the MCM, which will encode it and fan it out to the SCM.

#### **Master Clock Module (MCM)**

The Master Clock Module (MCM) is the heart of the system. It will receive, via an optical link, a 1 Hz and a 100 MHz signal from the GPS system, which is located up-stream close to the beam monitoring hardware. It will also receive a spill counter and real time spill signal from the accelerator via optical links. It will also receive triggers generated by the GTM. It will arbitrate between the cosmic and spill triggers and might also generate calibration triggers.

The 100 MHz, 1 Hz, spill counter and trigger signals are encode onto an optical link operating at 1 GHz, which is fanned out to all Slave Clock Modules and the FGD and TPC electronics. This scheme ensures that the entire readout is synchronised to each other. The same timing signals will also be sent to the GTM. There will be two independent MCM, one for the INGRID and one for the off-axis detector.

#### **Slave Clock Module (SCM)**

There will be three SCM in the off-axis detector, one for each subdetector (SMRD/POD/ECAL). The SCM has two functions. In a global run it will take the signals from the MCM and fan them

	milestone	date
1.	BEB and TFB prototype ready	12/06
2.	1st vertical slice finished	06/07
3.	Start BEB production	06/07
4.	Finished BEB production	12/07
5.	2nd vertical slice finished	06/08
6.	Start of TFB production	10/08
7.	Finished TFB production	10/09
8.	Finished TFB testing	12/09
9.	Electronics commissioned	09/10

Table 10.2: Electronics construction milestones

out to the RMMs of its sub-detector. Its function is entirely passive in this mode. However, it is possible for the SCM to locally generate all timing signal and thus allow each sub-detector to run independently for commissioning and calibration purposes. No synchronisation to the GPS or beam will be possible in this mode. In this mode the SCM will also be able to generate additional signal to allow the triggering of external calibration equipment. The INGRID detector will not have a SCM as it is operated independently from the off-axis detector.

## 10.3 Construction Schedule

The construction schedule is summarised in table 10.2 and detailed in the following sub-sections.

### 10.3.1 TFB

The 1st TFB prototype is currently being build and tested (Nov 2006). Development of the required firmware is progressing in parallel. After testing the 1st prototype will be available for use in the vertical slice test at the end of 2006. After reviewing requirements, the final version of the TFB and its associated firmware will be developed during 2007, becoming available, after testing, at the end of 2007.

Preparations for the TFB volume production (any market survey/call for tender required) will be carried out during the second half of 2007, allowing a pre-production series to be launched early in 2008. Following acceptance tests the full production will commence July 2008.

A 12 month production period is foreseen, finishing June 2009. Detailed QA and burn-in testing will be performed, keeping pace with production.

Because of the relatively large numbers of TFBs involved the volume testing needs special consideration. It is envisaged that two systems will be required. One will be installed at the manufacturer (to be operated by them) to allow identification of faulty boards as soon as they come off the production line, localising faults to particular regions or components on the board. This allows rapid rework/repair giving high level of confidence that boards delivered to us will subsequently be fault free. We have used this approach successfully in a previous large-scale manufacturing task. The second system will be used in-house for the detailed production acceptance and TFB characterisation, QA and burn-in (prolonged operation under power) tests. This system would accept multiple boards to keep up with production. It is likely (and desirable) that the manufacturer's system would simply be a cut-down version of the in-house system (simplified operation, less detailed and hence quicker testing).

Preliminary planning for the production test systems will be undertaken in the last quarter of 2006. The detailed hardware, firmware and software developments required for the test systems will occur during a 12 month period beginning April 2007, to enable both systems to be in place before the TFB volume production begins in July 2008.

### **10.3.2 Back-end boards (BEB): RMM, GTM, SCM, MCM**

All the BEB are, as described earlier, variants of a single opto-electrical I/O board, which is controlled by a high-end FPGA. CCLRC/RAL has delivered similar boards for ATLAS and the requirements and methods employed are quite similar to those.

We will first use off-the-shelf development boards to develop the firmware for the RMM, GTM and MCM. By April 2007 we will be able to build a system to readout a sufficient number of TFBs to form a vertical slice test (see below). We will also produce a small simple PCB to adapt this development board connectors to the connectors that will be used in the final system. This work will be contracted out and is included in the equipment costs for this WP along with the development boards required.

The Lead Design Engineer will be responsible for all aspects of the project management, design, testing and commissioning of the system.

In the following year we will design and produce all the common BEB modules with the correct number of channels required for the system. There will be one FPGA based PCB design which has three functions in the system; RMM, GTM and MCM. Three separate sets of FPGA firmware will be required for this design.

The lead Design Engineer will be responsible for the Project Management, PCB design of the Common Module, production of the module as well as some aspects of the firmware design. The Firmware Design Engineer will be responsible for designing the initial versions of most of the FPGA firmware for all three versions of the firmware required to run on the module. The PCB Design Engineer will carry out the PCB design including any minor iteration. The Test Engineer will carry out JTAG and other post manufacturing testing of the Boards once they have returned from Manufacture.

The Lead Design Engineer and the Firmware Design Engineer will also cover aspects of the test software required for verification of the system.

From April 2008 we will carry out the main commissioning phase with the Design Engineer providing support for this process. This will include supporting installation, system tests and any Firmware improvements required. We expect most of this work to be finished by April 2009 and will finish the commissioning phase soon after ECAL installation.

### **10.3.3 TPS**

We will use a commercial power supply system (probably by Wiener) to provide power to the TFBs and BEBs. A total of 48 TFBs and 1 RMM will be supplied from a single unit. The high voltage for the photo detectors will be either supplied externally or generated on the TFB. This work will be done by the end of 2007. After sourcing and customising commercial power supplies in 2008, they will install and commission them during 2009/10.

### **10.3.4 Vertical Slice Test**

We plan that all the prototypes will be brought together for a first test at the end of 2006. This vertical slice will include photosensors, TFB prototype, RMM and MCM prototype, and the DAQ. It will verify the basic functions of the entire readout system as described in this proposal. We estimate that it will take 3 months to make all the systems work together.

This test will be repeated with the final TFB, photosensor and BEB before any large scale production of the TFBs.

## **10.4 Installation/commissioning**

The electronics forms an integral part of the different sub-detectors. Its installation is described in the relevant sections of the ECAL, POD, SMRD and INGRID.

# Bibliography

- [1] Minerva CDR at [http://minerva.fnal.gov/minerva\\_cdr.pdf](http://minerva.fnal.gov/minerva_cdr.pdf)
- [2] Details of the TRIP-t ASIC can be found at <https://plone4.fnal.gov/P1/AFEIIUpgrade/AFEIIProto/AFEIIdocs/>

# Chapter 11

## Data Acquisition

### 11.1 Introduction

The data acquisition (DAQ) system of the T2K 280m detector will be required to collect raw data from all subdetectors and log formatted event data to persistent storage media for later analysis. Provision of run control and interfaces to online monitoring and detector control systems to facilitate effective operation of the experiment will also be necessary. We propose to implement a scalable, flexible system that will realise these needs. The same DAQ architecture will be used for the on-axis (INGRID) detector, which will be handled by a second installation of the DAQ, independently of the off-axis detector.

#### 11.1.1 DAQ System Requirements

The proposed readout electronics for the scintillator-based detectors, as described in Chapter [Electronics], present data from those detectors on a Gigabit Ethernet physical layer. The TPC and FGD readout systems also implement this interface; it is therefore a natural requirement that the DAQ system be able to make use of Gigabit Ethernet as the primary medium for data transfer.

The detailed requirements for the specific functionality that the DAQ will be required to provide will necessarily be developed during the initial phase of the project. However, there are a number of general requirements for the system:

- Interface to and acquire data from multiple subdetector systems
- Support a sustained data transfer and logging rate consistent with the scientific demands of the experiment
- De-randomise, build and format full event data for logging to persistent storage
- Allow sufficient operational flexibility such that subdetectors can be included and excluded from data-taking on a run by run basis
- Support the ability to readily implement local DAQ instances to support standalone debugging and commissioning of various subdetectors and subsystems
- Provide a high-level user interface to allow data-taking operation of the experiment
- Implement an interface to the detector control system to allow slow control and monitoring of the sensors and front-end electronics
- Provide an interface and access to data for online processes, such as online monitoring, to allow the quality of the data being obtained from the experiment to be monitored in near-real time.

The exact data transfer rate that the DAQ system will be required to support is highly dependent on a number of factors: the noise rate of the sensor finally selected for the scintillator-based detectors; the cosmic event triggering scheme implemented in the front-end electronics; and the cosmic trigger rate required to generate sufficient data to calibrate the detector in a timely fashion. The dominant contribution to the data rate from these detectors will arise from uncorrelated noise hits below approximately 1.5 photo-electrons present in cosmic triggers.

### Triggering and Data Transfer Rates

Triggering is performed in hardware as described in the Electronics and Timing System chapter. In brief, trigger signals generated from accelerator beam spill signals, cosmic ray coincidences formed by trigger cards on the SMRD electronics, or self generated triggers for special calibration runs such as charge injection, are distributed to all electronics boards by the timing system. These initiate a fixed but configurable length electronics integration gate to digitize the detector activity. In addition the timing system distributes a trigger type, a trigger counter and a spill counter which is attached to the data in the front end.

For physics running, the DAQ will log all spill triggers, cosmic ray triggers and provide sufficient singles data for calibration and monitoring of the photo-sensor gains. In estimating the maximum data transfer rates, we assume the following. The beam spill is  $5.17\mu\text{s}$  long with a repetition rate of 3.53s, representing a spill-trigger rate of  $\sim 0.3$  Hz. To provide sensitivity to decay electrons and background sampling near the spill, the DAQ will read out all detector activity from  $1\mu\text{s}$  before the spill to  $\sim 10\mu\text{s}$  after the spill. Since the electronics has a 300ns integration time and a maximum pipeline depth of 48 gates, the total readout window for spills will be just under  $15\mu\text{s}$  in length. Cosmic ray triggers will be generated at a rate of 20Hz, the maximum capability of the TPC, and the readout window will be  $1\mu\text{s}$  in length. A worst case scenario of 1 MHz noise rate per photo-sensor is assumed. Using a readout size of 8 bytes per hit, this generates a total raw data rate of 9.5 MB/s from the off-axis scintillator detectors and 1.5 MB/s from the on-axis INGRID, as shown in table 11.1. The contribution

Sub-detector	Nr channels	Spill Trigger (kHz)	Cosmic Trigger (kHz)	Total MB/s
ECAL	22764	102	455	4.25
POD	11000	50	220	2.06
FGD	8448	38	169	1.6
SMRD	8600	39	172	1.6
ND280m	50812	229	1016	9.5
INGRID	7840	35	157	1.5

Table 11.1: Raw data rates from worst-case noise in the scintillator detectors. This dominates any contribution from beam or cosmic ray events

from physics to these raw rates (a few thousand hits per trigger) is a few 100 kB/s which is small in comparison. Triggering the TPC at this rate generates an additional 2 MB/s (see the TPC chapter).

Assuming that no subsequent filtering or reduction (e.g. higher level triggering) is applied to the data, this would lead to a total logged data rate of 11.5 MB/s from the off-axis detector. This is well within the ability of a system based upon Gigabit Ethernet and modern commodity computers, which could log data to persistent storage at a rate of several tens of megabytes per second. However, this would place an unacceptable burden on the computing infrastructure required for the experiment. The DAQ system will therefore be required to implement some form of data processing and reduction to reduce the rate generated by the scintillator-based subdetectors. This is performed in the front end processor nodes as described below. The flexibility to acquire and store the “raw” data from the subdetectors to allow for commissioning, monitoring and diagnostics will of course be preserved, albeit at a reduced rate.

In addition, the DAQ will be required to perform special calibration runs, such as charge injection, HV and threshold scans, for the configuration and calibration of the electronics and photosensors, and (should such a system be implemented on the detector) light injection runs for detector debugging. The mode of operation and requirements for such runs are not yet fully established, though the raw data rates are configurable via both direct control (e.g. LI flashing) and partitioning of the detector.

### 11.1.2 The Proposed DAQ Implementation

In order to minimise the cost, effort and risk associated with this work package, it is proposed to base the system on an existing DAQ software framework. There are a number of these freely-available, which have been successfully deployed on a range of small and medium scale high energy and nuclear physics experiments and are supported by their authors and the community at large. The currently favoured choice is MIDAS (<http://midas.psi.ch/>), which is used extensively at a number of laboratories around the world. However, a final decision will be made on the basis of a careful evaluation of the possibilities once the detailed requirements for the DAQ system have been established.

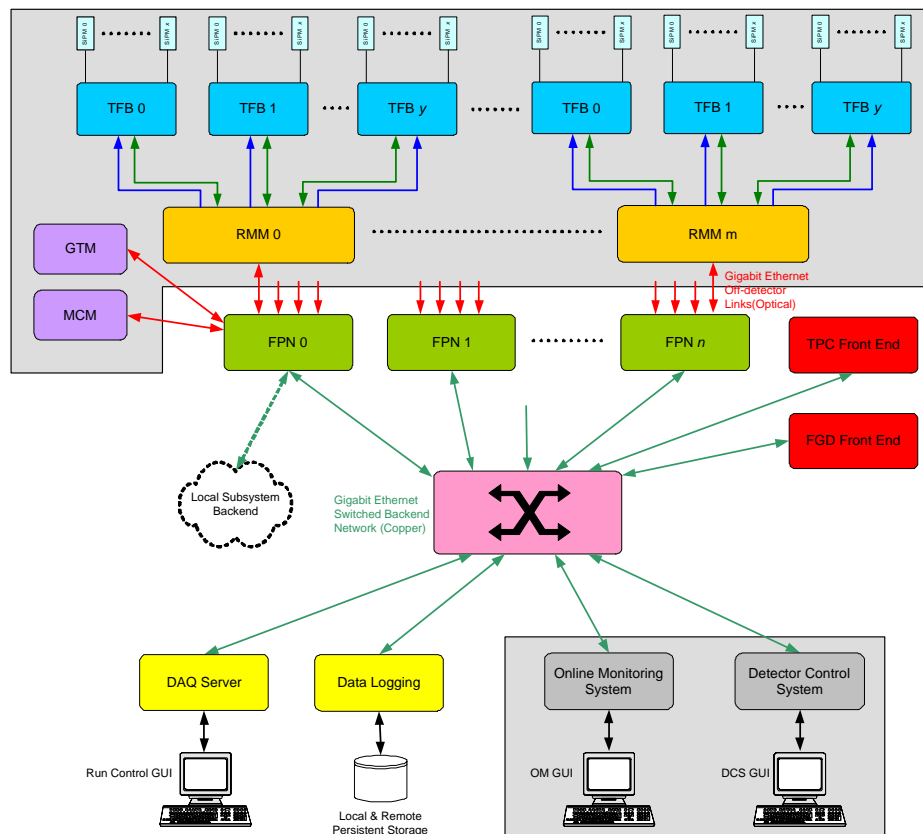


Figure 11.1: Conceptual design of the data acquisition system, showing its relationship to the front-end electronics of all subdetectors and the detector control and online monitoring systems. The IN-GRID system will be identical, though without the TPC and FGD components. The acronyms are explained in the text.

Fig. 11.1 shows the current conceptual design for the DAQ system and its relationship to the front-end electronics and other online systems, such as detector control and online monitoring. The interfacing to the front-end electronics for the scintillator-based subdetectors, as described in the electronics chapter, will be developed within this work package. The interface to the TPC electronics will be provided by the TPC group which will integrate its data at the gigabit switch prior to event building in the DAQ. The FGD, which will use different electronics to the other scintillator detectors, will likewise present its data to the DAQ. The use of a common software framework, with an existing,

well-defined programming interface for integrating custom systems, provides a significant advantage here.

The architecture shown is driven by the considerations outlined above and the working assumption that the MIDAS framework will be employed. However, the basic components and functionality will remain largely unchanged should another framework be selected. The function of each component is described in the following sections.

### The Front-end Processing Node

The Front-end Processing Node (FPN) is responsible for receiving raw data streamed over optical Gigabit Ethernet links from the Readout Merger Modules (RMMs) of the scintillator subdetector front-end electronics. The FPN will conform to the application programming interface (API) supported by the streaming firmware present on the RMMs and will provide the primary interface to the functionality of the front-end electronics. The FPN will consist of a commercially available PC running the GNU/Linux operating system, offering an excellent price-to-performance ratio. Fig. 11.2 shows the functional blocks implemented in the FPN.

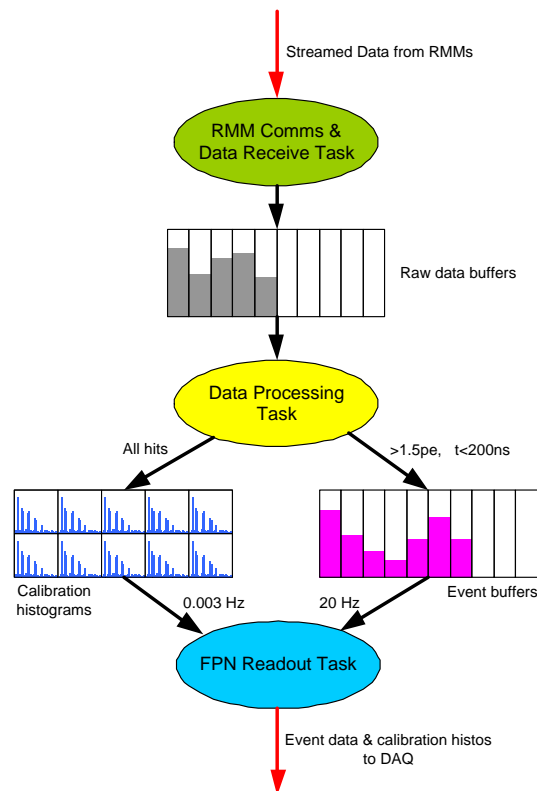


Figure 11.2: A schematic representation of the functionality of the DAQ Front-end Processing Node (FPN).

Using the cosmic readout and triggering scheme described earlier at a trigger rate of 20 Hz, the per-link rate is approximately 600 kB/s. It is anticipated that a two-to-one multiplexing of the RMM links into each FPN can be achieved, yielding a total of 15 FPNs required. In order to substantially reduce the data logging rate, the FPN will perform histogramming of data for calibration purposes. All hits from cosmic triggers will be histogrammed on a channel-by-channel basis in local memory. The histograms will then be inserted into the data stream for readout and storage at a significantly lower rate, for instance once every few minutes. This rate can be flexibly tuned to optimise data storage constraints against the calibration requirements for the detector. The local processing and storage requirements (a few MB per FPN) are not significant.

In order to match the event output for cosmic ray events to the offline needs, a programmable threshold will be applied to all hits read out for these triggers, for example passing only hits above 1.5 photo-electrons. In order to further tighten the selection of hits associated with cosmics triggers, which will have a well-known timing, a simple time cut (e.g. all hits within 200 ns of the trigger) could readily be applied. Note that the processing applied here is on a trivial, hit-by-hit basis and does not require any reconstruction of event topology. All hits passing these cuts will be written to buffers for subsequent readout by the DAQ backend. This will reduce the raw data rate to less than 1-2 MB/s. Hits from triggers associated with the 0.3 Hz beam spill rate could be buffered for readout with or without such cuts being applied, according to need.

### **The Back-end Network**

The FPNs communicate with the downstream components of the DAQ via the back-end network. Given the modest data rates expected in the scheme proposed here, this network will consist of a single, commercially-available Gigabit Ethernet network switch. Additional capacity and flexibility could however be readily achieved adding further switches if required.

The backend network provides the physical interface between the DAQ and the TPC and FGD subsystems. These also implement a Gigabit Ethernet interface and will participate in the DAQ on an equal basis with the other subsystems.

### **The Data Logging Node**

This component is responsible for collecting the full data streams from all front-end subsystems, assembling them into full events and logging them to persistent storage. Event building utilises information tagged to the readout in the front end electronics and is a relatively straight forward task. Each front end component attaches the following to the readout from each trigger:

- Trigger Counter
- Trigger Type
- Spill Counter, if appropriate
- GPS Time Stamp

The information is distributed across the detectors by the timing system as part of the trigger distribution scheme, as described in the electronics chapter, which ensures synchronous triggering and common trigger tagging. The DAQ will use the trigger counter and the GPS timestamps to match data from the different detector components and build events. The redundancy offered by these two sources provides valuable integrity checks. There will be sufficient buffering within the node to accommodate any latency differences between the sub-detectors. A likely scenario for providing a robust data logging scheme is for this node to write data files to local disk. These are then copied to the ultimate destination (e.g. a tape robot at a remote laboratory) by an archival task that runs asynchronously from the DAQ; this scheme provides a solution that is robust against external problems such as transient off-site network failures.

This node would again be implemented using a standard PC of similar specification to those used for the FPNs. The logging node could also provide other local storage media, such as high-capacity tape drives, according to the needs of the experiment.

### **The DAQ Server and Run Control**

The DAQ server controls the state and operating mode of the DAQ, coordinating data acquisition activities. The precise nature of the server and its realisation in software will be dependent on the

framework selected for the project. However, it will be required to provide a number of elements: maintain the global state machine representing the current state of data acquisition; control and store configuration data allowing components in the front-end systems and DAQ to be flexibly set-up and included or excluded from the data taking on demand; and a graphical user interface (GUI) to allow users to control the DAQ.

Since the facilities in proximity to the detector are limited, remote operation of the DAQ is foreseen as a requirement. A natural mechanism for delivering the run control interface is the World Wide Web; appropriate authentication mechanisms to prevent uncontrolled access to the system will be provided.

### **Local Subsystem Backends**

In order to provide flexibility for independent development, commissioning and debugging of detector subsystems, it is foreseen to provide the backend functionality of the DAQ on a local basis as necessary. Since the scope and performance requirements of these local systems is limited, the full backend could easily be provided by a single node. A number of the DAQ frameworks available allow for flexible configuration in this way.

Local DAQ systems will clearly be required during the development, testing, commissioning and integration of the various subdetectors and their electronics. Provision of support for the setup and initial use of such systems at other sites has been factored into the manpower resources provided by the DAQ work package. Any hardware over and above the experiments DAQ required for independent sub-detector development will be provided by the appropriate subdetector group.

### **Interface to the Detector Control Systems**

The Detector Control Systems are described elsewhere in this document. The DAQ will provide an interface to this system and will transmit control and monitoring data to and from the scintillator detector electronics on the DAQ network. This avoids the need for an additional network interface to the front end which greatly simplifies the overall design and robustness of the system. The interface will conform to the API of the software framework adopted (e.g. MIDAS).

### **Online Software**

Essential online processes, such as an online monitoring and event display, will utilise offline reconstruction and display software to minimise duplication of effort and ensure a consistent approach to data analysis. The DAQ will provide interfaces to these systems over which data may be accessed in close to real time via the software framework. The detailed nature of the interfaces will be determined as the designs of these systems evolve.

## **11.2 Inputs**

The DAQ package depends on inputs from a number of sources:

- Specification, design and delivery of the front-end electronics
- Physics studies and simulations for triggering and data requirements
- Calibration requirements for scintillator detectors
- Experimental facility and infrastructure design
- Experiment operational requirements

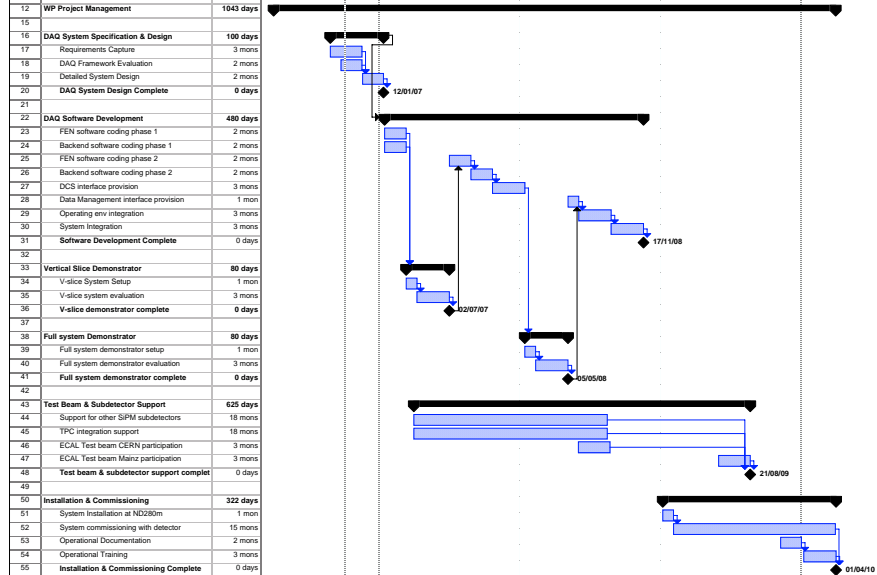


Figure 11.3: Schedule and main milestones for DAQ work package.

The structure and schedule for this work package has been defined to take into account these inputs. The objectives for this work package are broken down into a number of tasks, which are described below. The schedule for these tasks is shown as a Gantt chart in Fig. 11.3.

## 11.3 Objectives and Milestones

### 11.3.1 TASK I: DAQ System Specification and Design

The first task in this work package is to undertake the detailed specification and design of the DAQ system, which requires the following activities:

- Capture and develop the detailed requirements for the functionality and performance of the system, as determined by the scientific needs of the experiment.
- Evaluate possible DAQ software frameworks and select the most appropriate for the needs of T2K.
- Undertake the detailed design of the system based on the requirements and capabilities of the selected framework.
- Prepare a Technical Design Report describing the design and functionality of the system. This will be particularly important in order to ensure that all communication between the DAQ and other subsystems is appropriate and to agreed standard interfaces.

The milestone for completion falls in the fourth quarter of FY 2006/07.

### 11.3.2 TASK II: DAQ Software Development

This task encompasses the main software development effort for the DAQ system and includes the following items:

- Develop the FPN task software (including calibration processing) and interface to the DAQ framework. There will be several phases of development here as the various demonstrator systems, described below, are integrated with the front-end electronics and evaluated.

- Provide any customisation of the backend software. This will cover any additional functionality needed for the DAQ backend nodes (DAQ server, run control GUI, data logging node etc.) which may be required. Again, this will be phased around the demonstrator system tasks.
- Provide the Detector Control System interface. This will be developed according to the choice of implementation of that system. Since the DAQ provides the primary connection to the front-end electronics via the off-detector links, this interface will be used to control and monitor the electronics (bias voltages, temperatures, etc.).
- Integrate the DAQ into the experimental operating environment. This will include any work necessary to allow the DAQ to operate within the experimental computing infrastructure, for instance provision of data archiving scripts.
- Develop a fully integrated DAQ system. This covers the development and deployment of the software necessary to fully manage and operate the DAQ from a system perspective, including expert management scripts, software update tools etc.

The milestone for the completion of all DAQ software development falls during the third quarter of FY 2008/09.

### **11.3.3 TASK III: Vertical Slice Demonstrator**

The purpose of this task is to assemble and demonstrate a fully-working vertical slice of the photosensor, front-end electronics (or prototypes thereof) and data acquisition system and evaluate its performance. A period of system setup and debugging prior to system evaluation is scheduled.

The milestone for the successful demonstration and evaluation of a DAQ vertical slice is the end of the fourth quarter of FY 2006/07.

### **11.3.4 TASK IV: Full System Demonstrator**

The objective of this task is to demonstrate a full prototype DAQ system that incorporates sufficient elements of the final system to adequately characterise the likely final performance. Again, a period of system setup and debugging is scheduled prior to the full system evaluation.

The milestone for the demonstration of the full DAQ system is scheduled for the beginning of the first quarter of FY 2007/08.

### **11.3.5 TASK V: Test Beam and Subdetector Support**

This purpose of this task is to provide support for the use of the DAQ system during test beam campaigns. Since basic DAQ systems will be required during the commissioning of front-end electronics for other subdetectors, support for these activities is required also and will be provided by the sub-detector groups with assistance from the DAQ group. Finally, support for the integration of the TPC and FGD subsystems into the DAQ environment is foreseen.

The milestone for the completion of test beam and subdetector support task is the beginning of the second quarter of FY 2008/09.

### **11.3.6 TASK VI: Installation and Commissioning**

The objective of the final task is to install and commission the final DAQ system at the 280m site on both the off-axis and INGRID near detectors and cover the commissioning of the full detector prior to data taking with the neutrino beam. The initial installation is scheduled for January 2009, in conjunction with the installation of the INGRID and partially-completed off-axis detector. Commissioning will take place as the sub-detector front ends become available and will be complete in time for the

start of operations. As other sub detectors are installed (e.g. ECAL) they will be incorporated into the readout. It is planned to provide DAQ support throughout the period until the construction phase is completed.

## **11.4 Outputs**

The output from this work package is a functional, installed and commissioned data acquisition system for both the on and off-axis 280m detectors.

# Chapter 12

## Comissioning schedule + run plan

Figure 12.1 shows the current plan of ND280 detectors. The construction of the ND280 facility will start at the beginning of Apr. 2007. The pit excavation and the construction of the underground floors will be completed by Mar. 2008.

The magnet will be installed on the underground floor B1 before the ND280 building construction, which will start in July 2008 and will be finished in 2008. From Jan. 2009, we will install a part of detectors: N-GRID, tracker(TPC and FGD) and a part of SMRD, for commissioning with neutrino beams which will be delivered from Apr. 2009.

With this partial ND280, we can measure the neutrino beam direction by the on-axis neutrino monitor N-GRID to give important information for neutrino beam line operation, and also can perform measurement of  $\nu_\mu$  and  $\nu_e$  spectrum by the tracker via CCQE interactions.

Following the commissioning for three months with the partial ND280, we will install POD and remaining SMRD during a break in 2009 summer then will do data taking with the ND280(without ECAL). Finally we will install ECAL in Jan.2010 to complete ND280 and will be able to carry out measurement of  $\gamma$ 's and  $\pi^0$ 's with the expected ND280 performance for other reactions than CCQE, which enables us to aim the goal of T2K experiment.



# Chapter 13

## Reference

### 13.1 Neutrino experimental hall

The neutrino experimental hall is called the ND280 hall (the neutrino detector hall at 280m from the target point). The location of the ND280 hall is shown in Figure 13.1.

The ND280 hall is being designed as follows, which is drawn in Figure 13.2.

The ND280 hall has a pit with a diameter of 17.5m and a depth of about 34m, which incorporates both the on-axis detector (INGRID) and off-axis detectors. The B1 floor, which is about 23m deep, is for the off-axis detector. The off-axis detector is nearly located on the line between the target point and the SK position. The B2 floor, which is about 29m deep, is for the horizontal part of the on-axis detector. The B3 floor, which is about 34m deep, is for the deepest part of the vertical on-axis detector. The current nominal off-axis angle is 2.5 degrees and the on-axis beam line passes at about 1.5m above the B2 floor. This facility design can accommodate with the off-axis case of 2.0 ~ 2.5 degrees with the condition that the on-axis detector covers the  $\pm 4$ m area.

The hut with a size of about 21m  $\times$  37m covers the pit, and has a 10ton crane. The hut is a little bit shifted to the north with respect to the pit center in order to use the north area in the hut for the unloading of detector components and for the detector preparation (loading area). The effective height of the crane is 4m and its dead space is about 3m from the north and south walls and 2m from the east and west walls. The hut has an entrance shutter 5m wide and 3.9m high. There are a 6-people elevator and stairs. Some area in the hut at the ground floor is used for the electricity preparation and the cooling water preparation.

The construction of the ND280 hall and the installation of the detectors will be done in the following steps starting in Spring 2007.

1. The excavation of the pit.
2. The construction of the underground floors.
3. The installation of the magnet yokes and coils using external cranes.
4. The construction of the hut including the 10ton crane.
5. The installation of the on-axis detector.
6. The installation of the off-axis detector.

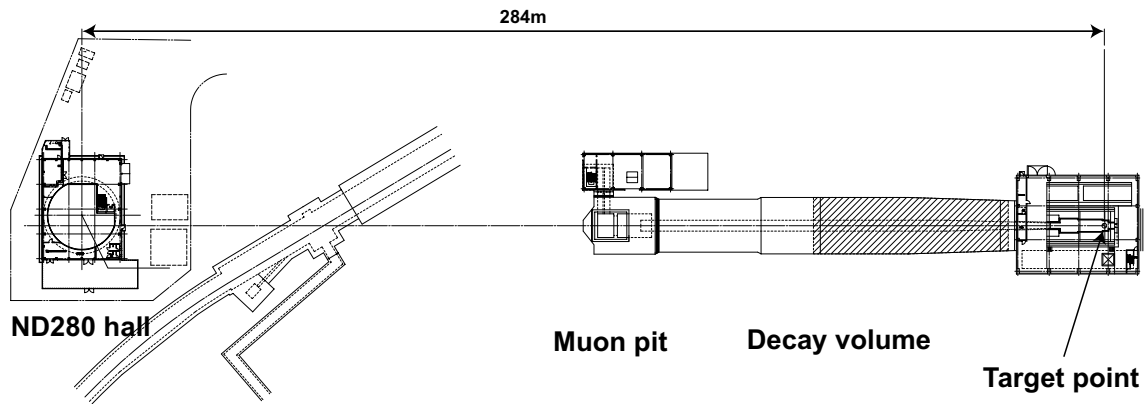


Figure 13.1: Location of the muon pit and the ND280 hall.

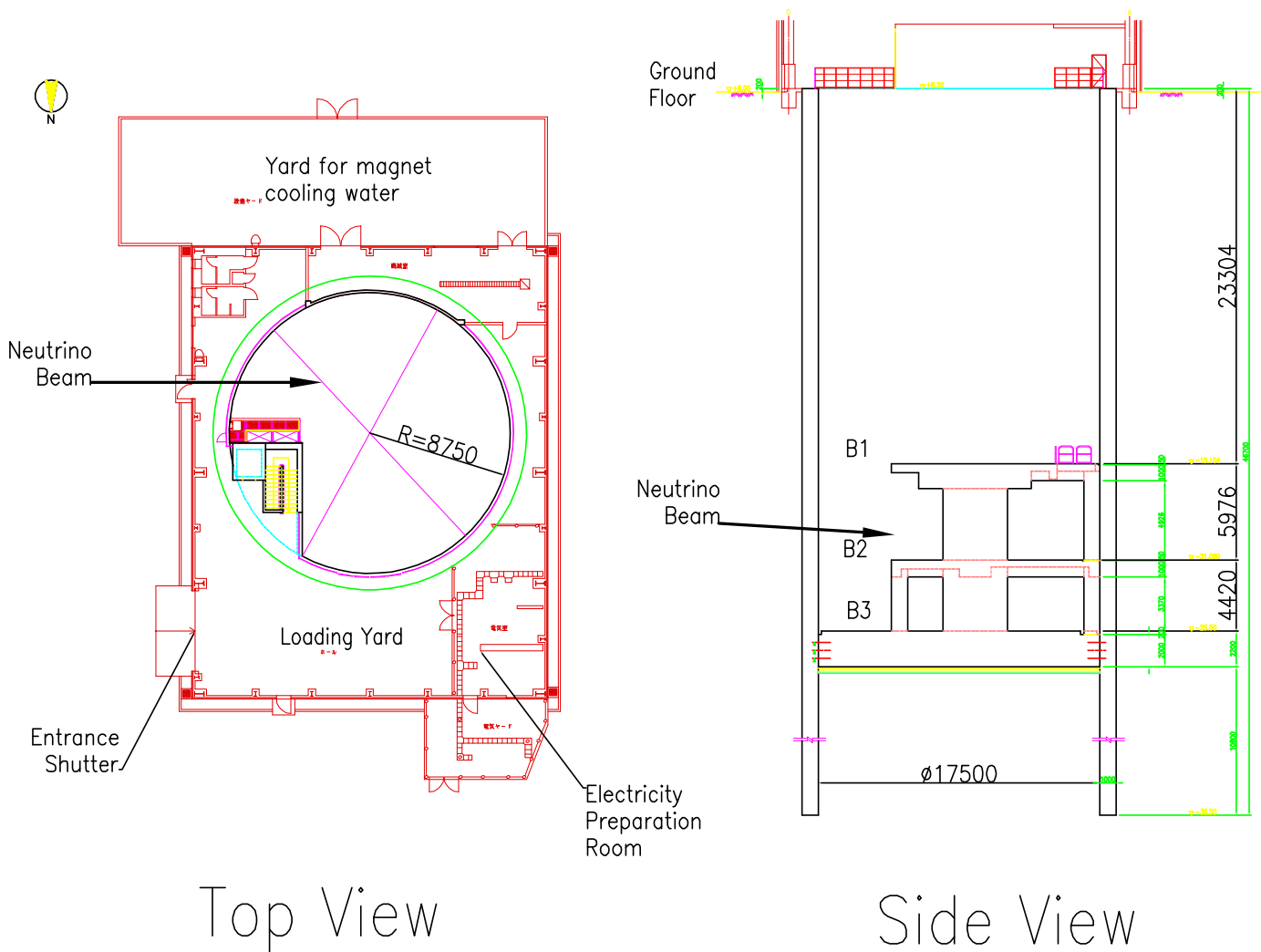


Figure 13.2: Current design of the ND280 hall.